Aims and Scope

The aim of the quarterly journal Archives of Thermodynamics (AoT) is to disseminate knowledge between scientists and engineers worldwide and to provide a forum for original research conducted in the field of thermodynamics, heat transfer, fluid flow, combustion and energy conversion in various aspects of thermal sciences, mechanical and power engineering. Besides original research papers, review articles are also welcome.

The journal scope of interest encompasses in particular, but is not limited to:

- Classical and extended non-equilibrium thermodynamics
- Thermodynamic analysis including exergy
- Thermodynamics of heating and cooling
- Thermodynamics of nuclear power generation
- Thermodynamics in defence engineering
- Advances in thermodynamics
- Experimental, theoretical and numerical heat transfer
- Thermal and energy system analysis
- Renewable energy sources including solar energy
- Secondary fuels and fuel conversion
- Heat and momentum transfer in multiphase flows
- Nanofluids
- Energy transition
- Advanced energy carriers
- Energy storage and efficiency
- Energy in buildings
- Hydrogen energy
- Combustion and emissions
- Turbomachinery
- Thermal and energy system analysis
- Integrated energy systems
- Distributed energy generation
- Thermal incineration of wastes
- Waste heat recovery.

Co-published by

Institute of Fluid Flow Machinery
Polish Academy of Sciences

Committee on Thermodynamics and Combustion
Polish Academy of Sciences

Editorial Office
IMP PAN Publishers
Institute of Fluid Flow Machinery, Fiszera 14, 80-231 Gdańsk, Poland,
Phone: (+48) 58-341-12-71 int. 230, e-mail: redakcja(at)imp.gda(.)pl
https://www.imp.gda.pl/archives-of-thermodynamics/
Journals PAS – Electronic Library Polish Academy of Sciences
https://journals.pan.pl/ather

Subscription outside Poland
From 2024, Archives of Thermodynamics appear only in electronic version as an open access journal. However, printed archive volumes or issues are still available. The price of a full volume outside Poland is **120 EUR**. The price of a single issue is **30 EUR**. Archived volumes or issues are available on request. Orders should be sent directly to IMP PAN Publishers:
Institute of Fluid-Flow Machinery,
Fiszera 14, 80-231 Gdansk, Poland,
e-mail: redakcja(at)imp.gda.pl or jfrk(at)imp.gda(.)pl or jrybka(at)imp.gda(.)pl.
Payments should be transferred to the bank account of IMP PAN:
IBAN 28 1130 1121 0006 5498 9520 0011 at Bank Gospodarstwa Krajowego; Code SWIFT: GOSKPLPW.

Prenumerata w Polsce
Od 2024, czasopismo ukazuje się tylko w formie elektronicznej otwartej. Osiągalne są jednak wydania papierowe archiwalne. Cena pojedynczego numeru wynosi **50 PLN**. Cena rocznika **200 PLN**. Zamówienia z określeniem numeru (rocznika), nazwiskiem i adresem odbiorcy należy kierować bezpośrednio do Wydawcy:
Instytut Maszyn Przepływowych PAN
ul. Fiszera 14, 80-231 Gdańsk,
e-mail: redakcja(at)imp.gda(.)pl lub jfrk(at)imp.gda(.)pl lub jrybka(at)imp.gda(.)pl.
Wpłaty prosimy kierować na konto Instytutu Maszyn Przepływowych PAN:
nr 28 1130 1121 0006 5498 9520 0011 w Banku Gospodarstwa Krajowego.

Articles in Archives of Thermodynamics are abstracted and indexed within:
Applied Mechanics Reviews • Arianta • Baidu Scholar • BazTech • Cabell's Directory • Celdes • Chemical Abstracts Service (CAS) – CAplus • CNKI Scholar (China National Knowledge Infrastucture) • CNPIEC • EBSCO (relevant databases) • EBSCO Discovery Service • Elsevier – SCOPUS • ESCI (Emerging Sources Citation Index) • Genamics JournalSeek • Google Scholar • Inspec • Index Copernicus • J-Gate • Journal TOCs • Naviga (Softweco) • Paperbase • Pirabase • POL-index • Polymer Library •Primo Central (ExLibris) • ProQuest (relevant databases) • ReadCube • Referativnyi Zhurnal (VINITI) • SCImago (SJR) • Summon (Serials Solutions/ProQuest) • TDOne (TDNet) • TEMA Technik und Management • Ulrich's Periodicals Directory/ulrichsweb • Web of Science • WorldCat (OCLC)

Contents

In memoriam: Professor Marian Trela (1941–2025), Deputy Editor-in-Chief of Archives of Thermodynamics (2006–2021)

Professor Marian Trela was born on 18.12.1941 in Książ Wielki, Poland. He graduated in 1965 from the Faculty of Machine Design of the Technical University of Gdańsk. Then he started working at the Institute of Fluid-Flow Machinery of the Polish Academy of Sciences in Gdańsk (IMP PAN), where he worked until 2015.

At the beginning of his scientific career, he dealt with problems of thermodynamic cycles, especially two-medium cycles with low-boiling agents in the low-temperature part of the cycle, encountering for the first time the problems of heat exchange and hydrodynamics of two-phase flows. He defended his doctoral thesis on the modelling of two-phase vapour-liquid flows at the Faculty of Shipbuilding of the Technical University of Gdańsk in 1972.

In the 1970s, he dealt with problems of heat exchange during steam condensation, heat exchange in fin-tube exchangers and during sudden expansion of water with high parameters. He was also concerned with coal liquefaction issues. At that time, while being on a research internship at the University of Kentucky, USA, he obtained interesting experimental results related to sudden expansion of hot water, among others the possibility of obtaining the so-called "negative pressures".

In the 1980s, he conducted research on problems of heat and mass transfer in two-phase mist flow. The Professor's original achievements in this area include the development of rational models of droplet separation and their effect on heat exchange. His scientific achievements in this area were honoured with an individual award from the Scientific Secretary of the Polish Academy of Sciences in 1982. He continued his work on these topics, covering issues related to the behaviour of the liquid phase on the channel wall in two-phase flow. The above topics gave rise to his doctoral (habilitation) thesis entitled "Thermo-hydrodynamic issues of the liquid phase on the wall in two-phase flow", which he defended at the Institute of Fluid-Flow Machinery of the Polish Academy of Sciences in Gdańsk in 1990.
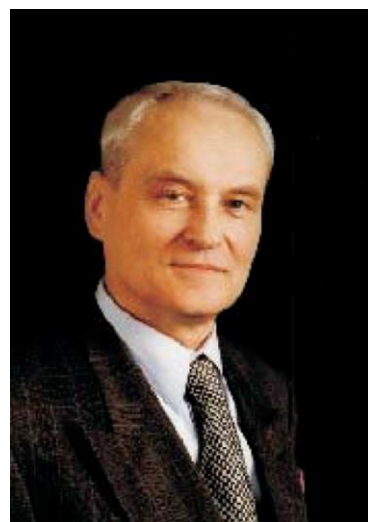
In the 1990s, Prof. M. Trela conducted research on: direct condensation on a cold liquid layer, steam condensation on densely ribbed pipes in condensate drainage conditions, the effect of surface contamination and the presence of air and steam velocity on steam condensation, the spread of free liquid jets on the surface of bodies of various geometry.

The summary of Prof. M. Trela's scientific achievements in the field of two-phase flows and heat exchange is the monographic book entitled "Motion and heat exchange of thin liquid layers" published in 1998 as volume 23 in the series "Fluid Flow Machinery", Ossolineum, Wrocław.

In 1999, he obtained the academic title of Professor of Technical Sciences.

In the years 2000 and 2010, Prof. M. Trela dealt with modelling physical phenomena in supercritical two-phase steam-water jets in conditions of strong thermal imbalance, and also with the effect of electric field on the condensation of vapours of dielectric media. In addition to the basic research, Prof. Marian

Trela was active in the field of applied research. He implemented his system for measuring and monitoring the amount of air in the condensers of large power plants.

Prof. M. Trela was Head of the Heat Exchange Department at IMP PAN in the years 1993−2012. In the years 2002−2012, he also served as Head of the Centre of Fluid Thermomechanics at IMP PAN. He was also a member of the Scientific Council of IMP PAN. He was appointed a member of the Committee of Thermodynamics and Combustion of the Polish Academy of Sciences, including its Thermodynamics Section, a member of the Multiphase Flows Subsection of the Committee of Mechanics of the Polish Academy of Sciences, and a member of the Section of Fundamentals of Machine Operation of the Committee of Machine Construction of the Polish Academy of Sciences.

Prof. M. Trela was the author of 2 dissertations, 3 monographs, and the author or co-author of approximately 200 articles and scientific papers published in journals and materials from national and international conferences. He also authored and co-authored of over 120 unpublished scientific research papers and expert opinions prepared for the industry.

He supervised 4 completed PhD theses. He also conducted didactic work at the University of Warmia and Mazury in Olsztyn and at the Higher School of Gdańsk (currently Academy of Finance and Business Vistula).

He was awarded Bronze and Gold Crosses of Merit. The Subsection of Multiphase Flows and Non-Newtonian Fluids of the Section of Fluid Mechanics of the Committee of Mechanics of the Polish Academy of Sciences awarded him a distinction in the form of the "Medal for outstanding achievements in the field of multiphase flows".

An outstanding scientist was associated with the journal Archives of Thermodynamics. His cooperation with the journal took various forms. He was the author or co-author of numerous articles published in the journal, the first of which was published very soon after the journal was founded, in 1990. Then, based on his thorough knowledge of the subject, he reviewed manuscripts submitted for publication. From 2006 to 2021, he served as Deputy Editor-in-Chief of the journal.

Professor Marian Trela passed away on 19.03.2025. He will forever remain in our memory as an outstanding specialist in the field of thermodynamics and fluid flow machinery. His openness, willingness to help other people and his respect for others made him not only an authority in his field, but also a true friend and mentor. His contribution to the development of science, his wisdom and kindness will inspire us for many years to come. He will forever remain in our grateful memory as a person with a big heart, a warm colleague and friend who, throughout his life, earned the respect of all who knew him.

AoT Editorial Board

Liquid crystal thermography supported by PIV and DII as modern and unique tools for technical and biomedical research and diagnosis – mini review

Jan A. Stąsiek, Michał E. Klugmann*, Dariusz P. Mikielewicz

Gdańsk University of Technology, Faculty of Mechanical Engineering and Ship Technology, ul. Narutowicza 11/12, 80-233 Gdańsk, Poland
*Corresponding author email: michal.klugmann@pg.edu.pl

Abstract

Liquid Crystals Thermography, Particle Image Velocimetry, Infrared Imaging Thermography and Digital Infrared Imaging have been successfully used in non-intrusive technical, industrial and biomedical studies and applications. These four tools (based on the desktop computers) have come together during the past two decades to produce a powerful advanced experimental technique as a judgment of quality of information that cannot be obtained from any other imaging procedure. A brief summary of the history of this technique is reviewed, principal methods and tools are described and some examples are presented mostly from our own research. Automated data evaluation allows us to determine the heat and flow visualization and locate the area of suspicious tissue in the human body. Anyway with this objective, a relatively new experimental technique has been developed and applied to the study of heat and mass transfer and for biomedical diagnosis.

1. Introduction

The beginning of the 21st century is a time of intensive scientific and research work related to micro- and nanotechnology, highly efficient energy conversion technology and methods of limiting its impact on the degradation of the natural environment. Research teams dealing with heat and mass exchange must face new challenges in the design and construction of modern and highly efficient process devices even for biomedical screened. Typical and idealized cases given in the specialist literature are no longer sufficient to solve current technical or technological problems. To cite two of them as an example: cooling of gas turbine blades or cooling of electronic systems, associated with complex geometry, non-uniform boundary conditions, and the action of aggressive and usually non-stationary flow. To investigate temperature and then heat transfer coefficient distributions (usual in Nusselt number form) on film heated models in channels with ribs turbulators has already been conducted by Baughn et al. [1], Bergles [2], Ciofalo et al. [3], Fiebig [4], Fiebig et al. [5], Hippensteele et al. [6], Jacobi et al. [7], Jones et al. [8,9], Leiner et al. [10], Mikielewicz et al. [11], Simonich and Moffat [12], Stasiek et al. [13–17], Tanda et al. [18–21] and the ones investigated in [22–25]. Designers of thermal devices expect more precise information on local values of the heat transfer coefficient, not only its average values. The flow pattern produced by transverse vortex generators (ribs) was visualized using a planar beam of double-impulse laser tailored by a cylindrical lens and oil particles. Sequential images of the particles in

Nomenclature

B – blue as the basic spectral colour
G – green as the basic spectral colour
I – intensity of any colour
R – red as the basic spectral colour
H – hue
l – linear dimension
S – saturation
x – distance

Abbreviations and Acronyms

CCD – charge-coupled device
CCIR– Comité Consultatif International des Radiocommunications
CFRP– carbon fibre-reinforced polymer

ChLC– cholesteric liquid crystals
CMOS– complementary metal-oxide-semiconductor
CR – computer radiography
DII – digital infrared imaging
FPS – frames per second
HSI – hue, saturation, intensity (model)
IR – infrared radiation
LCT – liquid crystal thermography
MRI – magnetic resonance imaging
NDT – non-destructive testing
PIV – particle image velocimetry
RGB – red, green, and blue (colour model)
SLC – smectic liquid crystal
TLC – thermochromic liquid crystal

a cross-sectional plane taken with a charge-coupled device (CCD) video camera from the downstream side of the flow were stored on a personal computer to obtain distributions of velocity vectors by means of the particle image velocimetry (PIV) method developed by Hiller and Kowalewski [26], Kowalewski et al. [27−29], Raffel et al. [30], Tanaka [31] and Tropea et al. [32]. Also in experimental investigations of the film cooling effectiveness for model turbine blades, the liquid crystal thermography (LCT) technique is presented. The film cooling and visualization of the few different jets holes configurations in steady-state and transient performance were performed experimentally above all by Satta and Tanda [33], Borda et al. [34] and Ekkad and Singh [35]. Therefore with this objective, a new experimental technique has been developed and applied to the study of heat and mass transfer and also for biomedical diagnosis by application of colour images for skin examination. Automated evaluation allows us to determine the heat and flow visualization and locate the area of suspicious tissue in the human body [36]. In medical case, the use of digital infrared imaging (DII) and LCT is based on the principle that metabolic activity and vascular circulation in both pre-cancerous tissue and the area surrounding a developing breast cancer is almost always higher than in normal breast tissue. These temperature variations may be among the earliest signs of breast cancer or orthopaedic cases and/or a pre-cancerous state of the breast as presented in [37−42] and the recently presented study by Kesztyüs et al [43]. These expectations are met by automated and fully computerized LCT based on the physicochemical properties of, among others, helical cholesterol esters, digital-computer and analogue analysis of colour images. It enables not only the study of complex geometries or the influence of non-uniform boundary conditions, but also pulsating and turbulent flows of large scales and low frequencies. Situations of such complex heat exchange can be found in most devices in which energy conversion processes take place. The analog-digital liquid crystal thermography supported by PIV [32] are excellent and recognized measurement methods used to study advanced thermal and flow processes in major scientific centres in the world and in Poland. LCT theoretically enables visualization of two-dimensional temperature and velocity fields with single-pixel accuracy and learning about the influence of many thermophysical and flow factors on the formation of laminar and turbulent boundary layers [44−53]. Or-

ganisation of scientific research using liquid crystal thermography and image anemometry will allow verification of established stereotypes in measurement techniques and empirical relationships obtained on the basis of low-precision (global) measurements, but still used in engineering practice and medical research [37,38].

2. RGB and HSI colour models

The perception of the spectrum of electromagnetic waves (colours) is an individual phenomenon. The colour of the setting sun at the same time can be interpreted by different people as red, dark red or light red. The variety of colour definitions indicates the different sensitivity of the human eye to absorbing light, photosensitive retinal receptors and colour perception. The problem of unambiguous colour description complicates the way and methods of defining colours, as in everyday Polish hue and colour are synonyms.

Colour is perceived thanks to photosensitive cells in the retina of the eye, called rods and cones. Rods are sensitive to the degree of quality (scotopic vision), and cones to colour (photopic vision). The human eye has its limited colour resolution, i.e. sometimes it is unable to see the difference between two colours with different spectrums, treating them as the same. It shows a different degree of sensitivity to a specific colour, which is determined by the individual and knowledge in using the sense of sight. The human eye contains three types of cones, with different spectral characteristics. Three dyes participate in the perception of colours, reacting with different sensitivities to the wavelength of electromagnetic radiation [54]:

- erythrolabe − sensitive mainly to the wavelength corresponding to red,
- chlorolabe − sensitive mainly to the wavelength corresponding to green,
- cyanolabe − sensitive mainly to the wavelength corresponding to blue.

On this basis, the RGB colour model was developed, widely used in devices analysing and displaying images, such as digital cameras, camcorders, monitors and televisions, etc. It is obvious to manufacturers and users of colour monitors, cameras and computer graphics that colour is a combination of three basic colours (primary colours) – red, green and blue (RGB). Additive

mixing of primary colours, i.e. RGBs, allows obtaining "millions" of colours of visible light. The history of research and considerations on the essence of colours and their impact on humans is much longer than the history of research on the properties of electromagnetic radiation.

Considerations on the creation of colours and their qualifications were undertaken by, among others, Pythagoras, Aristotle, Plato, Robert Grosseteste, Leon Battista Alberti and Leonardo da Vinci. A breakthrough in the study of colour was the discovery of Isaac Newton, made during his research on the dispersion of white light in a prism and the reverse process, during which he obtained white light again [54]. The colour triangle, drawn up in the mid-19th century by James Clerk Maxwell (1831−1879), illustrating the method of obtaining different colours by an appropriate combination of three primary colours: red, green and blue placed at the vertex of the triangle, became the basis for the technology of colour printing, photography and colour television. The colour system proposed by Maxwell and the scientific considerations conducted by his successors led to the establishment of a standardized colourimetric system in 1931 by the International Commission on Illumination (Commission Internationale de l'Eclairage − CIE) [55]. The CIE 1931 system and its later version CIE 1976 (Fig. 1), derived from Maxwell's triangle, are based on the recognition of red (R), green (G) and blue (B) as the basic spectral colours, which are described in the standardized trichromatic coordinate system X, Y, Z, also known as relative visual efficiency of cones. Due to the individual (individual) perception of colours by humans, many digital models describing the space of colours visible to humans have been developed. One of the more successful and used models is HSI (hue, saturation, intensity):

- hue (H) – specifies numerical shades of colour (on an angular scale from 0 to 360°),
- saturation (S) – is the saturation, deviation of the colour from white,
- intensity (I) – is the quality of colour, which indicates whether the colour is closer to white or black.

This model assumes that colours perceived by humans can be described using these three coordinates, provided that the points are located on the surface of a solid of a double-sided cone.
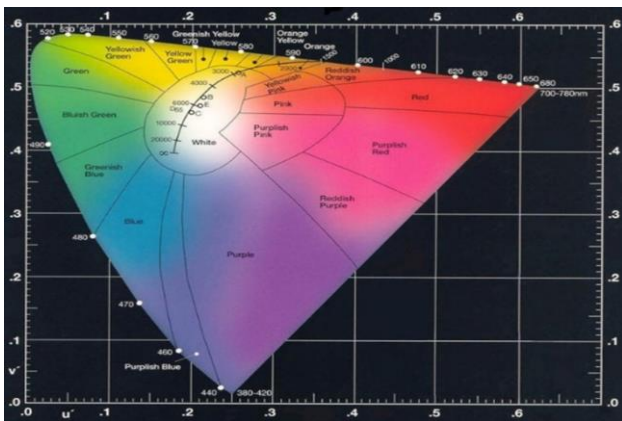
Fig. 1. The map of the 1976 chromaticity diagram is similar in nature to the triangle colour map. At the end points of the chart, the colour primaries (as defined by the CIE in 1976) are shown [55].

Figures 2 and 3 show two models of colour description: the first is based on the traditional model built on a cube, in which the basic colours are assigned to the appropriate corners of the solid, and the second is based on the HSI (Hue, Saturation and Intensity) model, where the intensity axis changing from black to white is marked and a cross-section of the solid is shown corresponding to the changing values of colour (H) and its saturation (S).
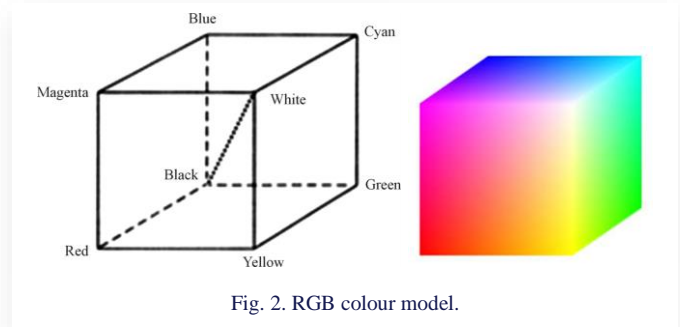
Fig. 2. RGB colour model.
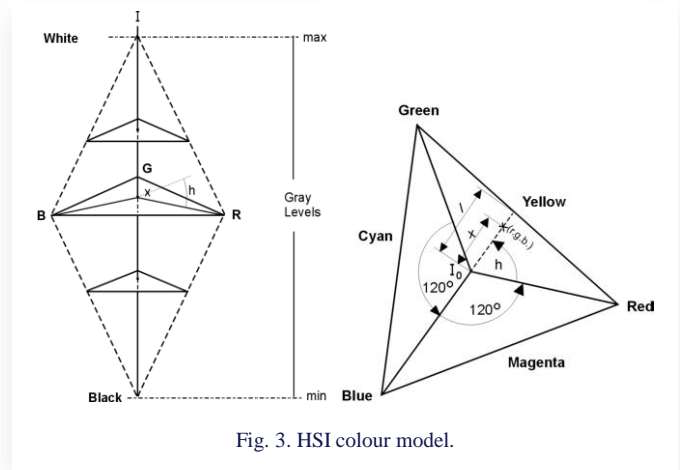
Fig. 3. HSI colour model.

Mathematically, it is relatively simple to change the colours of the image from the RGB model to the HSI model. If the coordinates of the colours or "hues" are defined by the coordinates as in Fig. 3, the intensity of any colour is defined by the formula:

$$I = \frac{R+G+B}{3}. \tag{1}$$

Accordingly, hue (colour) is represented by the angle of the vector rotating about the white colour point located inside the CIE 1976 colour map from the origin, which defines the colour red (Fig. 3 down). This value is given by the formula:

$$H = \frac{1}{360}\left[90 - \arctan\left(\frac{F}{\sqrt{3}}\right) + \{0, G > B; 180, G < B\}\right], \tag{2}$$

where:

$$F = \frac{2R-G-B}{G-B}. \tag{3}$$

The colour saturation is appropriately determined by the formula (4) in the following form:

$$S = 1 - \left[\frac{min(R,G,B)}{I}\right] = \frac{x}{l}. \tag{4}$$

For example, in Eq. (4), assuming the smallest values of R/I, G/I and B/I equal to 1, we get a saturation of 0, which means white. When using an 8-bit computer, all the values or attributes of colours change from 0 to 255. Colour image processing can be much less complicated and quicker to execute if colour images captured from RGB video sources can be digitally converted from RGB data to HSI data reported in [54,56,57].

The saturation of a chosen hue can be decreased by moving away from the pure hues parameter of the diagram toward its centre to the point where red, green and blue mix equally into white. Each step toward the diagram's centre represents a decrease in saturation [55].

3. Thermochromic liquid crystal

The history of research on liquid crystals dates back 120 years. In 1888, Austrian botanist F. Reinitzer [36] accidentally discovered the "anomalous" behaviour of cholesterol benzoate when heated. This compound melted at 145.5°C. However, the resulting liquid was not clear, had a very high viscosity and showed colour effects. Only at 177.5°C did it transition to a transparent liquid. German physicist O. Lehmann [58] became interested in this phenomenon, considering the state of the turbid liquid to be a separate state of matter, to which he gave the name liquid crystal. Currently, an alternative term is also in use − mesophase (from the Greek mezos − intermediate). The liquid crystal phase is characterized by rheological properties similar to those of liquids (the lack of a rigid crystal lattice causes a lack of elasticity of shape and allows flow), although it usually has significant viscosity. At the same time, however, liquid crystals exhibit anisotropy of physical properties, which means that physical quantities measured in different directions take different values. This feature is characteristic of solid crystals and does not occur in liquids, with the numerical anisotropy values generally being lower for liquid crystals than for solids. For many years, liquid crystals were treated as a kind of physical curiosity, and it was not until the 1960s that research on these substances began to develop rapidly, related to their role in biological systems and technical applications. Most applications of liquid crystals are based on the ease with which relatively weak external stimuli can change the macroscopic properties of the liquid crystal. This allows for the construction of devices that detect changes in various physical quantities and electronically controlled information imaging systems. Cholesteric liquid crystals (ChLC), after several decades of collecting research material, found application in science and technology, initially in thermography and defectoscopy, and then in the detection of organic compound vapours, electromagnetic radiation and ultrasound.

3.1. Structure and classification

At present, many different structures occurring in liquid crystal states are known. Due to the method of obtaining, liquid crystals are divided into thermotropic - formed after melting solid crystals and lyotropic − formed after dissolving a mesogenic substance in a suitable solvent. The thermotropic mesophase can be enantiotropic − occurring during heating and cooling or monotropic − if it appears only during cooling of the substance from the isotropic liquid state [54].

The order of molecules in the liquid crystal state depends on their shape, molecular properties and the nature of intermolecular interactions. The vast majority of molecules of mesogenic compounds have the shape of elongated rods or flat disks. Substances with elongated molecules can form a smectic mesophase, i.e. a smectic liquid crystal (SLC). In this type of mesophase, the molecules lie in mono- or bimolecular layers equally spaced from each other. Within one layer, there may also be various types of constraints imposed on the mutual position of the centres of gravity of the molecules, which distinguishes different types of smectic phases. The unit vector n parallel to the local average direction of the order of the long molecular axes − the so-called director, is in smectic either approximately perpendicular to the planes of the smectic layers or inclined to them at a certain angle. Individual types of smectic phases are usually described by capital letters of the Latin alphabet.

Elongated molecules can also form nematic order, i.e. nematic liquid crystal (NLC). In this type of liquid crystal phase, the molecules are free to rotate around the long molecular axis and translate, maintaining approximately the order relative to neighbouring molecules (Fig. 4).
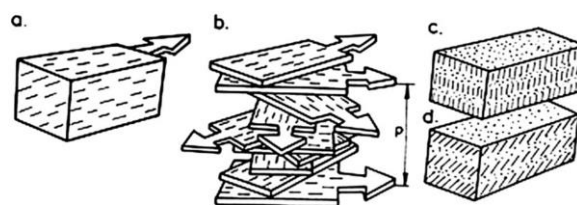
Fig. 4. Molecular arrangement in different types of mesophases. The direction n is represented by arrows: a) nematic, b) cholesteric, c) smectic A, d) smectic C.

If the molecules of a mesogenic compound have a centre of structural asymmetry (they are chiral), then due to the presence of spatial obstacles, the substance takes on a molecular order that is not nematic but twisted nematic, also called cholesteric. In a twisted nematic, the molecules lie in monomolecular layers, within which the order is quasi-nematic, as a result of which the molecular structure takes the shape of a screw (helicoids) as shown in Figure 4b. Such a twisted structure is equivalent to a nematic, but it determines the existence of several specific physical properties. The name ChLC is increasingly replaced by the one given above − twisted nematic.

3.2. Applications of ChLC

For the practical application of cholesteric liquid crystals (ChLC), optical phenomena that are characterized by significant sensitivity in response to external stimuli are of primary importance. Selective reflection of light and optical activity and circular dichroism should be mentioned here. The most frequently measured quantities are: temperature of occurrence of colours or colour transitions, wavelength of maximum selective reflection, intensity of selectively reflected light. The selection of the measurement method is determined by substantive and functional needs (including the required accuracy and sensitivity

of the measurement, time, costs and conditions of its performance and method of recording results). B&H Liquid Crystal Devices Ltd [59] presents some applications of ChLC depending on the working temperature.

In medicine, thermography was used, for example, when taking thermograms of the eye and eye socket. Using a solid layer of ChLC applied or by applying a thermographic foil, it is possible to determine the boundaries of the inflammatory process and detect separate foci of inflammatory infiltrates at different stages of their development. In comprehensive examinations of patients, liquid crystal thermography allows for obtaining information about the location of purulent-inflammatory foci, malignant and non-malignant tumours, as well as their metastases to lymph nodes and lymphatic vessels. This method enables observation of changes in the inflammatory state and allows the selection of the most rational surgical access to the inflammatory focus. Cancerous tissue emits significantly more energy than normal tissue. Rapid cell division is associated, among other things, with increased metabolism, which causes an increase in temperature and can be detected visually using thermography. In the case of breast cancer in women, a temperature increase of 0.5 K is often a sign of a benign tumour, while an increase of 2 K suggests a malignant tumour. In material testing, non-destructive testing (defectoscopy) with methods such as X-ray, ultrasound or magnetic resonance occupy an important place. In recent years, there has been development of device defectoscopy based on the use of liquid crystal thermography.

The distribution of temperature measured on the surface of an object is related to the properties of the material and the operating characteristics of the device. The temperature distribution is influenced by both the amount of heat dispersion (thermal dissipation) and thermal diffusivity. A typical example of the use of this method is the location of damage in joints. There is a high current density at the fault site, and therefore a high temperature, so it can be located very precisely.

3.3. Calibration of ChLC

Before starting temperature measurements and data recording with a computer-vision system, the characteristics of the measuring section consisting of a liquid crystal layer, light sources and a camera-video-computer system must be determined. It should be done on an experimental stand so that the optical conditions during calibrations and then the experiment are comparable. Both the temperature range of the colour response and the colour response temperature can be selected depending on the needs of the experiment in the range from −30°C to +120°C with a temperature range from 0.5°C to 20°C.

The type of liquid crystal selected for the experiment also depends on the type of means used to analyse the resulting colour images. In the described experiment, a computer-vision analysis technique is used that excludes the possibility of different interpretations of the same image depending on the way of perceiving colours. In such a case, the best material is a liquid crystal with a narrow temperature range. In the presented measurements, the liquid crystal film was manufactured by MERC Ltd. [57] The symbol R30C5WA means a colour response temperature range of 5°C and a colour response temperature of 30°C, i.e. the possibility of measurement in the temperature range from 30 to 35°C. The experimental stand for calibration of liquid crystal film is shown in Fig. 5. The layer of liquid crystal film is placed between a brass marking plate and an 8 mm thick plexiglass plate. This allows the change in the colour of the liquid crystal layer to be viewed through the plexiglass under the influence of changes in the temperature of the brass plate. The whole is insulated with a layer of polystyrene. The brass plate has dimensions of $210 \times 170 \times 8$ mm. To obtain a linear temperature distribution in the characteristic plate, one end of it is cooled with thermostated water and the other is heated with an electric heater with adjustable power.
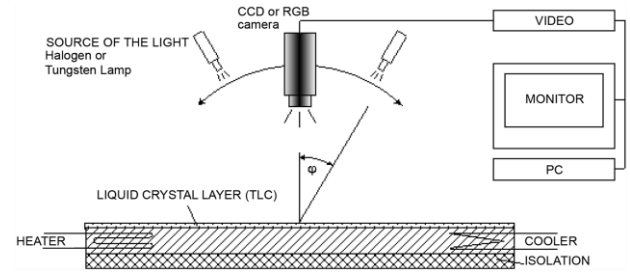
Fig. 5. Calibration brass plate with liquid crystal layer attached.

Fig. 6. The distribution of the colour component pattern on the liquid crystal layer measured by RGB colour camera.

For the applied R30C5WA liquid crystal layer as a foil with the colour component pattern (see Fig. 6), calibration was performed using halogen and tungsten lighting (Figs. 7 and 8). Analysis of the averaged values of the gauge curves showed that halogen lighting is more advantageous and useful for thermographic applications and it was selected for further measurement procedures.
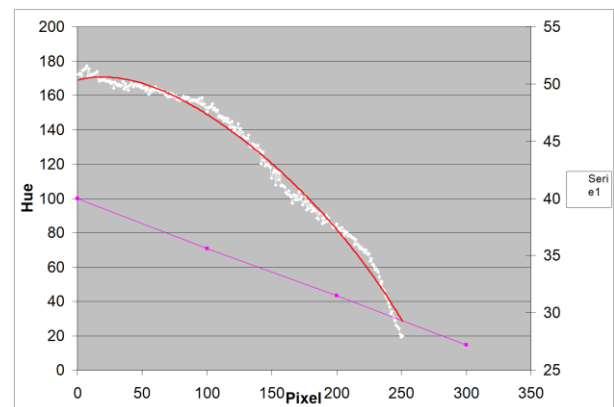
Fig. 7. Averaged value of the feature curves of the liquid crystal film under halogen illumination.
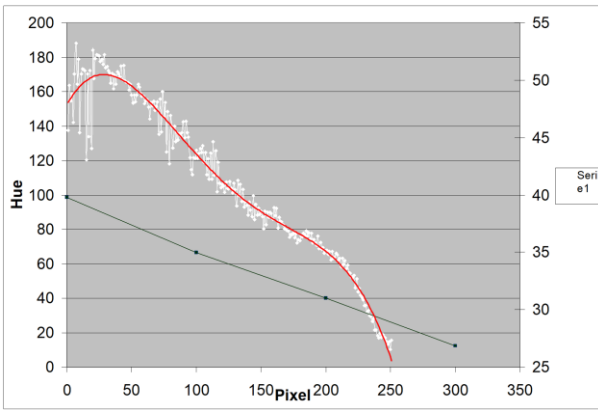
Fig. 8. Averaged value of the feature curves of the liquid crystal film under tungsten illumination.

3.4. Visualization of velocity and temperature fields in cavity

The liquid crystal technique is used not only in air flows, but also in other fluids. The distributions of the temperature field and velocity vectors were visualized using a liquid crystal in a pure solution form or microcapsules, both as trace particles inside the fluid or as a coating of the flowing surface. The encapsulated form of liquid crystal can be mixed directly with water, glycerine or silicone oil. It is recommended to create dilute solutions, i.e. 0.01–0.02% by weight [16,17]. Too much liquid crystal causes a milky colouration of the dilutes and when reflecting light, it causes blurring of colours. The structure of the flow together with the movement of the particles can be recorded using a photo camera or a video camera. With the flash of a white light knife "cutting through the flow" (similar to the PIV method), both the temperature of the coloured molecule and its flow direction (when several images of the same molecule are taken) can be recorded.

3.5. Particle Image Velocimetry

Digital image anemometry (known as Particle Image Velocimetry − PIV), as a measurement method of fluid mechanics, originates from visualization techniques used for hundreds of years, most often allowing only a qualitative assessment of the structure of the tested flow [30]. Visualization methods consist in observing marker particles, called seed particles, found in a moving fluid (e.g. smoke in the air, small pieces of wood in a river or specially selected particles in laboratory measurements) and determining, based on the observed movement of these particles, the nature of the flow of interest to us. The observation can be made here directly using the researcher's "eye" or using equipment enabling image recording. It is important that the observed marker particles are appropriately selected for the analysed movement − so that the tested flow "carries" them along with it. Their density must be close to the density of the flowing substance and their size must be suitably small. This will eliminate the influence of gravity and inertial factors and allow us to assume that the observed movement of particles is identical to the movement of the fluid carrying them. Most often, various types of powders, liquid droplets, smoke and pollen are used as seed particles, depending on the type of flowing medium (gas, liquid) and the nature of the flow. PIV consists in recording moving marker particles with a digital camera and further numerical analysis of the obtained image sequences, as a result of which we obtain instantaneous, full velocity fields of the moving fluid.

A typical diagram of the measuring techniques used in the PIV technique is shown in Fig. 9.
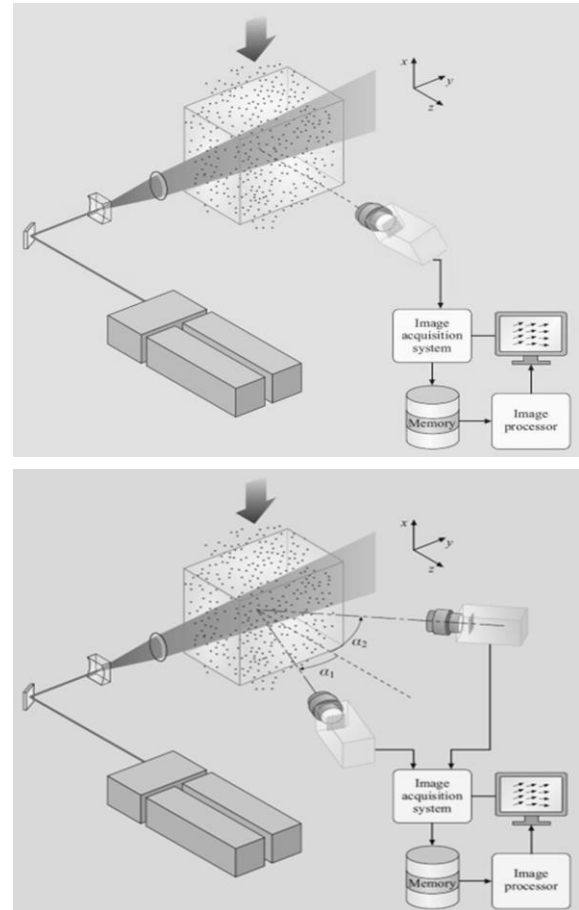
Fig. 9. Schematic of a typical PIV measurements with one camera (up), and two cameras (down) [32].

The tested flow with the addition of marker particles is illuminated by a narrow plane of light, the so-called light knife. Halogen lamps are used as the light source, and currently most often lasers, from which the light beam is directed at the tested flow by means of a system of mirrors and a cylindrical lens and formed into a light knife. The use of the light knife is intended to separate the tested, interesting cross-section of the flow from the rest of the measurement domain. Thanks to this, only the tested cross-section is visible on the recorded images, and the remaining part is darkened and not subject to recording. The obtained images of moving particles are subjected to further numerical analysis aimed at precisely determining their displacements between individual registrations. At present, the PIV measurements are performed by using small droplets of synthetic oil DEHS (Di-Ethyl-Heksyl-Sebacat). The oil drops volumetric concentration was very low hence they did not affect the flow structure.

12

The use of the PIV method entails certain limitations and conditions that must be met by images intended for analysis, namely:

- sufficiently high concentration of marker particles in images; a small number of particles does not allow the use of fast Fourier transforms (FFT),
- as even as possible saturation and brightness of the recorded images; large changes in the degree of exposure within the analysed area introduce the need to use filtering, which should average the brightness over the entire image,
- large differences in speed between individual image fragments favour the occurrence of interferences and distortions in the obtained velocity field, which occur when a larger number of lifted markers leave the analysed area due to too high speeds,
- the time interval between successive images should not be too small; small displacements have a directly proportional effect on measurement inaccuracies.

The path between obtaining digital images and obtaining vector graphs that are a graphical representation of velocity fields leads through a series of activities performed by a computer program; from manipulating graphic files, through typical mathematical operations, to using the functions controlling the system's graphical interface to visualize vector graphs. Mathematical calculations mainly come down to determine the correlation coefficients of image fragments in order to find particle displacements, and to convert them into velocity fields. In digital image anemometry, FFT is used to determine image correlation. These are algorithms for numerical calculation of the Fourier transform and the inverse Fourier transform.

4. IR Photography (IRP)

Infrared radiation as presented in Fig. 10 [60] can be used to remotely determine the temperature of objects and for imaging using differences in the thermal radiation of bodies [32]. For bodies at room temperature, this technique is called thermography, and for hot bodies, pyrometry. Thermography is used primarily in military and industrial applications, but the technology is reaching the public market in the form of infrared cameras. The most popular and comprehensive thermal cameras available for industrial and commercial buildings or energy conversion devices are FLIR products.
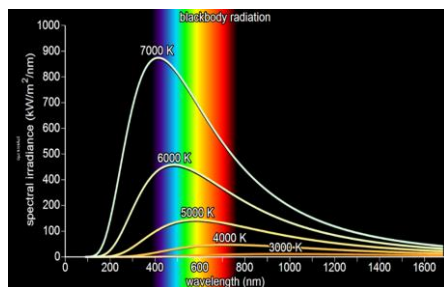
Fig. 10. Spectral irradiance graphs as a function of wavelength and temperature.

The FLIR T440bx thermal camera is based on infrared radiation and used in current investigations (Fig. 11). It offers all the latest FLIR features in a brilliant resolution. The real standout for the T440bx camera is FLIR's new MSX Thermal Image Enhancement. Multispectral imaging camera (MSX) combines the thermal and visible images into one data-rich image a completely new fusion technology. Easily identify intersecting walls, mechanical data plates and heat transfer elements or even whole furnaces and combustion systems, all while still viewing in full infrared. The FLIR T440bx series also offers a flexible, efficient and variably universal method of gathering and analysing equipment data with its high temperature range (−20°C to 650°C), multiple hot spot measurements, humidity and dew point measurements, wi-fi connectivity and sensitive to 0.03°C temperature changes.

Fig. 11. FLIR's T440bx IR camera.

In general, taking into account the advantages and disadvantages of this measurement technique, objects emit infrared radiation across a spectrum of wavelengths, but sometimes only a limited region of the spectrum is of interest because sensors usually collect radiation only within a specific bandwidth. Thermal infrared radiation also has a maximum emission wavelength, which is inversely proportional to the absolute temperature of the object, in accordance with Wien's displacement law. Therefore, the infrared band is often subdivided into smaller sections.

5. Experimental open wind tunnel

The experimental open wind tunnel was designed and constructed at the Institute of Energy of the Gdańsk University of Technology [11]. Thanks to its universal design, it allows for testing a wide range of geometries with a small expenditure of resources needed to adapt the measurement section to subsequent experiments. Figure 12 shows a diagram of the wind tunnel for modelling of heat exchanger elements.
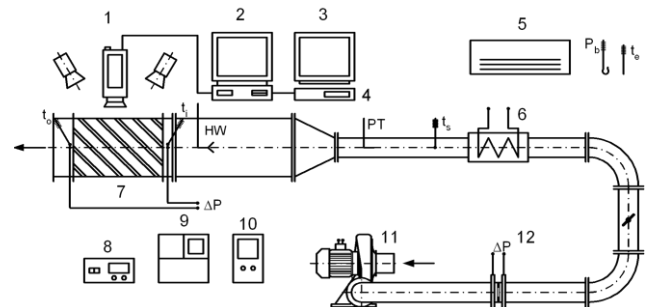
Fig. 12. Open low speed wind tunnel, 1 – RGB camera (TK-1070), 2 – PC, 3 – monitor (RGB-VMR 200), 4 – recorder/backup, 5 – air conditioning system, 6 – heater, 7 – LC mapping section, 8 – digital micro-manometer FC012, 9 – DISA hot wire system (HW), 10 – variac, 11 – fan, 12 – orifice, PT – Pitot tube.

In the air preparation section, an MPA 90T fan is installed with a maximum capacity of 1200 nm^3/h with automatic and smooth regulation of the rotational speed using an inverter, which allows for obtaining Reynolds numbers Re of up to approximately $1.5 \cdot 10^5$ in the measurement rectangular section (D_h = 69.11 mm).

The fan is connected by a steel spiral pipe to the heater and then to the control section. Thanks to the placement of the orifice with a dial measurement (D = 100 mm, d = 50.12 mm and module m = 0.2512), it is possible to estimate the amount of air flowing through the station before the heater, whose regulated power (N = 1800 W) allows heating the compressed air to the desired temperature.

The air prepared in this way is forced into the control section made of 8 mm thick plexiglass. Initially, it is a tube with a diameter of d = 90 mm and length of L_1 = 1080 mm, then a diffuser with a length of L_2 = 330 mm and a rectangular stabilizing section with a length of L_3 = 810 mm. Inside the round channel, a control measurement of the amount of air flowing and its parameters is carried out using a Pitot tube and a digital micro-manometer FC012 from Furness Controls Limited UK. This part of the control section is also used to calibrate the wire anemometer probe (DISA-thermo-anemometer type 55M01), which is used to measure the height of air turbulence at the inlet to the measuring section during the experiment.

The modelling (mapping) section, is supplied via a bypass valve which allows the hot air supply to be cut off if necessary. The modelling section is illuminated from above by a set of tungsten or halogen lamps and the colour images are recorded by using a computer vision system.

The mapping section, which is an 8 mm thick plexiglass plate and a 0.15 mm thick liquid crystal foil, is washed by the air flowing around that supplies heat to the ribbed surface. Know-ledge of the heat flux density and local temperature values obtained using liquid crystal thermography enables the calculation of local values of heat transfer coefficients and then Nusselt numbers using the gauge curve of the liquid crystal layer (Fig. 7) [17–19].

Thermographic measurements of stationary and non-stationary two-dimensional temperature fields in the measuring section of the model heat exchanger were aimed at determining the heat transfer coefficients and the Nusselt number. Local surface temperatures were assessed based on hue measurements, which were then converted into the temperature in Kelvin or Celsius scale using the gauge curve of the liquid crystal layer. In many cases, as mentioned above, remarkable enhancement of local and spatially averaged surface heat transfer rates is possible with rib turbulators, in spite of the lower local Nusselt number at certain locations along the ribbed surfaces.

The test surface that is analysed contains a collection of rib turbulators that are perpendicular and angled with respect to the flow stream (Fig. 13) [13,14]. However, to determine the surface heat flux, the convective power is provided by the thermofoil heaters.

Spatially resolved temperature distributions along the bottom rib turbulator test surface are determined using a liquid crystals foil and true-colour image processing system commercially available from Data Translation Ltd. [56] and Hallcrest [54].
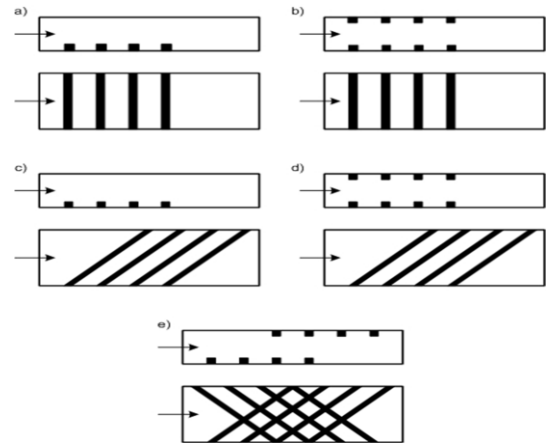
Fig. 13. Schematic view of four types of transverse vortex generators.

6. Examples of experimental results

In the following examples, the TLC's foil sheet and unsealed TLC's tracers have been applied to measure both the surface temperature and velocity, and temperature fields in a glycerol-filled cavity under free convection. For human body screening or biomedical situations, few images using Thin Layer Chromatography (TLC) and IR-Photography techniques are also presented.

6.1. Temperature measurement on the ribbed surface and square section column

Figures 14 and 15 show photographs of the colour distribution of the liquid crystal layer on the ribbed surface and around a square section column. A pattern of the Nusselt number Nu reconstructed by false colour images of the heat transfer from a surface with square columns is presented in Fig. 16.
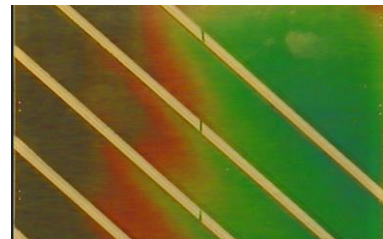
Fig. 14. Photograph of the colour distribution of the liquid crystal layer on the ribbed surface.
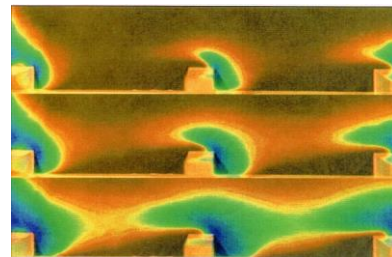
Fig. 15. Photograph of the colour distribution of the liquid crystal layer around a square section column.

14
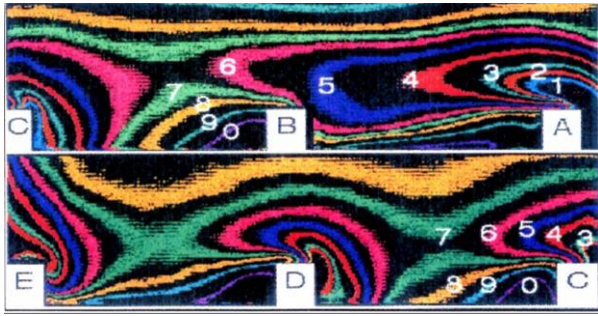
Fig. 16. Pattern of the Nusselt number Nu reconstructed by false colour images of the heat transfer from surface with columns for Re = 20 000 (No. 0: Nu = 79; 9: 99; 8: 113; 7: 123; 6: 136; 5: 147; 4: 160; 3: 175; 2: 185; 1: 209).

Figures 17 and 18 show (for geometry a and b, see Fig. 13) the local streamwise Nusselt number distribution between the selected ribs (out of several dozen) of the central zone of the model heat exchanger. Thermal flow tests were performed for four values of the Reynolds number, i.e. 9000, 16 000, 26 000 and 35 500. The analysis of the experimental results showed that flow turbulisation using simple transverse ribs leads to the best effects (the highest average values of the heat transfer coefficient are obtained for the perpendicular ribs). Turbulators set at angles other than perpendicular to the air flow contribute to the improvement of heat exchange to a lesser extent.
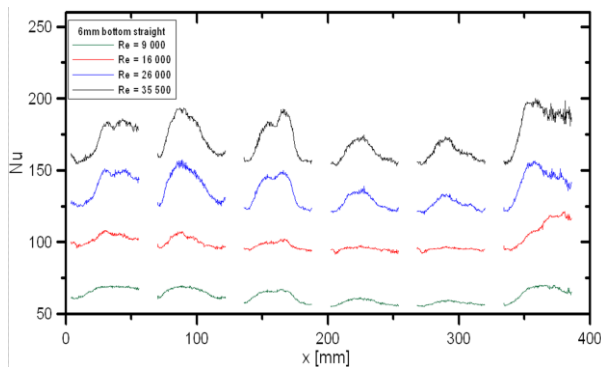
Fig. 17. Local streamwise Nusselt number distribution between the ribs in the boundary layer for ribbed bottom walls and ribs perpendicular to the flow (configuration a in Fig 13) [13].
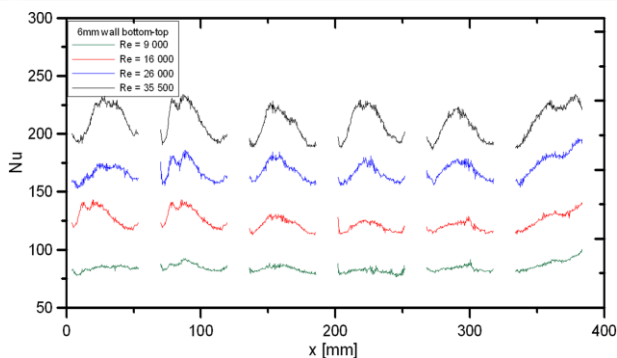
Fig. 18. Local streamwise Nusselt number distribution between the ribs in the boundary layer for ribbed bottom and top walls and ribs perpendicular to the flow (configuration b in Fig. 13) [13].

6.2. PIV measurements

For the numerical verification of local and averaged thermographic measurements of Nusselt numbers, knowledge of the turbulence level and flow velocity is required. These values can be obtained based on PIV anemometric measurements (Fig. 19). The sample results are presented in Fig. 20. The area scanned by the PIV method was in all cases located in the mid-vertical plane between side walls.
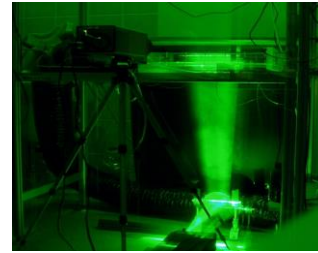
Fig. 19. Laser light sheet visualisation during a velocity measurement.
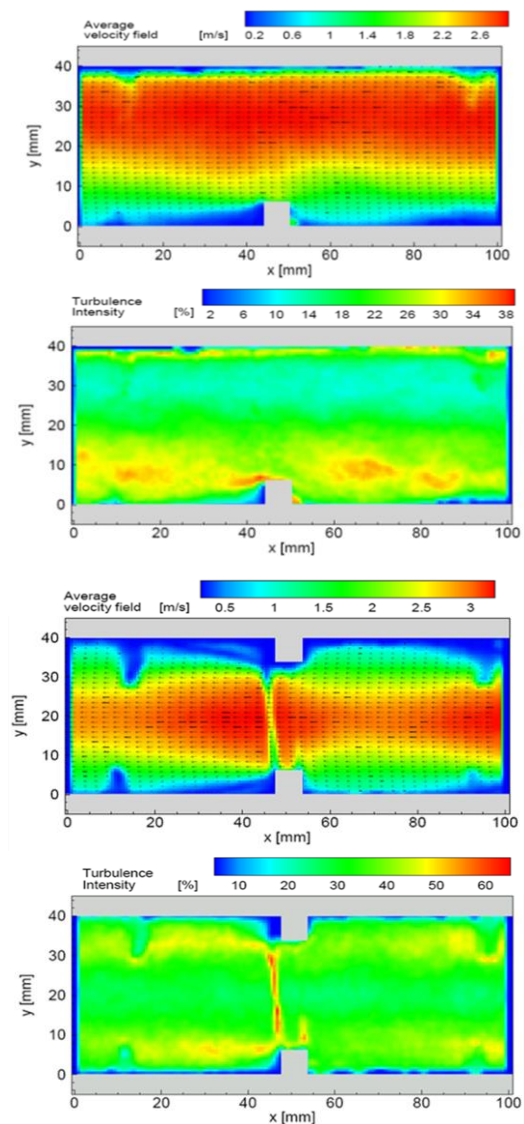
Fig. 20. PIV measurements for ribbed channel and Re = 9000: averaged velocity field and turbulence intensity for geometry with ribbed walls – upper for configuration 13a, and lower for configuration 13b [50].

15

Figure 20 shows an average velocity field and turbulence intensity (averaged over 100 instantaneous velocity fields) for a geometry with a ribbed bottom wall and ribbed bottom and top wall (ribs height is 6 mm) and flow perpendicular to the ribs (geometry a and b in Fig. 13). The Reynolds number is 9000 and the maximum velocity for these cases is about 3.0 m/s located in the top part of the channel. It also shows that the flow is turbulent with the maximum turbulence intensity about of 38% in the vicinity of the rib and a relatively small turbulence intensity in the top part of the channel (about 10%). In the case presented in Fig. 20, the maximum turbulence intensity is higher than 65% and located in the middle of the channel close to the ribs.

6.3. Natural convection in a closed cavity

The liquid crystal technique was used not only in air flows, but also in other fluids. The distributions of the temperature field and velocity vectors were visualized using a liquid crystal in a pure solution form or microcapsules, either as trace particles inside the fluid or as a coating of the flowing surface. The encapsulated form of the liquid crystal can be mixed directly with water, glycerine or silicone oil. It is recommended to create dilute solutions, i.e. 0.01–0.02% by weight. Too much liquid crystal causes a milky colouration of the diluent, and reflected light causes blurring of colours. The structure of the flow together with the movement of the molecules can be recorded using a camera or a camcorder. Together with the flash of the light knife "cutting through the flow", both the temperature of the molecule (colour) and the direction of the flow (when we take several pictures of one molecule) can be recorded. The undisputed leader in the study of fluid behaviour in closed spaces is T. Kowalewski [27–29,32]. Figure 21 shows the measurement results obtained by him in the cavity (filled with water) under conditions of free convection.
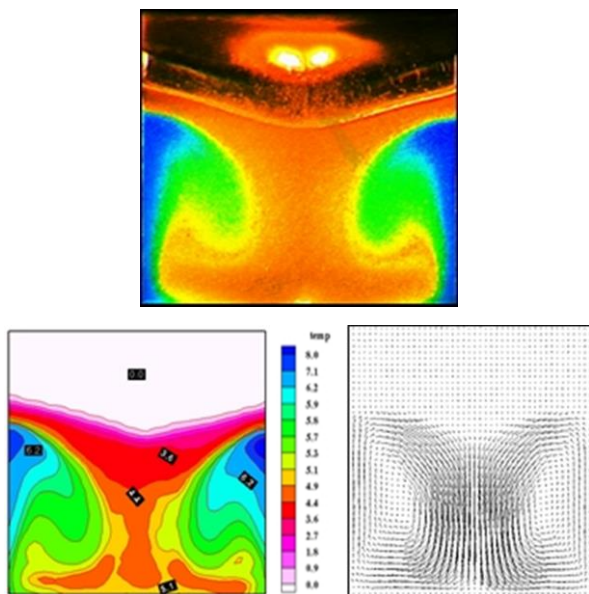
Fig. 21. Freezing of water under a cold surface in a lid cooled cavity. Recorded image of TLC tracers (up), evaluated temperature and velocity fields (down). Time step: 3600 s after cooling starts; isothermal lid temperature $T_c = -10°C$, external temperature $T = 20°C$ [16,27,28].

In the second experiment (as an example of TLC applications), there was a visualization of free convection in a closed space with glycerol (cavity) with dimensions $L = 180$ mm of length, $H = 30$ mm of height and $W = 60$ mm of width. The white light source in which the moving particles of liquid crystal were observed was a Xenon Flash Lamp. Colour images of moving particles were recorded at intervals of 1 to 15 seconds. Usually, several shots were recorded on one film frame. This colour anemometry resembling PIV was extended with temperature measurement, creating the so-called PIVT (particle image velocimetry and thermometry). Based on the photograph obtained in this way, two-dimensional velocity and temperature fields can be determined. An example of a two-dimensional velocity and temperature field is shown in Fig. 22. The photographs were taken from a horizontal to a vertical position every 30 degrees. Among other things, coloured Benard cells were recorded for the first time.
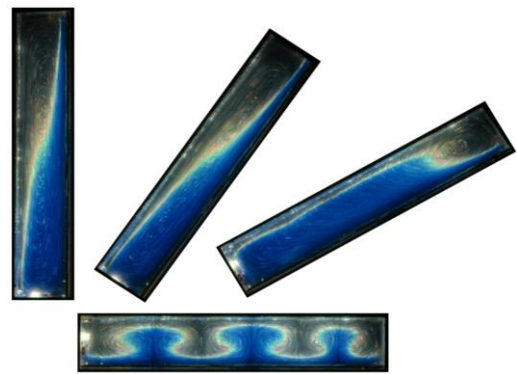
Fig. 22. Temperature and velocity visualisation in glycerol-filled cavity under free convection using TLC (Ra = 1.2·10⁴, Pr = 12.5·10³); $D_T = 10$ K; dimension of cavity: $L = 180$ mm, $H = 30$ mm, $W = 60$ mm. The horizontal position showing the Benard cells.

6.4. Flow visualization of gas model turbine blades cooled by air

Effective methods of gas turbine blades cooling and improving of their effectiveness require the use of modern and unique design solutions. Due to the high temperature of the inlet gas to the first gas turbine rims, there is the constructional and technological problem of designing shafts and blades properly cooled so as to prevent blade erosion (while exceeding the melting point).

The cooling system should provide the lowest mixing intensity and the best thermal barrier for the blade. On the other hand, the coolant mass flow has to be minimized as low as possible, because it influences the compressor and engine overall efficiency. However, the experimental set-up presented in this paper is able to provide complementary data of flow-field around film-cooled turbine blades and heat transfer under turbulent conditions. Examples of modified gas turbine blades are shown in Fig. 23 (up). Within this objective, a new experimental technique, inclusively with LCT has been developed and applied to the study of aerodynamic and aerothermal blade turbine design with the effusive cooling concept. Steady-state and transient methods were used during experiments to capture colour images during LCT experiments.

Fig. 23. Gas turbine blades with cooling holes (up) and view of the test section for the model turbine blade cooling system (down) [35].

6.4.1. Experimental facility

Experiments were carried out in a modernized open low-speed wind tunnel presented in Chapter 5 (Fig. 12). The air is pumped into the system through the fan with an automatic speed regulation, which allows us to change the flow over a wide speed range in the further part of the research section. The air flowing out from the checking section goes afterwards to the diffuser section followed by the stabilizing section and subsequently to the test section, which is the last section of the component wind tunnel and is illuminated by the annular lamps, which are commonly used in photography.

The colour temperature of light obtained through these lamps is 5000 K and is similar to daylight. It is also important to have a uniform density of luminous intensity of light in the measuring section so that the four cameras can work and record the experiment in the same range of parameters of light. The brightness of the lamps also affects the optical density parameter of the CMOS sensors of the installed cameras. Four special high speed cameras designed for taking high quality images are used, which allow us to transfer frames at a speed of 87 FPS.

The cameras are equipped with modern Pentax lenses with a focal length of 6 mm that enables us to obtain high quality images from a distance of 20 cm from the object, and two spherical lenses. The lens has a high brightness (f 2.9) and a viewing angle 57°. The white balance of the camera and the shutter are set individually for each camera when changing the location and lighting within the measuring section. The cameras are connected to the computer using the GBit Ethernet cable. The computer has specially designed software, which synchronizes all of the cameras to trigger at the same time. This enables the camera to take four different images of one object made at the same time determined to an accuracy of 2 ms. The software also allows us

to store data as a single frame to BMP, and each frame is described in detail and includes a timestamp. Subsequently, frames are stored on a disk storage, where they are collected for further processing by the main computer.

The lower part of the test section is constructed as a flat channel made of plexiglass with a thickness of 8 mm, and the upper side is closed by a modified blade profile made of aluminium. The jet section for secondary flow consists of 16 holes with 2 mm diameter each. The jet section can be located at different positions along the profile. They are marked as 1–2, 3–4, 5–6, 7–8 and 9–10 (Fig. 24).
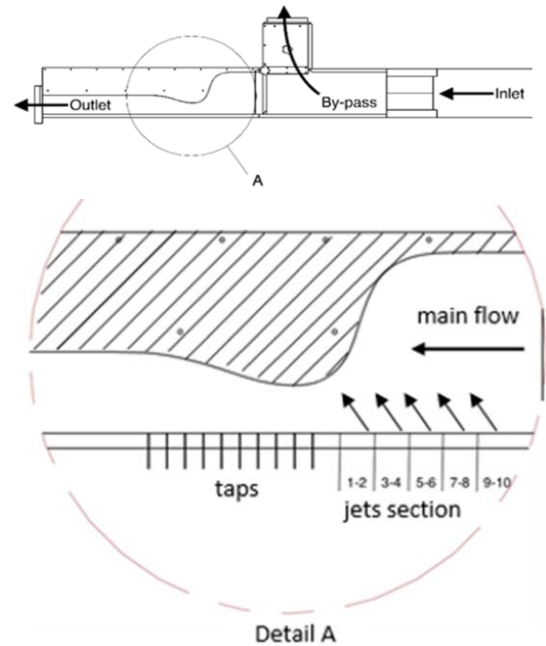
Fig. 24. View section of model turbine blade geometry [34].

For the experimental principle pressure transducers, air flow meters and thermocouples were selected and installed at specific locations in the test rig to measure the pressure, flow rate and temperature for the main and secondary flows. The test section is equipped with a bypass, which enables different air flows for use with transient as well as steady-state LCT techniques (Fig. 24).

Numerical simulations for the section design were carried out in order to obtain the pressure distribution in the channel similar to the blade cascade. The simulations were performed by means of the FINE/Turbo NUMECA code with the Autogrid 5 mesher for cascade configuration.

An example of velocity and static pressure contours in the blade passage is shown in Fig. 25. Numerical simulations for the cascade allow us to determine the pressure distribution on the profile wall, which is considered the reference for the test section design. In Fig. 26 (up), an example of pressure distribution for the test section is shown. It is compared with the results obtained for the cascade. The velocity magnitude distribution at the middle plane of the designed test section is shown in Fig. 26 (down). A properly adjusted shape of the upper wall provides the desired pressure distribution on the lower flat wall. The experimental investigations are carried out on the lower wall.
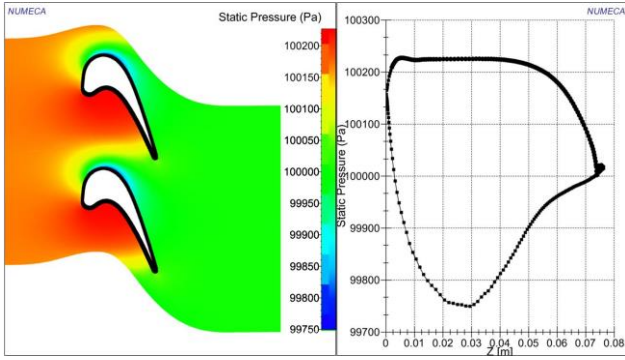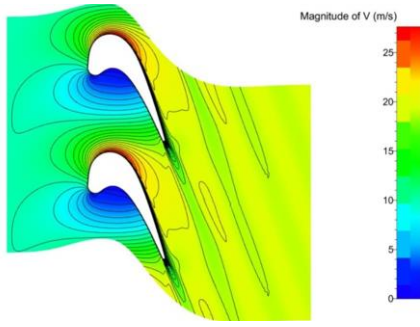
Fig. 25. Velocity magnitude in cascade (up)
and static pressure cascade (down) [34].
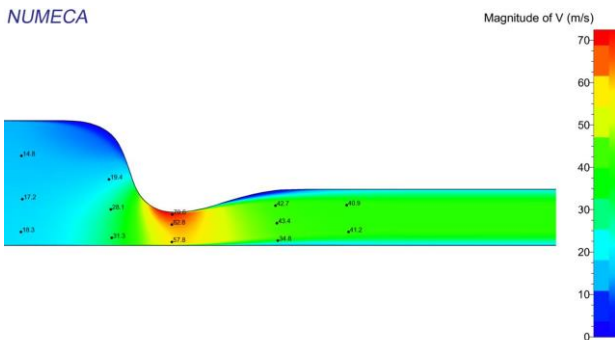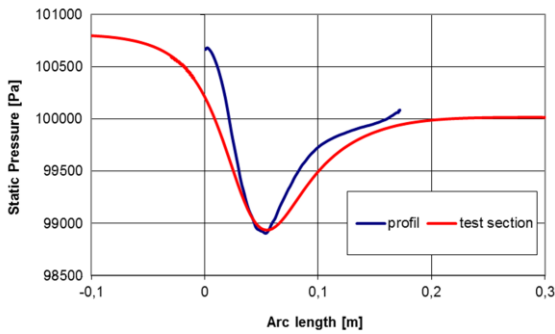
Fig. 26. Static pressure distribution on the suction side of the profile
and flat plate (up) and velocity in the test section (down) [34].

6.4.2. Results of LC experiments

The selected results of LCT measurements of steady-state flow are shown below. The experiment was conducted for 3 Reynolds numbers (Re = 87 000, Re=105 000 and Re = 122 000) of air

flow in the main channel and for two overpressures (ΔP): $\Delta P =$ 5% and $\Delta P = 15\%$. The relative pressure or overpressure is defined as a difference between the total pressure at the inlet to the set of jets and that of the main flow inside the channel. Figure 27 presents a visualisation of air flow on the blade surface for Re = 105 000, which corresponds to a velocity of 12 m/s. Figure 28 presents similar results, but for Re = 122 000, which corresponds to a velocity of 14 m/s and for the jet section located at position 7–8. In both examples, hue is converted to the Kelvin temperature using the curve of the calibration nomogram.

Fig. 27. Visualization of air flow on blade surface. Jet position 1–2,
Re = 105 000, T_a = 315 K, T_j = 299 K, T_{av} = 313.3 K, ΔP = 5% [51].
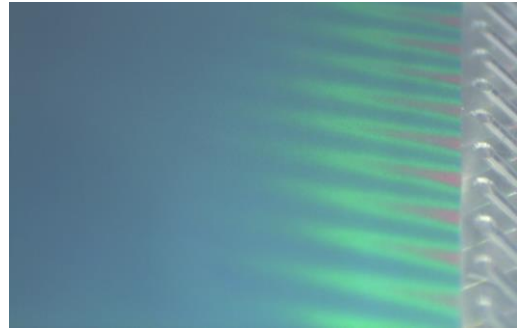
Fig. 28. Visualization of air flow on blade surface. Jet position 7–8,
Re = 122 000, T_a = 315 K, T_j = 299 K, T_{av} = 310.9 K, ΔP = 15% [51].

The jet section of the secondary flow is located inside the test section at position 1–2 (see Fig. 24), which is the closest to the profile narrowing. The temperature of air in the main channel was equal T_a = 315 K, while the temperature of air coming from jets was equal T_j = 299 K, and the average temperature of the surface covered by liquid crystal foil T_{av} = 310.9 K; this is an average temperature for the flat plate covered by liquid crystals sheets and "washed" by air. The local hue values versus distance from the jets outlet are presented in Fig. 29.

The results of cooling effectiveness visualization in the turbine inter-blade passage (at the end-wall) using transient LCT measurements are shown in Fig. 30. In this figure, a colour image was obtained with the use of liquid crystals thermography for Re = 122 000 and transient performance.

Measurements were taken for a few time steps, calculated from the moment of hot air entry to the test section (t+ is time in seconds). Before the measurements, hot air flowed through a by-pass and then was directed to the test section by a three-way

18

valve. The air temperature was kept constant and equal $T_a = 315$ K. Recently the steady-state technique of LCT has been used by F. Satta and G. Tanda [33] to map the heat transfer co-efficient distributions at the end-wall of the turbine blade cas-cade.
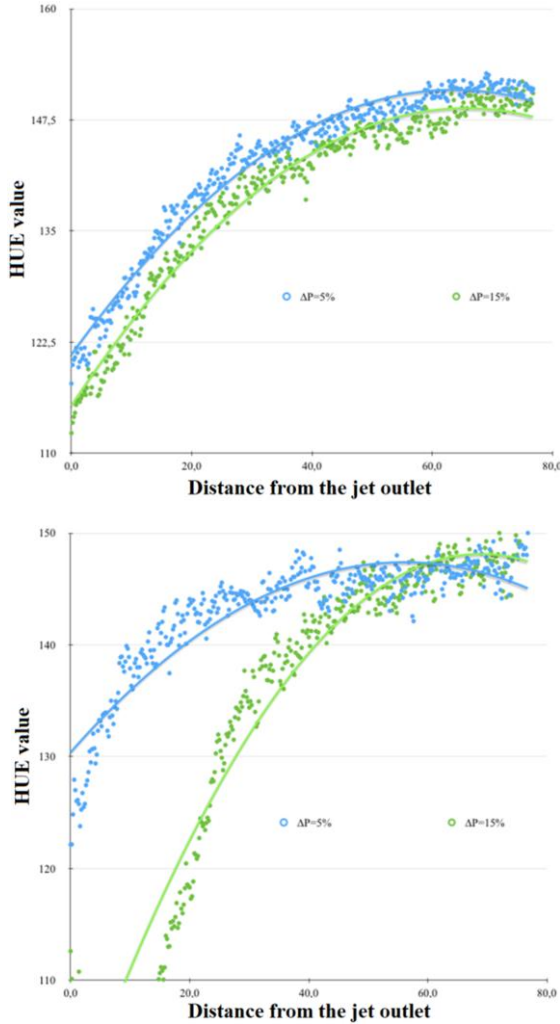
Fig. 29. Local hue value versus distance from jets outlet.
Jets position 1–2, Re = 105 000, $T_a = 315$ K, T_j =299 K (up),
jets position 7–8, Re = 122 000, $T_a = 315$ K, T_j =299 K (down) [51].
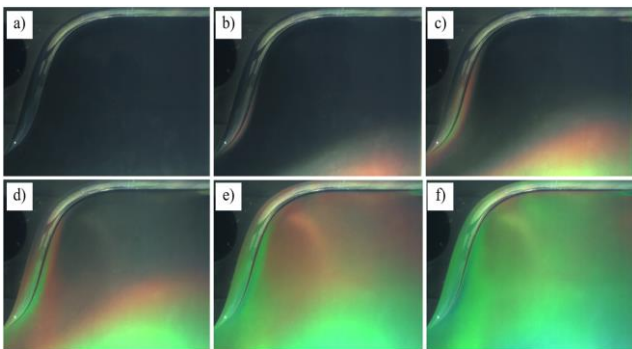
Fig. 30. End-wall of model turbine blade temperature distribution:
colour image. Re = 122000, $T_a = 315$ K, t+12s, time steps:
a) t+0s, b) t+4s, c) t+8s, d) t+12s, e) t+16 s, f) t+20s [50].

6.5. Investigations of using TLC in defectoscopy

Strugała et al. [51] proposed and described a new method for non-invasive testing of impact damage in carbon fibre reinfor-ced polymer (CFRP) using thermo-optical techniques (Fig. 31). Compared to previously used techniques, for example computer radiography (CR), this method is low-cost and does not require complicated equipment. Since the recording takes place using conventional cameras (see Fig. 32), this method can also be used in field research. The comparative analysis showed that this technique can be a full-fledged accurate tool for an NDT method for the diagnosis of impact damage in CFRP (Fig. 33).
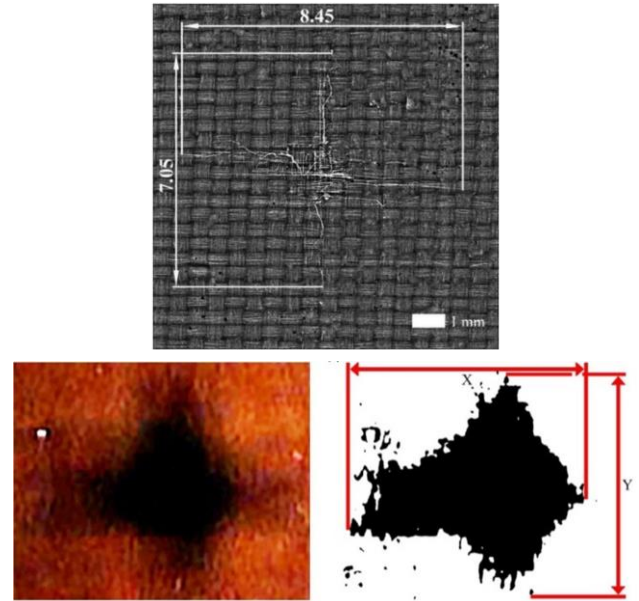
Fig. 31. X-ray image of cracked CFRP sample (up), TLC image of dam-aged area and its post-processing for quantitative analysis (down).
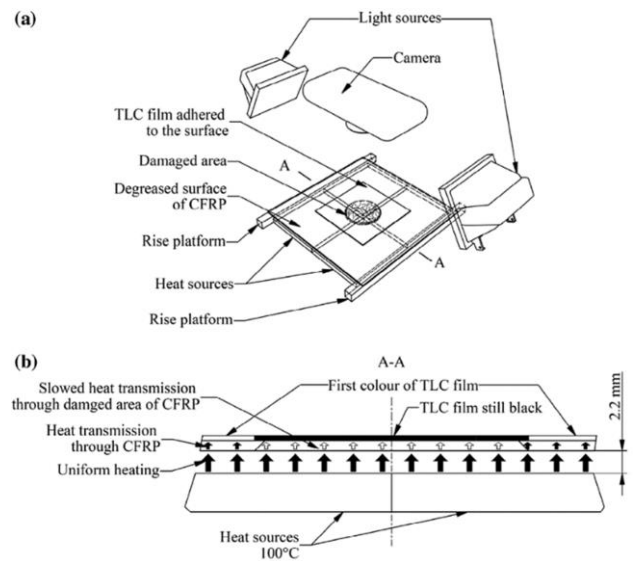
Fig. 32. Schematic drawings of (a) experiment station for sheet of lami-nated thermochromic liquid crystal film tests, (b) cross-section (A–A) with representation of heat transmission through an impacted specimen with the adhered sheet of laminated TLC film.
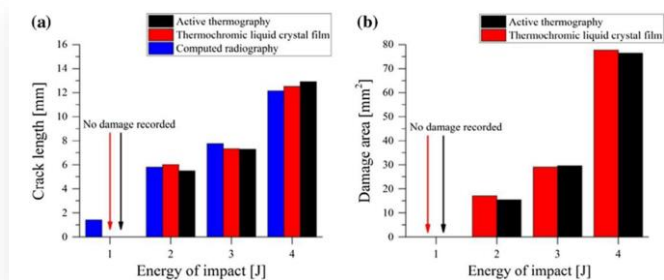
Fig. 33. Comparison of the NDT methods depending on the impact energy where: (a) comparison of the average crack length vs impact energy for three NDT methods, (b) comparison of the damage area vs impact energy measured by means of active thermography and laminated thermochromic liquid crystal film.

The use of liquid crystals significantly reduces the hardware costs of diagnostics without affecting the quality of results, compared to expensive thermal imaging cameras. The key disadvantages of the TLC film technique are negligible in terms of the applied procedure for performing the tests.

6.6. Medical applications

In medical applications, thermochromic liquid crystal and infrared thermography are used for examinations of breast cancer, thyroid dysfunction, lymphatic congestion, vascular and nervous system disorders, abdominal inflammation, muscle disorders, rheumatological conditions, orthopaedic diseases and many others [37–42]. It is used for both men and women. Diagnostics and prevention are definitely a better and cheaper solution than treatment. This is also the purpose of medical thermography, a test that allows you to visualize physiological changes in the body in the early stages of their development.

Thermography is a state-of-the-art non-invasive screening procedure (non-contact, radiation-free) that uses heat detection to locate areas of temperature differences in the body. Most pathological processes manifest themselves as increased heat, and some neurological processes exhibit excessive cold or hypothermia. For example, breast disease can be detected by looking for areas of excessive or increasing heat, which may indicate areas of angiogenesis or growth of blood vessels supplied by a growing tumour.

Unlike X-ray, ultrasound magnetic resonance imaging (MRI), and virtually all other modern medical imaging modalities are designed to capture anatomical information, while thermochromic liquid crystal and medical infrared technology are designed to capture more physiological information. Examples of two thermograms of human hands performed by LCT (left) and DII (right) [42,50] are shown in Fig. 34.
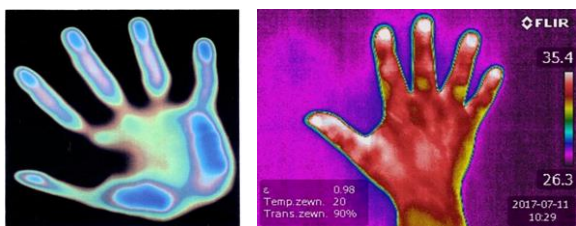
Fig. 34. Examples of two thermograms of human hands performed by LCT (left) and DII (right) [42,50].

6.6.1. Breast thermography

The distribution of temperature on the surface of the human body is determined by the temperature of the tissues of internal organs, the thermal conductivity of muscle and fat tissue, and the thermal emission of the skin. Hence, the temperature measured on the skin surface is a function of temperature of the internal organ and thermal properties of the tissues separating this organ from the body surface. An important role is also played by the processes of heat losses by convection and radiation through the skin, including gas exchange between the skin and the environment. Thermographic examinations are used both in the assessment of changes recorded on the skin surface and in relation to parenchymal organs located close to the skin surface. They provide opportunities for monitoring the circulatory system in both large and small vessels. It should be emphasized that very often temperature changes are one of the earliest symptoms of ongoing pathological processes. Therefore, both diagnostic methods, i.e. LCT and DII, are suitable for breast cancer screening (see Figs. 35 and 36).
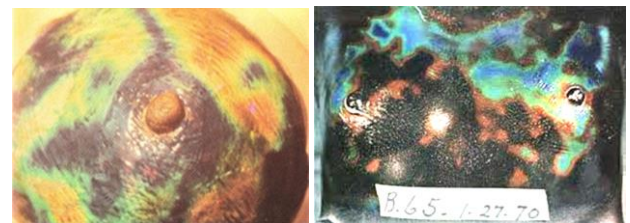
Fig. 35. Two examples of detection of breast cancer (dark region) by liquid crystal thermography. The blue and dark colours correspond to the higher temperature caused by inflammation [39].
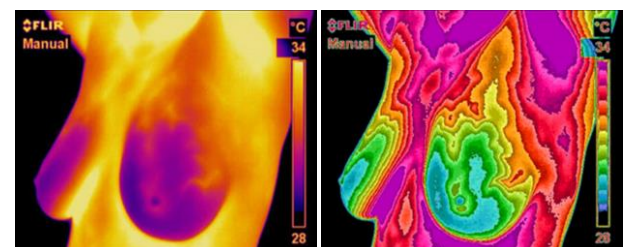
Fig. 36. Infrared image of human breast – left and a normal limited vascular pattern – right [38].

This kind of medical diagnosis (Figs. 35 and 36) should be confirmed by other independent methods (mammography ultrasound and MRI) in the case of disease suspicions.

6.6.2. Orthopedic application of LCT

In clinical studies of unspecified inflammatory conditions of orthopaedic diseases, liquid crystal thermography (LCT) can help in their identification. With its help, it is possible to localize the change and its extent, which may have an inflammatory, post-traumatic, degenerative, infectious or neoplastic origin. Most of these cause changes in the temperature of the synovial membrane and connective tissue, which can be recorded using very sensitive liquid crystals. On the basis of such changes, the level

of pathological changes can be estimated very quickly, and an example of such a disease is Raynaud's and Buerger's phenomenon, the pathological changes of which are presented using a thermogram as shown in the figures bellow:

* Raynaud's phenomenon (Symptoma Raynaud) is a vasomotor disorder characterized by sudden, well-demarcated blanching, then cyanosis and redness of the fingers, toes and rarely the nose and auricles, accompanied by numbness and pain. This happens because of spasms of blood vessels in those areas. The spasms happen in response to cold, stress or emotional upset (Fig. 37).
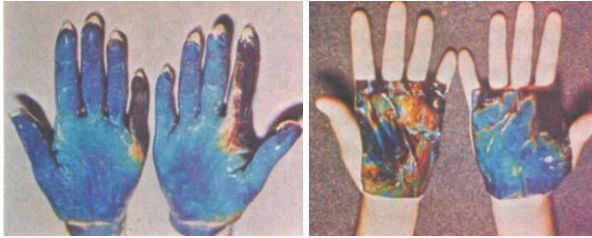
Fig. 37. Raynaud LC thermograms of vascular disease (left), and hand tumours (right) [40].

* Buerger's disease (known as Thromboangiitis Obliterans), is an inflammation of small and medium-sized blood vessels. Although any blood vessel can be affected, it usually presents with blockages in the arteries in the feet and hands, leading to severe pain and tissue damage (Fig. 38).
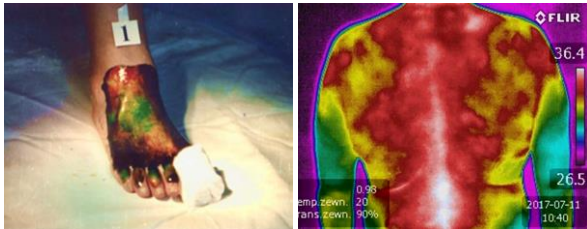
Fig. 38. Visualisation (by use of LCT) of lack of blood circulation caused by Buerger's disease (left) and DII thermogram of human back effected by muscular tensions (right) [39,50].

6.7. Advantages and disadvantages of TLC and DII

For surface or human body temperature measurement, special care is necessary to avoid specula light reflections form, irradiating or pulses, however some advantages and disadvantages of the use of TLC and DII are presented below:

❖ Advantages of TLC:
* Provides a quick visual qualitative observation of the surface temperature profile.
* Can be calibrated with a digital colour camera and isothermal surface control to provide accurate quantitative temperature fields to +/− 0.1°C.
* Typically operate between −30°C to 120°C with bandwidths of 0.1°C to 30°C.
* A high spatial resolution of around 1 μm, depends on camera optics.

* Provides both transient and steady-state surface temperature profiles.
* A fast time response of around 100 ms.
* Thermometry uses visible light and is independent of surface emissivity.
* Relatively cheap technique: camera, recorder, lighting etc.

❖ Disadvantages of TLC:
* Requires a stable uniform white light source with no infrared IR or ultraviolet UV components.
* IR will cause radiant heating of the surface, and UV will degrade the liquid crystal compounds.
* Must be calibrated in-situ using the same optics as the final experiment.
* Test subject must be prepared before measurements and the liquid crystals can be difficult to apply to complex surface geometries.
* Can be intrusive due to changes in the heat conduction properties of the body.
* Cannot be used for large subjects such as houses etc.

❖ Advantages and disadvantages of DII.
* Thermography has been shown effective as a standalone test for either breast cancer screening or diagnosis in detecting early stage breast cancer.
* Thermography has only been cleared by the official regulatory as an "adjunctive " tool – meaning for use alongside a primary test like mammography.
* Thermogram is no substitute for mammogram, it works by detecting increases in temperature.
* If the thermography detects any abnormalities, the person should seek further screening, which may include a mammogram. If a mammogram confirms that a lamp is present, the doctor may recommend an ultrasound or MRI scanning and a biopsy.
* Thermography produces a high number of false-positive and false-negative results and estimates of its sensitivity vary widely.
* In a positive way, thermography offers the following benefits: it is not painful, it is not invasive and it does not involve radiation.

7. Conclusions

Advanced experimental techniques, in this case, true-colour image processing of liquid crystal patterns, particle image velocimetry and infrared imaging allow new approaches to old problems and open up new areas of research and applications. Image processing data make available quantitative full field information about the distribution of temperature, heat transfer and adjunctive medical pathogenesis and diagnostics. It is evident from our research that liquid crystal and infrared imaging techniques have many applications, not only in testing but also in industry, medicine and home.

The presented overview provides an introduction to thermochromic liquid crystals, digital infrared imaging and particle image velocimetry, how these measurement techniques and methods work and how they are used.

References

[1] Baughn, J.W., Ireland, P.T., Jones. T.V., & Saniel, N. (1989). A comparison of the transient and heated-coating methods for the measurement of local heat transfer coefficients on a pin fin. *ASME Journal of Heat and Mass Transfer*, 111(4), 871−881. doi: 10.1115/1.3250800

[2] Bergles, A.E. (1997). Augmentation of heat transfer, single phase. In: *International encyclopaedia of heat and mass transfer* (Ed. Hewitt G.F., Shires G.L., Polezhaev Y.V.), 68−73, CRC Press, Boca Raton, Florida, USA.

[3] Ciofalo, M., Di Piazza I., & Stasiek, J.A. (2000). Investigation of flow and heat transfer in corrugated-undulated plate heat exchangers. *Heat and Mass Transfer*, 36, 449−462. doi: 10.1007/S002310000106

[4] Fiebig, M. (1996). Vortices: tools to influence heat transfer – recent developments. *Proceeding of 2nd European Thermal-Sciences and 14th UIT National Heat Transfer Conference*, 1, (pp. 41−56), 29−31 May, Rome. Italy.

[5] Fiebig, M., & Mitra, N.K. (1998). Experimental and numerical investigation of heat transfer enhancement with wing-type vortex generators. Chapter 8. In: *Computer Simulations in Compact Heat Exchangers*, (Ed. Sunden B., Faghri M.), *Computational Mechanics Publications*, 1, (pp. 227−254), Southampton, UK and Boston, USA

[6] Hippensteele, S.A., Russel, L.M., & Stepka, F.S. (1983). Evaluation of a Method for Heat Transfer Measurements and Thermal Visualization Using a Composite of a Heater Element and Liquid Crystals. *International Journal of Heat and Mass Transfer*, 105(1), 184−189. doi: 10.1115/1.3245539

[7] Jacobi, A.M., & Shah, R.K. (1995). Heat Transfer Surface Enhancement Through the Use of Longitudinal Vortices: A Review of Recent Progress. *Experimental Thermal and Fluid Science*, 11(3) 295−309. doi: 10.1016/0894-1777(95)00066-U

[8] Jones, T.V., & Hippensteele, S.A. (1998). *High-resolution heat transfer coefficient mops applicable to compound-curve surfaces using liquid crystals in a transient wind tunnel*. NASA Technical Memorandum 89855.

[9] Jones, T.V., Wang, Z., & Ireland, P.T. (1992). The use of liquid crystals in aerodynamic and heat transfer experiments. *Proc. 1st I. Mech. E. Seminar on optical methods and Data Process-ing in Heat and Fluid Flow*, 51−54, City University, London, UK.

[10] Leiner, W., Schulz, K., Behle, M., & Lorenz, S. (1996). Imaging techniques to measure local heat and mass transfer. *Proc. 3nd I. Mech. E. Seminar Optical Methods and Data Processing in Heat and Fluid Flow*, 1−13, City University, London, UK.

[11] Mikielewicz, D., Stasiek, A., Jewartowski, M., & Stasiek, J. (2012). Measurements of heat transfer enhanced by the use of transverse vortex generators. *Applied Thermal Engineering*, 49, 61−72. doi: 10.1016/j.applthermaleng.2011.11.013

[12] Simonich, J.C., & Moffatt, R.J. (1982), New technique for mapping heat transfer coefficient contours. *Review of Scientific Instruments*, 53(5), 678−683. doi: 10.1063/1.1137041

[13] Stasiek, J. (1998). Experimental study of heat transfer and fluid flow across corrugated-undulated heat exchanger surfaces. *International Journal of Heat and Mass Transfer*, 41, 899−914. doi: 10.1016/S0017-9310(97)00168-3

[14] Stasiek, J. (1997). Thermochromic liquid crystals and true-colour image processing in heat transfer and fluid flow research. *Heat and Mass Transfer*, 33, 27−33, Springer-Verlag. doi: 10.1007/S002310050158

[15] Stasiek, J., Ciofalo, M., & Wierzbowski, M. (2004). Experimental and Numerical Simulations of Flow and Heat Transfer in Heat Exchanger Elements Using Liquid Crystal Thermography. *Journal of Thermal Science*, 12(2), 133−137. Article ID: 1003-2169(2004)02-0133-05

[16] Stasiek, J.A., & Kowalewski, T.A. (2002). Thermochromic liquid crystals applied for heat transfer research. *Opto-Electronics Review*, 10(1), 1−10.

[17] Stasiek, J., Stasiek, A., Jewartowski, M., & Collins, M.W. (2006). Liquid crystal thermography and true-colour digital image processing. *Optics & Laser Technology*, 38(4−6,), 234−256. doi: 10.1016/j.optlastec.2005.06.028

[18] Tanda, G. (2001). Heat Transfer and Pressure Drop in a Rectangular Channel With Diamond-Shaped Elements. *International Journal of Heat and Mass Transfer*, 44, 3529–3541. doi: 10.1016/S0017-9310(01)00018-7

[19] Tanda, G. (2004). Heat Transfer in Rectangular Channels With Transverse and V-Shaped Broken Ribs. *International Journal of Heat and Mass Transfer*, 47, 229–243. doi: 10.1016/S0017-9310(03)00414-9

[20] Tanda, G., & Abram, R. (2009). Forced Convection Heat Transfer in Channels With Rib Turbulators Inclined at 45 deg. *ASME Journal of Turbomachinery*, 131. doi: 10.1115/1.2987241

[21] Tanda, G., Stasiek, J., & Collins, M.W. (1995). Application of holographic interferometry and liquid crystal thermography to forced convection heat transfer from a rib-roughened channel. *8th Int. Conference on Energy and Environment* (pp. 434−441), Shanghai, China. doi: 10.1615/1-56700-052-5.610

[22] Utriainen, E., & Sunden, B. (2002). Evaluation of the Cross Corrugated and Some Other Candidate Heat Transfer Surfaces for Microturbine Recuperators. *ASME Journal of Engineering for Gas Turbines and Power*, 124 (3). doi: 10.1115/1.1456093

[23] Valencia, A., Fiebig, M., Mitra, N.K., & Leiner, W. (1992). Heat transfer and flow loss in a fin-tube heat exchanger element with wing-type vortex generators. *Heat Transfer, 3rd UK National Conference Incorporating 1st European Conference on Thermal Sciences*, 16−18 September, Birmingham, UK.

[24] Vogel, G., Graf, A.B.A., von Walfersdorf, J., & Weigand, B. (2003). A Novel Transient Heater-Foil Technique for Liquid Crystal Experiments on Film-Cooled Surfaces. *ASME Journal of Turbomachinery*, 125, 529−537. doi: 10.1115/1.1578501

[25] Wierzbowski, M., & Stasiek, J. (2002). Liquid crystals technique application for heat transfer investigation in a fin-tube heat exchanger element. *Experimental Thermal and Fluid Science*, 26, 319−323. doi: 10.1016/S0894-1777(02)00143-7

[26] Hiller, W.J., & Kowalewski, T.A.(1986). Simultaneous measurements of temperature and velocity fields in thermal convective flows. In: *Flow Visualization IV* (Ed. Veret C., pp. 617−622). Hemisphere Publishing Corporation. Washington.

[27] Kowalewski, T.A., & Cybulski, A. (1996). Experimental and numerical investigations of natural convection in freezing water. *Int. Conference on Heat Transfer with Change of Phase in Mechanics*, Mechanics, 61, 7−16, Kielce, Poland.

[28] Kowalewski, T.A., Cybulski, A., & Rebow, M.(1998). Particle image velocimetry and thermometry in freezing water. *8th International Symposium On Flow Visualization*, Sorrento (Ed. Carlomagno G.M. and Grant I.), CD ROM Proc., 24.1−24.8, Edinburgh.

[29] Kowalewski, T.A., & Rebow, M.(1999). Freezing of water in the differentially heated cubic cavity, *International Journal of Computational Fluid Dynamics*, 11(3), 193−210. doi: 10.1080/10618569908940874

[30] Raffel, M., Willert, Ch.E., & Kompenhans, J. (1998). *Particle Image Velocimetry* (1st ed.). Springer Berlin, Heidelberg, Germany. doi: 10.1007/978-3-662-03637-2

[31] Tanaka, T. (1998). Visualisation of the temperature field in thermal storage tanks by using the thermosensitive liquid crystals sus-

pension method. *International Symposium Fluid Control, Measurement, Mechanics and Flow Visualisation*, 212−215.

[32] Tropea, C., Yarin, A.L., & Foss, J. (Eds). (2007). *Springer Handbook of Experimental Fluid Mechanics*. Springer-Verlag, Berlin, Heidelberg. Germany.

[33] Satta, F, & Tanda, G. (2014). Measurement of local heat transfer coefficient on the end wall of a turbine blade cascade by liquid crystal thermography. *Experimental Thermal and Fluid Science*, 58, 209−215. doi: 101016/j.expthermflusci.2014.07.005

[34] Borda, T., Flaszyński, P., Doerffer, P., Jewartowski, M., & Stasiek, J. (2015). Flow visualization and heat transfer investigations on the flat plate with stream-wise pressure gradient. *12th International Symposium on Experimental Computational Aerothermodynamics of Internal Flows*, Lerici, Italy.

[35] Ekkad, S.V., & Singh, P. (2021). Liquid Crystal Thermography in Gas Turbine Heat Transfer. A Review on Measurement Techniques and Recent Investigations. *Crystals*, 11(11) 1332, doi: 10.3390/cryst11111332

[36] Reinitzer, R. (1888). Beiträge zur Kenntniss des Cholestrins. *Monatshefte für Chemie*, Wien, 9, 421−441. doi: 10.1007/BF01516710

[37] Polidori, G., Renard, Y., Lorimier, S., Pron, H., Derrau, S., & Taiar, R. (2017). Medical Infrared Thermography assistance in the surgical treatment of axillary Hidradenitis Suppurativa: A case report. *International Journal of Surgery Case Reports*, 34, 56−59. doi: 10.1016/j.ijscr.2017.03.015

[38] Seymour, T. (2019). *Breast thermography: what you need to know*. https://www.medicalnewstoday.com [accessed 22 Jan. 2025].

[39] Żmija, J., Klosowicz, S., & Borys, S. (1989). *Cholesteric Liquid Crystals in a Detection of Radiation*. WNT, Warsaw (in Polish).

[40] Shlens, M., Stoltz, M.R., & Benjamin, A. (1975). Orthopaedic applications of liquid crystal thermography. *The Western Journal of Medicine*, 122, 367−370.

[41] Podbielska, H., & Skrzek, A. (Eds.). (2014). *Biomedical applications of thermovision*. Wroclaw University of Technology, Poland (in Polish).

[42] Stasiek, J., & Jewartowski, M. (2017). Liquid Crystals, PIV and IR-Photography in Selected Technical and Biomedical Applications. *IOP Conf. Series: Materials Science and Engineering*, 249, 012010. doi: 10.1088/1757-899X/249/1/012010

[43] Kesztyüs, D., Brucher, S., Wilson, C., & Kesztyüs, T. (2023). Use of Infrared Thermography in Medical Diagnosis, Screening, and Disease Monitoring, A Scoping Review. *Medicina*, 59(12), doi: 10.3390/medicina59122139

[44] Moffat, R. J. (1990). Experimental Heat Transfer. *Proc. 9th Int. Heat Transfer Conference*, 1, 187−205, 19−24 August, Jerusalem, Israel. doi: 10.1615/IHTC9.1900

[45] Dierking, I. (2014). Chiral Liquid Crystals: Structures, Phases, Effects. *Symmetry*, 6(2), 444−472. doi: 10.3390/sym6020444

[46] Klein, E.J. (1968). Application of liquid crystals to a boundary layer flow visualisation. *American Institute of Aeronautics and Astronautics. Meeting: Aerodynamic Testing Conference*, 8−10 April, San Francisco, USA.

[47] Klein, E.J., & Margozzi, A.P. (1969). *Exploratory investigation on the measurement of skin friction by means of liquid crystals*. NASA TM-X-1774.

[48] Stasiek, J., & Collins, M.W. (1996). The use of liquid crystals and true-colour image processing in heat and fluid flow experiments. *Atlas of Visualization*, 2, CRC Press, Inc., New York, USA.

[49] Bagavathiappan, S, Lahiri, B.B., Saravanan, T., Philip, J., & Jayakumar, T. (2013). Infrared thermography for condition monitoring – A review. *Infrared Physics & Technology*, 60, 35−55, doi:10.1016/j.infrared.2013.03.006

[50] Stąsiek, J., Jewartowski, M., & Stąsiek, A. (2016). *Liquid crystal thermography and image anemometry in selected technical applications*. AGNI Publisher Pruszcz Gdanski, Poland (in Polish).

[51] Strugała, G., Klugmann, M., Landowski, M., Szkodo, M., & Mikielewicz, D. (2018). A universal NDT method for examination of low energy impact damage in CFRP with the use of TLC film. *Non-destructive Testing and Evaluation*, 33(3), 315−328, doi: 10.1080/10589759.2018.1428323

[52] Bizzarri, M., Conti, P., Glicksman, L.R., Schito, E., & Testi, D. (2024). Evaluation by Liquid Crystal; Thermography of Transient Surface Temperature Distribution in Radiant Floor Cooling Applications and Assessment of Analytical and Numerical Models. *Journal of Heat and Mass Transfer*, 146(5), doi: 101115/1.4064707

[53] Kumar, D., Choudhury, R., & Layek, A. (2022). Application of liquid crystal thermography for temperature measurement of the absorber plate of solar air heater. *Materials Today; Proceedings*, 59, 605−611, doi: 1016/j.matpr.2021.12.09

[54] Hallcrest Ltd. (2014). *Handbook of Thermochromic Liquid Crystal Technology*. LCR Hallcrest.

[55] C.I.E. (1976). *UCS Chromaticity Diagram*. https://www.ledtronics.com (Google Scholar) [accessed 22 Jan. 2025].

[56] Data Translation Ltd. (1991). *Image Processing Handbook*. USA.

[57] MERC Ltd. (1994). *Poole, Dorset, UK Thermochromic Liquid Crystals – Manufacturer's catalogue*.

[58] B.D.H. Limited. *Advanced Materials Division*. UK.

[59] B & H Liquid Crystal Devices Ltd. (1992). London, UK.

[60] *Beginnings of Quantum Mechanics*. http://260h.pbworks.com [accessed 22 Jan. 2025].

Appendix

Figures 39, 40 and 41 show early results from liquid crystal thermography, where the heat transfer coefficients were determined from colour photographs taken with a photo camera. The resulting temperature distributions and subsequently Nusselt numbers on the surfaces in question were taken manually from the images projected onto a screen and reproduced with hand-coloured markers. For comprehensive quantitative local heat transfer data, the visibly sharp line of the spectrum was obtained at different fluid temperatures for the same Reynolds number. Afterwards as shown above the subsequent thermographic studies were carried out using full automatic colour image processing from Data Translation Ltd., USA.
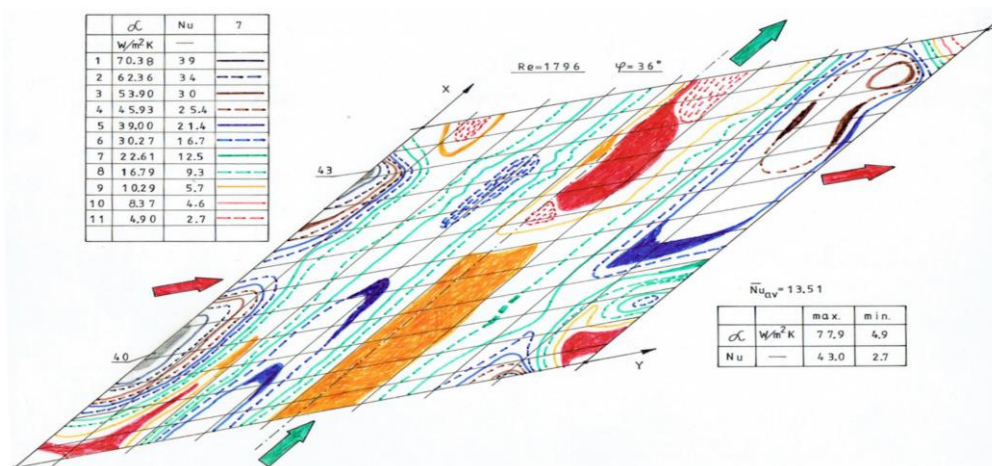
Fig. 39. Visualisation of the distribution of local Nusselt number values on the lower corrugated surface;
b = 36 deg, Re = 1796, P/Hi = 3.67 (manual method).

Fig. 40. Visualisation of the distribution of local Nusselt number values on the lower corrugated surface;
b = 36 deg, Re = 3394, P/Hi = 3.67 (manual method).
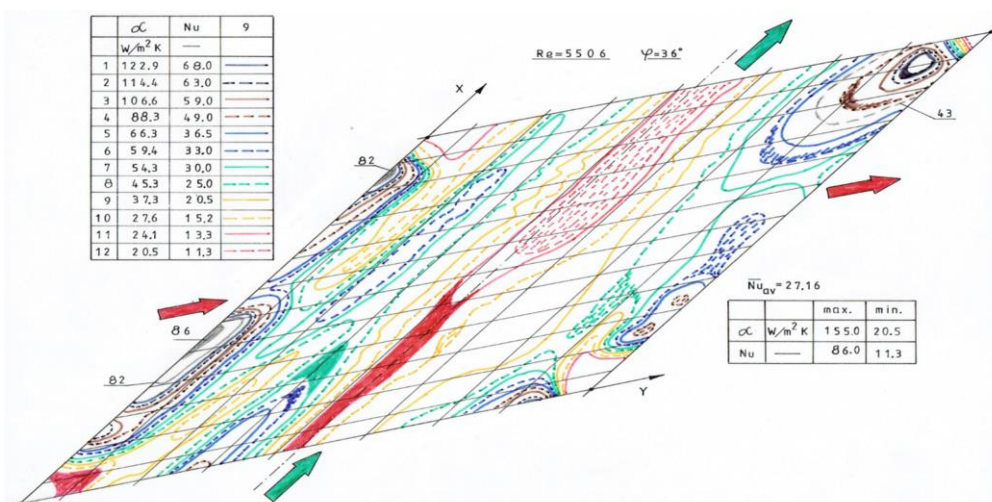
Fig. 41. Visualisation of the distribution of local Nusselt number values on the lower corrugated surface;
b = 36 deg, Re = 5506, P/Hi = 3.67 (manual method).

ARCHIVES OF THERMODYNAMICS

Comprehensive optimization of a novel thermo-hydraulic machine for mechanical power generation

Asmaa Guelib[a], Djallel Zebbar[b*], Zakaria Rahmani[b], Souhila Zebbar[b],
Kouider Mostefa[b], Sahraoui Kherris[b], Said Mekroussi[a]

[a]Research Laboratory of Industrial Technologies, Departmentof Mechanical Engineering, Faculty of Applied Sciences,
Ibn Khaldoun University, B.P. 78 Zaâroura 14000 Tiaret, Algeria
[b]Laboratory of Mechanical Engineering, Materials and Structures, Faculty of Sciences and Technology, Tissemsilt University –
Ahmed ben Yahia Elwancharissi, Benhamouda B.P 182, 38010 Tissemsilt, Algeria
*Corresponding author email: djallel.zebbar@univ-tissemsilt.dz

Abstract

This paper is dedicated to the multi-aspect optimization of a novel thermo-hydraulic machine with liquid piston operating according to organic Rankine cycle, designed for mechanical power generation from low temperature reservoirs. This involves the implementation of thermodynamic and hydraulic analyses. Several issues have been identified in thermo-hydraulic machines built to date, particularly the limitation imposed by the location of the expansion phase under the equilibrium dome, which constrains maximum output work. This issue is addressed through the application of steam superheating followed by the organic Rankine cycle. The thermodynamic analysis showed that the R1233zd is the most suitable working fluid for the suggested novel machine within the temperature range of 65−130°C. The selection of the best working fluid was followed by the dimensioning of the hydraulic part of the machine under optimal operating conditions. A new parameter was introduced to link the gas and hydraulic sides of the machine. It is about the time scale of the cycle which influences significantly the mechanical output power. Furthermore, mathematical modelling of the hydraulic part of the machine concludes that high mechanical power output can only be achieved only in modes of operation with high thermal efficiencies. Conversely, operational modes with high second law efficiencies fail to deliver high mechanical power levels. These two conclusions can be regarded as equivalent to the various postulates of the second law of thermodynamics.

Keywords: Thermo-hydraulic machine; Organic Rankine cycle; Liquid piston; Mechanical power generation

1. Introduction

Fossil fuels, including coal, oil, and gas, have served as the backbone of the global energy supply for the past century. However, since the beginning of the twenty-first century, their extensive use is increasingly recognised as unsustainable due to several significant issues. Foremost among these are their environmental impacts. Large quantities of greenhouse gases, particularly carbon dioxide (CO_2), are released through the combustion of fossil fuels, contributing significantly to global warming and climate change. Another critical issue is the non-renewable nature of fossil fuels, which presents inherent limitations [1].

Nomenclature

d – diameter of the hydraulic pipe, m
D – diameter of the transfer cylinder, m
f – frequency, 1/s
g – gravitational acceleration, m/s^2
GWP – global warming potential
h – specific enthalpy, J/kg
H – height, m
K – flow coefficient, m^3/s
$\dot{m}$ – mass flow rate of the cycle, kg/s
ODP – ozone depletion potential
P – power, W
p – pressure, Pa
Q – specific heat exchanged during transformation, J/kg
Re – Reynolds number
T – temperature, K
v – specific volume, m^3/kg
$\dot{V}$ – flow rate, m^3/s
V – velocity, m/s
W – specific work, J/kg
y – extraction ratio

Greek symbols

ΔH – height difference, m
Δp – pressure difference, Pa
η – efficiency
v – specific volume, m^3/kg
ρ – density of the fluid, kg/m^3

σ – kinematic viscosity, m²/s
τ – duration of a thermodynamic cycle, s

Subscripts and Superscripts

cond – condenser
evap – evaporator
exp – expansion
h – height
hyd – hydraulic
in – inlet
II – second
l – low
LT – work-transfer liquid
max – maximal
min – minimal
opt – optimal
sc – superheated
th – thermal
vs – valves

Abbreviations and Acronyms

CAPILI – Carnot with piston liquid
CT, CT' – transfer cylinders
FLP – pressurized fluid of liquid piston
ORC – organic Rankine cycle
ORPILI – organic Rankine cycle with liquid piston
OTEC – ocean thermal energy conversion

The widespread adoption of non-conventional energy sources and technologies to reduce reliance on fossil fuels has been driven by the pursuit of a sustainable and clean environment [2]. These energy sources, known as renewable energy sources, offer numerous advantages beyond their economic and social benefits. They encompass solar, wind, geothermal, biomass, and ocean thermal energy.

Solar energy, including both thermal solar energy and photovoltaic (solar electrical), stands out as one of Earth's major available energy sources compared to other forms. Its utilization spans a long history of applications in residential, vehicular, aerospace and naval sectors [3]. Wind energy is another significant player in the global energy market, representing a substantial and growing sector in renewable energy production [4].

Geothermal energy taps into the Earth's internal heat. Beneath the Earth's crust lies a layer of dense, molten rock that often contains water reservoirs, occasionally surfacing as hot springs. When not naturally accessible, this heated water can be extracted through drilling. It serves as a virtually cost-free energy source, whether used directly as hot water, steam, or heat, or to generate electricity [5].

Biomass energy, also known as bioenergy, derives from the conversion of biomass into various forms of energy such as electricity, heat, power, or transportation fuels. Biomass qualifies as a renewable energy source due to its ability to cultivate, harvest, and regenerate trees and plants within short timeframes. Additionally, this process consistently yields residues, wastes, and gases [6].

In addition, ocean thermal energy has gained significant recognition over the past decade as a renewable energy source for sustainable energy production systems. Ocean thermal energy conversion (OTEC) technology harnesses clean power from the natural thermal gradient between different layers of seawater. This temperature gradient is considered a self-replenishing energy source [3], driven by natural processes within the ocean.

Low-temperature energies, including industrial waste heat, low-temperature geothermal energy, and solar thermal energy, present promising solutions for enhancing energy efficiency and sustainability [7]. Power generation plays a crucial role in utilizing and recycling these low-temperature heat sources [8]. Thermo-hydraulic energy conversion systems, which transform thermal energy into hydraulic or mechanical energy, are increasingly gaining attention for their potential applications in both power generation and industrial processes. These systems are particularly suitable for generating mechanical power from low-temperature heat reservoirs such as solar and geothermal sources.

Consideration should be given to thermo-hydraulic conversion systems, such as those employing liquid piston technology to generate power. Liquid pistons are devices that utilize a liquid to produce mechanical movement or perform work, a concept pioneered by Humphrey in 1909 [9]. Humphrey later advanced this technology by developing an internal combustion engine based on the Atkinson cycle, which found extensive use in pumping stations and irrigation applications.

Liquid piston technology has undergone significant evolution and has found application across various fields and systems.

Van de Ven et al. [10] advocated for the liquid piston concept as a solution to challenges encountered in designing fluid engines and Stirling pumps. This concept is also integral to the operation of steam and refrigeration machines [11–13].

The thermo-hydraulic process CAPILI (Carnot with piston liquid) illustrates the application of liquid piston technology, marking significant advancements in renewable energy. This technology has been successfully utilized in OTEC power production [14], as well as in residential applications [15]. This thermo-hydraulic process can operate either in engine mode, where the evaporator temperature is higher than the condenser temperature (used for cogeneration or electricity production), or in receiver mode, where the evaporator temperature is lower than the condenser temperature (employed for heat pump or refrigeration purposes) [16]. The CAPILI process, whether configured as an engine or heat pump, is designed in two primary configurations: the "1st type" or the "2nd type," corresponding to these operational modes. The 2nd type CAPILI process closely adheres to the Carnot cycle, while the 1st type CAPILI process exhibits slight deviations [15].

The CAPILI engine typically comprises two cylinders connected to separate heat exchangers (evaporator and condenser), operating at different pressures. The transfer of work between the machine and its surroundings is facilitated by a hydraulic/mechanical converter, through which a liquid circulates alternately between the evaporator and the condenser during the isothermal phases of the cycle [16]. The work-transfer liquid (LT) in the CAPILI machine is required to have a very low saturation pressure (such as oil) at the process operating temperatures and must be immiscible with, and ideally denser than, the working fluid [15]. The working fluids used in these machines include pure substances or azeotropic mixtures (such as hydrocarbons, hydrofluorocarbons (HFCs), H_2O, etc.), which closely approximate or mimic the Carnot cycle (motor or receiver).

For a comprehensive understanding of the current study, it is essential to review previous research conducted on the CAPILI thermo-hydraulic machine. This process has been extensively investigated in several prior studies [14–19]. Semmari et al. [14] extensively examined the CAPILI process, investigating its performance, selecting appropriate working fluids, and developing dynamic models to simulate its behavior within OTEC power plants. Mauran et al. [15] presented the thermo-hydraulic CAPILI process with the primary objective of achieving optimal efficiency. They conducted a comprehensive analysis of thermodynamic cycles, explored various applications such as trigeneration, and assessed the system's performance and sustainability advantages. Additionally, the same authors [15] emphasized the potential of the CAPILI system to enhance energy efficiency and reduce greenhouse gas emissions in both residential and commercial sectors. Stitou [16] provided a comprehensive analysis of the CAPILI thermo-hydraulic process, offering analytical tools and effective solutions for examining the transformation and conversion of thermal energy through thermo-hydraulic processes. Borgogno et al. [17] investigated the application of the CAPILI process in trigeneration for residential areas, while Semmari et al. [18] conducted experimental validation of an innovative analytical model for a thermo-hydraulic CAPILI

system designed for re-sidential use, emphasizing hydraulic resistance as a foundational concept. Zebbar et al. [19] conducted a thermodynamic analysis of a machine operating under the first type of CAPILI cycle, designed to convert low-grade heat sources such as solar and geothermal energy into mechanical power. They identified n-butane (R-600) as the optimal working fluid, achieving peak thermal efficiencies of 20.3%, Carnot efficiencies of 23%, and second law efficiencies of 88% at specific operating temperatures of 30°C for the condenser and 120°C for the evaporator.

This brief review encompassed renewable energy sources for sustainable environments, previous studies on liquid pistons, and the thermo-hydraulic CAPILI process. It has highlighted several shortcomings in the current CAPILI machine.

In the previous research on the CAPILI thermo-hydraulic process, the working fluid undergoes continuous state changes, alternating between liquid and vapour phases. A significant challenge involves compressing a two-phase mixture or extracting work from an isentropic two-phase expansion [20]. The liquid piston plays a crucial role in overcoming this challenge, enabling the CAPILI cycle to operate without the necessity for superheating or subcooling the working fluid prior to expansion or compression. Consequently, thermodynamic irreversibilities are minimized in CAPILI cycles, leading to an enhanced overall efficiency of the cycle [20]. Furthermore, the patent of the Research Laboratory in Engineering, Materials and Structures [21], filed in March 2022 at the Algerian National Institute of Industrial Property (*Institut National Algérien de la Propriété Industrielle*), identified a critical issue with the CAPILI cycle related to the location of the expansion phase under the equilibrium dome. This positioning maintains the maximum temperature in the cycle significantly above the critical temperature of the working fluid, thereby restricting the maximum output work or mechanical power per unit mass of the working fluid. Moreover, in the same patent [21], it is reported that the CAPILI machine depends on a very complex control system consisting of several solenoid valves and sensors to reverse the direction of flow in the hydraulic motor and finally, the existing thermo-hydraulic CAPILI machine has a condensate transfer pump driven by an electric motor, which is far from practical.

The issues mentioned above were addressed in the Research Laboratory in Engineering, Materials and Structures patent [21] through several advancements. Firstly, steam superheating was introduced to raise the average temperature of heat input within the cycle, transitioning it into an organic Rankine cycle variant known as ORPILI (organic Rankine with piston liquid). Secondly, the proposed novel configuration of the ORPILI thermo-hydraulic machine reduced the number of solenoid valves by implementing a mechanical transmission. Thirdly, a steam turbine was integrated to drive the transfer pump, enhancing the efficiency and performance of the system.

This study aims to argue in favour of the novel ORPILI machine through thermo-hydraulic analysis. The primary objective is to increase the specific mechanical work output (or mechanical power) of the thermo-hydraulic machine while maintaining efficiencies similar to those of the CAPILI cycle. This enhancement is made possible by integrating a steam superheater, which

allows for an increase in the average temperature of the heat input into the cycle. Hence, the move to the organic Rankine cycle with superheating.

Therefore, the following objectives are set for this study:

- Develop a comprehensive thermodynamic model and analysis for the proposed ORPILI cycle.
- Evaluate the performance of the ORPILI cycle using different working fluids (e.g. R600a, R600, R1234ze, R1234yf, R1233zd, and SESE36).
- Dimension the hydraulic components of the proposed machine according to the input thermal power.

These objectives are crucial for substantiating the efficiency and feasibility of the ORPILI machine, as discussed earlier.

This paper is structured as follows: first, a description of the novel configuration of the thermo-hydraulic machine is presented in Section 2. A thermodynamic analysis is discussed in Section 3, followed by the results and discussion in Section 4. Section 5 provides the hydraulic analysis, with the main findings discussed in Section 6. Finally, concluding remarks are presented in Section 7.

2. Description of the novel concept of the organic Rankine thermo-hydraulic machine with liquid piston

2.1. Structure

The component layout of the proposed thermo-hydraulic system is illustrated in Fig. 1. The system consists of an evaporator (3) connected to the heat source at the high-temperature, $T_{evap} = T_h$, a condenser (4) connected to the heat sink at the low-temperature, $T_{cond} = T_l$, two insulated work-transfer cylinders (1) and (19), steam turbine (5), a transfer pump (6) driven by superheated steam for transferring the condensate to the evaporator, and to maintain the pressure difference or drop between the

evaporator and the condenser ($\Delta p = p_{evap} - p_{cond}$), a superheater (2), two hydraulic motors (7) and (8) coupled through a pair of gears (9) and (11), a generator (10), a 2-way solenoid valve (12) and (13), an extraction steam valve (14), four non-return valves (15)−(18) and level sensors (20) and (21).

2.2. Principle of operation

The novel thermo-hydraulic machine presented in this work operates as follows: heat is introduced in the evaporator (3), where the working fluid evaporates and proceeds into the superheater (2). Then, the steam passes through the solenoid valve (12) and enters the work-transfer cylinder (19). The steam acts on the surface of the liquid which plays the role of liquid piston. It is possible to insert a movable wall such as a diaphragm between the liquid and the steam to avoid their direct contact. The pressurized fluid of the liquid piston (FLP) passes into the hydraulic motor (7), which is coupled to a generator (10) via a freewheel. The FLP then moves to the work-transfer cylinder (1) through the non-return valve (16). During this phase, the solenoid valve (13) connects the steam space in the work transfer cylinder (1) with the condenser (4) at a pressure p_{cond}. The condensate in the condenser (4) is pumped to the evaporator (3) by pump (6), which is driven by the steam turbine (5). The steam turbine (5) is supplied from the superheater (2) through the extraction valve (14). In addition to transferring the condensate, the pump maintains the pressure drop between the evaporator and the condenser ($\Delta p = p_{evap} - p_{cond}$). When the free level of FLP reaches the designated level detected by the level sensor (20), the non-return valves (16) and (18) are activated to change the direction of flows. In this case, the superheated steam passes into the work transfer cylinder (1). The pressure created by the steam above the surface of the liquid piston returns the hydraulic oil to the hydraulic motor (8) through the non-return valve (16). The hydraulic motor (8) is coupled to the generator (10) via a pair of
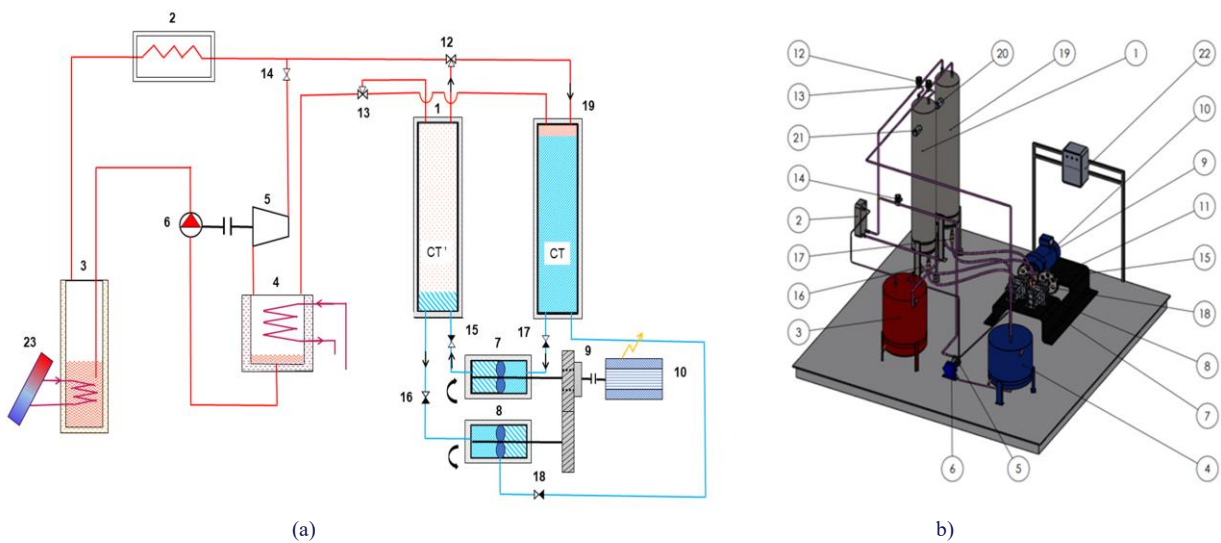
Fig. 1. (a) Schematic and (b) 3D drawing of the novel ORPILI thermo-hydraulic machine : (1) − work-transfer cylinder CT', (2) − superheater, (3) − evaporator, (4) − condenser, (5) − steam turbine, (6) − transfer pump, (7) and (8) − hydraulic motors, (9) − gear, (10) − generator, (11) − gear, (12) and (13) − 2 way solenoid valve, (14) − extraction steam valve, (15)−(18) − non-return valves, (19) − work-transfer cylinder CT, (20) and (21) − level sensor, (22) − panel board, (23) − solar collector.

gears (9) and (11) and the freewheel. Then, the hydraulic oil exits the hydraulic motor (8), passes through the non-return valve (18), and enters the work transfer cylinder (19). The liquid piston then pushes the working fluid steam towards the condenser (4) via the solenoid valve (13). Once the FLP has reached the designated level, which is detected by the level sensor (21), the solenoid valves (12) and (13) are activated, and the cycle begins again.

2.3. Description of the thermodynamic cycle

The operation of the proposed system's ORPILI cycle involves two half cycles, where the roles of the work-transfer cylinders are alternated. The working fluid follows the thermodynamic cycle denoted as (1-2-3-4-5), illustrated schematically in Mollier's p-h diagram (pressure vs. enthalpy) in Fig. 2, depicting the fundamental processes and heat transfers within the system. This novel machine operates on a Rankine-type cycle using superheated steam, with a steam generator operating at high pressure and temperature (T_{evap}, p_{evap}), and a condenser operating at low pressure and temperature (T_{cond}, p_{cond}).

The working fluid undergoes four processes: compression, evaporation, expansion, and condensation in sequence to complete a cycle.

The liquid-phase working fluid at low-pressure p_l at state **1** is directed into the pump, where it is isentropically compressed to match the operating pressure of the evaporator at state **2** at high pressure p_h. The pump operates without any heat transfer occurring around it.

2→4: Isobaric heat addition. The working fluid enters the evaporator as a compressed liquid at state **2** and leaves as a superheated vapor at state **4**.

4→5: Isentropic expansion. The superheated vapour at state **4** exits the evaporator and enters the CT, where it undergoes isentropic expansion. The pressure and the temperature of vapour drop during this process to the values at state **5**. During this process, the vapour displaces the transfer liquid (LT) towards the CT' until the liquid reaches the high level.

Fig. 2. Mollier p-h diagram of the proposed system.

5→1: Isobaric heat rejection in the condenser. The vapour displaced from the CT' during the previous process undergoes isobaric condensation in the condenser.

The performance analysis of the ORPILI thermodynamic cycle for various working fluids is carried out using the mathematical model presented in the next section.

3. Thermodynamic analysis

The ORPILI thermo-hydraulic machine proposed in this study operates within the following temperature ranges: superheating temperatures range from 65°C to 130°C, while evaporation occurs between 60°C and 120°C. However, the temperature at the condenser remains constant at 30°C. These temperature ranges were chosen to evaluate the thermodynamic efficiencies of the machine when using different working fluids.

In this context, various refrigerants are used in low-temperature applications to meet specific performance and environmental criteria, including HFC such as R134a, R152, and others. These refrigerants are harmless to the ozone layer, as they possess a zero ozone depletion potential (ODP) due to the absence of chlorine atoms [22]. Furthermore, HFCs have been subject to regulations under the Kyoto Protocol and the European F-Gas Regulation, aiming to gradually phase out their use by 2030. This is due to their high global warming potential (GWP), which exceeds 150 [23].

Compared to chlorofluorocarbons (CFCs), hydrochlorofluorocarbons (HCFCs) and HFCs, hydrocarbon-based refrigerants (HC) offer a more environmentally friendly alternative. They have a negligible impact on ozone depletion (ODP = 0) and exhibit a minimal potential for contributing to global warming (GWP ≈ 20). However, it should be noted that these refrigerants are highly flammable, necessitating stringent safety measures in both production and usage. Certain hydrocarbons, such as R600a (butane), find application in limited amounts in domestic refrigeration systems, such as household refrigerators [22].

Lastly, hydrofluoroolefin (HFO) gases such as R1234yf, R1234ze, R1233zd, etc. are considered as a new generation of refrigerants (4th generation) and are intended to replace older refrigerants like freons (R134a and R32) in various refrigeration engineering applications (refrigeration, heat pumps, air conditioning, automotive air conditioning, etc.) [23].

Taking into account the aforementioned arguments, the following working fluids are adopted and evaluated for the present ORPILI cycle: R600a, R600, R1234yf, R1234ze, R1233zd, and SES36.

In the thermodynamic analysis, the inputs and outputs of the condensate pump are characterised by the enthalpies h_1 and h_2, respectively, which are dependent on temperature and pressure.

The fluid state at the turbine inlet can be specified by the evaporating pressure and superheat degree. Using CoolProp library [24], parameters such as specific enthalpy and entropy can be calculated. The mathematical equations employed for the thermodynamic analysis of the ORPILI cycle, as detailed in Subsection 2.3, together with the thermal and second law efficiencies, are presented in Table 1. The work performed by the
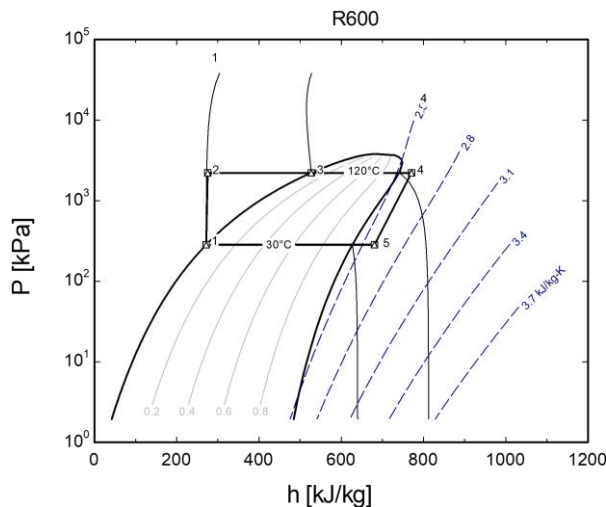
Table 1. Formulas for ORPILI system.

Item	Thermodynamic formula	No.
Pump work	$W_{pump} = (h_2 - h_1) = v_1(p_2 - p_1)$	(1)
Turbine work	$W_{turbine} = y(h_4 - h_5)$	(2)
Energy balance	$W_{turbine} = W_{pump}$	(3)
	$y(h_4 - h_5) = (h_2 - h_1)$	(4)
	$y = \dfrac{(h_2 - h_1)}{(h_4 - h_5)}$	(5)
Expansion work	$W_{exp} = (1 - y)(h_4 - h_5)$	(6)
Net work developed by the cycle	$W_{cycle} = W_{exp} - W_{pump}$	(7)
Thermal efficiency of the cycle	$\eta_{th} = \dfrac{W_{cycle}}{Q_{in}} = \dfrac{((1-y)(h_4 - h_5)) - (h_2 - h_1)}{(h_4 - h_2)}$	(8)
2nd law efficiency	$\eta_{II} = \dfrac{\eta_{th}}{\eta_{Carnot}}$	(9)

pump is given by Eq. (1), while the work generated by the turbine is expressed in Eq. (2). The system's energy balance, outlined in Eqs. (3) and (4), allows for the calculation of the steam extraction ratio, as shown in Eq. (5). The specific expansion work is defined by Eq. (6), whereas the net specific work of the cycle is determined by Eq. (7). The thermal efficiency of the cycle (Eq. (8)) is calculated by the ratio of the net specific work to the specific heat input, while the second law efficiency given by Eq. (9) is used to assess the system's performance relative to the ideal thermodynamic process.

4. Results and discussion of the thermodynamic analysis

The variations in thermal (η_{th}) and second law (η_{II}) efficiencies for the six refrigerants are shown in Table 2, which is, in fact, the synthesis of the results of several previous calculations. These calculations involved determining the thermal and second law efficiencies for various superheat temperatures, each time the evaporation temperature (T_{evap}) was fixed. The superheat temperature was varied within the range of $T_{evap} + 5°C$ to 130°C. Within this range, the thermal and second law efficiencies were

calculated. The retained values correspond to the maximum efficiencies.

It is evident from this table that the thermodynamic cycle of the novel ORPILI thermo-hydraulic machine operating with the refrigerants R1234yf and R1234ze develops lower thermal efficiencies compared to other fluids, equal to 11.6% and 13.9 %, respectively. This indicates that these working fluids are not suitable for this type of machine.

Furthermore, the machine achieves optimal performance within the temperature range of 65°C to 120°C when using refrigerants R600a, R600, R1233zd, and SES36. Among these, the maximum thermal efficiencies recorded are 16.1%, 16.9%, 17.5%, and 15.6%, respectively.

The thermal efficiency (η_{th}) reaches a maximum value of 17.5% with the refrigerant R1233zd at a superheat temperature (T_{sc}) of 130°C, matching to a second law efficiency (η_{II}) equal to 78.7%. The corresponding Carnot efficiency and pressure drops are about 22.4% and 1416.4 kPa, respectively (Fig. 3). Based on the aforementioned selection criteria, the results suggest that R1233zd fluid is the most suitable.

The hydrofluoroolefin gas R1233zd is identified as the most suitable working fluid for CAPILI applications, serving as a re-

Table 2. Thermal and second law efficiencies according to the superheated temperature.

T_{sc} (°C)	R600a η_{th}	R600a η_{II}	R600 η_{th}	R600 η_{II}	SES36 η_{th}	SES36 η_{II}	R1233zd η_{th}	R1233zd η_{II}	R1234ze η_{th}	R1234ze η_{II}	R1234yf η_{th}	R1234yf η_{II}
65	0.078	0.871	0.080	0.888	0.072	0.799	0.081	0.903	0.077	0.852	0.073	0.817
70	0.089	0.855	0.090	0.873	0.082	0.789	0.092	0.889	0.086	0.833	0.082	0.795
75	0.098	0.839	0.100	0.859	0.091	0.779	0.102	0.877	0.095	0.815	0.090	0.773
80	0.107	0.824	0.109	0.846	0.099	0.769	0.112	0.864	0.103	0.797	0.097	0.752
85	0.115	0.809	0.118	0.832	0.107	0.759	0.121	0.852	0.110	0.779	0.103	0.729
90	0.122	0.7941	0.126	0.819	0.115	0.748	0.129	0.840	0.117	0.760	0.109	0.707
95	0.129	0.780	0.133	0.807	0.122	0.739	0.137	0.829	0.123	0.743	0.113	0.683
100	0.135	0.767	0.140	0.794	0.129	0.728	0.144	0.817	0.127	0.724	0.116	0.699
105	0.141	0.752	0.147	0.782	0.135	0.718	0.151	0.806	0.132	0.704	–	–
110	0.147	0.739	0.153	0.770	0.141	0.709	0.158	0.796	0.136	0.683	–	–
115	0.152	0.725	0.158	0.758	0.146	0.699	0.164	0.785	0.139	0.698	–	–
120	0.156	0.711	0.164	0.746	0.151	0.689	0.170	0.774	–	–	–	–
125	0.159	0.698	0.164	0.747	0.156	0.679	0.175	0.764	–	–	–	–
130	0.161	0.702	0.169	0.736	0.155	0.676	0.175	0.766	–	–	–	–
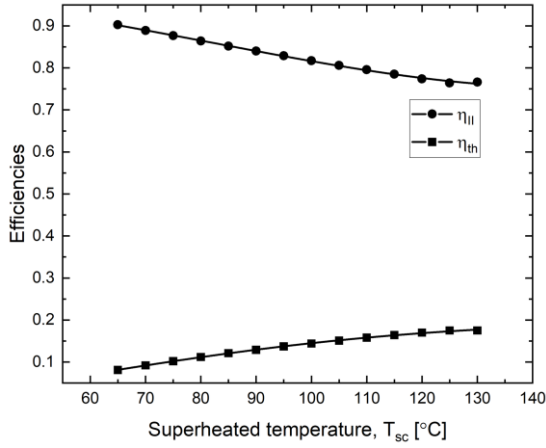
Fig. 3. Variation of efficiencies (η_{th}, η_{II}) with the superheated temperature of R1233zd as the working fluid.

placement for R123, which was previously extensively utilized in organic Rankine cycle (ORC) applications. In addition, R1233zd has a limited environmental impact, is completely non-flammable, and is non-toxic [25].

5. Hydraulic analysis

In this section, mathematical modelling of the hydraulic part of the novel ORPILI thermo-hydraulic machine configuration is addressed. This aspect of the study highlights the originality of the proposed concept. Based on the calculations carried out and the selection of the suitable working fluid R1233zd for this system application, a series of analyses have been developed to study the behaviour of the hydraulic system (Fig. 4) within the new proposed cycle with the fluid R1233zd. These analyses demonstrate the impact of changes on the overall cycle, particularly with variations in temperatures: $T_{sc} = 65{-}130°C$, $T_{evap} = 60{-}120°C$, and $T_{cond} = 30°C$.

Hence, two operating cases are highlighted and analysed. The first one corresponds to the operating regime with a maximum value of thermal efficiency $\eta_{th\_max} = 17.5\%$ and

pressure drop equal $\Delta p = 1416.4$ kPa, while the second case corresponds to the operating regime with a maximum value of second law efficiency $\eta_{II\_max} = 90.25\%$ and a pressure drop $\Delta p = 235.3$ kPa. However, in both cases, the total height corresponding to the height between the transfer liquid levels in transfer cylinders is adopted equal to $\Delta H = (H_1 - H_2) = 0.1$ m (Fig. 4). This hypothesis is demonstrated later. Finally, the density of the transfer liquid is adopted equal to $\rho = 900$ kg/m³.

5.1. Mathematical modelling

Figure 4 illustrates the transfer of the liquid (LT) from one cylinder to another, passing through the hydraulic converter and valves. The valves control the flow of the transfer liquid in and out of the hydraulic converter, respectively.

Table 3. Mathematical formulations used in hydraulic analysis.

Formula	
$p_{evp} + \dfrac{\rho V_1^2}{2} + \rho g H_1 = p_{cond} + \dfrac{\rho V_2^2}{2} + \rho g H_2 + \dfrac{P_{hyd}}{\dot{V}_{LT}} + \Delta P_{minor\_losses}$	(10)
$P_{hyd} = -\dfrac{8\rho K_{total}\dot{V}_{LT}^3}{\pi^2 d^4} + (\Delta p + \Delta H \rho g)\dot{V}_{LT}$	(11)
$K_{total} = 2K_{vs}d + K_{entrance} + 2K_{elbow} + K_{exit}$	(12)
$\dfrac{8\rho K_{total}\dot{V}_{LT}^3}{\pi^2 d^4} - (\Delta p + \Delta H \rho g)\dot{V}_{LT} + P_{hyd} = 0$	(13)
$\dot{V}_{LT}^3 - C_1\dot{V}_{LT} + C_2 = 0$	(14)
$C_1 = \dfrac{(\Delta p + \Delta H \rho g)g\pi^2 d^4}{8K_{total}}$	(15)
$C_2 = \dfrac{P_{hyd}g\pi^2 d^4}{8K_{total}}$	(16)
$\Delta \leq 0 \rightarrow \dfrac{C_2^2}{4} - \dfrac{C_1^3}{27} \leq 0$ [14]	(17)
$\dfrac{\left(\dfrac{P_{hyd}g\pi^2 d^4}{8K_{total}}\right)^2}{4} \leq \dfrac{\left[\dfrac{(\Delta p + \Delta H \rho g)g\pi^2 d^4}{8K_{total}}\right]^3}{27}$	(18)
$K_{total} \leq \dfrac{\pi^2 d^4(\Delta p + \Delta H \rho g)^3}{54\rho P_{hyd}^2}$	(19)
$P_{available} = \Delta p\dfrac{\pi D^2}{4}\Delta Hf = \Delta p\dfrac{\pi D^2}{4}\dfrac{\Delta H}{\tau}$	(20)
$P_{admissible} = P_{hyd}\dot{V}_{LT\_admissible}$	(21)
$\dot{V}_{LT\_admissible} = V_{admissible}\pi\dfrac{d^2}{4}$	(22)
$Re_{admissible} = \dfrac{V_{admissible}d}{\sigma}$	(23)
$K_{total\_min} = K_{total}P_{available} = \dfrac{\pi^2 d^4(\Delta p + \Delta H \rho g)^3}{54\rho P_{available}^2}$	(24)
$K_{total\_max} = K_{total}P_{admissible} = \dfrac{\pi^2 d^4(\Delta P_t)^3}{54\rho P_{available}^2}$	(25)
$\dot{V}_{LT} = \pi d^2\sqrt{\dfrac{\Delta P_t}{8\rho K_{total}}}$	(26)
$\dot{V}_{LT\_min} = \dot{V}_{LT}K_{total\_min}$	(27)
$\dot{V}_{LT\_max} = \dot{V}_{LT}K_{total\_max}$	(28)
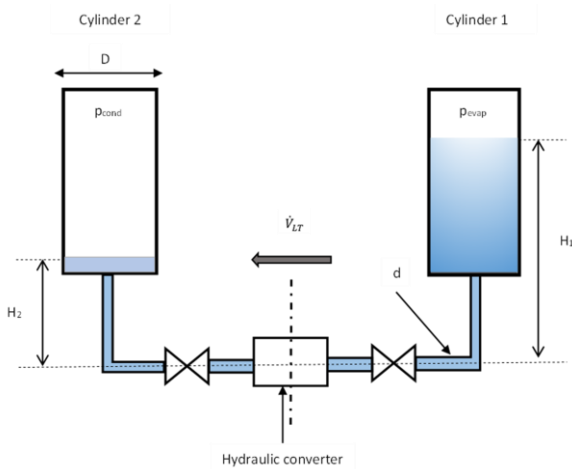
Fig. 4. Hydrostatic scheme of the hydraulic part of the power plant [20]; H_1 and H_2– heights relative to the reference plane, $\dot{V}_{LT}$ – flow rate.

In order to make the analysis smooth and clear, the following definitions are imperative (as detailed in Table 3). Hydraulic power denoted as P_{hyd}, is defined as the power consumed by the hydraulic converter, Eq. (11). It can be determined by utilizing the Bernoulli equation, Eq. (10), and taking into account the minor losses characterized by their flow coefficient. These los-ses occur in various circumstances such as entry to a pipe from a tank, exit from a pipe into a tank, bends in a pipe, valves, and so forth (Fig. 4). The total flow coefficient (K_{total}) of the above-mentioned minor losses is determined using Eq. (12). The values of loss coefficients for the threaded elbow (K_{elbow}), the entry to a pipe from a cylinder ($K_{entrance}$), and the exit from a pipe into cylinder (K_{exit}) can be found in [26]. Moreover, the loss coefficient of the valves (K_{vs}) which is related to the nominal diameter is determined based on [27].

In fact, the hydraulic analysis was carried out using Bernoulli's equation between two points located in the evaporator and condenser. The purpose of this analysis at this stage is to size the hydraulic circuit, specifically to define the diameter d based on the hydraulic power consumed by the hydraulic converter. By assuming a constant pressure difference (Δp), a maximum value of hydraulic power is obtained, which allows for determining the maximum diameter (d) of the circuit.

Even when assuming a constant pressure difference to estimate the hydraulic power, the thermal (Eq. (8)) and second law (Eq. (9)) efficiencies are not affected by this assumption. The efficiencies in question were calculated from the net specific work of the thermodynamic cycle, Eq. (7).

However, it would also have been possible to calculate the available mechanical power ($P_{available}$) defined as the mechanical power imparted by the engine cycle to the transfer liquid, from the net work of the cycle (W_{cycle}, Eq. (7)), provided that the mass flow rate of the cycle ($\dot{m}$) was known ($P_{available} = W_{cycle}\dot{m}$). This is equivalent to determining the duration τ of the thermodynamic cycle or its frequency f.

The available mechanical power (Eq. (20)) depends on the diameter of the transfer cylinder, which is set at $D = 1$ m in this study, the height or vertical distance traversed by the transfer liquid, the pressure differential (Δp), and ultimately, the frequency ($f = 1/\tau$) of a single thermodynamic cycle. At this stage of the study, it is only possible to vary the cycle duration (τ) within a hypothetical range. This power may be transmitted either wholly or partially to the turbine, contingent upon the hydraulic circuit losses (comprising bends, valves, etc.), which, in turn, hinge upon the diameter of the transfer piping and the volumetric flow rate of the transfer liquid. However, a portion of this available mechanical power ($P_{available}$) at the transfer cylinders is expended in overcoming the losses in the hydraulic circuit, deduced directly from Eq. (11). Meanwhile, the remaining is transformed by the hydraulic converter into mechanical power.

Furthermore, among the conditions that must be taken into consideration are the flow velocity limits to maintain the integrity and performance of the system. It emerges that the flow velocity (or admissible speed) can go up to 6 m/s [28], which will considerably increase the admissible power and in return will increase the specific power of the new power plant. In fact, it is a recommended flow velocity for hydraulic pipes to avoid transitioning to the rough turbulent regime.

Under these circumstances, admissible power refers to the maximum allowable power that a hydraulic system or component can handle without exceeding its design limitations or causing damage. The admissible power ($P_{admissible}$, Eq. (21)) can be determined by replacing the admissible speed ($V_{admissible}$) in the hydraulic power (Eq. (11)), taking into account several factors, including the design, materials, and operating circumstances of the hydraulic components.

Also, substituting the admissible speed in the Reynolds number equation gives the admissible Reynolds number (Re$_{admissible}$, Eq. (23)). Along with the admissible speed ($V_{admissible}$), the admissible Reynolds number is also affected by the kinematic viscosity of the hydraulic fluid (σ).

The selection of the hydraulic oil viscosity grade should align with the typical operating temperature. It is important to remember that viscosity is a measure of the oil's resistance to flow, so in hydraulic systems that are dependent on flow, viscosity is important with respect to both lubrication and energy transmission [29]. According to [29], hydraulic systems normally use oil with a viscosity range of 32–68 cSt at 40°C. However, in a thermo-hydraulic machine where the hydraulic oil comes into contact with the superheated vapour, the choice of the hydraulic oil depends on the temperature of the superheated vapour. For instance, a temperature of 100°C requires a hydraulic oil with a minimum viscosity of 15 cSt, i.e. a hydraulic oil ISO VG 150. At a temperature of 130°C and a viscosity of 15 cSt, the selection of an ISO VG 460 hydraulic oil is necessitated. This requirement can be substantiated through reference to oil viscosity-temperature charts, as documented in sources [30−32]. In this case, the power plant must be started by heating the hydraulic oil to a temperature greater than 40°C so that the kinematic viscosity is less than 600 cSt.

Moreover, finding the flow rate via the turbine is possible by solving the cubic equation (14). The discriminant (Δ) of this cubic equation has to be negative in order to get real solutions [14].

The definition of the maximum value of K_{total} that may be utilized to find real solutions for the flow rate in cubic equation (14) is made possible by inequality (19). Equations (24) and (25) establish the minimum and maximum values of K_{total} at the two powers $P_{admissible}$ and $P_{available}$, respectively.

Finally, to ensure the proper functioning of the turbine, it is necessary for the hydraulic power (Eq. (11)) to be positive. Through this condition, the relation of flow rate can be deduced (Eq. (26)). By substituting the expressions of the minimum and maximum total flow coefficient (Eqs. (24) and (25)) into the equation of flow rate (Eq. (26)), a condition on this flow rate is obtained in Eqs. (27) and (28).

6. Results and discussion of the hydraulic analysis

Figures 5a and 5b illustrate the evolution of hydraulic power for different diameters. They depict the maximum hydraulic powers and optimal flow rates for each diameter. For a given diameter of the hydraulic circuit piping, the shape of the hydraulic power curve is parabolic. Several readings can be inferred from this figure. The power is zero at the two points of intersection of the

curve with the axis representing flow rate. The first point corresponds to the converter's idle state with zero volumetric flow rate. The second point also corresponds to the converter's idle state with maximum volumetric flow rate and maximum pressure losses in the hydraulic circuit. The hydraulic power is maximum for a well-considered value of pressure losses and consequently a well-determined volumetric flow rate. The value of pressure losses at this point can only be minimal. In other words, the pressure losses of the hydraulic circuit, as a function of the volumetric flow rate for a given diameter, can vary from a minimum value when the converter is at rest to their maximum value when the converter is once again at rest (Figs. 5a and 5b). However, for a determined diameter of the hydraulic circuit, the hydraulic power reaches its maximum value, which corresponds to an optimal volumetric flow rate, i.e. minimum pressure losses in the circuit.

To take advantage of this determined maximum hydraulic power for a given diameter, it is necessary for the power available at the transfer cylinder to be greater than or equal to the hydraulic power. This implies that the available mechanical power at the transfer cylinder, which in turn depends on the frequency of the thermodynamic cycle (f) or the duration of a thermodynamic cycle (τ) (Eq. (20)). The latter depends on the temperatures and/or pressures of the hot and cold reservoirs, the working fluid, heat transfer parameters (exchange surfaces, heat transfer coefficient, temperature jumps, etc.). In this case, in the absence of real data and with the aim of completing this analysis, we can assume a frequency for which the available mechanical power at the transfer cylinder is equal to the hydraulic power, represented by the horizontal line passing through the maximum P_{hyd} for a given diameter.

It is observed that the available mechanical power at the transfer cylinder increases with the growth of the frequency of the thermodynamic cycle. This means that the higher the number of cycles per second, the greater the available mechanical power at the transfer cylinder ($P_{available}$).

In the first case (Fig. 5a), with the maximum value of thermal efficiency $\eta_{th\_max} = 17.5\%$ and a pressure drop $\Delta p = 1416.4$ kPa, the maximum hydraulic power is 5.3 kW for $d = 0.02$ m. However, it is equal to 0.4 kW for the second case (Fig. 5b) with the maximum value of second law efficiency $\eta_{II\_max} = 90.2\%$ and a pressure drop $\Delta p = 235.3$ kPa for the same diameter. When the diameter is $d = 0.046$ m, in both first and second cases, the maximum hydraulic power increases to 27.8 kW and 1.9 kW, respectively. These findings suggest that different types of converters must be selected in each case. For the first case, both the hydraulic turbine and piston-converter are suitable due to the relatively high pressure differential and high hydraulic power. However, for the second case, only a hydraulic turbine is suitable due to the low-pressure differential between the transfer cylinders.

However, it is crucial to emphasize that high mechanical powers can be produced only at the high thermal efficiency operating mode. In contrast, operating modes with high second low efficiencies cannot provide high levels of mechanical powers.

As previously noted, a total height of 0.1 m was selected for ΔH. This decision is supported by the relatively minor influence of ΔH on hydraulic power, as illustrated in Fig. 6. It is clear that ΔH is significantly related to the duration of the thermodynamic cycle (τ), and thus to the frequency (f). Specifically, a slower thermodynamic cycle corresponds to a higher value of ΔH.

The permissible range of flow rates according to the pressure drop in transfer cylinders obtained for both studied cases are shown in Figs. 7a and 7b. They are likewise compared to those obtained by Semmari et al. [14]. Consequently, the resulting working area built according to the minimum and maximum total flow coefficients is identical to the one obtained by Semmari et al. [14] for their thermo-hydraulic machine. Nonetheless, in

(a)   (b)
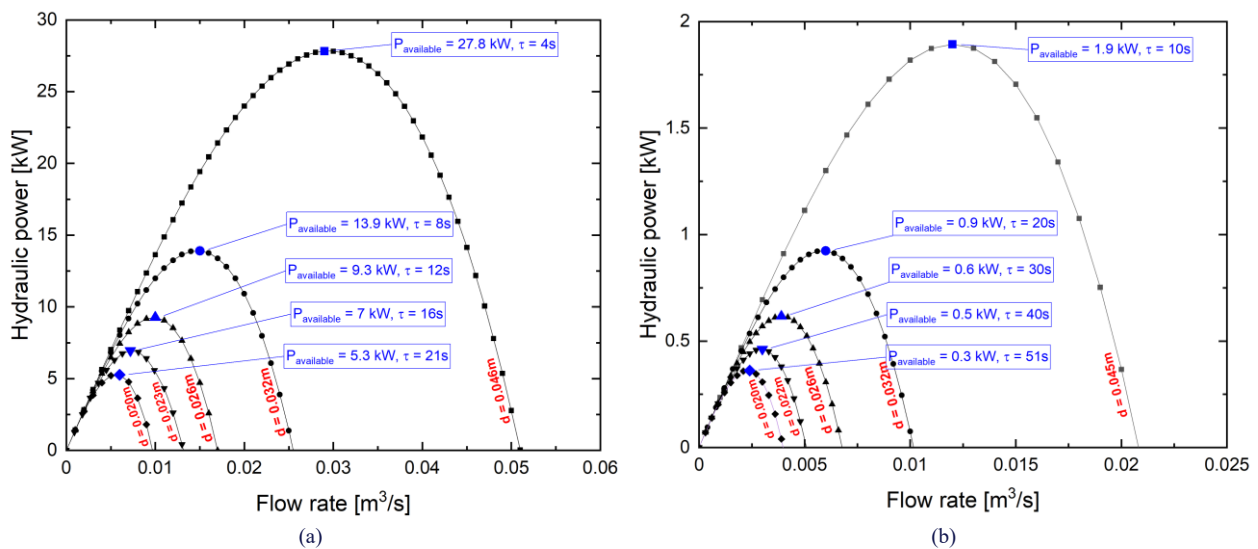
Fig. 5. Variation of the hydraulic power according to the volume flow rate: (a) case 1 − $\Delta p = 1416.4$ kPa and $\eta_{th\_max} = 17.5\%$, (b) case 2 − $\Delta p = 235.3$ kPa and $\eta_{II\_max} = 90.25\%$.
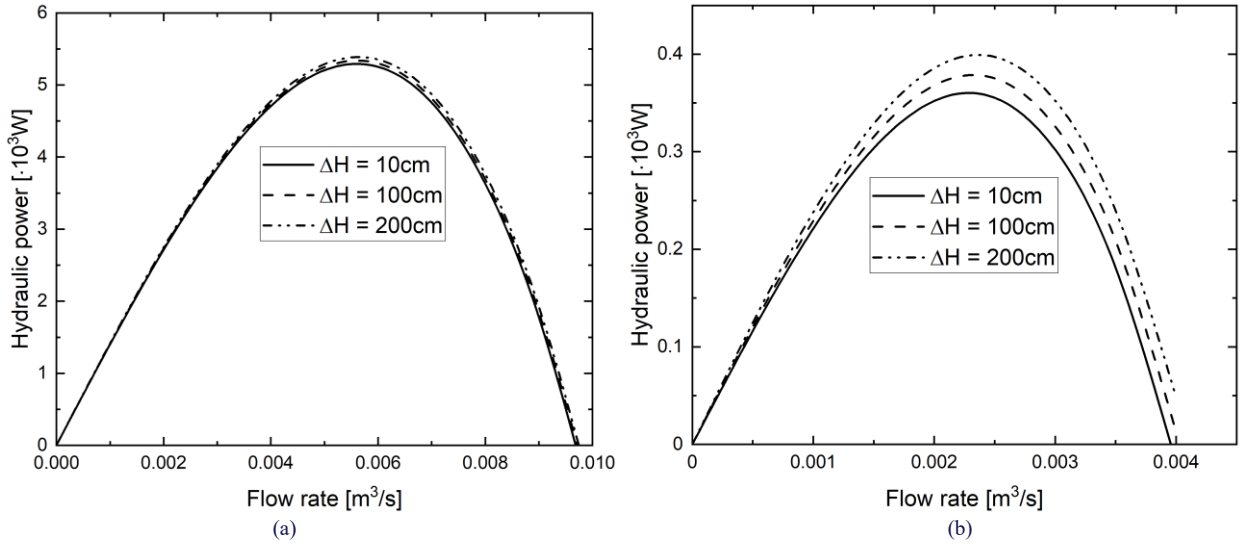
Fig. 6. Variation of the hydraulic power with the flow rate and the total height ΔH for $d = 0.02$ m: (a) case $1 - \Delta p = 1416.4$ kPa and $\eta_{th\_max} = 17.5\%$, (b) case $2 - \Delta p = 235.3$ kPa and $\eta_{II\_max} = 90.25\%$.
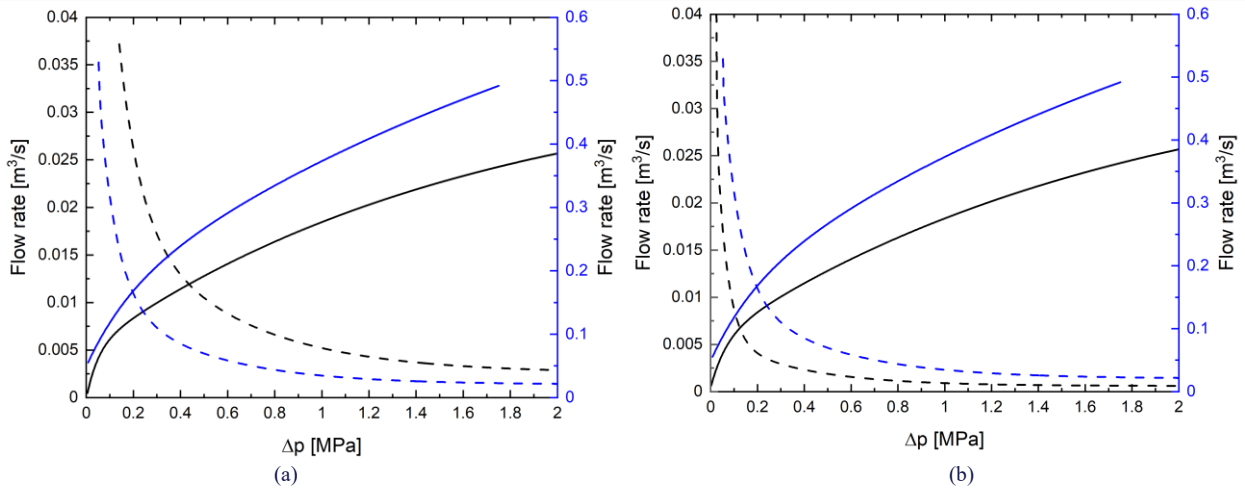
Fig. 7. Comparison of the allowed flow rates according to the pressure drop for $d = 0.03$ m in transfer cylinders obtained for both studied cases with those obtained by Semmari et al. [14]: — flow rate (K_{total_min}) for the present study, — flow rate max studied by Semmari et al. [14], - - flow rate (K_{total_max}) for the present study, - - flow rate min studied by Semmari et al. [14].

the aforementioned work, flow rates seem to be a little bit over-rated. To clarify the disparity in flow rates ranges, the homogeneity of the hydraulic power expression provided by Semmari et al. was checked through a dimensional analysis. It appears that the term containing the loss coefficient looks to have a unit of m³/s when it should really be expressed in watts!

As previously mentioned, solving Eq. (14) enables the determination of the flow rate through the turbine that satisfies the condition $\dot{V}_{LT\_min} < \dot{V}_{LT} < \dot{V}_{LT\_min}$. The set of retained solutions for flow rates and pressure drops is located between the two curves. This information is valuable when comparing various gases and operating regimes. It is clear that, as you move to the left (i.e. with decreasing pressure drop), the range of flow rates narrows. Conversely, moving to the right broadens the range of flow rates.

Admissible powers and admissible Reynolds numbers versus diameter are depicted in Table 4 for cases 1 and 2 at the admissible speed $V_{admissbile}$ of 6 m/s. It can be observed that in

case 1 the admissible power increases from 2.6 kW to 574.5 kW as the diameter increases. Similarly, for case 2 the admissible power increases from 0.3 kW to 73.6 kW as the diameter increases. The hydraulic system can accommodate higher power levels, suggesting that a larger diameter enables better fluid flow and can meet higher power demands. However, it is important to ensure that the power is not simultaneously exceeded in a hydraulic system. Operating at excessive admissible power levels can lead to increased wear, pressure drops, and potential system failures.

Additionally, the Reynolds number in Table 4 increases at the admissible speed as the diameter increases, ranging from 8 000 to 120 000 for cases 1 and 2, respectively. This increase in the Reynolds number at the admissible speed indicates a transition from a smooth turbulent regime, characterized by a Reynold number ranging between 2 300 and 100 000 [26]. Hence, the obtained results show that in both cases when the pipe diameter

34

Table 4. Variations of admissible and available mechanical powers and Reynold numbers according to diameters.

Case 1				Case 2			
Δp = 1416.4 kPa corresponding to η_{th_max} = 17.5%				Δp = 235.3 kPa corresponding to η_{II_max} = 90.25%			
d (m)	$P_{admissible}$(kW)	$Re_{admissible}$	$P_{available}$ (kW)	d (m)	$P_{admissible}$(kW)	$Re_{admissible}$	$P_{available}$ (kW)
0.02	2.6	8000	5.3	0.02	0.3	8000	0.4
0.03	5.8	12000	11.9	0.03	0.8	12000	0.8
0.04	10.3	16000	21.2	0.04	1.4	16000	1.4
0.05	16.1	20000	33.0	0.05	2.1	20000	2.3
0.06	23.1	24000	48.4	0.06	3.1	24000	3.2
0.07	31.5	28000	64.3	0.07	4.2	28000	4.4
0.08	14.2	32000	84.3	0.08	5.5	32000	5.7
0.10	64.2	40000	130.9	0.10	8.5	40000	8.9
0.125	100.3	50000	203.7	0.125	13.3	50000	13.8
0.15	144.3	60000	292.8	0.15	19.1	60000	19.9
0.20	256.1	80000	505.7	0.20	33.5	80000	34.5
0.25	399.6	100000	778.0	0.25	51.7	100000	53.0
0.30	574.5	120000	1101.5	0.30	73.6	120000	74.8

remains under 0.25 m, the flow regime is still far from the rough turbulent regime.

Another careful reading from Table 4 allows to underline another established fact when comparing the available and admissible powers. The available power exceeds the admissible one by an average value of 51% and 4%, respectively for the two cases. This suggests that the operating regime with a maxi-mum value of second law efficiency η_{II_max} = 90.25% (case 2) is able to convert all the available power at the transfer cylinders more efficiently than the one with a maximum value of thermal efficiency η_{th_max} = 17.5% (case 1). However, the only drawback is that a power plant operating according to case 2 cannot provide high levels of mechanical powers and have a relatively low specific power.

7. Conclusions

In summary, this work examines a unique ORPILI thermo-hydraulic machine that was first conceived by the Research Laboratory in Engineering, Materials and Structures. The study is thought of as a multi-aspect optimization of the new concept of a power plant and it is divided into two primary sections: thermodynamic and hydraulic analysis. Hence, the following major conclusions are drawn based on the obtained results:

- Among several suggested working fluids, the thermodynamic analysis has shown that the R1233zd is the most appropriate for mechanical power generation from low temperature reservoirs. It is demonstrated that thermal and second law efficiencies can reach maximum values of 17.5% and 90.3%, respectively. However, high mechanical powers can be produced only at high thermal efficiencies operating mode. On the other hand, operating modes with high second low efficiencies cannot provide high levels of mechanical powers.
- For a given diameter of the hydraulic circuit piping, the shape of the hydraulic power curve is parabolic. However, the hydraulic power reaches its maximum value, which corresponds to minimum pressure losses in the circuit, i.e. the optimal volumetric flow rate.

- It is shown that there is a certain operating area with allowed values of flow rate and pressure drop in transfer cylinders. The boundaries of this area are determined by the minimum and maximum values of the total flow coefficients.
- A power plant operating with a maximum value of second law efficiency cannot provide high levels of mechanical powers and have a relatively low specific power. To develop a significant power, it will be necessary to opt for a power plant operating with a maximum value of thermal efficiency, i.e. relatively high specific power.

The last conclusion aligns with several postulates of the second law of thermodynamics. It evokes the initial observation made by Nicolas Leonard Sadi Carnot during his analysis of steam engines, when he realized that there was a fundamental limit to the amount of work generated from a given amount of heat. In light of this, more studies will need to be done. Their primary focus will be on the transfer cylinders and the mechanical gearbox with the freewheel.

References

[1] Shah, Y.T. (2022). *Advanced power generation systems: Thermal sources* (1st ed.). CRC Press. doi: 10.1201/9781003328087

[2] Yilmaz, F. (2019). Energy, exergy and economic analyses of a novel hybrid ocean thermal energy conversion system for clean power production. *Energy Conversion and Management*, 196, 557–566. doi: 10.1016/j.enconman.2019.06.028

[3] Khaligh, A., & Onar, O.C. (2010). *Energy harvesting: Solar, wind, and ocean energy conversion systems*. CRC Press. doi: 10.1201/9781439815090

[4] Tong, W. (2010). Fundamentals of wind energy. *WIT Transactions on State of the Art in Science and Engineering*, 44, 3–48. doi: 10.2495/978-1-84564-205-1/01

[5] Igwe, C.I. (2021). Geothermal energy: A review. I*nternational Journal of Engineering Research & Technology*, 10(3). doi: 10.17577/IJERTV10IS030164

[6] Benti, N.E., Gurmesa, G.S., Argaw, T., Aneseyee, A.B., Gunta, S., Kassahun, G.B., Aga, G.S., & Asfaw, A.A. (2021). The current status, challenges and prospects of using biomass energy in Ethiopia. *Biotechnology for Biofuels*, 14(1), 209. doi: 10.1186/s13068-021-02060-3

[7]   Pan, Y., Yang, F., Zhang, H., Yan, Y., Yang, A., Liang, J., & Yu, M. (2022). Performance prediction and working fluid active design of organic Rankine cycle based on molecular structure. *Energies*, 15(21), 8160. doi: 10.3390/en15218160

[8]   Pan, L., & Wang, H. (2013). Improved analysis of organic Rankine cycle based on radial flow turbine. *Applied Thermal Engineering*, 61(2), 606−615. doi: 10.1016/j.applthermaleng.2013.08.019

[9]   Humphrey, H.A. (1909). An internal-combustion pump, and other applications of a new principle. *Proceedings of the Institution of Mechanical Engineers*, 77(1). doi: 10.1243/PIME_PROC_1909_077_019_02

[10]   Van de Ven, J.D., & Li, P.Y. (2009). Liquid piston gas compression. *Applied Energy*, 86(10), 2183−2191. doi: 10.1016/j.apenergy.2008.12.001

[11]   Van de Ven, J.D. (2009). Mobile hydraulic power supply: Liquid piston Stirling engine pump. *Renewable Energy*, 34(11), 2317−2322. doi: 10.1016/j.renene.2009.01.020

[12]   Motamedi, M., Ahmadi, R., & Jokar, H. (2018). A solar pressurizable liquid piston stirling engine: Part 1, mathematical modeling, simulation and validation. *Energy*, 155, 796−814. doi: 10.1016/j.energy.2018.05.002

[13]   Ahmadi, R., Jokar, H., & Motamedi, M. (2018). A solar pressurizable liquid piston stirling engine: Part 2, optimization and development. *Energy*, 164, 1200−1215. doi: 10.1016/j.energy.2018.08.197

[14]   Semmari, H., Stitou, D., & Mauran, S. (2012). A novel Carnot-based cycle for ocean thermal energy conversion. *Energy*, 43(1), 361−375. doi: 10.1016/j.energy.2012.04.017

[15]   Mauran, S., Martins, M., Stitou, D., & Semmari, H. (2012). A novel process for engines or heat pumps based on thermal-hydraulic conversion. *Applied Thermal Engineering*, 37, 249–257. doi: 10.1016/j.applthermaleng.2011.11.026

[16]   Stitou, D. (2013). *Transformation, Conversion, Stockage, Transport de l'énergie thermique par procédés thermochimiques et thermo-hydrauliques*. Habilitation à Diriger des Recherches en Énergétique − Génie des Procédés, Université de Perpignan. https://tel.archives-ouvertes.fr/tel-00841655

[17]   Borgogno, R., Mauran, S., Stitou, D., & Marck, G. (2017). Thermal-hydraulic process for cooling, heating and power production with low-grade heat sources in residential sector. *Energy Conversion and Management*, 135, 148–159. doi: 10.1016/j.enconman.2016.12.064

[18]   Semmari, H., Mauran, S., & Stitou, D. (2017). Experimental validation of an analytical model of hydraulic motor operating under variable electrical loads and pressure heads. *Applied Energy*, 206, 1309–1320. doi: 10.1016/j.apenergy.2017.10.010

[19]   Zebbar, D., Guelib, A., Kherris, S., Zebbar, S., Mostefa, K., & Kaddouri, N. (2019). Thermodynamic study and analysis of thermohydraulic cycle for power generation. *Recueil de mécanique*, 3(2), 299−305 (in French). doi: 10.5281/zenodo.2581463

[20]   Semmari, H. (2012). *Production d'électricité par procédé thermo-hydraulique. Application à l'exploitation de l'énergie thermique des mers*. Thése de doctorat, Université de Perpignan (in French).

[21]   Zebbar, D., Guelib, A., Rahmani, Z., Zebbar, S., & Kherris, S. (2022). *Machine thermohydraulique pour la production continue de puissance mécanique avec piston liquide fonctionnant suivant le cycle de Rankine*, Algeria. Patent No. 220156.

[22]   Martins, M. (2010). *Nouveau procédé thermo-hydraulique appliqué au rafraîchissement solaire de l'habitat. Analyse et optimisation thermodynamiques*. Thèse de doctorat, Université de Perpignan (in French).

[23]   Maalem, Y., Madani, H., & Mehemmai, M. (2023). Modélisation mathématique et simulation numérique des performances de refroidissement de différentes unités de réfrigération à compression de vapeur: application de nouveaux fluides frigorigènes. *Revue des Sciences et Science de l'ingénieur*, 10 (1), 21−39 (in French).

[24]   Bell, I.H., Wronski, J., Quoilin, S., & Lemort, V. (2014). Pure and Pseudo-pure fluid thermophysical property evaluation and the open-source thermophysical property library CoolProp. *Industrial & Engineering Chemistry Research*, 53(6), 2498–2508. doi: 10.1021/ie4033999

[25]   Borgogno, R. (2017). Procédé thermo-hydraulique solaire appliqué à la trigénération dans le secteur résidentiel. Thése de doctorat, Université de Perpignan (in French). https://tel.archives-ouvertes.fr/tel-01620245

[26]   Çengel, Y.A., & Cimbala, J.M. (2006). *Fluid mechanics: Fundamentals and applications*. McGraw-Hill Higher Education.

[27]   Regin. *GF2/GF3 Rev. C 2– and 3–way DIN-standard flanged valve*. https://www.regincontrols.com/globalassets/pimmedia-files/documents/gf2_gf3_ps10097_en.pdf [accessed 7 Jul. 2024].

[28]   Savić, V., Knežević, D.M., Lovrec, D., Jocanović, M., & Karanović, V. (2009). Determination of pressure losses in hydraulic pipeline systems by considering temperature and pressure. *Strojniški vestnik − Journal of Mechanical Engineering*, 55(4), 237−243 UDC 621.643

[29]   Pirro, D.M., Wessol, A.A., & Wills, J.G. (2001). *Lubrication fundamentals* (2nd ed.). CRC Press.

[30]   Oil viscosity/temperature chart. OEM Dynamics. https://oemdynamics.us/documents/InstructionBooks/viscosity.pdf [accessed 7 Jul. 2024].

[31]   Majumdar, S.R. (2003). Oil hydraulic systems: Principles and maintenance. McGraw-Hill.

[32]   Chapple, P. (2002). Principles of hydraulic system design (1st ed.). Coxmoor Publishing Company.

Numerical investigation on vapour-liquid equilibrium and gas solubility in hydrocarbons for binary and ternary systems

Mohammad Reza Goodarzi, Hojat Ghassemi[*]

School of Mechanical Engineering, Iran University of Science and Technology, Narmak, Tehran, P.O.B. 16765-163, Iran
*Corresponding author email: h_ghassemi@iust.ac.ir

Abstract

Vapour-liquid equilibrium calculation is crucial in oil industry and multi-phase systems such as droplet evaporation. This paper presents a comprehensive numerical analysis of phase equilibrium in multi-component systems at various pressures and temperatures, accounting for high-pressure phenomena including thermodynamic non-ideality and inert gas effects. The phase equilibrium is determined by solving the fugacity equation iteratively to find the equilibrium mole fractions in both liquid and vapour phases. The Peng-Robinson equation of state is used to handle non-idealities and calculate fugacity coefficients. This study details the procedure for computing vapour-liquid equilibrium and evaluates N_2, O_2, and CO_2 solubility in liquid alkanes such as heptane, dodecane, and hexadecane. Model performance is validated against experimental data for binary and ternary systems, showing good agreement. Results indicate that density and molecular attractive forces impact gas dissolution. Increased pressure and gas density enhance solubility in the liquid phase, while temperature effects vary between subcritical and supercritical regions. The study also highlights differences in gas solubility between heavy and light fluids.

Keywords: Vapour-liquid equilibrium; Gas solubility; Fugacity; High pressure; Hydrocarbons; Binary and ternary systems

1. Introduction

Phase equilibrium calculation is important in fuel droplet evaporation, combustion, distillation process design, and nitrogen/carbon dioxide injection in enhanced oil recovery techniques. Therefore, using a simple and practical model to calculate equilibrium mole fractions in numerical models is essential [1,2]. Figure 1 shows a droplet that is evaporating in a gaseous environment. The problem is calculating equilibrium mole fractions of species at the interface, where vapour-liquid equilibrium (VLE) coexists. At low pressures (near or below 1 atm), the dis-solved gas and real-gas effects are negligible; consequently, Raoult's law can accurately predict the equilibrium mole fractions [3]. At high-pressure conditions, a comprehensive model should consider solubility and real-gas behaviour. In an extensive review, Mühlbauer and Raal [4] have studied two methods to determine the phase equilibrium at high pressures. Two primary approaches, combined and direct methods, have been developed. The combined method utilizes activity and fugacity coefficients to describe the non-idealities of the liquid and vapour phases, respectively. It reliably represents complex systems at low to medium pressures but faces difficulties at high-pressure regions.

Nomenclature

a – parameter in the Peng-Robinson equation of state representing the intermolecular attractive force, $Nm^4/kmol^2$

b – coefficient in Peng-Robinson equation of state, $m^3/kmol$

f – fugacity, N/m^2

g – Gibbs function, J/kg

k_{ij} – binary interaction coefficient

n – mole number

N – number of species

T – temperature, K

P – pressure, N/m^2

R_u – universal gas constant, J/ (mol K)

V – volume, m^3

x – mole fraction

Z – compressibility factor

Greek symbols

μ – chemical potential, J/kg

γ – activity coefficient

φ – fugacity coefficient

ν – molar specific volume, $m^3/kmol$

ω – acentric factor

Subscripts and Superscripts

c – critical

l – liquid phase

v – vapour phase

i, j – individual component

r – reduced

Abbreviations and Acronyms

EOS – equation of state

VLE – vapour-liquid equilibrium
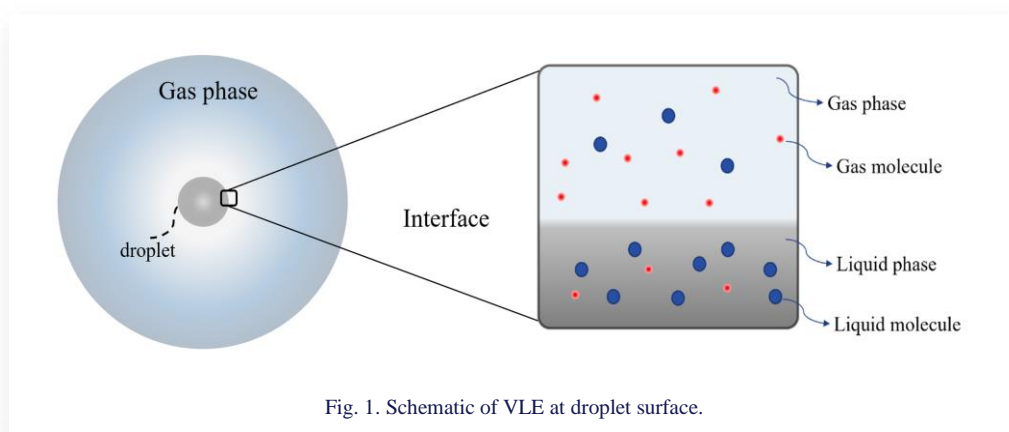
Fig. 1. Schematic of VLE at droplet surface.

In contrast, the direct method overcomes these challenges and requires fewer binary interaction coefficients. However, there are difficulties in using this model for complex polar systems. Rojas et al. [5] studied the effect of the equation of state (EOS) on the solubility of hydrogen gas in pyrolysis gasoline. Considering the cubic EOS of Redlich-Kwong, the classical quadratic mixing rules, and the correlation function S93 for hydrocarbons and S72 for hydrogen gas, the average absolute relative deviation on the prediction of solubility of hydrogen in pyrolysis gasoline was reported as 3.1%. Ghosh [6] showed that Ping-Robinson and Redlich-Kwong have acceptable accuracy in computing phase equilibrium among the cubic equation of states. Lyu et al. [7] studied the solubility of carbon dioxide in methanol in the temperature range of 213 K to 273 K and up to 3 MPa pressure based on the γ-φ method. This study calculated the activity coefficient from Wilson and non-random two-liquid models. They showed that the Wilson model has better accuracy in determining the mole fraction. Chaparro et al. [8] measured and modelled VLE and surface tension for the hexane + ethanol + cyclopentyl methyl ether. The theoretical predictions of vapour–liquid equilibrium using Peng-Robinson Stryjek-Vera equation of state and non-random two-liquid model (NRTL) are in good agreement with the reported experimental data of the ternary mixture. Laursen et al. [9] proposed a straightforward VLE device with

vapour phase recirculation to test the gas solubility using liquid phase sampling. Höhler [10] introduced a novel apparatus for investigating gas solubility in solvents, such as alcohols and ketones, across a temperature range of 253 K to 453 K. They showed that adding acetone can increase gas solubility. Yang et al. [11] studied the impact of non-ideal VLE on multi-component droplet evaporation. The results suggest that an ideal VLE model may result in incorrect evaporation process predictions when the component structures, like those of ethanol and isooctane, exhibit considerable differences. Ray et al. [12] studied the effect of pressure, temperature, and liquid phase composition on the solubility of gas in a ternary system. It was observed that gas solubility in the liquid phase increases significantly at high pressures. In the numerical studies carried out in this field, the procedure of computing the mole fraction of components in ternary systems and more has not been outlined in detail. Nor have the effect of pressure and temperature on the gas solubility at different compositions in the liquid phase been investigated.

This paper aims to provide a more fundamental understanding of VLE and gas dissolution in the liquid phase by considering non-ideal behaviour across a wide range of pressures and temperatures. Additionally, a detailed procedure for determining equilibrium mole fractions in ternary systems, which is not adequately covered in existing literature, is described. This model

could eventually be applied to studies of droplet evaporation or combustion under high-pressure conditions. As validation, the vapour-liquid equilibrium of six systems is compared against existing experimental data. Extensive research has investigated the impact of pressure, temperature, and composition on VLE.

2. Numerical model

2.1 Phase equilibrium at high pressures

Three criteria must be met at the liquid- and vapour-phase interface to establish phase equilibrium in a multi-component mixture. First, thermal equilibrium must be achieved in both phases. Additionally, mechanical forces at the interface should be balanced. These two criteria indicate that temperature and pressure at the liquid- and vapour-phase interface must be equal [13]. In summary, the criteria for temperature and pressure equilibrium can be expressed as follows:

$$T^v = T^l, \tag{1}$$

$$P^v = P^l, \tag{2}$$

where P and T represent pressure and temperature, and superscripts v and l refer to the vapour and liquid phases, respectively. It is also necessary for the chemical potential to be equal at the interface of both phases. If this criterion is not met, mass transfer will occur from one phase to another [13]. Since the partial molar Gibbs function is equivalent to the chemical potential, it can be written for each species as follows:

$$\mu_i^v = \mu_i^l \rightarrow g_i^v = g_i^l, \quad i = 1,2,\dots,N, \tag{3}$$

where μ is the chemical potential, g refers to the Gibbs function, and N represents the number of species in the system. Gibbs function of ith species in the mixture is defined as follows:

$$dg_i = R_u T d(\ln f_i)_T, \tag{4}$$

where R_u is the universal gas constant, and f refers to fugacity. According to Eq. (4), Eq. (3) is rewritten in terms of fugacity as follows:

$$\ln f_i^v = \ln f_i^l \rightarrow f_i^v = f_i^l, \quad i = 1,2,\dots,N. \tag{5}$$

In Eq. (5), f_i is defined as [2]

$$f_i = x_i \varphi_i P \tag{6}$$

or

$$f_i = x_i \gamma_i f_i^0 \tag{7}$$

where x, φ, γ, and f^0 denote mole fraction, fugacity coefficient, activity coefficient, and standard-state fugacity. Although Eqs. (6) and (7) can be defined for any phase, Eq. (6) is usually used for the vapour phase (known as φ method), and Eq. (7) is employed for the liquid phase (known as γ method). Although the γ method is simpler to use at low pressures, when the system's temperature is above one of the species' critical temperatures, it can be challenging to use γ methods. In this condition, it is preferred to use the φ method for both phases [13].

In this study, Eq. (6) is employed to calculate the mole fraction in both phases, known as φ-φ method. In reference [14], the following equation is proposed to calculate the fugacity coefficient, which can be used for any substance and in any phase:

$$R_u T \ln(\varphi_i) = \int_V^\infty \left[\left(\frac{\partial P}{\partial n_i}\right)_{T,V,n_j} - \frac{R_u T}{V}\right] dV - R_u T \ln Z. \tag{8}$$

In Eq. (8), Z is the compressibility factor, V is the volume, and n_j is the mole number of the jth species. According to this equation, the fugacity coefficient is a function of temperature, pressure, and mole fraction. The right-hand side of Eq. (8) is calculated using the equation of state. Due to simplicity and acceptable accuracy, cubic equations of states are utilized. Among these equations, the Peng-Robinson equation of state considers the real-gas behaviour of the gas phase at high pressures and provides better accuracy in predicting the mole fraction of components.

The Peng-Robinson equation of state can be written as follows [14]:

$$P = \frac{R_u T}{v-b} - \frac{a}{v(v+b)+b(v-b)}, \tag{9}$$

where v is the molar volume, a and b are functions of critical temperature and pressure for pure substances. In a multi-component mixture, these coefficients are functions of critical temperature, critical pressure, and mixture composition, which are calculated using mixing rules [14]. Parameter a accounts for attractive forces between molecules while parameter b represents the volume occupied by a molecule. Equation (9) can be written as a cubic polynomial in terms of v as follows:

$$v^3 + \left(b - \frac{R_u T}{P}\right)v^2 + \left(\frac{a}{P} - 3b^2 - 2\frac{bR_u T}{P}\right)v +$$

$$+ \left(b^3 + \frac{R_u T b^2}{P} - \frac{ab}{P}\right) = 0. \tag{10}$$

Equation (10) has either one or three roots depending on the number of phases in the system. In a two-phase system where both liquid- and vapour phases coexist, the largest root represents the molar volume of the vapour, and the smallest root is the molar volume of the liquid. In other cases, if only one phase exists in the system, the equation has one positive root. If there are two positive roots as a solution, one is physically meaningless.

By combining the compressibility factor definition ($Z = Pv/(R_u T)$) and Eq. (10), the Peng-Robinson equation of state can be written as follows:

$$Z^3 - (1-B)Z^2 + (A - 2B - 3B^2)Z +$$

$$- (AB - B^2 - B^3) = 0. \tag{11}$$

The values of A and B are defined as follows:

$$A = \frac{aP}{R_u^2 T^2}, \tag{12}$$

$$B = \frac{bP}{R_u T}, \tag{13}$$

39

$$a = \sum_{i=1}^{N} \sum_{j=1}^{N} x_i x_j a_{ij}, \qquad (14)$$

$$b = \sum_{i=1}^{N} x_i b_i, \qquad (15)$$

$$b_i = \frac{0.0778 R_u T_{ci}}{P_{ci}}, \qquad (16)$$

$$a_{ii} = \frac{0.457254 R_u^2 T_{ci}^2}{P_{ci}} \left[1 + f(\omega_i)\left(1 - \sqrt{T_{ri}}\right)\right]^2, \qquad (17)$$

$$a_{ij} = \left(1 - k_{ij}\right)\sqrt{a_{ii}a_{jj}}, \qquad (18)$$

$$T_{ri} = \frac{T}{T_{ci}}, \qquad (19)$$

$$f(\omega) = 0.3746 + 1.5423\omega - 0.2699\omega^2. \qquad (20)$$

In these equations, subscript c refers to critical parameters, T_{ri} stands for the reduced temperature, ω represents the acentric factor, and k_{ij} is the binary interaction coefficient, which is independent of temperature, pressure, and mole fraction and is usually assumed to be zero in density calculation [3]. However, considering this parameter as zero in the phase equilibrium calculation can lead to significant errors. The value of k_{ij} is taken from [3]. By solving Eq. (11), the compressibility factor of the mixture for the liquid phase (Z^l) and the vapour phase (Z^v) can be determined. Additionally, combining Eqs. (8) and (9) define the fugacity coefficient as follows:

$$\ln \varphi_i = \frac{b_i}{b R_u T} (Pv - RT) - \ln\left[\frac{P}{R_u T}(v - b)\right] +$$

$$- \frac{a/b R_u T}{\sqrt{4+v}} \left[\frac{2\sum_j x_j a_{ij}}{a} - \frac{b_i}{b}\right] \ln\left[\frac{2v + (2+\sqrt{8})b}{2v - (2+\sqrt{8})b}\right]. \qquad (21)$$

By using the definition of the compressibility factor, Eq. (21) can be reformulated as follows:

$$\ln \varphi_i = \frac{b_i}{B}(Z - 1) - \ln(Z - B) +$$

$$+ \frac{A}{B\sqrt{8}} \left[\frac{b_i}{b} - \frac{2\sqrt{a_i}}{a}\sum_j x_j \sqrt{a_j}\left(1 - k_{ij}\right)\right] \ln\left[\frac{Z + (1+\sqrt{2})B}{Z + (1-\sqrt{2})B}\right]. \qquad (22)$$

In summary, to establish phase equilibrium between a multicomponent liquid and vapour mixture, Eqs. (1), (2), and (5) must be satisfied. The equilibrium mole fraction of ith species in the mixture can be calculated using Eq. (5), which can be written as follows:

$$f_i^v = f_i^l \rightarrow x_i^v \varphi_i^v = x_i^l \varphi_i^l. \qquad (23)$$

For a system comprising N species (where $N > 1$), $2N$ mole fractions are determined: N mole fractions in the liquid phase and N mole fractions in the vapour phase. Therefore, there must be a total of $2N$ equations to close the system of equations. N equations can be obtained from Eq. (23). Additionally, since the sum of mole fractions in the liquid- and vapour-phase is equal to unity, two more equations are added to the system of equations as follows:

$$\sum_{i=1}^{N} x_i^v = 1, \qquad \sum_{i=1}^{N} x_i^l = 1. \qquad (24)$$

Hence, for a binary system ($N = 2$), Eqs. (23) and (24) yield a system of 4 equations. However, if there are more than two components in the system, additional equations are required. In such cases, by specifying the mole fraction ratios of components, the number of equations becomes equal to the number of unknowns, resulting in a system of $2N$ equations and $2N$ unknowns. For example, in a ternary system such as heptane-hexadecane-nitrogen, the system of equations is:

$$x_1^v \varphi_1^v = x_1^l \varphi_1^l, \qquad (25)$$

$$x_2^v \varphi_2^v = x_2^l \varphi_2^l, \qquad (26)$$

$$x_3^v \varphi_3^v = x_3^l \varphi_3^l, \qquad (27)$$

$$\sum_{i=1}^{3} x_i^v = 1, \qquad (28)$$

$$\sum_{i=1}^{3} x_i^l = 1, \qquad (29)$$

$$\frac{x_1^l}{x_2^l} = \text{constant}. \qquad (30)$$

Subscripts 1, 2, and 3 refer to heptane, hexadecane, and nitrogen, respectively. In a ternary system, Ray et al. [12] considered the mole fraction ratio (Eq. (30)) as the initial value in the liquids, while Juanos et al. [15] considered it as the stoichiometric mole ratio in a quaternary system. This assumption is acceptable since the amount of dissolved gas in the liquid phase is small compared to the other components.

Following the methodology outlined by Ray et al. [12], the procedure for determining the mole fractions of the liquid- and vapour-phase under thermodynamically equilibrium conditions at a certain pressure and temperature can be summarized as follows:

1) The temperature, pressure, and initial mole fractions of species in the liquid phase ($x_i^{l,old}$) are known.
2) The initial mole fractions of species in the vapour phase ($x_i^{v,old}$) are computed using Raoult's law.
3) By solving the Peng-Robinson equation of state using $x_i^{l,old}$ and $x_i^{v,old}$, the compressibility factors for both phases are determined (Eq. (11)).
4) The fugacity coefficients for each species in the liquid and vapour phases are calculated using Eq. (22).
5) Employing the mole fraction of the liquid phase ($x_i^{l,old}$), the mole fractions of the vapour phase components are determined by Eq. (23). The mole fraction of the last component is calculated using Eq. (24).
6) The mole fraction of dissolved gas in the liquid phase is calculated using Eq. (23), while the mole fractions of other components in the liquid phase are determined using Eq. (24) along with the known component ratio specified in Eq. (30).
7) Steps 3 to 6 are repeated until the convergence condition is met ($\left|x_i^{new} - x_i^{old}\right| < 10^{-6}$).

3. Results and discussion

3.1. Validation

Four binary systems and two ternary systems, for which experimental data are available in the literature, were selected to validate the model. This collection encompasses a wide range of
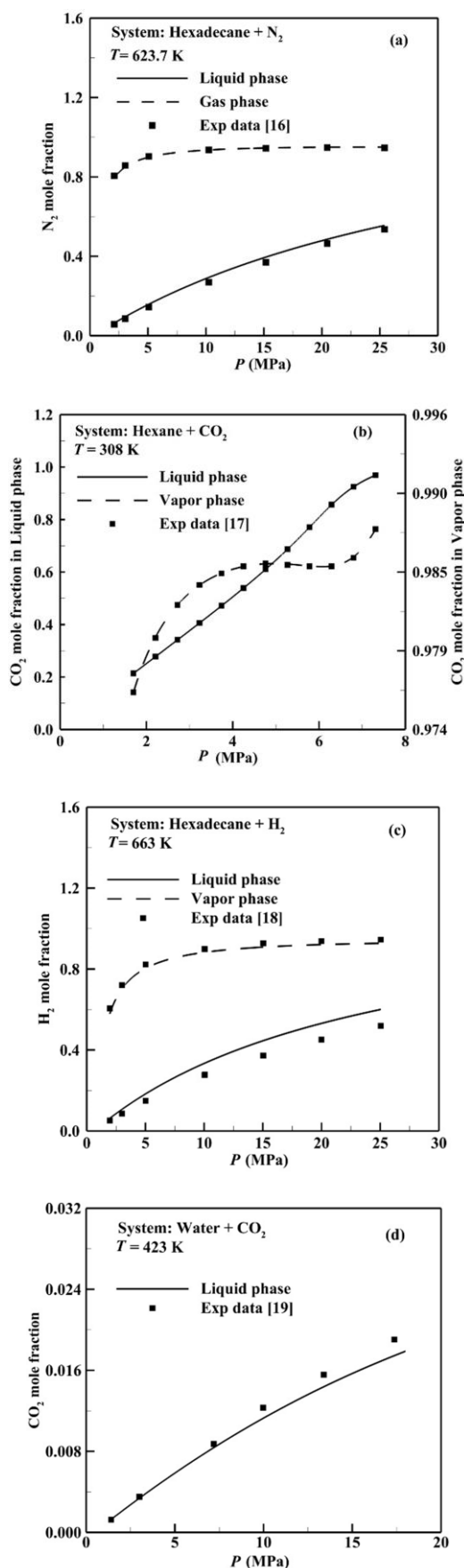
Fig. 2. Comparison results of the presented model for binary systems with experimental data: (a) hexadecane-nitrogen, (b) hexane-carbon dioxide, (c) hexadecane-hydrogen, (d) water-carbon dioxide.

systems, from light gases like hydrogen to heavy gases such as carbon dioxide, and from liquids with small molecules like water to those containing larger molecules like hexadecane.

Figure 2 shows a comparison of the predicted values and measured data reported by Lin et al. [16] for the hexadecane-nitrogen system (Fig. 2a), − Lay et al. [17] for the hexane-carbon dioxide system (Fig. 2b), − Lin et al. [18] for the hexadecane-hydrogen system (Fig. 2c), and − Søreide et al. [19] for water-carbon dioxide system (Fig. 2d). The predicted values agree with the experimental data in binary systems.

Experimental data from Uribe-Vargas et al. [20] for the hexane-decane-nitrogen system and Dima et al. [21] for the water-methane-carbon dioxide system have been employed to validate the numerical model for ternary systems. According to Fig. 3, the current model demonstrates good agreement with experimental data in ternary systems.

(a)

(b)
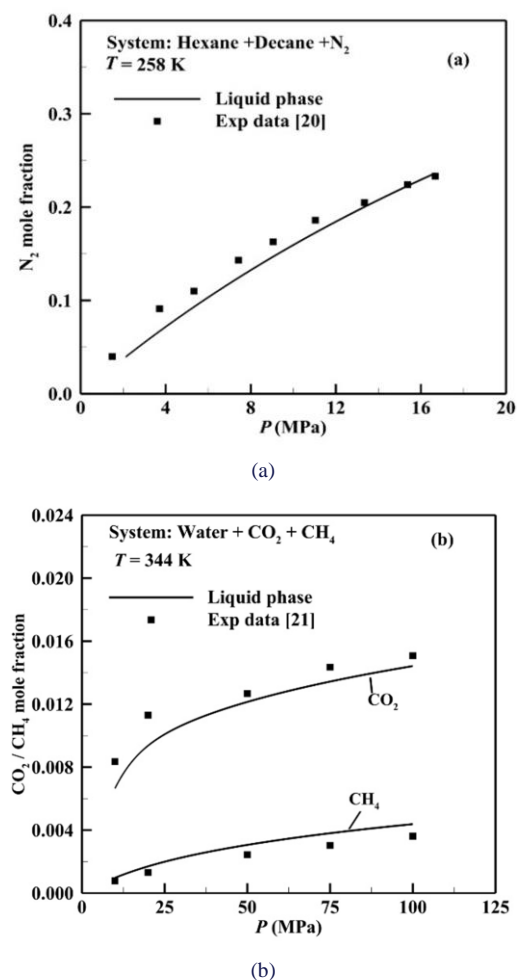
Fig. 3. Comparison of the presented model results with experimental data: (a) hexane-decane-nitrogen, (b) water-methane-carbon dioxide.

3.2. Results

The study further investigates the effect of pressure and temperature on the solubility of ambient gases in the liquid phase. For this purpose, liquid hydrocarbons, including heptane, dodecane, and hexadecane, were used in the presence of nitrogen,

Table 1. Properties of considered substances.

Substance	Chemical formula	Critical temperature (K)	Critical pressure (MPa)	Molecular mass (g/mol)	Acentric factor
Liquid					
Hexane	C_6H_{14}	507.50	3.025	86.177	0.300
Heptane	C_7H_{16}	540.20	2.740	100.202	0.350
Decane	$C_{10}H_{22}$	617.70	2.110	142.285	0.490
Dodecane	$C_{12}H_{26}$	658.00	1.820	170.338	0.576
Hexadecane	$C_{16}H_{34}$	723.00	1.400	226.446	0.718
Water	H_2O	647.14	22.064	18.015	0.344
Gas					
Hydrogen	H_2	32.98	2.016	2.016	-0.217
Nitrogen	N_2	126.20	28.014	28.014	0.037
Oxygen	O_2	154.58	31.999	31.999	0.000

Fig. 4. Phase equilibrium diagram of the heptane-nitrogen system at constant reduced temperature using presented model. Numbers on the graph are heptane reduced temperature.

Fig. 5. Phase equilibrium diagram of the heptane-nitrogen system at constant reduced pressure using presented model. Numbers on the graph are heptane reduced pressure.

Fig. 6. Variation of parameter a for heptane and nitrogen.

oxygen, and carbon dioxide. The properties of these substances are listed in Table 1. In this study, heptane was chosen as a light hydrocarbon with high volatility, while hexadecane was selected as a heavy hydrocarbon with low volatility. Dodecane, on the other hand, represents a hydrocarbon with average molecular mass.

3.2.1. Binary systems

The effect of pressure and temperature on the solubility of nitrogen, oxygen, and carbon dioxide in heptane, dodecane, and hexadecane in a binary system has been investigated using the presented model.

Figure 4 shows the equilibrium concentrations for nitrogen in the heptane-nitrogen system at seven different reduced temperatures ($T_r = T/T_c$). It is evident that at a constant reduced temperature, the dissolved gas in the liquid phase increases almost linearly with increasing pressure. In the gas phase, the nitrogen mole fraction experiences an upward trend and gradually diminishes as it approaches the heptane boiling point or critical mixing point. This behaviour is because, with increasing pressure, some heptane in the vapour enters the liquid phase and condenses, resulting in an increase in the nitrogen mole fraction. However, as the condition approaches the boiling point or mixing point, the heptane in the liquid phase turns into vapour, and the nitrogen mole fraction in the gas phase decreases. Finally, nitrogen mole fractions in liquid- and vapour-phase meet at the boiling and critical mixing points in subcritical and supercritical regions, respectively.

Figure 5 presents the variation of nitrogen mole fraction in the heptane-nitrogen system as a function of reduced temperature in five different reduced pressures ($P_r = P/P_c$). In subcritical regions where heptane reduced pressure is less than one, as the temperature of the liquid phase increases, the amount of gas dissolved in the liquid phase generally decreases and vanishes at the liquid's boiling point. In this case, the attraction between molecules decreases as the temperature increases.
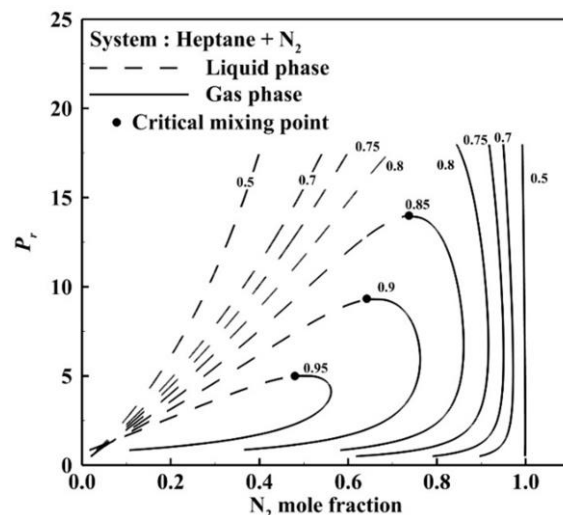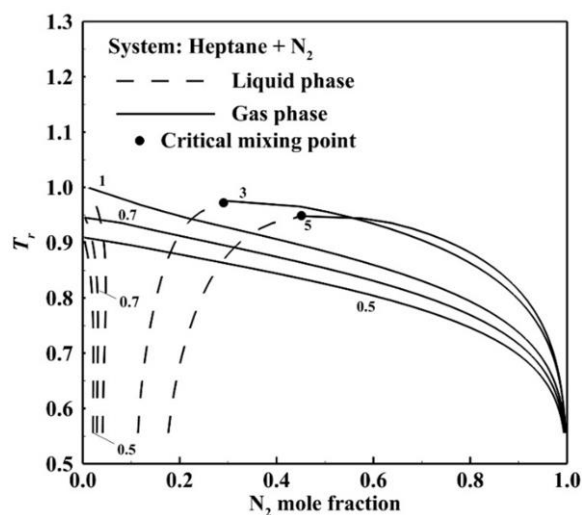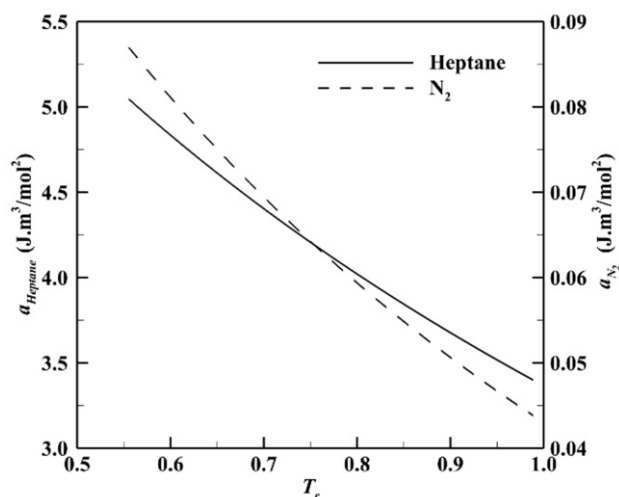
As mentioned earlier, parameter a in the Peng-Robinson equation of state represents the intermolecular attractive force. The variation of this parameter with respect to temperature is shown in Fig. 6. Results indicate that increasing temperature decreases the attractive force between molecules in both heptane and nitrogen. However, this mitigation notably impacts the liquid phase at lower temperatures, resulting in easier dissolution of gas molecules. With a further increase in temperature, the attractive force between gas molecules also decreases. Consequently, a smaller amount of gas dissolves in the liquid. In addition (look back at Fig. 5), vaporization becomes dominant as the temperature of heptane approaches its boiling point. Within an isolated system, where the total mass remains constant, the evaporation of heptane is anticipated to result in an elevation of nitrogen mole fraction. However, contrary to expectations, this elevation does not occur. Accordingly, it can be concluded that nitrogen escapes from the liquid phase to the gas phase with the evaporation of heptane. In fact, with increasing temperature, decreasing attractive force between nitrogen molecules (parameter a) plays a controlling role in determining the equilibrium mole fraction. When the pressure exceeds the critical liquid pressure, an increase in temperature continuously increases the amount of gas solubility and reaches its maximum at the critical mixing point. The liquid phase exhibits gas-like characteristics with increasing temperature and approaching the critical state. Hence, nitrogen dissolves into the liquid phase more easily. It is apparent that even at relatively low temperatures, for example, 300 K (reduced temperature of about 0.55), the nitrogen mole fraction in the liquid phase increases with increasing pressure. For example, at a reduced pressure of 0.5, the amount of nitrogen dissolved in the liquid phase is approximately 0.025, while at a reduced pressure of 5, it is about 0.2, which emphasizes the importance of considering gas solubility in models such as droplet evaporation at high pressures.

Figure 7 compares nitrogen solubility in three hydrocarbons: heptane, dodecane, and hexadecane, at various reduced pressures. Figures 7a and b show the nitrogen mole fractions in subcritical pressures. According to these figures, with an increase in a reduced temperature, nitrogen solubility gradually increases, reaching local maximum values and decreasing rapidly. It can be seen that as the molecular weight of the liquid increases, the amount of dissolved gas decreases. In other words, with the reduction in the volatility of hydrocarbons, less nitrogen dissolves into the liquid phase. Specifically, in all cases, nitrogen exhibits the lowest solubility in hexadecane as a heavy hydrocarbon, whereas it demonstrates the highest solubility in heptane as a representative of light hydrocarbons. The difference vanishes for reduced temperature near unity, and dissolved nitrogen sharply drops to zero. Figures 7c and d depict the solubility of nitrogen in different liquids against reduced temperatures at two supercritical pressures. Similar to subcritical conditions, the solubility of nitrogen is higher for lighter liquids. However, in contrast, the solubility monotonically increases as temperature increases.

Figure 8 compares the solubility of different gases (nitrogen, oxygen, and carbon dioxide) in dodecane as a function of the reduced pressure. The findings reveal a positive correlation
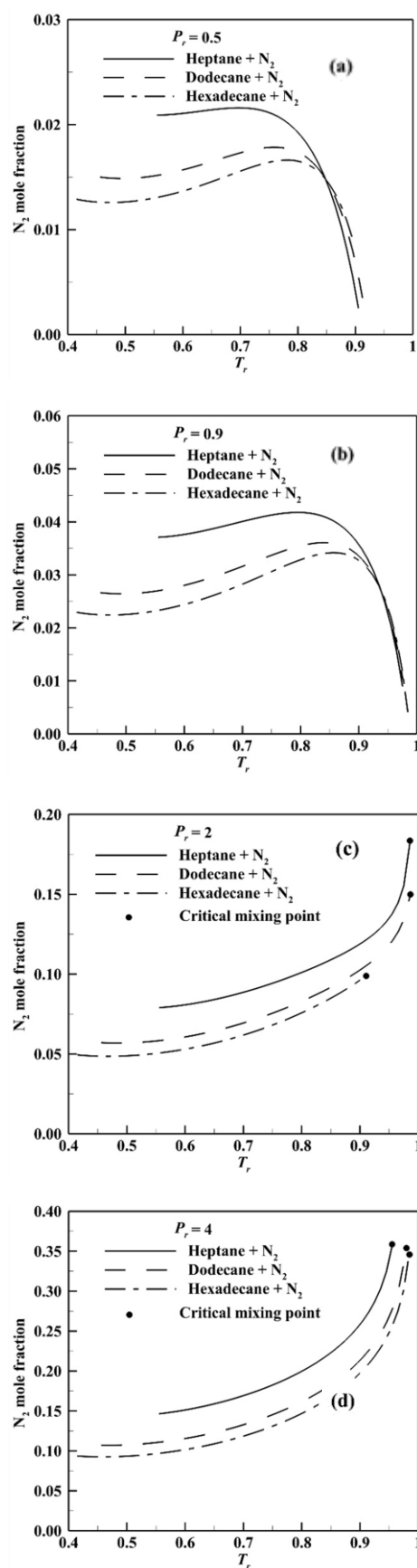
Fig. 7. Comparison of nitrogen solubility in three hydrocarbons, heptane, dodecane, and hexadecane at different hydrocarbon's reduced pressures: (a) $P_r = 0.5$, (b) $P_r = 0.9$, (c) $P_r = 2$, (d) $P_r = 4$.

between the molecular mass of the gas and its solubility. The solubility of carbon dioxide is approximately 5 to 6 times greater than nitrogen at lower temperatures. With rising temperatures, the solubility of carbon dioxide experiences a sharp decline, whereas the variations in the mole fractions of nitrogen and oxygen occur at a slower pace. The results indicate that the lighter gas dissolves less in a liquid, regardless of pressure.

It contrasts with the previous finding that a gas dissolves less in heavier liquid at a given pressure. It is also worth mentioning that the results of the dodecane-CO_2 system are in agreement with the experimental data of Camacho-Camacho [22].

The disparity in gas solubility can be attributed to the attractive force between molecules. Figure 9 shows the value of the parameter a for substances studied in this paper. Figure 9a presents the value of attractive force for nitrogen, oxygen, and carbon dioxide. It can be seen that the value of this parameter for carbon dioxide is about four times higher than nitrogen in 300 K. Indeed, the attractive force between carbon dioxide molecules is much higher than that of nitrogen. Consequently, carbon dioxide demonstrates substantially higher solubility than nitrogen, particularly under low-temperature conditions. The value of this parameter for oxygen is approximately 1.3 times greater than that of nitrogen. As a result, the solubility levels of nitrogen and oxygen in Fig. 8 demonstrate a similar magnitude. Figure 9b illustrates the liquids studied in this work. Through a comparison between this figure and Fig. 7, it becomes evident that with an increase of molecular attractive force in the liquid phase, the amount of gas dissolved in the liquid decreases, with nitrogen gas demonstrating the highest amount of solubility in heptane and the least amount of solubility in hexadecane. Parameter a depends on the critical temperature and pressure. Since the critical temperature and pressure depend on the molecular mass, parameter a also depends on the molecular mass. Therefore, it can

Fig. 8. Comparison of nitrogen, carbon dioxide, and oxygen solubility in dodecane at different reduced pursuers:
(a) $P_r = 0.5$, (b) $P_r = 0.9$, (c) $P_r = 2$.
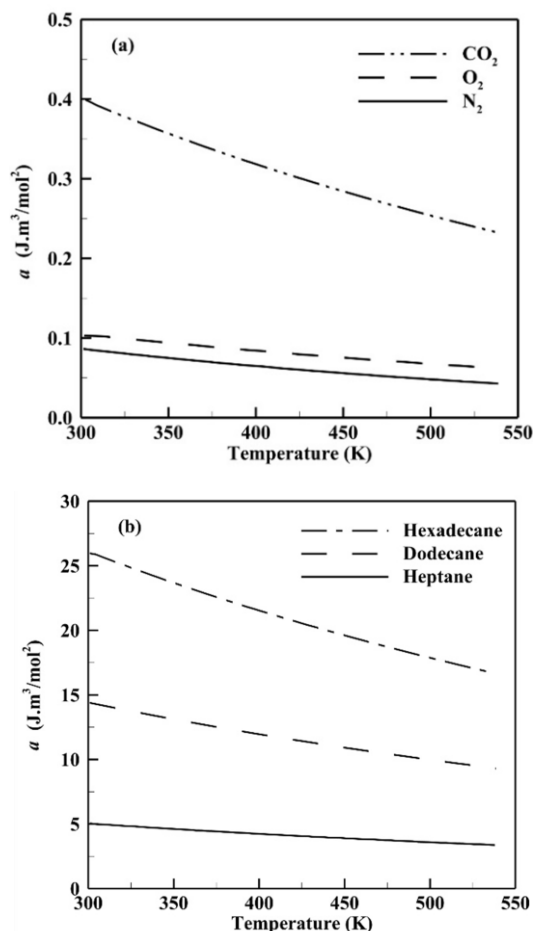
Fig. 9. Value of parameter a in different substances:
(a) gas substances, (b) liquid substances.

be claimed that an increase in the molecular mass of the gas leads to an increase in its solubility within the liquid phase. However, gas solubility decreases in the liquid by increasing the molecular mass. As the density of liquids and gases decreases with increasing temperature, it could be claimed that parameter a and density are directly associated with each other, and the density of the species subsequently impacts gas solubility.

Figure 10 illustrates the effect of pressure on the solubility of nitrogen at 300 K in three hydrocarbons: heptane, dodecane, and hexadecane. It is evident in Fig. 10a that with an increase in pressure, nitrogen solubility increases in all cases. As mentioned earlier, the attractive force in the Peng-Robinson equation of state for a pure substance only depends on the temperature. Therefore, at a constant temperature, its value remains constant with increasing pressure. Hence, in this case, this variable does not play any role in the difference between gas solubility in the liquid phase. With increasing pressure, gas density increases, and more gas is placed in a particular volume. As shown in the figure, hexadecane dissolves more nitrogen than heptane. Differences in the solubility of liquids at a given temperature and pressure are related to their different reduced states. For example, 4 MPa corresponds to reduced pressure of 1.46 and 2.86 for heptane and hexadecane, respectively. Therefore, hexadecane experiences more pressure for dissolving the nitrogen. Figure 10b shows the nitrogen solubility with respect to the reduced pressure of liquids. Compared to Fig 10a, an utterly reverse dependency on the pressure is seen. For a given reduced pressure,

heptane can dissolve more gas into itself. It is dependent on the real state of the liquid; $T = 300$ K corresponds to a reduced temperature of 0.55, while the reduced temperature for hexadecane is 0.42. In the first case, the dissolution should be more.

3.2.2. Ternary system

The subsequent discussion encompasses three ternary systems: heptane-hexadecane-nitrogen, dodecane-heptane-nitrogen, and dodecane-hexadecane-nitrogen. The initial mole fraction of each component in the liquid phase is tabulated in Table 2. In the presented model, the temperature was considered 300, 350, and 500 K, and the pressure was changed from 0.5 MPa to 10 MPa.

Table 2. Initial mole fraction of liquid components.

System	C_7H_{16}	$C_{16}H_{34}$	$C_{16}H_{34}$	N_2
$C_7H_{16} + C_{16}H_{34} + N_2$	0.7	0.3	–	–
$C_{12}H_{24} + C_7H_{16} + N_2$	0.3	–	0.7	–
$C_{12}H_{24} + C_{16}H_{34} + N_2$	–	0.3	0.7	–

Figure 11 illustrates the variation of liquid- and vapour-phase mole fractions as a function of pressure at a constant temperature of 350 K. Figure 11a shows that the mole fraction of
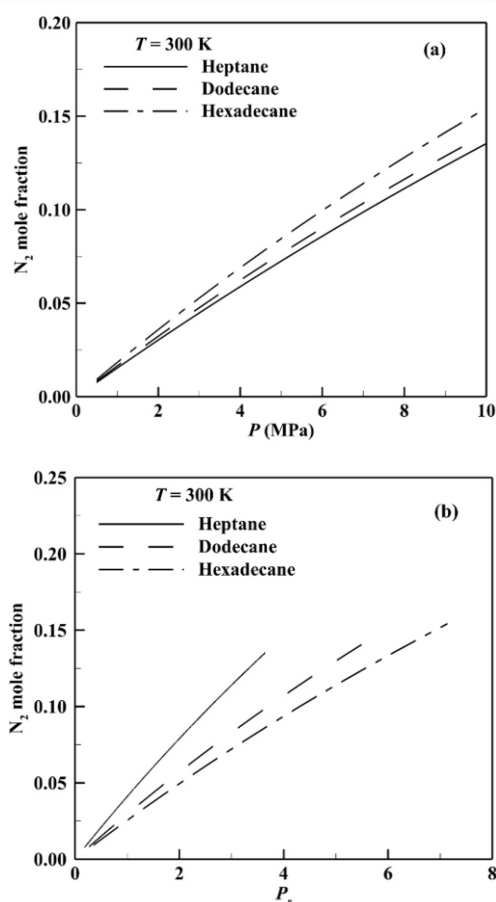
Fig. 10. Effect of pressure on nitrogen solubility at 300 K vs. (a) pressure and (b) reduced pressure.
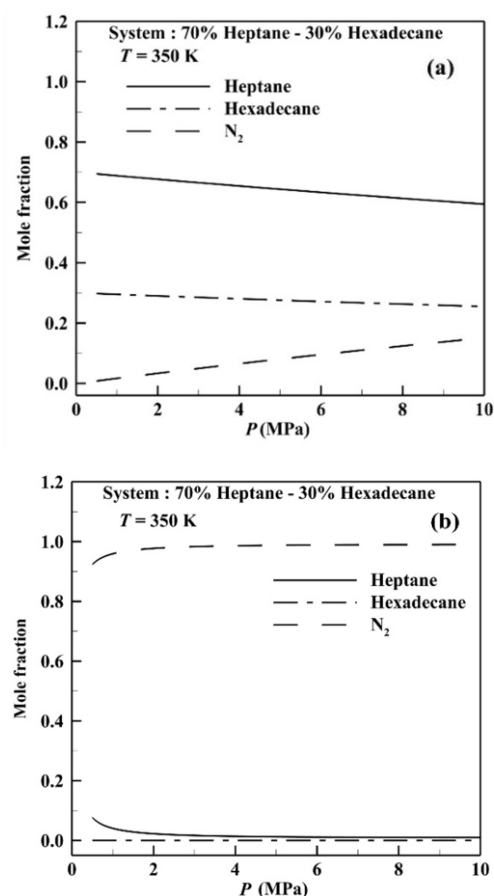
Fig. 11. Mole fractions in 70% heptane-30% hexadecane-nitrogen system using presented model: (a) in the liquid phase and (b) in the gas phase.

nitrogen dissolved in the liquid phase increases with increasing pressure. In this case, the gas solubility behaviour in the ternary system is identical to that of binary systems. Meanwhile, the mole fraction of heptane and hexadecane has constantly decreased due to the nitrogen mole fraction increase. Figure 11b presents mole fractions in the gas phase. It can be observed that the mole fraction of heptane and hexadecane in the gas phase decreases with increasing pressure. Because the volatility of heptane is higher than that of hexadecane, the mole fraction of heptane in the gas phase is continuously higher.

Figure 12a depicts the variations in the nitrogen mole fraction in the liquid phase in a 70% heptane-30% hexadecane mixture as a function of pressure at 350 K and 500 K. The results show that the amount of nitrogen dissolved in the liquid phase has increased with an increase in temperature. Figure 12b displays the attractive force between the mixture's molecules in the liquid phase in terms of pressure. It can be seen that similar to binary systems, this parameter's value has decreased with an increase in temperature. The reduction in the parameter a within the liquid phase has increased the gas solubility in the liquid phase. An important observation is the decrease in nitrogen solubility as the temperature increases at lower pressure. In this case, with the increase in temperature, the liquid mixture is closer to its boiling temperature, and the solubility decreases like the binary system. As the pressure increases and moves further away from the boiling point of the mixture's lighter component, the gas solubility at 500 K is higher than at 350 K, which can be attributed to the parameter a. As Fig. 12b shows, the attractive force in the liquid mixture decreases by pressure, and the slope is more acute at higher temperatures. Here, it is worth noting that the density of the mixture is lower at higher temperatures. Therefore, the solubility of the gas encounters less resistance at higher temperatures. This figure depicts that the sensitivity of the solubility to the pressure is higher at higher temperatures.
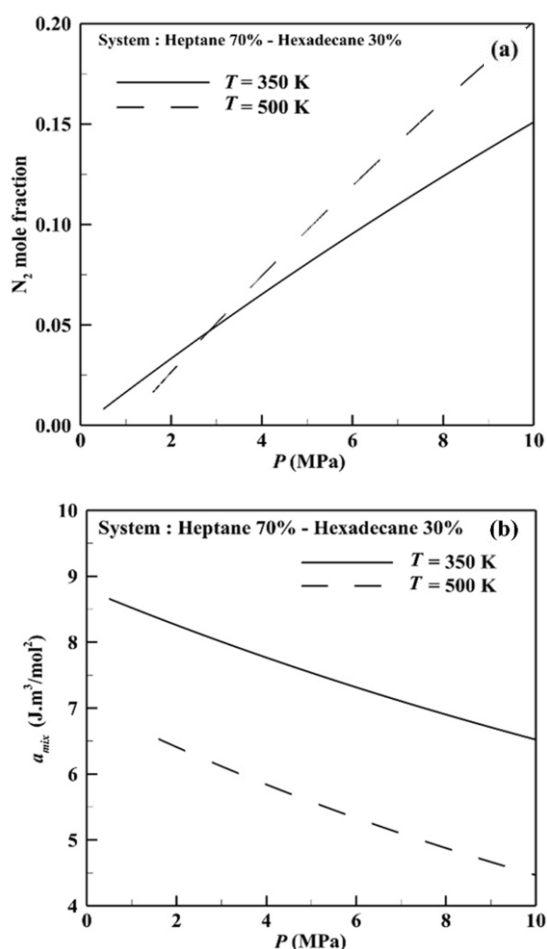
Figure 13 compares nitrogen solubility in different concentrations of heptane and hexadecane mixture at 300 K. It is evident that nitrogen solubility increases at a constant reduced pressure by increasing heptane concentration (lighter hydrocarbon). For instance, at reduced pressure 2, the mole fraction of nitrogen in pure hexadecane is approximately 0.05. By adding heptane to hexadecane and increasing heptane concentration to 30%, the nitrogen mole fraction changes to 0.06. At this reduced pressure, nitrogen solubility in a 70% heptane-30% hexadecane mixture is about 0.07, while in pure heptane, it is approximately 0.08. These results accentuate the use of this comprehensive model to calculate species concentration, especially for light hydrocarbon mixtures at high pressures.
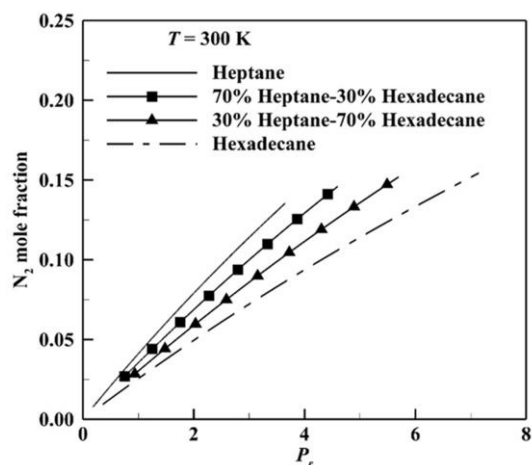
Fig. 13. Effect of pressure on nitrogen solubility in different concentrations of heptane and hexadecane mixture at 300 K using the presented model. The mixture reduced pressure is calculated from [14].

Fig. 12. Model predictions of (a) dissolved nitrogen mole fraction and (b) attractive force, in 70% heptane-30% hexadecane-nitrogen system at 350 K and 500 K.

Figure 14 shows how adding heptane and hexadecane to dodecane affects nitrogen solubility. Nitrogen dissolution is compared in two systems of 70% dodecane-30% heptane and 70% dodecane and 30% hexadecane. Adding heptane as a light and volatile hydrocarbon to dodecane increases nitrogen dissolution compared to the dodecane-hexadecane mixture. As the reduced pressure increases, this difference becomes noticeable. For example, at reduced pressure 5, the amount of nitrogen dissolved in the dodecane-heptane mixture is about 11% more than in the dodecane-hexadecane mixture.
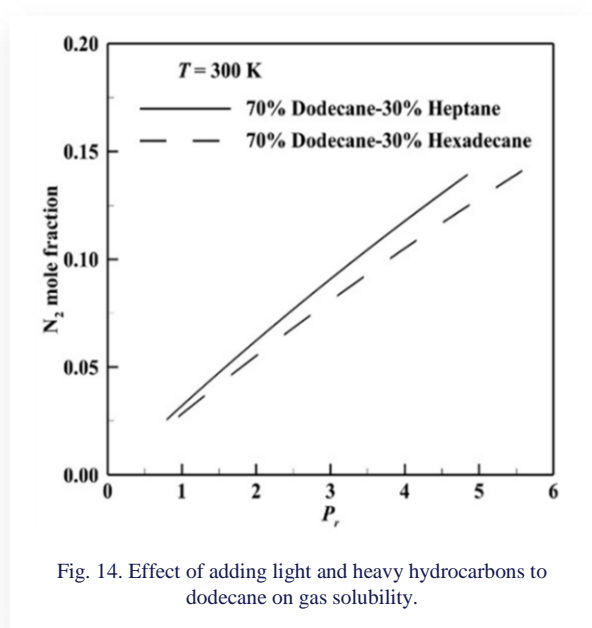
Fig. 14. Effect of adding light and heavy hydrocarbons to dodecane on gas solubility.

6. Conclusions

For studying the evaporation of droplets at high pressures, accurately estimating equilibrium mole fractions is crucial for determining droplet lifetime and evaporation rate. An iterative process using the fugacity coefficients of all species in both phases is employed to estimate phase equilibrium. This model accounts for all effects related to high pressure, including gas solubility in liquids, high-pressure phase equilibrium, and gas-phase non-idealities. The procedure of solving related equations, which is not covered in the literature, is described in detail. A system of 4 and 6 equations for binary and ternary system, respectively, are set with appropriate initial conditions, accompanying with Peng-Robinson equation of state. Compared to experimental data published in the literature, the numerical model is quantitatively validated and shows satisfactory agreement. The presented model can investigate the solubility of different ambient gases in various liquid hydrocarbons under subcritical and supercritical conditions. The primary conclusions of this study are as follows:

1) The attractive force term within the Peng-Robinson equation of state significantly impacts solubility with temperature variations. In the liquid phase, reduction in the parameter a, which represents the intermolecular attraction force, improves gas dissolution. Hydrocarbons with lower molecular weights, exhibiting reduced attractive forces, display a propensity for higher gas solubility as temperature rises. Conversely, concerning gases, a heavier gas with a higher attractive force tends to dissolve more in a particular liquid.

2) Gas solubility declines as the temperature rises in the subcritical region, while dissolved gas rises and achieves its maximum value at the critical mixing point in the supercritical region. In both subcritical and supercritical regions, dissolved gas in the liquid phase increases as pressure rises.

3) Adding heptane as a light hydrocarbon to a mixture increases gas solubility at a given temperature, while heavy hydrocarbons like hexadecane reduce solubility.

Although the presented model is simple and can be used for a wide range of substances at different temperatures and pressures, it is unreliable near liquid critical points. Also, due to the complexities of polar molecules, there is a need to provide a comprehensive model for polar systems.

References

[1] Sirignano, W.A. (2010). *Fluid dynamics and transport of droplets and sprays* (2nd ed.). Cambridge University Press. doi: 10.1017/CBO9780511806728

[2] Lynch, M. (2001). Phase behavior. *Current Opinion in Colloid and Interface Science*, 6(4), 402−404. Henry L. Doherty Memorial Fund of AIME, Society of Petroleum Engineers. doi: 10.1016/ S1359-0294(01)00109-1

[3] Riazi, M. R. (2005). *Characterization and Properties of Petroleum Fractions* (1st ed.). ASTM International.

[4] Mühlbauer, A.L., & Raal, J.D. (1995). Computation and thermodynamic interpretation of high-pressure vapour–liquid equilibrium – a review. *The Chemical Engineering Journal and The Biochemical Engineering Journal*, 60(1−3), 1–29. doi: 10.1016/ 0923-0467(95)02980-X

[5] Rojas, M., Figueira, F., & Zeppieri, S. (2014). Prediction of hydrogen solubility in PYGAS with equations of state. *Journal of Computational Methods in Sciences and Engineering*, 14(1−3), 137–153. doi: 10.3233/JCM-140492

[6] Ghosh, P. (1999). Prediction of vapor-liquid equilibria using Peng-Robinson and Soave-Redlich-Kwong equations of state. *Chemical Engineering and Technology*, 22(5), 379–399. doi: 10.1002/(SICI)1521-4125(199905)22:5<379::AID-CEAT379> 3.0.CO;2-Q

[7] Lyu, Z., Ma, H., Zhang, H., & Ying, W. (2018). Solubility of carbon dioxide in methanol from 213.15 K to 273.15 K: Measurement and modeling. *Fluid Phase Equilibria*, 471, 40–54. doi: 10.1016/j.fluid.2018.04.014

[8] Chaparro, G., Cartes, M., & Mejía, A. (2020). Vapor–liquid equilibrium at 94 kPa and surface tension at 298.15 K for hexane+ ethanol+ cyclopentyl methyl ether mixture. *Fuel*, 279, 118415. doi: 10.1016/j.fuel.2020.118415

[9] Laursen, T., & Andersen, S.I. (2002). High-pressure vapor- liquid equilibrium for nitrogen + methanol. *Journal of Chemical and Engineering Data*, 47(5), 1173–1174. doi: 10.1021/je020006z

[10] Höhler, F., Deschermeier, R., Rehfeldt, S., & Klein, H. (2018). Gas solubilities of carbon dioxide in methanol, acetone, mixtures of methanol and water, and mixtures of methanol and acetone. *Fluid Phase Equilibria*, 459, 186–195. doi: 10.1016/j.fluid.2017. 12.004

[11] Yang, W., Xia, J., Wang, X.Y., Wan, K.D., Megaritis, A., & Zhao, H. (2021). Predicting evaporation dynamics of a multicomponent gasoline/ethanol droplet and spray using non-ideal vapour-liquid equilibrium models. *International Journal of Heat and Mass Transfer*, 168, 120876. doi: 10.1016/j.ijheatmasstransfer.2020. 120876

[12] Ray, S., Sree Harsha, V.V., & Raghavan, V. (2019). Prediction of vapor-liquid equilibrium of ternary system at high pressures. *Archives of Thermodynamics*, 40(2), 137–149. doi: 10.24425/ ather.2019.129545

[13] Koretsky, M.D. (2012). *Engineering and chemical thermodynamics* (2nd ed.) John Wiley & Sons.

[14] Poling, B.E., Prausnitz, J.M., & O'Connell, J.P. (2001). *Properties of gases and liquids*. McGraw-Hill Education.

[15] Jorda J.A., & Sirignano, W.A. (2017). Analytical/computational approach to liquid spray heating and vaporization at supercritical pressures. *Ilass−Europe, 28th European Conference on Liquid Atomization and Spray Systems*, 6–8 Sept., Valencia, Spain, 686–693. doi: 10.4995/ilass2017.2017.4615

[16] Lin, H.M., Kim, H., & Chao, K.C. (1981). Gas-liquid equilibria in nitrogen + *n*-hexadecane mixtures at elevated temperatures and pressures. *Fluid Phase Equilibria*, 7(2), 181–185. doi: 10.1016/0378-3812(81)85020-0

[17] Nemati Lay, E., Taghikhani, V., & Ghotbi, C. (2006). Measurement and correlation of CO_2 solubility in the systems of CO_2 + toluene, CO_2 + benzene, and CO_2 + *n*-hexane at near-critical and supercritical conditions. *Journal of Chemical and Engineering Data*, 51(6), 2197–2200. doi: 10.1021/je0602972

[18] Lin, H.-M., Sebastian, H.M., & Chao, K.-C. (1980). Gas-liquid equilibrium in hydrogen + n-hexadecane and methane + n-hexadecane at elevated temperatures and pressures. *Journal of Chemical and Engineering Data*, 25(3), 252–254. doi: 10.1021/je60086a012

[19] Søreide, I., & Whitson, C.H. (1992). Peng-Robinson predictions for hydrocarbons, CO_2, N_2, and H_2S with pure water and NaCI brine. *Fluid Phase Equilibria*, 77, 217–240. doi: 10.1016/0378-3812(92)85105-H

[20] Uribe-Vargas, V., & Trejo, A. (2004). Vapor-liquid equilibrium of nitrogen in an equimolar hexane + decane mixture at temperatures of 258, 273, and 298 K and pressures to 20 MPa. *Fluid Phase Equilibria*, 220(2), 137–145. doi: 10.1016/j.fluid.2004.03.009

[21] Dhima, A., de Hemptinne, J.-C., & Jose, J. (1999). Solubility of hydrocarbons and CO_2 mixtures in water under high pressure. *Industrial and Engineering Chemistry Research*, 38(8), 3144–3161. doi: 10.1021/ie980768g

[22] Camacho-Camacho, L. E., Galicia-Luna, L.A., & Elizalde-Solis, O. (2011). Vaporth–liquid equilibria of binary and ternary systems containing carbon dioxide, alkane, and benzothiophene. *Journal of Chemical & Engineering Data*, 56(11), 4109–4115. doi: 10.1021/je200586g

Normal and failure operation mode of resistojet thruster – experimental research on the laboratory model

Jan Kindracki*, Michał Romanowski

Institute of Heat Engineering, Faculty of Power and Aeronautical Engineering, Warsaw University of Technology.
Nowowiejska 21/25, 00-665 Warsaw, Poland
*Corresponding author email: jan.kindracki@pw.edu.pl

Abstract

Rocket thrusters of various types are used in space to change orbits, maneuver, and position control. The progressive trend in miniaturization of satellites also entails changes in propulsion systems. In recent years, electric rocket thrusters have become increasingly important. Resistojets are one of the simplest types offering thrust ranging from several to hundreds of millinewtons and use two types of energy: potential (pressure) and electrical. Electrical energy added by a resistive element − a heater − allows a significant increase in the temperature and specific impulse of the working medium. The paper considers the case of damage or lack of electrical power to the heater, which changes the engine operating mode from resistojet to coldgas. Experimental tests were carried out on a model of resistojet thruster operating in atmospheric conditions, both with the heater on and off. For the resistojet mode (heater on), three different variants of the flow delay to the heater activation time were considered. The analysis of results showed how the key propulsion parameters of the thruster change: specific impulse, total impulse, thrust and mass flow rate. For the tested model engine, wherein the resistojet mode the temperature was higher by approximately 120°C compared to coldgas, and approximately a 30% increase in specific impulse was observed. This demonstrates the advantages of the resistojet, where a heater failure "only" causes a reduction in the propulsion potential and not its complete loss. The spaceship or a satellite with resistojet thruster onboard has still the opportunity to accomplish mission goals.

Keywords: Thruster; Coldgas; Resistojet; Normal operation

1. Introduction

Different rocket propulsion systems have been used for almost 70 years to conquer space. All of them can be divided into chemical, nuclear, electric, and thermal [1]. Advances in the third one are low propellant use, resulting in small thrust compared to other propulsion systems. Small forces are not a drawback in satellites where they are desired. They are divided into three groups: electrothermal, electrostatic, and electromagnetic. From all of them, electrothermal propulsions give relatively high thrust without the demand of an enormous power supply [2]. In this type, heat is the energy obtained from electricity used to expand and later expel gas through the nozzle, creating thrust. The first way to reach this force is arcjet with propellant heated by electric discharge in its flow, but it demands quite a huge current. It contrasts resistojets where power conditioning is simpler. A heat exchanger is a resistance wire through which fuel flows, gaining temperature and pressure.

Kindracki J., Romanowski, M.

In the case of damage to the heater, this thruster could also serve as a cold gas propulsion in backup mode. Thus, part of the mission objectives may be saved if a less efficient thruster is still available. That family of thrusters needs only a valve that controls the flow of the working medium: gas, liquid [3] or even solid [4]. Both resistojet and cold gas operate with a wide group of propellants, such as gaseous hydrogen, carbon dioxide, nitrogen oxygen, hydrocarbons, and noble gases or liquid hydrazine, ammonia, and water [2]. Important information is whether the fuel is flammable, toxic, or reactive [5]. Those properties could limit use for safety reasons or possible damage to a stand.

Short reviews show that the thrust for cold gas is reaching values of a few millinewtons up to newtons [3,6,7]. It has a specific impulse typically between 300 m/s to 750 m/s, can operate under a 10 W power supply, and has a total weight below 2 kg. The same paper described resistojets with thrust from 10−200 mN and a specific impulse of 500–1500 m/s. Much more power is needed: 15–100 W which typically enables reaching 500−700°C. In the papers [8,9], researchers found that if there is an available bigger power source, the increase of specific impulse in resistojet thruster achieves 1.66−1.83 times higher than cold gas [8,9]. Thrust value could be enlarged by using multiple nozzles [10].

A resistojet thruster uses two types of energy: the potential energy of the pressure of the working medium located in the engine chamber and electrical energy, which increases its gas temperature, thereby increasing the engine's propulsion parameters. The profit from using electricity increases with the temperature of the working medium heated using a resistive circuit − a heater. The efficiency of the restistojet thruster is influenced by several factors: the type of gas used, the amount of pressure, and the temperature of the medium. During thruster operation, several different failure scenarios are possible, but one does not completely exclude the further use of a partially damaged engine. Such a scenario causes damage to the heater or a lack of electricity to power it. The paper describes a laboratory model of a resistojet thruster working in two modes: as a resistojet and in the case when the heater is a failure as cold gas.

2. The research stand

The research stand was built to conduct measurements of thruster performance. It consists of gas and power supply systems, a heating chamber, a nozzle, and a measurement system. A scheme of the stand is presented in Fig. 1a and Fig. 2 view of the real setup. The research thruster was made of 316 AISI stainless steel with three flow channels ending with a convergent-divergent nozzle. Two engine channels are connected to resistance heaters, increasing the working gas temperature. The third channel, located close to the outer wall, was used to recover heat from the walls of the inner channels. It decreases heat losses from the heaters to the walls. The heaters are supplied with 0.3 mm resistance wire, sheathed with ceramic insulation. The wire and ceramic insulation were enclosed in an Inconel alloy cover. The possibility of safe use of heating wire was up to 1000°C. It has an external diameter of 1 mm and a resistivity of 9 Ω/m. The research thruster is connected to a system equipped with a 24 V electromagnetic valve, a Venturi measuring tube upstream of the valve, static pressure sensors, and a buffer tank with a pressure regulator. The working gas was fed to the buffer tank from a high-pressure cylinder. The working gas is synthetic air (oxygen and nitrogen).
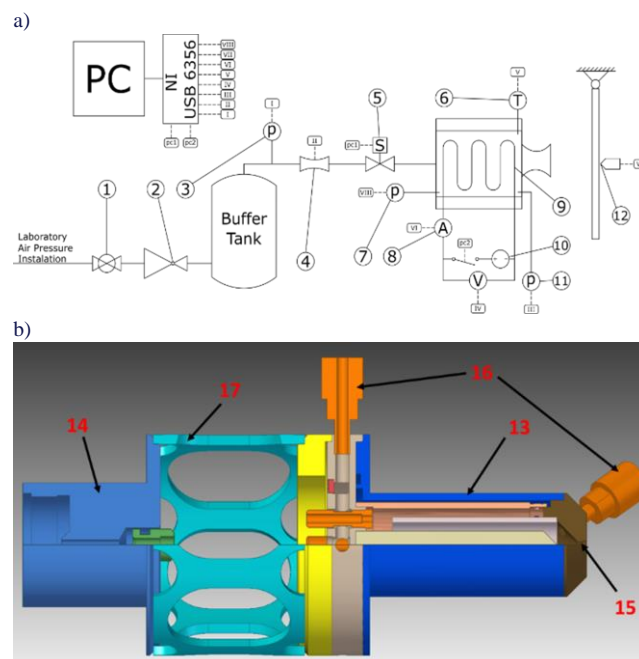
Fig. 1. The research stand: a) scheme: 1 – valve, 2 – pressure regulator, 3 – pressure in the feeding line (in front of the Venturi), 4 – Venturi tube, 5 – electromagnetic valve, 6 – temperature after the heater, 7 – pressure before the heater, 8 – current sensor, 9 – heater in the constructed thruster, 10 – power supply, 11 – pressure sensor at the nozzle inlet, 12 – baffle plate measurement system; b) view of the thruster: 13 – heater chamber (φ15 x 5 mm), 14 – control valve, 15 – nozzle, 16 – pressure/temperature ports, 17 – thermal barrier.

The measurement system was based on a National Instruments USB 6356 measurement card with 8 analog channels and a maximum sampling frequency of 1 MHz Keller PAA-23 pressure sensors with various measurement ranges were used, depending on the location. A Czaki company type K thermocouple was used to measure working medium temperature in three locations: the buffer tank and the inlet and outlet heating channel. The mass flow rate was calculated from the Venturi tube meas-
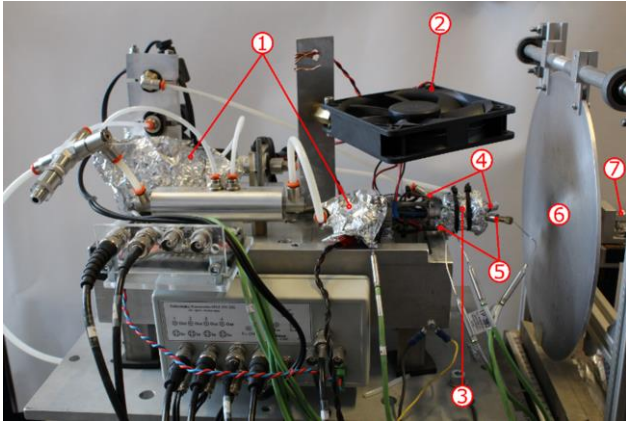
Fig. 2. View of the research stand. 1 – thermal isolation, 2 – cooling fan, 3 – isolation on the constructed thruster, 4 – pressure sensor connectors, 5 – thermocouple connectors, 6 – baffle plate, 7 – force sensor.

urements using the relation described in [11].

The model of resistojet thruster consists of three channels. After opening the control valve, the working medium flows towards the outlet nozzle and increases its temperature. The increase of the temperature of the working medium effectively can be controlled by the power (temperature) of the heater and the heat exchange surface, which affects the length of the flow channel. In the described thruster model, both parameters were optimally selected in the paper [11], taking into account the limitations related to the maximum temperature of the heater and the length of the heating channel itself. For the maximum temperature, the strongest limitation was the maximum temperature of the heater material – in this case, 1000°C was the limit. For the dimensions of the thruster model, a solution with three channels was adopted (two of them have heaters) where the flow is reversed twice before it reaches the nozzle, which is associated with pressure losses but reduces the surface-to-volume ratio of the thruster, which significantly minimizes heat losses.

3. Experimental results

A matrix of variable parameters was adopted to compare both thruster operating modes. Two parameters were selected: flow time and the flow activation time delay compared to the heater activation time. The flow time is related to the possibility of implementing the shortest possible single control pulse in the thruster. For a cold gas thruster, the times of single pulses can be counted in milliseconds. However, it should be noted that the structure of such an engine is very simple – it is a control valve and an outlet nozzle. For a resistojet engine, this time is longer because the flow channel's length must be considered. The channel should be long enough to increase the working medium temperature. The extension of the channel affects the inertia of the working medium flow, but on the other hand, it affects the possibility of increasing its temperature. Therefore, the resistojet thruster must have longer operating times for a single pulse. So, the length of a single pulse for the resistojet thruster is the limiting value.

The second important question to answer is when the flow will be turned on, in comparison to the time of heater switching.

Heating of the heater takes some finite time, and activating the heater at the same time as the flow means that in the initial period, the resistojet thruster will work in cold gas mode. The time to reach the operating temperature will be longer due to the cooling effect of the working medium flow. Therefore, turning on the heater before starting the flow is reasonable. This means that working gas starts to flow around the warmed heater wire and almost immediately switches to working in resistojet mode. Therefore, the second tested parameter is the delay time (flow activation time relative to the activation time of the heater), but this parameter was only tested for resistojet mode. These parameters for all examined cases are shown in Table 1.

Table 1. Experiments matrix: a combination of the flow time and delay time for both cases of thruster work.

Delay time [s]	Flow time [s]					
	Coldgas			Resistojet		
	2	5	10	2	5	10
0	CG-Case 0.2	CG-Case 0.5	CG-Case 0.10	RJ-Case 0.2	RJ-Case 2.5	RJ-Case 0.10
1				RJ-Case 1.2	RJ-Case 2.5	RJ-Case 1.10
2				RJ-Case 2.2	RJ-Case 2.5	RJ-Case 1.10

The case name: "Name-Case X.Y" contains information about the working mode: "Name": CG – coldgas, RJ – resistojet, and X – delay time in second, Y – flow time in second, respectively. Each measurement point was repeated at least three times, each time returning the initial temperature of the stand to the same value. The cooling fan (2) shown in Fig. 2 was used for this purpose. Figure 3 shows the test stand's typical course of the measured parameters. The engine thrust was measured using the baffle plate method, which allows for spatial separation between the thruster and the plate with a force sensor. This means that vibrations caused by, e.g. actuation of valves, do not affect the thrust measurement. Thanks to the knowledge of the mass flow rate, it is also possible to calculate the specific impulse – the basic parameter of a rocket thruster.
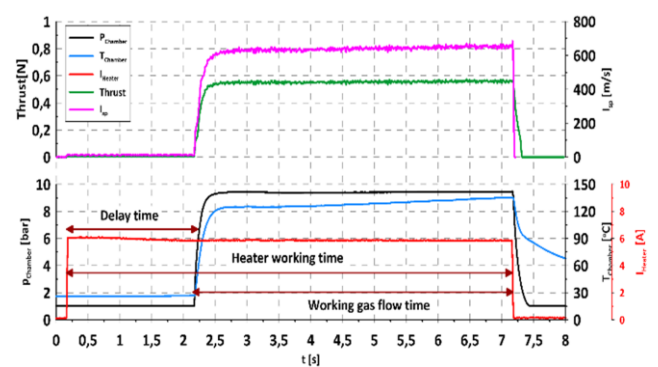
Fig. 3. Typical course of measured parameters.

The experiment mentioned above (Fig. 3), where the delay time was 2 s and the flow time was 5 s, is analyzed in detail in Fig. 4. It will see the heater warming up time, which shows a decrease in the current from 6.05 A to a stabilized value of 5.85 A

(change of electrical resistance as a function of temperature). The heater current in the following part of the experiment ranges within ±0.66%, which shows how stable the energy transfer to the working gas was. The pressure at the outlet of a heating channel is varied within ±0.6%, and the temperature of the working gas about 340 ms after flow starts reaches approximately 125°C and increases by approximately 10 degrees for the next 5 seconds. It means that the thruster walls have not achieved a steady state.
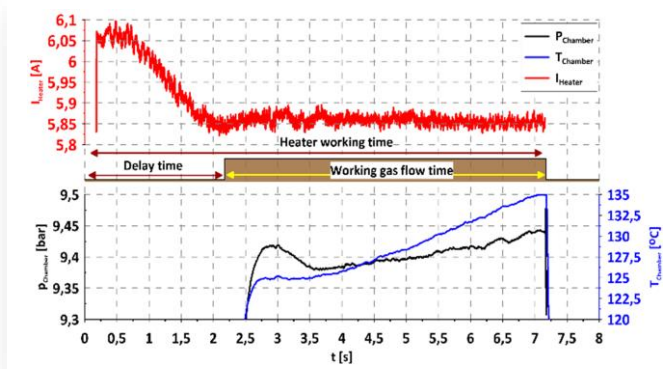
Fig. 4. Course of selected parameters of the experiment.

For all experiments performed, similar curves were obtained, as presented above. The propulsion parameters should be compared to the operation of the thruster in both modes (CG and RJ): the specific impulse and the total impulse were selected. A comparison of the specific impulse for the CG and RJ operating modes with three different delay times of turning on the flow (for RJ mode) is shown in Fig. 5, and the calculated values, including the total impulse, are shown in Table 2. To determine the theoretical ones, it was assumed that the thruster in the CG mode operates on a working medium at a temperature of 25°C, while in RJ mode with 150°C. In both modes, the same pressure was assumed in the engine chamber.
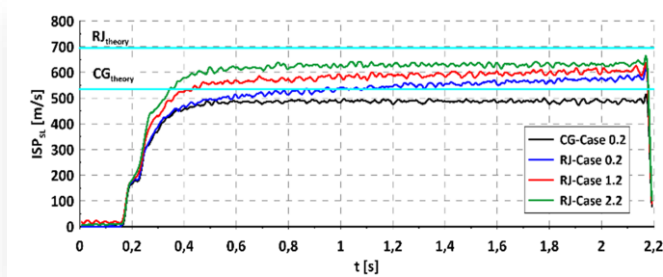
Fig. 5. Specific impulse in the function of time for all cases with 2 s of gas flow. Beginnings of flow are shifted to place them in one moment.

Table 2. Calculated propulsion parameters for both work modes of a thruster.

Case	ISP_t [m/s]	ISP_r [m/s]	I_{TT} [Ns]	I_{TR} [Ns]	I_{TR}/I_{TT} [%]
CG 0.2	535	487.5	1070.2	856.2	80
RJ 0.2		550.6		944.6	64.9
RJ 1.2	694.5	590.3	1389.3	1033.9	74.5
RJ 2.2		629.7		1105.7	79.5

Looking at the calculated parameters, two conclusions can be drawn. Firstly, it is beneficial to use a delay in starting the flow to the starting of the heaters, which increases the total impulse by 161 Ns (17%). Secondly, using a heater in the thruster increases the total impulse value in the RJ mode by approximately 29% compared to the CG mode.

Analyzing the graphs shown in Fig. 6, it can be concluded that the flow time is not important for the obtained specific impulse values. However, they confirm the validity of a delay in turning on the flow.
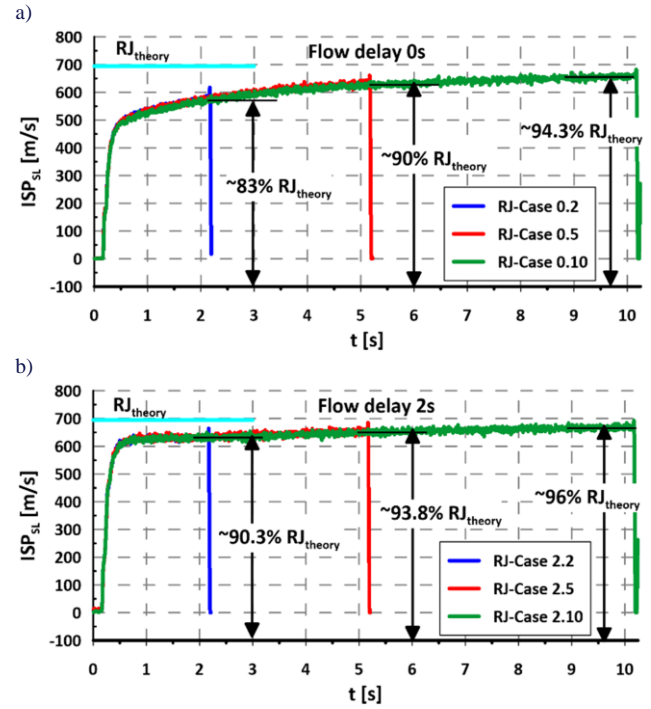
Fig. 6. Specific impulse in a function of time with different flow times: 2 s, 5 s, 10 s for: a) delay time – 0 s; b) delay time – 2 s.

From the driven spaceship's perspective, the most important parameter is the engine thrust. The transition from the RJ mode (e.g. in a failure situation) to the CG mode causes a slight increase in the thrust value (see Fig. 7) – in this case, the change is between 6.3% and 9.3%. This is because gas at a higher temperature has a larger specific volume, which causes a different mass flow rate through the same thruster geometry, confirmed by the graph shown in Fig. 8. The mass flow rate for the CG mode was assumed as 100%. For the RJ mode of operation, this flow value decreases. For short pulses of thruster operation, the drop depends on the delay time; for long operating times, it stabilizes at the same level. This is due to the thruster reaching the same operating temperature value – it is reached faster for cases where the delay time is longer.

The large impact of the delay time on the propulsion parameters is well illustrated by how fast the temperature at the nozzle inlet increases (see Fig. 9). We assume that the nominal temperature value for this analysis can be taken as a value between 9 and 10 seconds of the working time. If the flow is started with the heater, it takes as much as 5.805 s to reach 90% of the nominal value; for a 1 s delay, this time drops to 5.15 s, and for a 2 s delay, it drops to 3.247 s. If we take 75% as the reference level

of the nominal value, these times are as follows: 3.155 s, 2.05 s and 0.2 s. For comparison, the temperature at this same point of the inlet nozzle is also shown; for three experiments with different working times, these differences do not exceed 0.4°C.

4. Summary

A research stand was presented, and experimental tests were carried out for a resistojet thruster, which can operate in normal and emergency modes. The tests were carried out for two main cases: in the coldgas mode - the influence of the duration of operation of a single pulse was checked; for the resistojet mode, the influence of operation time and the delay time of starting the flow to the time of starting the heater was examined. For the resistors operating mode, it was found that the delay in opening the flow is very significant. The efficiency (represented by the total impulse) increases significantly from 67.9% to almost 80%. From a control law point of view, the ideal shape of the thruster control pulse is a rectangle; in reality, we can only fol-low this shape. Experimental cases with a delay time of 2 second are most similar to the required shape. In the case of a failure scenario for a thruster, in the form of the inability to turn on the heater, the thruster can be switched to cold gas mode. The total impulse will also be 80% of the theoretical value while the mass flow rate increases and the thrust decreases slightly. From a control system point of view, the thruster delivers the same level of thrust, but the onboard resources for the propulsion system wear out faster; in other words, the time of its use is shortened. In many cases, such a failure scenario of the propulsion system allows for saving at least part of the mission objectives.

The conducted research allows for quantitative estimation of one of the emergency scenarios and is a starting point for planning research using a vacuum chamber, in which these effects can be examined in conditions more similar to real ones.

Acknowledgments

References

[1] Sutton, G.P, & Biblarz, O. (2107). *Rocket Propulsion Elements*. (9th ed.) Wiley.

[2] Tajmar, M. (2012). *Advanced Space Propulsion Systems*. Springer.

[3] Tummala, A.R., & Dutta A. (2017). An Overview of Cube-Satellite Propulsion Technologies and Trends. *Aerospace,* 4(4), 58. doi: 10.3390/aerospace4040058

[4] Cervone, A., Mancas A., & Zandbergen B. (215). Conceptual Design of a Low-pressure Micro-resistojet Based on a Sublimating Solid Propellant. *Acta Astronautica,* 108, 30−39. doi: 10.1016/j.actaastro.2014.12.003

[5] Zakirov, V., Sweeting M., Lawrence, T., & Sellers, J. (2001). Nitrous Oxide as a Rocket Propellant. *Acta Astronautica*, 48(5−12), 353−362. doi: 10.1016/S0094-5765(01)00047-9

[6] Lemmer, K. (2017). Propulsion for CubeSats. *Acta Astronautica*, 134, 231–243. doi:10.1016/j.actaastro.2017.01.048.

[7] Leomanni, M., Garulli A., Giannitrapani A., & Scortecci F. (2016). Propulsion options for very low Earth orbit microsatellites. *Acta Astronautica*, 133, 444–454, doi: 10.1016/j.actaastro. 2016.11.001.

[8] Cifali, G., Gregucci, S., Andreussi, T., & Andrenucci, M. (2017). Resistojet thrusters for auxiliary propulsion of full electric platforms. *35th International Electric Propulsion Conference*, 8−12 October, Atlanta, Georgia, USA. http://electricrocket.org/IEPC/IEPC_2017_371.pdf [accessed 22 Nov. 2024].

[9] Hejmanowski, N., Woodruff, C.A., Burton, R.L., Carroll, D.L., & Cardin, J.M. (2015). CubeSat High Impulse Propulsion System (CHIPS). *62nd JANNAF Propulsion Meeting (7th Spacecraft Propulsion)*, 1–5 June, Nashville, TN, USA.

[10] Schmuland, D., Carpenter, C., & Masse, R. (2012). Mission applications of the mrs-142 cubesat high-impulse adaptable monopropellant propulsion system (champs). *48th AIAA/ASME/SAE/ASEE Joint Propulsion Conference & Exhibit*. 30 July−01 August, Atlanta, Georgia, USA. doi: 10.2514/6.2012-4269

[11] Kindracki, J., Paszkiewicz, P., & Mężyk, Ł. (2019). Resistojet Thruster with Supercapacitor Power Source – Design and Experimental Research. *Aerospace Science and Technology* 92, 847−857. doi: 10.1016/j.ast.2019.07.010
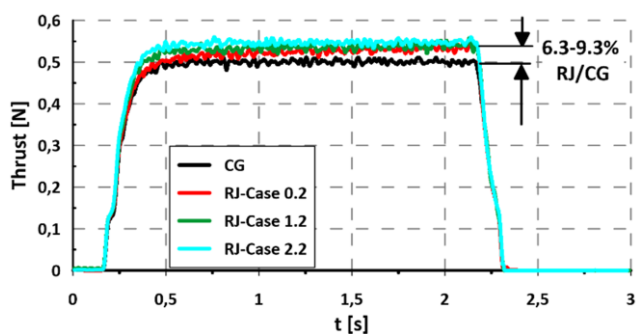
Fig. 7. Comparison of thrust as a function of time for CG and RJ work mode.
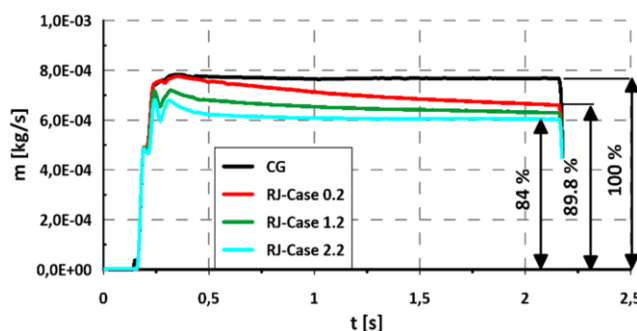
Fig. 8. Comparison of mass flow rate as a function of time for CG and RJ work mode.
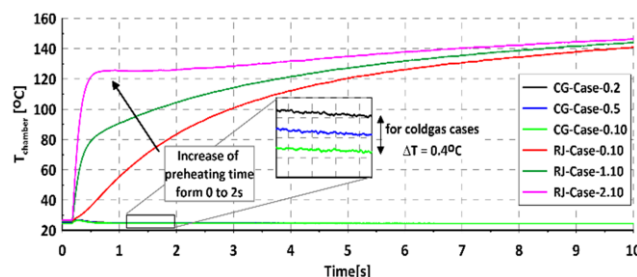
Fig. 9. Comparison of temperature profiles in CG and RJ working mode.

ARCHIVES OF THERMODYNAMICS

Investigations of the influence of leakage and diffusion of hydrogen-doped natural gas pipelines by numerical simulation

Xiang Zhou[a], Dewen Kong[a*], Teng Ren[b]

[a]Jiangsu Vocational College of Information Technology, No. 1 Qianou Road, Huishan District, Wuxi City, Jiangsu 214153, China
[b]Shenyang University of Technology, Shenyang, Liaoning 110023, China
*Corresponding author email: kongdwdw@outlook.com

Abstract

The leakage of natural gas pipelines will waste energy and damage the environment. Research on the leakage and diffusion features of hydrogen-doped natural gas is beneficial to the safe management of natural gas pipelines. This paper established a numerical model used for simulating and computing the diffusion of hydrogen-doped natural gas. Then, simulation experiments were conducted. First, the model accuracy was verified through experiments, and the appropriate mesh number of the model was determined. Then, the influence of different hydrogen blending ratios and various leakage hole diameters on the leakage and diffusion of gas was calculated. Under the same diffusion time, the higher the hydrogen content in the gas, the higher the diffusion rate of methane and hydrogen, and the diffusion rate of hydrogen had the most obvious change. Under the same diffusion time, the closer to the leakage hole, the higher the concentration of natural gas, and the concentration at the monitoring points at the same level differed little.

Keywords: Hydrogen mixing; Natural gas; Leakage; Numerical simulation

1. Introduction

With the continuous adjustment of the global energy structure and rapid development of clean energy, natural gas, as an environmentally friendly and efficient form of energy occupies an important position in the energy supply system [1]. Methane is the primary constituent of natural gas, and the products after combustion are carbon dioxide and water, which will not pollute the environment. Hydrogen, as a flammable gas, will not pollute the environment because its combustion product is water [2]. For the two combustible gases mentioned above, pipelines are usually used to transport them, and the addition of hydrogen to natural gas has the potential to enhance the efficiency of combustion, cut down carbon emissions, and make hydrogen and natural gas share a set of transportation pipelines, saving construction costs. However, natural gas pipelines will be damaged during use due to ageing or other unexpected factors. The damage may lead to natural gas leakage, which will not only cause energy waste but also may cause fire once the concentration of leakage is too high [3]. Meanwhile, high-concentration natural gas will also pose a threat to human health. Thus, investigating the characteristics of leakage and diffusion of hydrogen-doped natural gas pipelines has great practical significance and can offer a theoretical background for engineering practice and safety

Zhou X., Kong D., Ren T.

Nomenclature

A – diagonal matrix of M
B – resultant external force, N/m³
$C_{1\varepsilon}$, $C_{2\varepsilon}$, $C_{3\varepsilon}$ – turbulence constants
D – non-diagonal matrix of M
G_b – production of turbulent kinetic energy by buoyancy, J/(m³s)
G_k – production of turbulent kinetic energy by flow, J/(m³s)
J_i – diffusion flux of the i-th component, kg/(m²s)
k – turbulent kinetic energy, J/kg
M – molar mass of gas, kg/mol
M – coefficient matrix,
p, P – pressure, Pa
p' – corrected pressure, Pa
R – gas constant, J/(mol K)
S_i – source of mass, kg/(m³s)
S_m – source of momentum, N/m³

S_k – source term, J/(m³s)
S_ε – source term, J/(m³s²)
t – time, s
T – pipe temperature, K
U – velocity field, m/s
v – gas velocity, m/s
x – gas displacement, m
Y_i – mass fraction of the i-th gas component
Y_M – contribution of the fluctuating dilatation in compressible turbulence to the overall dissipation rate, J/(m³s)

Greek symbols

γ – specific heat ratio
ε – dissipation rate of turbulent kinetic energy, J/(kg s)
μ_{eff}, μ_l, μ_t – effective, laminar, turbulent viscosity, Pa s
ρ – gas density, kg/m³
σ_k – turbulence constant

administration in related fields. Moortgat et al. [4] described the scenario of shallow groundwater pollution caused by natural gas leakage due to horizontal drilling and hydraulic fracturing in the process of exploitation. They used the numerical model of gas phase migration related to leaking natural gas wells to simulate working conditions, which provides an effective contribution to evaluating the leakage frequency of faulty natural gas wells and reducing leakage events. Shan et al. [5] designed a practical approach combining a Bayesian network with a bow-tie model for assessing the risk of natural gas pipeline leakage. The analysis of the case revealed that negligence in signage, implicit signage, excessive load, and design flaws in auxiliary equipment were identified as the primary factors inducing natural gas pipeline leakage. Wu et al. [6] established a Bayesian inference-iterative ensemble Kalman filter model for estimating source terms (leak location and leakage rate) and forecasting gas concentration distribution. Lee et al. [7] utilized a restricted quantity of sensors for the early detection of chemical leaks, thereby facilitating prompt and suitable initial response. Zandi et al. [8] conducted research on natural gas leaks resulting from pipeline failures in both atmospheric and porous conditions using a three-dimensional simulation methodology. Li et al. [9] compared the disparities in the distribution of hydrogen-blended natural gas flow fields released from three pipeline leakage sources: gas flowing downwards in a vertical pipe with a leak hole on the pipe wall, gas flowing upwards in a vertical pipe with a leak hole on the pipe wall, and a leak hole at the end of a horizontal pipe. In this article, a numerical model was designed to simulate the diffusion of hydrogen-doped natural gas, and simulation experiments were also conducted.

2. Materials and methods

2.1. Experimental environment

The numerical simulation of hydrogen-doped natural gas pipeline leakage and diffusion was conducted on a laboratory server with the Windows 10 operating system, 32 G memory, and Core I7 processor.

2.2. The numerical model of gas diffusion

The relevant mathematical models involved in the simulation of leakage and diffusion of hydrogen-doped natural gas pipelines include the governing equations and the turbulent motion equations, where the governing equations are:

$$\frac{\partial \rho}{\partial t} + \nabla \cdot (\rho v) = 0,$$

$$\frac{\partial (\rho v)}{\partial t} + \nabla \cdot (\rho v^2) = -\nabla p' + \nabla \cdot (\mu_{eff} \nabla v) + B + S_m, \quad (1)$$

$$\frac{\partial (\rho Y_i)}{\partial t} + \nabla \cdot (\rho v Y_i) = -\nabla J_i + S_i.$$

The first governing equation is a continuity equation, the second is a momentum conservation equation, and the third is a component conservation equation. ρ represents the gas density, v – gas velocity, t represents time, μ_{eff} represents the effective viscosity, p' is the corrected pressure, B is the resultant of all the external forces, S_m is the source of momentum, Y_i is the mass fraction of the i-th component in the gas, J_i is the diffusion flux of the i-th component, and S_i is the source of mass [10].

The governing equations ensure the basic rules to be followed by the gas in the numerical simulation process [11], and the simulation of the gas flow needs the application of the turbulent motion equations. In this paper, a common k-ε turbulence model [12] is adopted. The reason for choosing this turbulence model is that it is a semi-empirical formula summarized from experimental phenomena, so it has extensive applications, low computational cost, and reasonable accuracy. Its formula is:

$$\frac{\partial}{\partial t}(\rho k) + \frac{\partial}{\partial x}(\rho k v) = \frac{\partial}{\partial x}\left(\left(\mu_l + \frac{\mu_t}{\sigma_k}\right)\frac{\partial k}{\partial x}\right) +$$

$$+ G_k + G_b - \rho \varepsilon - Y_M + S_k,$$

$$\frac{\partial}{\partial t}(\rho \varepsilon) + \frac{\partial}{\partial x}(\rho \varepsilon v) = \frac{\partial}{\partial x}\left(\left(\mu_l + \mu_t + \frac{\mu_t}{\sigma_k}\right)\frac{\partial \varepsilon}{\partial x}\right) +$$

$$\text{(2)}$$

$$+ C_{1\varepsilon}\frac{\varepsilon}{k}(G_k + C_{3\varepsilon}G_b) - C_{2\varepsilon}\rho\frac{\varepsilon^2}{k} + S_\varepsilon,$$

where k denotes the turbulent kinetic energy, ε denotes the dissipation rate of turbulent kinetic energy, μ_l is the laminar viscosity coefficient, μ_t is the turbulent viscosity [13], G_k is the turbulent kinetic energy produced by mean velocity gradients, G_b is the turbulent kinetic energy produced by buoyancy, Y_M represents the contribution of the fluctuating dilatation in compressible turbulence to the overall dissipation rate, S_k, S_ε are source terms, $C_{1\varepsilon}$, $C_{2\varepsilon}$, $C_{3\varepsilon}$ and σ_k are turbulence constants.

The governing equations and turbulent motion equations are used to simulate the leakage and diffusion of the blended gas. This paper adopts the SIMPLE algorithm to solve the equation iteratively. The basic flow is as follows:

① The subject of numerical simulation is modelled. In order to facilitate the calculation, the model is simplified, and the side of the damaged pipe opening facing the atmosphere forms a closed two-dimensional rectangular space with the atmospheric space (The closure here is used to limit the spatial range of calculations rather than to enclose atmospheric space) [14].

② After the two-dimensional rectangular space is divided into grids and given boundary conditions, the initial working conditions are set, including the initial velocity distribution and pressure distribution.

③ The velocity field is predicted according to the initial pressure, and the prediction equation [15] is:

$$MU = -\nabla p, \tag{3}$$

where U is the velocity field, p is the pressure field, and M is the coefficient matrix.

④ The new pressure field is obtained using the pressure correction equation:

$$\nabla(A^{-1}\nabla p) = \nabla(A^{-1}D), \tag{4}$$

where A is the diagonal matrix of M and D is the non-diagonal matrix.

⑤ The velocity field is corrected using the corrected pressure field:

$$U = A^{-1}D - A^{-1}\nabla p. \tag{5}$$

⑥ It is determined whether the corrected velocity field satisfies Eq. (1). If not, it returns to step ③; if it does, then the iteration stops.

2.3. Numerical simulation

The schematic plot of the numerical simulation model of the simulation experiment is displayed in Fig. 1.
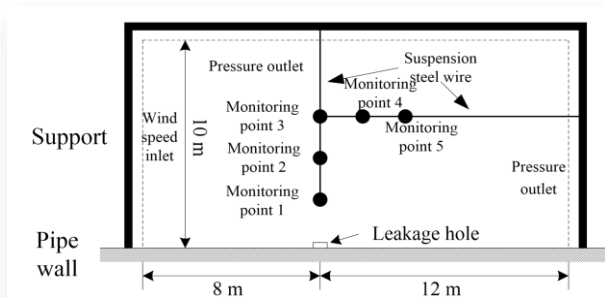
Fig. 1. Schematic plot of the numerical simulation model.

The model was simplified into a closed two-dimensional rectangular space, i.e. the two-dimensional rectangular space composed of the pipe wall and dashed line frame in Fig. 1, to simplify the calculation. The space is 10 m high and 20 m long, and the leakage hole is 8 m away from the left side. In the rectangular space, the left boundary is the wind speed inlet, the upper and right boundaries are pressure outlets, and the leakage hole is the natural gas velocity inlet. In addition, the thick black lines in Fig. 1, as well as the black dots and thin connecting lines, are part of the actual scaled model that will be validated for effectiveness later. Here, the numerical model was overlapped with the actual scaled model. The numerical model is represented by the region formed by pipe walls and dashed lines in the figure.

2.4. Experimental items

(1) Validation of numerical model

To facilitate operation during the numerical simulation, the model was simplified to some extent, which led to some errors between the calculated results and the actual results. Therefore, to guarantee the precision of the simulation under various working conditions, the validity of the numerical model was verified first. To assess the effectiveness of the numerical model, an equal scale model was built, and then a support was set up outside the two-dimensional rectangular space as shown in Fig. 1. A gas sensor was set on the monitoring points 1–5 using the support. The monitoring point 1 was 2 m above the leakage hole, and the interval between adjacent monitoring points was 2 m. The sensors on the monitoring point were fixed by suspending steel wires according to Fig. 1. The steel wires were as thin as possible to guarantee the sensors' stability.

Because the wind speed in the natural environment is difficult to control, the test environment was wind-free, the pressure in the pipeline was 3.0 MPa, the diameter of the leakage hole was 10 mm, the hydrogen mixing ratio of natural gas was 5%, and the leakage rate was 2.3 m³/h. The same conditions were substituted into the numerical model. In the numerical model, the number of grid cells in the two-dimensional rectangular space was set to 4 875, 5 425 and 6 387, respectively. The deviation between the calculation results of the numerical model at the monitoring point and the actual results was compared under different grid numbers when the diffusion was carried out for 5, 10, and 15 seconds.

(2) Influence of hydrogen mixing ratio on leakage and diffusion

During the numerical simulation, the hydrogen blending ratio was set to 0%, 5%, 10%, 15% and 20%, the pressure in the pipeline was set to 3.0 MPa, the diameter of the leakage hole was 10 mm, and the number of grid cells was set to 5 427. The computation formula for the gas leakage velocity [16] at the leakage hole is:

$$v = \frac{P}{\rho}\sqrt{\frac{M}{RT} \cdot \gamma \cdot \left(\frac{2}{\gamma+1}\right)^{\frac{\gamma+1}{\gamma-1}}}, \tag{6}$$

where P is the pipeline pressure, ρ is the gas density, M is the molar mass of the gas, γ is the specific heat ratio, R is the gas

constant, and T is the pipe temperature.

(3) The change of diffusion concentration when gas leaks

When conducting the numerical simulation, the hydrogen mixing ratio was set to 20%, the diameter of the leakage hole was set to 10 mm, the pipeline pressure was set to 3.0 MPa, and the number of grid cells was set to 5 427. The mass fraction change of natural gas and hydrogen at each monitoring point within 20 s after the diffusion began was simulated.

2.5. Experimental results

Before using the model to simulate the leakage, the validity of the model was verified first, and the calculation error and time consumption of the numerical model under different grid cell numbers were compared. The final results are presented in Table 1. Under the same number of grid cells, with the increase of

simulated diffusion time, the average error between the mass fraction of methane and hydrogen at the monitoring point calculated by the model and the actual value did not change significantly, nor did the standard deviation of the error change significantly. In other words, the model's simulated calculation of gas diffusion was relatively stable. Under the same simulated diffusion time, although the calculation time of the model under the 4 875 grid count was the least, the calculation error and the standard deviation of the error were large, while the model under the 5 425 grid count and the 6 387 grid count had relatively smaller calculation errors and standard deviations, with little difference between them. However, the model under the 6 387 grid count consumed more simulated calculation time. Therefore, this paper used a model with a grid size of 5 425 cells for the subsequent simulated calculation.

Table 1. Validity verification of the numerical model with different grid cell numbers.

Diffusion time, s	Number of grid cells	Average error of methane mass fraction, %	Standard deviation of methane mass fraction error, %	Average error of hydrogen mass fraction, %	Standard deviation of hydrogen mass fraction error, %	Simulation time, s
5	4 875	2.34	1.11	2.33	1.12	1.22
	5 425	1.53	0.53	1.52	0.52	1.23
	6 387	1.52	0.53	1.51	0.53	1.48
10	4 875	2.53	1.22	2.52	1.23	1.89
	5 425	1.61	0.52	1.60	0.51	1.90
	6 387	1.51	1.23	1.51	0.52	2.05
15	4 875	2.52	1.25	2.50	1.24	2.03
	5 425	1.62	0.53	1.61	0.52	2.06
	6 387	1.53	0.56	1.51	0.53	2.41

The numerical model was employed to simulate the leakage and diffusion of gas under various hydrogen mixing ratios. The diffusion rates of methane and hydrogen are shown in Fig. 2. With the passage of leakage diffusion time, the diffusion rates of methane and hydrogen in natural gas eventually tended to be stable, and the rates of methane and hydrogen diffusion tended to be consistent in the end. Under the same diffusion time, the higher the hydrogen proportion in the gas, the higher the diffusion rate of methane and hydrogen, and the diffusion rate of hydrogen had the most apparent change.

The numerical model was employed to simulate the natural gas leakage and diffusion with 20% hydrogen and 10 mm leakage hole diameter. The concentration variation at the monitoring points during diffusion is shown in Table 2. With the passage of diffusion time at each monitoring point, the gas concentration presented a trend of rapid rise at first, then a slow decline, and finally stability. At the same time after the beginning of diffusion, the gas concentration at the monitoring points closer to the leakage hole was higher, while the gas concentration at the monitoring points at the same height level was not significantly different.
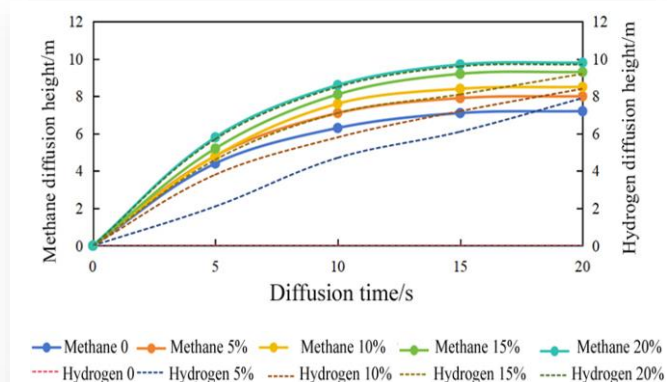
Fig. 2. Diffusion rates of methane and hydrogen under various hydrogen mixing ratios.

Table 2. Changes in concentration at the monitoring points.

Monitoring point	Gas concentration, %	0 s	5 s	10 s	15 s	20 s
1	Methane	0	24.5	20.6	18.5	18.3
	Hydrogen	0	6.3	5.2	4.6	4.5
2	Methane	0	22.1	18.9	17.8	17.6
	Hydrogen	0	5.6	4.8	4.4	4.2
3	Methane	0	19.8	17.8	16.9	16.7
	Hydrogen	0	4.9	4.6	4.1	4.1
4	Methane	0	18.9	16.7	13.4	13.2
	Hydrogen	0	4.7	4.2	3.3	3.2
5	Methane	0	18.7	16.6	10.3	10.1
	Hydrogen	0	4.6	4.1	3.2	3.1

3. Discussion

The incorporation of hydrogen into natural gas has the potential to decrease carbon dioxide emissions while maintaining optimal combustion efficiency. At the same time, the two types of gas share a set of transmission pipelines, and there is no need to lay additional pipelines for hydrogen, which greatly saves construction costs [17]. However, unexpected factors during use, such as earthquakes, hail, construction excavation, etc., and ageing due to long-time use may cause cracks or damage to the pipeline. When the pipeline transmits hydrogen-doped natural gas, the high pressure of the gas will produce loads on the inner wall of the pipeline. Once there is a gap in the wall of the pipeline, the gas will escape from the gap under the action of pressure difference, forming a natural gas leakage [18]. The leakage of natural gas will cause energy loss and produce a negative impact on the surrounding environment. In addition, once the leakage concentration reaches a certain level, it may also cause an explosion, further deepening the loss of the pipeline. Therefore, studying the leakage and diffusion characteristics of natural gas pipelines can provide an effective reference for pipeline construction and management.

When analyzing the leakage and diffusion characteristics of natural gas pipelines, the most direct method is to directly observe the leaking natural gas near the pipeline [19]. In this method, on the one hand, natural gas is usually colourless, which is difficult to observe by the naked eye directly, and the detection sensor can only provide the local gas distribution state. On the other hand, the natural gas pipeline is a public facility, and it is impossible to destroy it anytime and anywhere for the purpose of experiment. With the development of technology, the computing power of computers is getting stronger and stronger. By building mathematical models and using computers to perform calculations [20], the characteristics of natural gas leakage and diffusion can be numerically simulated.

The paper used a mathematical model of gas diffusion to simulate the leakage of hydrogen-mixed natural gas. In this process, in order to facilitate calculation, the area where hydrogen-doped natural gas leaks from the pipeline is simplified as a two-dimensional rectangular space. The effectiveness of the numerical model was verified by using an actual scaled model. Subsequently, the numerical model was used to test the influence of hydrogen-doped ratios on leakage diffusion and changes in concentration during the diffusion process. When the number of grid cells increased from 4 875 to 5 425, the error of the numerical model decreased, but the computation time increased. However, when the number of grid cells increased from 5 425 to 6 387, there was no significant change in the error of the numerical model, but the computation time still increased. The reason for this is that an increase in grid quantity means an increase in details in the numerical model, allowing for more accurate calculations. However, this improvement has marginal effects: once a certain number of grid cells is reached, it becomes difficult to further reduce calculation errors while the computational workload continues to rise. In the same diffusion time, the higher the hydrogen content in hydrogen-doped natural gas, the higher the diffusion rate of methane and hydrogen. The variation in diffusion rate was most significant for hydrogen. This is because hydrogen is less dense than natural gas, making it more diffusive. Additionally, the disturbance caused by the rapid diffusion of hydrogen also drives the diffusion of natural gas.

In conclusion, based on the effect of hydrogen content in hydrogen-doped natural gas on the diffusion of leaked natural gas, when preventing the risk of leakage in hydrogen-doped natural gas pipelines, it is advisable to first focus on the concentration of hydrogen in natural gas. While ensuring the combustion performance of hydrogen-doped natural gas, efforts should be made to minimize the concentration of hydrogen as much as possible.

4. Conclusions

This paper established a numerical model used to simulate how the hydrogen-doped natural gas diffuses. Then, simulated experiments were performed. Firstly, the validity of the numerical model was verified through experiments, and the appropriate mesh number of the model was selected. Then, the effect of various hydrogen-doped ratios and different leakage hole diameters on the leakage and diffusion of the hydrogen-doped natural gas was analyzed using simulation. When the number of grid cells was 5 425, there was little difference between the results calculated by the model and the actual results. The errors were relatively stable, and the calculation time was less. Under the same diffusion time, the higher the hydrogen proportion in the gas, the higher the diffusion rate of methane and hydrogen, and the diffusion rate of hydrogen had the most obvious change. The gas concentration in each monitoring point presented a trend of rapid rise at first, then a slow decline, and finally tended to be stable as the diffusion time elapsed. The closer to the leakage hole, the higher the concentration of the natural gas, but there was little difference between the monitoring points at the same level.

References

[1] Chamberlain, S.D., Ingraffea, A.R., & Sparks, J.P. (2016). Sourcing methane and carbon dioxide emissions from a small city: Influence of natural gas leakage and combustion. *Environmental Pollution*, 218, 102–110. doi: 10.1016/j.envpol.2016.08.036

[2] Wang, D., Liu, P., Hua, C., Zhang, H., Shi, C., & Du, J. (2023). Research on natural gas leakage diffusion of urban underground pipeline and its explosion hazard. *KSCE Journal of Civil Engineering*, 27(2), 590–603. doi: 10.1007/s12205-022-1795-5

[3] Ren, L., Ni, Y., Liu, Q., & Chen, J. (2022). Experimental and numerical prediction model for the dangerous radius of natural gas leakage in soil. *ACS Omega*, 7(35), 30879–30893. doi: 10.1021/acsomega.2c02545

[4] Moortgat, J., Schwartz, F.W., & Darrah, T.H. (2018). Numerical modeling of methane leakage from a faulty natural gas well into fractured tight formations. *Ground Water*, 56(2), 163–175. doi: 10.1111/gwat.12630

[5] Shan, X., Liu, K., & Sun, P. L. (2017). Risk analysis on leakage failure of natural gas pipelines by fuzzy Bayesian network with a bow-tie model. *Scientific Programming*, 2017, 1–11. doi: 10.1155/2017/3639524

[6] Wu, J., Cai, J., Liu, Z., Bai, Y., Yuan, S., & Zhou, R. (2023). BI-IEnKF coupling model for effective source term estimation of

natural gas leakage in urban utility tunnels. *Tunnelling and Underground Space Technology*, 136, 105080. doi: 10.1016/j.tust.2023.105080

[7] Lee, H., Lee, D., & Shin, L.D. (2024). Efficient gas leak simulation surrogate modeling and super resolution for gas detector placement optimization. *Computers and Chemical Engineering: An International Journal of Computer Applications in Chemical Engineering*, 181, 108508.1–108508.13. doi: 10.1016/j.compchemeng.2023.108508

[8] Zandi, E., Alemrajabi, A.A., Emami, M.D., & Hassanpour, M. (2022). Numerical study of gas leakage from a pipeline and its concentration evaluation based on modern and practical leak detection methods. *Journal of Loss Prevention in the Process Industries*, 80, 104890. doi: 10.1016/j.jlp.2022.104890

[9] Li, Y., Wang, Z., & Shang, Z. (2024). Analysis and prediction of hydrogen-blended natural gas diffusion from various pipeline leakage sources based on CFD and ANN approach. *International Journal of Hydrogen Energy*, 53, 535–549. doi: 10.1016/j.ijhydene.2023.12.018

[10] Dezfouli, A.M., Saffarian, M.R., Behbahani-Nejad, M., & Changizian, M. (2022). Experimental and numerical investigation on development of a method for measuring the rate of natural gas leakage. *Journal of Natural Gas Science and Engineering*, 104, 104643. doi: 10.1016/j.jngse.2022.104643

[11] Baker, A. (2024). Fort Worth hotel explosion likely caused by natural gas leak injures 21. *Natural Gas Intelligence*, 43(25).

[12] Wang, B., Chen, L., Lin, W., Wu, D., Fang, Y., & Li, Z. (2022). Research on gas diffusion of natural gas leakage based on Gaussian plume model. *Arabian Journal of Geosciences*, 15(7), 1–8. doi: 10.1007/s12517-022-09922-6

[13] Mei, Y. & Shuai, J. (2022). Research on natural gas leakage and diffusion characteristics in enclosed building layout. *Process Safety and Environmental Protection*, 161, 247–262. doi: 10.1016/j.psep.2022.03.040

[14] Mujtaba, S.M., Lemma, T.A., & Vandrangi, S.K. (2022). Gas pipeline safety management system based on neural network. *Process Safety Progress*, 41, S59–S67. doi: 10.1002/prs.12334

[15] Miao, X., Zhao, H., & Xiang, Z. (2023). Leakage detection in natural gas pipeline based on unsupervised learning and stress perception. *Process Safety and Environmental Protection*, 170, 76–88. doi: 10.1016/j.psep.2022.12.001

[16] Hu, Q.J., Tang, S., He, L.P., Cai, Q.J., Ma, G.L., Bai, Y., & Tan, J. (2021). Novel approach for dynamic safety analysis of natural gas leakage in utility tunnel. *Journal of Pipeline Systems Engineering and Practice*, 12(1), 1–12. doi: 10.1061/(ASCE)PS.1949-1204.0000498

[17] Su, Y., Li, J., Yu, B., Zhao, Y., Han, D., & Sun, D. (2023). Modeling of hydrogen blending on the leakage and diffusion of urban buried hydrogen-enriched natural gas pipeline. *Computer Modeling in Engineering and Science*, (8), 1315–1337. doi: 10.32604/cmes.2023.026035

[18] Ebrahimi-Moghadam, A., Farzaneh-Gord, M., & Deymi-Dashtebayaz, M. (2016). Correlations for estimating natural gas leakage from above-ground and buried urban distribution pipelines. *Journal of Natural Gas Science and Engineering*, 34, 185–196. doi: 10.1016/j.jngse.2016.06.062

[19] Liao, K., Wang, Y., Chen, D., He, G., Huang, Y., Zhang, S., Qin, M., & He, T. (2023). Parametric study on natural gas leakage and diffusion in tunnels. *Journal of Pipeline Systems Engineering and Practice*, 14(2). doi: 10.1061/JPSEA2.PSENG-1396

[20] Zhang, B., Kang, R., Zhu, H., Yuan, Q., Gong, F., Wu, Y., & Zhou, X. (2024). Study of multisource leakage diffusion and explosion risk of underground natural gas pipelines. *Journal of Pipeline Systems Engineering and Practice*, 15(1), 1–16. doi: 10.1061/JPSEA2.PSENG-1499

ARCHIVES OF THERMODYNAMICS

Thermomagnetic convection and entropy generation in a hybrid nanofluid filled wavy-walled cavity heated non-uniformly

Nirmalendu Biswas[a], Dipak Kumar Mandal[b*], Nirmal K. Manna[c], Ali Cemal Benim[d]

[a]Department of Power Engineering, Jadavpur University, Salt Lake, Kolkata-700106, India
[b]Department of of Mechanical Engineering, Government Engineering College Samastipur, Bihar-848127, India
[c]Department of Mechanical Engineering, Jadavpur University, Kolkata-700032, India
[d]Department Mechanical and Process Engineering, Duesseldorf University of Applied Sciences, Germany
*Corresponding author email: dipkuma@yahoo.com

Abstract

In this work, thermomagnetic convection and irreversibility production in a hybrid nanofluid-filled wavy-walled porous thermal system containing a semi-circular heated bottom is presented. Both the sidewalls of the enclosure are cooled and undulated with varying undulation numbers. The lower wall is partially undulated following a semi-circular-shaped object and is heated isothermally. The horizontal walls are insulated. The cavity is occupied with Cu-Al_2O_3/water-based hybrid nanofluid and porous substances under the impact of the evenly applied horizontal magnetic field. This work significantly contributes to the existing research rendering an exhaustive understanding of the hydrothermal flow-physics as well as irreversibility production of a hybrid nanofluid in the cavity having surface undulation. The Galerkin weighted finite element method is utilized to solve the mathematical model. The hydrothermal performance of the thermal system is considerably influenced by various pertinent factors such as Darcy-Rayleigh number, Darcy number, Hartmann number, and number of undulations. The wall undulations have a critical role in altering the hydrothermal performance. Heatlines are used to analyse heat transport dynamics from the protruded hot surface to the heat sink. The protruded heater wall induces the formation of a hot upward plume in the nearest fluid layers. The flow divides into two parts forming a pair of circulations due to symmetrical cooling at the sidewalls. The flow behaviours are significantly dampened by increasing the Hartmann number. The associated total entropy generation is also demonstrated. This study contributes to the existing domain knowledge and provides insights for designing and optimizing similar thermal systems.

Keywords: Magnetohydrodynamic flow; Nanofluid flow; Hybrid wavy-wall heating; Entropy generation; Heat transfer

1. Introduction

The intriguing interplay of thermomagnetic convective phenomena and irreversibility generation within an undulated enclosure occupied with a hybrid nanofluid, subject to non-uniform heating, stands as a captivating challenge at the forefront of contemporary research in fluid dynamics and thermal sciences. This study delves into the captivating realm of magnetohydrodynamics (MHD), where magnetic fields influence the dynamics of fluids with electrical conductivity, particularly under the impact of temperature gradients. In the multifaceted arena of scientific exploration, this intersection of magnetic fields with fluid dynamics holds sway over a multitude of applications, each more intriguing than the last [1].

Nomenclature

A — amplitude, m
B — strength of magnetic field, N A^{-1}m^{-2}
c_p — specific heat, J kg^{-1}K^{-1}
Da — Darcy number
Ec — Eckert number
F_c — Forchheimer constant
g — gravitational acceleration, m^2/s
H — length scale, cavity height, m
Ha — Hartmann number
k — thermal conductivity, W m^{-1}K^{-1}
K — porous medium permeability, m^2
L — length of enclosure, m
n — undulation number
NS — dimensionless entropy generation
Nu — Nusselt number (average)
p — pressure, Pa
P — dimensionless pressure
Pr — Prandtl number
Ra — Rayleigh number (fluid-based)
Ra$_m$ — Darcy-Rayleigh number
S — entropy generation, W m^{-3}K^{-1}
T — temperature, K
u, υ — velocity components, m s^{-1}
U, V — dimensionless velocity components
x, y — Cartesian coordinates, m
X, Y — dimensionless Cartesian coordinates

Greek symbols

α — thermal diffusivity, m^2 s^{-1}
β — coefficient of thermal expansion, K^{-1}
ε — porosity
θ — dimensionless temperature
λ — undulation amplitude
μ — dynamic viscosity, N m^{-2}s
v — kinematic viscosity, m^2 s^{-1}
Π — heat function
ρ — density, kg m^{-3}
σ — electrical conductivity, μS cm^{-1}
φ — hybrid nanoparticles concentration
ψ — stream function

Subscripts and Superscripts

a — ambient
c — cold
d — dissipation
f — base fluid
gen — generation
h — hot
c — cold
loc — local
mf — magnetic
min — minimum
max — maximum
r — property ratio
s — solid
tg — thermal gradient
tot — total
vd — viscous

Abbreviations and Acronyms

MHD — magnetohydrodynamics

Magnetic fields can be harnessed to control and manage the transport of heat, momentum, and mass in multiphysical systems [2]. When magnetic fields are applied to fluid flows, they can alter local fluid velocities and modify the underlying flow physics. This is particularly relevant when dealing with complex systems that involve porous materials and nanofluids or hybrid nanofluids, which are colloidal mixtures of suspended nanoparticles in a base fluid [3].

The application of magnetic fields finds use in a wide array of modern technologies and industries [4]. For instance, it plays a crucial role in microfluidic devices [5], the manufacturing of crystals, electronic circuit cooling [6], heat exchange units, anti-vibrating systems, and molten metal flow regulators in nuclear reactors [7]. Moreover, magnetic fields have revolutionized medical science [8], contributing to advancements in specific medicine transport, cancer therapy and tumour treatment, magnetic endoscopy, control of blood flow during operation, gastro-intestinal complaint management, biological waste transportation, and more [9].

Magnetothermally controlled systems work in complicated environments with porous media, hybrid nanofluids, and thermal gradients in many sophisticated applications [10]. The geometry and boundary conditions of these systems play a critical role in their design and analysis [11]. Surface undulation or cor-

rugation, which enhances the surface area, can significantly influence near-wall transport processes, thereby altering the thermo-flow behaviour within thermal systems [12]. Researchers have tackled the modelling and analysis of such systems, which become even more challenging in the presence of porous structures and nanofluids or hybrid nanofluids. For instance, studies have investigated free convection in wavy-walled enclosures with varying undulation numbers, with varying results depending on the specific conditions [13]. Investigations into buoyancy-driven thermal convection flow in porous cavities having undulated walls that produce heat have similarly shown an increasing trend in heat transfer with an increase in the number and peak of the undulations [14]. Because of their improved thermal conductivity, hybrid and nanofluids have become more and more common [15]. This makes them useful in a variety of applications, even when flow-hindering porous materials exist [16]. Sarkar et al. presented a detailed overview of the developments of hybrid nanofluids [17]. A detailed review of the heat transfer enhancement utilizing nanofluid flow through a porous medium has been presented by Kasaeian et al. [18]. Several researchers have also studied the impact of surface morphology on the enhanced heat transfer in the presence of hybrid nanofluid [19,20], magnetic field [21,22], and others. Very recently Bahmani et al. [23] numerically studied the MHD buoyant convec-

tive process in different wavy-walled cavities packed with porous substances and reported the enhanced heat transfer with the existence of a curved surface.

Hamid et al. [24] in a recent study, examined the thermal convection in a cavity having curvilinear hot corners and with the existence of a central circular heated cylinder. They found enhanced heat transfer up to 400% when the heated cylinder radius increased. Pandit et al. [25] studied the impact of partial wavy walls on the hydrothermal convection of hybrid nanofluid in a porous cavity with the existence of multi-segmented magnetic fields. They achieved notably enhanced heat transfer up to 38% compared to traditional cavity. Better fluid mixing is made possible by the increased surface area and broken thermal boundary layers. The application of a segmented magnetic field with strategic orientation may lead to heat transfer enhancements of up to 26%. Guedri et al. [26] analysed the effect of wall waviness of a trapezoidal porous container filled with (multi-walled carbon nanotube-Fe$_3$O$_4$/water (MWCNT-Fe$_3$O$_4$/water) hybrid nanofluid under MHD effects on the heat transport phenomena. They achieved 26% enhanced heat transfer due to the increase in permeability. Mandal et al. [27] examined the impact of surface undulations on the convective heat transport in a porous cavity filled with hybrid nanofluid subjected to non-uniform multi-frequency heating and magnetic field. They found that at higher frequencies, heat transport increases up to 261.49%. Furthermore, compared to without undulations, an increase in the undulation height of the wavy sidewalls results in 13.41% enhanced heat transfer. In a corrugated porous cavity packed with Ag-MgO hybrid nanofluid, Al-Dulaimi et al. [28] studied the enhanced conjugate thermal convection. Further details could be found in [29,30]. In fact, current research has shown that increasing surface undulation does not always lead to improved heat transfer, highlighting the complexity of the relationship between undulation and heat transfer enhancement [31].

In this context, the current study investigates the behaviour of hybrid nanofluids in a confined cavity having surface undulations and the influence of a magnetic field. The study aims to shed light on how multiphysical factors, such as porous structure, nanofluids, and magnetizing fields, interact in irregular geometries. The cavity has an adiabatic top wall, wavy sidewalls that allow for cooling, and a partially heated bottom. The left sidewall receives the magnetic field applied perpendicularly. We alter a number of flow-regulating factors, such as the concentration of hybrid nanoparticles, the length of the active heating length, the strength of the magnetic field, the Darcy-Rayleigh number, and the Darcy number. This study contributes to our understanding of complex multiphysical phenomena in irregular geometries, offering insights that may find practical applications in solar thermal systems, thermal mixing processes, biomedical systems, and more. It is worth noting that this work differs significantly from our earlier studies, as it explores the impact of partial magnetic fields in a novel and previously unexplored geometry.

2. Problem geometry and mathematical modelling

The geometry under consideration is a two-dimensional wavy-walled enclosure, as illustrated in Fig. 1. This square-shaped enclosure has a length, denoted as L, and a height, denoted as H. Both the sidewalls of the cavity is not straight; it follows a wavy pattern described by the expression

$$y = 0.5A[1 - \cos(2n\pi y)], \tag{1}$$

where A and n denote the amplitude and wavy undulation number, respectively. The wavy walls are subject to isothermal cooling at a temperature T_c. The heating element is located on the central semicircular part of the bottom wall. The straight portions and the top horizontal wall are insulated.
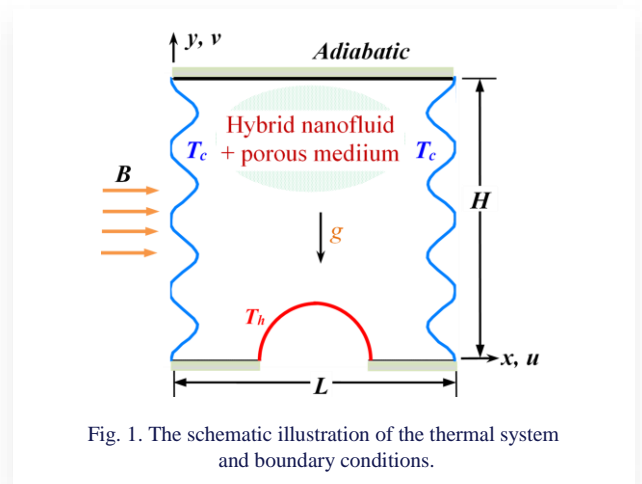
Fig. 1. The schematic illustration of the thermal system and boundary conditions.

This thermal system incorporates a hybrid nanofluid, a unique mixture consisting of Cu-Al$_2$O$_3$ nanoparticles dispersed within a host fluid. These nanoparticles are identical, spherical in shape, and have an average diameter of approximately 1 nm. The concentration of these nanoparticles within the hybrid nanofluid is maintained at a level below 3%. Importantly, following prior research [31], we ensure that there is no agglomeration or sedimentation of these nanoparticles within the fluid. The host fluid, in our case, is water, characterized by a Prandtl number (Pr) of 5.83. Furthermore, the porous medium is modelled utilizing the Forchheimer-Brinkman-Darcy model [32,33]. To simplify the mathematical model and ensure its practicality, we make several key assumptions:

- The magnetic Reynolds number (induced) is still very small, particularly at lesser concentrations of nanoparticles and lower magnetic field intensities. Because of this, the effects of induced magnetic fields, displacement currents, Joule heating, and the Hall effect are neglected [34].
- We also neglect the impact of radiative heat transfer and viscous dissipation effect, in line with earlier studies [35].

These assumptions allow us to focus on the primary thermomagnetic convection and entropy generation phenomena within our system, facilitating a more tractable mathematical model and a deeper understanding of the core dynamics.

The governing equations of continuity, momentum, and energy equations can be obtained in the dimensional form as follows, presuming the previously stated assumptions:

$$(X, Y) = (x, y)\frac{1}{H}, \quad (U, V) = (u, v)\frac{H}{\alpha_f},$$

$$\theta = \frac{T - T_c}{T_h - T_c}, \quad P = \frac{(p - p_a)H^2}{\rho \alpha_f^2}, \tag{2a}$$

$$Pr = \frac{\nu_f}{\alpha_f}, \quad Da = \frac{K}{H^2}, \quad F_c = \frac{1.75}{\sqrt{150\varepsilon^3}},$$

$$Ra_m = \frac{g\beta_f(T_h - T_c)KH}{\nu_f \alpha_f}, \quad Ha = BH\sqrt{\frac{\sigma_f}{\mu_f}}. \tag{2b}$$

The following dimensionless equations [34,35] are the resultant converted equations stated as

$$\frac{\partial U}{\partial X} + \frac{\partial V}{\partial Y} = 0, \tag{3}$$

$$\frac{1}{\varepsilon^2}\left(U\frac{\partial U}{\partial X} + V\frac{\partial U}{\partial Y}\right) = -\frac{\partial P}{\partial X} + \frac{\nu}{\nu_f}\frac{Pr}{\varepsilon}\left(\frac{\partial^2 U}{\partial X^2} + \frac{\partial^2 U}{\partial Y^2}\right) +$$
$$-\left(\frac{\nu}{\nu_f}\frac{Pr}{Da} + \frac{F_c\sqrt{U^2 + V^2}}{\sqrt{Da}}\right)U, \tag{4}$$

$$\frac{1}{\varepsilon^2}\left(U\frac{\partial V}{\partial X} + V\frac{\partial V}{\partial Y}\right) = -\frac{\partial P}{\partial Y} + \frac{\nu}{\nu_f}\frac{Pr}{\varepsilon}\left(\frac{\partial^2 V}{\partial X^2} + \frac{\partial^2 V}{\partial Y^2}\right) +$$
$$-\left(\frac{\nu}{\nu_f}\frac{Pr}{Da} + \frac{F_c\sqrt{U^2 + V^2}}{\sqrt{Da}}\right)V + \tag{5}$$

$$-\frac{\rho_f}{\rho}\frac{\sigma}{\sigma_f}Ha^2\, Pr\, V + \frac{\rho_f}{\rho}\frac{\beta}{\beta_f}Ra_m\frac{Pr}{Da}\theta,$$

$$\left(U\frac{\partial \theta}{\partial X} + V\frac{\partial \theta}{\partial Y}\right) = \frac{\alpha}{\alpha_f}\left(\frac{\partial^2 \theta}{\partial X^2} + \frac{\partial^2 \theta}{\partial Y^2}\right). \tag{6}$$

The boundary conditions related to transport equations (3) through (6) are assumed to be $\theta = 1$ and $\theta = 0$, respectively, $\partial\theta/\partial Y = 0$ at the cavity's horizontal walls, left and right walls, and zero velocity ($U = V = 0$) for each boundary wall.

The working medium (Cu-Al$_2$O$_3$/water hybrid nanofluid) comprises host fluid (water), and Al$_2$O$_3$ and Cu nanoparticles. The concentration φ designates the volume-based presence of the nanoparticles. The properties of the liquid phase and the two distinct types of nanoparticles (Al$_2$O$_3$ and Cu) are presented in Table 1 [36].

Table 1. Characteristics of Al$_2$O$_3$ and Cu nanoparticles and water [36].

Parameter	Unit	Water	Al$_2$O$_3$	Cu
α	m^2 s^{-1}	1.47×10^{-7}	131.7×10^{-7}	1.11×10^{-4}
β	K^{-1}	21×10^{-5}	0.85×10^{-5}	1.67×10^{-5}
c_p	J kg^{-1}K^{-1}	4179	765	385
k	W m^{-1}K^{-1}	0.613	40	401
ρ	kg m^{-3}	997.1	3970	8933
μ	kg m^{-1}s^{-1}	9.09×10^{-4}	–	–

The thermal properties of the hybrid nanofluid are computed based on experimental models and empirical correlations, as shown in Table 2. Here, the combination of nanoparticles (Cu and Al$_2$O$_3$) and the host fluid (water) are signified by the symbols s and f, respectively. Additionally, the expression for dynamic viscosity, and thermal and electrical conducting properties [35] are incorporated in accordance with the traditional theoretical models. Nevertheless, the Brinkman model and the Maxwell model, two traditional expressions for thermal conductivity and viscosity, are unable to adequately forecast these characteristics for the hybrid nanofluids [36]. As shown in Table 3, precise values for the Cu-Al$_2$O$_3$/water hybrid nanofluid's thermal conductivity and viscosity are used from the experiments [36] to solve the aforementioned drawbacks.

In the post-processing stage, the solved primitive variables (U, V, θ) are used to produce several relevant dimensionless values. Based on an entropy generation (S_{gen} or NS_{gen}) analysis, the systems' deviation from ideal operation (reversible) is assessed.

Table 2. Relationships for the hybrid nanofluid Cu-Al$_2$O$_3$/water properties [35].

Thermodynamic properties	Relationships
Density (ρ)	$\rho = (1 - \varphi)\rho_f + \varphi\,\rho_s$
Thermal conductivity (k)	$k = k_f\left[\dfrac{(k_s + 2k_f) - 2\varphi(k_f - k_s)}{(k_s + 2k_f) + \varphi(k_f - k_s)}\right]$
Thermal diffusivity (α)	$\alpha = \dfrac{k}{\rho c_p}$
Electrical conductivity (σ)	$\sigma = \sigma_f\left[1 + \dfrac{3\left(\frac{\sigma_s}{\sigma_f} - 1\right)\varphi}{\left(\frac{\sigma_s}{\sigma_f} + 2\right) - \left(\frac{\sigma_s}{\sigma_f} - 1\right)\varphi}\right]$
Thermal expansion coefficient ($\rho\beta$)	$(\rho\beta) = (1 - \varphi)(\rho\beta)_f + \varphi\,(\rho\beta)_s$
Specific heat capacity (ρc_p)	$(\rho c_p) = (1 - \varphi)(\rho c_p)_f + \varphi(\rho c_p)_s$
Viscosity (μ)	$\mu = \dfrac{\mu_f}{(1 - \varphi)^{2.5}}$

Magnetic field effects, fluid flow, and temperature gradient are all present in the current systems. As a result, irreversibility falls into three categories: irreversibility caused by thermal gradients (S_{tg} or NS_{tg}), irreversibility caused by fluid friction (viscous dissipation) (S_{vd} or NS_{vd}), and irreversibility caused by magnetic fields (S_{mf} or NS_{mf}). Here are the equations for the local irreversibility production rate (S_{gen} and NS_{gen}) as well as the dimensional (S) and dimensionless (NS) influences [34]:

$$S_{gen} = \underbrace{S_{tg}}_{} + S_{vd} + S_{mf} = \overbrace{\frac{k}{T^2}\left[\left(\frac{\partial T}{\partial x}\right)^2 + \left(\frac{\partial T}{\partial y}\right)^2\right]}^{S_{tg}} +$$

$$+ \overbrace{\frac{\mu}{T}\left[2\left(\frac{\partial u}{\partial x}\right)^2 + 2\left(\frac{\partial u}{\partial y}\right)^2 + \left(\frac{\partial u}{\partial y} + \frac{\partial v}{\partial x}\right)^2\right]}^{S_{vd}} + \overbrace{\frac{\sigma B^2}{T}v^2}^{S_{mf}}, \tag{7}$$

$$NS_{gen} = \frac{S_{gen}}{\frac{k_f}{H^2}} = NS_{tg} + NS_{vd} + NS_{mf} =$$

$$= \underbrace{\frac{1}{(\theta + \theta_r)^2} \frac{k}{k_f} \left[\left(\frac{\partial \theta}{\partial X} \right)^2 + \left(\frac{\partial \theta}{\partial Y} \right)^2 \right]}_{NS_{tg}} +$$

$$+ \underbrace{\frac{EcPr}{(\theta+\theta_r)} \frac{\mu}{\mu_f} \left[2 \left(\frac{\partial U}{\partial X} \right)^2 + 2 \left(\frac{\partial V}{\partial Y} \right)^2 + \left(\frac{\partial U}{\partial Y} + \frac{\partial V}{\partial X} \right)^2 \right]}_{NS_{vd}} +$$

$$+ \underbrace{\frac{EcPrHa}{(\theta+\theta_r)} \frac{\sigma}{\sigma_f} V^2}_{NS_{mf}}. \tag{8}$$

Equation (8) includes the Eckert number (Ec) and the temperature ratio reference parameter (θ_r), which are specified as

$$\theta_r = \frac{T_c}{T_h - T_c}, \tag{9}$$

$$Ec = \frac{\alpha_f^2}{H^2 c_{pf}(T_h - T_c)} = \sqrt[3]{\frac{(g \alpha_f \beta_f)^2}{T_h - T_c}} \; Pr^{-\frac{2}{3}} Ra^{-\frac{2}{3}}. \tag{10}$$

One possible global characteristic of the systems is their total entropy generation (NS_{tot}). It is calculated as the result of integrating the generation of local entropy over the whole flow domain:

$$NS_{tot} = \iint NS_{gen} dX dY. \tag{11}$$

Using the local and average Nusselt numbers (Nu), which are provided by, the heated wavy wall's average and local rates of heat transfer:

$$Nu_{loc} = \frac{k}{k_f} \left(-\frac{\partial \theta}{\partial n} \Big|_{hw} \right), \tag{12a}$$

$$Nu = \frac{k}{k_f} \frac{1}{s} \int_0^s \left(-\frac{\partial \theta}{\partial n} \Big|_{hw} \right) dS, \tag{12b}$$

where s stands for both the appropriate coordinate point and the real length of the wavy wall. Streamlines are used to graphically represent localized fluid flow patterns inside flow geometries. The stream function (ψ) is used to generate streamlines from the solved velocity field. The expression for the stream function is

$$-\frac{\partial \psi}{\partial X} = V \quad \text{and} \quad \frac{\partial \psi}{\partial Y} = U. \tag{13}$$

3. Numerical technique

The finite element method (FEM) is employed to discretize the transport equations. The method of solving the equations is iterative and continues until the residuals meet a predetermined convergence threshold, usually set at a strict level so that the residuals are $\leq 10^{-6}$. This methodology conforms to accepted procedures in the field and guarantees the simulations' correctness and stability [31,35]. The flexible finite element analysis program offers a reliable foundation for resolving challenging multiphysics issues. It is the perfect fit for this study because of its ability to handle linked physical phenomena like heat transfer, fluid flow, and magnetic fields with ease. Because of this meticulous selection, the computational investigations have a solid foundation in precise and confirmed data, which supports the numerical model.

Prior research has thoroughly validated the accuracy and dependability of the selected numerical approach [31,35]. These validations include a thorough evaluation of the computational outcomes in comparison to experimental data as well as cross-validation with other numerical simulations. The computational and experimental results are consistently observed, which highlights the resilience of the approach and validates the veracity of the simulated results.

Additionally, a thorough validation investigation is conducted by comparing the computed findings with the results of Ghasemi et al. [38] to validate our computational results. To assess the accuracy of numerical approaches for forecasting heat transfer for magnetohydrodynamic free convective process in the cavity, the present solver outcome is compared with the published results of Ghasemi et al. [38]. This work uses a horizontal magnetic field, an Al_2O_3/water nanoliquid, and a square geometry having heating and cooling from the vertical sides. The comparison is carried out for different values of Ha ($= 0 - 60$) and φ ($= 0\%$, and 2%) at Ra $= 10^5$. The comparative results are shown in Table 3 using ψ_{max}. The two results of the comparison exhibit excellent agreement. These comparative assessments show that MHD-free convection in a confined cavity may be predicted using the current numerical technique.

Table 3. Comparing ψ_{max} of the present results and results of Ghasemi et al. [38] for varying Ha and φ at Ra $= 10^5$.

Ha	Ghasemi et al. [38]		Present simulation	
	$\varphi = 0\%$	$\varphi = 2\%$	$\varphi = 0\%$	$\varphi = 2\%$
0	11.053	11.313	11.014	11.275
30	5.710	5.682	5.693	5.878
45	3.825	3.729	3.813	3.922
60	2.518	2.518	2.614	2.677

In addition, a grid refinement test was methodically carried out to confirm that the grid size had no discernible impact on the numerical simulations. To guarantee the precision and dependability of the simulations, this test is essential. All of the geometric shapes that were used in the grid generation for the current two-dimensional challenges were created using the finite element method. However, in this study, a finer mesh structure is utilized for the extensive simulations, which provides the correct results. Hence, no mesh independence study is presented here.

4. Results and discussion

Here, we delve into the intricate thermal transport phenomena occurring within the cavity, characterized by wavy left and right walls, heated from the bottom in the form of a semi-circle, and subjected to the effect of an external flat magnetic field [39]. Our investigation unveils a rich tapestry of insights, with the results elucidated through the visualization of key parameters, including streamlines (ψ), isotherms (θ), heatlines (Π), and the average Nusselt number (Nu). We explore a wide range of controlling variables, spanning various undulation numbers ($n = 1, 2, 4, 6, 8$), Darcy-Rayleigh numbers ($1 \leq Ra_m \leq 10^4$), Darcy numbers ($10^{-4} \leq Da \leq 10^{-2}$), and Hartmann numbers ($0 \leq Ha \leq 70$).

Furthermore, the irreversibility study as a result of fluid friction, thermal, and magnetic force are also assessed. The porosity and volumetric concentration of hybrid nanofluids are taken as $\varepsilon = 0.8$ and $\varphi = 0.1\%$.

4.1. Magneto-thermal transport structures

4.1.1. Flow signatures

Figure 2 encapsulates the flow signatures within the cavity, offering a visual narrative of how fluid dynamics evolve under different parameter regimes. The variations in wavy wall undulations ($n = 1, 2, 4$ and 6), Darcy-Rayleigh number ($Ra_m = 10, 10^2, 10^3, 10^4$), and Rayleigh number ($Ra = 10^4, 10^5, 10^6, 10^7$) are meticulously examined at $Da = 10^{-3}$ and $Ha = 10$. Our observations reveal intriguing insights into the flow patterns within the cavity. Notably, as the Rayleigh number rises, the change from pure conduction dominance to convection mode becomes evident, manifesting as an increase in flow velocity. This transition is mainly marked in the presence of strong convection, where the flow velocity triples (as observed at $Ra = 10^5$ and 10^6).

The interplay of wavy wall undulations and Rayleigh numbers elucidates the impact of geometric configuration on flow behaviour. This exploration of basic flow patterns, as depicted in Fig. 2, lays the foundation for the in-depth investigations and analyses that follow in this study. These flow signatures serve as a critical reference point for our subsequent discussions and findings, shedding light on the underlying physics governing the system's response to varying parameters. Utilizing a half-circular wall at the centre of the bottom surface enhances the heating effect, while the elongated wavy walls contribute to an extended cooling surface. The central half-circular bottom heating results in an upward flow of heated water that returns over both wavy sidewalls. The presence of surface waviness at the sidewalls plays a pivotal role in altering the directions of flow velocity, leading to the formation of distinct circulation patterns. At lower Darcy-Rayleigh numbers, undulations have no remarkable im-
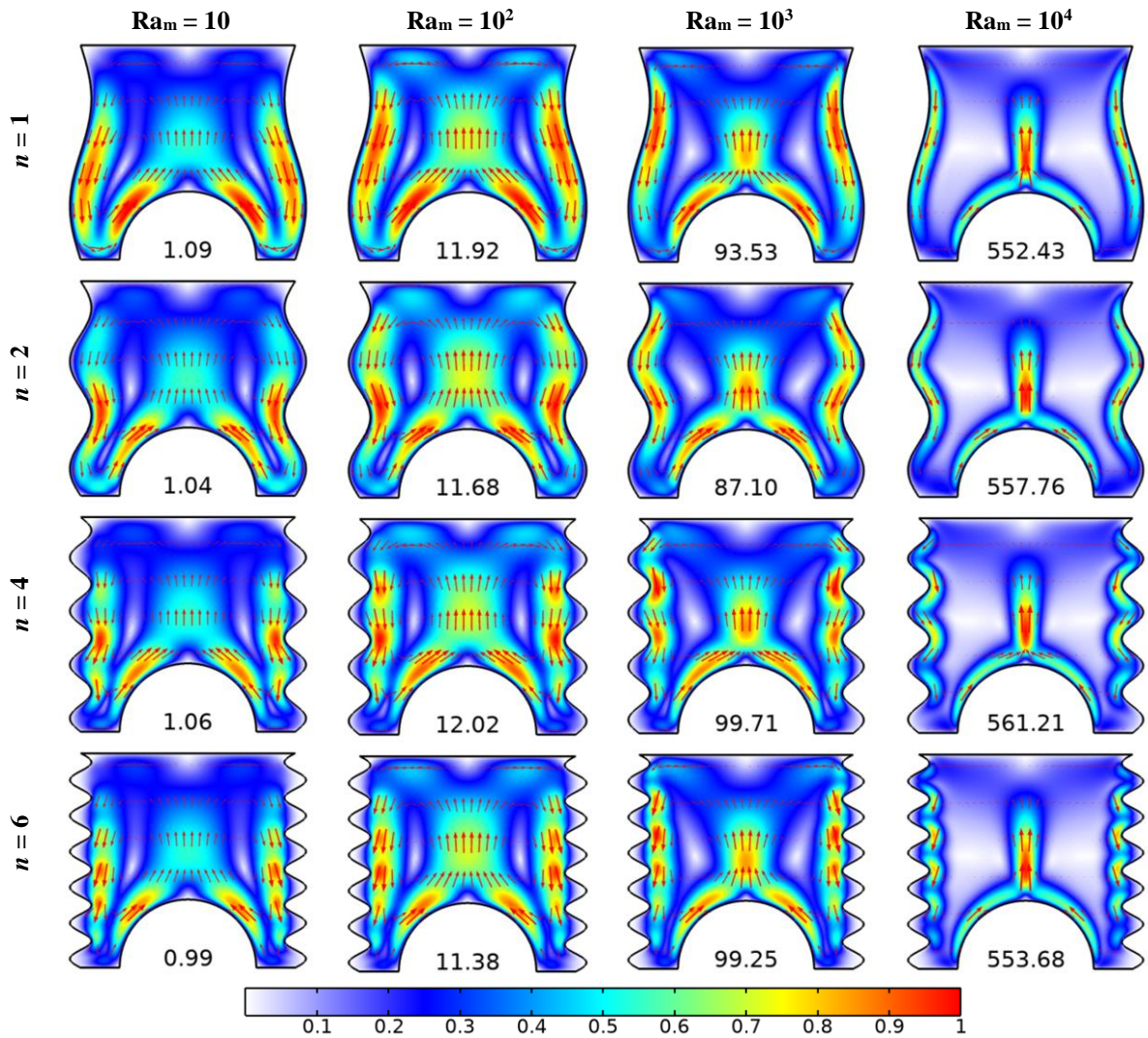
Fig. 2. Flow signatures varying with undulations ($n = 1, 2, 4,$ and 6) and Darcy-Rayleigh numbers ($Ra_m = 10, 10^2, 10^3, 10^4$) at different Rayleigh numbers ($Ra = 10^4, 10^5, 10^6, 10^7$), for $Da = 10^{-3}$, $Ha = 10$. The value below each figure indicates maximum velocity (dimensionless).

pact on velocity magnitude. However, at higher Ra_m values, particularly for $n = 4$, a substantial increase in velocity is observed. A rise in Ra_m leads to a significant enhancement in flow velocity. This heightened velocity is particularly confined to the central region and adjacent to the wavy walls, reflecting the complex interplay of buoyancy-driven flow physics and geometric configuration.

4.1.2. Streamline evolution

Figure 3 provides a comprehensive view of the evolving flow circulation patterns within the cavity, allowing us to unravel critical insights into the system's behaviour under varying conditions. This analysis was conducted for various undulations ($n = 1, 2, 4$ and 6) and Darcy-Rayleigh numbers ($Ra_m = 10, 10^2, 10^4$)

while keeping Darcy number fixed at 10^{-3} and Hartmann number at 30. It yields several noteworthy observations.

The formation of streamlines reveals the emergence of two symmetrical circulations within the cavity, indicative of the complex interplay between buoyancy-driven flow and geometric configuration. As the Darcy-Rayleigh number reaches 10^4, signifying the dominance of convection, the strength of these circulations intensifies significantly. This escalation in circulation strength is a hallmark of the transition from conduction to convection-dominated flow regimes. Interestingly, the presence of more undulations at the cold wavy walls leads to a phenomenon where flow stagnates at the vertical walls, causing a retardation in circulation strength. Consequently, an increase in the number of undulations results in a reduction in circulation

Fig. 3. Evolution of flow circulation at various undulations ($n = 1, 2, 4$ and 6) and Darcy-Rayleigh numbers ($Ra_m = 10, 10^2$ and 10^4), for $Da = 10^{-3}$, $Ha = 30$. The values below each figure indicate ψ_{max} and ψ_{min}, respectively.

strength. This effect is particularly pronounced at lower Ra_m values, emphasizing the intricate relationship between wall waviness and flow dynamics. In contrast, at higher Ra_m values, especially at $Ra_m = 10^4$, an intriguing phenomenon is observed. The circulation strength reaches an optimum value when the number of undulations is set at $n = 4$. This suggests that, under specific conditions, the presence of moderate wall undulations can enhance circulation strength, highlighting the subtle balance between geometric complexity and flow dynamics. These insights into streamline evolution offer a deeper understanding of how fluid circulations respond to varying parameters within the cavity. They underscore the role of convection dominancy, wall waviness, and the interplay of these factors in shaping circulation patterns and flow behaviour.

4.1.3. Isotherm evolution

Figure 4 presents a comprehensive depiction of the evolving isotherm patterns within the cavity, offering critical insights into the distribution of static temperature under varying conditions. This analysis was conducted for various undulations ($n = 1, 2, 4$ and 6) and Darcy-Rayleigh numbers ($Ra_m = 10, 10^2, 10^4$) while keeping Darcy number fixed at 10^{-3} and Hartmann number at 30, unveils several notable observations.

The formation of isotherms showcases intriguing behaviour. Initially, these isotherms assume a circular shape at the heating wall and gradually transform into elliptical patterns as they ascend toward the top wall. This transition from circular to elliptic isotherms reflects the complex interplay of heat transfer mecha-
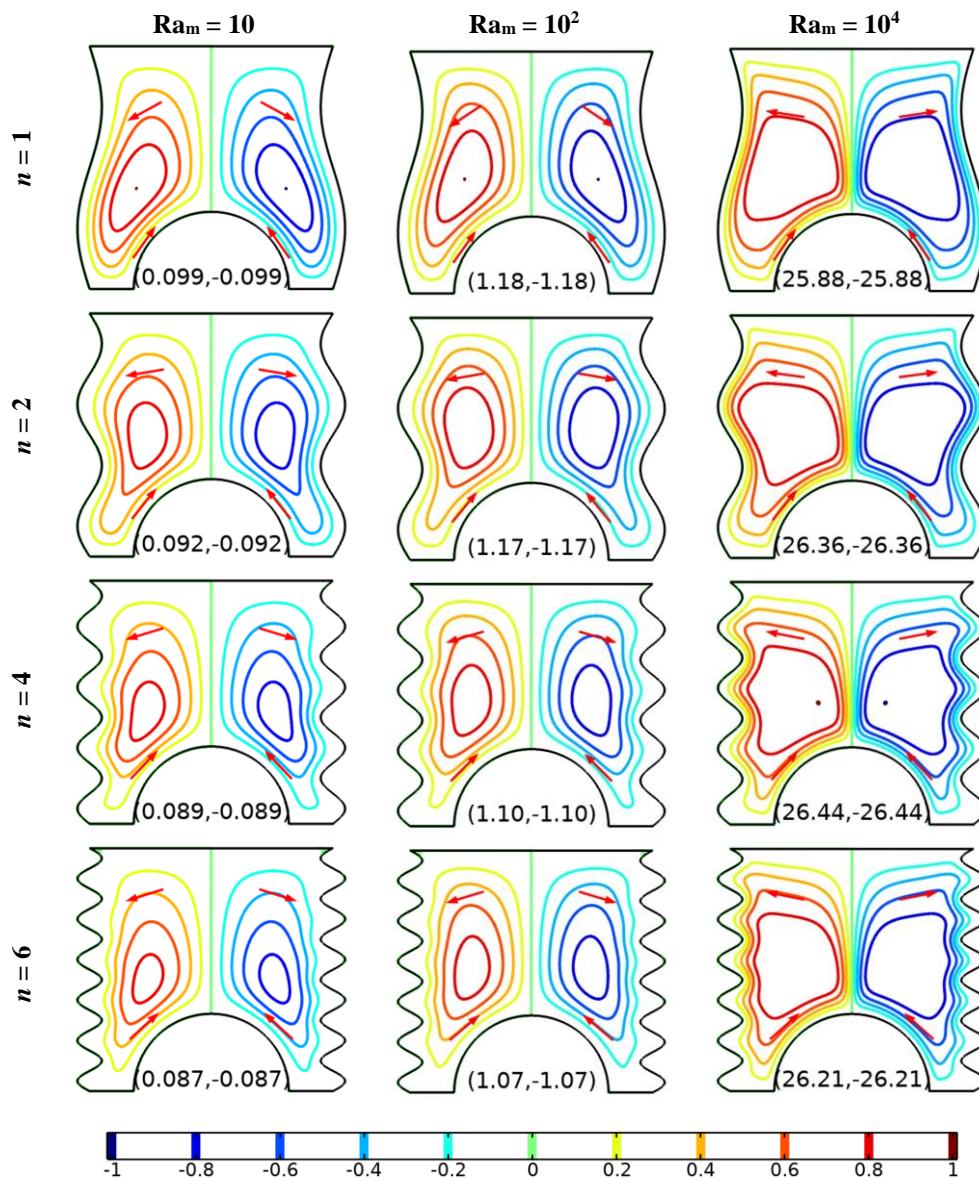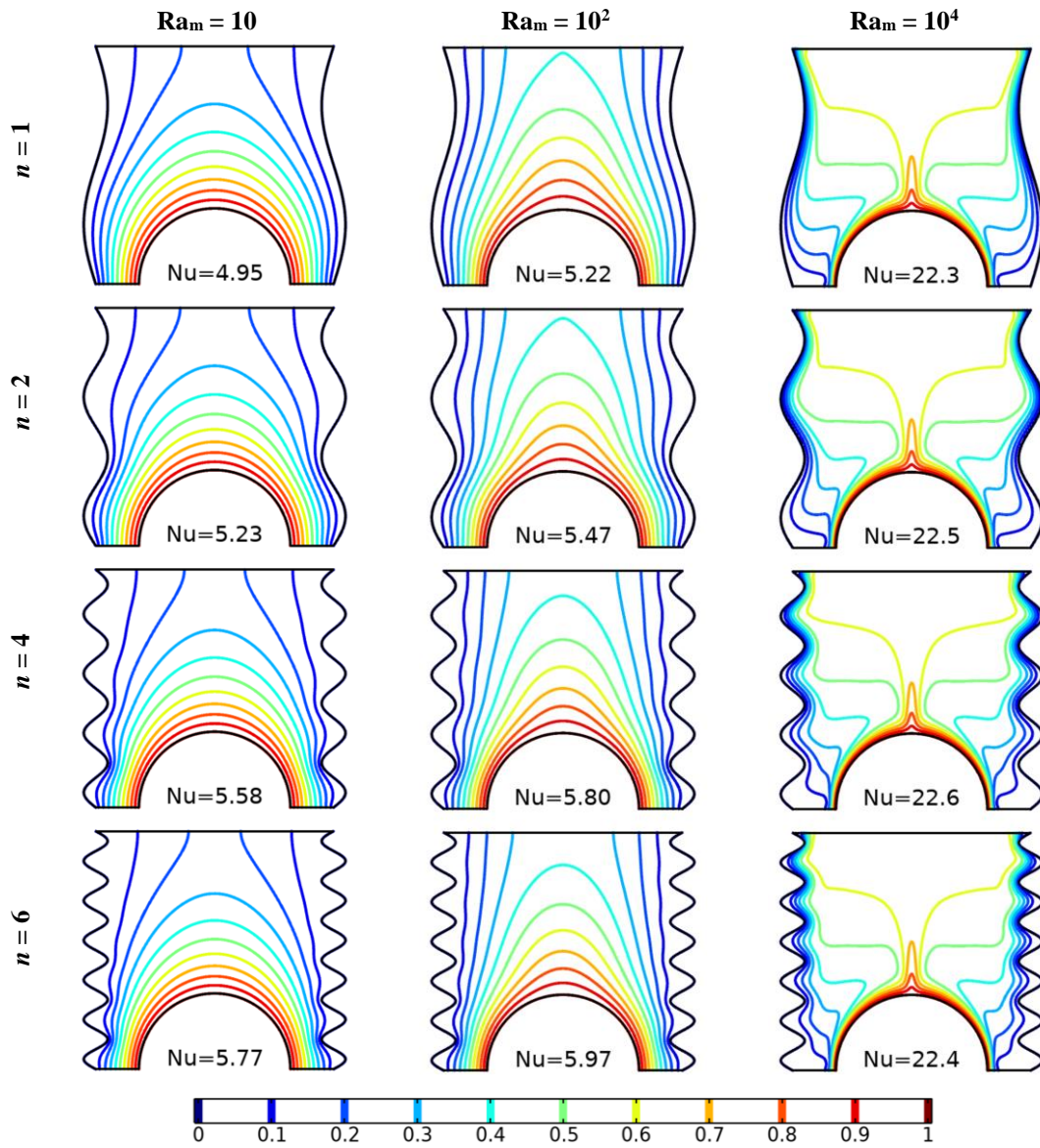

Fig. 4. Evolution of static temperature at various undulations ($n = 1, 2, 4$ and 6) and Darcy-Rayleigh numbers ($Ra_m = 10, 10^2$ and 10^4), for $Da = 10^{-3}$, $Ha = 30$.

nisms within the cavity. As the Darcy-Rayleigh number increases, signifying the onset of convection, a notable phenomenon emerges. The hot isotherms stratify horizontally over the top of the cavity, indicating a more efficient heat transfer process. This stratification is a clear indicator of enhanced heat transfer, leading to a rise in the Nusselt number. The presence of wavy cold walls further amplifies heat transfer, with increasing wavy undulations leading to an increase in the effective cold surface area. Consequently, the Nu value reaches its optimum at $Ra_m = 10^4$ when the number of undulations is set at $n = 4$.

However, an intriguing observation emerges when undulations are further increased. Beyond this optimum point, a reduction in heat transfer is noted. This phenomenon may be attributed to flow separation at the vertical walls, which disrupts the convective heat transfer process. These insights into isotherm evolution shed light on the complex dynamics of temperature distribution within the cavity. They underscore the role of convection, wall waviness, and their interplay in shaping temperature patterns and heat transfer efficiency. The findings also highlight the delicate balance between geometric complexity and heat transfer performance within this unique thermal system.

4.1.4. Magneto-thermofluid flow patterns

The Hartmann number, representing the influence of an external magnetic field that opposes the fluid flow, serves as a pivotal controlling parameter in this study. The profound alterations in flow physics induced by varying Ha values (Ha = 0, 50 and 70) are meticulously examined to understand the magnetic field's
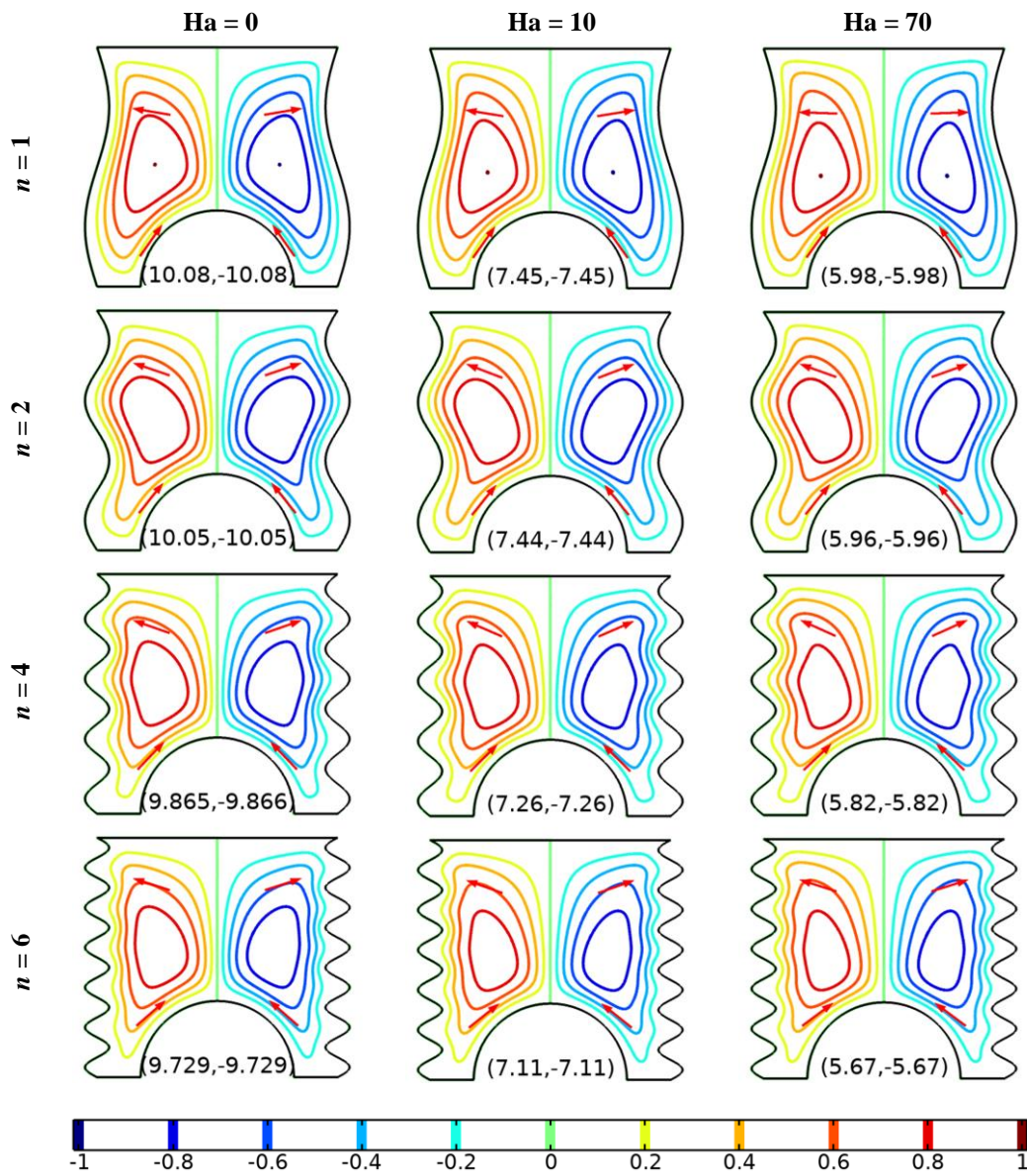
Fig. 5. Magnetic field (Ha) effect on the evolution of flow circulation at various undulations ($n = 1, 2, 4$ and 6), Hartmann number (Ha = 0, 10 and 70), for $Ra_m = 10^3$, Da = 10^{-3}. The values below each figure indicate ψ_{max} and ψ_{min}, respectively.
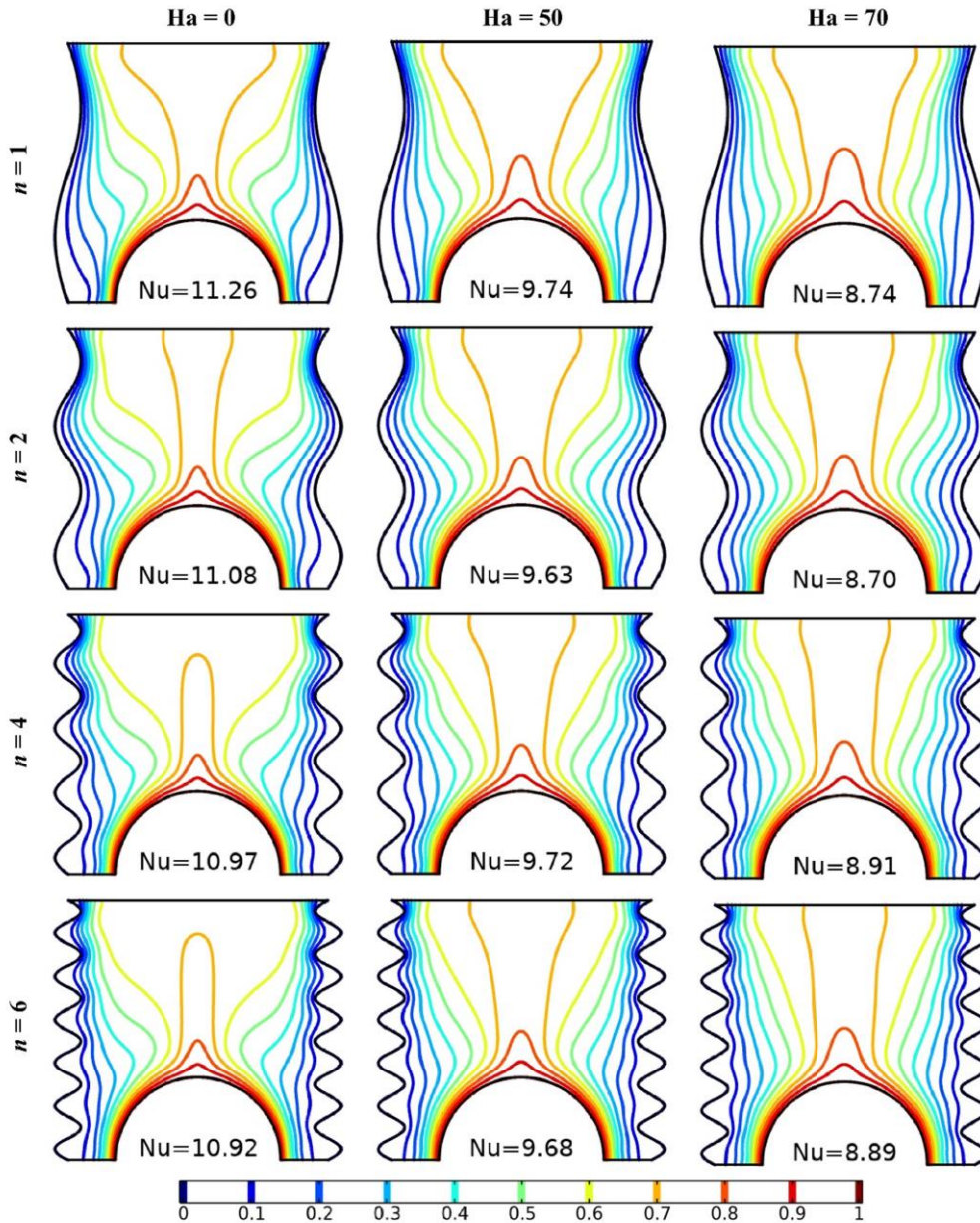
Fig. 6. Magnetic field (Ha) effect on the evolution of static temperature at various undulations (n = 1, 2, 4 and 6),
Hartmann number (Ha = 0, 50 and 70) for $Ra_m = 10^3$, Da = 10^{-3}.

impact on the system's behaviour (as depicted in Fig. 5). It shows that, as Ha values increase, reflecting a stronger magnetic field's dampening effect on the flow, a noticeable change in flow dynamics unfolds. This effect is observed across different undulation numbers (n = 1, 2, 4 and 6). Secondly, the flow strength experiences a steady reduction with increasing Ha values. This phenomenon underscores the magnetic field's ability to restrain fluid motion, leading to diminished circulation within the cavity. Moreover, the magnetic field's influence extends to the distribution of static temperature within the cavity, as illustrated in Fig. 6. At the heated wall, isotherms become progressively thicker with the rise in Ha values. This phenomenon indicates that the magnetic field's presence results in a more pronounced impact (reducing local temperature gradient near the heater as well as cooler surfaces), affecting heat transfer patterns within the cavity. These observations emphasize the pivotal role of the Hartmann number in modulating flow circulation and temperature distribution within the system. The magnetic field's ability to alter flow strength and temperature gradients holds significant implications for the overall thermal performance of the cavity, particularly in scenarios where magnetohydrodynamics plays a critical role.

4.2. System analysis from design perspectives

In the pursuit of understanding the intricate thermal system from a design perspective, we delve into the profound influence of Darcy parameters, particularly the Darcy number, which characterizes the permeability of the porous medium and its resistance to fluid flow. To assess the impact of Da on fluid flow

physics, we examine its effects at Da = 10^{-4}, 10^{-3} and 10^{-2} (as depicted in Fig. 7). As we elevate the Da values, signifying a reduction in the porous medium's resistance to flow, a clear trend emerges — flow circulation within the cavity decelerates. This observation aligns with the fundamental physics of porous media, where lower Da values correspond to higher resistance and, consequently, slower fluid flow. Streamline contours, which are invaluable in revealing flow patterns, consistently exhibit symmetric behaviour across all combinations of the Darcy number and undulation parameter. The system exhibits two counter-rotating circulations, with fluid rising along the mid-vertical plane of this intricate thermal setup. However, the intriguing revelation here is that as Da increases from 10^{-4} to 10^{-2}, the circulation strength diminishes. This unexpected decline in flow rate with increasing Da at a constant modified Rayleigh

number (the Darcy-Rayleigh number) is attributed to the reduction in fluid-based Rayleigh number. The Rayleigh number is inherently responsible for driving flow within the confined domain due to temperature gradients. This insight into the interplay between Da and flow circulation underscores the significance of porous media characteristics in shaping fluid dynamics within the cavity. Moreover, it highlights the nuanced relationship between resistance to flow and circulation strength − a critical consideration in optimizing the design of thermal systems with porous components. Turning the attention to the distribution of static temperature, we uncover additional insights into the impact of Da, as illustrated in Fig. 8. Isotherms, which provide valuable information about the mode of temperature transfer (convection or conduction), exhibit distinct behaviour as Da varies. At lower Da values (Da = 10^{-4}, 10^{-3}), isotherms exhibit intricate and wavy patterns, indicative of strong convection heat transfer.
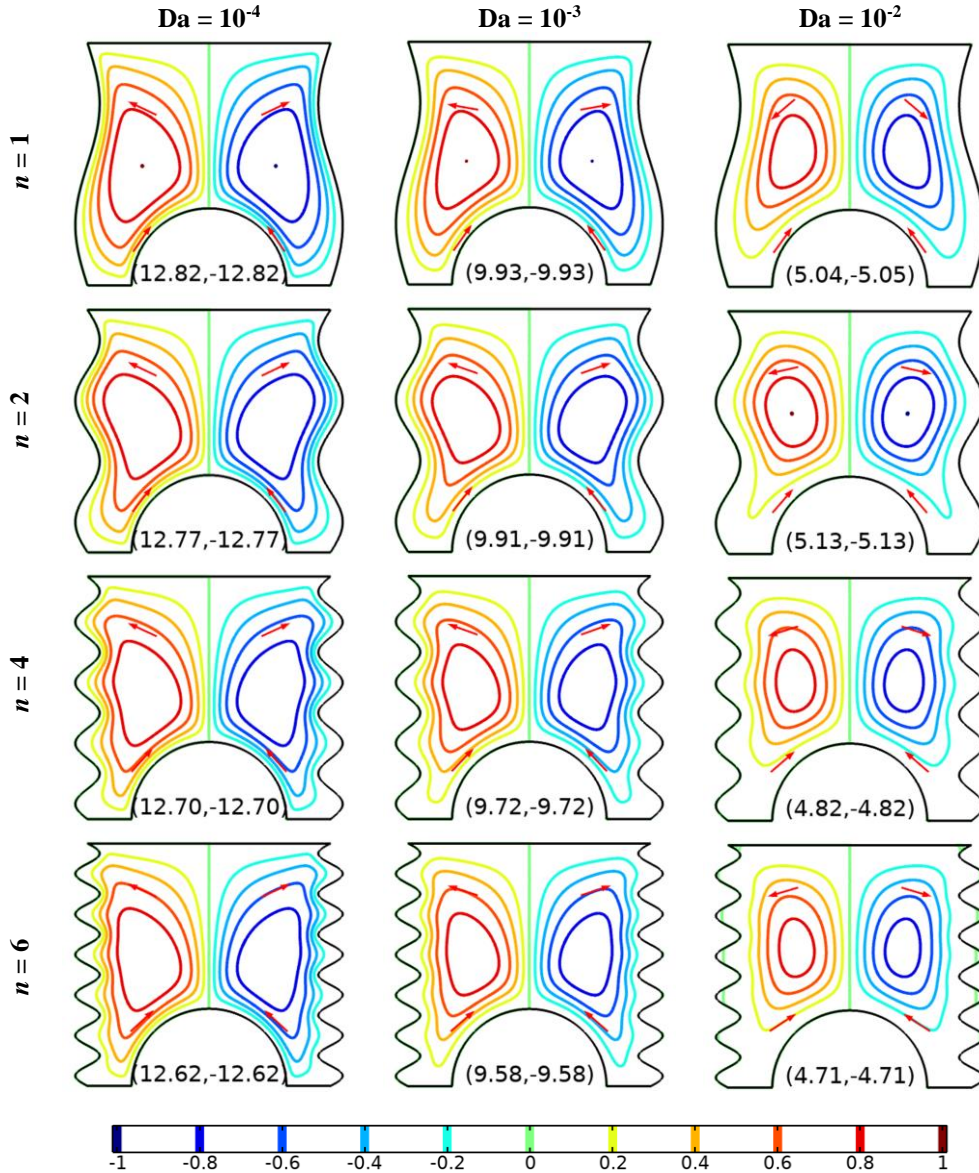
Fig. 7. Evolution of flow circulation at various undulations (n = 1, 2, 4 and 6) and Darcy numbers (Da = 10^{-4}, 10^{-3} and 10^{-2}), for Ra_m = 10^3, Ha = 10. The values below each figure indicate ψ_{max} and ψ_{min}, respectively.
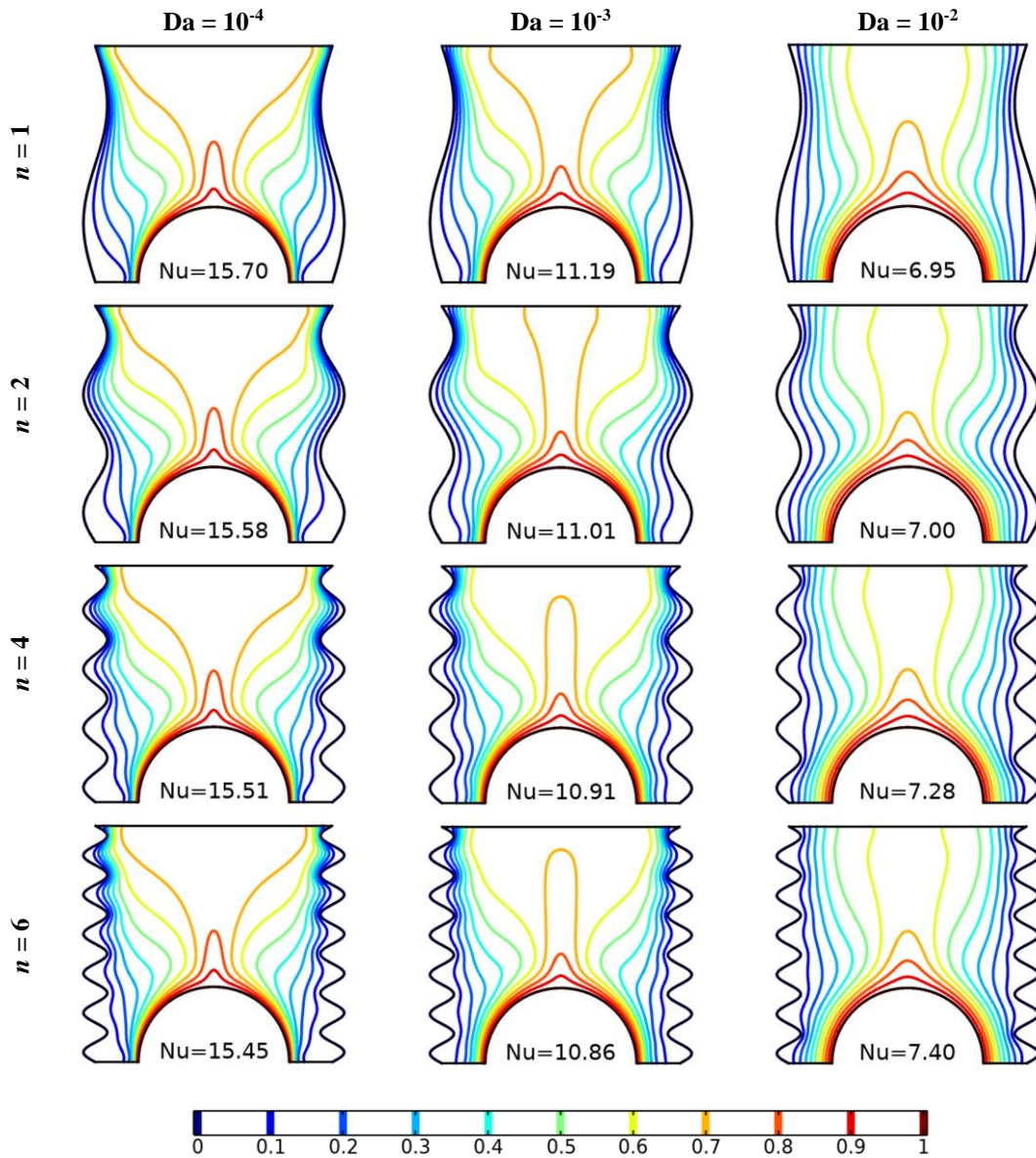
Fig. 8. Evolution of static temperature at various undulations ($n = 1, 2, 4$ and 6) and Darcy numbers (Da = 10^{-4}, 10^{-3} and 10^{-2}), for $Ra_m = 10^3$, Ha = 10.

As Da increases, isotherm contours spread more towards the top wall and become notably smoother. Additionally, the clustering of isotherms and streamlines over the lower portion of the semi-circular wall and the upper regions of the undulated sidewalls diminishes at higher Da values. This shift in thermal boundary layer dynamics impacts the local Nusselt number and normal temperature gradient, resulting in a significant reduction in the average Nusselt number, as indicated below the figures. The highest average Nu magnitude is observed at low Da values and sharply decreases as Da increases. These findings emphasize the intricate interplay between fluid flow, porous medium charac-teristics, and heat transfer within the cavity. They underscore the

critical role of Da in shaping both flow and temperature distri-bution, offering valuable insights for the design and optimiza-tion of thermal systems involving porous media.

4.3. Heatline visualization

In the quest to unravel the intricate mechanisms of thermal en-ergy transport within the cavity, we turn our attention to heatline visualization (as depicted in Fig. 9). This technique offers valu-able insights into how thermal energy moves across different configurations of the system, characterized by varying Darcy-Rayleigh numbers and undulations (n), while maintaining a con-
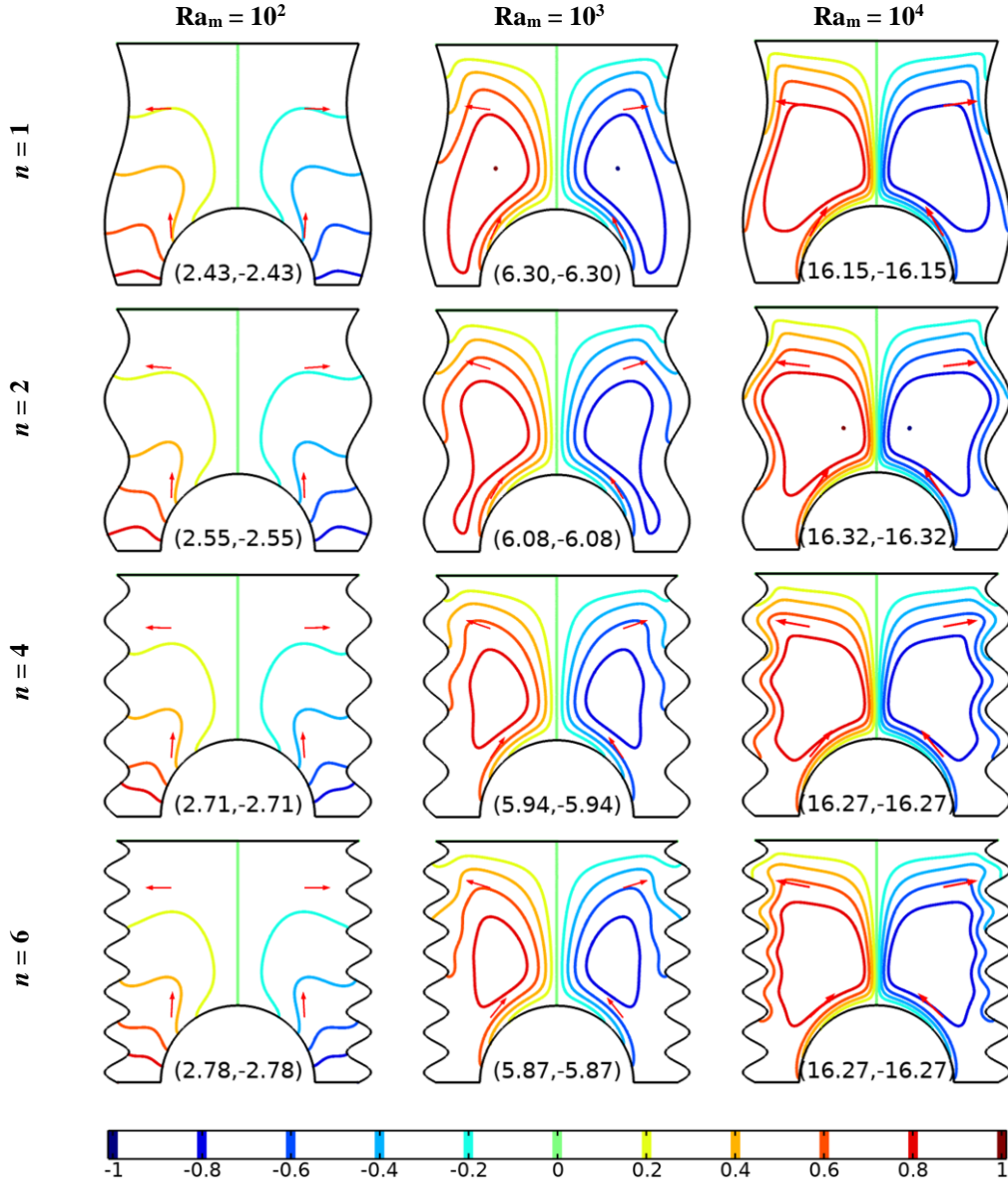
Fig. 9. Heatline visualization at various undulations (n = 1, 2, 4 and 6) and Darcy-Rayleigh numbers (Ra_m = 10^2 to 10^4), for Da = 10^{-3} and Ha = 30. The values below each figure indicate Π_{max} and Π_{min}, respectively.

stant Darcy number (Da = 10^{-3}) and Hartmann number (Ha = 30).

As we manipulate Ra_m, a noticeable shift in the heat transport mechanism becomes apparent. At low Ra_m values, heatlines exhibit straightforward paths from the hot wall to the cold wall, indicating a dominance of conduction-driven heat transfer. However, as Ra_m increases, these heatlines disperse, tracing larger and more convoluted paths towards the cold wall. This transformation signifies a transition from conduction-dominated to convection-dominated heat transfer. Notably, at high Ra_m values, two symmetrical circulations emerge within the cavity, driven by intensified convective forces. Furthermore, heatlines with varying undulations showcase enhanced energy

transport from the hot wall, emphasizing the influence of wall waviness on thermal dynamics.

The impact of magnetic fields, quantified by the Hartmann number, on heatline patterns is explored in Fig. 10. We find that the magnetic damping effect causes the energy recirculations to diminish as Ha grows. In the absence of a magnetic field (Ha = 0), representing non-MHD flow, energy recirculations are more robust, resulting in the strongest heat flow. Conversely, as Ha rises to 50 or 70, energy circulation diminishes, leading to reduced heat transfers. Regions with congested heatlines indicate strong flowing heat flux, primarily located near the vertex of the semicircular heater.
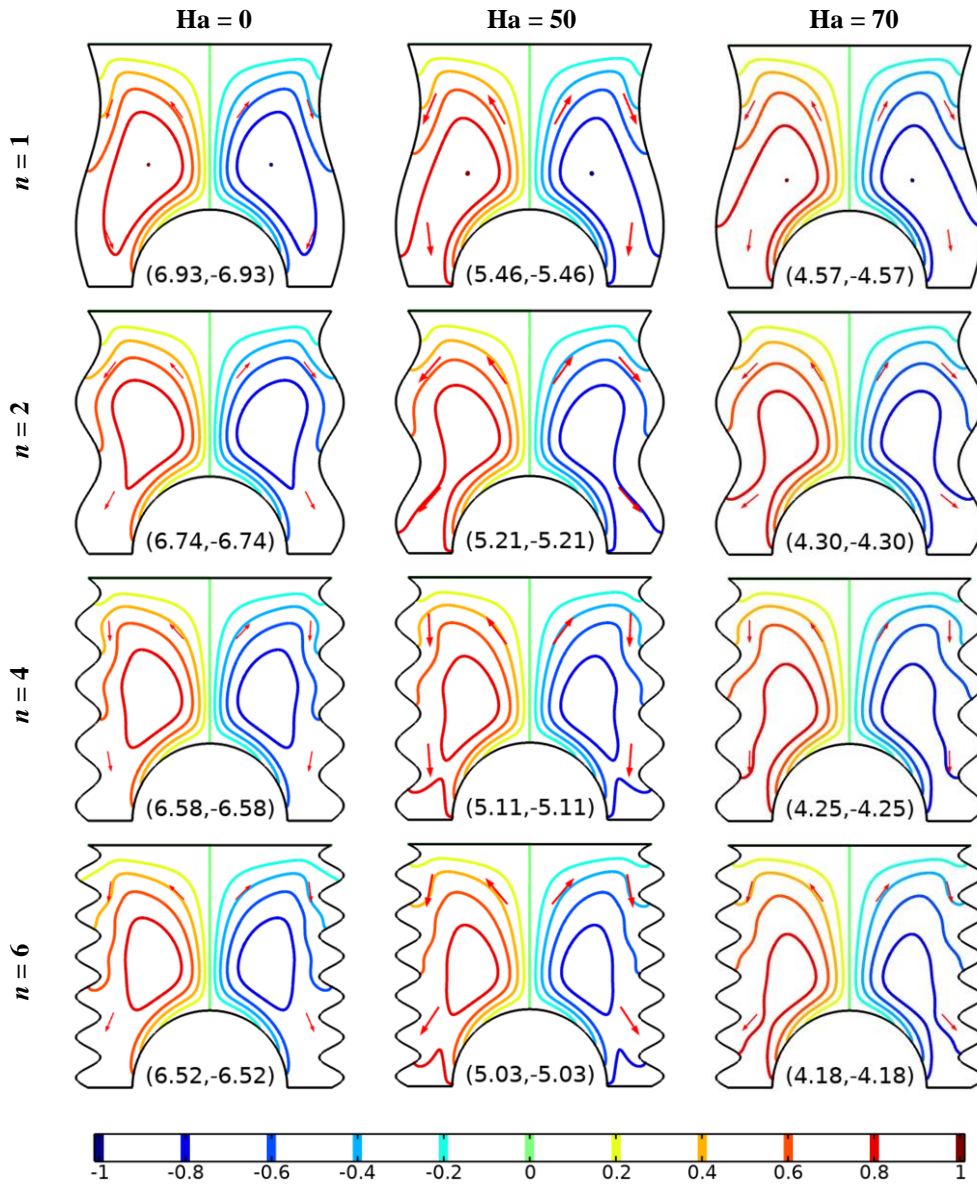
Fig. 10. Evolution of heatlines at various undulations ($n = 1, 2, 4$ and 6) and Hartmann numbers (Ha = 0, 50 and 70), $Ra_m = 10^3$, for Da = 10^{-3}. The values below each figure indicate Π_{max} and Π_{min}, respectively.

The investigation into the impact of the Darcy number on heatline patterns, while keeping $Ra_m = 10^3$ and Ha = 10 constant, reveals intriguing insights (as depicted in Fig. 11). Surprisingly, as Da increases, allowing for less-resisting flow, the heat flow within the system decreases. This counterintuitive observation contradicts the expectation that increased permeability, associated with higher Da values, should lead to enhanced heat flow. However, this behaviour aligns with our earlier streamline results, demonstrating the intricate interplay between porous medium characteristics, resistance to flow, and heat transfer. Notably, at Da = 10^{-4}, characterized by a high fluid-based Rayleigh number (Ra = 10^7), heatline contours exhibit greater magnitude,

indicative of strong fluid circulation. At Da = 10^{-2}, a transitional behaviour emerges, bridging the gap between conduction-dominated and convection-dominated heat transfer.

4.4. Thermodynamic irreversibility generation

In pursuit of comprehending the intricate thermodynamic aspects of the system, we delve into the analysis of entropy generation, a fundamental parameter shedding light on the thermodynamic irreversibilities inherent to the thermal system. This analysis proves indispensable in understanding the efficiency and performance of the system under varying conditions, enabling
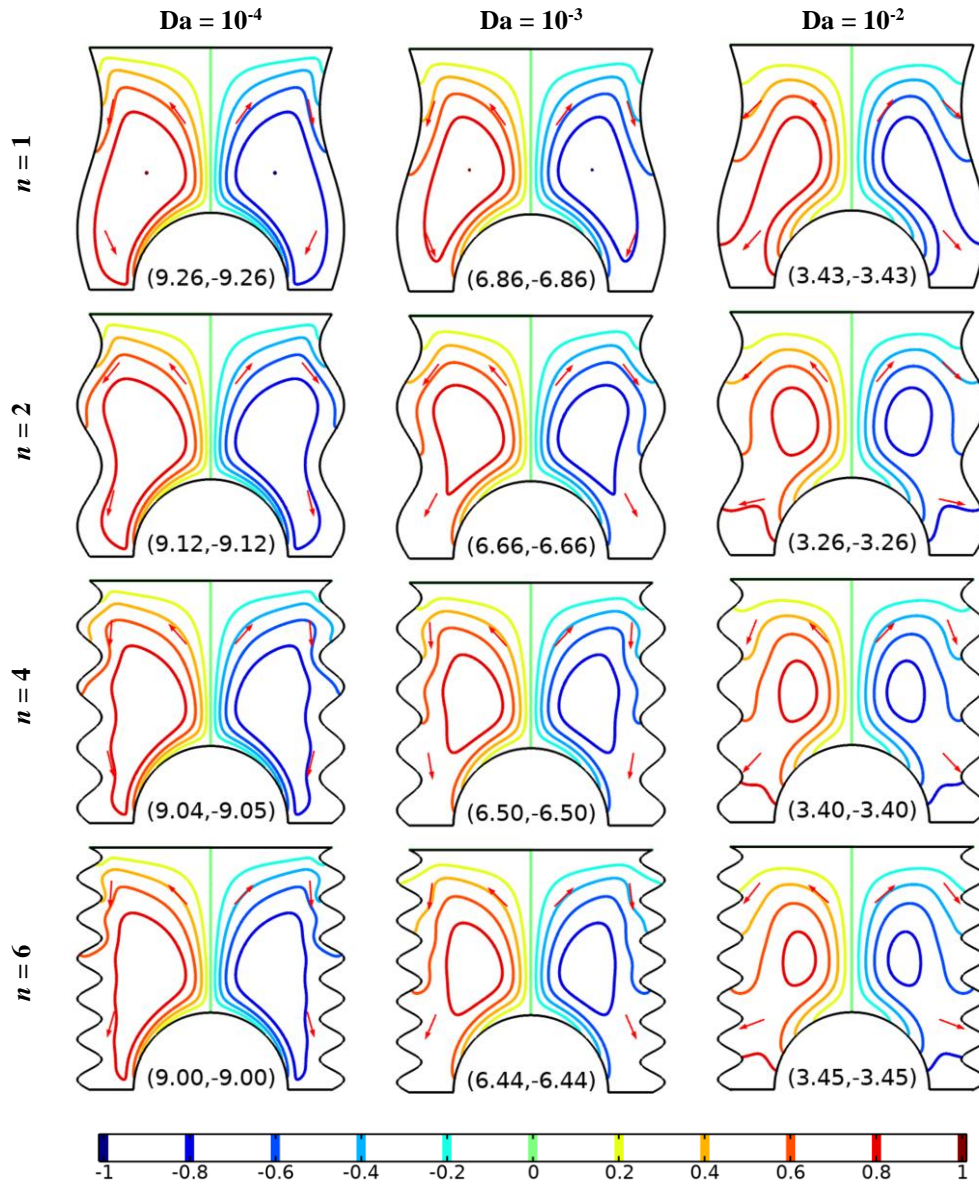
Fig. 11. Evolution of heatlines at various undulations ($n = 1, 2, 4$ and 6) and Darcy numbers (Da $= 10^{-4}, 10^{-3}, 10^{-2}$), for Ra$_m = 10^3$, for Ha $= 10$. The values below each figure indicate Π_{max} and Π_{min}, respectively.

us to make informed design choices. First and foremost, the examination of normalized local total irreversibility generation (*NS*) reveals intriguing insights, as depicted in Fig. 12. At lower Darcy-Rayleigh numbers (Ra$_m = 10^2$), *NS* is predominantly conduction-dominated, signifying the prevalence of heat transfer through conduction mechanisms. Interestingly, *NS* reaches its maximum in the vicinity of the heating and cooling zones within the cavity, gradually diminishing as one moves toward the top

adiabatic wall. However, as Ra$_m$ increases, transitioning the system towards a more convective regime, the distribution of total entropy generation becomes significantly affected. The presence of convection, driven by higher Ra$_m$ values, leads to elevated fluid velocities and consequently, an increase in entropy production (*NS*). The regions experiencing the most pronounced temperature gradients, found near the heating and cooling zones, correspond to the areas with the highest *NS* values.
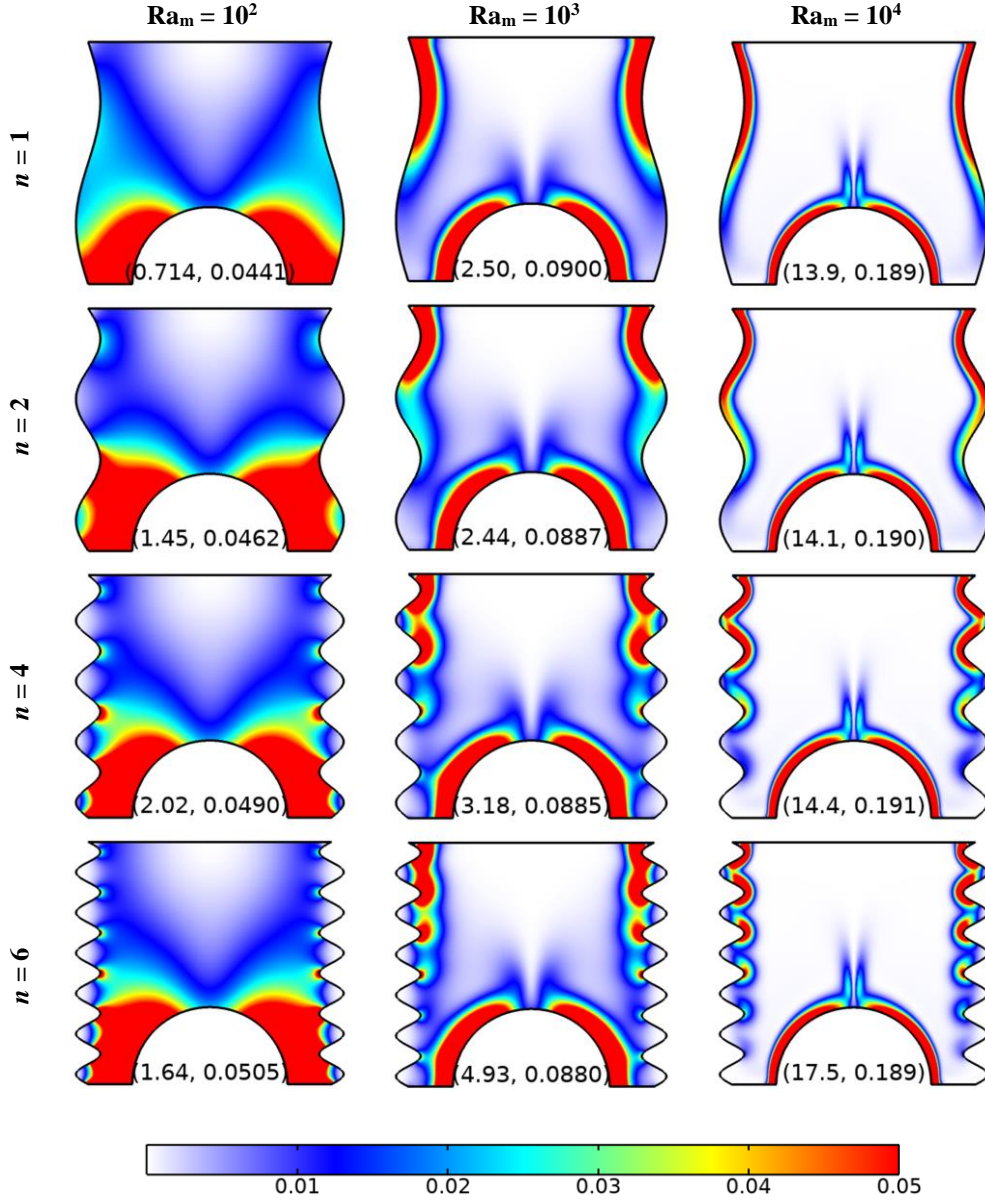
Fig. 12. Effect of Darcy-Rayleigh number Ra_m ($Ra_m = 10^2$ to 10^4) and n ($n = 1, 2, 4$ and 6) on normalized total irreversibility generation, for $Da = 10^{-3}$ and $Ha = 30$. The values below each figure indicate NS_{max} and NS_{tot}, respectively.

Moving forward, Fig. 13 provides insights into the irreversibility generation resulting from viscous dissipation. Here, the interplay between various system parameters, such as Ra_m, n, Da and Ha, becomes apparent. As Ra_m increases, marking a shift towards stronger convective effects, the fluid velocity intensifies, contributing to increased entropy production due to viscous dissipation (NS_{vd}). The zones of heightened entropy generation become more concentrated along the active walls, emphasizing the complex interplay between thermal convection, magnetic fields, and viscous dissipation. Figure 14 further delves into the impact of the magnetic field (Ha) on irreversibility generation, highlighting the opposing role it plays in fluid circulation. As Ha values increase, the magnitude of magnetic field-induced irreversibility (NS_{mf}) experiences a corresponding rise. This behaviour underscores the significant influence of Ha on entropy generation and its crucial role in understanding the thermodynamic dynamics of the system.

In summary, entropy generation analysis provides invaluable insights into the multifaceted irreversibilities present in the thermal system. Higher Ra_m values intensify these irreversibilities due to the amplification of convection effects, while augmented magnetic fields enhance magnetic field-induced irreversibilities. Additionally, the Darcy number, which represents flow resistance within the porous medium, exerts a pivotal influence on the generation of irreversibilities. The intricate interplay of these multiphysical phenomena underscores the complexity of entropy generation and highlights its significance in discerning the hierarchy of thermodynamic irreversibilities within the system.
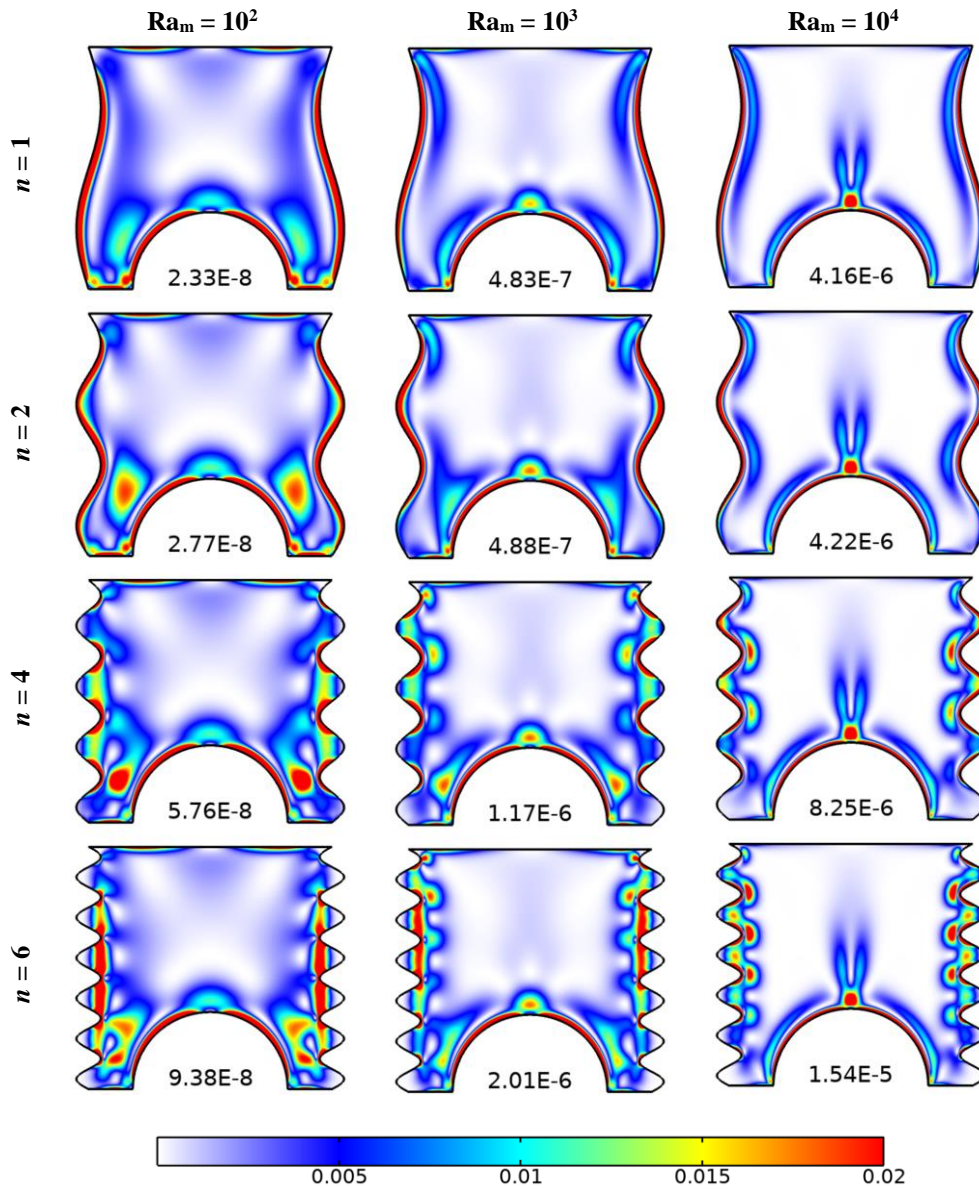
Fig. 13. Effect of Darcy-Rayleigh number ($Ra_m = 10^2$ to 10^4) and n ($n = 1, 2, 4$ and 6) on irreversibility generation due to viscous dissipation, for $Da = 10^{-3}$ and $Ha = 10$. The value below each figure indicates maximum NS_{vd} (dimensionless).

This analysis not only contributes to a deeper understanding of the system's behaviour but also informs decisions in the design and optimization of thermally driven systems involving porous media and magnetic fields. Variations in heat transfer alteration are typically measured using the Nusselt number, as depicted in Fig. 15. It has been observed that the presence of undulations in wavy walls tends to enhance heat transfer, particularly at low Darcy-Rayleigh numbers, where conduction dominates. As Ra_m increases, Nu also increases, but the influence of the undulation number is not significant. In terms of the Darcy number, which represents flow resistance in porous media, higher Da values lead to reduced heat transfer due to the corresponding decrease in the fluid-based Rayleigh number. The impact of the undulation number on heat transfer in this context is not prominent. Regarding the Hartmann number, which affects fluid circulation and heat transfer, higher Ha values tend to dampen fluid flow, similar to the Darcy number, resulting in reduced heat transfer rates. However, it is worth noting that lower undulation levels exhibit better heat transfer under low Ha regimes.
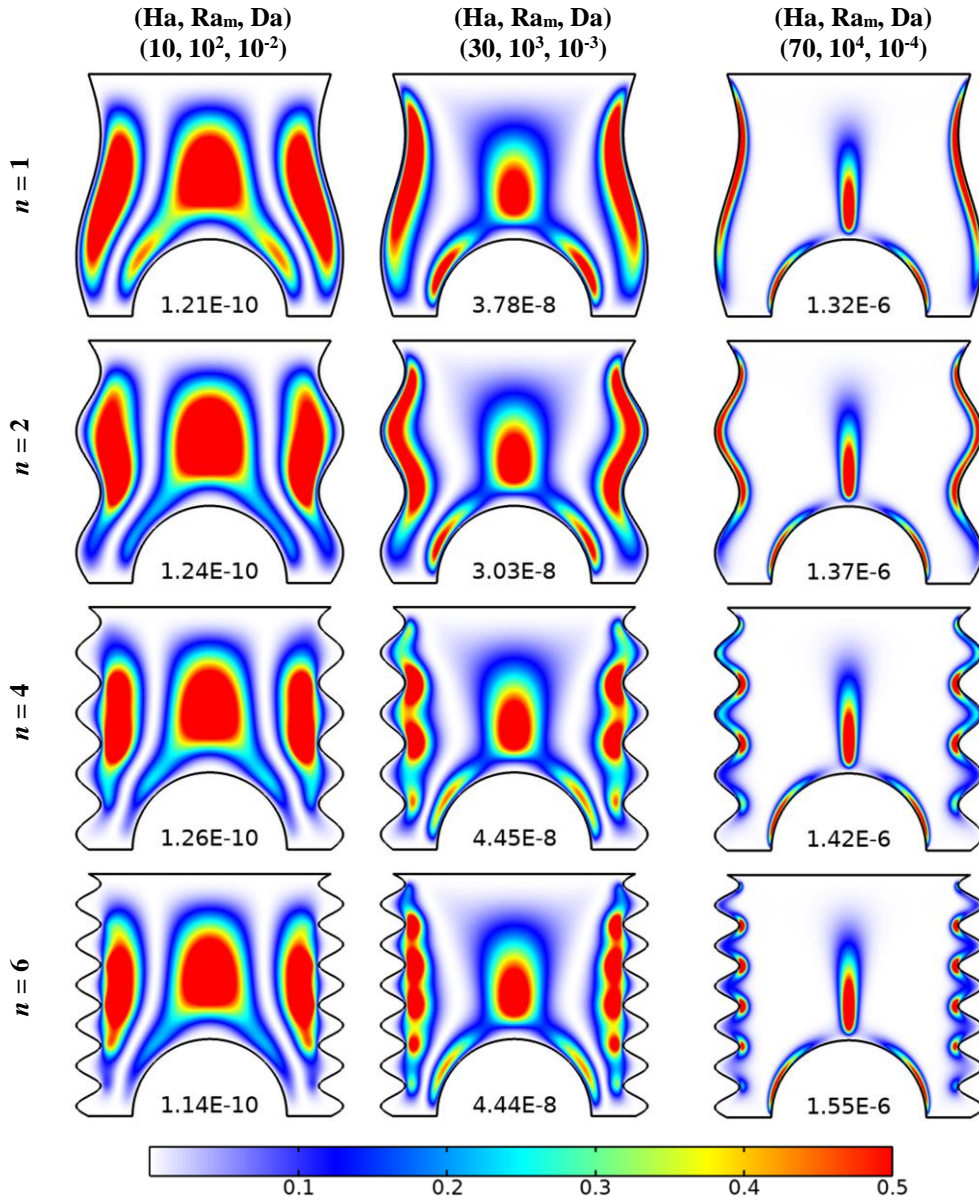
Fig. 14. Effect of Hartmann number (Ha = 10, 30, 70) and n (n = 1, 2, 4 and 6) on irreversibility generation due to magnetic field. The value below each figure indicates maximum NS_{mf} (dimensionless).

Entropy generation, represented by the irreversibility (NS), is depicted for all considered cases in Fig. 16. Higher values of the Darcy-Rayleigh number exacerbate irreversibility due to increased convection effects, whereas elevated magnetic fields and Darcy numbers lead to a reduction in irreversibility. At higher Ra_m values, greater undulations exhibit increased irreversibility. Moreover, more undulations result in higher irreversibility across all considered Hartmann and Darcy values.

5. Concluding remarks

This work comprehensively explores the intricate interplay of multiple physical parameters that govern thermal transport and entropy generation in a complex enclosure. This investigation

has provided valuable insights and noteworthy findings that contribute to the understanding of thermal systems involving porous media and magnetic fields. Here, we summarize the key conclusions drawn from this research:

It is observed that the undulations in the wavy walls significantly influence the flowing fluid and heat transfer patterns within the enclosure. The undulations not only alter the flow direction but also enhance heat transfer due to the increased surface area, with optimum heat transfer occurring at specific undulation values.

This study has shown that the Darcy number, representing flow resistance within the porous domain, plays a crucial role in governing fluid flow and heat transfer. Surprisingly, higher Da values, which should theoretically allow for increased flow, led
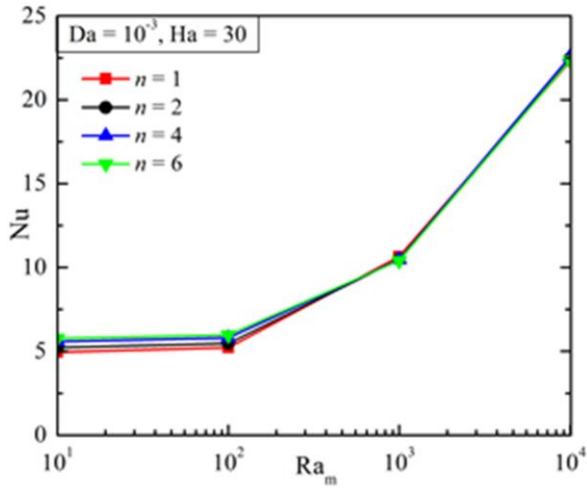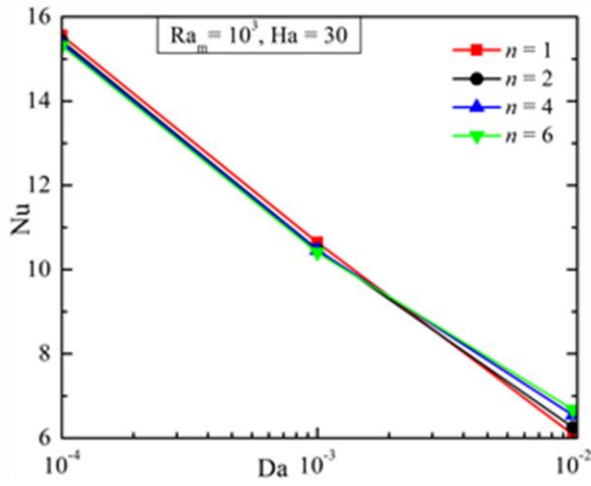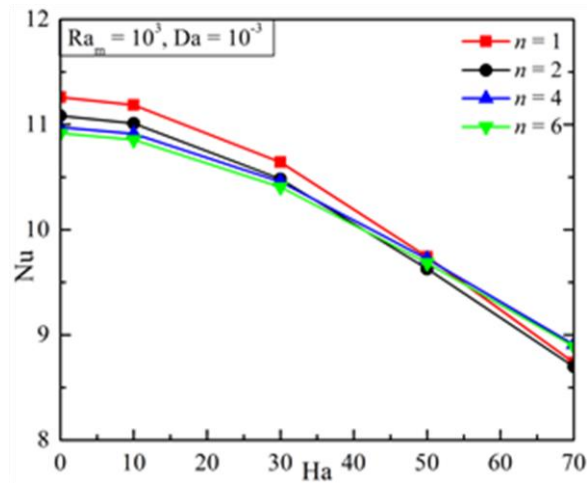
Fig. 15. Average Nu for the various undulation parameters (n) for changing (a) Ra_m (= 1–10^4) when Da = 10^{-3}, Ha = 30, (b) Da (=10^{-4}–10^{-2}) when Ra_m = 10^3, Ha = 30, and (c) Ha (= 0–70) when Ra_m = 10^3, Da = 10^{-3}.
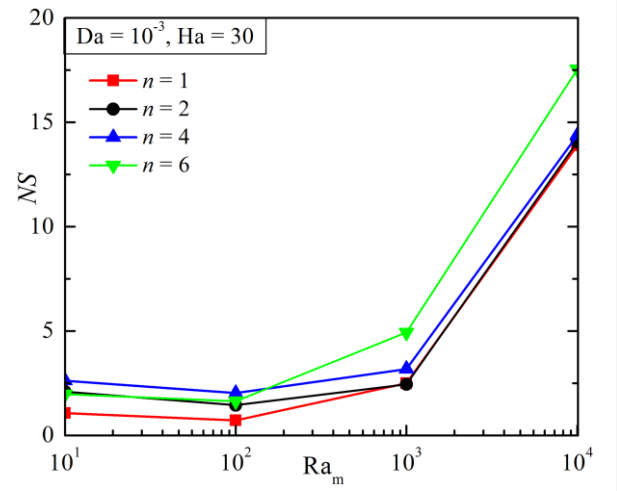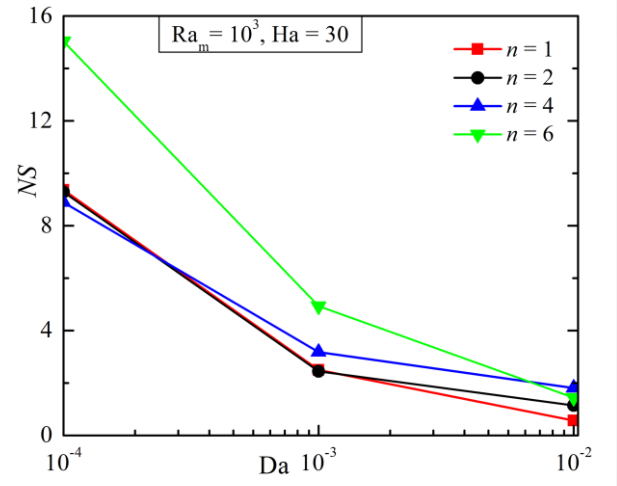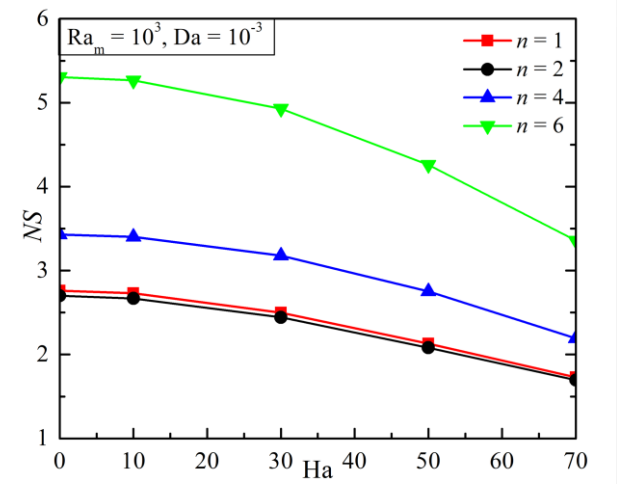
Fig. 16. Total NS for the various undulation parameters (n) for changing (a) Ra_m (= 1–10^4) when Da = 10^{-3}, Ha = 30, (b) Da (=10^{-4}–10^{-2}) when Ra_m = 10^3, Ha = 30, and (c) Ha (= 0–70) when Ra_m = 10^3, Da = 10^{-3}.

to reduced flow rates and heat transfer due to the reduced fluid-based Rayleigh number (Ra).

The existence of an external magnetic field, quantified by the Hartmann number, impacts fluid circulation and heat transfer. Higher Ha values dampen fluid flow, leading to changes in circulation patterns and altered heat transfer rates.

Present findings elucidate the intriguing flow signatures and heatline patterns within the cavity. We have noted the formation of distinctive circulation patterns depending on the heater-cooler positions, leading to variations in flow direction and velocity magnitude. Heatlines have revealed the transition from conduction-dominated to convection-dominated heat transfer as the Darcy-Rayleigh number increases.

The analysis of entropy generation has provided valuable insights into the irreversibilities present in the thermal system. Higher Ra_m values intensify these irreversibilities due to stronger convection effects, while elevated magnetic fields enhance magnetic field-induced irreversibilities. The Darcy number has been identified as a key parameter influencing entropy generation.

In summary, the findings of this study imply that the fluid flow and heat transport phenomena in a thermal system are strongly influenced by the shape of the heating, as well as cooling surfaces. Such findings are very effective for designing a compact heat exchanger, chemical reactor, bio-microfluidic devices, etc. The current research might be expanded into three-dimensional models under various boundary conditions for unstable fluid flow.

Data availability statement

The data that support the findings of this study are available from the corresponding author upon reasonable request.

References

[1] Hartmann, J. (1937). Hg-dynamics I. Theory of the laminar flow of an electrically conductive liquid in a homogeneous magnetic field. *Det Kgl. Danske Vidensk-abernes Selskab. Mathematisk-fysiske Meddelelser*, 15(6).

[2] Manna, N.K., & Biswas, N. (2021). Magnetic force vectors as a new visualization tool for MHD convection. *International Journal of Thermal Sciences*, 167, 107004. doi: 10.1016.j.ijthermalsci.2021.107004

[3] Barnothy, M.F. (ed) (1964). *Biological Effects of Magnetic Fields*. Plenum Press. New York

[4] Rashidi, S., Esfahani, J.A., & Maskaniyan, M. (2017). Applications of magnetohydrodynamics in biological systems – a review on the numerical studies. *Journal of Magnetism and Magnetic Materials*, 439, 358–372. doi: 10.1016/j.jmmm. 2017.05.014

[5] Ozoe, H.(2005). *Magnetic Convection*. Imperial College Press, Singapore.

[6] Ganguly, R., Sen, S., & Puri, I.K. (2004). Thermomagnetic convection in a square enclosure using a line dipole. *Physics of Fluids*, 16(7), 2228–2236. doi: 10.1063/1.1736691

[7] M'hamed, B., Sidik, N.A.C., Yazid, M.N.A.W.M., Mamat, R., Najafi, G., & Kefayati, G.H.R. (2016). A review on why researchers apply external magnetic field on nanofluids. *International Communications in Heat and Mass Transfer*, 78, 60–67. doi: 10.1016/j.icheatmasstransfer.2016.08.023

[8] Manna, N.K., Mondal, C. Biswas, N., Sarkar, U.K., Öztop, H.F., & Abu-Hamdeh, N.H. (2021). Effect of multibanded magnetic field on convective heat transport in linearly heated porous systems filled with hybrid nanofluid. *Physics of Fluids*, 33, 053604. doi: 10.1063/5.0043461

[9] Kabeel, A.E., El-Said, E.M.S., & Dafea, S.A. (2015). A review of magnetic field effects on flow and heat transfer in liquids: Present status and future potential for studies and applications. *Renewable and Sustainable Energy Reviews*, 45, 830–837. doi: 10.1016/j.rser.2015.02.029

[10] Khaled, A.-R.A., & Vafai, K. (2003). The role of porous media in modeling flow and heat transfer in biological tissues. *International Journal of Heat and Mass Transfer*, 46(26), 4989–5003. doi: 10.1016/S0017-9310(03)00301-6

[11] Manna, N.K., Mondal, M.K., & Biswas, N. (2021). A novel multi-banding application of magnetic field to convective transport system filled with porous medium and hybrid nanofluid. *Physica Scripta*, 96(6), 065001. doi: 10.1088/1402-4896/abecbf

[12] Shenoy, A., Sheremet, M., & Pop. I. (2016). *Convective flow and heat transfer from wavy surfaces. Viscous fluids, porous media and nanofluids*, CRC Press, Taylor & Francis Group, New York. doi: 10.1201/9781315367637

[13] Dalal, A., & Das, M.K. (2006). Natural convection in a cavity with a wavy wall heated from below and uniformly cooled from the top and both sides. *ASME Journal of Heat and Mass Transfer* 128(7), 717–725. doi: 10.1115/1.2194044

[14] Cheong, H.T., Sivasankaran, S., & Bhuvaneswari, M. (2017). Natural convection in a wavy porous cavity with sinusoidal heating and internal heat generation. *International Journal of Numerical Methods for Heat & Fluid Flow*, 27(2), 287–309. doi: 10.1108/HFF-07-2015-0272

[15] Al-Srayyih, B.M., Gao, S., & Hussain, S.H. (2019). Natural convection flow of a hybrid nanofluid in a square enclosure partially filled with a porous medium using a thermal non-equilibrium model. *Physics of Fluids*, 31, 043609. doi: 10.1063/1.5080671

[16] Babar, H., Sajid, M.U., & Ali, H.M. (2019). Viscosity of hybrid nanofluids: A critical review. *Thermal Science*, 23(3B), 1713–1754. doi: 10.2298/TSCI181128015B

[17] Sarkar, J., Ghosh, P., & Adil, A.(2015). A review on hybrid nanofluids: Recent research, development and applications. *Renewable and Sustainable Energy Reviews*. 43, 164–177. doi: 10.1016/j.rser.2014.11.02 3

[18] Kasaeian, A., Daneshazarian, R., Mahian, O., Kolsi, L., Chamkha, A.J., Wongwises, S., & Pop, I.(2017). Nanofluid flow and heat transfer in porous media: A review of the latest developments. *International Journal of Heat and Mass Transfer*, 107, 778–791. doi: 10.1016/j.ijheatmasstransfer.2016.11.074

[19] Biswas, N., Mandal, D.K., Manna, N.K.,. Gorla, R.S.R., & Chamkha, A.J. (2021). Magnetohydrodynamic thermal characteristics of water-based hybrid nanofluid filled non-Darcian porous wavy enclosure: effect of undulation. *International Journal of Numerical Methods for Heat & Fluid Flow*, 32(5), 11742−1777. doi: 10.1108/HFF-03-2021-0190

[20] Biswas, N., Manna, N.K., Chamkha, A.J. & Mandal, D.K. (2021). Effect of surface waviness on MHD thermo-gravitational convection of Cu−Al₂O₃−water hybrid nanofluid in a porous oblique enclosure. *Physica Scripta*, 96(10), 105002. doi: 10.1088/1402-4896/ac0f94

[21] Mandal, D.K., Biswas, N., Manna, N.K., Gorla, R.S.R., & Chamkha, A.J. (2022). Magneto-thermal convection of hybrid nanofluid in a non-Darcian porous complex wavy enclosure. *The European Physical Journal Special Topics*, 231, 2695–2712. doi: 10.1140/epjs/s11734-022-00595-6

[22] Biswas, N., Mondal, M.K., Mandal, D.K., Manna, N.K., Gorla, R.S.R., & Chamkha, A.J. (2022). A narrative loom of hybrid nanofluid filled wavy walled tilted porous enclosure imposing a partially active magnetic field. *International Journal of Mechanical Sciences,* 217, 107028. doi: 10.1016/j.ijmecsci.2021.107028

[23] Bahmani, M., Babagoli, M., Jalili, P., Jalili, B., & Ganji, D.D. (2024).The numerical study on the MHD natural convection trend of square/circle corrugated porous media. *Journal of Engineering Research* (in press). doi. 10.1016/j.jer.2024.05.012

[24] Hamid, M., Usman, M., Khan, W.A., Haq, R.U., & Tian, Z. (2024). Characterizing natural convection and thermal behavior in a square cavity with curvilinear corners and central circular obstacles. *Applied Thermal Engineering*, 248(A), 123133. doi: 10.1016/j.applthermaleng.2024.123133

[25] Pandit, S., Mondal, M.K., Manna, N.K., Sanyal, D., Biswas, N., & Mandal, D.K. (2024). Synergistic effects of multi-segmented magnetic fields, wavy-segmented cooling, and distributed heating on hybrid nanofluid convective flow in tilted porous enclosures. *International Journal of Thermofluids,* 4, 100826. doi: 10.1016/j.ijft.2024.100826

[26] Guedri, K., Zaim, A.N., Sajadi, S.M., Jasim, D.J., Aissa, A., Salahshour, S., Almuhtady, A., Younis, O., Baghaei, S., & Al-Kouz, W. (2024). Investigation of free convection in a wavy trapezoidal porous cavity with MWCNT-Fe$_3$O$_4$/Water hybrid nanofluid under MHD effects: Galerkin finite element analysis. *Case Studies in Thermal Engineering*, 56, 104243. doi: 10.1016/j.csite.2024.104243

[27] Mandal, D.K., Mondal, M.K., Biswas, N., Manna, N.K., Al-Farhany, K., Mitra, A., & Chamkha, A.J. (2024). Convective heat transport in a porous wavy enclosure: nonuniform multi-frequency heating with hybrid nanofluid and magnetic field. *Heliyon*, 10 (9), e29846. doi: 10.1016/j.heliyon.2024.e29846

[28] Al-Dulaimi, Z., Kadhim, H.T., Jaffer, M.F., Al-Manea, A., Al-Rbaihat, R., & Alahmer, A. (2024). Enhanced conjugate natural convection in a corrugated porous enclosure with Ag-MgO hybrid nanofluid. *International Journal of Thermofluids*, 21, 100574. doi: 10.1016/j.ijft.2024.100574

[29] Said, M.A., Togun, H., Abed, A.M., Biswas, N., Mohammed, H.I., Sultan, H.S., Mahdi, J.M., & Talebizadehsardari, P. (2024). Evaluation of wavy wall configurations for accelerated heat recovery in triplex-tube energy storage units for building heating applications. *Journal of Building Engineering*, 94, 109762. doi: 10.1016/j.jobe.2024.109762

[30] Manna, N.K., Saha, A., Biswas, N., & Ghosh, K. (2024). Shape matters: Convection and entropy generation in magneto-hydrodynamic nanofluid flow in constraint-based analogous annular thermal systems. *Numerical Heat Transfer, Part A: Applications*, 1−33. doi: 10.1080/10407782.2024.2347585

[31] Chatterjee, D., Biswas, N., Manna, N.K., & Mandal, D.K. (2023). Magneto-nanofluidic convection and entropy generation in discretely heated cylindrical annuli with central conducting obstructions. *Journal of Magnetism and Magnetic Materials*, 569, 170442. doi: 10.1016/j.jmmm.2023.170442

[32] Maxwell, J. (1904). *A treatise on electricity and magnetism* (2nd ed.). Oxford University Press, Cambridge.

[33] Brinkman, H.C. (1952). The viscosity of concentrated suspensions and solutions. *The Journal of Chemical Physics*, 20(4), 571−580. doi: 10.1063/1.1700493

[34] Chatterjee, D., Biswas, N., Manna, N.K., & Sarkar, S. (2023). Effect of discrete heating-cooling on magneto-thermal-hybrid nanofluidic convection in cylindrical system. *International Journal of Mechanical Science*, 238, 107852. doi: 10.1016/j.ijmecsci.2022.107852

[35] Halder, A., Bhattacharya, A., Biswas, N., Manna, N.K., & Mandal, D.K. (2024). Convective heat transport and entropy generation in butterfly-shaped magneto-nanofluidic systems with bottom heating and top cooling. *International Journal of Numerical Methods for Heat & Fluid Flow*, 34(2), 837−877. doi: 10.1108/HFF-06-2023-0353

[36] Suresh, S, Venkitaraj, K, Selvakumar, P, & Chandrasekar, M. (2012). Effect of Al$_2$O$_3$–Cu/water hybrid nanofluid in heat transfer. *Experimental Thermal and Fluid Science*, 38, 54–60. doi: 10.1016/j.expthermflusci.2011.11.007

[37] Biswas, N., Chatterjee, D., Sarkar, S., & Manna, N.K. (2024). Magneto-nanofluidic thermal transport and irreversibility in semicircular systems with heated wavy bottom under constant fluid volume and cooling surface constraints. *International Journal of Numerical Methods for Heat & Fluid Flow*, 34(2), 1021−1059. doi: 10.1108/HFF-06-2023-0354

[38] Ghasemi, B., Aminossadati, S.M., & Raisi, A. (2011). Magnetic field effect on natural convection in a nanofluid-filled square enclosure. *International Journal of Thermal Sciences*, 50(9), 1748–1756. doi: 10.1016/j.ijthermalsci.2011.04.010

[39] Pandit, S., Mondal, M.K., Manna, N.K., Sanyal, D., Biswas, N., & Mandal, D.K. (2024). Synergistic effects of multi-segmented magnetic fields, wavy-segmented cooling, and distributed heating on hybrid nanofluid convective flow in tilted porous enclosures. *International Journal of Thermofluids*, 24, 100826. doi: 10.1016/j.ijft.2024.100826

Numerical Analysis of Heat Transfer of CuO-Water Nanofluid Through a Square Channel with Heated Inner Triangular Groove

Baradi Lavanya[a,b], Gosukonda Srinivas[c], Baluguri Suresh Babu[d*], Oluvole Daniel Makinde[e]

[a]Bharatiya Engineering Science & Technology Innovation University, Gorantla, Andhra Pradesh- 515231, India.
[b]St. Francis College for Women, Hyderabad, Telangana-500 016, India.
[c]Geethanjali college of Engineering and Technology, Hyderabad, Telangana-500 016, India.
[d]Sreyas Institute of Engineering and Technology, Hyderabad, Telangana-500 068, India.
[e]Stellenbosch University, Private Bag X2, Saldanha 7395, South Africa.
*Corresponding author email: bsureshmaths@gmail.com.

Abstract

This paper investigates the flow and heat transfer characteristics of CuO–water nanofluid in a square channel with an inner triangular groove that is continuously heated. By applying a transverse magnetic field, the governing coupled and nonlinear equations are solved using the Galerkin finite element method across various Reynolds numbers. The analysis provides comprehensive insights into the effects of different parameters through stream plots and contour plots. The heat transfer rate, represented by the Nusselt number (Nu), is graphically presented for the heated inner triangular groove and thoroughly discussed. Results indicate that the flow rate significantly influences heat transfer, particularly for high Reynolds numbers, with notable effects observed in both the upper and lower parts of the channel. Optimal heat transfer is achieved at a 3% concentration of CuO nano-particles, highlighting the potential for enhanced thermal performance in such configurations.

Keywords: Heat transfer; CuO-water nanofluid; Square channel; Inner triangular groove; Finite element method

1. Introduction

Heating systems have always been extensively studied across various fields. Researchers have continually sought to enhance the heat transfer rate and efficiency of heating systems through a variety of techniques, both experimentally and numerically, using active and passive methods. Energy exchange occurs when two systems with different temperatures come into contact, although there can also be a temperature differential within a single system. Heat transfer is the process that facilitates the transport of energy. With advancements in microelectronics and micro-manufacturing technologies, higher performance and integration of electronic devices are now achievable. This has

raised concerns among heat transfer researchers due to the thermal management challenges that come with increased performance and integration.

Heat transfer, although not directly measurable or observable, can be inferred through its effects. It involves the movement of energy due to a temperature difference between solid, liquid, or gaseous objects. The study of heat transfer encompasses the production, use, conversion and exchange of thermal energy across physical systems within the field of thermal engineering.

CuO-water nanofluid has many applications in industries. The literature contains numerous research works. In particular, Karami et al. [1] did a computer simulation of turbulent flow convection in a cylinder with rectangular grooves. He looked at

Nomenclature

B_0 – constant applied magnetic field, A/m
C_p – specific heat, J/(kg K)
g – gravitational acceleration, m/s^2
Gr – Grashoff number
k – thermal conductivity, W/(m K)
L – characteristic length, m
M – magnetic field parameter
Pr – Prandtl number
q – heat source parameter, W/m^2
Q_h – dimensionless heat source parameter
Re – Reynolds number
t – dimensional time, s
T – dimensional temperature, K
T_0 – temperature at triangular groove, K
T_∞ – temperature at upper plate of the channel, K
u, v – dimensional velocity, m/s
U, V – dimensionless velocities
U_0 – characteristic velocity, m/s

x, y – dimensional space variables, m
X, Y – dimensionless space variables
Ø – volume fraction of the nanoparticles

Greek Symbols

α – thermal diffusivity, m^2/s
β_T – coefficient of thermal expansion, 1/K
Θ – dimensionless temperature
μ – dynamic viscosity, Pa·s
ρ – density, kg/m^3
σ – electrical conductivity, S/m
φ_j – shape function at j^{th} node

Subscripts and Superscripts

f – base fluid (water)
nf – nanofluid (CuO-water)
s – metal particle (CuO)

Abbreviations and Acronyms

FEM – finite element method

how CuO nanoparticles at different volume fractions affect heat transfer for different Reynolds numbers. Dehghani-Ashkezari and Salimpour [2] studied how water-titanium oxide nanofluid boiled in pools on different grooved surfaces and found that the shape of the grooves has a big effect on how heat moves through the surface. In their study, Boukerma and Kadja [3] looked at the convective heat transfer of Al$_2$O$_3$/water-ethylene glycol (EG) and CuO/(W-EG) nanofluids in a round tube with laminar flow. According to Jafarimoghaddam and Aberoumand [4], nanofluids improve the flow properties in rib-groove channels, with the Nusselt number going up as the volume fraction goes up and down as the nanoparticle diameter goes down. Srinivas et al. [5] studied the natural chemical reaction between the metal particle and the solvent, along with the decomposition of the metal particle. Researchers also examined the behaviour of the nanofluid viscosity in relation to its flow and heat transfer. Gupta et al. [6] explored how to resolve the unsteady flow problem of a hybrid nanofluid on a stretched surface in a porous medium. This study examines the form factor analysis by evaluating four geometries: brick, lamina, platelet and blade.

The experiments of heat and mass transfer through many geometries, like horizontal and vertical channels, are available in the literature. Balasubramanian and Mukeshkumar [7] conducted additional research and determined that the size of the nanoparticles and their thermal conductivity significantly influence the efficacy of heat transfer. Navaei et al. [8] investigated the impact of various nanofluids and geometrical parameters on rib-grooved channels. They discovered that the heat transfer properties varied based on the basal fluids. Rimbault et al. [9] noted that nanofluids exhibit minor improvements in heat transfer compared to water due to their low particle volume fractions. Ahmed et al. [10] used a turbulence model to look into the turbulent forced convection of nanofluids in channels that are triangularly corrugated and have different Reynolds numbers. The objective was to emphasize the impact of rib dimensions on heat transfer.

The finite element method (FEM) has become a crucial computational tool in engineering and applied sciences, solving complex problems in structural, thermal, fluid, and electromagnetic domains. FEM applications span various fields, including mechanical engineering, civil engineering, bioengineering, and materials science, providing accurate simulations of heat flow in systems with intricate shapes and varying thermal properties. Ekiciler [11] did a test to see how new hybrid nanofluids (TiO$_2$-Cu/EG) and the shape of a triangular rib in a duct changed the flow and transfer of heat. They discovered that a volume fraction of 4% is necessary. Suresh Babu et al. [12] created a mathematical model that includes thermo-diffusion and diffusion-thermal effects for heat and mass transfer in a variable-width vertical channel between two fluids that don't mix. In the research by Gupta et al. [13], they look at how radiation and Thompson and Troian boundary slip affect the flow of a nanofluid that is made up of kerosene oil and CNT-Fe$_3$O$_4$ over an exponentially stretched porous sheet. The Reynolds viscosity model views the viscosity as temperature-dependent. Ahmed et al. [14] used the finite volume method to study the impact of nanofluid volume on entropy and turbulent kinetic energy. Vatani and Mohammed [15] numerically examined the effects of rib groove shapes and nanofluids on heat and fluid flow in horizontal channels.

Also, FEM has a lot of advantages; it can handle complex geometries like a square channel with different shapes of grooves. FEM is well-suited for problems with boundary and interface complexities. Ajeel et al. [16], Alipour et al. [17], Hussein et al. [18], and Naphon and Nakharintr [19] conducted a study that explored various nanofluid configurations and their effects on turbulent flow and heat transfer. Gosty et al. [20] examine the phenomena of heat, mass, and fluid flow in a vertical channel holding two immiscible fluids, with an emphasis on slip effects. Upreti et al. [21] analyze Au-TiO$_2$/ethylene glycol hybrid nanofluid flow across a narrow needle. In a homogeneous magnetic field, fluid parameters like dynamic viscosity and thermal conductivity rely on nanoparticle shape and temperature. They also examine quadratic convection with quadratic thermal

radiation and use the Cattaneo-Christov heat flow model to explain heat transfer. Some researchers, like Avramenko et al. [22] and Ajeel et al. [23] looked into the thermal and hydraulic properties of turbulent nanofluid flow. Other researchers, like Khudheyer et al. [24] and Pourfattah et al. [25] looked into how nanoparticles and rib angles affect heat transfer. Sailaja et al. [26] conducted research on forced and free convective heat transfer through a two-dimensional nanofluid flowing past a stretching vertical plate. In a study by Akdag et al. [27] they measured how heat moved through water-based Al$_2$O$_3$ nanofluids in a wavy mini-channel. They found that the size and number of nanoparticles had a big effect on how well the heat moved. Uniyal et al. [28] examined it in depth. They conducted a thorough investigation into the integration of phase change materials and nanofluids into evacuated tube solar water heaters, an area that has witnessed significant advancements recently. Gosty et al. [29] conducted a study that explores the transmission of heat and mass in a vertical channel filled with immiscible fluids, specifically viscous and micropolar fluids. Bhandari et al. [30] looked into modifying the design of the microchannel heat sink to enhance thermo-hydraulic performance.

The aforementioned research reveals that while traditional studies concentrate on straightforward flow patterns, this study delves into the distinctive impact of the triangular groove, amplifying the heat transfer effects. So the primary objective of this work is to investigate the flow and heat transfer characteristics of CuO-water nanofluid through a square channel with a heated inner triangular groove. The groove geometry disturbs the flow, and the induced temperature due to the geometry plays a vital role in heat transfer analysis. This study aims to help improve the thermal management of advanced cooling systems in high-performance settings by using CuO nanoparticles, which are known for being excellent at transferring heat, and look at how they change heat transfer under different flow conditions. Detailed computational simulations provide a deeper understanding of the intricate heat transfer phenomena in advanced engineering applications such as solar water heaters and industrial heat exchangers.

2. Mathematical Formulation

To mathematically formulate the flow and heat transfer of a fully developed nanofluid in a square pipe with an isosceles triangular groove at the bottom, the following assumptions need to be considered:

- Flow direction: The nanofluid flows in the *z*-axis direction.
- Cross-sectional geometry: The cross-section is square with an isosceles triangular groove at the bottom.
- Boundary conditions: Vertical walls: Adiabatic.
- Top wall: Constant temperature T_∞.
- Inclined triangular walls: Constant temperature T_0.
- Bottom wall: Adiabatic (excluding the triangle).
- $T_0 > T_\infty$.

The typical cross section as shown in Fig. 1, is assumed for the numerical study.
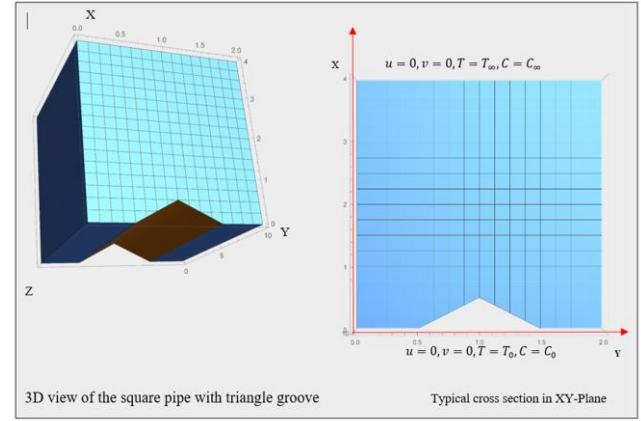
Fig. 1. Geometry of the problem

Under these assumptions, the flow system is assumed to follow the Bussinesq approximation and as per the Buongiorno model, the equations governing the flow, heat and mass transfer are obtained as follows:

$$\frac{\partial u}{\partial x} + \frac{\partial v}{\partial y} = 0, \tag{1}$$

$$\rho_{nf}\left(\frac{\partial u}{\partial t} + u\frac{\partial u}{\partial x} + v\frac{\partial u}{\partial y}\right) = \mu_{nf}\left(\frac{\partial^2 u}{\partial x^2} + \frac{\partial^2 u}{\partial y^2}\right) +$$
$$+ (\rho\beta_T)_{nf} g(T - T_\infty) - \sigma_{nf}B_0^{\,2}u, \tag{2}$$

$$\rho_{nf}\left(\frac{\partial v}{\partial t} + u\frac{\partial v}{\partial x} + v\frac{\partial v}{\partial y}\right) = \mu_{nf}\left(\frac{\partial^2 v}{\partial x^2} + \frac{\partial^2 v}{\partial y^2}\right), \tag{3}$$

$$\frac{\partial T}{\partial t} + u\frac{\partial T}{\partial x} + v\frac{\partial T}{\partial y} = \alpha_{nf}\left(\frac{\partial^2 T}{\partial x^2} + \frac{\partial^2 T}{\partial y^2}\right) - \frac{Q}{(\rho C_p)_{nf}}. \tag{4}$$

The boundary conditions are:
at $t \geq 0$, at the inner triangular groove

$$u = 0, \quad v = 0, \quad T = T_0, \tag{5a}$$

at $t \geq 0$, $y = L$, $\forall x$

$$u = 0, \quad v = 0, \quad T = T_\infty. \tag{5b}$$

All the above equations are made dimensionless using the following forms:

$$X = \frac{x}{L}, \quad Y = \frac{y}{L}, \quad t' = t\frac{U_0}{L},$$
$$U = \frac{u}{U_0}, \quad V = \frac{v}{U_0}, \quad \theta = \frac{T - T_\infty}{T_0 - T_\infty}, \tag{6}$$

where L is the characteristic length and U_0 is the characteristic velocity.

Thermophysical properties considered for this CuO water nanofluid are taken from the work of Pak and Cho [31].

$$\rho_{nf} = (1 - \emptyset)\rho_f + \emptyset\rho_s, \tag{7}$$

$$(\rho C_p)_{nf} = (1 - \emptyset)(\rho C_p)_f + \emptyset(\rho C_p)_s, \tag{8}$$

$$\frac{k_{nf}}{k_f} = \frac{k_s + 2k_f + 2\emptyset\,(k_s - k_f)}{k_s + 2k_f - \emptyset\,(k_s - k_f)}, \tag{9}$$

$$(\rho\beta)_{nf} = (1-\emptyset)(\rho\beta)_f + \emptyset(\rho\beta)_s, \tag{10}$$

$$\alpha_{nf} = \frac{k_{nf}}{(\rho C_p)_{nf}}, \tag{11}$$

$$\frac{\mu_{nf}}{\mu_f} = \frac{1}{(1-\emptyset)^{2.5}}, \tag{12}$$

$$\frac{\sigma_{nf}}{\sigma_f} = 1 + \frac{3\left(\frac{\sigma_S}{\sigma_f}-1\right)\emptyset}{\left(\frac{\sigma_S}{\sigma_f}+2\right)-\left(\frac{\sigma_S}{\sigma_f}-1\right)\emptyset}. \tag{13}$$

Values of thermophysical properties given in Table 1 are considered to get the numerical solution.

Table 1. Values of thermophysical properties.

Physical properties	Copper (CuO)	Water
C_p, J/(kg·K)	385	4,179
ρ, kg/m³	8,933	997.1
k, W/(m·K)	401	0.613
$\beta_T \times 10^{-5}$, 1/K	1.67	27.6
μ, kg/(m·s)	-	8.55×10^{-4}
σ, S/m	0.064	0.05

In view of Eqs. (5) to (13), the governing Eqs. (1) to (4) are modified as follows:

$$\frac{\partial U}{\partial t} + U\frac{\partial U}{\partial X} + V\frac{\partial U}{\partial Y} = \frac{\frac{1}{(1-\emptyset)^{2.5}}}{1-\emptyset+\emptyset\left(\frac{\rho_S}{\rho_f}\right)}\frac{1}{Re}\left(\frac{\partial^2 U}{\partial X^2}+\frac{\partial^2 U}{\partial Y^2}\right)+$$

$$+\left(1-\emptyset+\emptyset\left(\frac{\beta_S}{\beta_f}\right)\right)\frac{Gr}{Re^2}(\theta)-\left(1+\frac{3\left(\frac{\sigma_S}{\sigma_f}-1\right)\emptyset}{\left(\frac{\sigma_S}{\sigma_f}+2\right)-\left(\frac{\sigma_S}{\sigma_f}-1\right)\emptyset}\right)M\,U, \tag{14}$$

$$\frac{\partial V}{\partial t} + U\frac{\partial V}{\partial X} + V\frac{\partial V}{\partial Y} = \frac{\frac{1}{(1-\emptyset)^{2.5}}}{1-\emptyset+\emptyset\left(\frac{\rho_S}{\rho_f}\right)}\frac{1}{Re}\left(\frac{\partial^2 V}{\partial X^2}+\frac{\partial^2 V}{\partial Y^2}\right), \tag{15}$$

$$\frac{\partial \theta}{\partial t} + U\frac{\partial \theta}{\partial X} + V\frac{\partial \theta}{\partial Y} = \frac{\frac{k_S+2k_f+2\emptyset(k_S-k_f)}{k_S+2k_f-\emptyset(k_S-k_f)}}{1-\emptyset+\emptyset\left(\frac{(\rho c_p)_S}{(\rho c_p)_f}\right)}\frac{1}{Pr}\frac{1}{Re}\left(\frac{\partial^2 U}{\partial X^2}+\frac{\partial^2 U}{\partial Y^2}\right)+$$

$$-\frac{Q_h}{1-\emptyset+\emptyset\left(\frac{(\rho c_p)_S}{(\rho c_p)_f}\right)}\frac{1}{Pr}\frac{1}{Re}. \tag{16}$$

where the dimensionless numbers are given as follows:

$$Gr = \frac{g\beta_T(T_\infty-T_0)L^3}{v_f^2}, \qquad Pr = \frac{v_f}{\alpha_f}, \qquad M = \frac{\sigma_f B_0^2}{\rho_f L}, \tag{17}$$

$$Ar = \frac{Gr}{Re^2}, \qquad Re = \frac{LU_0}{v}.$$

After applying the forms given in Eq. (6) the boundary conditions given in Eqs. (5a) and (5b) becomes as below:
at $t \geq 0$, at the inner triangular groove

$$U = 0, \qquad V = 0, \qquad \theta = 1, \tag{18a}$$

at $t \geq 0$, on the upper plate

$$U = 0, \qquad V = 0, \qquad \theta = 0. \tag{18b}$$

The rate of heat transfer (Nusselt number) at the inner triangular groove is calculated using the formula:

$$Nu = -\frac{k_{nf}}{k_f}\left\{\int_A^B \frac{\partial \theta}{\partial X}dY + \int_B^C \frac{\partial \theta}{\partial X}dY\right\}. \tag{19}$$

3. Method of solution

The coupled nonlinear system of partial differential equations governing the flow and heat transfer, as described in Eqs. (14) to (16), is solved subject to the boundary conditions specified in Eq. (18). The Galerkin finite element method (FEM) is employed to solve this system as per the flow chart given in Fig. 2.

Numerical calculations are carried out using the Mathematica 10.1 program, and the results are presented in the form of contour and stream graphs. Additionally, a table showing the rate of heat transmission (Nusselt number Nu) is provided. During the computations, the region is partitioned into 316 elements. The number of elements (316) is determined by testing the convergence of Nu by means of trial and error. When determining the grid size and calculating the outcomes of the governing variables for different values of a given parameter, the remaining parameters are kept constant as follows: $\emptyset = 3\%$, $M = 5$, $Q = 5$, $Gr = 5$, $Pr = 6.99$.
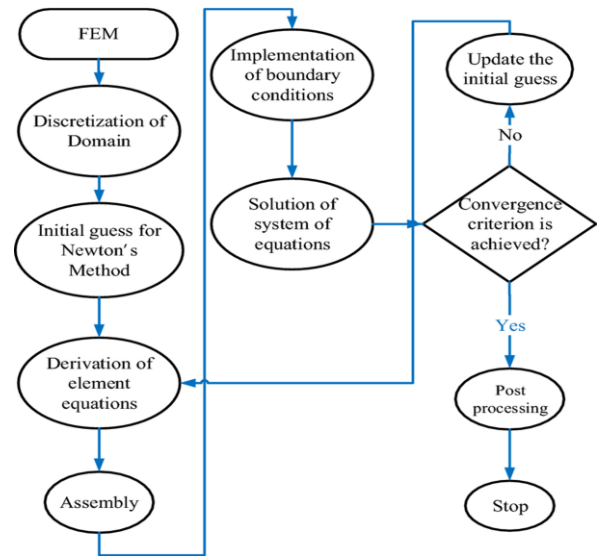
Fig. 2. Flow chart of the numerical method

This approach ensures that the FEM discretization is sufficiently refined to capture the detailed behaviour of flow, heat, and mass transfer processes within the square channel featuring a heated inner triangular groove. The convergence tests confirm the accuracy and reliability of the numerical solutions obtained.

The element wise stiffness matrix will be calculated using the following system of equations:

$$\begin{bmatrix} x_1 \\ x_2 \\ x_3 \\ x_4 \end{bmatrix} * \begin{bmatrix} u \\ v \\ \theta \\ s \end{bmatrix} = \begin{bmatrix} y_1 \\ y_2 \\ y_3 \\ y_4 \end{bmatrix}$$

where:

$$x_1 = \iint \varphi_j \Big(\frac{\partial U}{\partial t} + U\frac{\partial U}{\partial X} + V\frac{\partial U}{\partial Y} - \frac{\frac{1}{(1-\emptyset)^{2.5}}}{\Big(1-\emptyset+\emptyset\big(\frac{\rho_s}{\rho_f}\big)\Big)} \frac{1}{Re}\Big(\frac{\partial^2 U}{\partial X^2} + \frac{\partial^2 U}{\partial Y^2}\Big) +$$

$$+ \Big(1 - \emptyset + \emptyset\big(\frac{\sigma_s}{\sigma_f}\big)\Big) M^2 U\Big) dxdy,$$

$$x_2 = \iint \varphi_j \Big(\frac{\partial U}{\partial t} + U\frac{\partial U}{\partial X} + V\frac{\partial U}{\partial X} - \frac{\frac{1}{(1-\emptyset)^{2.5}}}{\Big(1-\emptyset+\emptyset\big(\frac{\rho_s}{\rho_f}\big)\Big)} \frac{1}{Re}\Big(\frac{\partial^2 U}{\partial X^2} + \frac{\partial^2 U}{\partial Y^2}\Big) +$$

$$+ \Big(1 - \emptyset + \emptyset\big(\frac{\sigma_s}{\sigma_f}\big)\Big) M^2 U\Big) dxdy,$$

$$x_3 = \iint \Big(\varphi_j \Big(\frac{\partial \theta}{\partial t} + U\frac{\partial \theta}{\partial X} + V\frac{\partial \theta}{\partial Y} - \frac{\frac{k_s+2k_f+2\emptyset(k_s-k_f)}{k_s+2k_f-\emptyset(k_s-k_f)}}{(1-\emptyset+\emptyset(\frac{(\rho C_p)_s}{(\rho C_p)_f}))} \frac{1}{Pr}\frac{1}{Re} \times$$

$$\times(\frac{\partial^2 \theta}{\partial X^2} + \frac{\partial^2 \theta}{\partial Y^2}) + \frac{Q_h}{(1-\emptyset+\emptyset(\frac{(\rho C_p)_s}{(\rho C_p)_f}))} \frac{1}{Pr}\frac{1}{Re}\theta +$$

$$+ N_b\Big(\big(\frac{\partial S}{\partial Y}\big)\big(\frac{\partial \theta}{\partial Y}\big) + \big(\frac{\partial S}{\partial X}\big)\big(\frac{\partial \theta}{\partial X}\big)\Big) + N_t\big((\frac{\partial \theta}{\partial X})^2 + \big(\frac{\partial \theta}{\partial Y}\big)^2\big)\Big)\Big) dxdy,$$

$$x_4 = \iint \Big(\varphi_j\big(\big(\frac{\partial S}{\partial t}\big) + U\big(\frac{\partial S}{\partial X}\big) + V\big(\frac{\partial S}{\partial Y}\big) - N_b L_n \Big(\frac{\partial^2 S}{\partial X^2} + \frac{\partial^2 S}{\partial Y^2}\Big)\Big) dxdy,$$

$$y_1 = \iint \varphi_j \left[\Big(1 - \emptyset + \emptyset\big(\frac{\beta_s}{\beta_f}\big)\Big) \frac{Gr}{Re^2}\Big(\theta + \frac{Gc}{Gr}s\Big) \right] dxdy,$$

$$y_2 = 0,$$

$$y_3 = 0,$$

$$y_4 = N_t \iint \varphi_j (\frac{\partial^2 \theta}{\partial X^2} + \frac{\partial^2 \theta}{\partial Y^2}) dxdy,$$

where the integral is done on the domain under consideration.

Each dependent variable at every 3 nodded triangular elements of the discretized domain is taken as:

$$\sum_{j=1}^{3}\sum_{i=1}^{3} u_i \varphi_j, \qquad\qquad \sum_{j=1}^{3}\sum_{i=1}^{3} v_i \varphi_j,$$

$$\sum_{j=1}^{3}\sum_{i=1}^{3} S_i \varphi_j, \qquad\qquad \sum_{j=1}^{3}\sum_{i=1}^{3} \theta_i \varphi_j.$$

The φ_j is the shape function at j^{th} node of the triangular element. The above system of equations is solved with the given approximations. This approach ensures that the FEM discretization is sufficiently refined to capture the detailed behaviour of the flow, heat and mass transfer processes within the square channel featuring a heated inner triangular groove. The convergence tests confirm the accuracy and reliability of the numerical solutions obtained.

4. Results and discussion

The results of numerical simulations, obtained through the Galerkin finite element method (FEM) using Mathematica 10.1, provide detailed insights into the heat and mass transfer charac-

teristics of CuO-water nanofluid in a square channel with a heated inner triangular groove. The computational domain, discretized into 316 elements, ensures a high level of accuracy, as confirmed by the convergence tests of the Nusselt number. The results are presented in the form of contour and stream plots, which visually depict the flow patterns and temperature distributions within the channel. These plots highlight the effects of the triangular groove and the presence of CuO nanoparticles on the overall heat transfer performance. Additionally, the analysis of Nu provides a quantitative measure of the heat transfer rate, allowing for a detailed discussion of the impact of various parameters on thermal efficiency. The discussion focuses on the influence of the flow rate, magnetic field, and nanoparticle concentration on the heat transfer and fluid flow characteristics. The findings for all significant variations are illustrated in stream plots from Fig. 3 to Fig. 8, providing a clear depiction of the stream field profiles. These findings are presented for three distinct flow regimes: laminar conditions at low Reynolds numbers (Re = 10), transition conditions at moderate Reynolds numbers (Re = 100), and at high Reynolds numbers (Re = 5000). The effects of varying CuO particle volume fractions and Reynolds numbers on the flow and heat transfer are analysed.

4.1. Stream plots

Figures 3−6 show that at a Reynolds number (Re) of 10, the flow pattern is distinctly laminar and smooth, indicating stable and uniform flow characteristics. However, as the Reynolds number increases to 100 and 5000, the flow transitions to more complex states, exhibiting significant changes in behaviour. For Re = 100, the flow begins undergo the transition, showing the early stages of instability and the development of non-uniformties. At Re = 5000, the flow becomes fully turbulent, characterized by chaotic and irregular patterns. In both the transitional (Re = 100) and turbulent (Re = 5000) cases, the flow is notably non-uniform across the channel, regardless of the percentage of metal particle composition. This non-uniformity is particularly pronounced around the heated triangular groove, where the recirculation zones and vortices are more prominent. Gravity influences the flow near the lower half of the channel, causing fluid accumulation and complex flow patterns around the groove. However, significant flow changes are also observed in the upper half of the channel. The presence of higher concentrations of CuO particles amplifies these effects. At higher particle concentrations, the fluid exhibits increased thermal conductivity and altered viscosity, which contribute to the more pronounced flow alterations. The CuO particles enhance the heat transfer but also lead to more complex flow interactions, especially in the upper half of the channel. This results in a distinct presence of fluid with higher particle content in this region, affecting the overall flow dynamics and heat transfer efficiency within the channel.

The magnetic field parameters play a crucial role in understanding and predicting the dynamics of magnetized fluids. The strength of the magnetic field is a fundamental parameter that directly influences the behaviour of the fluid. Higher magnetic field strengths lead to stronger interactions of CuO particles with the fluid, affecting its flow patterns, stability and transport prop-

Fig. 3. Stream plots for Ø = 1% for different Reynolds numbers: Re = 10, 100 and 5000, respectively.

Fig. 4. Stream plots for Ø = 2% for different Reynolds numbers: Re = 10, 100 and 5000, respectively.

Fig. 5. Stream plots for Ø = 3% for different Reynolds numbers: Re = 10, 100, 5000 respectively.

Fig. 6. Stream plots for Ø = 4% for different Reynolds numbers: Re = 10, 100 and 5000, respectively.

erties. Figures 7−10 show that there is a slight flow disturbance observed when the magnetic field parameter varies from $M = 2$ to $M = 10$ at Re = 10 (laminar flow). A uniform flow near the inner triangular groove up to $M < 8$ is noticed. But for M > 8, the flow behaviour changes significantly. However, lower magnetic field parameters are strongly recommended to reduce the flow turbulence to a greater extent.

Figures 11−14 illustrate the temperature distribution within the channel, highlighting the impact of the heat source on thermal gradients. The presence of the heated triangular groove introduces localized high-temperature regions, resulting in significant thermal expansion of the fluid and variations in the density of both the fluid and CuO particles. This thermal expansion causes deformation of the streamlines at the heat source, particu-

Fig. 7. Stream plots for $M = 2$ for different Reynolds numbers: Re = 10, 100 and 5000, respectively.

Fig. 8. Stream plots for $M = 5$ for different Reynolds numbers: Re = 10, 100 and 5000, respectively.
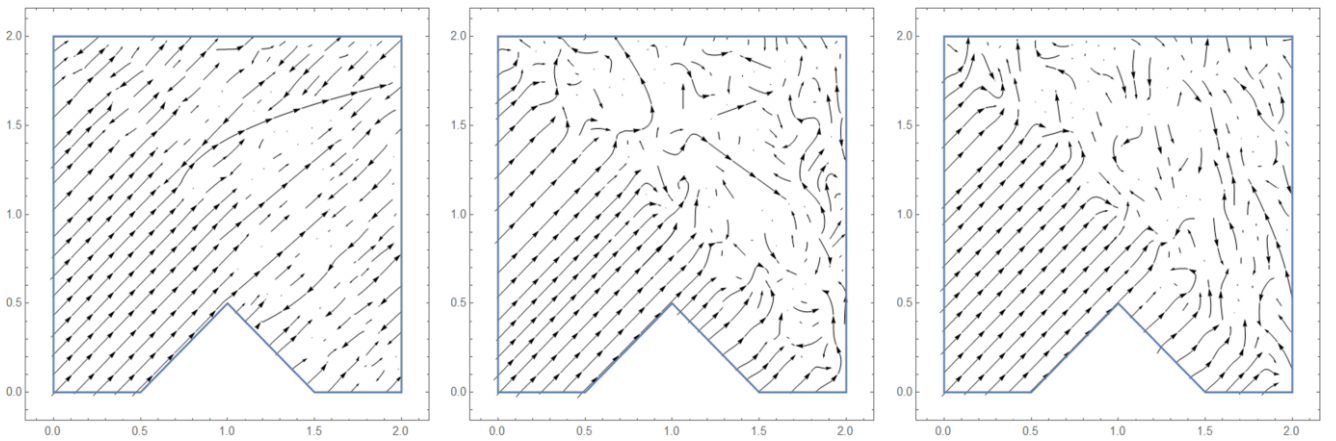
Fig. 9. Stream plots for $M = 8$ for different Reynolds numbers: Re = 10, 100 and 5000, respectively.
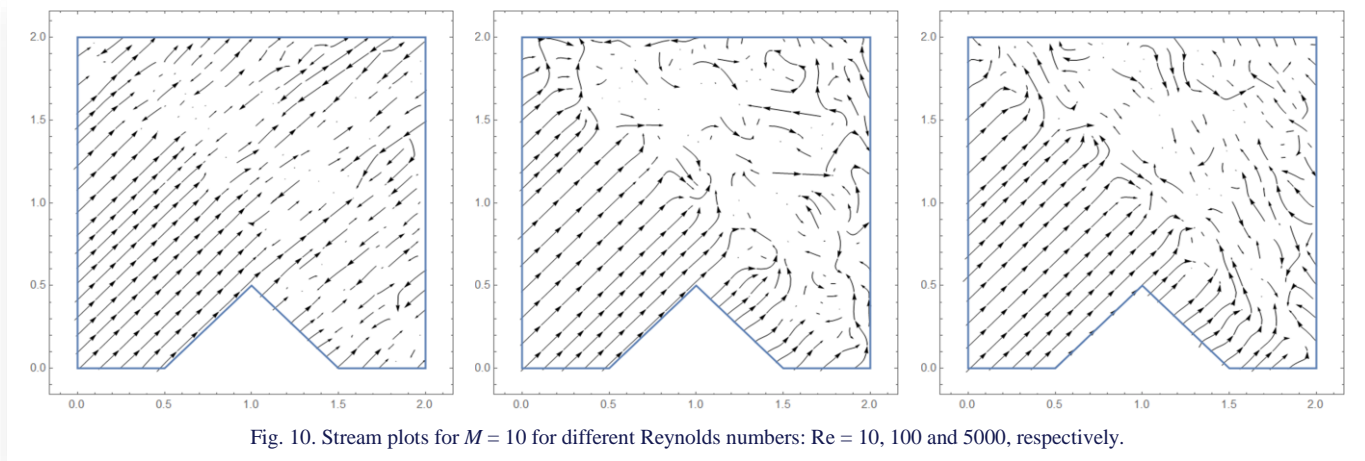
Fig. 10. Stream plots for $M = 10$ for different Reynolds numbers: Re = 10, 100 and 5000, respectively.

larly around the triangular groove, indicating changes in the flow pattern induced by the heat. In these regions, the streamlines exhibit noticeable curvature or deviation, corresponding to areas of convective motion where heat is being transported through the fluid. The thermal gradients create buoyancy effects, which further alter the flow pattern. This is especially evident in the upper half of the channel, where turbulence is more pronounced. The internal heat source acts as an additional factor, intensifying the disturbances in this region. The results show that the heat source significantly influences the temperature field, causing more pronounced disturbances and complex flow behaviour near the upper half of the channel. The increased tur-

bulence and convective heat transfer lead to greater mixing and enhanced thermal diffusion, reflected in the curved and deviated streamlines. These effects underscore the crucial role of thermal gradients and heat sources in shaping the flow and temperature distribution within the channel.

4.2. Contour plots

Figures 15−18 illustrate the temperature distribution contours for various heat source values in different flow regimes. At lower values of the heat source parameter (Q) in laminar flow, the temperature is predominantly higher in the lower part of the

Fig. 11. Stream plots for $Q = 5$ for different Reynolds numbers: Re = 10, 100 and 5000, respectively.

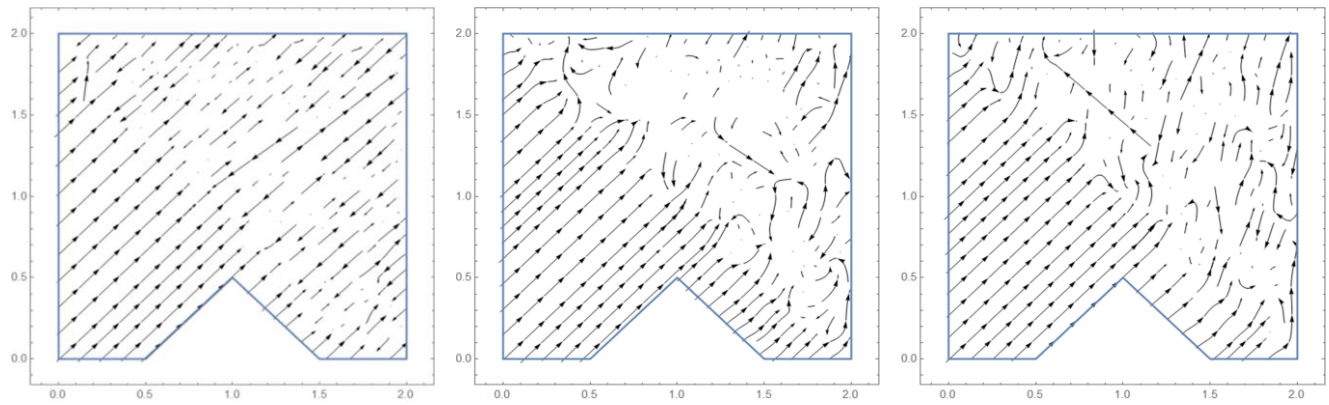Fig. 12. Stream plots for $Q = 12$ for different Reynolds numbers: Re = 10, 100 and 5000, respectively.

90
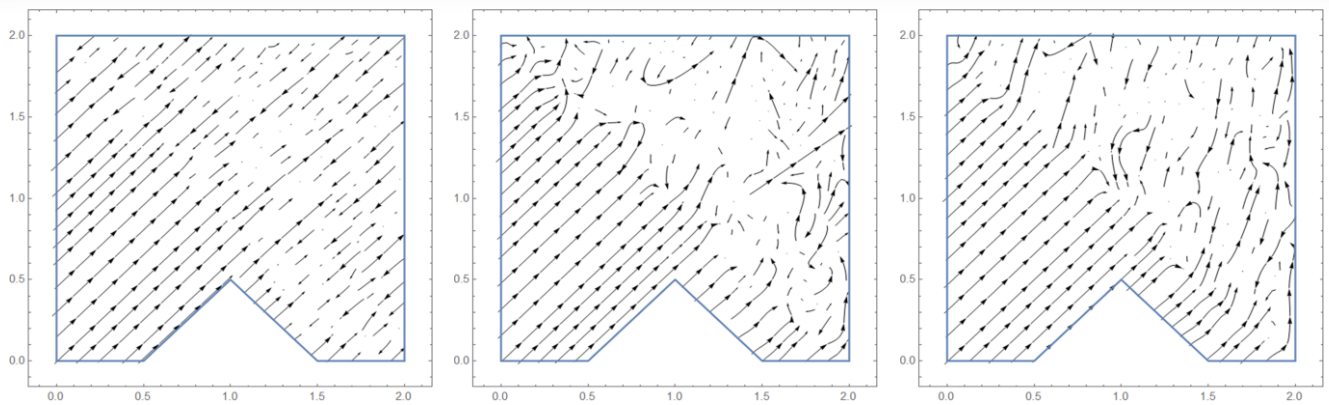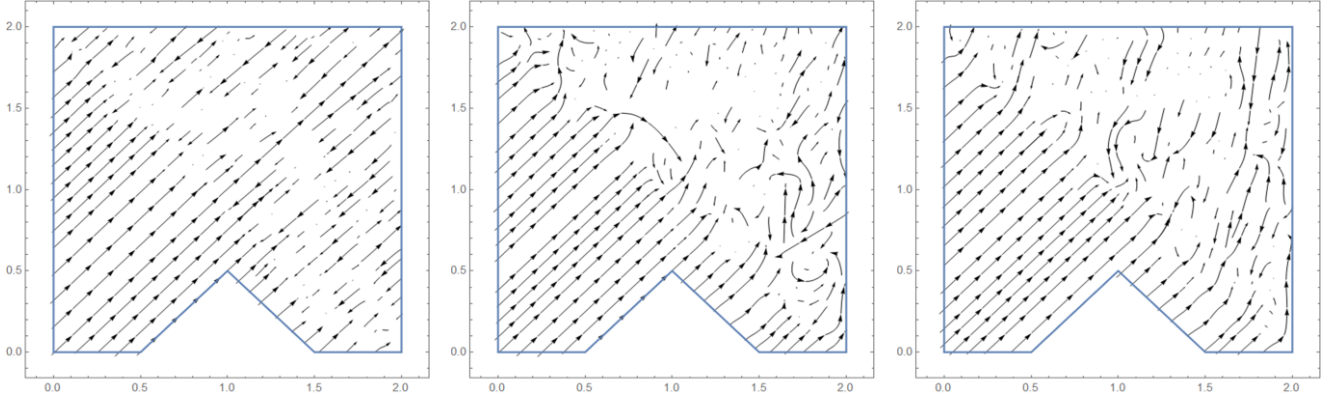
Fig. 13. Stream plots for $Q = 15$ for different Reynolds numbers: Re = 10, 100 and 5000, respectively.
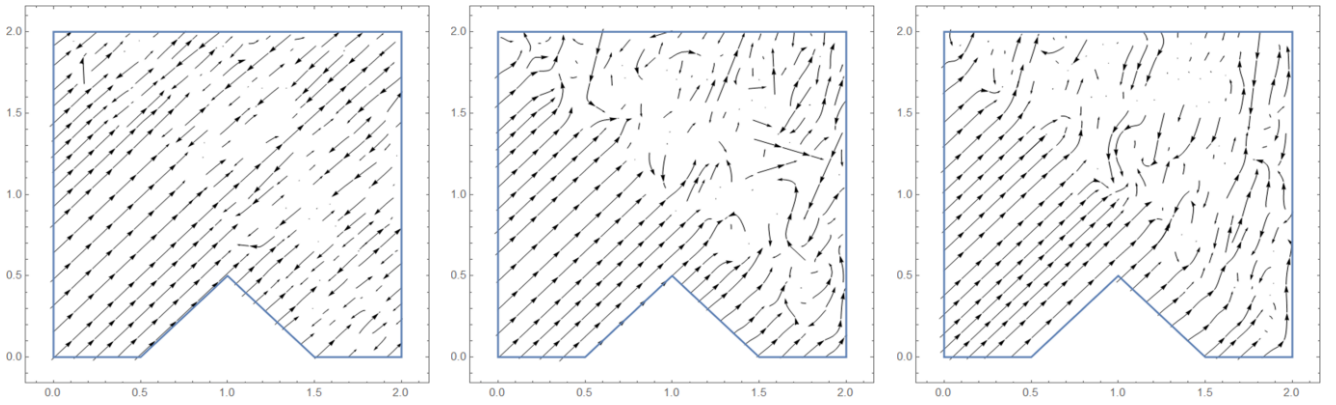
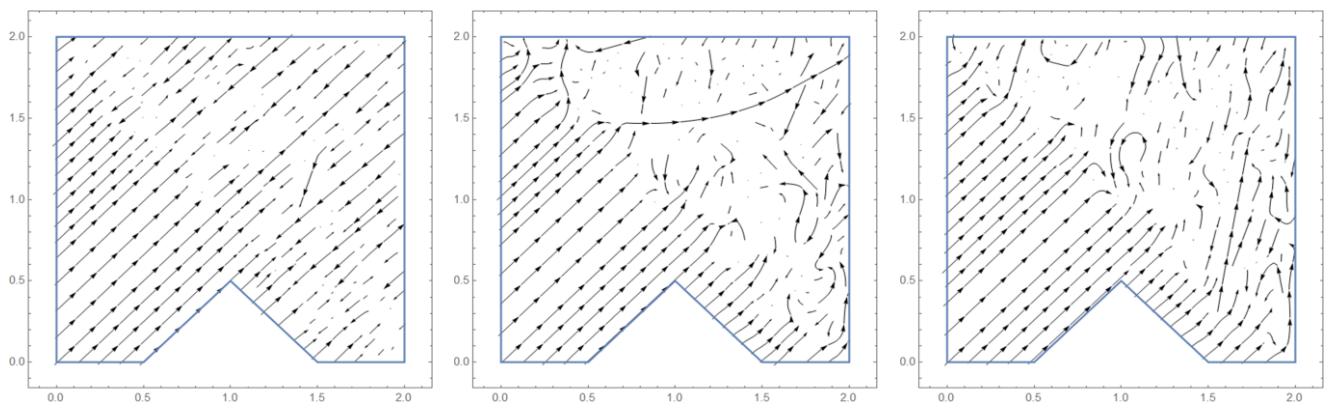Fig. 14. Stream plots for $Q = 24$ for different Reynolds numbers: Re = 10, 100 and 5000, respectively.

channel due to the relatively lower heat generation, which causes heat to accumulate near the bottom before it can be adequately dispersed. As the heat source parameter increases, the temperature distribution becomes more uniform, indicating better heat dispersion throughout the channel, suggesting that higher heat source values enhance convective heat transfer, reducing localized temperature peaks. For flows with a higher Reynolds number, the influence of increasing the heat source parameter on the temperature distribution is less pronounced, as

higher Reynolds numbers correspond to more turbulent flow regimes that inherently enhance mixing and heat transfer. Thus, even with an increase in Q, the already efficient heat transfer mechanism due to turbulence mitigates significant changes in the temperature distribution.

The combined effect of internal and external heat sources becomes more significant at higher Reynolds numbers, likely due to the enhanced convective heat transfer capabilities in turbulent flows, which can more effectively integrate and distribute
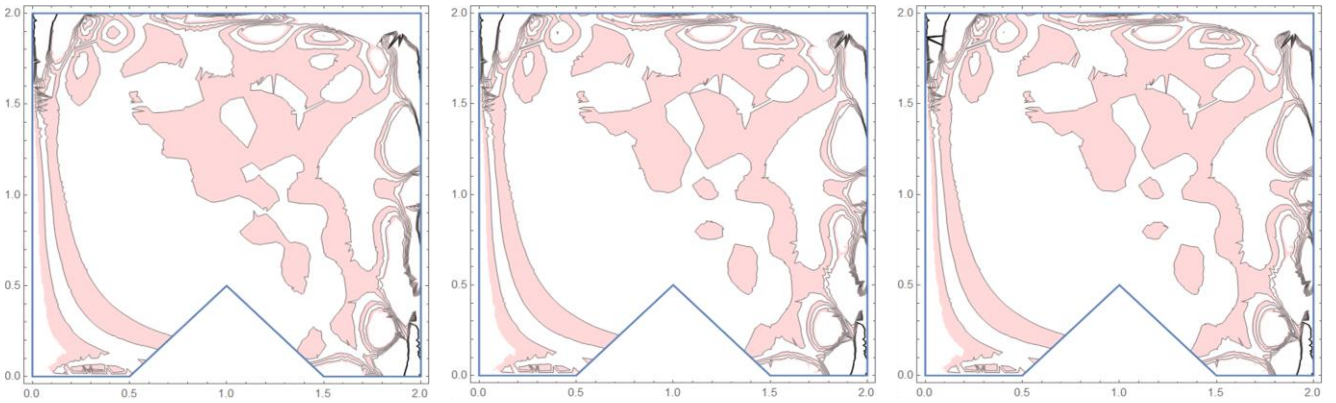
Fig. 15. Contour plots for $Q = 5$ for different Reynolds numbers: Re = 10, 100 and 5000, respectively.
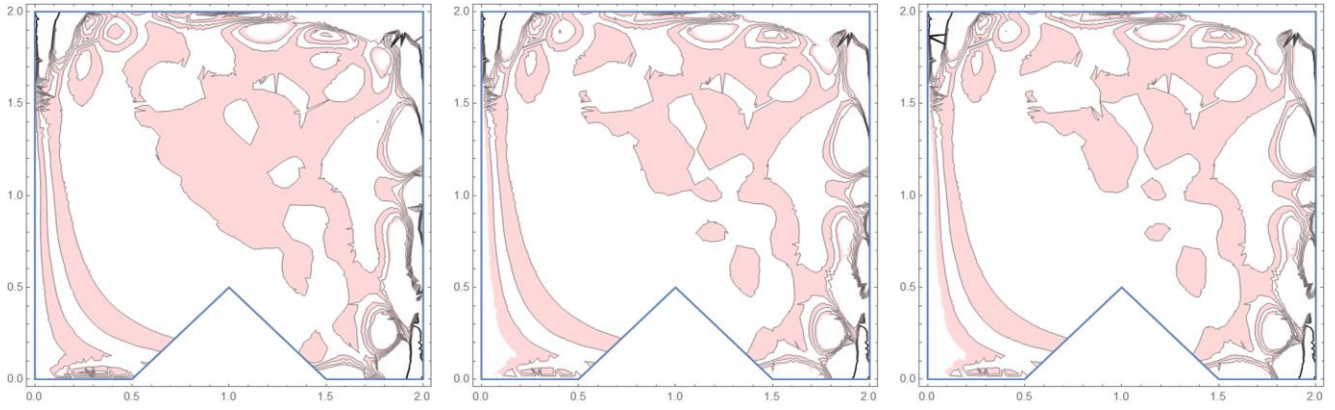
Fig. 16. Contour plots for $Q = 12$ for different Reynolds numbers: Re = 10, 100 and 5000, respectively.
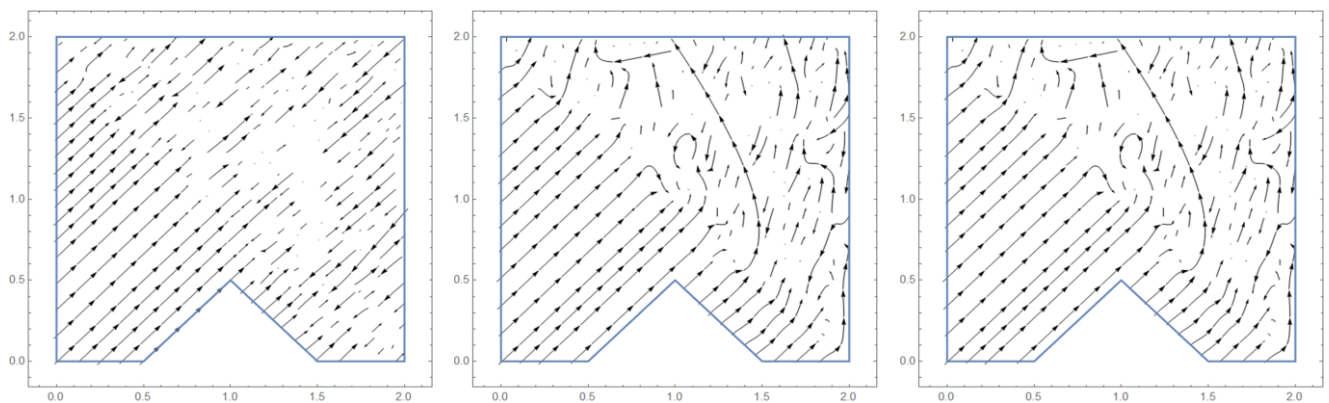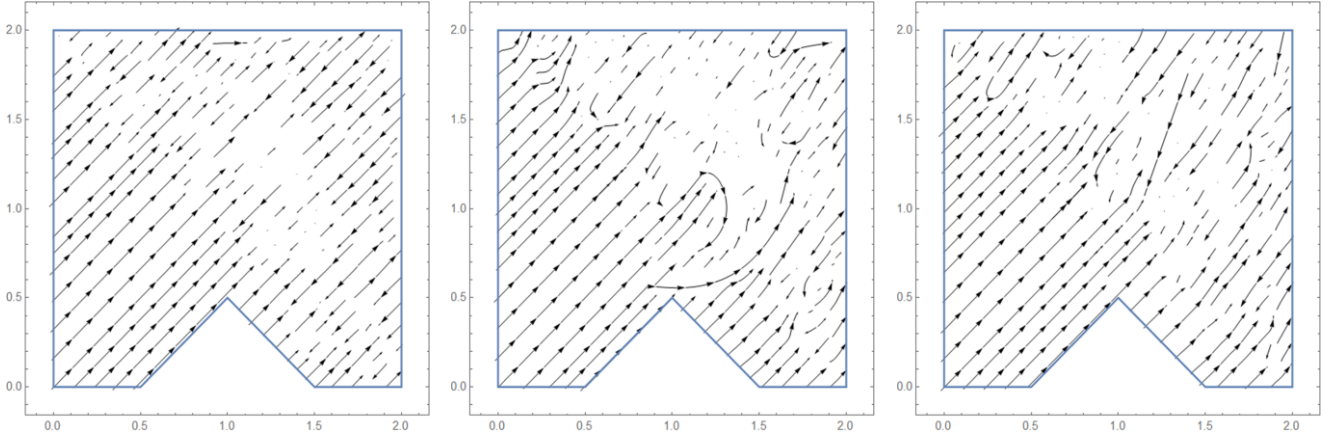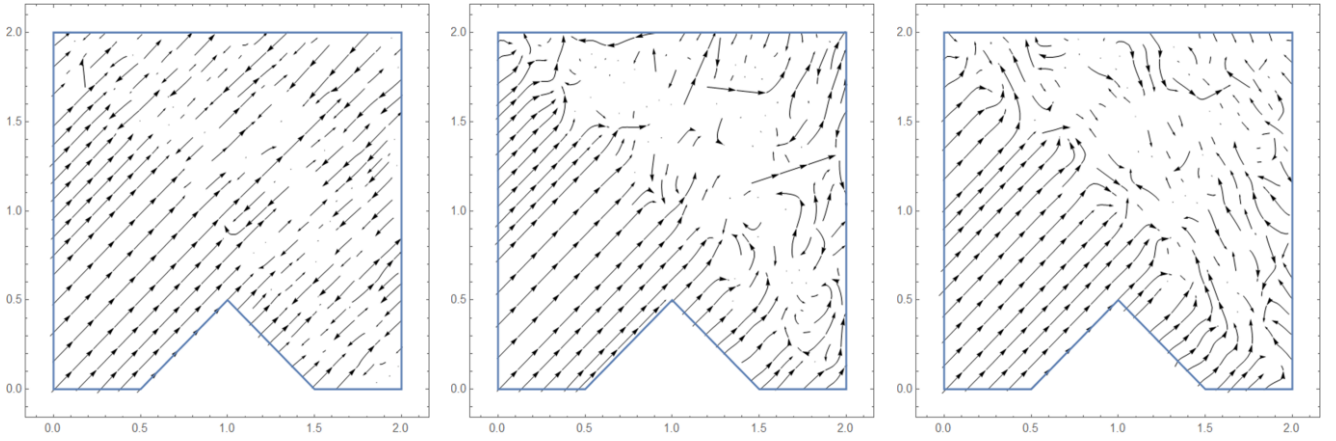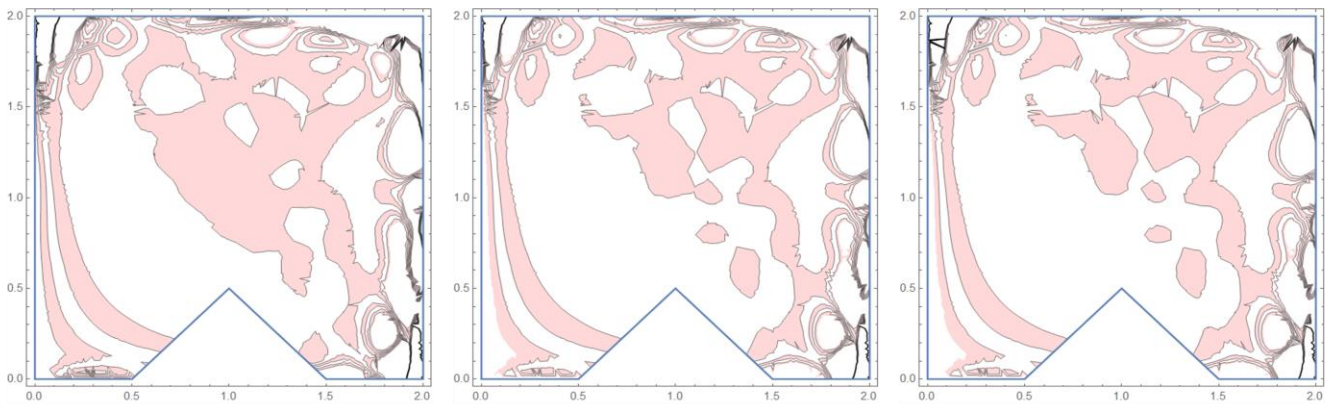

Fig. 17. Contour plots for $Q = 15$ for different Reynolds numbers: Re = 10, 100 and 5000, respectively.
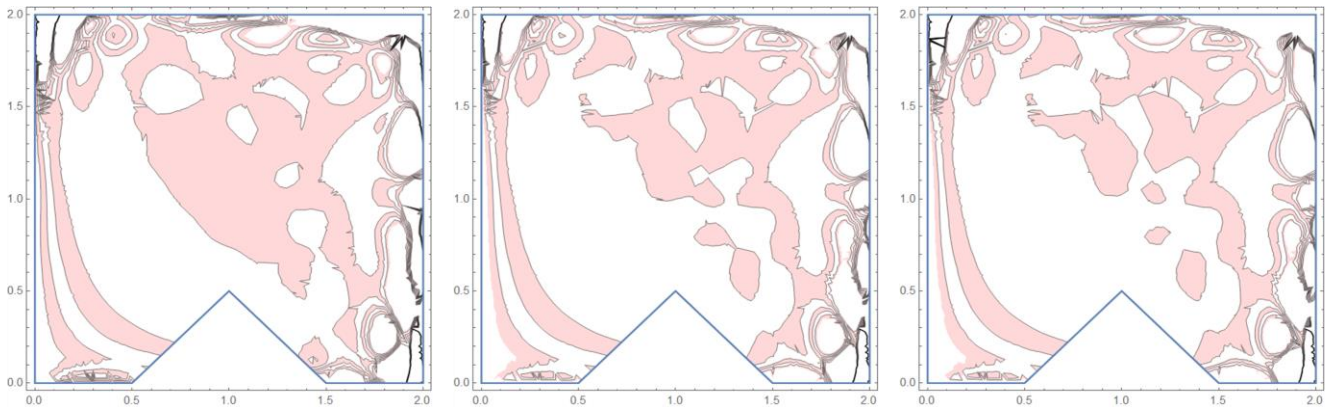
Fig. 18. Contour plots for $Q = 24$ for different Reynolds numbers: Re = 10, 100 and 5000, respectively.

heat from both sources compared to laminar flows. For all variations of the heat source parameter and Reynolds number, the temperature is consistently higher on the right wall compared to the left wall, possibly due to asymmetries in the flow field or in the placement of heat sources, causing a preferential accumulation of heat on the right side. This observation indicates a potential directional bias in heat transfer within the channel, which may need to be addressed depending on the application or desired thermal management outcomes.

As per Figs. 19−23, the temperature dissemination is larger at high Reynolds numbers for all percentages of CuO particles. This is due to the Brownian motion of CuO particles in the fluid. Further, the thermal boundary layer is found larger near the right wall of the channel than the left wall. The temperature dissemination is found larger near the heat source or bottom of the channel. The dissemination of heat to the top wall is found larger for low Reynolds numbers at all variations of metal particle concentrations.

Figure 24 presents the Nusselt number (Nu), which quantifies the rate of heat transfer across laminar, transitional and turbulent flow regimes. The results indicate that the heat transfer rate increases up to a 3% concentration of metal particles (CuO), beyond which it decreases. This decrease suggests the potential occurrence of particle agglomeration at higher concentrations, impacting heat transfer efficiency. Importantly, this trend is consistent across all Reynolds numbers investigated in this study. For lower Reynolds number flows, the internal heat source sig-

nificantly boosts heat transfer rates. However, for higher Reynolds numbers, the heat transfer rate shows less predictable behaviour due to the random movement of particles in the fluid, which can disrupt thermal gradients and flow patterns.

The magnetic field parameter (M) exhibits varying effects on the heat transfer rate depending on the Reynolds number. In laminar flow, increasing M reduces Nu due to decreased flow induced by the magnetic field. Conversely, at higher Reynolds
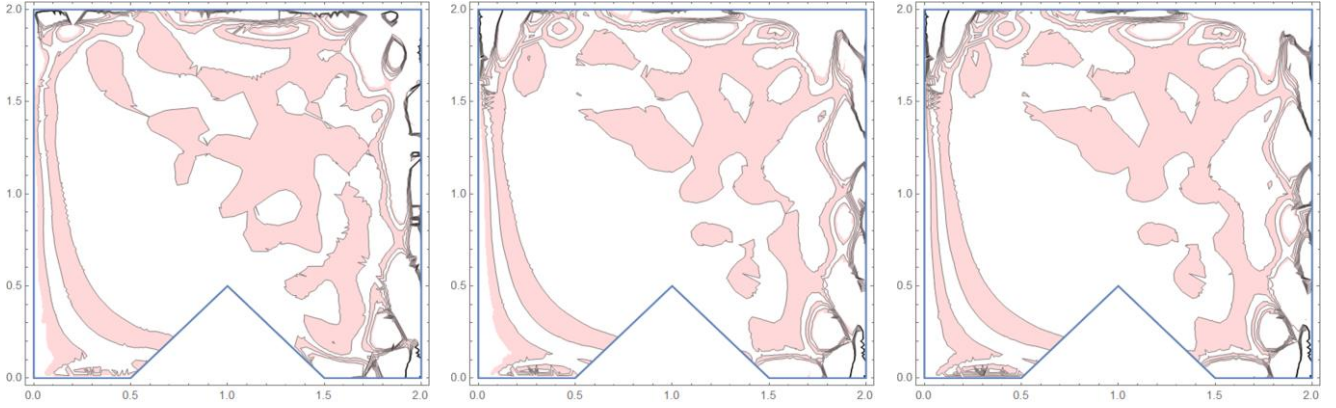
Fig. 19. Contour plots for Ø = 1% for different Reynolds numbers: Re = 10, 100 and 5000, respectively.
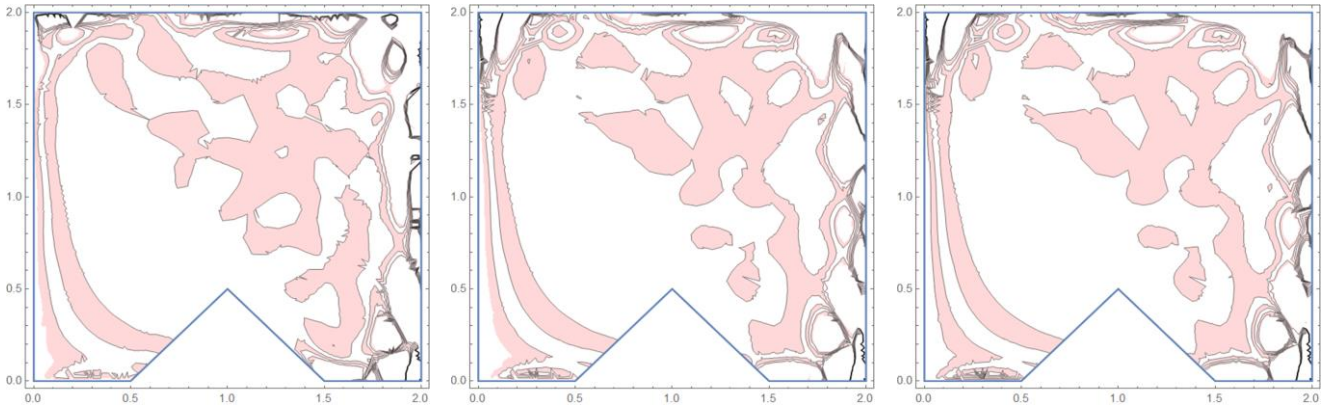
Fig. 20. Contour plots for Ø = 2% for different Reynolds numbers: Re = 10, 100 and 5000, respectively.
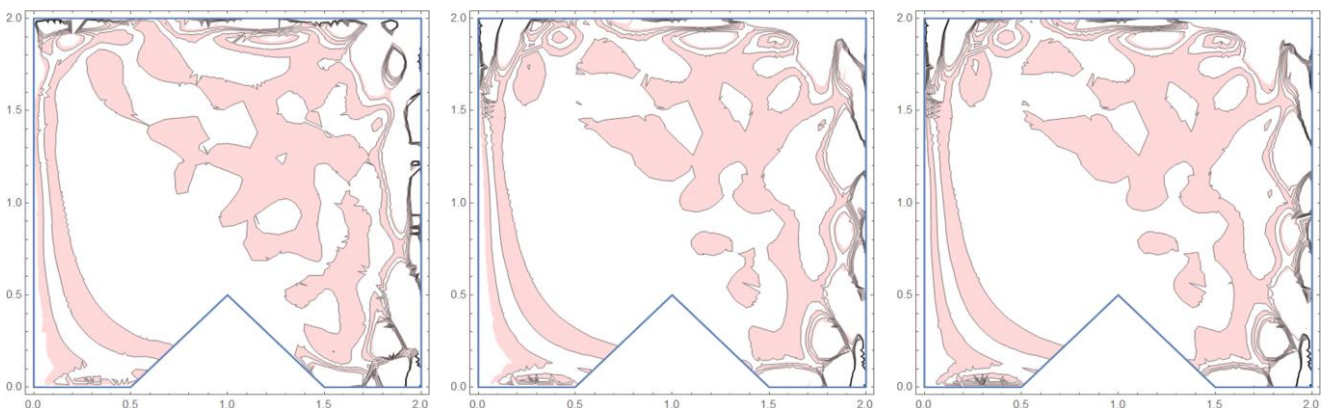
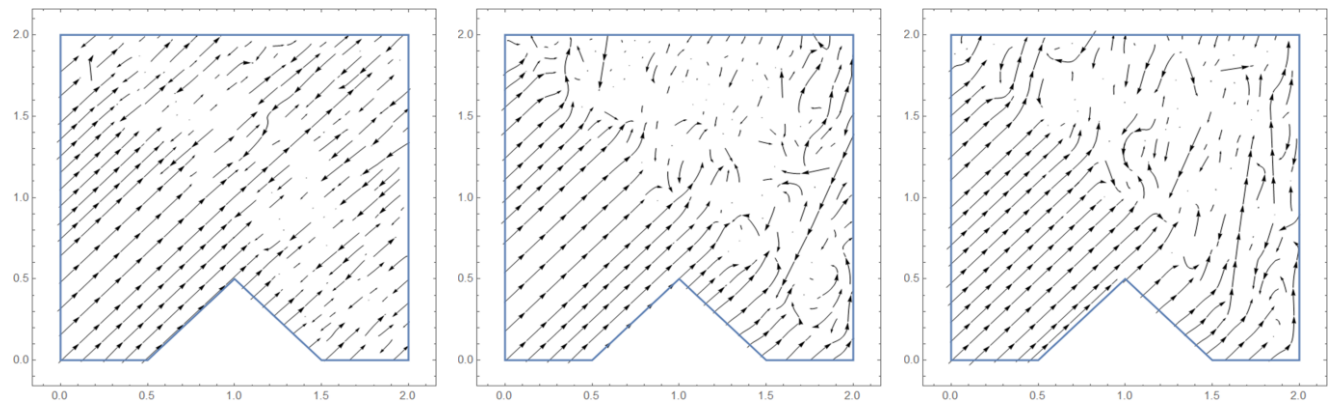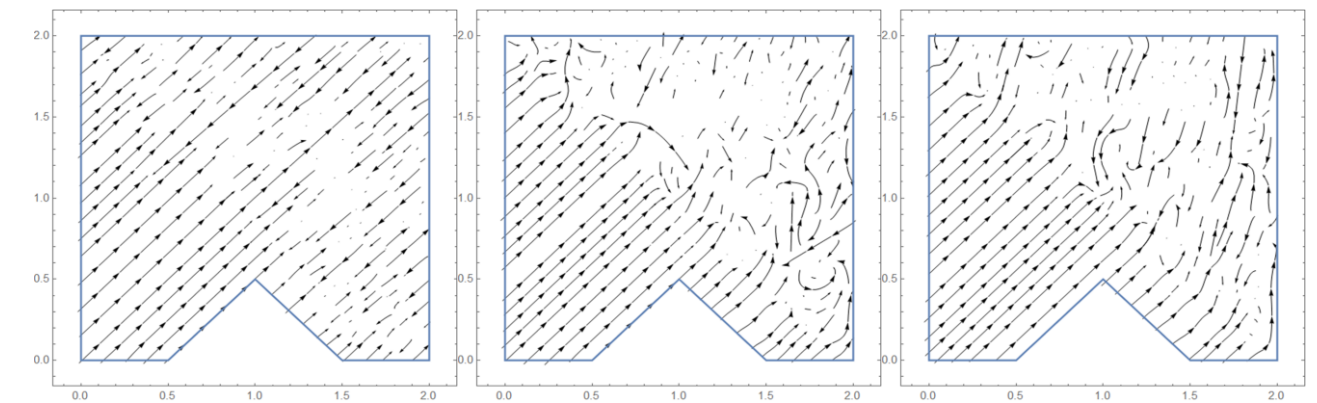Fig. 21. Contour plots for Ø = 3% for different Reynolds numbers: Re = 10, 100 and 5000, respectively.
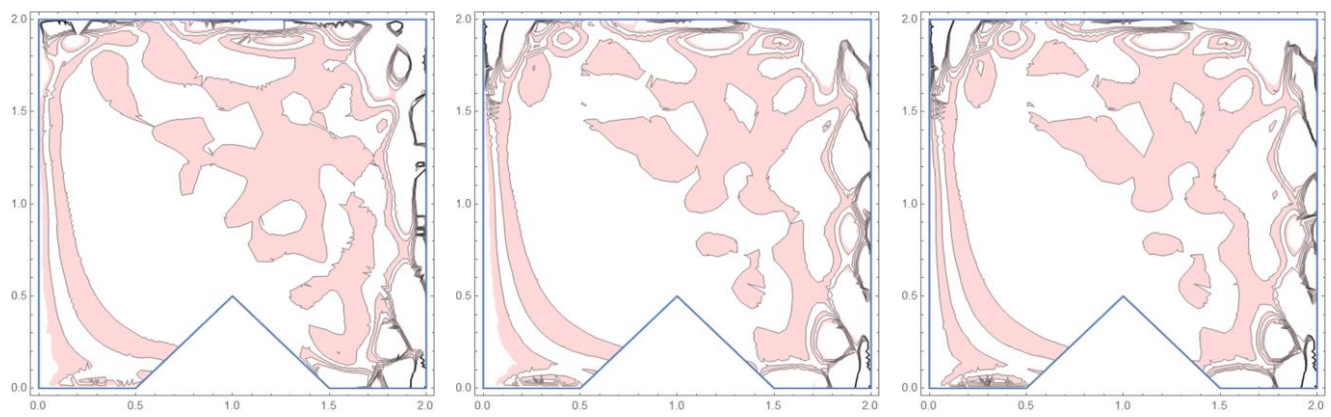
Fig. 22. Contour plots for $M = 5$ for different Reynolds numbers: Re = 10, 100 and 5000, respectively.
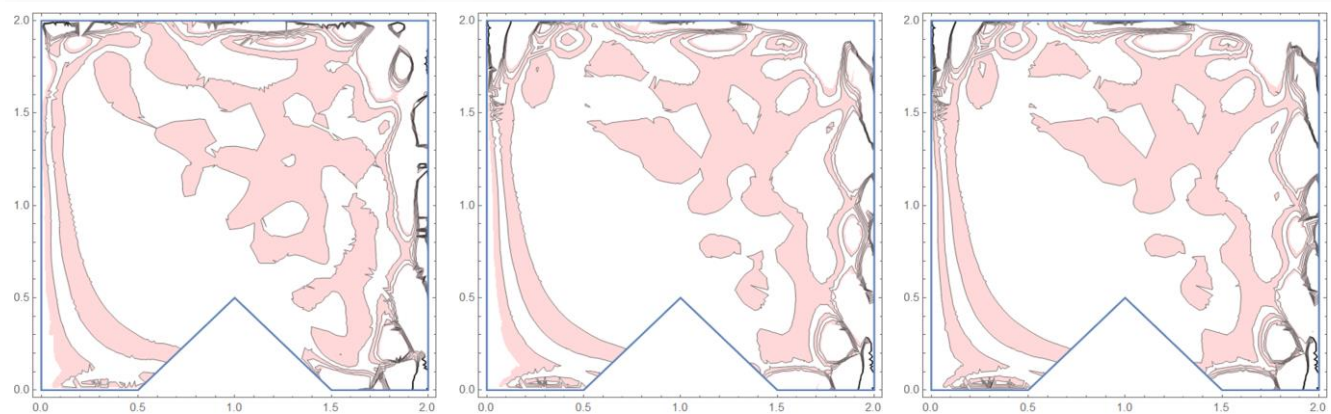
Fig. 23. Contour plots for $M = 10$ for different Reynolds numbers: Re = 10, 100 and 5000, respectively.
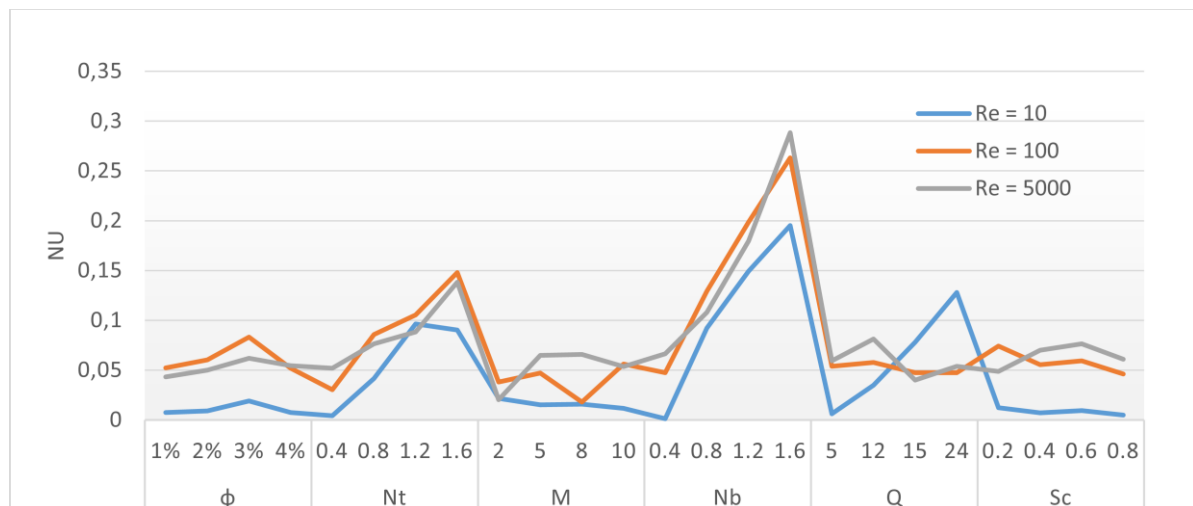
Fig. 24. Nusselt numbers for corresponding variations of parameters.

numbers, the random movement of metal particles may counteract this effect, leading to an increase in Nu with higher M. In summary, Fig. 11 highlights the complex interplay of metal particle centration and magnetic field effects on heat transfer efficiency across different flow conditions. These findings contribute to understanding and optimizing heat transfer processes in nanofluid-based systems under varying operational parameters.

5. Conclusions

The numerical study of flow and heat transfer in CuO-water nanofluid is carried out. The following conclusions are drawn:

1. The stream plots indicate that, at moderate and high Reynolds numbers, the flow in the upper part of the channel significantly weakens, while it remains controlled in the lower part. This behaviour is influenced by the presence of the heat source in the form of a triangular groove. Additionally, the dispersion of CuO metal particles within the fluid contributes to this flow pattern.

2. At higher Reynolds number flows, an increase in the internal heat source typically results in a higher temperature. However, this temperature rise can be mitigated by adjusting the Brownian motion parameter in such flows, especially when Reynolds numbers are high.

3. For effective heat transfer the CuO particle concentration less than 3% is recommended. The magnetic field shows an inconsistent pattern in heat transfer.

4. Limitations: The entire work is limited to heat transfer analysis with the defined geometry. Also, the flow of the fluid is for fixed Reynolds numbers.

5. Future work: This study can be extended to include mass transfer analysis and investigate the impact of additional physical effects, such as variable physical properties, diffusion, or slip conditions. These extensions will provide a more comprehensive understanding of the coupled heat and mass transfer phenomena in the geometry under consideration.

References

[1] Karami, F., Abbasian Arani, A.A., Akbari, O.A., Pourfattah, F., & Toghraie, D. (2023). Numerical study of location and depth of rectangular grooves on the turbulent heat transfer performance and characteristics of CuO-water nanofluid flow. *Heliyon*, 9(3), e14239. doi: 10.1016/j.heliyon.2023.e14239

[2] Dehghani-Ashkezari, E., & Salimpour, M.R. (2018). Effect of groove geometry on pool boiling heat transfer of water-titanium oxide nanofluid. *Heat and Mass Transfer, 54*(11), 3473–3481. doi: 10.1007/s00231-018-2388-1

[3] Boukerma, K., & Kadja, M. (2017). Convective heat transfer of Al2O3 and CuO nanofluids using various mixtures of water-ethylene glycol as base fluids. *Engineering, Technology and Applied Science Research, 7*(2), 1496–1503. doi: 10.48084/etasr.1051

[4] Jafarimoghaddam, A., & Aberoumand, S. (2016). On the implementation of Cu/ethylene glycol nanofluids inside an annular pipe under a constant wall temperature boundary condition. *Heat Transfer−Asian Research, 46*(7), 647–655. doi:10.1002/htj.21235

[5] Gosukonda, S, Gorti, V.P.N.S., Baluguri, S.B., & Sakam, S.R. (2015). Particle spacing and chemical reaction effects on convective heat transfer through a nano-fluid in cylindrical annulus. *Procedia Engineering*, 127, 263–270. doi:10.1016/j.proeng.2015.11.359

[6] Gupta, T., Pandey, A.K., & Kumar, M. (2024). Shape factor and temperature-dependent viscosity analysis for the unsteady flow of magnetic Al2O3–TiO3/C2H6O2–H2O using Legendre wavelet technique. *Pramana*, 98(2), 1–19. doi: 10.1007/s12043-024-02756-9

[7] Balasubramanian, R., & Mukeshkumar, P.C. (2017). Performance of the heat transfer behavior of triethylene glycol (TEG) based CuO and SiN nanofluids in a rectangular pipe under the turbulent flow condition. *Advances in Natural and Applied Sciences, 11*(8), 331–341.

[8] Navaei, A.S., Mohammed, H.A., Munisamy, K.M., Yarmand, H., & Gharehkhani, S. (2015). Heat transfer enhancement of turbulent nanofluid flow over various types of internally corrugated channels. *Powder Technology*, 286, 332–341. doi: 10.1016/j.powtec.2015.06.009

[9] Rimbault, B., Nguyen, C.T., & Galanis, N. (2014). Experimental investigation of CuO–water nanofluid flow and heat transfer inside a microchannel heat sink. *International Journal of Thermal Sciences*, 84, 275–292. doi: 10.1016/j.ijthermalsci.2014.05.025

[10] Ahmed, M.A., Yusoff, M.Z., Ng, K.C., & Shuaib, N.H. (2015). Numerical investigations on the turbulent forced convection of nanofluids flow in a triangular-corrugated channel. *Case Studies in Thermal Engineering, 6*, 212–225. doi: 10.1016/j.csite.2015.10.002

[11] Ekiciler, R. (2021). Effects of novel hybrid nanofluid (TiO2–Cu/EG) and geometrical parameters of triangular rib mounted in a duct on heat transfer and flow characteristics. *Journal of Thermal Analysis and Calorimetry*, 143(2), 1371–1387. doi: 10.1007/s10973-020-09913-3

[12] Suresh Babu, B., Srinivas, G., & Reddy, B.R.K. (2011). Finite element analysis of free convection flow with MHD micropolar and viscous fluids in a vertical channel with dissipative effects. *Journal of Naval Architecture and Marine Engineering*, 8(1), 59–69. doi: 10.3329/jname.v8i1.5808

[13] Gupta, T., Pandey, A.K., & Kumar, M. (2024). Effect of Thompson and Troian slip on CNT-Fe3O4/kerosene oil hybrid nanofluid flow over an exponential stretching sheet with Reynolds viscosity model. *Modern Physics Letters B*, 38(2), 2350209. doi: 10.1142/S0217984923502093

[14] Ahmed, F., Fuad, M., Akter, F., Gugulothu, R., Jilugu, R.K., Alam, S.B., & Kumar, D. (2021). Investigation of entropy and turbulence characteristics of water-based Al2O3, TiO2, and graphene-oxide nanoparticles in a triangular rod array. *Materials Today: Proceedings,* 47(11), 3364–3369. doi: 10.1016/j.matpr.2021.07.160

[15] Vatani, A., & Mohammed, H.A. (2013). Turbulent nanofluid flow over periodic rib-grooved channels. *Engineering Applications of Computational Fluid Mechanics*, 7(3), 369–381. doi: 10.1080/19942060.2013.11015473

[16] Ajeel, R.K., Salim, W.S.I.W., & Hasnan, K. (2018). Thermal and hydraulic characteristics of turbulent nanofluids flow in trapezoidal-corrugated channels: Symmetry and zigzag shaped. *Case Studies in Thermal Engineering*, 12, 620–635. doi: 10.1016/j.csite.2018.09.011

[17] Alipour, H., Bahiraei, M., & Mashayekhi, R. (2017). Influence of T-semi attached rib on turbulent flow and heat transfer parameters of a silver-water nanofluid with different volume fractions in a three-dimensional trapezoidal microchannel. *Physica E: Low-dimensional Systems and Nanostructures*, 88, 60–76. doi: 10.1016/j.physe.2017.01.014

[18] Hussein, A.M., Sharma, K.V., Bakar, R.A., & Kadirgama, K. (2013). The effect of cross-sectional area of tube on friction factor and heat transfer nanofluid turbulent flow. *International Communications in Heat and Mass Transfer*, 47, 49–55. doi: 10.1016/j.icheatmasstransfer.2013.06.004

[19] Naphon, P., & Nakharintr, L. (2015). Turbulent two-phase approach model for the nanofluids heat transfer analysis flowing through the minichannel heat sinks. *International Journal of Heat and Mass Transfer*, 82, 388–395. doi: 10.1016/j.ijheatmasstransfer.2014.11.019

[20] Gosty, V., Srinivas, G., & Babu, B.S. (2024). Numerical investigation of slip effects on heat and mass transfer in a vertical channel with immiscible micropolar and viscous fluids of variable viscosity. *Heat Transfer*, 53(7), 3987–4012. doi: 10.1002/htj.22659

[21] Upreti, H., Das, A., Kumar, P., & Kumar, M. (2023). Exploring the nanoparticle's shape effect on boundary layer flow of hybrid nanofluid over a thin needle with quadratic Boussinesq approximation: Legendre wavelet approach. *Journal of Thermal Analysis and Calorimetry*, 148(22), 12669–12686. doi: 10.1007/s10973-023-12502-9

[22] Avramenko, A.A., Shevchuk, I.V., & Muratov, V.S. (2015). Heat transfer at film condensation of moving vapor with nanoparticles over a flat surface. *International Journal of Heat and Mass Transfer*, 82, 316–324. doi: 10.1016/j.ijheatmasstransfer.2014.11.007

[23] Ajeel, R.K., Salim, W.S.W., & Hasnan, K. (2018). Numerical investigations of flow and heat transfer enhancement in a semicircle zigzag corrugated channel using nanofluids. *International Journal of Heat and Technology*, 36(4), 1292–1303. doi: 10.18280/ijht.360430

[24] Khudheyer, A.F., Hasan, Z., Shuaib, A.N., & Al-Amery, S. (2021). Turbulent heat transfer for internal flow of ethylene glycol-Al2O3 nanofluid in a spiral grooved tube with twisted tape inserts. *Journal of Thermal Engineering*, 7(4), 761–772. doi: 10.18186/thermal.950571

[25] Pourfattah, F., Karami, F., Abbasian Arani, A.A., & Akbari, O.A. (2017). The numerical investigation of angle of attack of inclined rectangular rib on the turbulent heat transfer of Water-Al2O3 nanofluid in a tube. *International Journal of Mechanical Sciences*, 131, 1106–1116. doi: 10.1016/j.ijmecsci.2017.07.002

[26] Sailaja, B., Srinivas, G., Babu, B.S., & Kumar, G.K. (2020). Free and forced convective heat transfer through a nanofluid in two dimensions past moving vertical plate. *South East Asian Journal of Mathematics & Mathematical Sciences*, 16, 1–15. doi: 10.36963/IJTST.2020070302

[27] Akdag, U., Akcay, S., & Demiral, D. (2014). Heat transfer enhancement with laminar pulsating nanofluid flow in a wavy channel. *International Communications in Heat and Mass Transfer*, 59, 17–23. doi: 10.1016/j.icheatmasstransfer.2014.07.016

[28] Uniyal, A., Maheshwari, N., Sharma, P.K., & Raturi, S. (2022). Recent advancements in evacuated tube solar water heaters: A critical review of the integration of phase change materials and nanofluids with ETCs. *Energies*, 15(23), 8999. doi: 10.3390/en15238999

[29] Gosty, V., Srinivas, G., Babu, B.S., Goud, B.S., Hendy, A.S., & Ali, M. R. (2024). Influence of variable viscosity and slip on heat and mass transfer of immiscible fluids in a vertical channel. *Case Studies in Thermal Engineering*, 58, 104368. doi: 10.1016/j.csite.2024.104368

[30] Bhandari, P., Sharma, R., Singh, A., & Yadav, N. (2024). A review on design alteration in microchannel heat sink for augmented thermohydraulic performance. *Ain Shams Engineering Journal*, 15(2), 102417. doi: 10.1016/j.asej.2023.102417

[31] Pak, B.C., & Cho, Y.I. (1998). Hydrodynamic and heat transfer study of dispersed fluids with submicron metallic oxide particles. *Experimental Heat Transfer*, 11(2), 151–170. doi: 10.1080/08916159808946559

Performance Characteristics Investigation of a Solar Rankine Cycle Powered Air Conditioning System for Residential Buildings using Low GWP Working Fluids

Youcef Maalem[a], Hakim Madani[b*]

[a]Ecole Nationale Polytechnique de Constantine (ENPC), BP75 A, Nouvelle Ville RP, 25000 Constantine, Algeria
[b]LESEI, Department of Mechanical Engineering, Faculty of Technology, University of Batna 2, 05000 Batna, Algeria
*Corresponding author email: h.madani@univ-batna2.dz

Abstract

Screening for eco-friendly working fluids with high-energy efficiency is one of the highest challenges in the air conditioning sector. The present research aims to investigate and compare the performance characteristics of fourteen promising low global warming potential working fluids, less than 150, in solar organic Rankine cycle powered vapour compression cycle for air conditioning of residential buildings. The working fluids selected are R152a, R161, R1234yf, R1234ze(E), R1233zd(E), R290, R1270, R600a, R600, R601a, R601, R13I1, RE170 and R123. The performance characteristics investigated are the organic Rankine cycle efficiency (η_{ORC}), the ratio (WRm) of network output (W_{net}) for the organic Rankine cycle to mass flow (m_{ORC}) rate for organic Rankine cycle, volumetric flow ratio (VFR), expander size parameter (SP), cooling power (Q_{eva}) of vapour compression cycle, coefficient of performance (COP_{VCC}) of vapour compression cycle, coefficient of performance ($COPs$) of the organic Rankine cycle–vapour compression cycle system, the ratio ($CPRm$) of cooling power (Q_{eva}) to ($m_{ORC}+m_{VCC}$), and the total efficiency of solar air conditioning system (η_t). The investigated results proved that the working fluid RE170 (global warming potential = 1) is the most suitable working fluid for the organic Rankine cycle–vapour compression cycle system through the comprehensive comparison of η_{ORC}, WRm, VFR, SP, Q_{eva}, COP_{VCC}, $COPs$, $CPRm$ and η_t for the fourteen working fluids.

Keywords: Solar Rankine cycle; Air conditioning system; Thermodynamic analysis; Performance characteristics

1. Introduction

In recent years, environmental preservation and energy conservation have grown in significance in residential buildings [1] due to the annual energy consumption behaviour of the growing population. The steadily increasing demand in the world for cooling and heating applications is in major part met by the vapour compression systems. Furthermore, in response to increasing environmental concerns, there has been a growing focus on utilizing eco-friendly working fluids that offer high-energy efficiency.

Actually, energy systems that provide comfort, like the domestic air-conditioning system, contribute considerably to the energy consumption − electric power provided to residential buildings during the summer and especially during the peak time due to the temperature difference between the condenser and evaporator of the system [2,3].

To solve this problem, several researchers therefore have presented solutions to reduce the electricity consumption of these systems under these conditions. One of the solutions to tackle this issue is the utilization of thermal energy from clean sources of sustainable energy such as solar energy to reduce the

Nomenclature

A_{col} – solar collector aperture area, m^2
CMR – compression ratio in compressor
COP_S – coefficient of performance for ORC-VCC
COP_{VCC} – coefficient of performance for VCC
$CPRm$ – ratio of Q_{eva} to overall mass flows of ORC-VCC, kWs/kg
EPR – expansion ratio in expander
h_1 – enthalpy at expander inlet, kJ/kg
h_{2s} – enthalpy at expander outlet based on isentropic process, kJ/kg
h_3 – enthalpy at working fluid pump inlet, kJ/kg
h_4 – enthalpy at working fluid pump outlet, kJ/kg
h_{4s} – enthalpy at working fluid pump outlet based on isentropic process, kJ/kg
h_5 – enthalpy at evaporator outlet, kJ/kg
h_{6s} – enthalpy at compressor outlet based on isentropic process, kJ/kg
h_7 – enthalpy at evaporator inlet, kJ/kg
I – direct solar radiation intensity, kW/m^2
m_{ORC} – mass flow rate for ORC, kg/s
m_{VCC} – mass flow rate for VCC, kg/s
P_5 – pressure at evaporator outlet, kPa
P_6 – pressure at compressor outlet, kPa
Pc – cooling power per collector square meter, kW/m^2
Q_{eva} – cooling power, kW
Q_{gen} – useful energy gained from the solar collector, kW
SP – expander size parameter, m
T_{amb} – ambient temperature, °C
T_{con} – condensation temperature in the condenser, °C
T_{eva} – evaporation temperature in the evaporator, °C
T_{gen} – generation temperature in the generator, °C

T_m – solar collector temperature, °C
v_1 – specific volume of working fluid at expander inlet, m^3/kg
v_2 – specific volume of working fluid at expander outlet, m^3/kg
V_1 – volumetric flow of working fluid at expander inlet, m^3/s
V_2 – volumetric flow of working fluid at expander outlet, m^3/s
VFR – volumetric flow ratio
W_{com} – compressor work input, kW
W_{exp} – expander work output, kW
W_{net} – net power output of ORC, kW
W_{pump} – working fluid pump power consumption, kW
WRm – ratio of W_{net} to m_{ORC}, kWs/kg

Greek symbols
η_{com} – compressor isentropic efficiency
η_{exp} – expander isentropic efficiency
η_{ORC} – organic Rankine cycle efficiency
η_{pump} – working fluid pump isentropic efficiency
η_{Solar} – thermal efficiency of solar collector
η_t – total efficiency of solar air conditioning system
ρ_1 – density of working fluid at expander inlet, kg/m^3
ρ_2 – density of working fluid at expander outlet, kg/m^3

Abbreviations and Acronyms
COP – coefficient of performance
ETC – evacuated tube collectors
FPC – flat plate collectors
GWP – global warming potential
ORC – organic Rankine cycle
VCC – vapour compression cycle
VCR – vapour compression refrigeration

electric power produced from gas turbine used for air-conditioning.

In particular in warm climate countries, such as the south of Algeria, solar radiation is the most sufficient in those areas, where it still has untapped potential, and air-conditioning systems driven by solar energy are very useful applications in these countries. These systems are economically attractive and acceptable in environmental terms. In the context of recent developments in the field of energy engineering from a building energy point of view [4], there is a lot of potential for lowering the amount of electric power used in the domestic air-conditioning system by utilizing solar thermal energy by using modern technologies [5].

Among these technologies, there are two promising energy systems for converting solar energy into processes that involve thermal comfort by use of either the absorption/adsorption refrigeration cycles or the thermo-mechanical air conditioning systems [6–8]. Although absorption and adsorption are still the dominant technologies in solar air-conditioning and cooling, the gradual removal of absorption chiller operating limits and the recent developments in organic Rankine cycle (ORC) equipment [9] to extract work from low-grade thermal sources to lower residential electric consumption [10] have sparked increasing attention in thermo-mechanical air conditioning systems.

Currently, the use of low-grade thermal sources to operate an ORC–VCC system for air-conditioning and cooling with

working fluids has become the subject of renewed interest and has been reported by many researchers.

Molés et al. [11] examined a hybrid ORC–VCR system operating under diverse conditions, powered by low-temperature heat sources and employing low global warming potential (GWP) fluids, including R134a, for both power generation and refrigeration cycles. They came to the conclusion that R1336mzz(Z) and R1234ze(E), respectively, are the best candidates for the power and refrigeration cycles.

Asim et al. [12] looked at the working fluid selection and performance of a VCR–ORC system, which recovers the waste heat. R600a-R123 was selected as the fluid pair for the integrated system based on thermodynamics (energy and exergy) and thermo-economic analysis, where the authors found that the systems combined coefficient of performance (COP) could be raised from 3.10 to 3.54.

Saleh [13] introduced novel hydrofluoroolefins alongside conventional hydrofluorocarbons as potential working fluids for an ORC–VCR system utilizing low-grade thermal energy. This integrated system combines the vapour compression refrigeration cycle with the organic Rankine cycle to enhance overall efficiency and performance. With a maximum overall performance of 0.718 at a condenser temperature of 30°C and basic values for the remaining parameters, the results showed that working fluid R600 is the best candidate compared to the other substances suggested for the hybrid ORC–VCR system. Still, its flammability ought to draw sufficient notice.

Aphornratana and Sriveerakul [14] evaluated the suitability of the working fluids R22 and R134a for optimizing the heat-powered refrigeration cycle, specifically a combined Rankine–vapour–compression system. The system can be powered by low-grade thermal energy as low as 60°C and produce cooling temperatures as low as −10°C. The results showed that R134a achieves the best system performance.

A combined ORC–VCR system using R600, R600a, R245fa, and R601 as working fluids was theoretically analysed by Cihan [15]. The combined system is best suited for R601 fluid, according to the results.

Bu et al. [16] looked into six working fluids (R134a, R123, R245fa, R290, R600a, and R600) to find the best working fluids for an ORC–VCR system that is powered by geothermal energy. They concluded that R600a is the best option. Nevertheless, enough attention should be paid to R600a flammability.

Li et al. [17] investigated the performance of hydrocarbons including R290, R600, R600a and R1270 as working fluids in an ORC–VCC system. Their evaluation, considering total COP and the ratio of combined mass flow rates to cooling output, identified R600 as the optimal choice, contrasting with R1270, which emerged as the least preferred option.

Two distinct working fluids, R245fa and R134a, were used in the study of an ORC–VCR system by Wang et al. [18] for the organic Rankine cycle and conventional vapour compression cycle, respectively. The system's overall coefficient of performance was close to 0.50.

In the study of Yue et al. [19], the authors investigated the performance of an ORC integrated with a car air conditioning system using cyclopentane, pentane, R134a and R245fa as working fluids. Their findings indicate that, among the studied conditions, R134a demonstrated superior thermal and economic performance compared to the other fluids considered.

The combined ORC–VCR thermodynamic model was developed by Hu et al. [20] for ship air conditioning in order to effectively use cooling water and transfer waste heat from flue gases. Using five widely used working fluids (R22, R141b, R236ea, R218 and R601), the system performance was examined. It was determined through calculations that R601 was the best working fluid.

Eight working fluids (R290, R717, R600, R600a, R143a, R22, R152a and R142a) were used in an ORC–VCR system that was activated by low-grade sensible energy, according to Kim and Perez-Blanco's analysis [21]. The fluids were arranged in order of critical temperature. The findings showed that because of its relatively high efficiencies, R600a provides a sensitivity analysis in a few unique situations.

The thermal performance analysis of an ORC–VCR system with a common shaft was the focus of the study of Khatoon et al. [22]. Two refrigerants (R245fa and R290), were selected for the organic Rankine cycle and three (R245fa, R123 and R134a) were chosen for the vapour compression cycle. With propane serving as the working fluid in the organic Rankine cycle and R123 serving as the working fluid in the vapour compression cycle. The results indicated the highest efficiency of 16.48% and the highest coefficient of performance value of 2.85 at 40°C.

In order to determine which refrigerant would be best for the ORC–VCR system, Jeong and Kang [23] tested R123, R134a and R245ca. The R123 case has the highest thermal efficiency, it has been discovered.

Küçük and Kılıç [24] investigated a hybrid ORC–VCR system functioning under various conditions to generate power and cooling. The analysis employs the working fluids R114, R123, R600, R600a and R245fa in the ORC system, and R141b, R600a, R290, R134a, R123, R245fa and R143a in the VCRC subsystem. The results indicated that the R123-R141b fluid pair yields the optimal values for energy utilization factor, exergy efficiency, system coefficient of performance and net power.

In the research conducted by Wang et al. [25], the authors evaluated the performance of the ORC–VCR system utilizing a zeotropic mixture of R245fa/R134a (0.9/0.1) under diverse evaporation temperatures and cooling conditions. The interaction between cooling water temperature and flow rate on the performance of the ORC–VCR system is examined. They determined that the temperature of the cooling water exerts a more significant influence on the operational characteristics of the system than the flow rate of the cooling water. As the temperature of the cooling water decreases and its flow rate increases, the system's cooling capacity rises, whereas the coefficient of performance remains relatively stable.

Qureshi et al. [26] examined the performance of refrigeration systems using solar-based organic Rankine cycle (ORC) and vapour compression refrigeration (VCR) cycles. Dry natural hydro-carbons like n-decane, n-dodecane and toluene are used in ORC, while traditional working fluids like ethane, propane, iso-butane, isopentane and isohexane are used in VCR due to environmental concerns. The study found that solar thermal energy could be efficiently operated within 90ºC to 315ºC, reducing the need for conventional fossil fuels.

Al-Sayyab et al. [27] studied the performance of a modified organic Rankine-vapour compression cycle using ultra-low GWP fluids (R1234ze(E), R1243zf, and R1234yf). The system configured for three operational modes, significantly improved refrigerant efficacy. The R1234ze(E) power-cooling mode showed the highest COP increase, while incorporating a recapture heat exchanger improved power generation by 58%.

Based on the literature reviewed, consensus has yet to be reached on the optimal working fluid for ORC–VCR systems. Consequently, further research investigating the performance of working fluids in ORC–VCR systems remains necessary.

This study proposes and addresses to utilize the untapped potential of solar energy in warm climate countries, such as the south of Algeria for the operation of an ORC–VCC system by using the solar thermal collector, which is energy efficient in the application of air conditioning for residential buildings. The study contributes to the research of an optimal eco-friendly working fluid for the solar driven ORC–VCC system and the study of its performance characteristics. Therefore, fourteen promising working fluids have GWP less than 150 are investigated and compared under the same operating conditions to identify suitable fluids which may yield high system efficiencies.

The working fluids investigated are R152a, R161, R1234yf, R1234ze(E), R1233zd(E), R290, R1270, R600a, R600, R601a, R601, R13I1, RE170 and R123.

Table 1. Candidate working fluids and their basic properties [28,29].

Substance	Chemical formula	Physical properties data					Environmental data		Safety data
		M (g/mol)	NBP (°C)	T_{crit} (°C)	P_{crit} (MPa)	v_{crit} x10^3 (m³/kg)	GWP 100 yr	ODP	Safety group
R152a	CH_3-CHF_2	66.05	-24.0	113.3	4.517	2.72	133	0	A2
R161	C_2H_5F	48.1	-37.6	102.1	5.010	3.31	12	0	A3
R1234yf	$CF_3CF=CH_2$	114.0	-29.5	94.7	3.38	2.10	4	0	A2L
R1234ze(E)	$CHF=CHCF_3$	114.0	-18.9	109.4	3.635	2.04	6	0	A2L
R1233zd(E)	$CHCL=CH$-CF_3	130.5	18.3	165.6	3.57	2.10	7	0	A1
RE170	CH_3-O-CH_3	46.1	-24.8	127.2	5.34	3.65	1	0	A3
R290	C_3H_8	44.10	-42.1	96.7	4.25	4.58	~20	0	A3
R1270	CH_3-$CH=CH_2$	42.08	-47.7	92.4	4.67	4.58	<20	0	A3
R600a	iso-C_4H_{10}	58.12	-11.7	134.7	3.63	4.46	~20	0	A3
R600	C_4H_{10}	58.12	-0.55	152.0	3.80	4.39	~20	0	A3
R601a	$CH_3CH_2CH(CH_3)_2$	72.15	27.8	187.2	3.38	4.24	4	0	A3
R601	$CH_3(CH_2)_3CH_3$	72.15	36.1	196.6	3.37	4.31	4	0	A3
R13I1	CF_3I	195.9	-21.9	123.3	3.953	1.15	0	0	A1
R123	$CHCl_2CF_3$	152.93	27.5	183.68	3.67	1.81	90	0.020	B1

The basic properties of the candidate working fluids are given in Table 1. In this regard, the environmental impact of the working fluids is considered as the most important criterion [28,29].

2. System description

The schematic diagram of the solar driven ORC–VCC system under investigation is shown in Fig. 1(a). It comprises a base ORC (1-2-3-4-1) and a base VCC (5-6-3-7-5). The overall system consists of a solar collector (generator), an expander, a condenser, a feed pump, a compressor, a throttle valve and an evaporator. A single shaft between the expander and compressor joins the two cycles together. This system has an integrated configuration and uses the same working fluid in both cycles to minimize the problem associated with leaking of the working fluids.

Fig. 1(b) shows the T−s diagram of the solar driven ORC–VCC system. This system has eight fundamental transformations occurring during thermodynamic cycles (ORC and VCC), and the ORC and VCC condensation processes take place in a shared condenser at the same pressure.
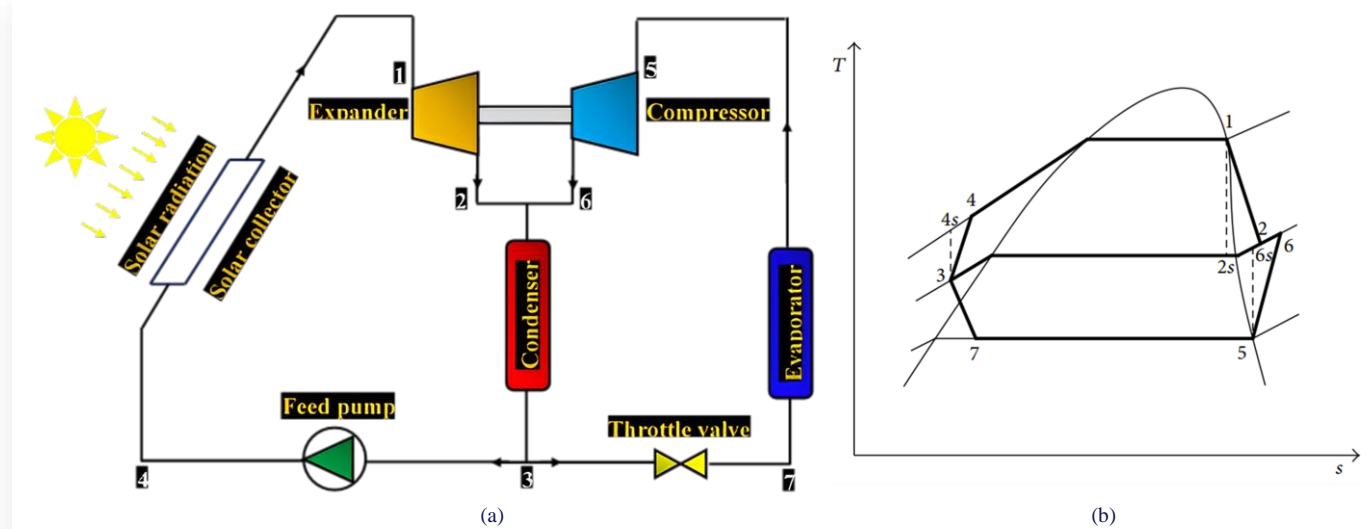
Fig. 1. Configuration (a) and T−s diagram (b) of a solar Rankine cycle powered air-conditioning system.

The operation processes of the subsystems ORC and VCC are described as follows:

o *Process* 1→2s: is an isentropic expansion process across the expander of ORC.
o *Process* 1→2: is the actual expansion process.
o *Process* 2→3: is a heat rejection (condensation) process across the condenser of ORC and VCC.
o *Process* 3→4s: is an isentropic pumping process across the pump of ORC.
o *Process* 3→4: is the actual pumping work.

o *Process* 4→1: is a heat addition process in the solar collector (generator) of ORC.
o *Process* 5→6s: is an isentropic compression across the compressor of VCC.
o *Process* 5→6: is the actual compression process.
o *Process* 6→3: is a heat rejection (condensation) process across the condenser of ORC and VCC.
o *Process* 3→7: is an isenthalpic expansion across the throttle valve of VCC.
o *Process* 7→5: is a heat absorption (evaporation) in the evaporator of VCC.

The working principle of this system is described below:

- In the ORC, the liquid working fluid is pressurized by the feed pump and sent into the solar collector to exchange heat with the solar energy to vaporize into high-temperature and high-pressure vapour (*process* 4→1). Then, high-pressure vapour drives an expander attached to a vapour compressor to do mechanical work (*process* 1→2). Following that operation, the vapour working fluid at the expander outlet is combined with the vapour working fluid at the compressor outlet, going through the condenser and cooling to a low-temperature and low-pressure liquid state (*process* 2→3). To finish a cycle process, the liquid working fluid eventually returns to the feed pump (*process* 3→4).

- In the subsystem VCC, after being depressurized by the throttle valve, the low-temperature and low-pressure liquid enters the evaporator and exchanges with air for heat exchange (*process* 7→5). Following heat exchange, the working fluid enters the compressor and is compressed into high pressure and temperature (*process* 5→6). It is mixed with the working fluid at the outlet of the expander in ORC, and then enters the condenser, where it is cooled to a liquid state (*process* 6→3). To finish a cycle process (*processes* 3→7), the liquid working fluid finally goes through the throttle valve once more.

3. Thermodynamic analysis

3.1. Assumptions

To perform the analysis of the solar driven ORC–VCC, the following assumptions are applied for modelling:

- The system works under steady state conditions.
- Solar collector (generator) has a uniform radial temperature distribution.
- No pressure losses in connection tubes and heat exchangers.
- The transformations in heat exchangers are isobaric.
- The working fluid leaving the generator, evaporator and condenser is assumed to be saturated.
- The variations in kinetic and potential energy are not considerable.
- The fluid undergoes a constant enthalpy process in the throttle valve (isenthalpic process) of the subsystem VCC.
- The work produced by the expander of the subsystem ORC is equal to the work consumed by the compressor of the subsystem VCC.
- The isentropic efficiencies of the pump (η_{pump}), expander (η_{exp}) and compressor (η_{com}) have a given value and are not affected by operating conditions.

Based on the above assumptions and referring to the system under investigation presented in Fig. 1, the thermodynamic models are developed and mentioned below.

3.2. Cycle modelling

This section presents the mathematical description of the solar driven ORC–VCC system.

Evacuated tube collectors (ETC) are used for solar heat collecting, considering their relatively higher performance compared to flat plate collectors (FPC) under low and medium temperatures [30]. The model of heat-collecting efficiency of ETC is described by Eq. (1) [31]:

$$\eta_{Solar} = a_0 - a_1 \frac{(T_m - T_{amb})}{I} - a_2 \frac{(T_m - T_{amb})}{I}, \tag{1}$$

where $a_0 = 0.721$, $a_1 = 0.89$ and $a_2 = 0.0199$ are the solar collector efficiency constants, a_0 is the efficiency of the collector, and a_1 and a_2 are the first and second heat loss coefficients. Here, T_m means the temperature of working fluid in the collector and T_{amb} means the ambient temperature. I represents the incident solar radiation per unit area of the collector about 4.8 kWh/m² for an Algerian climate location [32].

The calculation formulas of the components of the ORC subsystem are shown as follows:

- the output work of the expander can be expressed as:

$$W_{exp} = m_{ORC}(h_1 - h_{2s})\eta_{exp}; \tag{2}$$

- the required power to the pump is expressed by:

$$W_{pump} = \frac{m_{ORC}(h_{4s} - h_3)}{\eta_{pump}}; \tag{3}$$

- the useful energy gained from the solar collector (generator) is given by:

$$Q_{gen} = m_{ORC}(h_1 - h_4); \tag{4}$$

- the net power output of the ORC subsystem is defined as:

$$W_{net} = W_{exp} - W_{pump}; \tag{5}$$

- the net power output per unit mass flow rate of working fluid of the ORC subsystem:

$$WRm = \frac{W_{net}}{m_{ORC}} = \frac{W_{exp} - W_{pump}}{m_{ORC}}; \tag{6}$$

- the volumetric flow ratio is given by:

$$VFR = \frac{V_2}{V_1}, \tag{7}$$

with:

$$V_1 = \frac{m_{ORC}}{\rho_1}, \tag{8}$$

$$V_2 = \frac{m_{ORC}}{\rho_2}; \tag{9}$$

- the expander size parameter is defined as:

$$SP = \frac{\sqrt{V_2}}{\sqrt[4]{1000(h_1 - h_{2s})}}; \tag{10}$$

- the expansion ratio across the expander is given by:

$$EPR = \frac{v_2}{v_1}; \tag{11}$$

− the thermal efficiency of the ORC subsystem is defined as:

$$\eta_{ORC} = \frac{W_{net}}{Q_{gen}}. \qquad (12)$$

The calculation formulas of the components of the VCC subsystem are shown as follows:

− the output power of the expander is equal to the input power of the compressor:

$$W_{com} = W_{exp}, \qquad (13)$$

$$W_{com} = \frac{m_{VCC}(h_5 - h_{6s})}{\eta_{com}}; \qquad (14)$$

− the cooling capacity of the VCC subsystem produced from the solar energy is calculated by:

$$Q_{eva} = m_{VCC}(h_5 - h_7), \qquad (15)$$

with:

$$m_{VCC} = \frac{W_{com}\eta_{com}}{(h_5 - h_{6s})}; \qquad (16)$$

− the compression ratio across the compressor is given by:

$$CMR = \frac{P_6}{P_5}; \qquad (17)$$

− the coefficient of performance the VCC subsystem is given by:

$$COP_{VCC} = \frac{Q_{eva}}{W_{com}}. \qquad (18)$$

The calculation formulas of the performance indicators of the ORC–VCC system are shown as follows:

− the coefficient of performance for the ORC–VCC system is given by:

$$COP_S = \eta_{ORC}COP_{VCC}; \qquad (19)$$

− the ratio of Q_{eva} to overall mass flows of the ORC–VCC system is calculated by:

$$CPRm = \frac{Q_{eva}}{m_{ORC} + m_{VCC}}; \qquad (20)$$

− the overall thermal efficiency of the solar driven ORC–VCC system is defined as:

$$\eta_t = \eta_{Solar}COP_S; \qquad (21)$$

− the cooling power per square meter of the collector is calculated as follows:

$$Pc = \frac{Q_{eva}}{A_{col}}. \qquad (22)$$

Based on the theoretical model presented above, a simulation code is developed to simulate the performance characteristics of the solar driven ORC–VCC system with various working fluids.

The input values of operating parameters are listed in Table 2.

Table 2. Condition of simulation for the solar driven ORC-VCC system.

Parameter	Symbol	Typical value	Range
Working fluid mass flow in ORC	m_{ORC}	1.0 kg/s	−
Evaporation temperature	T_{eva}	−5°C	−
Generation exit temperature	T_{gen}	80°C	60–90°C
Condensation temperature	T_{con}	40°C	−
Ambient temperature	T_{amb}	40°C	−
Compressor isentropic efficiency	η_{com}	80	−
Expander isentropic efficiency	η_{exp}	85	−
Pump isentropic efficiency	η_{pump}	90	−
Solar radiation intensity	I	1000 W/m²	−

4. Results and discussion

4.1. Model validation

Before presenting the results of thermodynamic analysis, a brief discussion on validation of the present calculating program for system simulation would be appropriate.

Due to their similar integrated cycle configuration, data of Li et al. [17] are used as a reference for comparisons. Since the organic Rankine cycle is driven by a boiler instead of a solar collector in the reference, the product of coefficient of performance for ORC–VCC system is used as the index parameter for comparison under the same operating conditions ($m_{ORC} = 1$ kg/s, $T_{eva} = 5°C$, $T_{con} = 40°C$, $T_{boil} = 60–90°C$, $\eta_{exp} = 0.80$, $\eta_{com} = 0.75$ and $\eta_{pump} = 0.75$) and working fluids (R290, R600, R600a and R1270). Based on different boiler temperatures, Fig. 2 compares the product of the coefficient of performance for the ORC–VCC system between the current work and the reference.
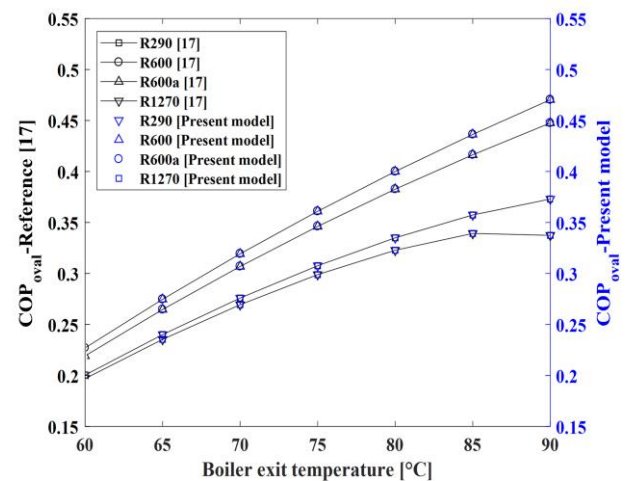
Fig. 2. Validation of the calculation model.

The comparison of results indicates a very good agreement between the results, which confirms the validity of our simulation model.

4.2. Performance characteristics

This section illustrates the strategy presented on working fluid selection in our case study. We propose to assess the performance characteristics of the solar-powered ORC–VCC with a temperature that ranges between 60–90°C and 1000 W/m^2 of beam solar radiation.

4.2.1. Influence of working fluid types on ORC subsystem

The influence of generation temperature (T_{gen}) on the parameters (η_{ORC}, WRm, VRF and SP) of ORC driven by solar energy using the investigated working fluids, while keeping the other operating conditions constant are presented in Figs. 3–6.

Figure 3 illustrates the influence of generation temperature (T_{gen}) on organic Rankine cycle efficiency (η_{ORC}) of the working fluids, namely R152a, R161, R1234yf, R1234ze(E), R1233zd(E), R290, R1270, R600a, R600, R601a, R601, R13I1, RE170 and R123.
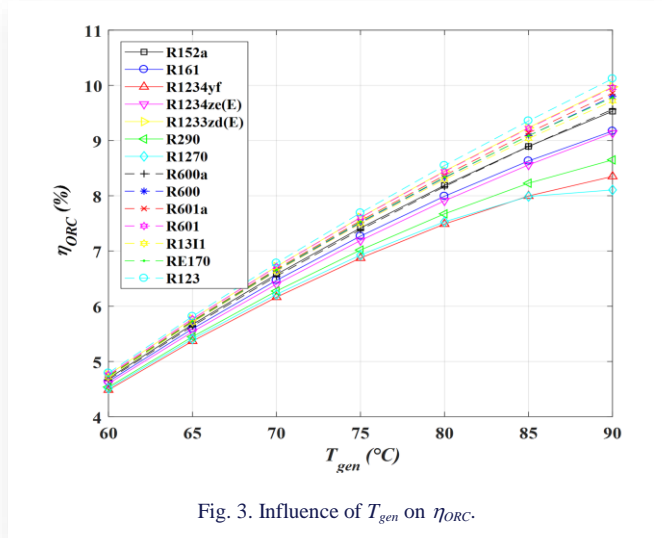
Fig. 3. Influence of T_{gen} on η_{ORC}.

It can be found from the figure profiles that the thermal efficiency of ORC depends largely on heat source temperatures, where it increases with the increase of T_{gen} for all investigated working fluids. This is because the increase of generation temperature results in enhancement of the heat added to the generator (Q_{gen}), which increases the thermal efficiency.

By comparing the simulation results of the thermal efficiency obtained for each working fluid, it can be seen that the differences in thermal efficiency between every working fluid are negligible when $T_{gen} < 70°C$. However, at $T_{gen} > 70°C$, the differences get noticeable, where it is obvious that the working fluid R123 exhibits the highest thermal efficiency among the investigated working fluids, followed by R601, R1233zd(E), R601a and RE170, whereas R1234yf and R1270 have the minimum thermal efficiency.

Figure 4 shows the effects of the generation exit temperature on the ratio WRm of ORC driven by solar energy using the working fluids R152a, R161, R1234yf, R1234ze(E), R1233zd(E), R290, R1270, R600a, R600, R601a, R601, R13I1, RE170 and R123.
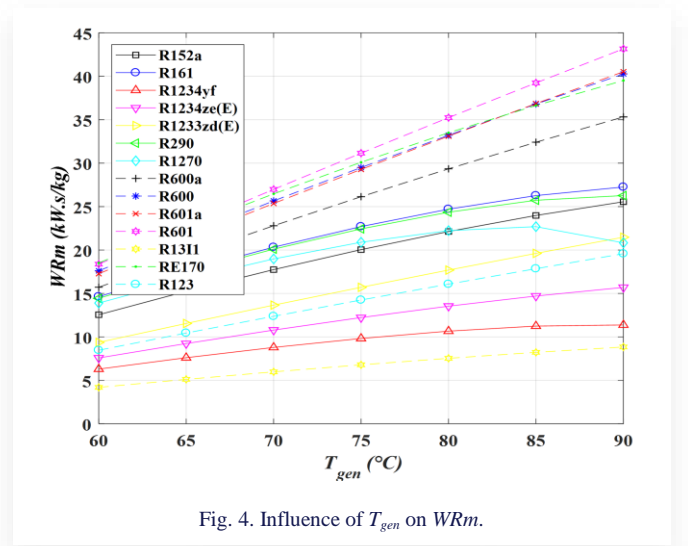
Fig. 4. Influence of T_{gen} on WRm.

The ratio WRm is defined as the ratio of net power output (W_{net}) of ORC to the ORC mass flow rate, reflecting the power capability of the working fluid per unit mass flow rate.

It can be found from the profiles of Fig. 4 that WRm exhibits the same behaviour as the thermal efficiency (η_{ORC}), where it rises as T_{gen} rises for every working fluid that has been studied. This is because, when the condensation temperature (T_{con}) is constant, h_{4s} and h_3 remain unchanged, but the difference between h_1 and h_{2s} increases with increasing T_{gen}, which causes WRm to increase.

By comparing the simulation results of WRm obtained for each working fluid, it can be found that R601 exhibits the highest WRm among the investigated working fluids, followed by RE170, R600 and R601a, whereas R13I1 and R1234yf have the minimum WRm under the generation temperature range considered.

The effect of generation temperature (T_{gen}) on VFR is illustrated in Fig. 5. The VFR is defined as the specific volume variation across the expander in an isentropic process, which accounts for the effect of compressibility through the expansion.
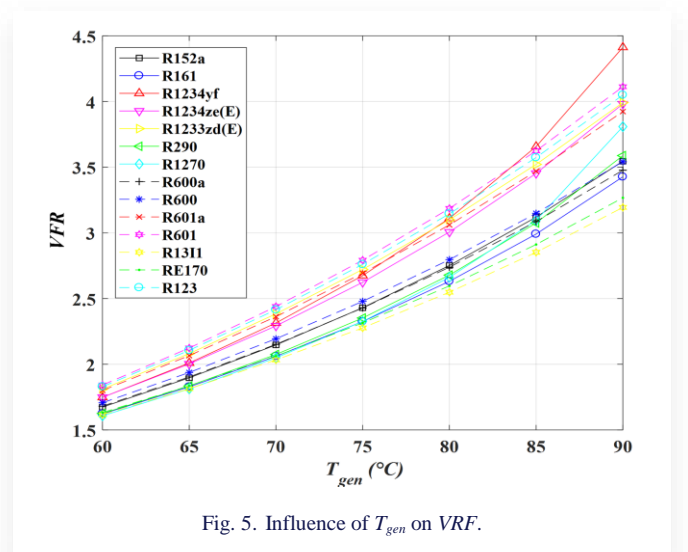
Fig. 5. Influence of T_{gen} on VRF.

As it is seen from Fig. 5, with the increase of T_{gen}, VFR for all working fluids increases. Examining the profiles of VFR for each working fluid in the figure, it can be found that the working fluids R601, R123 and R1233zd(E) have the highest VFR, while the working fluids R161, RE170, R600a and R13I1 have the lowest VFR. The low VFR leads to high η_{ORC}. This result is in line with what Macchi and Perdichizzi [33] found.

Macchi and Perdichizzi [33] state that higher turbine efficiency is produced by lower VFR values. Furthermore, according to Invernizzi et al. [34], the VFR needs to be less than 50 in order to attain a turbine efficiency of more than 80%. Since the VFR for all working fluids in this study is less than 4.5, a turbine efficiency of more than 80 % may be attained.

The variation of the expander size parameter (SP) with (T_{gen}) is plotted and presented in Fig. 6. According to Lakew and Bolland [35]; Stijepovic et al [36], SP is a measure of expander size that corresponds to the real expander size.
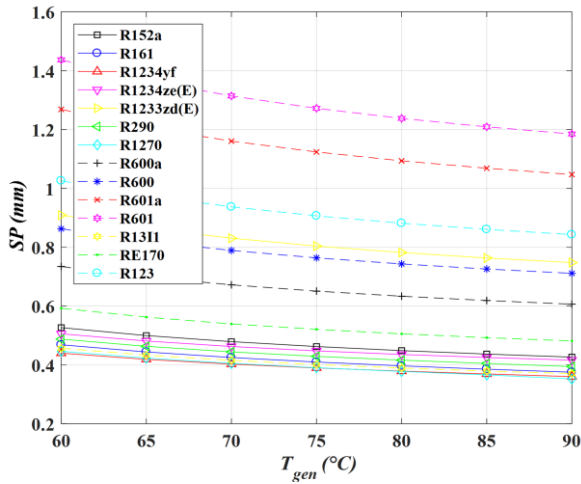
Fig. 6. Influence of T_{gen} on SP.

As it is seen from the figure, with the increase of generation temperature, SP for all working fluids decreases. This is explained by the fact that, according to Eq. (10), a higher generation temperature causes a greater enthalpy drop between the expander's inlet and outlet in addition to increasing thermal efficiency and resulting in a lower SP.

By comparing the simulation results of SP obtained for each working fluid, it can be observed that at all heat source temperatures, the working fluids R601, R601a and R123 have the highest SP, while the working fluids R1234yf, R1270, R161, R13I1, R1234ze(E), R152a and RE170) have the lowest SP.

According to Eq. (10), the working fluids R1234yf, R1270, R161, R13I1, R1234ze(E), R152a and RE170 have a higher pressure and density at the expander outlet, which lowers the volumetric flow of working fluids at the expander outlet (V_2), and consequently SP.

From the discussion above, it is evident that working fluid RE170 is the most suitable working fluid among the fourteen examined working fluids for ORC in the heat source temperature range of 60–90°C in terms of η_{ORC}, WRm, VFR and SP.

4.2.2. Influence of working fluid types on VCC subsystem

The influence of generation temperature (T_{gen}) on the parameters (Q_{eva} and COP_{VCC}) of VCC using the investigated working fluids while keeping the other operating conditions constant are presented in Figs. 7–8.

Figure 7 illustrates the influence of generation temperature (T_{gen}) on cooling power (Q_{eva}) of the working fluids, namely R152a, R161, R1234yf, R1234ze(E), R1233zd(E), R290, R1270, R600a, R600, R601a, R601, R13I1, RE170 and R123. It can be found from the figure profiles that the cooling power of the vapour compression cycle (VCC) depends largely on heat source temperatures, where it increases with the increase of T_{gen} for all investigated working fluids.
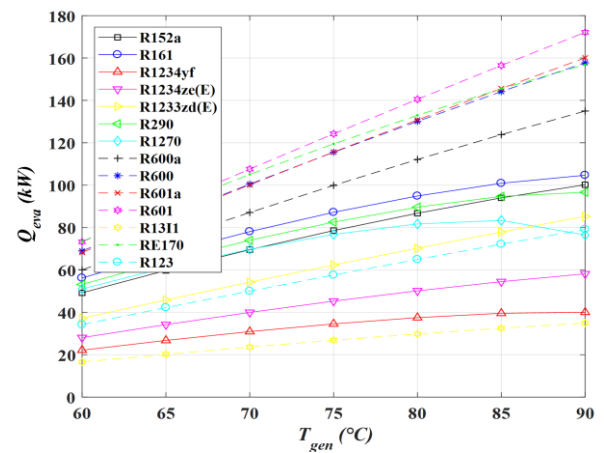
Fig. 7. Influence of T_{gen} on Q_{eva}.

By comparing the simulation results of the cooling power obtained for each working fluid, it can be seen that the working fluid R601 exhibits the highest cooling power among the investigated working fluids, followed by RE170, R600 and R601a, while R1234yf and R13I1 have the minimum cooling power.

The comparison of cycle performance COP_{VCC} among the 14 candidate refrigerants is illustrated in Fig. 8.
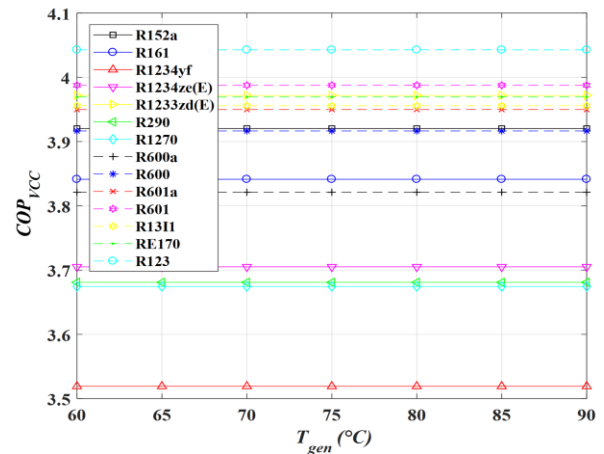
Fig. 8. Influence of T_{gen} on COP_{VCC}.

By comparing the simulation results of the coefficient of performance (COP_{VCC}) obtained for each working fluid, it can be seen that the working fluid R123 exhibits the highest coefficient of performance among the investigated working fluids, followed by R601, R1233zd(E) and RE170), while R1234yf, R1270 and R290 have the minimum coefficient of performance.

From the discussion above, it is evident that working fluids RE170 and R601 are the most suitable working fluids among the fourteen examined working fluids for the VCC system in the heat source temperature range of 60–90°C in terms of Q_{eva} and COP_{VCC}.

4.2.3. Influence of working fluid types on solar driven ORC–VCC system

The influence of generation temperature (T_{gen}) on the parameters $COPs$, $CPRm$ and η_t of the ORC–VCC system using the investigated working fluids while keeping the other operating conditions constant are presented below in Figs. 9–11.

Figure 9 represents the effect of the generation temperature on the coefficient of performance ($COPs$) of the ORC–VCC system using R152a, R161, R1234yf, R1234ze(E), R1233zd(E), R290, R1270, R600a, R600, R601a, R601, R13I1, RE170 and R123 as working fluids. It is observed from the figure that the coefficient of performance ($COPs$) of each working fluid increases with the increase in generation temperature.

Fig. 10. Influence of T_{gen} on $CPRm$.

As it is seen from the figure with the increase of generation temperature, the profiles of $CPRm$ for all working fluids increase. By comparing, the simulation results obtained for $CPRm$ for investigated working fluids, it can be found that RE170 exhibits the highest $CPRm$ among the investigated working fluids, followed by R601, R600 and R601a, while R1234yf and R13I1 have the minimum $CPRm$.

Figure 11 illustrates the influence of generation temperature (T_{gen}) on the total efficiency of the solar air conditioning system (η_t) using the investigated working fluids.

Fig. 9. Influence of T_{gen} on $COPs$.

Fig. 11. Influence of T_{gen} on η_t.

By comparing $COPs$ of the investigated working fluids, it would be observed that R123 exhibits the highest $COPs$ among the investigated working fluids, followed by R601, R1233zd(E), R601a, and RE170, while R1234yf and R1270 have the minimum $COPs$. This higher $COPs$ of R123, R601, R1233zd(E), R601a and RE170 is due the fact that the working fluids have higher values of η_{ORC} as evident in Fig. 2 and COP_{VCC} in Fig. 8, thus leading to the highest $COPs$ for R123, R601, R1233zd(E), R601a and RE170 in Fig. 9.

The influence of generation temperature on $CPRm$ is shown in Fig. 10. The $CPRm$ is defined as the ratio of Q_{eva} to ($m_{ORC}+m_{VCC}$), which reflects the refrigerating capacity of the working fluid per unit mass flow rate.

It can be found from the figure profiles that the total efficiency of the ORC–VCC system depends largely on heat source temperatures, where it increases with the increase of T_{gen} for all investigated working fluids.

It is obvious that R123 exhibits the highest total efficiency among the investigated working fluids, followed by R601, R1233zd(E), R601a and RE170, while R1234yf and R1270 have the minimum total efficiency.

From the discussion above, it is evident that the working fluids R601, R601a, R1233zd(E) and RE170 are the most suitable

working fluids among the fourteen examined working fluids for the ORC–VCC system in the heat source temperature range of 60–90°C in terms of *COPs*, *CPRm* and η_t.

5. Conclusions

In the present work, theoretical investigations of the performance characteristics were performed for a solar ORC powered VCC for an air conditioning system for residential buildings operating with low GWP working fluids, less than 150, in both cycles (ORC and VCC).

Fourteen promising working fluids R152a, R161, R1234yf, R1234ze(E), R1233zd(E), R290, R1270, R600a, R600, R601a, R601, R13I1, RE170 and R123 were selected and compared under the same operating conditions to identify the suitable working fluid which may yield the high system efficiency.

The performance characteristics studied include the organic Rankine cycle efficiency (η_{ORC}), the ratio (*WRm*) of net power output (W_{net}) for ORC to mass flow (m_{ORC}) rate for ORC, volumetric flow ratio (*VFR*), expander size parameter (*SP*), cooling power (Q_{eva}) of VCC, coefficient of performance (COP_{VCC}) of VCC, coefficient of performance (*COPs*) of the ORC–VCC system, the ratio (*CPRm*) of cooling power (Q_{eva}) to ($m_{ORC}+m_{VCC}$), and the total efficiency of solar air conditioning system (η_t).

Based on the results obtained from the present study, the main conclusions are listed as follows:

- The variation in the generation temperature has a significant impact on the performance characteristics of the solar ORC–VCC system.
- The performance parameters η_{ORC}, *WRm*, *VFR*, Q_{eva}, *COPs*, *CPRm* and η_t of investigated working fluids increase with the increasing of generation temperature.
- The expander size parameter (*SP*) of investigated working fluids decreases with the increasing generation temperature.
- The coefficient of performance (COP_{VCC}) of the VCC is unaffected by variations in the generation temperature.
- In terms of the parameter η_{ORC} of the ORC, the working fluids R601, R1233zd(E), R601a and RE170 have the maximum η_{ORC} among the fourteen examined working fluids in the heat source temperature range of 60–90°C.
- In terms of the parameter *WRm* of the ORC, the working fluids R601, RE170, R600 and R601a have the maximum *WRm* among the fourteen examined working fluids in the heat source temperature range of 60−90°C.
- In terms of the parameter *VFR* of the ORC, the working fluids R161, RE170, R600a and R13I1 have the lowest *VFR* among the fourteen examined working fluids in the heat source temperature range of 60–90°C.
- In terms of the parameter *SP* of the ORC, the working fluids R1234yf, R1270, R161, R13I1, R1234ze(E), R152a and RE170 have the lowest *SP* among the fourteen examined working fluids in the heat source temperature range of 60–90°C.
- In terms of the parameter Q_{eva} of the VCC, the working fluids R601, RE170, R600 and R601a have the maximum

Q_{eva} among the fourteen examined working fluids in the heat source temperature range of 60–90°C.

- In terms of the parameter COP_{VCC} of the VCC, the working fluids R123, R601, R1233zd(E) and RE170 have the maximum COP_{VCC} among the fourteen examined working fluids in the heat source temperature range of 60–90°C.
- In terms of the parameter *COPs* of the ORC–VCC system, the working fluids R123, R601, R1233zd(E), R601a and RE170 have the maximum *COPs* among the fourteen examined working fluids in the heat source temperature range of 60–90°C.
- In terms of the parameter *CPRm* of the ORC–VCC system, the working fluids RE170, R601, R600 and R601a have the maximum *CPRm* among the fourteen examined working fluids in the heat source temperature range of 60−90°C.
- In terms of the parameter η_t of the ORC–VCC system, the working fluids R601, R1233zd(E), R601a and RE170 have the maximum η_t among the fourteen examined working fluids in the heat source temperature range of 60−90°C.

By analysing the performance characteristics of investigated working fluids, the investigated RE170 fluid emerges with the best performances in most of the cases, which confirms that it could be a promising working fluid in terms of performance characteristics for ORC–VCC system.

Overall, from the view point of the performance characteristics and GWP, the working fluid RE170 (GWP = 1) is the most suitable working fluid for the ORC–VCC system through the comprehensive comparison of η_{ORC}, *WRm*, *VFR*, *SP*, Q_{eva}, COP_{VCC}, *COPs*, *CPRm* and η_t for the fourteen working fluids.

References

[1] Maalem,Y., Fedali, S., Madani, H., & Tamene, Y. (2020). Performance analysis of ternary azeotropic mixtures in different vapor compression refrigeration cycles. *International Journal of Refrigeration*, 119, 139–151. doi: 10.1016/j.ijrefrig.2020.07.021

[2] Li, C., Zhou, J., Cao, Y., Zhong, J., Liu, Y., Kang, C., & Tan, Y. (2014). Interaction between urban microclimate and electric air-conditioning energy consumption during high temperature season. *Applied Energy*, 117, 149–156. doi: 10.1016/j.apenergy.2013.11.057

[3] Martins, M., Mauran, S., Stitou, D., & Neveu, P. (2012). A new thermal hydraulic process for solar cooling. *Energy*, 41, 104–112. doi: 10.1016/j.energy.2011.05.030

[4] Maalem, Y., & Madani, H. (2024). Energetic performance investigation of ejector air conditioning cycles using the environment friendly gas R161 (Fluoroethane) as substitute to the phase-out R22 (Chlorodifluoromethane). *International Journal of Thermofluid Science and Technology*, 11, 110201. doi: 10.36963/IJTST.2024110201

[5] Zeyghami, M., Goswami, D.Y., & Stefanakos, E. (2015). A review of solar thermo-mechanical refrigeration and cooling methods. *Renewable and Sustainable Energy Reviews*, 51, 1428–1445. doi: 10.1016/j.rser.2015.07.011

[6] Egrican, A. N., & Karakas, A. (1986). Second law analysis of a solar powered Rankine cycle/vapor compression cycle. *Journal of Heat Recovery Systems*, 6, 135–141. doi: 10.1016/0198-7593(86)90073-1

[7] Louajari, M., Mimet, A., & Ouammi, A. (2011). Study of the effect of finned tube adsorber on the performance of solar driven

adsorption cooling machine using activated carbon-ammonia pair. *Applied Energy*, 88, 690–698. doi: 10.1016/j.apenergy.2010.08.032

[8] Luo, H., Wang, R., & Dai, Y. (2010). The effects of operation parameter on the performance of a solar-powered adsorption chiller. *Applied Energy*, 87, 3018–3022. doi: 10.1016/j.apenergy.2010.03.013

[9] Quoilin, S., Orosz, M., Hemond, H., & Lemort, V. (2011). Performance and design optimization of a low-cost solar organic Rankine cycle for remote power generation. *Solar Energy*, 85, 955–966. doi: 10.1016/j.solener.2011.02.010

[10] Tchanche, B.F., Lambrinos, G., Frangoudakis, A., & Papadakis, G. (2011). Low-grade heat conversion into power using organic Rankine cycles − A review of various applications. *Renewable and Sustainable Energy Reviews*, 15, 3963–3979. doi: 10.1016/j.rser.2011.07.024

[11] Molés, F., Navarro-Esbrí, J., Peris, B., Mota-Babiloni, A., & Kontomaris, K. (2015). Thermodynamic analysis of a combined organic Rankine cycle and vapor compression cycle system activated with low temperature heat sources using low GWP fluids. *Applied Thermal Engineering*, 87, 444–453. doi: 10.1016/j.applthermaleng.2015.04.083

[12] Asim, M., Leung, M.K.H., Shan, Z., Li, Y., Leung, D.Y.C., & Ni, M. (2017). Thermodynamic and Thermo-economic Analysis of Integrated Organic Rankine Cycle for Waste Heat Recovery from Vapor Compression Refrigeration Cycle. *Energy Procedia*, 143, 192–198. doi: 10.1016/j.egypro.2017.12.670

[13] Saleh, B. (2016). Parametric and working fluid analysis of a combined organic Rankine-vapor compression refrigeration system activated by low-grade thermal energy. *Journal of Advanced Research*, 7, 651–660. doi: 10.1016/j.jare.2016.06.006

[14] Aphornratana, S., & Sriveerakul, T. (2010). Analysis of a combined Rankine-vapour-compression refrigeration cycle. *Energy Conversion and Management*, 51, 2557–2564. doi: 10.1016/j.enconman.2010.04.016

[15] Cihan, E. (2014). Cooling performance investigation of a system with an organic Rankine cycle using waste heat sources. *Journal of Thermal Science and Technology*, 34(1), 101–109.

[16] Bu, X., Wang, L., & Li, H. (2013). Performance analysis and working fluid selection for geothermal energy-powered organic Rankine-vapor compression air conditioning. *Geothermal Energy*, 1, 1–14. doi: 10.1186/2195-9706-1-2

[17] Li, H., Bu, X., Wang, L., Long, Z., & Lian, Y. (2013). Hydrocarbon working fluids for a Rankine cycle powered vapor compression refrigeration system using low-grade thermal energy. *Energy and Buildings*, 65, 167–172. doi: 10.1016/j.enbuild.2013.06.012

[18] Wang, H., Peterson, R., Harada, K., Miller, E., Ingram-Goble, R., Fisher, L., Yih, J., & Ward, C. (2011). Performance of a combined organic Rankine cycle and vapor compression cycle for heat activated cooling. *Energy*, 36, 447–458. doi: 10.1016/j.energy.2010.10.020

[19] Yue, C., You, F., & Huang, Y. (2016).Thermal and economic analysis of an energy system of an ORC coupled with vehicle air conditioning. *International Journal of Refrigeration*, 64, 152–167. doi: 10.1016/j.ijrefrig.2016.01.005

[20] Hu, B., Guo, J., Yang, Y., & Shao, Y. (2022). Performance analysis and working fluid selection of organic Rankine steam compression air conditioning driven by ship waste heat. *Energy Reports*, 8, 194–202. doi: 10.1016/j.egyr.2022.01.094

[21] Kim, K.H., & Perez-Blanco, H. (2015). Performance analysis of a combined organic Rankine cycle and vapor compression cycle for power and refrigeration cogeneration. *Applied Thermal Engineering*, 91, 964–974. doi: 10.1016/j.applthermaleng.2015.04.062

[22] Khatoon, S., Almefreji, N.M.A., & Kim, M.H. (2021). Thermodynamic study of a combined power and refrigeration system for low-grade heat energy source. *Energies*, 14(2), 410. doi: 10.3390/en14020410

[23] Jeong, J., & Kang, Y.T. (2004). Cycle of a refrigeration cycle driven by refrigerant steam turbine. *International Journal of Refrigeration*, 27, 33–41. doi: 10.1016/S0140-7007(03)00101-4

[24] Küçük,E., & Kılıç, M. (2023). Exergoeconomic and Exergetic Sustainability Analysis of a Combined Dual-Pressure Organic Rankine Cycle and Vapor Compression Refrigeration Cycle. *Sustainability*, 15(8), 6987. doi: 10.3390/su15086987

[25] Wang, Z., Zhao, Y., Xia, X., Zhang, S., Xiao, Y., Zhang, X., & Chen, W. (2024). Experimental study of the thermodynamic performance of the ORC-VCC system with a zeotropic mixture. *Applied Thermal Engineering*, 250, 123534. doi: 10.1016/j.applthermaleng.2024.123534

[26] Qureshi.F.M., Chandio, M.W., Memon, A.A., Kumar, L., & Awad, M.M. (2024). Thermal analysis of solar energy based organic Rankine cycle cascaded with vapor compression refrigeration cycle. *Energy Nexus*, 14, 100291. doi: 10.1016/j.nexus.2024.100291

[27] Al-Sayyab, A.K.S., Mota-Babiloni, A., & Navarro-Esbrí, J. (2023). Performance Evaluation of Modified Compound Organic Rankine-Vapour Compression Cycle with Two Cooling Levels, Heating, and Power Generation. *Applied Energy*, 334, 120651. doi: 10.1016/j.apenergy.2023.120651

[28] Mota-Babiloni, A., Navarro-Esbrí, J., Barragán, A., Molés, F., & Peris, B. (2014). Drop-in energy performance evaluation of R1234yf and R1234ze (E) in a vapor compression system as R134a replacements. *Applied Thermal Engineering*, 71, 259–265. doi: 10.1016/j.applthermaleng.2014.06.056

[29] Calm, J.M., & Hourahan, G.C. (2011). Physical, safety, and environmental data summary for current and alternative refrigerants. *Proceedings of the 23rd International Congress of Refrigeration*, Prague, Czech Republic, 21–26 August 2011, ID 915.

[30] Sokhansefat, T., Kasaeian, A., Rahmani, K., Heidari, A.H., Aghakhani, F., & Mahian, O. (2018). Thermoeconomic and environmental analysis of solar flat plate and evacuated tube collectors in cold climatic conditions. *Renewable Energy*, 115, 501–508. doi: 10.1016/j.renene.2017.08.057

[31] Li, P., Li, J., Pei, G., Munir, A., & Ji, J. (2016). A cascade organic Rankine cycle power generation system using hybrid solar energy and liquefied natural gas. *Solar Energy*, 127, 136–146. doi: 10.1016/j.solener.2016.01.029

[32] Yaiche, MR., Bouhanik, A., Bekkouche, S.M.A., Malek, A., & Benouaz, T. (2014). Revised solar maps of Algeria based on sunshine duration. *Energy Conversion and Management*, 82, 114–23. doi: 10.1016/j.enconman.2014.02.063

[33] Macchi, E., & Perdichizzi, A. (1981). Efficiency Prediction for Axial-Flow Turbines Operating with Nonconventional Fluids. *Journal of Engineering for Power*, 103, 718–724. doi: 10.1115/1.3230794

[34] Invernizzi, C., Iora, P., & Silva, P.(2007). Bottoming micro-Rankine cycles for micro-gas turbines. *Applied Thermal Engineering*, 27, 100–110.doi: 10.1016/j.applthermaleng.2006.05.003

[35] Lakew, A.A., & Bolland, O. (2010). Working fluids for low-temperature heat source. *Applied Thermal Engineering*, 30, 1262–1268. doi: 10.1016/j.applthermaleng.2010.02.009

[36] Stijepovic, M.Z., Linke, P., Papadopoulos, A.I., & Grujic, A.S. (2012). On the role of working fluid properties in Organic Rankine Cycle performance. *Applied Thermal Engineering*, 36, 406–413. doi: 10.1016/j.applthermaleng.2011.10.057

ARCHIVES OF THERMODYNAMICS

Heat recovery from large scale brewery cooling system

Stefan Reszewski, Tomasz Hałon*

Wroclaw University of Science and Technology, Departmentof Thermal Sciences, Wyspianskiego 27, 50-370 Wroclaw, Poland,
*Corresponding author email: tomasz.halon@pwr.edu.pl

Abstract

This paper discusses 2 examples of using waste heat from a brewery cooling process with heat pumps. The first example is the transfer of condensation heat to the heat usable for bottling, mashing or in the return flow of a district heating system to increase the water temperature. The second is the use of superheating heat to increase the return water temperature of a district heating network or mashing, lautering or bottling. Both possible solutions for the use of heat pumps offer real possibilities of introducing part or all of the waste heat of the cooling system to the level of useful temperatures. The 1st concept (usage of heat of condensation and discharge gas heat) is much more interesting because it gives real savings for the plant and possibilities of selling heat to an external recipient. The temperature level is also sufficient to cover all own technological purposes at temperatures up to 70°C.

Keywords: Energy efficiency; Industrial heat pumps; District heating; Industrial refrigeration

1. Introduction

Nowadays, heat and electricity are key components of production costs in breweries [1], hence the desire to manage them in the best possible way. Additionally, waste heat utilization for breweries is, after waste water utilization/reduction or bio-waste usage [2,3], one of the most potent ways of decreasing the plants environmental impact [4]. The waste heat in a brewery is being rejected at a temperature range of 30−130°C [5]. While the usage of high temperature heat is not a problem, the heat with temperatures below 50°C is often wasted. One of the possibilities of using low temperature waste heat is to integrate it with its own heating/preheating system or local district heating. If the temperature level of the waste heat is low, it can be transformed using heat pumps [6].

In many plants, the results of the energy audit indicate specific improvements that should be applied to obtain the appropriate environmental effect [5,7]. However, auditors rarely delve into improving the efficiency of cooling processes.

Breweries have a constant need for moderate to low temperature cooling [8]. The plant analysed in this article has a very effective high-capacity compressor refrigeration system, with R717 or anhydrous ammonia (NH_3) as the refrigerant. The installation is constantly modernized and its operation is optimized in order to obtain the maximum efficiency. From the perspective of the optimization of the cooling system itself, there are few to no possibilities to improve the efficiency, but there are many possibilities of waste heat management. This opens up completely different possibilities for the plant, which, from the point of view of the brewery, could expand its activities with the commercial sale of heat for consumers or for its own needs. In the first case, the effect would be to increase the plant's income, and in the other case, it would reduce the plant's operating costs by increasing the energy efficiency. In both cases, the positive ecological effect is the reduction of primary energy, which directly translates into the reduction in carbon dioxide (CO_2) as well as other pollutant emissions.

Nomenclature

COP – coefficient of performance
e – emission
EC – emission coefficient
GWP – global warming potential
h – specific enthalpy, kJ/kg
ODP – ozone depletion potential
P – power, kW
Q – heating power, kW
T – temperature, ºC

Greek symbols

η – isentropic efficiency

Subscripts and Superscripts

a – annual
b – including irreversibility
c – condenser
g – heating
hp – heat pump
ref – refrigeration

Abbreviations and Acronyms

CHP – combined heat and power plant
DH – district heating

In the case of selling the heat to local district heating, there are two scenarios for existing municipal systems: connect the hot water to the supply pipeline at high temperatures or connect it to the return pipeline as a kind of preheating for the combined heat and power plant (CHP) [9,10].

In the case of using the heat for own purposes, it can be used either for hot water and heating of premises, or for production processes (as a direct heat source or a source for preheating) [5]. This article may be a guideline for both plant owners and energy auditors whose possibilities to improve efficiency are worth analysing. For plants with similar cooling systems, the presented solutions may turn out to be interesting

2. Materials and methods

2.1. Plant and cooling system description

The cooling system of the described brewery is an installation that uses R717 (ammonia) as a refrigerant. It is a single-stage installation equipped with a compressor rack system consisting of screw compressors and with three central filter dryers. The heat of condensation is dissipated by spray evaporative condensers. Refrigeration system receivers can be divided into 3 main groups:

- working on direct evaporation (tanks, fermentation tanks and air coolers),
- plate and shell-and-tube exchangers for cooling liquids (below 0°C monopropylene glycol solution necessary in the production process and for the air-conditioning cycle),
- accumulative water coolers.

The installed cooling capacity of the compressor unit is 18 600 kW with an evaporative condenser at a condensing temperature of $T_c = 25.5°C$ and an evaporator with an evaporation temperature of $T_0 = -7°C$. The developed power of the compressors' electric motors is 4400 kW under these conditions, while the spray-evaporative condensers are prepared to dissipate 24 950 kW with the use of 370 kW of fan power. The information received shows that there is a power reserve of 1800 kW on the side of the condensing unit, to cope with in the event of a failure of one of the compressors. In addition, one of the discharge lines has been equipped with a shell-and-tube exchanger

for heat recovery from superheated vapour with a nominal power of 1 MW. During the on-site inspection, it was found that it is possible to retrofit all discharge lines with heat recovery exchangers for superheated refrigerant.

Discharge high-temperature heat is mainly used to produce hot water at a temperature not exceeding 60°C. In the case of the described installation, it is not possible to obtain higher temperatures, therefore the heat is not used for the production of domestic hot water, but only for the heating of the office building in winter and transition periods, in which fan-convectors are installed. In summer, heat is dissipated into the outside air.

Obtaining higher water temperatures from the heat recovery system in the analysed system is unjustified due to the increase of condensing pressure, which in turn causes a decrease in the coefficient of performance (COP). In addition, it is difficult to obtain constant operating parameters of the heat recovery installation due to the variability of the heat flux, which is shown in Fig. 1. The discharge heat can not be used in winter, as the refrigeration system is not used frequently. Also, the temperature of the obtained medium makes the use of such a heat source questionable.

The specificity of the breweries is the fact that the demand for cooling power varies depending on the production volume,
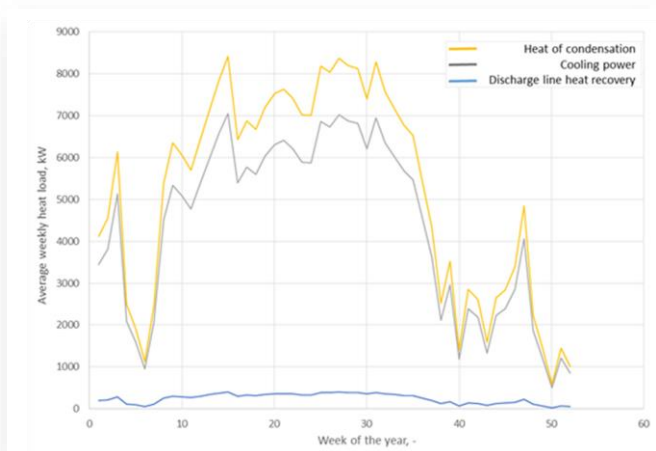

Fig. 1. Weekly heat exchangers load in the compressor refrigeration system. 1st week is in January, while 52nd week is in December.

which in turn depends on the beer sales, which increase with the outside air temperature. According to the data provided by the plant staff and shown in Fig. 1, the demand for cooling power decreases significantly in the winter months and the main reason for that is the decrease in sales. In the case of small and microbreweries, the heat usage depends on the brewing period − most of the high temperature is used during the first days of the process (mashing, malting, lautering), while the cooling effect is used at the end of the process. This creates problems with the efficient utilization of waste heat from the cooling system. On the other hand, for big plants, as in our case, the beverage production is constant and parallel, meaning that all processes occur at almost the same time, but for different batches of product.

Based on Fig. 1, the average cooling capacity of the plant varies significantly from 498 kW in week 50 (December) of the year to over 7050 in week 15 (April) and 7023 kW in week 27 (July). In view of the above, the waste heat load on the condensers varies from 600 kW to 8500 kW. After eliminating the extreme values, it can be assumed that an average of 6000 kW of waste heat can be recovered. The average annual cooling capacity developed by the cooling plant is $Q_0 = 4344$ kW. The average annual load of the condensers $Q_c = 5179$ kW.

From the data provided by the brewery technical staff, the average condensing pressure over the year is 10.2 bar. The evaporation pressure is virtually constant at 3.28 bar and is the same throughout the year for process reasons. In the months when the outside temperature makes it possible to lower the condensing pressure, it is around 9.2 bar. The automatic control system makes it possible to achieve this low condensing pressure and it is the optimum operating point for the system, which is impossible to achieve in the summer months. According to the data received from the brewery, the average coefficient of performance of the installation on the side of the condensing unit is COP = 4.45. However, to maintain such a low temperature of condensation, it is necessary to continuously optimize the process of heat extraction, which is associated with the cost of water evaporated in the spray evaporative condensers and the operation of fans used to disperse heat by forced convection.

The brewery staff did not provide us with the amount of heat utilized by the system, so we gathered data for different breweries from the literature [11−13] and calculated the heat shares consumed for different technological processes. It is presented in Table 1 together with the corresponding temperature levels.

2.2. Waste heat utilization concepts

The plant does not have large needs in terms of heat supply for office spaces, but its needs are not sufficiently met in winter, while in summer there is no real possibility of using waste heat. However, in the vicinity of the plant, there is a district heating network supplying heat to single-family housing estates as well as a number of plants, which realize their heating needs throughout the year using local boiler houses. Therefore, an attempt has been made to propose such solutions, which would contribute to waste heat management. One of them assumes the use of both superheated vapour and condensation heat, while the other presents a solution that uses only the superheated vapour heat. Both concepts are feasible and can benefit both the plant and other

Table 1 Brewery heat sources temperatures and heat shares in plants total heat consumption [11−13].

Heat source	Temperature, °C	Heat share, %
Mashing	45–70	25
Lautering	70–80	13
Bottling	70–80	10
Boiling	100	52
Cooling	2–20	20

heat consumers. The biggest benefit is in the reduction of emissions. In the first case, there is virtually no change to the existing refrigeration plant and in the second case, the change to the existing plant consists of adding superheated vapour heat recovery exchangers.

2.2.1. 1st case: Usage of heat of condensation and discharge gas

The concept is based on the implementation of a cooling and heating system realized by means of two-stage water/water heat pumps, using R717 as a refrigerant. A potential heat receiver taken into account is at the return of the district heating network - the increase of water return temperature reduces heat supplied by the heating plant. Supply and return temperatures vary from 70°C to 125°C and from 44°C to 60°C, for outdoor temperatures 14.4 and −18°C, respectively. We have chosen the return of the district heating as the heat receiver because it has a lower temperature than the supply, which will increase the heat pumps COP.

Another potential receiver, according to Table 1, is the bottling stage or first two parts of mashing (requiring 45−62°C). Bottling requires a temperature of 70°C, but it is performed directly by the heated water, so no additional heat exchange occurs in this step.

The criteria that were set for the design task are as follows:

- obtain heat at a temperature level of +70°C, which is suitable as a heat source for the district heating return during the whole year or for mashing or bottling (technological heat);
- the condenser has to remain evaporative-type, as it ensures sufficient heat dissipation even if there is no heat reception on the district heating or technological side;
- use the entire condenser heat load (heat of condensation and superheated discharge vapour);
- do not make significant structural changes to the plant's refrigeration system that could cause a decrease in its COP;
- minimize heat transfer losses of the produced heat at useful temperatures;
- produce heat with the lowest operating and investment costs;
- possibly increase the coefficient of performance of the plant's cooling system;
- reduce water and/or electricity consumption for the condenser drive;

- use techniques that avoid legal restrictions on the use of synthetic refrigerants;
- do not increase flow resistance in the district heating system.

The heat pumps lower heat source is the water used for cooling of spray-evaporative condensers, as there is no need to interfere with the cooling installation of the plant on the refrigerant side. The danger of a fatal influence of the heat recovery installation on the operation of the primary cycle is avoided. A water-to-water heat pump installation makes it possible to utilize all waste heat. The water used for condenser cooling would be cooled by about 3 to 4 K, which changes the dew temperature and has a beneficial effect on the cooling cycle of the refrigeration plant − COP is increased due to a lower condensation temperature. By installing heat pumps, it is possible to reduce the amount of water evaporated for dissipating the heat load of the plant's refrigeration system or to reduce the energy consumption of the condenser fans. The schematic and simplified drawing is shown in Fig. 2, which includes the utilization of the cooling effect in air conditioning (AC) systems etc.
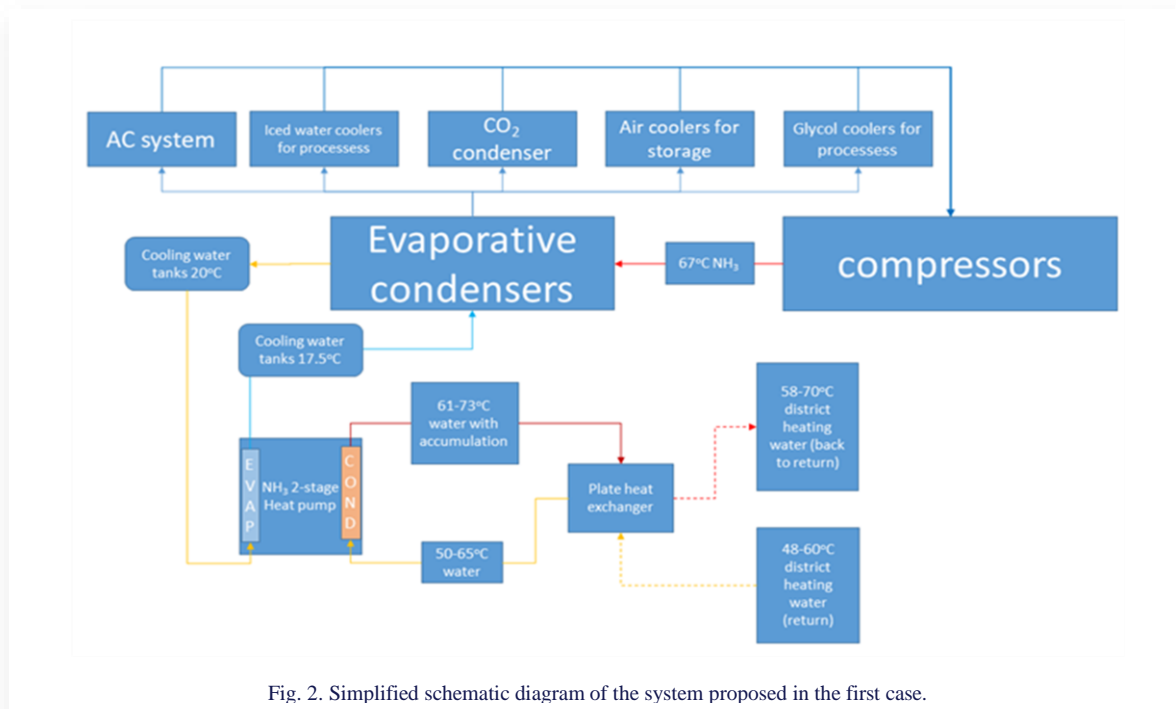
Fig. 2. Simplified schematic diagram of the system proposed in the first case.

2.2.2. 2nd case: Usage of discharge gas heat

The criteria that were set for the design task are as below:

- obtain heat at a temperature level up to +87°C, which is suitable as a heat source for the district heating network;
- utilize the heat of superheated vapours without changing the operating conditions of the refrigeration plant;
- do not make significant changes in the design of the plant's refrigeration system that could cause a decrease in its COP;
- minimize heat transfer losses of the produced heat at useful temperatures;
- produce heat with as little operating and investment cost as possible;
- use techniques that avoid legal restrictions on the use of synthetic refrigerants;
- do not increase flow resistance in the district heating system.

The water leaving the superheated vapour heat recovery system is too cold (up to 53.7°C) to be used for direct injection into the district heating network or for processes other than the first stage of mashing. Thus, it was decided to use single-stage high-temperature heat pumps that would be able increase the temperature of water leaving the heat recovery system.

The concept assumes the use of high-temperature single-stage water/water heat pumps for which the bottom heat source would be water used to remove the heat from the superheated vapours of the brewery's refrigeration system, and the refrigerant making the heat pump cycle would be R717. Such an approach, compared to the idea presented in the previous subsection, requires interference with the brewery's refrigeration plant and the installation of an exchanger to recover the heat of superheated vapours from the discharge line. It was decided to apply a high-temperature single-stage heat pump, which is able to heat up water returning from district heating network receivers from 60°C to 87°C.

Heat exchangers would be installed in the mixing branch. In such a solution, it is possible to increase the temperature of water returning from the district heating and to introduce heat to the consumers. For this purpose, it is necessary to install pumps to cover the hydraulic losses in the transmission on the supply pipe between the location of the mixing branch to the consumers and in the return pipe to the mixing branch with the heat exchangers of the additional heat source. It is also necessary to install a three-way mixing valve to change the flow through the heat

recovery system and to control the temperature in the heating network supply, which varies with the outside air temperature.

The system is designed to operate all year. What is variable is the system efficiency and the amount of heat supplied to the district heating network depending on the return temperature from the heating system consumers, load on the cooling system and load of the heating installation. The schematic and simplified drawing is shown in Fig. 3.

The application of such a solution, as opposed to the previous one, does not change the COP of the brewery's refrigeration
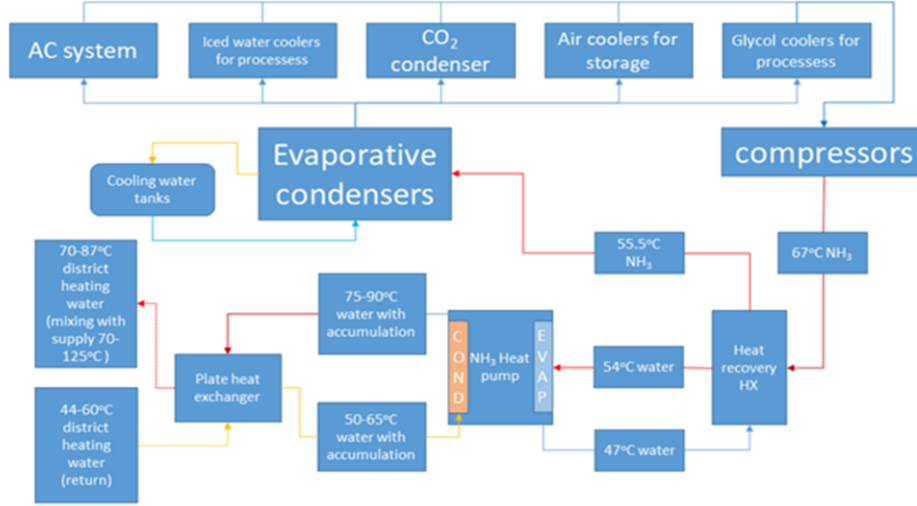
Fig. 3. Simplified schematic diagram of the system proposed in the second case.

system. It will also not significantly affect the savings on cooling water for spray-evaporative condensers. It only serves the purpose of utilizing the heat of superheated vapours in a useful way. In order to utilize it and feed it into the district heating network, it is necessary to use a heat pump capable of heating the return water from the district heating network by a minimum of 25 K.

2.3. Calculations

The cycle consists of four components: compressor, condenser, throttling valve and evaporator. Pressure drops are not considered in the ideal cycle. All refrigerants thermo-physical data were calculated using the CoolProp library [14].

For both the brewery refrigeration system and heat pumps, we first determined the pressure of evaporation and condensation for given saturation temperatures. The suction enthalpy h_1 was calculated at the evaporation pressure with a $3-10$ K superheat. The ideal enthalpy at discharge h_2 was calculated using the condensation pressure and under the assumption of isentropic compression $s_2 = s_1$. The real enthalpy h_{2b} was calculated assuming isentropic efficiency η:

$$h_{2b} = h_1 + \frac{h_2 - h_1}{\eta}. \quad (1)$$

Throttling was isenthalpic from the subcooled point h_3 ($2-5$ K) at the condensation pressure. The calculations do not take into account the power consumed by the pumps, as this is highly dependent on the length and height of the pipeline.

The coefficient of performance for the refrigeration system

(COP$_{ref}$) is the ratio of its specific cooling power $h_1 - h_3$ to specific compression power $h_{2b} - h_1$ or real cooling power Q_0 to real compressor power consumption P in the case of the real COP. The coefficient of performance for the heat pump system (COP$_{hp}$) is the ratio of its specific condensation power $h_{2b} - h_3$ to specific compression power $h_{2b} - h_1$.

As stated in the system description, the brewery's refrigeration system works on R717, condensing temperature of $T_c = +25.5°C$ and evaporation temperature of $T_0 = -7°C$, superheat 10 K and subcooling 2 K. Knowing that the measured annual cooling COP was 4.45 we assumed the compressor isentropic efficiency (η) to be 0.63.

We performed simulations of the heat pump cycle working on two different pure low global warming potential (GWP) and zero ozone depletion potential (ODP) refrigerants: R290 (propane) and R717 (ammonia). We chose these refrigerants because there are many commercial heat pumps on the market for the two chosen refrigerants.

For the 1st case heat pump cycle, the following values were assumed: evaporation temperature $10-20°C$, condensation temperature 75°C. The assumed cooling power of the evaporator is $Q_0 = 5.179$ MW (the power from the refrigeration systems condensers). The compressor isentropic efficiency is $\eta = 0.78$ for the second stage and 0.83 for the first stage.

For the 2nd case heat pump cycle, the following values were assumed: evaporation temperature 43°C, condensation temperature 90°C. The assumed cooling power of the evaporator is $Q_0 = 1.2$ MW (the heat of superheated vapour from the refrigeration system compressors) and the compressor isentropic effi-

ciency $\eta = 0.78$.

The carbon dioxide emission caused by the electricity consumed by the system is equal to the used electricity P and carbon dioxide emission coefficient (EC_{CO2}):

$$e_{CO_2} = P_a \cdot EC_{CO2}. \tag{2}$$

The carbon dioxide emission factor can be taken from the annual data for a given country. In the exemplary brewery, the end user electricity is taken from the Polish electrical grid, so its $EC_{CO2} = 685$ kg/MWh [15]. In order to compare the carbon dioxide emissions of the electrical heat pump with the professional heat and power plant we used the value of $EC_{CO2} = 94.83$ kg/GJ [16], which corresponds to the direct burning of coal.

The exact compression power of the exemplary brewery's refrigeration plant is not known, but its mean yearly COP is equal to 4.45. The average annual compressor power P_a of the refrigeration system can be calculated as in Eq. (3):

$$P_a = \frac{Q_{0,ref}}{COP_{ref}}. \tag{3}$$

The heat losses from the preinsulated pipes connecting the brewery with local district heating (DH) depend on the type of insulation, pipe diameter and most importantly the distance and temperature. The average heat losses for our pipeline are between 18–80 W/m [17]. For the calculations we used the medium value of 49 W/m, knowing that the distance to the DH network was 1 km. It means that the transfer losses constitute less than 1% of the heating power in the first case and less than 4% in the second case.

3. Results and discussion

For R717 in the first case, the heat pump obtained $Q_c = 6.93$ MW of thermal power in the condenser with the use of $P = 1.75$ MW of electric power to supply the compressor. It translates to the heating COP of 3.95.

For R290 in the first case, the heat pump obtained $Q_c = 7.14$ MW of thermal power in the condenser with the use of $P = 1.97$ MW of electric power to supply the compressor, which translates to the heating COP of 3.64.

The heat pumps COP is higher for the R717 heat pump than for the R290, so this refrigerant was chosen. The advantage of this solution is that the current exemplary plant is also equipped with the refrigeration system working on R717, so both devices can be maintained by the same staff.

Heat pumps produce hourly 24.9 GJ of heat, which translates to 218 124 GJ/year supplied to the district heating at the average meteorological year in Central and Eastern Europe (Poland). If this amount of heat would come directly from burning coal then the emissions would equal 20 684.7 tons of CO_2. Instead, it comes from the electrical grid, so it consumes 15 330 MWh a year which translates to 10 501 tons of CO_2.

By investing in heat pumps to absorb the heat load of the condensers, the plant can additionally benefit from the lowering of condensation temperature of the existing refrigeration installation by about 1.5−2 K, which would increase its annual average efficiency by a further 8%. Currently, the average annual efficiency of the cooling system is COP = 4.86. Therefore, the

average annual electricity demand for the compressor (P_a) would decrease from 969 kW to 829 kW. The decrease of CO_2 emissions e_{CO2} caused by the decrease of the plants refrigeration system power consumption is 840 tons a year.

Further environmental and economic savings can be obtained by reducing the need for evaporating water in the cooling process of spray-evaporative condensers. In relation to the data on water consumption by the plant, with the consumption of 71 388 m^3 of water, the savings may be about 2500 m^3 a year.

For the second case: R717, the heat production is $Q_g = 1.45$ MW in the condenser at a temperature 90°C with the use of $P = 0.65$ MW of electric power to supply the compressor. It translates to the heating COP of 2.23.

Compared to the previous solution, the plant cannot count on electricity savings due to the lowering of the condensing temperature. Savings due to the reduction of water evaporation in spray evaporative condensers will be about 10 times lower than in the 1st case.

The cooling power constitutes on average 20% of the total heat usage in the brewery (Table 1). From the data of the brewery, we know that the average annual cooling system condenser power is 20% higher than the evaporator power (24% of the total). If this heat is used as a lower heat source for the heat pumps described in the 1st case, then the heat gained from the heat pumps could cover the demand for 31% of the total heat used in the brewery. According to Table 1, the temperatures obtained from this case are usable only for 2/3 of mashing and all bottling, which takes 26.5% of the total heat consumed by the brewery. This means that the heat pumps could work with safety allowance. This is the most rational usage of waste heat as the waste heat source. It is the most coherent with the needs for heat, compared to selling it to district heating.

If we proceed with the same calculations for the second case, then the heat pumps heat source (heat of superheat vapour) consists only of 5.5% of the total heat used in the brewery. This means that only 6.6% of the brewery's total heat consumption could be served by the heat pumps.

4. Conclusions

This paper discusses 2 examples of using waste heat from a brewery cooling process with heat pumps. The first example was the transfer of condensation heat to the heat usable for bottling, mashing or in the return flow of a district heating system to increase the water temperature. The second was the use of superheating heat to increase the return water temperature of a district heating network or mashing, lautering or bottling.

Both possible solutions for the use of heat pumps offer real possibilities of introducing part or all of the waste heat of the cooling system to the level of useful temperatures. The 1st concept (usage of heat of condensation and discharge gas heat) is much more interesting because it gives real savings for the plant and possibilities of selling heat to an external recipient. The temperature level is also sufficient for own technological purposes. The 2nd concept provides very small amounts of heat but on temperature levels that can be directly used for district heating. Both cases will be less effective if the distance between the brewery and the heat recipient is large. In our case, the distance of 1 km generated heat losses of less than 1–4%.

Looking more broadly when selling the heat to the municipal district heating, it should be analysed whether the heat generated by the heat pumps will be supplied to the district heating network, the source of which is a combined heat and power plant (CHP, cogeneration) or a heating plant. In the case of a heating plant, when heat is introduced to DH from another source the benefits are manifested directly in the reduction of fuel consumption and in an almost double decrease of annual carbon dioxide generation. In both cases, if the heat pumps and cooling devices were coupled with renewable energy sources, the decrease of environmental impact would be even higher. Unfortunately in the example considered here, that was impossible.

When the heat source for the heating network is a CHP plant, connecting additional heat sources to the network is even harmful. This is due to the fact that heat in district heating powered by cogeneration plants is a waste energy generated in the conversion of chemical energy contained in fuel into electricity. All CHP plants have a problem with heat management because it is not used for central heating in summer. The coherence of the solutions presented in cases 1st and 2nd does not coincide with the increase in demand for heat, which will result in the fact that any amount of heat introduced into the district heating network means that it must be dispersed in the environment by cooling towers. This situation could happen if a city has one company responsible for municipal district heating network and another for heat generation (for example city of Wrocław, Poland).

When analysing the feasibility of a heat recovery system, it is important to consider the issues of cooperation of the designed system with other systems and the global impact on the environment. Often, the environmental outcome is dependent on the cooperation of the heat sources and one may come to the wrong conclusion by considering only the local effect at the plant level. The final conclusion should therefore be as follows: the processed waste heat should only be fed into district heating networks whose sources are heat plants or local boiler houses.

References

[1] Olajire, A.A. (2020). The brewing industry and environmental challenges. *Journal of Cleaner Production*, 256, 102817. doi: 10.1016/j.jclepro.2012.03.003

[2] Siqueiros, E., Lamidi, R.O., Pathare, P.B., Wang, Y., & Roskilly, A.P. (2019). Energy recovery from brewery waste: experimental and modelling perspectives. *Energy Procedia*, 161, 24–31. doi: 10.1016/j.egypro.2019.02.054

[3] Garcia, C.M., Palomino, T.C., Godino, F.J.I., & Iglesias, F.A.C. (2014). Porosity of expanded clay manufactured with addition of sludge from the brewing industry. *International Journal of Energy and Environmental Engineering*, 5, 341–347. doi: 10.1007/s40095-014-0112-6

[4] Bär, R.M., Schmid, S., Zeilmann, M., Kleinert, J., Beyer, K., Glas, K., & Voigt, T. (2022). Simulation of energy and media demand of batch-oriented production systems in the beverage industry. *Sustainability*, 14. 1599. doi: 10.3390/su14031599

[5] Muster-Slawitsch, B., Weiss, W., Schnitzer, H., & Brunner, C. (2011). The green brewery concept – Energy efficiency and the use of renewable energy sources in breweries. *Applied Thermal Engineering*, 31(13), 2123–34. doi: 10.1016/j.applthermaleng.2011.03.033

[6] Jensen, J.K., Markussen, W B., Reinholdt, L., & Elmegaard, B.

(2015). Exergoeconomic optimization of an ammonia-water hybrid absorption-compression heat pump for heat supply in a spray-drying facility. *International Journal of Energy and Environmental Engineering*, 6, 195–211. doi: 10.1007/s40095-015-0166-0

[7] Fazelpour, F., Bakhshayesh, A., Alimohammadi, R., & Saraei, A. (2022). An assessment of reducing energy consumption for optimizing building design in various climatic conditions. *International Journal of Energy and Environmental Engineering*, 13, 319–329. doi: 10.1007/s40095-021-00461-6

[8] Hubert, S., Helmers, T., Gross, F., & Delgado, A. (2016). Data driven stochastic modelling and simulation of cooling demand within breweries. *Journal of Food Engineering*, 176, 97–109. doi: 10.1016/j.jfoodeng.2015.06.032

[9] Sayegh, M.A., Jadwiszczak, P., Axcell, B.P., Niemierka, E., Brys, K., & Jouhara, H. (2018). Heat pump placement, connection and operational modes in European district heating. *Energy and Buildings*, 166, 122–144. doi: 10.1016/j.enbuild.2018.02.006

[10] Siddiqui, S., Macadam, J., & Barrett, M. (2021). The operation of district heating with heat pumps and thermal energy storage in a zero-emission scenario. *Energy Reports*, 7, 176–83. doi: 10.1016/j.egyr.2021.08.157

[11] Sturm, B., Hugenschmidt, S., Joyce, S., Hofacker, W., & Roskilly, A.P. (2013). Opportunities and barriers for efficient energy use in a medium-sized brewery. *Applied Thermal Engineering*, 53(2), 397–404. doi: 10.1016/j.applthermaleng.2012.05.006

[12] Santonja, G.G., Karlis, P., Stubdrup, K.R., Brinkmann, T., & Roudier, S. (2019). Best Available Techniques (BAT) reference document for the food, drink and milk industries − Industrial Emissions Directive 2010/75/EU (Integrated Pollution Prevention and Control). European Commission: Joint Research Centre, Publications Office. https://data.europa.eu/doi/10.2760/243911 [accessed 6 Feb. 2024].

[13] Pino, A., Pino, F.J., & Guerra, J. (2019). Solar thermal and photovoltaics to supply heating and cooling demand for a microbrewery. In Proceedings of the ISES Solar World Congress and the IEA SHC Solar Heating and Cooling Conference for Buildings and Industry, 614–625. doi: 10.18086/swc.2019.12.12

[14] Bell, I.H., Wronski, J., Quoilin, S., & Lemort, V. (2014). Pure and pseudo-pure fluid thermophysical property evaluation and the open-source thermophysical property library coolprop. *Industrial and Engineering Chemistry Research*, 53(6), 2498–2508. doi: 10.1021/ ie4033999

[15] National Centre for Emissions Management (2023). Emissions indicators of CO_2, SO_2, NO_x, CO and total dust for electricity based on information contained in the National Database on Emissions of Greenhouse Gases and Other Substances for 2022. KOBiZE, Institute of Environmental Protection – National Research Institute (in Polish). https://www.kobize.pl/uploads/materialy/materialy_do_pobrania/wskazniki_emisyjnosci/Wska%C5%BAniki_emisyjno%C5%9Bci_dla_energii_elektrycznej_grudzie%C5%84_2022.pdf [accessed 6 Feb. 2024].

[16] National Centre for Emissions Management (2022). Calorific Values (CO) and CO2 Emission Factors (EC) in 2020 to Be Reported Under the EU Emissions Trading Scheme for 2023. KOBiZE, Institute of Environmental Protection – National Research Institute (in Polish). https://www.kobize.pl/uploads/materialy/materialy_do_pobrania/monitorowanie_raportowanie_weryfikacja_emisji_w_eu_ets/WO_i_WE_do_monitorowania-ETS-2023.pdf [accessed 6 Feb. 2024].

[17] Nowak-Ocłoń, M., &, Ocłoń, P. (2020). *Thermal and economic analysis of preinsulated and twin-pipe heat network operation*. Energy, 193, 116619. doi: 10.1016/j.energy.2019.116619

ARCHIVES
OF THERMODYNAMICS

Achieving optimum performance of a split air conditioner by using evaporative cooling

Hakim T. Kadhim*, Munadhil Aldamaad

Karbala Technical Institute, Al-Furat Al-Awsat Technical University (ATU), Karbala, 56001, Iraq
*Corresponding author email: dw.hkm@atu.edu.iq

Abstract

Split cooling devices are widely used in different regions of the world. These devices work in high ambient temperatures during the summer months in many countries, such as Iraq, which increases electrical energy consumption and decreases the coefficient of performance. In addition, high temperatures expose the devices to damage, which means more maintenance and costs. This work investigates the potential of using a direct evaporative cooling system integrated with a split air conditioning unit to enhance the cooling performance and provide optimum operational conditions. The use of evaporative cooling is to reduce the condenser temperature of the outdoor split unit in the extremely hot summer. The mathematical development of the related equation is used to predict the cooling effectiveness. The climate conditions have been selected according to the Karbala city, Iraq, as it has a dry and hot climate, in which the temperatures may exceed 50 C. The results demonstrated the possibility of obtaining a higher coefficient of performance compared to the standard value of 2.96 by utilizing the evaporative cooling system. This in turn reduces the electrical energy consumption and makes the devices operate in very appropriate conditions, which prolongs the life of the devices and preserves them from damage.

Keywords: Split air conditioner; Evaporative cooling; Electrical energy consumption; Coefficient of performance

1. Introduction

Two problems arise when using refrigeration and air conditioning devices in Iraq. The first is the electrical energy crisis and the attempt to reduce the use of electricity, and the second is the rise in climate temperatures, especially in the middle of summer, to be more than 50°C [1]. In addition, another problem appears in different cities of Iraq, Karbala as an example, that have high-rise buildings close to each other and equipped with cooling devices, which is a greater rise in temperatures as a result of the expulsion of heat from the cooling devices on the lower floors and its impact on the cooling devices on the upper floors. Increasing the air temperature in this manner significantly raises the temperature and pressure of the refrigerant gas exiting the compressor. This, in turn, results in a higher pressure ratio, which leads the cooling unit to consume more electricity and may eventually cause the compressor to stop working permanently.

The method of cooling air by allowing water to evaporate is known as evaporative cooling, so it is highly suitable and highly effective in hot and dry climates. The two qualities of being hot and dry make evaporative cooling perfect, as its effectiveness increases with the increasing temperature and decreasing humidity, unlike what can be seen with mechanical cooling systems, which have a reduced efficiency when the outside air temperature increases [2,3], but direct evaporative cooling is insufficient to achieve the level of temperature comfort requirem-

Nomenclature

A – surface area at air-water interface, m^2

c_{pu} – specific heat of the humid air, J/(kg K)

COP – coefficient of performance

h_c – coefficient of convection heat transfer, W/(m^2 K)

h_{LVS} – vapour specific enthalpy at surface temperature, J/kg

h_m – coefficient of mass transfer, kg/(m^2 s)

h_{VS} – vapour specific enthalpy at saturated surface temp., J/kg

$\dot{m}_a$ – mass flow rate of air, kg/s

Nu – Nusselt number

Pr – Prandtl number

Q – heat flux applied, W/m^2

Re – Reynolds number

R_{Le} – Lewis relationship

T – bulk temperature, °C

T_{cond} – air temperature at the condenser, °C

T_s – surface temperature, °C

T_1 – dry bulb temperature of the inlet air, °C

T_2 – dry bulb temperature of the outlet air, °C

W – humidity ratio, kg$_w$/kg$_a$

Greek symbols

ε – cooling effectiveness

ϑ – volume of the used evaporative, m^3

μ – dynamic viscosity, Pa·s

ρ_w – density, kg/m^3

Subscripts

a – air

s – surface

w – water

ents and relative humidity in very hot climates (such as the summer in Iraq), so it is fruitful to use evaporative cooling as pre-cooling to cool the condenser in split air conditions and thus obtain a high coefficient of performance and reduce the use of electrical energy and provide suitable working conditions.

Several researches have been conducted focusing on cooling the condenser of the split cooling device to enhance its performance. Hwang et al. [4] experimentally evaluated a 9 kW (2.6 tonnes) split heat pump system using an advanced styling of the evaporative-cooled condenser. It involves a tank of an acrylic box, 0.94 m wide, 0.66 m long and 0.66 m high. The tubes of the condenser were submerged in a cooling water tank to remove the heat from the condensing process. The rotating disks were partially submerged in the water bath as the air was blown over them. The disks transport a small layer of water from the bath to the air stream, where it evaporates. Compared to the baseline air-cooled results, the new design showed better performance, with a capacity increase of 1.8 to 8.1% and a COP increase of 11.1 to 21.6%. The disadvantages of Hwang's system are that it is too complicated, heavy and large. Goswami et al. [5] investigated the improvement of air-to-air vapour compression air conditioner performance by the application of indirect evaporative cooling. The system was modified with a media pad evaporative cooler, pump and source of water. The results show that an electric energy saving of twenty per cent was obtained by utilizing an evaporative-cooled air condenser.

Wang et al. [6] studied experimentally the possibility to increase the coefficient of performance of an air conditioning system using an evaporative cooling condenser. The data revealed an inverse relation between COP and the condenser inlet dry bulb temperature. The saturated temperature of the condenser increased from 2.4°C to 6.6°C by utilizing the evaporative cooling. It is also indicated that an increase in the mass flow rate of the refrigerant that passes through the evaporator results in the increase of COP from 6.1% to 18%. Elshiaty et al. [7] conducted practical experiments to evaluate the coefficient of performance and energy reduction in an air conditioning package unit. A comparison between two identical air conditioners was carried out, one was an ordinary air conditioner and the second was upgraded with a pump, water supply and nozzles that spray wa-

ter onto the condenser, including optimized water consumption sprayers. The findings demonstrated that the coefficient of performance and the consumption of electrical power mainly rely on the surrounding conditions due to their effects on condensing temperature and pressure. The evaporative cooling enhanced COP by around 42.2% and reduced the electrical power consumption by 14.55%.

For an experimental evaluation of the energy saving utilizing different kinds of evaporative cooling systems, Chaktranond and Doungsong [8] retrofitted the condensing part in a split air conditioner unit with a water sprayer, cellulose corrugated pad, water source and a pump. The authors illustrated an increase in the consumption of electrical power energy of around 4% when the ambient temperature was raised by 1°C. In addition, it was found that a decrease in power consumption of around 15% with an increase in COP by up to 48% due to large contact surface between air-stream and water. In regions where temperatures range from 50 °C to 60 °C, Alhamdo et al. [9] experimentally and theoretically investigated how to enhance condenser performance to improve the temperature of the evaporator outlet fluid. The result indicated that applying the spray water on the condenser is the best technique for improving the performance. The authors also presented a cost-benefit analysis related to the cost-benefit ratio, net present value, life cycle cost and payback period.

In Iraq, where temperatures can rise to 55°C, Eidan et al. [10] investigated the impact of condenser evaporative pre-cooling on a tiny air conditioner of window type. They claimed that pre-cooling lowers the consumption of the peak power, and increases the working range to extremely high temperatures. It was also reported that the compressor can operate at a voltage of 16% less than 220 V by the use of evaporative pre-cooling.

To improve the cooling performance and reduce the consumption of electrical energy, this work attempts to explore the possibility of integrating a split air conditioning unit with a direct evaporative cooling system. A mathematical equation is developed to predict the cooling effectiveness which results in avoiding high costs of the experimental tests. The significance of this work lies in its contribution to offering ideal operating conditions for a split air conditioning unit that works in regions

under an extremely hot and dry climate and/or installed within high-rise buildings such as in the case of Karbala city. As far as the authors are aware, no previous studies have addressed this particular issue.

2. Optimum operational conditions

There is an increasing interest in reducing electrical energy consumption as a result of global warming and energy crisis. Therefore, conserving energy and using environmentally friendly devices is very important, especially in hot regions with temperatures of 45−50ºC and long summers, where the use of electrical energy for cooling devices reaches 70% of the total energy used [6]. Increasing the outside air temperature increases the pressure and temperature of the refrigerant in the condenser unit, which in turn increases electrical energy consumption and reduces the cooling capacity of the cycle because, in a high-temperature environment, the refrigerant passing through the condenser might not completely condense, causing a mixture of liquid and vapour to enter the evaporator. Thus, the coefficient of performance of the cooling device decreases greatly as the outside air temperature rises [11]. The COP decreases by about 2−4% with each degree of increase in the temperature of the condenser [12,13]. The standard value of COP is 2.96 [14], which is at an outdoor air temperature approximately equal to 32.2ºC), and it is required to use evaporative cooling to cool the condenser when the outside air temperature is higher than 32.2ºC [15]. The addition of evaporative cooling to cool the condenser leads to lowering the temperature and pressure of the refrigerant in the condenser, thus increasing COP, reducing electrical energy consumption, increasing the duration of the cooling unit, and not stopping the cooling device, as the device is exposed to refrigerant pressures suitable for the compressor and obtaining high cooling capacities.

3. Equipment and system setup

3.1. Types of condensers

In heat pumps, condensers come in three different varieties: evaporative, water and air-cooled. The type used in conventional small tonnage is mainly air-cooled which needs a high air flow rate to enhance the performance. The bigger tonnage market uses water-cooled condensers, which rely on heat transfer from the refrigerant tube to the water flow.

The air-cooled condenser has a lower heat transfer coefficient compared to the water-cooled condenser. In the evaporative condensers, the evaporation of water into the air stream produces cooling. As a result, the water-cooled condensers require more water pumping and chemical treatment. Only sensible heat transfer is used in the air-cooled condenser, but both sensible and latent heat transfers are used in the evaporative condenser. Because of this, the evaporative condenser requires less airflow rate than an air-cooled condenser, allowing the present design to use a smaller fan and motor.

One of the main benefits of using an evaporative condenser over an air-cooled condenser is the lowered condensing temperature. More heat transfer is provided to the evaporative conden-

ser by latent heat transfer, increasing its overall heat transfer coefficient over that cooled only by air. The condensing temperature of the evaporative condenser is lowered because of the smaller temperature differential caused by the improved overall heat transfer coefficient for a comparable quantity of transferred heat. Furthermore, rather than the dry-bulb temperature, the condensing temperature of this strategy is restricted by the air's wet-bulb temperature.

3.2. Performance of different refrigerants

R-410A typically operates in near-critical conditions when used in air conditioning systems at high outside temperatures. When the outside temperature rises, especially over 35ºC, the R-410A system performance can deteriorate more quickly than the R-22 system performance.

R-410A and R-22 air conditioners running at a high ambient temperature were compared by Payne et al. [16]. The identical condenser and evaporator heat exchangers were used to evaluate the two air conditioning systems. Normalized ratios were used to compare the R-410A system's capacity and COP to those of the R-22 system. At 35ºC, the capacities of the R-410A and R-22 systems matched, while at 27 ºC, the COPs matched. The authors reported that the ratio of the normalized capacity, R-22 against R-410A, declined from 1.05 to 0.90, and COP decreased from 1.05 to 0.80 when the ambient temperature was changed from 25ºC to 55ºC. The R-410A system appeared to be further susceptible to the rising outdoor temperature, according to the data.

In a thorough modelling study of comparing R-410A to R-22 systems, Rice [17] essentially verified the same findings. Thus, when subjected to an identical condenser evaporative precooling load, the R-22 apparatus experiences a less relative power reduction in comparison to the R-410A apparatus. Put differently, the refrigerant functions throughout a wide range of enthalpy changes in the two-phase area, which enhances the overall effectiveness of heat transfer from the condenser and allows it to reject more heat into the ambience at a fixed mass flow rate. As a result, precooling benefits energy savings for R-410A systems more than it does for R-22 units. Utilizing water for evaporative cooling only when the dry bulb temperature rises over 32.2ºC is one way to conserve water, as opposed to utilizing it throughout the cooling season. To optimize the annual operating cost savings and minimize water use, it may be advantageous for R-22 to utilize water only when dry bulb temperatures surpass 32.2ºC. It is important to note, nevertheless, that utilizing R-410A results in far larger annual and peak energy reductions than using R-22. Additionally, if the equipment is used at all dry bulb temperatures rather than just when the dry bulb surpasses 32.2ºC, R-410A can save even more energy [15].

3.3. Modelling of direct evaporative cooler

The transformation of sensible heat into latent heat is the basic idea behind direct evaporative cooling. The ambient air wet-bulb temperature is represented by the lowest temperature that can be reached. The unsaturated air cools through the process of heat and mass transfer.

The following definition applies to the total differential heat flow:

$$\delta Q = dA[h_c(T_s - T_a) + \rho_w h_{LVS} h_m(W_s - W_a)]. \quad (1)$$

Assuming that the vapour and air are ideal gases, the following can be determined using the mixture's specific enthalpy, which is the total of the individual enthalpies:

$$\delta Q = \frac{h_c dA}{c_{pu}}\left[(h_s - h_a) + \frac{(W_s - W_a)}{R_{Le}}(h_{LVS} - R_{Le}h_{VS})\right]. \quad (2)$$

If the magnitude of $R_{Le} = 1$, then, the second term in Eq. (12) can be ignored:

$$\delta Q = \frac{h_c dA}{c_{pu}}(h_s - h_a). \quad (3)$$

It can be written as

$$\delta Q_s = h_c dA(T_s - T_a). \quad (4)$$

The following relation is used to determine the effectiveness of direct evaporative cooling [18]:

$$\varepsilon = \frac{T_1 - T_2}{T_1 - T_s}. \quad (7)$$

Accordingly,

$$\varepsilon = 1 - \exp\left(-\frac{h_c A}{\dot{m}_a c_{pu}}\right). \quad (8)$$

The following relationship determined the coefficient of convection heat transfer across an evaporative medium of cellulose as reported by Dowdy and Karabash [19]:

$$\text{Nu} = 0.10\left(\frac{l_e}{l}\right)^{0.12}\text{Re}^{0.8}\text{Pr}^{0.33}, \quad (9)$$

where l_e is defined as

$$l_e = \frac{\vartheta}{A}. \quad (10)$$

3.4. System description

The study was conducted in Karbala, Iraq, located at a latitude of 32º and longitude of 44º. The maximum temperature in this city during the summer is 49.5ºC, according to data from the Iraqi Meteorological Organization [1]. That was on August 12, 2022, and the relative humidity at that temperature was 12%. Thus, this day is selected in the current work starting from 8 a.m. to 5 p.m.

The hot outside air passes through the cooling pad unit, to which water is pumped from the top. The hot outside air is evaporatively cooled, and then the air enters the condensing unit and the refrigerant entering into the condensing unit is cooled, as shown in Fig. 1.

4. Result and discussion

The air temperature as it exits the cooling pad unit and enters the condensing coil (T_{cond}) was calculated at different times of the day (from eight in the morning until five in the evening). Figure 2 shows the change in dry bulb outdoor air temperature,

relative humidity and temperature of the air exit from the cooling pad unit at different periods of the daytimes.

The temperature of the air leaving the cooling pad unit (T_{cond}) increases with time and then decreases with increasing temperature and decreasing humidity. This helps the split air-conditioning unit perform well during peak hours, as increases COP and decreases electrical energy consumption. It is interested to mention that the average temperature of the air leaving the cooling pad unit in the extreme summer of the Karbala city is less than 32.2ºC at which the standard COP is 2.96. Therefore, COP of the split air-conditioning unit that uses evaporative cooling is always higher than the standard COP in the city of Karbala.

It can be concluded that the use of evaporative cooling in the split air condition unit is considered a very good solution to con-
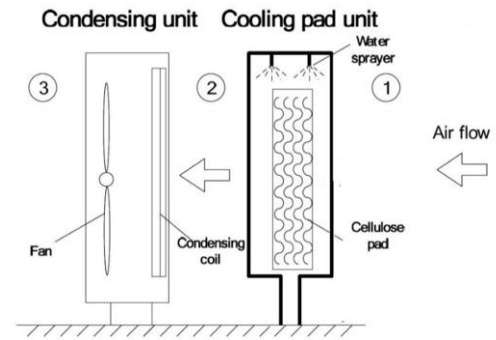
Fig. 1. A schematic illustration of the evaporative cooling system.
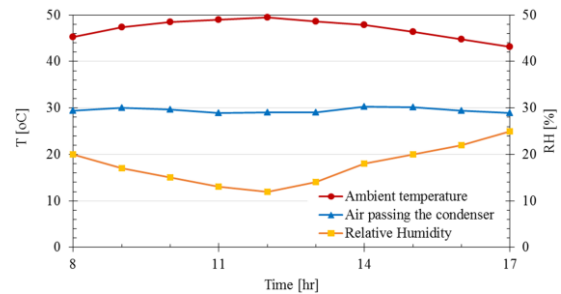
Fig. 2. Change of outside air temperature, relative humidity, and temperature of air passing the condenser (T_{cond}) with time.

front high temperatures, increase electrical energy consumption, and obtain COP higher than the standard at all times of summer.

The psychometric chart's process lines for the condenser's outdoor air temperature were constructed using the relative humidity and dry bulb. The enthalpy change through the evaporative-cooled condenser (referred to as DEC) and conventional condenser (referred to as CV) is shown in Fig. 3. Process line 1 to 2 demonstrates how the sensible heat transferred from the refrigerant raised the air temperature through the traditional condenser while maintaining a steady humidity ratio. The refrigerant phase change was the initial cause of the heat released into the air from the condenser. But in the case of the evaporative cooled condenser, latent heat transfer from the evaporation of water passing through the wetted medium caused the air temperature to drop from T_1 to T_3, and the humidity ratio to rise from
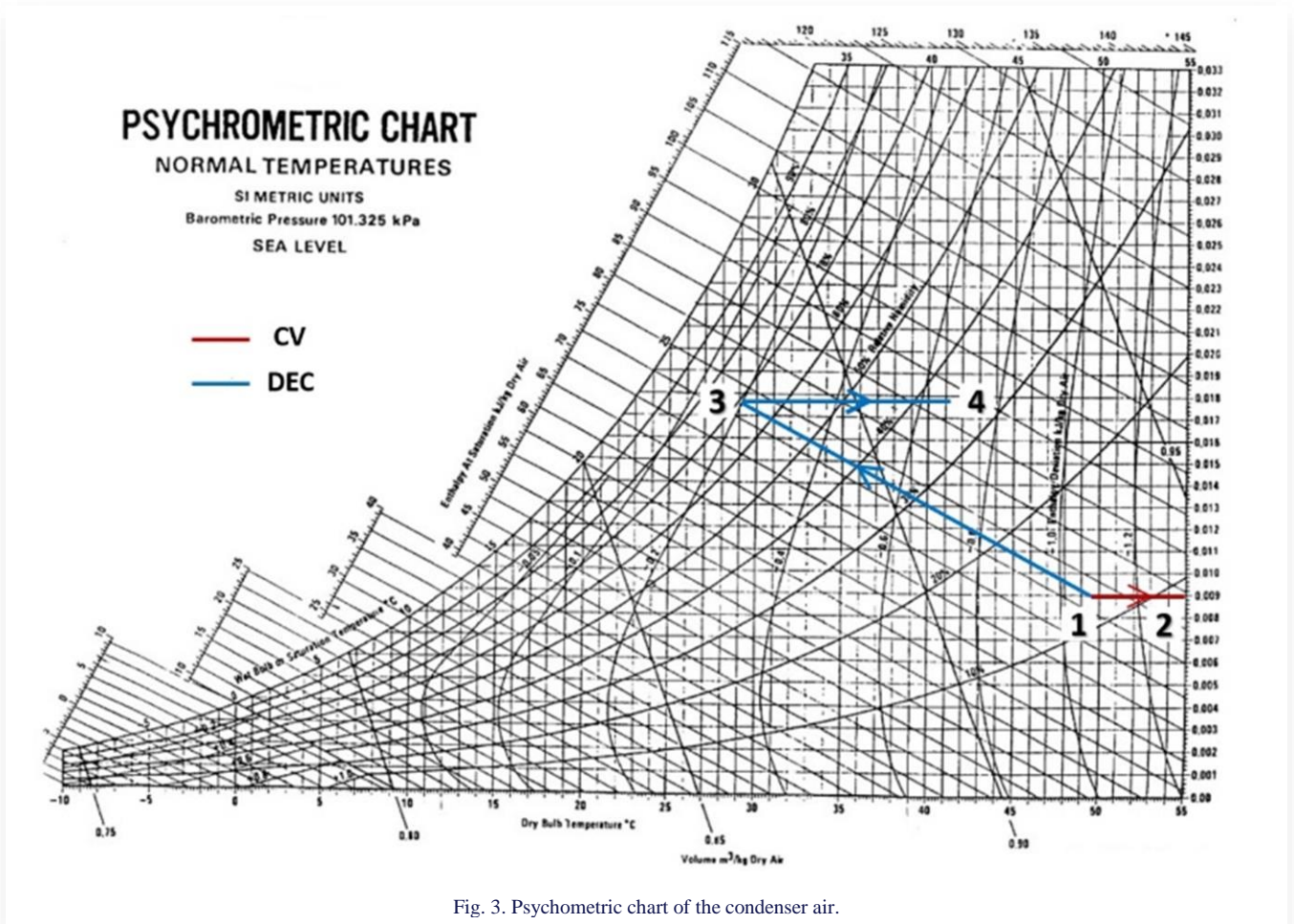
Fig. 3. Psychometric chart of the condenser air.

W_1 to W_3. This process is represented by line 1−3 in Fig. 3, known as an adiabatic process or a constant enthalpy line. The process line 3−4 illustrates the temperature of the air passing across the condenser which increases by the sensible heat transfer obtained from the heat rejected by the refrigerant inside the condenser. The chart shown in Fig. 3 indicates that the evaporative cooled condenser has a process line of 1−3−4, whereas the traditional condenser has a process line of 1−2. The wetted cooling pad surface drew heat from the surrounding air during the process of evaporative cooling, which led to sensible heat loss from the air and consequent latent heat uptake by the water.

5. Conclusions

Using an air-cooled condenser in hot climates, especially in the middle of summer when temperatures are more than 50ºC, leads to a rise in the pressure and temperature of the refrigerant gas coming out of the compressor, which in turn increases the electrical energy consumption and decreases the coefficient of performance, and may end up causing the compressor to stop working ultimately.

Using an evaporative cooling condenser to be integrated with a split air condition unit leads to the following conclusions:

- The use of evaporative cooling in a split air conditioner enhances performance, making it an effective method for reducing energy consumption and maintaining high values of coefficient of performance through the summer. The performance enhancement is achieved by lowering the condensing temperature.

- Considering the extremely hot summer in the Karbala city, the air temperature leaving the cooling pad unit reaches below 32.2ºC. As a result, the typical COP of 2.96 is exceeded.

- The required amount of the evaporative condenser's airflow rate is lower than that for air-cooled condensers.

- By using the same condenser evaporative pre-cooling, the R-410A system receives a greater reduction in the relative power compared to the R-22 system. Consequently, it can be suggested that the R-410A system is highly exposed to increasing external temperature.

- The current findings show the potential of reducing the required chemical treatment and water pumping for water-cooled condensers.

References

[1] *Iraqi Agrometeorological Network*. https://www.agromet.gov. iq/eng/index.php [accessed 3 Aug 2022].

[2] Foster, R.E. (1998). Evaporative air-conditioning contributions to reducing greenhouse gas emissions and global warming. *Proceedings of American Society of Heating, Refrigerating and Air-Conditioning Engineers, Toronto*.

[3] Aldamaad, M.A., & Kadhim, H.T. (2023). Theoretical investigation of combining cooling tower and cooling coil with direct evaporative cooler. *International Journal of Air-Conditioning and Refrigeration*, 31(12), 12. doi: 10.1007/s44189-023-00028-6

[4] Hwang, Y., Radermacher, R., & Kopko, W. (2001). An experimental evaluation of a residential-sized evaporatively cooled condenser. *International Journal of Refrigeration*, 24(3), 238−249. doi: 10.1016/S0140-7007(00)00022-0

[5] Goswami, D.Y., Mathur, G.D., & Kulkarni, S.M. (1993). Experimental investigation of performance of a residential air conditioning system with an evaporatively cooled condenser. *Journal of Solar Energy Engineering*, 115(4), 206–211. doi: 10.1115/1.2930051

[6] Wang, T., Sheng, C., & Nnanna, A.G.A. (2014). Experimental investigation of air conditioning system using evaporative cooling condenser. *Energy and Buildings*, 81, 435−443. doi: 10.1016/j.enbuild.2014.06.047

[7] El Shiaty, R., Swilem, A.M.S., Abdelwali, H., & Yousuf, A. (2018). Evaluation of energy saving in a package air conditioner with optimum atomized water spray type evaporative system (Case Study: A villa in Kuwait). *American Journal of Engineering Research*, 7(12), 277−285.

[8] Chaktranond, C., & Doungsong, P. (2010). An experimental evaluation of energy saving in a split-type air conditioner with evaporative cooling systems. *International Transaction of Engineering Management & Applied Sciences Technology*, 1(1), 9−18.

[9] Alhamdo, M.H., Theeb, M.A., & Abdulhameed, J.J. (2015). Using evaporative cooling methods for improving performance of an air-cooled con-denser. *Universal Journal of Mechanical Engineering*, 3(3), 94−106. doi: 10.13189/ujme.2015.030304

[10] Eidan, A.A., Alwan, K.J., AlSahlani, A., & Alfahham, M. (2017). Enhancement of the performance characteristics for air-conditioning system by using direct evaporative cooling in hot climates. *Energy Procedia*, 142, 3998−4003. doi: 10.1016/j.egypro.2017.12.311

[11] Dossat, R.J. (1991). *Principal of Refrigeration*, Prentice Hall, New Jersey.

[12] Cengel, Y.A., Boles, M.A., & Kanoğlu, M. (2011). *Thermodynamics: An Engineering Approach* (5 ed.). McGraw-Hill, New York.

[13] Hajidavalloo, E. (2007). Application of evaporative cooling on the condenser of window-air-conditioner. *Applied Thermal Engineering*, 27(11-12), 1937−1943. doi: 10.1016/j.applthermaleng.2006.12.014

[14] Hu, S.S., & Huang, B.J. (2005). Study of a high efficiency residential split water-cooled air conditioner. Applied thermal engineering, 25(11-12), 1599−1613. doi: 10.1016/j.applthermaleng.2004.11.011

[15] Shen, B., New, J., & Ally, M. (2019). Energy and economics analyses of condenser evaporative precooling for various climates, buildings and refrigerants. *Energies*, 12(11), 2079. doi: 10.3390/en12112079

[16] Payne, W.V., & Domanski, P.A. (2002). A comparison of an R22 and an R410A air conditioner operating at high ambient temperatures. *International Refrigeration and Air Conditioning Conference*. 532. http://docs.lib.purdue.edu/iracc/532 [accessed 3 Aug. 2022].

[17] Rice, C.K. (2005). *Investigation of R-410A Air conditioning system performance operating at extreme ambient temperatures up to the refrigerant critical point*. Final report. Oak Ridge National Laboratory. doi: 10.13140/RG.2.2.34623.71848

[18] Aldamaad, M.A., & Kadhim, H.T. (2024). Theoretical study of cooling effectiveness based on heat and mass transfer in direct evaporative system. *AIP Conference Proceedings*, 3199, 020009. doi: 10.1063/5.0217224

[19] Dowdy, J.A., & Karabash, N.S. (1987). Experimental determination of heat and mass transfer coefficients in rigid impregnated cellulose evaporative media. *ASHRAE Transactions*, 93(2), 382−395.

ARCHIVES
OF THERMODYNAMICS

Thermodynamic modelling of a power generation plant using solar concentrators assisted by organic Rankine cycle for João Pessoa city, Brazil

Taynara G. S. Lago[a*], Beatriz R. P. Padilha[b], Felipe S. Teixeira[a], João A. Lima[a]
Adriano S. Marques[a] and Carlos M. S. Santos[c]

[a]Department of Renewable Energy Engineering, Centre of Renewable and Alternative Energy, Federal University of Paraíba, João Pessoa – PB, Brazil
[b]Postgraduate Program in Energy Planning, Faculty of Mechanical Engineering, State University of Campinas, Campinas – SP, Brazil.
[c]Centre for Exact and Technological Sciences, Federal University of Recôncavo da Bahia, Cruz das Almas –BA, Brazil.
*Corresponding author email: taynara@cear.ufpb.br

Abstract

The potential for generating electricity through solar energy makes Brazil a very promising country in this segment, with several possibilities for the use of solar energy, whether in the thermal or photovoltaic part, due to the high incidence of solar radiation throughout much of the country, especially in the Northeast region. In this study, an analysis of the performance of the organic Rankine cycle (ORC) that produces electricity using solar concentrators was performed. The fluids used in the system were classified as dry type – toluene, isobutane, isopentane, R227ea, R113, R114, R245fa and R600. During the study, the energy and exergy analysis of the system was conducted for different evaporator pressures (500−2500 kPa), and two types of solar collectors were tested (parabolic trough collector and parabolic compound collector). In addition, a system case study was simulated for radiation and temperature conditions in the city of João Pessoa, Brazil. Based on this analysis, the performance of the cycle components was examined, and the first and second law efficiencies of the system were compared for different configurations. The solar collector (parabolic trough collector) proved to be the most suitable for the studied cycle. With the adequate selection of the refrigerant, collector and evaporation pressure, the first and second law efficiencies of the cycle improve up to 41% and 44%, respectively. For the city of João Pessoa, the highest exergy efficiency occurs in the month of January, the hottest month of the year when the sun shines brightly, and the lowest exergy efficiency occurs in the month of June.

Keywords: Organic Rankine cycle; Renewable energy; Concentrated solar power; Thermal and exergetic analysis

1. Introduction

Thermodynamic modelling of organic Rankine cycles (OCRs) has been the subject of increasing interest in the fields of engineering. These cycles, based on the principle of the classic Rankine cycle, are fundamental for the efficient generation of energy from renewable and sustainable sources. Unlike conventional cycles that use water as the working fluid, organic Rankine cycles employ organic compounds with low boiling points as working fluids, enabling the utilization of low-temperature heat sources such as waste heat from industrial processes or solar energy. The increasing interest in renewable and environmentally friendly sources of energy has driven research and development efforts towards power generation systems based on this technology.

Lago T.G.S., Padilha B.R.P., Teixeira F.S., Lima J.A., Marques A.S., Santos C.M.S.

Nomenclature

a_1, a_2, a_3 – heat loss coefficients, 1/K, W/(m² K), W/(m² K²)
A – area, m²
C_p – specific heat at constant pressure, kJ/(kg K)
DNI – direct normal irradiance, W/m²
Ex – exergy, kW
h – specific enthalpy, kJ/kg
Δh – enthalpy change, kJ/kg
$\dot{m}$ – mass flow rate, kg/s
P – pressure, kPa
$\dot{Q}$ – heat transfer rate, kJ/kg
s – entropy, kJ/(kg K)
T – temperature, K
v – specific volume, m³/kg
w – work, kJ/kg
$\dot{W}$ – power, kW

Greek symbols

ε – effectiveness of the heat exchanger
η – efficiency
ψ – exergy, kJ/kg

Subscripts and Superscripts

a – solar collector aperture
amb – ambient
b – pump
$collector$ – solar collector

con – condensation
$condenser$ – condenser
$evaporator$ – evaporator
$f, fluid$ – fluid
i – point in the cycle
in, out – inlet, outlet
liq – liquid
o – dead-state conditions
$Pump,isen$ – isentropic pump process
rad – radiation
$regenerator$ – regenerator
sun – surface of the sun
t – turbine
$ther$ – overall thermal
$Turbine,isen$ – isentropic turbine process
$II, Collector$ – second law of the collector
$II, Condenser$ – second law of the condenser
$II, Evaporator$ – second law of the evaporator
$II, Regenerator$ – second law of the regenerator
$II, Turbine$ – second law of the turbine

Abbreviations and Acronyms

CPC – compound parabolic collector
FPC – flat plate solar collector
HTF – heat transfer fluid
ORC – organic Rankine cycle
PTC – parabolic trough collector

Colonna et al. [1] provided a bibliographic review, illustrating the concept of organic Rankine cycles, emphasizing that these cycle technologies offer flexibility in terms of capacity and temperature for thermal energy conversion applications. The authors highlight that these systems have broad applications in co-generation systems, involving both heating and cooling, as well as thermal energy distribution systems. In this study, the fundamental elements of the thermodynamic cycle, such as the working fluid, design aspects, and the advantages and disadvantages in comparison to other technologies, are detailed.

According to Loni et al. [2], the relationship between solar irradiation and the use of solar thermal energy combined with thermodynamic cycles is a promising technology due to the high compatibility between the operating temperature of the collectors and the temperature required for the cycle to function, meeting the minimum conditions to achieve viable efficiency. In this perspective, research and development efforts in the context of using it as a secondary source of energy employ these solar collector systems in subprocesses of the cycles, such as enhancing boiler heating.

Petrollese et al. [3] investigated the solar energy concentrate ion plant (CSP) with an organic Rankine cycle integrated into the Ottana solar facility as a means of concentrating solar technologies for power supply. In this case, the thermal plant consists of a CSP unit (630 kW) with thermal storage coupled to a 400 kW concentrated photovoltaic plant with electrochemical storage, acting to promote planned energy profiles for the succeeding day based on meteorological data and weather forecasts. Regarding the CSP plant, it was determined that the ORC performance is inherently related to the thermal oil operational profiles, inlet temperature, and ambient temperature. Therefore, the researchers emphasized the significant importance of the daily start-up and shut-down phases of the ORC unit to enhance the overall plant performance.

Ancona et al. [4] conducted an analysis of a prototype of an organic Rankine cycle coupled to a commercial model of a solar collector, aiming to reduce the annual costs of electricity for a household. Initially, the collector surface and the tank were sized to simulate the performance of organic fluids and low-global warming potential mixtures. Results show that the system with R134a can cover approximately 39% of the yearly electricity demand, corresponding to more than 1150 kWh.

An optimization analysis of the low-temperature solar organic Rankine cycle was conducted by Delgado-Torres and García-Rodríguez [5]. The study involved examining twelve potential working fluids for ORC and four stationary solar collector models to determine the most efficient system with the minimum required area. One viable application observed by the authors is the integration of the organic Rankine cycle with solar thermal energy and the low-energy consumption desalination technology, reverse osmosis. Jing et al. [6] developed a mathematical model to optimize a system of low temperature solar thermal electric generation based on compound parabolic concentrators (CPC) and an organic Rankine cycle working with HCFC-123, and evaluated its annual performance in different areas of Canberra, Singapore, Bombay, Lhasa, Sacramento and Berlin. Kumar and Shukla [7] investigated the application of benzene as the working fluid for the ORC system to assess the performance of the organic Rankine cycle. The thermal solar plant modelled for this study features a binary cycle, where the

first cycle operates with the heat transfer fluid in a liquid state, and the second cycle operates with the organic fluid, benzene. To analyse the efficiency behaviour, output powers of 8 kW, 9 kW, and 10 kW were applied. The best result was obtained at the 9 kW power level, where the ORC system efficiency ranged from 32.87% to 54.98%, with the turbine outlet temperature varying from 259.53°C to 127.22°C.

Sonsaree et al. [8] proposed a model for a small-scale solar organic Rankine cycle power plant in Thailand with R-245af, operating with a compound parabolic concentrator, evacuated-tube or flat-plate collectors as the devices for generating heat. The maximum power output, the CO_2 emission, and the economic analysis in terms of the levelised cost of electricity were analysed. Stand et al. [9] proposed in their study an idea for a hybrid solar-biomass system for electricity generation in remote areas in Colombia. In this case, the hybridization integrates the supercritical Brayton cycle (SBC) and organic Rankine cycle, a solar field composed of concentrated solar tower technology, and coconut shell biomass. For the elaboration of this work, energy and exergy analysis were necessary for the following scenarios: solar-biomass hybrid SBC-ORC, SBC-ORC/Solar, and SBC-ORC/Biomass. The study concluded that the solar-biomass hybrid system SBC-ORC presented the best exergetic efficiency among the three cases, thus showing the possibility of implementing this project. Additionally, they also highlighted the coconut shell's high calorific value and the dissemination of its energetic use to contribute to the socioeconomic development of the agricultural sector in Colombia.

Gupta et al. [10] reviewed the main thermodynamic methods applied in organic Rankine cycles, with the authors' primary focus being on the issue of multi-utilization of ORC to couple concentrated solar collectors with an environmentally viable biomass system, where ORC would supply more than one type of energy, i.e. applied in the context of thermal and electrical energy conversion.

The storage system in thermal solar energy projects is essential for utilizing electrical energy during periods of reduced solar irradiation. Therefore, based on this scenario, Lakhani et al. [11] developed a dynamic model applied to the thermal energy storage system using latent heat in solar thermal power plants with an organic Rankine cycle. The mentioned energy storage system consists of a shell-and-tube heat exchanger where the phase change material is stored on the shell side, while the heat transfer fluid (HTF) flows through the tubes. Through this mechanism, HTF can meet the plant's nighttime demand during moments when the organic fluid cannot reach the saturation temperature.

Li et al. [12] performed an experimental study on a parabolic trough concentrated solar ORC system by using nitrate salt as the heat transfer and storage medium, and a single screw expander for power conversion. They carried out energy and exergy analyses of the overall system evaluating the dynamic changes in the temperature of PTC, molten salt tank and ORC. It was observed that the collector efficiency, expander efficiency and ORC efficiency were relatively lower than the published data. In accordance with Ahmadi et al. [13], organic Rankine cycles originating from a geothermal source can be technically viable, favouring the substitution of conventional fossil energy

sources. The choice of a hybrid system that operates under favourable low-temperature conditions, such as geothermal energy (below 150°C), enables a systematic approach in which the authors emphasize the economic aspect of the ORC's efficiency applied in this context.

The nanofluid acting as the working fluid has a long history of experiments and scientific foundation that enabled the manufacturing of specific thermodynamic components for this type of fluid. Therefore, Saadatfar et al. [14], through a modelling program, designed the thermodynamic cycle to produce energy, heating and cooling using an organic Rankine cycle with nanofluid as the working fluid. This research involved a comparison between an organic nanofluid and a base fluid, namely silver nano pentane and pure pentane, respectively. The established analysis concluded that the best cycle efficiency results were found for the organic nanofluid, requiring smaller heat exchangers and expanders.

More recently, Rejeb et al. [15] developed a 3E mathematical model (energy, exergy and economic) to simulate and optimize a poligeneration system (H_2, O_2, electricity and heat production) consisting of solar photovoltaic thermal collectors with organic Rankine cycle, proton exchange membrane (PEM) electrolyser and liquefied natural gas. They used the non-dominated sorting genetic algorithm II (NSGA-II) to estimate the optimal results for the proposed system with the energy efficiency, cost rate and net output power as the objective functions.

Youtao et al. [16] evaluated a direct vapour generation for a solar organic Rankine cycle (DVG-ORC) system under different operating conditions. The results show that the evaporation temperature has different impacts on the system performance. R245ca and R1336mzz(Z) exhibit a higher net output power at different evaporation temperatures, with R1336mzz(Z) only reducing it by 3.73–5.26% compared to R245ca. In addition, R1336mzz(Z), of low global warming potential (GWP), demonstrates the highest system efficiency, making it the most suitable working fluid for the DVG-ORC system due to its environmental friendliness and safety.

Maytorena and Buentello-Montoya [17] simulated a parabolic trough collector system filled with benzene under solar irradiation for use in an organic Rankine cycle. Different inlet temperatures (465, 475 and 485 K), mass fluxes (168, 336 and 504 kg/(m^2s)), and solar-concentrated heat fluxes (15.1, 18.5 and 22.2 kW/m^2) are used in the simulations. The results indicate that increasing the mass flow rate decreases the fluid evaporation rate, the fluid evaporation rate is directly affected by the solar heat flux and the mass flux affects the point where evaporation begins (tube lengths of 10, 15 and 25 m for mass fluxes of 168, 336 and 504 kg/(m^2s), to 15.1 kW/m^2, respectively).

Based on recent literature, this article aims to explore the thermodynamic modelling of these innovative cycles, highlighting their benefits, challenges and potential applications. It also aims to encourage studies related to the search for more sustainable fluids, collaborating to intensify the research and development of ORC plants applied to solar thermal systems in the context of electric generation. Its main contribution is a study of the potential of a solar power generation plant using the organic Rankine cycle in a city in the northeast region of Brazil, the city

of João Pessoa (never studied), through an energy and exergy analysis with different fluids and solar concentrators in a simple plant without storage, which can be applied by entrepreneurs in the region and reproduced by other researchers for mapping resources in other regions.

2. Method and materials

Figure 1 shows a methodological routine flowchart of the study. The methodological procedures applied in the work were based on mathematical modelling and simulation of a traditional conventional regenerative Rankine cycle scheme with the coupling of solar concentrators as a heat source. The input data are cycle parameters, concentrator characteristics, type of fluids and solar irradiance. With this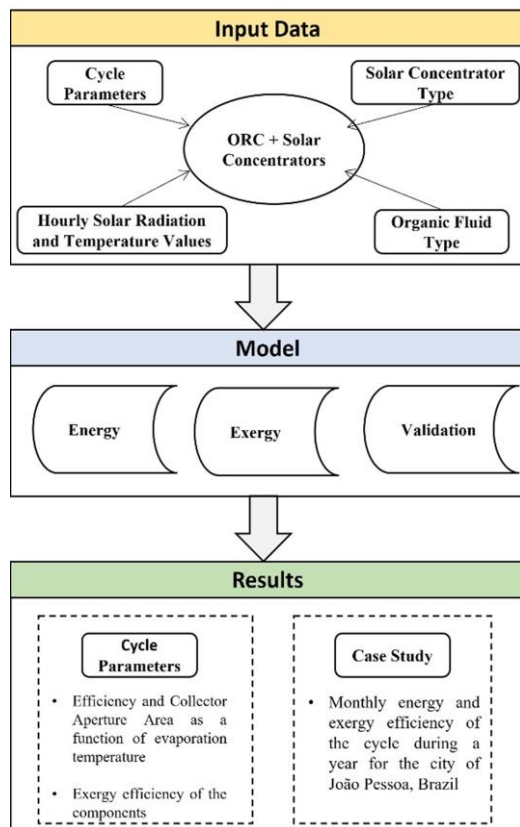 data, an energetic and exergy analysis is made. The efficiency results are reported as a function of the evaporation temperature.

2.1. Cycle studied

Figure 2 shows the typical low-temperature organic Rankine cycle configuration with solar concentrators in the heat supply function as the hot source for system operation. The processes in Fig. 2 are:

- Process 1−2: The working fluid enters the pump as a saturated liquid and leaves under pressure as a subcooled liquid. There is no heat transfer during the process.
- Process 2−3: With the compression of the liquid performed by the pump, the compressed fluid is slightly heated in the regenerator using the saturated vapour that leaves the turbine.
- Process 3−4: Heat is supplied to the compressed liquid in the evaporator due to heat exchange with the fluid from the solar field. The temperature of the organic Rankine fluid increases at constant pressure, passing the fluid to a superheated state.
- Process 4−5: After the expansion of the fluid performed by the turbine, there is a decrease in the temperature and pressure properties until it enters the regenerator.
- Process 5−6: Saturated vapour passes through the regenerator to heat the compressed fluid.
- Process 6−1: Heat rejection in the condenser. The saturated vapour becomes saturated liquid.
- Process 7−8: Solar field fluid is pumped to the solar concentrator.
- Process 8−9: Solar fluid is heated in a solar concentrator.
- Process 9−7: Solar fluid supplying heat to organic fluid in the evaporator.

This type of configuration is not only applicable to solar collectors but also in other applications, such as in geothermal energy systems, due to its simplicity and low cost.

The system was mathematically modelled in the software EES − Engineering Equation Solver. To develop the model, the mass and energy balance equations were adopted for control volumes in a steady state regime, with negligible kinetic and potential energy variations and flow without a pressure drop. The equations and conditions adopted are described in the following sections.
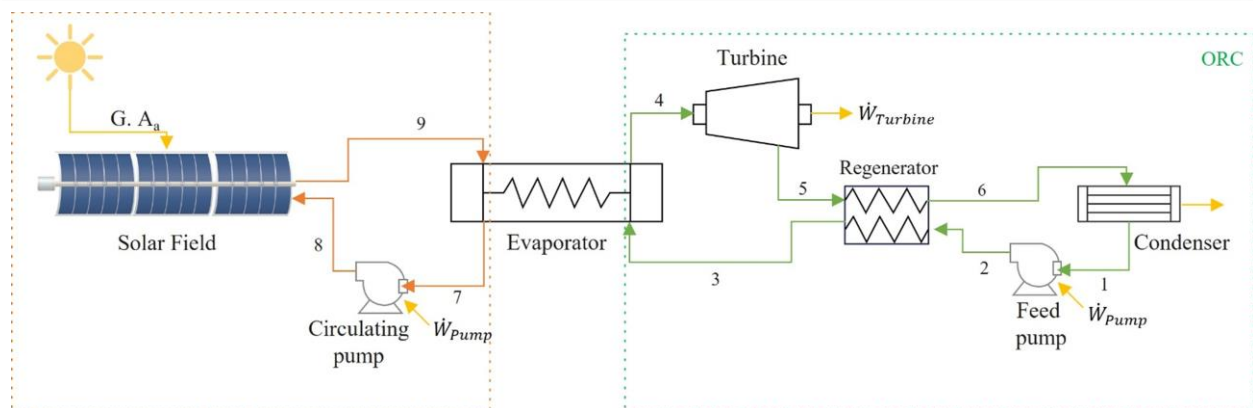

Fig. 1. Flowchart of methodology used in the research.

Fig. 2. Organic Rankine cycle with solar concentrators.

2.2. The energy analysis of the cycle studied

An energy analysis is performed for the studied cycle, through the equation of the first law of thermodynamics applied to all cycle components. The energy equations of the cycle components are described as follows:

Figure 3 shows the control volume in the turbine. In this equipment, work is produced, so the energy balance is described by

$$\dot{W}_{Turbine} = \dot{m}(h_4 - h_5). \tag{1}$$

Fig. 3. Turbine control volume.
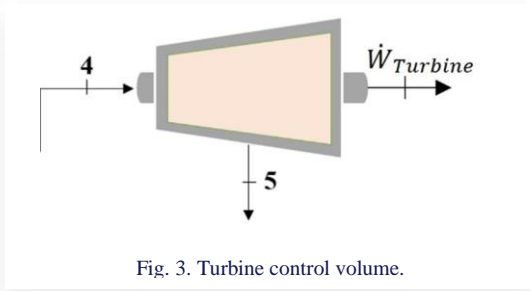
Through the isentropic efficiency of the turbine, it is possible to determine the real work between 4 and 5 and the enthalpy at the output, according to the following equation:

$$\eta_{Turbine,isen} = \frac{h_4 - h_5}{h_4 - h_{5s}}. \tag{2}$$

Figure 4 shows the control volume in the condenser. In this heat exchanger, the heat exchange between 6 and 1 is given by the following equation:

$$\dot{Q}_{condenser} = \dot{m}(h_6 - h_1). \tag{3}$$
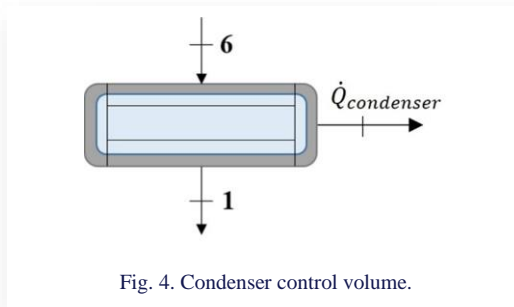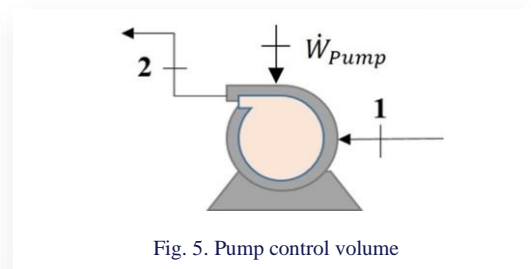
Fig. 4. Condenser control volume.

Figure 5 shows the volume control in the pump. The pump fluid is an incompressible fluid, i.e., $v_1 = v_2$, so the pump work between 1 and 2 is given by the following equations:

Fig. 5. Pump control volume

$$-w_{Pump} = \int vdP \cong v_1(P_2 - P_1) = h_{2s} - h_1, \tag{4}$$

$$h_{2s} = h_1 + v_1(P_2 - P_1). \tag{5}$$

Through the isentropic efficiency of the pump, it is possible to determine the real work between 1 and 2 and the enthalpy at the output, according to the following equation:

$$\eta_{Pump,isen} = \frac{h_{2s} - h_1}{h_2 - h_1}. \tag{6}$$

Figure 6 shows the control volume in the regenerator. The heat transfer in the regenerator is calculated by the following equation:

$$\dot{Q}_{regenerator} = \varepsilon \dot{m} C_p (T_5 - T_2). \tag{7}$$

Fig. 6. Regenerator control volume.
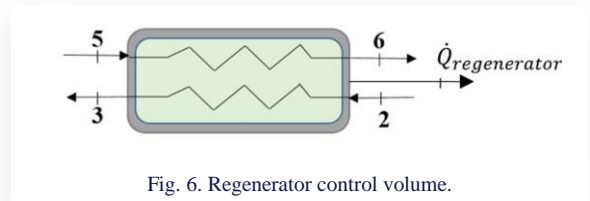
Figure 7 shows the control volume in the evaporator. The heat transfer in the evaporator is calculated by the following Eqs. (8)–(13):

Fig. 7. Evaporator control volume.
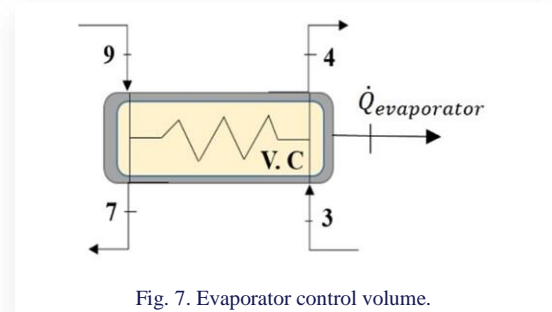
$$\dot{Q}_{evaporator} = \dot{m}(h_4 - h_3), \tag{8}$$

$$\eta_{ORC} = \frac{\dot{W}_{liq}}{\dot{Q}_{evap}} = 1 - \frac{\dot{Q}_{condenser}}{\dot{Q}_{evaporator}}, \tag{9}$$

$$\eta_{ther} = \eta_{ORC} \cdot \eta_{collector}, \tag{10}$$

$$A_a = \frac{\dot{Q}_{evaporator}}{\text{DNI} \cdot \eta_{collector}}, \tag{11}$$

$$\eta_{ther} = \frac{\dot{W}_{liq}}{\text{DNI} \cdot A_a}. \tag{12}$$

Considering that there are no heat losses to the surroundings in the evaporator between the ORC and the solar collector circuit and taking into account the definition of the collector efficiency and the overall efficiency of the solar ORC in the configuration with heat transfer fluid, the thermal efficiency is given by

$$\eta_{ther} = \frac{\dot{W}_{liq}}{\text{DNI} \cdot A_a} = \eta_{collector} \left[\eta_{ORC} + \frac{\Delta h_{\text{HTF},7 \to in(8)}(\eta_{ORC} - 1)}{\Delta h_{\text{HTF},in(8) \to out(9)}} \right]. \tag{13}$$

2.3. The exergy analysis of the organic Rankine cycle

Exergy is a thermodynamic property that defines the maximum theoretical work that can be obtained as the reference environment interacts to equilibrium with the system of interest. Therefore, T_o represents the dead-state temperature for exergy calculations, h_o and s_o stand for the enthalpy and entropy of the operating fluid in the dead-state conditions (at the pressure and temperature), respectively. Additionally, h_i and s_i represent enthalpy and entropy for each point in the cycle. Using these variables, exergy ψ_i is determined for each point in the cycle according to the following equation:

$$\psi_i = h_i - h_o - T_o(s_i - s_o). \tag{14}$$

The second-law efficiency of various devices with steady-state flow can be determined based on its general definition, which is the ratio of the recovered exergy to the supplied exergy. The second-law efficiencies of the turbine, condenser, evaporator, and regenerator can be defined through Eqs. (15)–(18), respectively:

$$\eta_{II,Turbine} = \frac{\dot{W}_{liq}}{(\psi_4 - \psi_5)}, \tag{15}$$

$$\eta_{II,Condenser} = 1 - \left[\frac{T_o(s_6 - s_1) + \frac{\dot{Q}_{condenser}}{T_{con}}}{\dot{m}(\psi_6 - \psi_1)}\right], \tag{16}$$

$$\eta_{II,Evaporator} = \frac{\dot{m}_{fluid}(\psi_4 - \psi_3)}{\dot{m}_{HTF}(\psi_9 - \psi_7)}, \tag{17}$$

$$\eta_{II,Regenerator} = \frac{\dot{m}_{fluid}(\psi_3 - \psi_2)}{\dot{m}_{HTF}(\psi_5 - \psi_6)}. \tag{18}$$

The exergetic efficiency, or the second law of a coupled system, can help reduce irreversibility in the system and increase the efficiency of thermal processes. The increased efficiency, in turn, reduces the energy required by the systems, given that the expression for the exergetic efficiency can be defined by (Hepbasli [18])

$$\eta_{II,Collector} = \frac{\dot{m}_{HTF}(\psi_9 - \psi_8)}{Ex_{rad}}. \tag{19}$$

The exergy of solar radiation was calculated using the Petela equation presented in Eq. (20) (Hepbasli [18]):

$$Ex_{rad} = A_a \cdot DNI \cdot \left[1 + \frac{1}{3}\left(\frac{T_o}{T_{sun}}\right)^4 - \frac{4}{3}\frac{T_o}{T_{sun}}\right]. \tag{20}$$

The term within parentheses has a value of 0.934 for the surface temperature of the sun at 6000 K and an ambient temperature of 298 K.

2.4. Refrigerant fluid selection

Due to the huge variety of working fluids available for use in organic Rankine cycles, it was necessary to carry out the selection of representative fluids for computer simulation. The criteria for the selection were:
- Critical temperature higher than the minimum study temperature;
- Dry fluids, i.e. $\theta < 87°$ (θ is the angle of inclination of the tangent line to the saturated vapour curve (dT/ds), humid

$\theta > 93°$; isentropic fluids $\theta \cong 90°$, evaluated at the saturation temperature for 80% of the critical pressure);
- Give preference to hydrocarbons, as they have a simpler molecular structure and lower cost;
- Search for fluids of distinct thermodynamic properties to enrich comparisons;
- Toxicity category A by the American Society of Heating, Refrigerating and Air-Conditioning Engineers (ASHRAE).
- Fluids used in the literature, to verify their efficiency, since they have already been selected for this purpose in other studies.

Applying the criteria described above, a shortlist of 8 potential fluids was arrived at for study: toluene, isobutane, isopentane, R227ea, R113, R114, R245fa, R600.

Table 1. Solar collectors and operating temperature range.

Type of Collector	Operating Range (°C)
Flat plate collector	80–100
Evacuated tube collector	80–160
Compound parabolic collector	120–170
Parabolic trough collector	170–300

2.5. Solar collectors

Table 1 shows collectors for heating water or producing energy and their operating temperature range (Nafey and Sharaf [19]).

Given various types of solar collectors, three types of collectors are most studied: flat plate collector (FPC), parabolic trough collector (PTC) and compound parabolic collector (CPC). Linear Fresnel reflectors and solar towers have the characteristic of having their performance determined by the geometry of the solar field and the arrangement of the individual mirrors, and there is no efficiency equation independent of the geometric configuration. The efficiency equations for parabolic, evacuated tube, flat plate and compound parabolic collectors are easier to find in the literature.

Among the collectors with an experimentally determined efficiency curve, only the parabolic trough and compound parabolic trough collectors are widely used for power production. These choices are related to the temperature range linked to the efficiency of these two collectors for concentration systems, since they are the main collectors used in this type of application (Kalougirou [20]). For this reason, these two classes of collectors were simulated, according to Eq. (21) and Table 2:

$$\eta_{collector} = \eta_0 - a_1(\bar{T}_f - T_{amb}) - \frac{a_2(\bar{T}_f - T_{amb})}{DNI} - \frac{a_3(\bar{T}_f - T_{amb})^2}{DNI}. \tag{21}$$

Table 2. Parameters of solar collectors.

Type	Collector	η_0	a_1	a_2	a_3
PTC	EuroTrough	0.750	0.039	0.0003	0.000045
CPC	CPC Aosol 1.12X²	0.736	4.610	0.0000	0.000000

This collector efficiency is related to the efficiency of zero loss (η_0), heat loss coefficients with temperature (a_1, a_2, a_3), and finally, the technical parameters of irradiance on the collector (DNI) and the average temperatures of the fluid flowing inside the collector ($\bar{T}_f$) and the surroundings (T_{amb}).

2.5. Validation

To ensure the accuracy of the thermodynamic model developed within the scope of this study and the reliability of the obtained results, this model must be validated by studies in the literature. In order to verify the developed model, the organic Rankine cycle was simulated in a manner analogous to the work of Delgado-Torres and García-Rodríguez [5] comparing collector efficiency parameters, ORC efficiency and overall efficiency (thermodynamic and solar cycle). The calculated parameters included the heat supplied by the system, i.e. by the solar concentrators, the rejected heat, as well as the work of the pumps and turbines, which were already considered in a situation close to reality, without assuming compression and expansion as isentropic.

Table 3 reports the results found by the thermodynamic simulation of the organic Rankine cycle in comparison with the results of Delgado-Torres and García-Rodríguez [5]. With the consolidated program in EES, different configurations were investigated for the solar ORC cycle. Table 3 shows the parameters considered in the simulation.

Table 3. Input parameters for the proposed simulation.

Fluids of the Organic Rankine Cycle	Isobutane; Isopentane; Toluene; R245fa
Isentropic efficiency of the turbine (η_t)	0.75
Isentropic efficiency of the pump (η_b)	0.80
Effectiveness of the regenerator (ε)	0.80
Evaporation pressure	500–2500 kPa
Working fluid in the collector	Terminol-VP1
Ambient temperature (T_{amb})	25°C
Condensation temperature (T_{cond})	25°C;
Average irradiance on the collector (DNI)	1000 W/m²
Net power generated	1 kW
Solar collectors used	FPC; PTC; CPC

For the simulated cycle, the Terminol-VP1 fluid was chosen due to its suitability for use in solar concentrating systems. It was also verified that it meets the desired temperature requirement, remaining non-flammable within the temperature and pressure range used in the simulation proposed by this study. Furthermore, to gather information regarding the average fluid temperature in the collector ($\bar{T}_f$), temperatures of 300°C were assumed for the parabolic trough collector, 170°C for the compound parabolic collector, and 100°C for the flat plate solar collector, in a non-concentrated configuration, to obtain results with a high level of reliability for this temperature range applied to both collectors [20]. The pumping power of the heat transfer fluid was neglected.

The System Advisor Model (SAM) software was used to study the direct normal irradiation of the location of CEAR – Center for Alternative and Renewable Energy. The representative average days of each month were chosen according to those recommended by Klein [21]. The average values for direct solar radiation corresponding to each representative day, according to data from the year 2020, can be seen in Fig. 8, showing the average direct normal irradiance (DNI) for each month of the year over a one-day period. This analysis is important for developing the calculations set out above. The normal direct irradiance of João Pessoa for each typical day chosen shows variations throughout the 24 hours analysed depending on meteorological factors, such as cloudiness and rain. The hottest months in João Pessoa are from November to March. However, the graph for 2020 showed atypical behaviour for December and February. June is the coldest month.
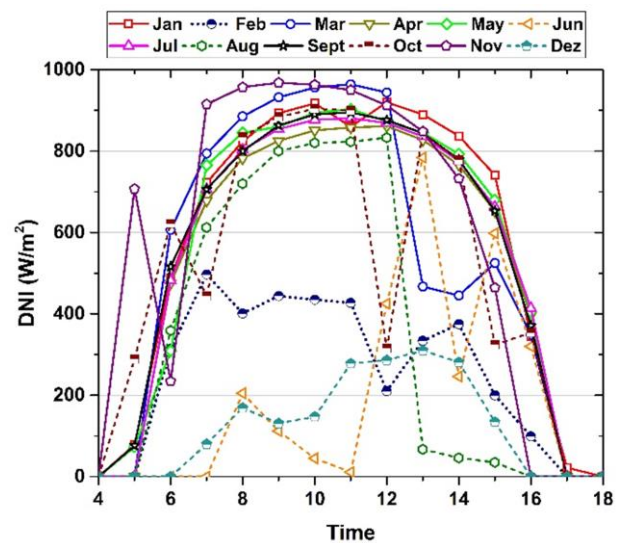
Fig. 8. Average DNI for each month of the year.

3. Results and discussion

3.1. Validation of the ORC with benchmark

Table 4 presents the verified efficiency results of the organic Rankine cycle and the global efficiency of the solar cycle for different collectors and fluids. The calculated results of the present study are quite satisfactory and show good agreement with the reference work by Delgado-Torres and García-Rodríguez [5] used for validation, with percentage errors of less than 5%.

3.2. Cycle with parabolic trough collector

Figure 9 shows the energetic and exergetic efficiency of the organic Rankine cycle for the parabolic trough collector (PTC) collector. This collector presented a greater range of use of organic fluids for the solar organic Rankine cycle, as it obtained the best overall system efficiency, in addition to the smaller opening areas required for installation. This is justified by the fact that the average operating temperature range is greater than that of other collectors, which makes it possible to obtain greater applicability for different fluids.

Table 4. Validation of the results of the present study with the reference work.

Cycle Parameters					Organic Rankine Cycle Efficiency			Solar Power Cycle Efficiency		
Collector	Fluid	P_{cond} (kPa)	P_{evap} (kPa)	T_2 (°C)	η_{ORC} (%) Reference	η_{ORC} (%) Present Study	Error (%)	η (%) Reference	η (%) Present Study	Error (%)
Aosol 1.12 X (CPC)	Isobutane	404.7	1400	95	9.95	9.86	0.90	3.91	3.98	1.79
	Isopentane	109.2	491.6	95	10.49	10.51	0.19	4.03	4.11	1.99
	R245fa	177.8	829.6	95	10.14	10.15	0.10	3.97	4.04	1.76
VITOSOL 200F (FPC)	Isobutane	404.7	1371	95	9.85	9.96	1.12	4.32	4.40	1.85
	Isopentane	109.2	491.6	95	10.49	10.51	0.19	4.45	4.54	2.02
	R245fa	177.8	829.6	95	10.14	10.15	0.10	4.39	4.47	1.82
VITOSOL 300 (Evacuated)	Isobutane	404.7	2395	145	14.94	14.41	3.55	8.11	7.96	1.85
	Isopentane	109.2	1288	145	16.40	16.48	0.49	8.51	8.78	3.17
	R245fa	177.8	2087	145	15.46	15.48	0.13	8.26	8.44	2.18

As shown in Fig. 9, the toluene fluid, which is a dry fluid, presents the highest efficiencies with the variation of evaporation pressure. This is related to the fluid saturation curve, in which the toluene saturation temperature is greater than that of other fluids analysed for the same simulated evaporation pressure. As can be seen, the cycle using toluene fluid at a pressure of 2500 kPa achieves 21.62% thermal efficiency and 23.61% exergy efficiency.
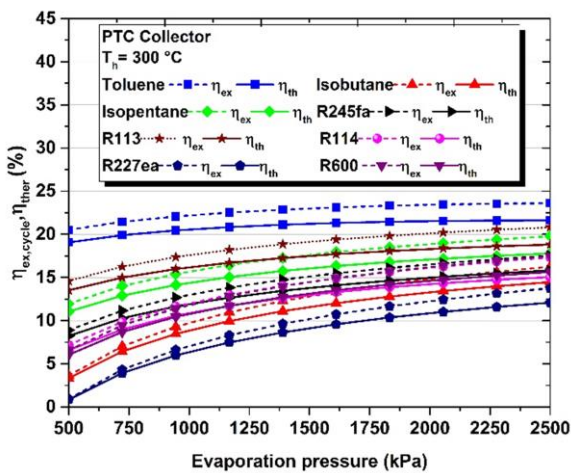

Fig. 9. Exergy and energy efficiency as a function of evaporation pressure for the PTC collector.

Figure 10 shows the variation in the mass flow in relation to the evaporation pressure. It can be noted that there is an inversely proportional relationship between these two variables, in which the circulating flow of fluid in the system decreases as the pressure increases. Toluene and isopentane were the fluids that presented the lowest mass flow values within the pressure range chosen for the simulation, in which the mass flow values did not exhibit significant variations. Furthermore, at higher pressures, the mass flow values did not vary significantly, remaining almost constant. Mass flow rates are directly related to the system size and required pumping power.
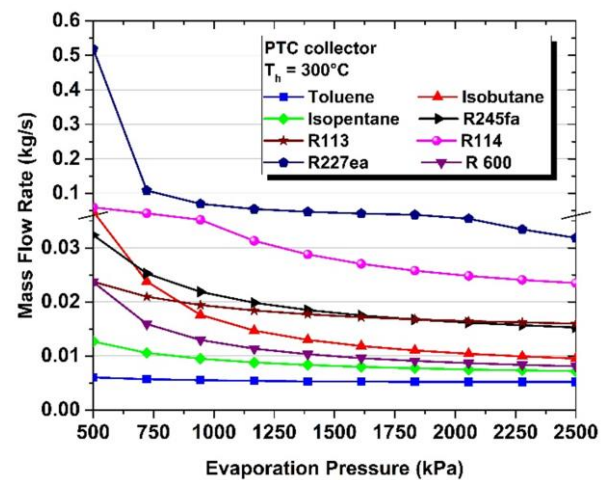

Fig. 10. Mass flow rate as a function of evaporation pressure for the PTC collector.

Figure 11 shows the variation in the opening area in relation to the evaporation pressure. The opening area decreases with the increasing evaporation pressure. R227ea fluid at 50 kPa pressure requires 117.8 m^2 and at 250 kPa pressure requires 8.3 m^2. Furthermore, a relationship can be seen in which not necessarily increasing the collector area will increase the cycle efficiency. In general, among the fluids analysed, the area values did not show sudden changes beyond a pressure of 1500 kPa. Toluene, R113 and isopentane fluids require smaller areas to install a solar plant of this model.

Figure 12 presents the exergy efficiency analysis of the turbine as a function of the evaporation pressure. For different fluid flow rates, the change in turbine exergy destruction depends on the evaporator pressure. If R227ea is chosen as the refrigerant, the exergy efficiency of the turbine is maximum, and the exergy efficiency increases from 84.27% to 85.18%. However, if toluene is used, the exergy efficiency increases from 80.71% to 82.45%.

Figure 13 shows the exergy efficiency of the condenser as a function of the evaporation pressure. When R227ea is used as
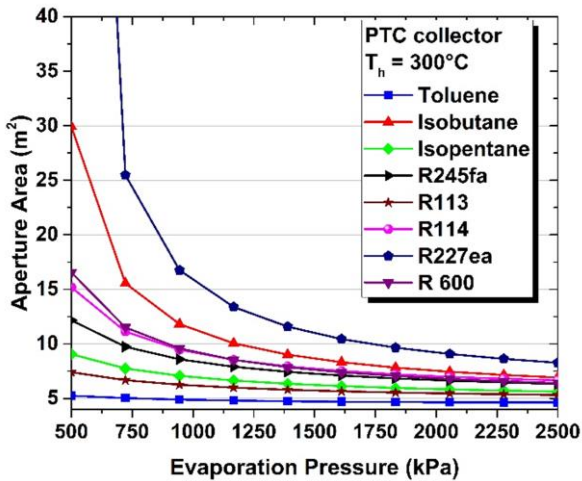
a refrigerant, depending on the evaporator pressure, the maximum variation in the exergy efficiency of the condenser is approximately 50.27%, ranging from 48.14% to 96.81%. However, if toluene is preferred, the variation in the condenser exergy efficiency is minimal and approximately 0.08%, ranging from 99.4% to 99.48%. For the different refrigerants, the changes in the regenerator exergy efficiency are shown in Fig. 14. When R227ea is used, the change in the exergy efficiency of the heat exchanger is maximum depending on the evaporator pressure, ranging from 25.44% to 52.85%. However, if toluene is chosen as the refrigerant, the change in the exergy efficiency of the heat exchanger is minimal at 1.18%.

Fig. 11. PTC collector aperture area as a function of evaporation pressure.

Fig. 14. Regenerator exergy efficiency as a function of evaporation pressure.
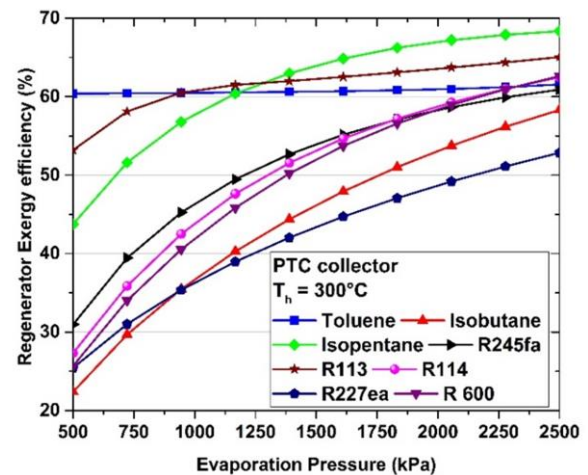
Fig. 12. Turbine exergy efficiency as a function of evaporation pressure.

Figure 15 shows the exergy efficiency of the evaporator as a function of the evaporation pressure. When R227 and R114 are used as refrigerants, the evaporator exergy efficiency is maximum and reaches up to 30% depending on the evaporator pressure.
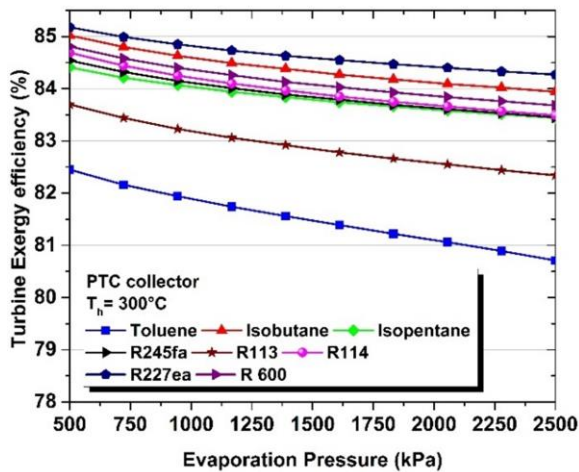

Fig. 13. Condenser exergy efficiency as a function of evaporation pressure.

Fig. 15. Evaporator exergy efficiency as a function of evaporation pressure.

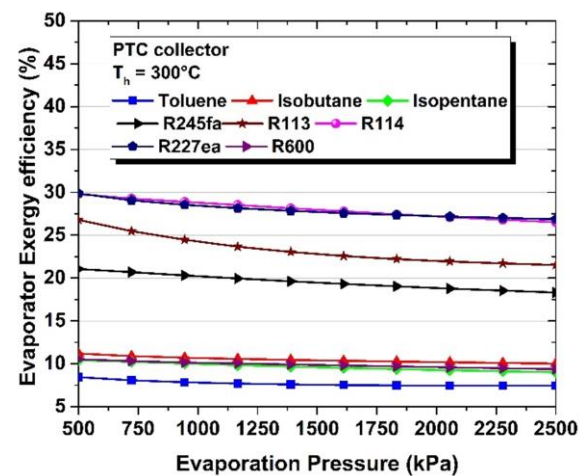## 3.3. Cycle with compound parabolic collector

Figures 16 and 17 show the resulting performance parameters and the variation in the mass flow for the compound parabolic collector (CPC) as a function of the evaporation pressure, respectively. For application in CPCs, the thermodynamic analysis showed an unfeasibility entropy generation for the toluene fluid within the recommended temperature operating range of the solar concentrator, a factor consistent with works found in current literature, in which there is the possibility of using isobutane and R245fa in these lower temperature ranges, in which they are common in geothermal applications [13]. As can be seen, using CPC collector in the cycle depending on the fluid only achieves 1.83% thermal efficiency and 2.02% exergy efficiency.
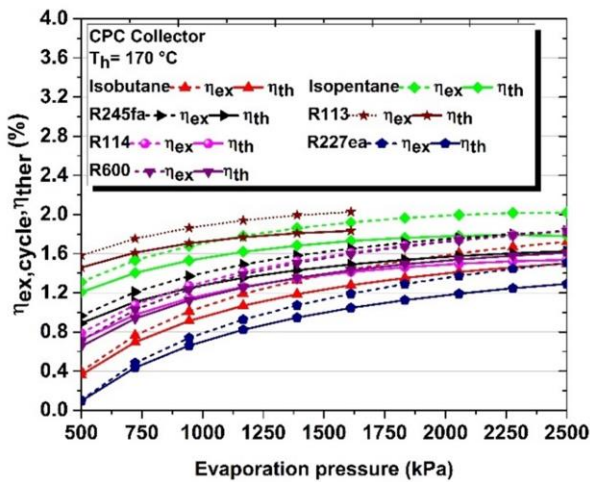
Fig. 16. Exergy and energy efficiency as a function of evaporation pressure for the CPC collector.
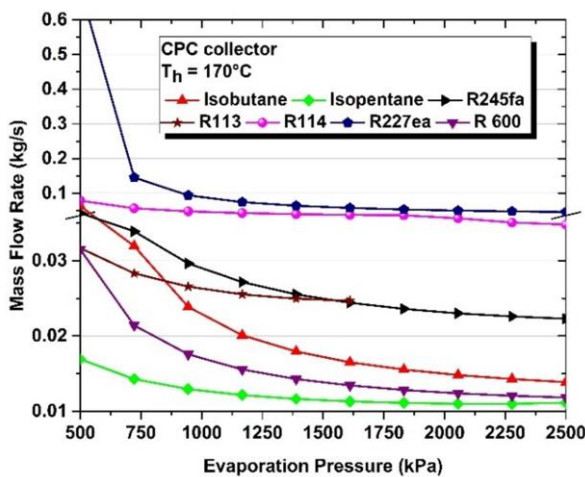
Fig. 17. Mass flow rate as a function of evaporation pressure for the CPC collector.

The efficiencies of the plant with the CPC concentrator for all fluids used in the simulation are very low. In addition, the areas calculated with these fluids (Fig. 18) make applications related to power plants with solar energy unfeasible from a prac-
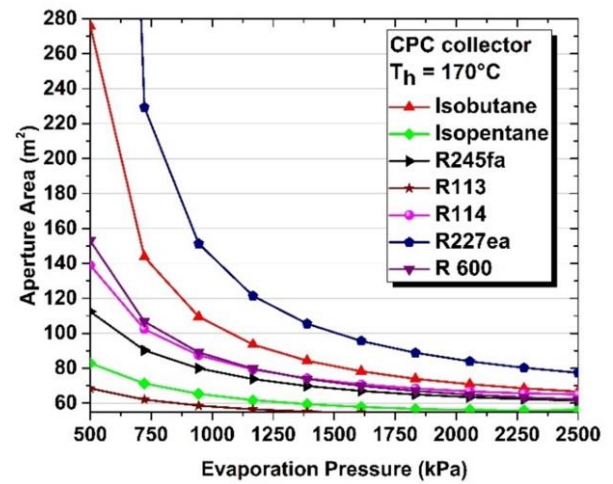
Fig. 18. CPC collector aperture area as a function of evaporation pressure.

tical point of view. It can be highlighted that for R600, the presence of a minimum area of 60 m² with low flow provides a maximum efficiency of 1.8% for this working fluid, and this should be the operating point selected in the case of using this working fluid coupled to CPC. Therefore, it is recommended to use another type of collector with higher temperatures, such as PTC, as it makes more sense to obtain greater efficiency and a smaller opening area.

3.4. Case study (João Pessoa, Brazil)

The effect of solar radiation and ambient temperature on the system performance in a city is evaluated in this section. The city of João Pessoa, in eastern Brazil, has impressive solar potential due to the abundance of solar radiation throughout the year. Therefore, it was chosen as an option for implementing the studied system.

Figures 19 and 20 demonstrate how solar irradiation and ambient temperature affect exergy and thermal efficiency, respec-
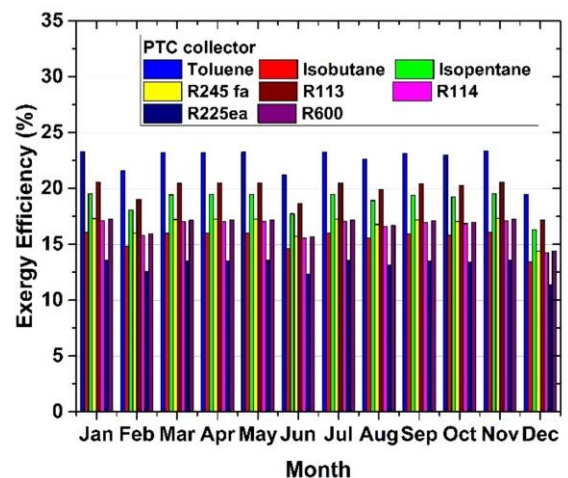
Fig. 19. System exergy efficiency with PTC collector for the year 2020 in the city of João Pessoa, Brazil.
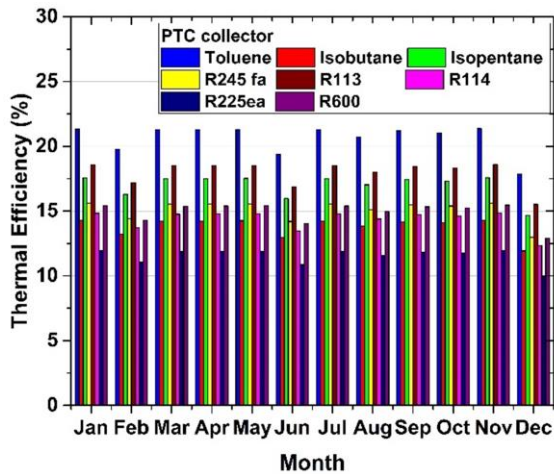
Fig. 20. System thermal efficiency with PTC collector for the year 2020 in the city of João Pessoa, Brazil.

tively. According to Fig. 19, the greatest exergy efficiency occurs in the months of January (21.37%), March (21.26%) and November (21.35%) − the hottest months of the year, when the sun shines intensely. Based on Fig. 8, the greater the solar irradiation, the greater the exergy and thermal efficiency. Unlike solar intensity, which positively affects exergy efficiency, an increase of the ambient temperature decreases exergy and thermal efficiency. Therefore, its lowest value occurs in June. December's results are atypical for the year 2020.

4. Conclusions

In this study, cycle energy and exergy analyses based on the evaporator pressure change were performed for a power generation plant using solar energy with different refrigerants. It can be concluded that:

- With the adequate selection of the refrigerant, collector, and evaporation pressure, the first and second law efficiencies of the cycle improve up to 41% and 44%, respectively.
- The best use of incident solar radiation occurred with the fluid toluene among the refrigerants used, due to the high thermal and exergy efficiency of the cycle, and presented the smallest opening area (4.6 m^2) required per unit kW, indicating that its adoption would result in a more compact solar field, while R227ea presented the lower thermal and exergy performance than other refrigerants.
- The parabolic trough collector achieved the best results from the point of view of energy (21.62%) and exergy (23.62%) efficiency, due to obtaining high temperatures, which resulted in the optimum concentration efficiency.
- The thermodynamic analysis of the compound parabolic collector showed an unfeasible entropy generation in the heat exchangers for isopentane and toluene, indicating the impossibility of using these working fluids within the selected pressure range at the maximum temperatures reached by this type of collector. The use of a compound parabolic collector in the cycle depending on the fluid achieves only 1.83% thermal efficiency and 2.02% exergy efficiency.

- Depending on the refrigerant and evaporator pressure, the exergy efficiency of the turbine reaches 86.22%, while that of the evaporator reaches 76.6%.
- For the city of João Pessoa, the highest exergy efficiency occurs in the months of January (21.37%) and November (21.35%), the hottest months of the year, when the sun shines brightly, and the lowest exergy efficiency occurs in the month of June (19.41%).

Finally, this study on the organic Rankine cycle with solar concentrators can assist research and development projects in the dissemination and maturation of the topic in the national territory, being another option to be analysed from an economic and environmental point of view for its more significant insertion in the Brazilian electrical matrix.

Acknowledgements

References

[1] Colonna, P., Casati, E., Trapp, C., Mathijssen, T., Larjola, J., Turunen-Saaresti, T., & Uusitalo, A. (2015). Organic Rankine cycle power systems: From the concept to current technology, applications, and an outlook to the future. *Journal of Engineering for Gas Turbines and Powe*r, 137(1), 1−19. doi: 10.1115/1.4029884

[2] Loni, R., Mahian, O.M., Markides, C.N., Bellos, E., Roux, W.G.L, Kasaeian, A., Najafi, G., & Rajaee, F. (2021). A review of solar-driven organic Rankine cycles: recent challenges and future outlook. *Renewable and Sustainable Energy Reviews*, 150, 111410. doi: 10.1016/j.rser.2021.111410

[3] Petrollese, M.; Cau, G., & Cocco, D. (2020). The Ottana solar facility: dispatchable power from small-scale CSP plants based on ORC systems. *Renewable Energy*, 147, 2932−2943. doi: 10.1016/j.renene.2018.07.013

[4] Ancona, M.A. Bianchi, M., Branchini, L., De Pascale, A., Melino, F., Peretto, A., Poletto, C., & Torricelli, N. (2022). Solar driven micro-ORC system assessment for residential application. *Renewable Energy*, 195, 167−181. doi: 10.1016/ j.renene.2022.06.007

[5] Delgado-Torres, A.M., & García-Rodríguez, L. (2010). Analysis and optimization of the low-temperature solar organic Rankine cycle (ORC). *Energy Conversion and Management*, 51(12), 2846−2856. doi: 10.1016/j.enconman.2010.06.022

[6] Jing, L., Gang, P., & Jie, J. (2010). Optimization of low temperature solar thermal electric generation with Organic Rankine Cycle in different areas. *Applied Energy*, 87(11), 3355–3365. doi: 10.1016/j.apenergy.2010.05.013

[7] Kumar, A., & Shukla, S.K. (2016). Analysis and performance of ORC based solar thermal power plant using benzene as a working fluid. *Procedia Technology*, 23, 454−463. doi: 10.1016/j.protcy.2016.03.050

[8] Sonsaree, S., Asaoka, T., Jiajitsawat, S., Aguirre, H., & Tanaka, K. (2018). A small-scale solar organic Rankine cycle power plant in Thailand: Three types of non-concentrating solar collectors, *Solar Energy*, 162, 541–560. doi: 10.1016/j.solener.2018.01.038

[9] Stand, L.M., Ochoa, G.V., & Forero, J.D. (2021). Energy and exergy assessment of a combined supercritical Brayton cycle −

133

ORC hybrid system using solar radiation and coconut shell biomass as energy source. *Renewable Energy*, 175, 119−142. doi: 10.1016/j.renene.2021.04.118

[10] Gupta, P.R., Tiwari, A.K., & Said, Z. (2022). Solar organic Rankine cycle and its poly-generation applications – A review. *Sustainable Energy Technologies and Assessments*, 49, 101732. doi: 10.1016/j.seta.2021.101732

[11] Lakhani, S.; Raul, A., & Saha, S.K. (2017). Dynamic modelling of ORC-based solar thermal power plant integrated with multitube shell and tube latent heat thermal storage system. *Applied Thermal Engineering*, 123, 458−470. doi: 10.1016/j.applthermaleng.2017.05.115

[12] Li, J.F., Guo, H., Wu, Y.T., Lei, B., Ye, F., Ma, C.F., Zhang, Y., & Jiao, X.L. (2022). Experimental investigation of solar organic Rankine cycle with parabolic trough concentrator using nitrate salt as heat transfer and storage fluid, *International Journal of Energy Research*, 46, 6847−6865. doi: 10.1002/er.7628

[13] Ahmadi, A., El Haj Assad, M., Jamali, D.H., Kumar, R., Li, Z.X., Salameh, T., Al-Shabi, M., & Ehyaei, M.A. (2020). Applications of geothermal organic Rankine Cycle for electricity production. *Journal of Cleaner Production*, 274, 122950. doi: 10.1016/j.jclepro.2020.122950

[14] Saadatfar, B., Fakhrai, R., & Fransson, T. (2014). Conceptual modeling of nano fluid ORC for solar thermal polygeneration. *Energy Procedia*, 57, 2696−2705. doi: 10.1016/j.egypro.2014.10.301

[15] Rejeb, O., Alirahmi, S.M., Assareh, E., El Haj Assad, M., Jemni, A., Bettayeb, M., & Ghenai, C. (2022). Innovative integrated solar powered polygeneration system for green hydrogen, oxygen, electricity and heat production. *Energy Conversion and Management*, 269, 116073. doi: 10.1016/j.enconman.2022.116073

[16] Jiang, Y., Zhang, X., Zhang, Z., Hao, L., Cao, Z., Li, S., Guo, B., Zheng, Y., Dong, C., & Zhao, L. (2024). Performance evaluation and working fluid screening of direct vapor generation for solar ORC using low-global warming potential (GWP) working fluids. *Energies*, 17, 3133. doi: 10.3390/en17133133

[17] Maytorena, V.M., & Buentello-Montoya, D.A. (2022). Multi-phase simulation and parametric study of direct vapor generation for a solar organic Rankine cycle. *Applied Thermal Engineering,* 216, 119096. doi: 10.1016/j.applthermaleng.2022.119096

[18] Hepbasli, A. (2008). A key review on exergetic analysis and assessment of renewable energy resources for a sustainable future. *Renewable and Sustainable Energy Reviews*, 12(3), 593−661. doi: 10.1016/j.rser.2006.10.001

[19] Nafey, A.S., & Sharaf, M.A. (2010). Combined solar organic Rankine cycle with reverse osmosis desalination process: Energy, exergy, and cost evaluations. *Renewable Energy*, 35(11), 2571−2580. doi: 10.1016/j.renene.2010.03.034

[20] Kalogirou, A.S. (2013). *Solar Energy Engineering: Process and Systems*. Academic Press.

[21] Klein, S.A. (1977). Calculation of monthly average insolation on tilted surfaces. *Solar Energy*, 19(4), 325−329. doi: 10.1016/0038-092X(77)90001-9

ARCHIVES OF THERMODYNAMICS

A study on ceramic sintering preparation process and properties with the addition of silicon carbide foaming agent

Haicheng Qi

Henan Mechanical and Electrical Vocational College, Mount Taishan Road, Longhu Town, Xinzheng City, Henan 454000, China
Author email: qihaichc@hotmail.com

Abstract

Foamed ceramics are widely used in construction as a building material. This article used potassium feldspar tailings as the primary raw material and added a silicon carbide (SiC) foaming agent to prepare samples through a sintering process. The impact of three factors − SiC content, sintering temperature and heat preservation time − on sample properties (such as bulk density and water absorption rate) was analyzed using a single-factor variable method. It was found that the increase in SiC content, sintering temperature, and heat preservation time increased pores inside the sample, thereby leading to a higher water absorption rate, lower compressive strength and higher mass loss rate, i.e., decreased sample performance. Overall, the optimal sintering process parameters were as follows: a SiC content of 1.0 wt%, a sintering temperature of 1,250°C and a heat preservation time of 30 minutes. Under these conditions, the obtained sample had a bulk density of 0.54 g/cm^3, a water absorption rate of 13.45%, a compressive strength of 4.75 MPa, a thermal conductivity of 0.06 W/(m·K) and an acid resistance mass loss of 1.21%, exhibiting the optimal performance. The experimental results provide appropriate SiC content and sintering parameters that can be applied in practice to obtain higher-performance foam ceramics.

Keywords: Silicon carbide; Foaming agent; Ceramics; Sintering preparation; Water absorption rate

1. Introduction

In the face of the escalating contradiction between energy supply and demand, the development of energy-saving products has become a current focus, and building energy efficiency is also an essential content [1]. With building energy consumption intensifying, waste reuse and energy-saving materials have been increasingly widely studied [2]. Foamed ceramics are environmentally friendly materials. Compared with ordinary ceramics, foamed ceramics perform better in heat preservation, insulation, sound insulation, and other aspects due to the formation of a large number of bubbles in the firing process [3]. Moreover, foamed ceramics have the characteristics of lightweight and high-strength. It can be used not only as an excellent filtration or carrier material [4] but also for artificial bone repair or drug-loaded materials [5]. In construction engineering, foamed ceramics, as a new building material, have also been extensively used for thermal insulation of external walls [6], reducing construction loads while achieving good effects. Due to the excellent performance of foamed ceramics, the preparation process and properties have also received more and more attention from researchers [7]. Sandoval et al. [8] prepared porous ceramics by using mullite as raw material and the direct foaming method (1,600 °C, two hours). They conducted an analysis of the microstructure in order to comprehend the impact of bovine serum albumin as a foaming and binding agent. Alias et al. [9] utilized treated desulfurization sludge to generate porous ceramics through foaming. They analyzed the porosity and mechanical

strength of the samples and found that the increased porosity significantly reduced the flexural strength of the samples after sintering at 1,200°C for three hours. Hu et al. [10] prepared porous ceramics using Al_2O_3-SiO_2, TiO_2 and silicon carbide (SiC) with low density and high porosity. Jia et al. [11] studied the properties of porous ceramics prepared by the freeze-gelation method. They discovered that the samples had relatively high mechanical strength and good adiabatic properties. According to the current practical requirements of foamed ceramics in building material applications, there is a higher demand for its various properties. Moreover, deeper research on energy-saving properties of building materials is also needed to face further development of green buildings. Currently, many materials have been applied to prepare foamed ceramics. This article conducted an in-depth study on the sintering preparation process of foamed ceramics using potassium feldspar tailings as raw material. The ceramic properties under different sintering preparation processes were analysed using the single-factor variable method. This paper contributes to further optimizing the preparation of foamed ceramics, improving their performance and achieving better application in the construction materials market.

2. Materials and methods

2.1. Experimental subjects

Produced by firing natural ores, ceramics are characterized by high hardness, low density, and corrosion resistance, and have extensive applications in daily life, art, culture and the construction industry [12]. With the progress of technology and evolving demands, there has been an increasing focus on researching various new types of ceramics [13].

Adding SiC foaming agent to cores can produce foamed (porous) ceramics, a novel functional material. Compared to regular ceramics, foamed ceramics exhibit significantly enhanced properties and further broaden their range of applications.

Foamed ceramics are light as abundant pores are generated during sintering. Moreover, their stable skeleton structure provides excellent strength, making them highly suitable for applications in the construction industry. The presence of pores allows for adequate heat and sound insulation, making them excellent thermal and acoustic insulating materials. Moreover, the high porosity enables reliable filtration and adsorption capabilities [14]. Additionally, foamed ceramics exhibit exceptional resistance to corrosion from acids and alkalis, providing a distinct advantage in scenarios like wastewater filtration and high-temperature dust removal [15].

The study of the preparation process for foamed ceramics holds significant practical value due to their excellent perfor-

mance and diverse application scenarios. It enables better control over product performance and ensures alignment with market demand.

2.2. Experimental materials

The following materials are considered:
(1) Potassium feldspar tailings: They are produced by a mining company in Henan Province. Their chemical composition contains a large amount of SiO_2 and Al_2O_3, making them suitable for ceramic preparation. Their main components are shown in Table 1.
(2) Silicon carbide (SiC) foaming agent: It is prepared by Sinopharm Group Chemical Reagent Co., Ltd., and is chemically pure. In a high-temperature environment, SiC can react with oxygen [16] to produce bubbles, and the reaction equations of this process are:

$$SiC + O_2 \rightarrow SiO_2 + CO \uparrow,$$

$$SiC + O_2 \rightarrow SiO_2 + CO_2 \uparrow.$$
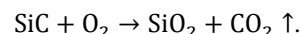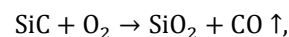
Table 1. Main chemical composition of potassium feldspar.

	Chemical composition, wt%
SiO_2	46.87
Al_2O_3	10.93
K_2O	9.46
Fe_2O_3	1.42
Na_2O	1.36

2.3. Experimental equipment

The main equipment used in the experiment is listed in Table 2.

2.4. Ceramic preparation process

The preparation process of ceramics is shown in Fig. 1. Based on Fig. 1, the preparation steps are outlined as follows:
(1) Potassium feldspar was ball-milled with the SiC foaming agent;
(2) A suitable amount of water was added to moisten the mixture, and then it was screened using a 100-mesh sieve;
(3) The mixture was pressed into a mould and pressed to form the desired shape;
(4) The moulded sample was dried in an oven for 12 hours;
(5) The ceramic embryo was sintered and foamed in a chamber furnace.

The sample was heated at a rate of 15°C/min to 300°C, kept at 300°C for 50 min, and heated again at a rate of 15°C/min until reaching the sintering temperature. After being held at this tem-

Table 2. Experimental equipment.

Equipment	Model number	Factory
Electronic balance	HZF-A200	Shanghai Shuangxu Electronics Co., Ltd.
Planetary ball mill	YXQM	Guangzhou Gurui Technology Co., Ltd.
Standard test sieve	100 mesh	Xinxiang Tongxin Machinery Co., Ltd.
Microcomputer control pressure tester	YAW-300	Xian County Rushi Technology Co., Ltd.
Vacuum drying oven	DZ-1BCIV	Tianjin Taisite Instrument Co., Ltd.
Chamber furnace	SX-G	Tianjin Zhonghuan Electric Furnace Co., Ltd.
Static water mechanics balance	JY5001	Hebei Ningke Instrument Co., Ltd.
Crucible	TC5645-30	Jinan Zhongbote Special Ceramics Co., Ltd.
Constant water bath pan	HH-2S	Shanghai Jingxin Industrial Development Co., Ltd.
TCi thermal conductivity analyzer	C-THERM	Shanghai RaocheLab Technology Development Co., Ltd.

Fig. 1. Flow chart of the ceramic preparation process.

2.5. Performance testing

The following parameters were investigated:

(1) Bulk density: The sample was dried in an oven until no further change in mass; its mass was called m, and its bulk density was calculated:

$$\rho = \frac{m}{V},\qquad(1)$$

where V is volume.

(2) Water absorption rate: The sample was weighed using a static water mechanics balance, and its mass of the sample was denoted as m_1. The sample was immersed in water until saturated and then dried, and its mass was denoted as m_2. The water absorption rate was calculated:

$$w_a = \frac{m_2 - m_1}{m_1} \times 100\%.\qquad(2)$$

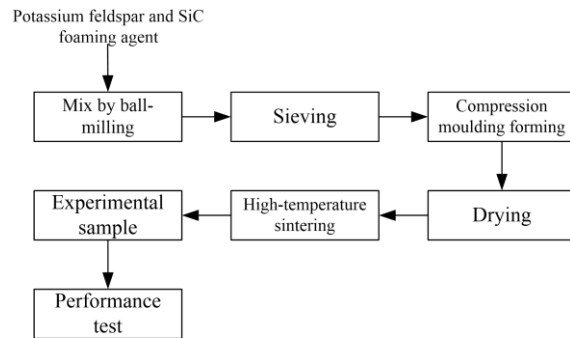(3) Compressive strength: Using a microcomputer-controlled pressure testing machine, the sample was cut into standard blocks. The area of pressure surface (S) is calculated. A pressure test was conducted. If the failure load was P, the compressive strength was

$$\sigma = \frac{P}{S}.\qquad(3)$$

(4) Thermal conductivity coefficient: it was determined using a TCi thermal conductivity meter.

(5) Acid resistance: The dry sample with a mass of m_5 was added with 20% sulfuric acid, boiled for one hour, washed and burned in a crucible at 700 °C until constant weight. After cooling at room temperature, its mass was weighed and denoted as m_4. The mass loss rate is calculated:

$$L = \frac{m_3 - m_4}{m_3} \times 100\%.\qquad(4)$$

3. Results and analysis

The properties of the sample mixed with different SiC contents are presented in Table 3.

It can be observed that an increase in SiC content resulted in a higher number of internal pores within the samples, leading to a decrease in bulk density and a significant increase in water absorption rate. Specifically, the water absorption rate of the 1.5 wt% SiC sample showed a 22.92% increase compared to the 0.5 wt% SiC sample. The increased SiC content contributed to

perature for a certain period of time, it was cooled down to room temperature to obtain the experimental sample.

This study investigated three parameters, namely SiC content, sintering temperature and holding time for sample preparation using a single-factor variable method [17]. The interpretation of these factors is shown below.

(1) SiC content: SiC content impacts the gas generation within the ceramic embryo, subsequently influencing the formation of porosity.

(2) Sintering temperature [18]: The sintering temperature affects the reaction of the foaming agent during the sintering process, thereby affecting the internal structure and properties of the sample.

(3) Heat preservation time: The sample may only foam adequately if the heat preservation time is short, resulting in small pores and high bulk density. Conversely, an excessively long heat preservation time can lead to continued growth of pores, resulting in thinner pore walls and reduced compressive strength. Therefore, selecting an appropriate heat preservation time is essential.

Table 3. Effect of SiC content on properties.

	0.5 wt%	1.0 wt%	1.5 wt%
Bulk density, g/cm³	0.51	0.43	0.35
Water absorption rate, %	7.11	18.02	30.03
Compressive strength, MPa	7.23	5.35	2.12
Thermal conductivity coefficient, W/(m·K)	0.07	0.06	0.05
Acid-resistance mass loss rate, %	0.92	1.12	3.16

a rise in the number of internal pores, which subsequently reduced the compressive strength and thermal conductivity of the samples. The compressive strength decreased from 7.23 MPa to 2.12 MPa, while the thermal conductivity decreased from 0.07 W/(m·K) to 0.05 W/(m·K). With the increase of pores, the contact area between the sample and acid increased, leading to decreased acid resistance. It can be concluded that the changes in water absorption rate, compressive strength, and mass loss were significant when increasing SiC content from 1.0 wt% to 1.5 wt%. Therefore, opting for a SiC content of 1.0 wt% was more suitable.

The properties of the samples mixed with 1.0 wt% SiC under a heat preservation time of 30 minutes at different sintering temperatures are presented in Table 4.

Table 4. Effect of sintering temperature on properties.

	1,200°C	1,250°C	1,300°C
Bulk density, g/cm³	0.68	0.54	0.42
Water absorption rate, %	3.84	13.45	48.94
Compressive strength, MPa	8.07	4.75	0.98
Thermal conductivity coefficient, W(m·K)	0.08	0.06	0.05
Acid-resistant mass loss rate, %	0.87	1.21	4.37

It can be observed that as the sintering temperature increased, the reaction of SiC became more intense, resulting in the formation of a more significant number of expansion pores in the embryo. However, as the sintering temperature continued to rise, there was a possibility of pore rupture and penetration, leading to an increase in the water absorption rate. Specifically, the water absorption rate increased by 9.61% from 1,200°C to 1,250°C and by 35.49% from 1,250°C to 1,300°C. These findings indicated that the sample contained more pores at higher sintering temperatures. Additionally, in the presence of multiple pores, the sample became more susceptible to cracking under pressure, decreasing compressive strength. The sample's compressive strength at 1,300°C was only 20.63% of that at 1,250°C. Similarly, the mass loss rate exhibited a significant increase, from 1.21% at 1,250°C to 4.37% at 1,300°C. While the sample demonstrated the lowest thermal conductivity coefficient at 1,300°C, their compressive strength and water absorption rate were poor. Therefore, a sintering temperature of 1,250°C was preferred.

Table 5 shows the properties of the samples under different heat preservation durations when the SiC content and sintering temperature were fixed at 1.0 wt% and 1,250°C.

According to Table 5, it can be observed that as the heat preservation time was extended, the bulk density of the sample decreased, and the water absorption rate increased. This was because a longer heat preservation time allowed for more complete foaming of the sample, resulting in a decrease in density, an increase in water absorption rate, and a decrease in compressive strength. For instance, at a heat preservation time of 60 minutes, the compressive strength was only 1.03 MPa, indicating a significant decrease of 78.32% compared to the 30-minute heat preservation time. The thermal conductivity coefficient increased when extending the heat preservation time from 50 minutes to 60 minutes, reaching 0.06 W/(m·K). This could be attributed to the appearance of more penetrating holes within the sample, enhancing gas convection and subsequently increasing the thermal conductivity coefficient. In addition, the mass loss rate in the acid resistance test also increased due to the increase of pores, rising from 1.21% at 30 minutes to 3.547% at 60 minutes. Thus, a heat preservation time of 30 minutes was more suitable.

Table 5. Effect of heat preservation time on performance.

	30 min	40 min	50 min
Bulk density, g/cm³	0.54	0.47	0.42
Water absorption rate, %	13.45	15.56	25.87
Compressive strength, MPa	4.75	2.02	1.46
Thermal conductivity coefficient, W/(m·K)	0.06	0.06	0.05
Acid-resistant mass loss rate, %	1.21	1.46	2.12

4. Conclusions

This study investigated the foamed ceramics prepared by sintering with SiC foaming agent to achieve better application of ceramic materials in practical construction projects. The results showed that increasing the amount of SiC led to more pores, higher water absorption rate, and lower compressive strength. An appropriate SiC content was found to be 1.0 wt%. Improving the sintering temperature resulted in a more complete reaction of the foaming agent, more pores, lower compressive strength and higher mass loss. An appropriate sintering temperature was determined to be 1,250°C. Extending the heat preservation time generated more internal pores in the samples, and the optimal time was 30 minutes.

A sample sintered using 1.0 wt% SiC at 1,250°C and insulated for 30 minutes exhibits good performance with a compressive strength of 4.75 MPa and a thermal conductivity coefficient of 0.06 W/(m·K), making it suitable for practical applications. However, this study also has some limitations. For instance, it only investigated the influence of sintering preparation processes on performance and lacked analysis of sample phase transitions and pore structures. In future work, a comparison will be made among more preparation methods, and the performance of the samples will be further analyzed.

References

[1] Zhang, P., Wang, W., Zheng, Y., & Hu, S. (2023). Effect of recycled aggregate and slag as substitutes for natural aggregate and cement on the properties of concrete: a review. *Journal of Renewable Materials*, 11(4), 1853–1879. doi: 10.32604/jrm.2023.024981

[2] Maslennikova, L.L., Babak, N.A., & Naginskii, I.A. (2019). Modern building materials using waste from the dismantling of buildings and structures. *Materials Science Forum*, 945, 1016–1023. doi: 10.4028/www.scientific.net/MSF.945.1016

[3] Rezaei, E., Barbato, M., Gianella, S., Ortona, A., & Haussener, S. (2019). Pressure drop and convective heat transfer in porous ceramic structures fabricated by additive manufacturing. *Journal of Heat Transfer*, 142(3), 032702. doi: 10.1115/1.4045732

[4] Shishkin, A., Aguedal, H., Goel, G., Peculevica, J., Newport, D., & Ozolins, J. (2021). Influence of waste glass in the foaming process of open cell porous ceramic as filtration media for industrial wastewater. *Journal of Cleaner Production*, 282, 124546. doi: 10.1016/j.jclepro.2020.124546

[5] Whitehouse, M.R., Dacombe, P.J., Webb, J.C.J., & Blom, A.W. (2013). Impaction grafting of the acetabulum with ceramic bone graft substitute mixed with femoral head allograft: High survivorship in 43 patients with a median follow-up of 7 years. *Acta Orthopaedica*, 84(4), 365–370. doi: 10.3109/17453674.2013.792031

[6] Feng, C., Guimares, A.S., Ramos, N., Sun, L., Gawin, D., Konca, P., Hall, C., Zhao, J., Hirsch, H., Grunewald, J., Fredriksson, M., Hansen K.K., Pavlik, Z., Hamilton, A., & Janssen, H. (2020). Hygric properties of porous building materials (VI): A round robin campaign. *Building and Environment*, 185, 1–14. doi: 10.1016/j.buildenv.2020.107242

[7] Wang, S., Zhang, X., Kuang, F., Li, J., Wang, Y., Wang, R., Wang, Y., Lin, X., & Li, J. (2019). Preparation and properties of a new porous ceramic material used in clean energy field. *Journal of Materials Science & Technology*, 35(7), 1255–1260. doi: 10.1016/j.jmst.2019.03.038

[8] Sandoval, M.L., Ramajo, L., & Camerucci, M.A. (2019). Cellular mullite materials processed by direct foaming and protein casting. *Journal of the European Ceramic Society*, 39(7), 2472–2483. doi: 10.1016/j.jeurceramsoc.2019.02.018

[9] Alias, S.I., Johar, B., Adam, S.N.F., Taib, M.A.A., Othman, F.F., & Yahya, H. (2022). Preparation of porous porcelain with treated flue gas desulfurization (FGD) sludges the foaming agent. *Key Engineering Materials*, 908, 245–249. doi: 10.4028/p-1xdpb0

[10] Hu, H., Zhong, H., & Zhang, B. (2022). Fabricating porous ceramic materials via phase separations in blends of cellulose acetate and ceramic nanoparticles. *Journal of the American Ceramic Society*, 105(8), 5461–5471. doi: 10.1111/jace.18497

[11] Jia, P., Watanabe, M., & Nakane, T. (2022). Development of porous ceramic thermal insulators. *Journal of the Technical Association of Refractories*, 42(2), 108.

[12] Yang, J., Xu, L., Wang, Z., Tang, Z., & Wu, H.Q. (2020). Preparation and properties of building decoration ceramic materials from spodumene flotation tailings. *Chemical Industry and Engineering Progress*, 39(9), 3777–3785. doi: 10.16085/j.issn.1000-6613.2019-1877

[13] Ochoa-Pérez, P., González-Crespo, A.M., García-Lucas, Á., Jiménez-Martínez, F.J., Vázquez-Rodríguez, M., & Pardo, L. (2021). FEA study of shear mode decoupling in nonstandard thin plates of a lead-free piezoelectric ceramic. *IEEE Transactions on Ultrasonics, Ferroelectrics, and Frequency Control*, 68(2), 325–333. doi: 10.1109/TUFFC.2020.2996083

[14] Dey, A., Kayal, N., Chakrabarti, O., Fortes, N.M., Innocentini, M. D. M., Molla, A. R., Sinha, P., & Dalui, S. (2021). Studies on processing of layered oxide-bonded porous sic ceramic filter materials. *International Journal of Applied Ceramic Technology*, 18(3), 869–879. doi: 10.1111/ijac.13717

[15] Ding, Y., Lu, Y., Yun, K., Liu, J., & Liang, N. (2021). The study on porosity controllable filter material for the integrated gasification combined cycle. *Solid State Phenomena*, 315, 10–15. doi: 10.4028/www.scientific.net/SSP.315.10

[16] Fang, W., Hou, L., & Li, Y. (2021). Foaming mechanism of SiC in steel slag foamed ceramics. *ISIJ International*, 61(3), 1043–1052. doi: 10.2355/isijinternational.ISIJINT-2020-271

[17] Zhu, X., Chi, R., Du, Y., Qin, J., Xiong, Z., Zhang, W., & Li, X. (2020). Experimental study on the key factors of low-loss threshing of high-moisture maize. *International Journal of Agricultural and Biological Engineering*, (5), 23–31. doi: 10.25165/j.ijabe.20201305.5653

[18] Safronova, N.A., Kryzhanovska, O.S., Dobrotvorska, M.V., Balabanov, A.E., Yavetskiy, R.P., Parkhomenko, S.V., Brodskii, R.Y., Baumer, V.N., Kosyanov, D.Y., Shichalin, O.O., Papynov, E.K., & Li, J. (2020). Influence of sintering temperature on structural and optical properties of Y2O3–MgO composite SPS ceramics. *Ceramics International*, 46(5), 6537–6543. doi: 10.1016/j.ceramint.2019.11.137

Physical and mathematical problems of 1D modelling of transonic two-phase flow in a convergent-divergent nozzle

Wojciech Angielczyk

Bialystok University of Technology, 45A Wiejska Street, 15-351 Bialystok, Poland
Author email: w.angielczyk@pb.edu.pl

Abstract

This work addresses the challenges associated with one-dimensional modelling of steady transonic two-phase flows illustrated through simulations of selected flow cases of the famous Moby Dick experiment. It primarily concentrates on the method for a fast determination of the transonic trajectory. The second proposed approach allows for determining trajectories describing the transonic flow with a normal shock wave. The first method is successfully verified by comparing its results with simulation results obtained from the (widely known and thoroughly verified) Wavefront Algorithm for High-speed Aerodynamics code, utilizing the Delayed Equilibrium Model. The first method mentioned is the author's proposition that is competitive to conventional (time-expensive) approaches such as the Newton Critical Point or achieving a steady flow description by asymptotical convergence of the time-dependent model's solutions, and it is a completely new consistent solution method. The second proposed method is an adaptation of the Rankine–Hugoniot jump conditions to a two-phase flow described by the Delayed Equilibrium Model. In the case of this method, the presented here analysis and results serve only as a proof of concept. Similar methods have been described before, but the results presented in this article, obtained with the Delayed Equilibrium Model, are unique. Also, a limited but coherent model of thermodynamic properties of a superheated liquid is presented and physically justified. This model was formulated earlier and is often used, but its comprehensive derivation has not been presented before.

Keywords: Transonic trajectory; Steady two-phase flow; Normal shock; Moby Dick experiment; Metastable liquid

1. Introduction

Flows encountered in machines and industry can be frequently classified as steady-state. These flows can be simulated using three-dimensional (3D) models of unsteady flow. Consequently, it may appear that current Computational Fluid Dynamics (CFD) methods adequately address the needs of designers, engineers and researchers. However, in practice, such methods are rarely employed at the initial stages of the flow analysis or description. This is mainly due to the extensive computational time required for CFD simulations with today's available computing

speed. The simulations are even more challenging when the fluid velocity magnitude passes through the value of the local sound speed [1]. Moreover, certain characteristics of the flow can only be evaluated through an analysis of the time-independent version of the model [2]. As a result, fast one-dimensional (1D) transonic steady-state approaches remain essential.

This article, therefore, reintroduces a fast general method of transonic trajectory determination (TTD) that is competitive with conventional time-consuming approaches (such as the Newton Critical Point [3] or asymptotical convergence of time-dependent solutions [4]). The method has been developed by the

Nomenclature

A – cross-section area of the flow channel, m^2
$\mathbf{A}$ – main matrix of the governing equation system
$\boldsymbol{b}$ – vector of the source terms
C – perimeter of the flow channel, m
c_p – specific heat at constant pressure, J/(kg K)
h – specific enthalpy, J/kg
l – dummy parameter
M – mass flow rate, kg/s
n – size of the velocity-state vector
p – absolute static pressure, MPa
q – heat flux, J/(s m^2)
r – channel radius, m
s – specific entropy, J/(kg K)
t – static temperature, ºC
T – absolute static temperature, K
v – specific volume, m^3/kg
$\boldsymbol{V}$ – vector tangent to the trajectory
w – velocity, m/s
x – saturated vapour mass fraction
y – saturation index
z – spatial coordinate, m

Greek symbols

α – void fraction
ρ – mass density, kg/m^3
$\boldsymbol{\sigma}$ – velocity-state vector
τ – shear stress, Pa
Ω – phase space

Subscripts and Superscripts

0 – intersection point of the subcooled liquid expansion curve with the saturated liquid line
B – flow channel inlet
c – critical
$calc$ – calculated
exp – experimental
IN – nozzle inlet
$onset$ – nucleation onset
sat – saturation
T – throat
w – wall

Abbreviations and Acronyms

CFD – computational fluid dynamics
DEM – delayed equilibrium model
HEM – homogeneous equilibrium model
HRM – homogenous relaxation model
IF – impossible flow
NCP – Newton critical point
PF – possible flow
PIF – possible-impossible flow
SMD LN – Super Moby Dick Long Nozzle experiment
TTD – transonic trajectory Determination
WAHA – wavefront algorithm for high-speed aerodynamics

author in a previous paper [5] but appears to be underappreciated and underutilized. This could be since in its original presentation [5] only the mathematical proof of its validity was given. Hence, this paper provides a more practical demonstration of the method's correctness. Namely, a confrontation of results obtained by application of the mentioned method with results obtained from the well-known Wavefront Algorithm for High-speed Aerodynamics (WAHA) code [6], utilizing the Delayed Equilibrium Model (DEM). To verify the method, selected flow cases of the Moby Dick experiment [7] were simulated and analysed.

The DEM was chosen because it is sufficiently complex in some mathematical aspects (the 5-component velocity-state vector) allowing for a demonstration of the method's universality. Moreover, previous studies have shown that it aligns closely with the subsonic results of the Moby Dick experiment, with excellent predictivity of the critical mass flow rate [8]. Nonetheless, any other two-phase homogeneous relaxation flow model could serve equally well for verification purposes [5]. In turn, the results of simulations using the WAHA code were selected as reference data, because the code has undergone extensive experimental validation [9]. Furthermore, simulations of the Moby Dick experiment conducted with the WAHA code were provided by the authors of the article [8].

The first known to the author attempts at formulating a general approach for Transonic Trajectory Determination (TTD) were conducted in the 1960s [10]. The cited report presents an approach, called the "optimum-point method", dedicated to single-equation nozzle flow models, including those with nonequi-

librium. However, single-equation flow models are generally too simplistic to accurately capture phenomena in flows other than gases. Consequently, this method lacks the generality needed for broader applications. The same report briefly describes other approaches but all of them focus on highly simplified models. In the late 1980s, significant advancements in TTD were made when the methodology of dynamical systems theory was successfully applied to a broad class of mathematical models describing 1D two-phase flows [2]. It was demonstrated that the direction of the transonic trajectory at the singular point can be determined using the aforementioned theory. This result was crucial for applying the shooting method to solve the initial-value problem (see Section 3). However, the models studied and the assumptions made, simplified the problem to the extent that the applied solution algorithms cannot be considered general methods. Subsequent work has tackled more complex flows, incorporating factors such as heat transfer between the fluid and the environment and friction effects. For instance, in [11], a version of the Newton Critical Point (NCP) method was applied to solve the compressible Euler equations, including gravity and heat source terms. While the method demonstrated speed and accuracy, this performance might be attributed to the simulations being limited to perfect gas flows without friction effects. Simultaneously, several codes were developed to describe 1D unsteady two-phase flows, including: RELAP5, TRAC, CATHARE, TRACE and WAHA. RELAP5 is a thermal-hydraulic simulation code developed for analysing flows and accidents related to light water nuclear reactor systems [12]. TRAC is a thermal-hydraulic code, devoted to nuclear reactor flows in general,

capable of handling non-equilibrium conditions [13]. CATH-ARE is an approach based on a six-equation two-fluid model, designed for reactor safety and accident analysis [14]. TRACE is a thermal-hydraulic simulation tool with multidimensional modelling capabilities, aimed at safety analysis of nuclear reactors [15]. WAHA is a 1D thermal-hydraulic code based on a six-equation two-fluid model for modelling transient flows such as water hammer and pressure wave propagation phenomena in piping systems [16]. It is capable of handling non-equilibrium conditions and flexible channels. RELAP5, CATHARE and WAHA are strictly 1D approaches while the remaining codes allow for 2D and 3D analysis. All the mentioned codes are transient flow approaches. Therefore, in the following years, the methods of solving the considered problems were dominated by the use of unsteady flow models in which the steady-state solution was obtained in asymptotic convergence of the transient-flow solutions. Although it was both practically verified and analytically demonstrated [17] that these traditional time-marching methods converge slowly. The most recent works, in which TTD did not involve the use of transient flow models, were conducted by teams that included the author of this paper. In [5], the developed methods were applied to modelling two-phase carbon dioxide flows. The determination of the critical mass flow rate in two-phase carbon dioxide flows using DEM and the Homogeneous Equilibrium Model (HEM) was investigated in [18]. Then, a development of the DEM was described in [19]. In these two papers, the methods proposed here were applied. In the most recent publication [20], the author critically analysed the relaxation equations used in modelling multiphase transonic flows. Admittedly, the proposed methods were not used, but many of the author's insights that emerged during the methods' development were applied.

The second proposed approach adopts the Rankine–Hugoniot jump conditions in a two-phase flow described by the DEM to predict the normal shock wave (that may potentially occur in the flow) and the trajectory following the shock. Thus, the proposal may be seen as not particularly innovative; However, to the best of the author's knowledge, this approach has only been theoretically outlined in the context of 1D modelling of steady transonic two-phase flows using the HEM and the Homogeneous Relaxation Model (HRM) [1]. More practically, in the context of the two-phase flows, it was investigated only in [21], but also with the application of a very simplistic model. Certainly, a similar method has not been used with the DEM. Furthermore, aside from this work, no practical (implementation-oriented) description of a comparable method has been published. This gap in the literature presents a unique opportunity to explore the method's applicability, which could lead to valuable insights into the research domain.

Nevertheless, the behaviour of normal shocks has been frequently investigated using transient models. For example, in [22], the WAHA code was applied to simulate the Moby Dick experiment flows that often contained a shock wave. Also, CFD methods were applied in similar kinds of simulations. For instance, the significant challenge of capturing shocks in steam turbines was addressed in [23]. In [24], the developed CFD model was successfully validated against the non-equilibrium condensation in Gyarmathy's nozzle under high-pressure conditions. Moreover, condensation-induced shock waves were well captured by this model. In [25], based on a CFD analysis, the Laval nozzle was designed to give a more significant pressure drop than a conventional nozzle by eliminating the shock wave strings at the nozzle throat.

2. The two-phase flow model and the submodels

2.1. Delayed Equilibrium Model

Due to the reasons explained in the introduction, the DEM was chosen to simulate the selected flow cases of the Moby Dick experiment. The DEM assumes the existence of three fractions, although it is treated as a two-phase model. Those fractions are the metastable liquid phase (subscript ML), the saturated liquid phase (subscript SL), and the saturated vapour phase (subscript SG). The metastable fraction is assumed to have the same pressure as the saturated phases but higher temperature, as it is assumed to undergo an isentropic expansion. Therefore, the DEM takes into account the thermal non-equilibrium effects, but it does not include the mechanical non-equilibrium effects (the velocities of the phases are equal since they are perfectly mixed – a homogenous mixture). The model consists of three conservation equations of mass, momentum, and energy, and two state equations (describing specific volume v and the specific enthalpy h), respectively:

$$w\frac{d\rho}{dz} + \rho\frac{dw}{dz} = -\rho w\frac{1}{A}\frac{dA}{dz}, \tag{1}$$

$$\frac{dp}{dz} + \rho w\frac{dw}{dz} = -\frac{\tau_w C}{A}, \tag{2}$$

$$\rho w\frac{dh}{dz} - w\frac{dp}{dz} = w\frac{\tau_w C}{A} + \frac{qC}{A}, \tag{3}$$

$$v = \rho^{-1} = (1-y)v_{ML} + (y-x)v_{SL} + xv_{SG}, \tag{4}$$

$$h = (1-y)h_{ML} + (y-x)h_{SL} + xh_{SG}. \tag{5}$$

Those equations describe a flow in a horizontal channel of variable cross-section area and contain the following quantities associated with the flowing two-phase mixture: p – the absolute static pressure, v – the specific volume, ρ – the mass density, w – the velocity, h – the specific enthalpy, x – the saturated vapour mass fraction, y – the saturation index. As well as the geometrical parameters of the flow channel (A – the cross-section area, C – the perimeter) that are functions of the spatial coordinate z measured from the channel inlet along its axis. Finally, τ_w is the wall shear stress (determined from the Lockhart-Martinelli model) and q is the heat flux. However, the last one is assumed to be zero since the flows in the transonic nozzle are treated as adiabatic.

The saturation index is defined as follows:

$$y = \frac{M_{SG} + M_{SL}}{M_{SL} + M_{SG} + M_{ML}} = \frac{M_{SG} + M_{SL}}{M} = x + \frac{M_{SL}}{M}, \tag{6}$$

where M stands for the two-phase mixture mass flow rate (the remaining M_S with appropriate subscripts stand for mass flow rates of the considered phases).

To complete the model, a mass balance equation for saturated fractions must be added to the system of Eqs. (1−5, 7). This closure equation has been developed for water [26] in the following form:

$$\frac{dy}{dz} = \left(C_1 \frac{c}{A} + C_2\right)(1-y)\left[\frac{p_{sat}(T_{ML})-p}{p_c - p_{sat}(T_{ML})}\right]^{C_3}, \qquad (7)$$

$C_1 = 0.008390, \quad C_2 = 0.633691 \text{ m}^{-1}, \quad C_3 = 0.228127.$

In the above relation, p_{sat} is the saturation pressure at the metastable liquid water temperature T_{ML} and p_c is water's critical pressure.

2.2. Metastable liquid thermodynamic properties model

The flow model presented in the previous section contains the thermodynamic variables of the metastable liquid phase, namely: v_{ML}, h_{ML} and T_{ML}. Therefore, it is required to formulate a submodel describing these quantities. Below, such a submodel is formulated. In fact, it is a simplified and limited version of the metastable liquid phase thermodynamic properties model, but it is consistent, simple, fast and clearly explained.

The specific enthalpy of the metastable fraction can be modelled based on the first law of thermodynamics in the form: $dh = vdp + Tds$ (s stands for the specific entropy). This form needs to be integrated from conditions determined by the intersection point of the subcooled liquid expansion curve with the saturated liquid line, up to conditions given by the mixture pressure p and temperature of the metastable liquid T_{ML}. If the properties in the mentioned intersection point are denoted with subscript 0 then the specific enthalpy of the metastable fraction is given by the following formula:

$$h_{ML}(p, T_{ML}) = h_0 + \int_{p_0}^{p}\left(v_{ML} + T_{ML}\frac{ds_{ML}}{dp}\right)dp. \qquad (8)$$

It is worth noticing that calculation of the specific enthalpy, with the above formula, requires utilization of a metastable liquid state equation to determine v_{ML} for given p and T_{ML}. As well as, additional assumptions/relations for calculating T_{ML} and ds_{ML}/dp. In this investigation (as in many others studies, e.g. [27,28]) it was assumed that the metastable liquid fraction is subjected to an isentropic expansion (thus $ds_{ML}/dp = 0$) and that it is incompressible:

$$v_{ML} = v_0, \qquad (9)$$

as a result, the metastable fraction specific enthalpy is a function of only pressure:

$$h_{ML}(p) = h_0 + \int_{p_0}^{p} v_0 \, dp = h_0 + v_0(p - p_0). \qquad (10)$$

In order to obtain an expression for T_{ML}, let us analyse the process starting from the state 0 by applying the first law of thermodynamics in the following way:

$$T_0 \, ds = dh - v_0 \, dp = k \, c_{p,0} \, dT - v_0 \, dp, \qquad (11)$$

where k is a correction factor that allows one to include the deviation of the considered process from the isobaric process. In the case of an ideal gas, the value of k is one, and the specific heat at constant pressure $c_{p,0}$ is constant. For simplicity, let us approximate the behaviour of the metastable liquid by those assumptions. Then, in the isentropic flow, the metastable liquid temperature is given by the following equation:

$$T_{ML} \approx T_0 + \int_{p_0}^{p}\frac{v_0}{c_{p,0}}dp = T_0 + \frac{v_0}{c_{p,0}}(p - p_0). \qquad (12)$$

2.3. Nucleation onset

Finally, the pressure at which nucleation in the metastable fraction starts must be specified. It should be noted that this quantity is decisive for the application of a metastable liquid flow model or a two-phase flow model. However, it may be related to the metastable liquid existence limits, which are determined based on the metastable liquid properties model [29]. Here, a simple approach is adopted (in order to be consistent with the WAHA code simulations), assuming that it is a function of the fluid temperature at the channel inlet T_{IN}:

$$p_{onset} = 0.965 \, p_{sat}(T_{IN}). \qquad (13)$$

2.4. Summary

Incorporating Eq. (4) and Eq. (5) into Eqs. (1−3), and then including Eq. (9) and Eq. (10) in the resulting system and Eq. (12) in Eq. (7), we derive a practical (ready for implementation) formulation of the model. This formulation consists of the equations for the conservation of mass, momentum, energy, and the closure Eq. (7), and it includes only the following gradients: $dA(z)/dz$, dp/dz, dx/dz, dy/dz, dw/dz, $dv_{SL}(p)/dz$, $dv_{SG}(p)/dz$. The first gradient is determined entirely by the flow channel geometry, while the last two depend solely on p. Moreover, in the applied Lockhart-Martinelli model $\tau_w = \tau_w(p, x, y, w)$, while A and C are functions of z. Thus, the practical formulation comprises four equations with four independent variables, which are the gradients of pressure p, vapour mass fraction x, saturation index y, and fluid velocity w.

3. Topological aspects of the modelling and conventional solution procedure

In a case where the flow channel inlet is fed with fluid/liquid in its supercritical, subcooled or metastable state, a single-phase flow model must be applied before a two-phase flow approach. The single-phase flow model consists of Eqs. (1)−(3) supplemented with state equations describing the supercritical, subcooled or metastable liquid properties. These governing equations operate until the nucleation onset. Subsequently, a two-phase flow model should be applied.

As long as the expansion goes from the supercritical state through subcooled and metastable liquid states the fluid compressibility remains low, ensuring that the flow is subsonic. Consequently, the single-phase flow model solutions could be determined by conventional forward-marching integration of the governing equations' system. However, the determination of the transonic solution of the DEM (or other two-phase flow models) is not that simple. It requires an in-depth topological analysis based on the dynamical systems theory, as conducted by Bilicki

et al. [2]. Below, only the essential elements of that analysis are presented, which are necessary to understand the foundation of conventional solution procedure as well as the proposed (in the next section) fast method.

3.1. General and autonomous form of the governing equation system

Practically all known one-dimensional models of a steady-state flow can be presented in the form of the following nonlinear ordinary first-order differential equation system [2]:

$$\mathbf{A}(\boldsymbol{\sigma}) \frac{d\boldsymbol{\sigma}}{dz} = \boldsymbol{b}(z, \boldsymbol{\sigma}). \tag{14}$$

The size and elements of the matrix $\mathbf{A}$ and the vector $\boldsymbol{\sigma}$ depend on the model type. The vector $\boldsymbol{\sigma}$ consists of n quantities describing a thermodynamic state of the fluid, and if necessary, the velocity of the fluid (in this case it is called the velocity-state vector). The elements of the matrix $\mathbf{A}$ depend only on $\boldsymbol{\sigma}'$s components, and $\boldsymbol{b}$'s elements additionally depend on the spatial coordinate z. The set of governing Eqs. (14) supplied with the vector $\boldsymbol{\sigma}_{\mathrm{B}} = [\sigma_{1,\mathrm{B}}, \sigma_{2,\mathrm{B}}, \ldots, \sigma_{n,\mathrm{B}}]$ (describing the flow inlet conditions, the inlet is located at z_B) creates an initial-value problem. A solution to the problem is a trajectory $\boldsymbol{\sigma}(z)$ in $n + 1$ dimensional phase space Ω, an approximation of which can sometimes be obtained by numerical integration of the equation system (14).

The system of Eqs. (14) can be solved with respect to the derivatives of $\boldsymbol{\sigma}$'s components by using Cramer's rule:

$$\frac{d\sigma_i}{dz} = \frac{N_i(z,\sigma)}{D(\sigma)}, \qquad i = 1, 2, \ldots, n, \tag{15}$$

where D denotes the determinant of $\mathbf{A}$, and N_i are determinants, each of which is created by replacing the i-th column of $\mathbf{A}$ with $\boldsymbol{b}$. The most practically useful form of the equation system is obtained by application of the dummy parameter l:

$$\frac{dz}{dl} = D, \qquad \frac{d\sigma_i}{dl} = N_i. \tag{16}$$

It is worth noticing that in the above autonomous form, the independent variable is not z but the dummy parameter l.

To complete this part, it should be noted that, in accordance with the previous section, the applied DEM uses a 5-component velocity-state vector defined as follows:

$$\boldsymbol{\sigma} = [z, p, x, y, w]. \tag{17}$$

3.2. Topological structure of the phase space

Each possible state of a system is represented as a point in the phase space Ω. For example, if in the mathematical model $n = 3$, then $\boldsymbol{\sigma}$ consists of three components—say, pressure p, enthalpy h, and velocity w. Consequently, the state of the fluid and flow in any cross-section of the flow channel is determined by the values of these three parameters, along with the spatial coordinate z. Thus, in this example, the phase space is 4-dimensional. In general, however, the phase space is $n + 1$ dimensional. For simplicity, the most interesting features of its structure are presented as projections onto the pressure p – spatial coordinate z plane, as shown in Fig. 1.
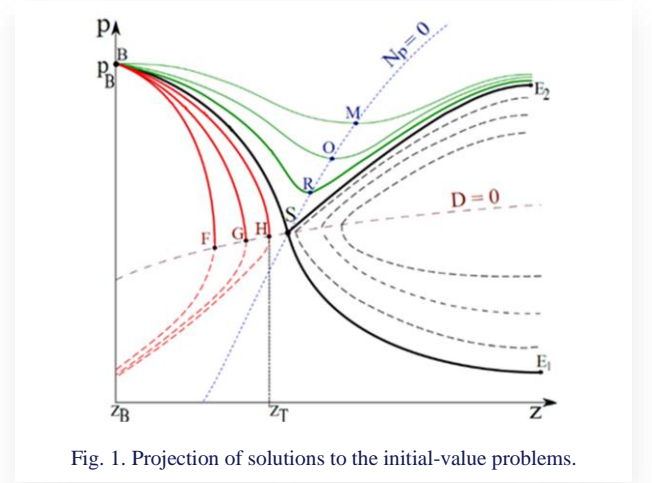

Fig. 1. Projection of solutions to the initial-value problems.

Accordingly, the black, green and red curves present projections of $n + 1$ dimensional trajectories on the $p-z$ plane. Each solid line is a projection of a solution to the initial-value problem mentioned in the previous subsection. The inlet conditions related to those flows differ only in the velocities. Consequently, all trajectories related to the solid lines start from the same values of the inlet pressure p_B, inlet density ρ_B and inlet specific enthalpy h_B but they are related to different mass flow rates.

Three distinct classes of points in the phase space must be distinguished:

1. **Regular points** at which $D \neq 0$. At each of these points, equation systems (14), (15) and (16) are equivalent. Any numerical forward-marching integration of system (14) starting from the inlet conditions $B = [z_B, \sigma_{1,\mathrm{B}}, \sigma_{2,\mathrm{B}}, \ldots, \sigma_{n,\mathrm{B}}]$ and proceeding toward the channel outlet through only the regular points, provides an appropriate approximation to a physically acceptable analytic solution. At such points, system (14) satisfies the existence and uniqueness requirements (only one trajectory passes through any regular point). A trajectory consisting of only regular points is fully subsonic or fully supersonic. Figure 1 shows projections of three subsonic trajectories − the green curves. They are called Possible Flow (PF) trajectories.

2. **Turning points** at which $D = 0$ and all $N_i \neq 0$. At those points, the systems (14) and (15) are not equivalent. Numerical integration of (14), in the vicinity of the turning point, produces a systematically accumulating numerical error. As a result, the integration could become impossible even before reaching the turning point. This is because $|d\sigma_i/dz| \to \infty$ while $D \to 0$. However, the autonomous system (16) satisfies the existence and uniqueness requirements at those points. Hence, during its numerical integration, one can simply pass through a turning point and can obtain a proper approximation of a trajectory that, at the turning point, changes direction along the z-axis (the red curves in Fig. 1). The one-dimensional steady-state flow cannot change direction in the channel. Therefore, those trajectories are physically acceptable only if they pass through a point of inlet conditions B and the turning point is located at the end of the channel. Consequently, the solutions that pass through turning points localized inside of the channel are called Im-

possible Flow (IF) trajectories.

In work [1], it was shown that $D = 0$ occurring at the channel end is also a choking criterion (or critical flow condition) since $D = 0$ means that at this point the fluid's velocity reaches the local speed of sound, and as a result, the mass flow rate and the subsonic part of the trajectory are unchangeable even despite a possible pressure drop occurring beyond the channel exit.

Figure 1 shows a projection of three IF trajectories (the red curves). They pass through the turning points F, G, H. Turning points determine the curve $D = 0$ (the projection of this curve is shown in Fig. 1 as the brown dashed line).

3. **Singular points** at which $D = 0$ and all $N_i = 0$. Here are considered only nondegenerate singular saddle points like S at which rank $(\mathbf{A}) = n - 1$ and through which exactly two trajectories pass. Namely, B-S-E$_1$ and B-S-E$_2$ in Fig. 1 (but only B-S-E$_1$ is "really" a transonic trajectory since on B-S-E$_2$ the velocity of the fluid reaches the speed of sound merely at point S to decrease just after it [1]).

According to Eq. (16), $dz = Ddl$ and $d\sigma_i = N_idl$. Therefore, at those points, finite changes Δz and $\Delta\sigma_i$ calculated by the numerical methods are equal to 0 regardless of the integration step size Δl. It means that the numerical algorithms cannot neither "start from" nor "pass through" this kind of points (they simply "get stuck" in these points - in the theory of differential equations, such points are called equilibrium points). Therefore, contrary to remaining trajectories, the transonic trajectory cannot be determined by a conventional numerical forward-marching integration (even of the system 16).

In [1], it was shown that when $D = 0$ and an arbitrary $N_i = 0$ then all remaining Ns also vanish.

3.3. Conventional solution method - NCP

Formally, NCP is a shooting method that starts from singular saddle points and uses the multidimensional, globally convergent Newton-Raphson algorithm to fit into given inlet conditions [11]. The general concept can be described in 4 steps:

1. Guess a singular saddle point coordinates.
2. Find the transonic trajectory passing through the singular saddle point (or at least, its subsonic part and related inlet conditions).
3. Calculate the deviation of the found solution at the channel inlet from the desired inlet values.
4. Figure out how to change the guessed singular point parameters (using the Newton-Raphson algorithm) to decrease the deviation calculated in the previous step.

Those steps are repeated until the aforementioned deviation is sufficiently low.

The above description (however excellent in describing the general concept) does not illustrate the enormous overall numerical operations number, and as a result, the huge time consumption connected with conducting the NCP procedure. The computation time is so high mostly due the step 4. This issue is extensively explained by the author in [30].

Nevertheless, NCP is still faster and more accurate than the asymptotical convergence to a steady state solution of the unste-

ady model solutions [11].

3.4. Possible-Impossible Flow algorithm

In fact, the Possible-Impossible Flow (PIF) algorithm is not able to determine the transonic trajectory related to given inlet conditions. Thus, it cannot be treated as a solution procedure for the problem considered. However, it is very fast and can be used as a preliminary step towards the solution. Since, with each PIF iteration, the region of phase space that contains the subsonic part of the sought trajectory is narrowed down. Thus, this trajectory part could be localized in an arbitrarily small region of the phase space (however, in practice, the numerical errors preclude restricting the region arbitrarily). The idea of PIF is based on the fact that the sought transonic trajectory lies between PF and IF trajectories (Fig. 1). As it was mentioned earlier, those trajectories can be easily obtained by numerical forward-marching integration of the equation system (16). The PIF algorithm has been widely used, for instance by Bouré et al. [31], or more recently by Lorenzo et al. [28] in the form that can be described in the following steps:

1. Calculate an intermediate mass flow rate $M = (M_{PF} + M_{IF})/2$ and related inlet velocity w.
2. Integrate system of Eqs. (16) from the inlet conditions and at each step, check if D has changed the sign.
3. If D has changed its sign before the end of the channel, then assign the value of M to M_{IF}. If D has not changed its sign before the end of the channel, then assign the value to M_{PF}.
4. If $(M_{IF} - M_{PF})$ is low enough then stop, otherwise go to point 1.

As a result of conducting the PIF algorithm, we obtain two values of the mass flow rate that are, respectively, the upper and lower limit for the critical mass flow rate. Similarly, we get two trajectories (IF and PF) that restrict the phase space to the region containing subsonic part of the sought transonic trajectory. Those "border" trajectories share with the transonic trajectory all values of the inlet parameters excluding velocity. The data obtained as a result of conducting the PIF algorithm are a basis for application of the fast transonic trajectory determination approach that is proposed in the next section.

In [30], the author proposed an even faster-converging version of the PIF algorithm.

4. Proposition of fast transonic trajectory determination approach

It is worth noting that the concept of a general procedure leading to TTD was initially, albeit imprecisely, introduced as early as in 1964 [10]: „The singularity problem can also be attacked by means of trial-and-error procedures, wherein numerous integrations are performed, each with a slightly different value for the mass flow (...). Once a subsonic solution is available that is sufficiently close to the critical one, the integration can then be started from a supersonic initial point obtained by extrapolating the subsonic solution across the singularity". The mentioned trial-and-error procedure is described in the previous subsection as the PIF algorithm, which at that time was not referred to by this name. However, the final step of the above procedure,

namely the extrapolation of the subsonic solution across the singularity, is the tricky part. It is crucial to precisely determine the point of the subsonic trajectory to start the extrapolation. From Fig. 1, it is evident that extrapolation from point R (or any point to its right) would fail, as it would result in a clear discontinuity in the obtained trajectory (or subsonic trajectory). Moreover, to extrapolate 'across the singularity' it is necessary to know where the singularity is located (the PIF algorithm does not localise it), and what 'across' means. Unfortunately, the author of [10] did not clarify those issues. He believed the approach would require a 'considerable consumption of computer time' and abandoned it. Instead, he developed a significantly less general method (briefly described in the introduction). In this section, not only are the 'mystery points' clearly identified and the procedures for their determination described, but also explanations are provided that refer to the previously characterized structure of the phase space and the initial-value problem, complementing and enhancing the aforementioned concept.

The proposed fast TDD method can be divided into four stages:

1. Conduction of the PIF algorithm in order to obtain approximations of trajectories around the singular saddle point.
2. Utilization of the obtained data for determination of the singular saddle point coordinates.
3. Determination of the direction of the transonic trajectory at the singular saddle point from the obtained data.
4. Integration "from" the singular point up to B and down to E_1.

4.1. Generalised method of singular saddle point determination

The proposed method utilises the fact that the saddle singular point is an intersection point of the following curves: $D(\boldsymbol{\sigma}) = 0$, $N_i(z, \boldsymbol{\sigma}) = 0$ (as shown in Fig. 1 or Fig. 2). In fact, the main determinant of the system of equations (14) D is not explicitly dependent on the spatial coordinate z. It depends on the components of the vector $\boldsymbol{\sigma}$. However, the solution of the initial-value problem determines value distributions of the components along the nozzle (Fig. 1) and thus it assigns a spatial coordinate for each value of D. Therefore, the points at which $D = 0$ can be presented (in any $\sigma_i - z$ plane) as curve $D(\boldsymbol{\sigma}(z)) = 0$ consisting of turning points that belong to different trajectories (e.g. point G and H in Fig. 2).
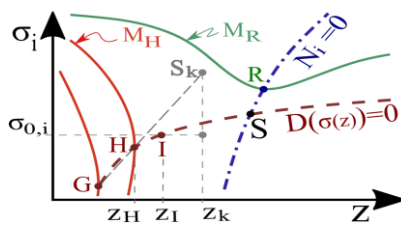

Fig. 2. Illustration of the singular saddle point S determination.

As a result of conducting the PIF algorithm, a set of trajectories is obtained. Each trajectory can be recognized as an IF or a PF trajectory (as explained earlier). However, to perform the considered procedure, only one last-found PF trajectory (green solid line in Fig. 2) and two last-found IF trajectories (red solid lines in Fig. 2) are required. Nevertheless, the PIF algorithm must be conducted at least to the iteration in which the turning point spatial coordinate of the last-found IF trajectory is not lower than the nozzle throat coordinate ($z_H \geq z_T$). The mentioned trajectories, together with the channel geometry, determine the related mass flow rates. The necessary two of them are presented in Fig. 2, namely, M_H and M_R.

Determination of the saddle singular point approximation requires the following steps:

1. Approximate the curve $D(\boldsymbol{\sigma}) = 0$ by the straight line passing through points G and H.
2. Determine a point $S_k(z_k, \sigma_k)$ that lies on the line. At this point $z_k = z_H + \Delta z$.
3. Take $M_i = M_H + \Delta z(M_R - M_H)/(z_R - z_H)$.
4. Use the gradient descent method (take $\boldsymbol{\sigma}_k = [\sigma_{k,1}, ..., \sigma_{k,n}]$ as a starting point) to determine $\boldsymbol{\sigma}_0 = [\sigma_{0,1}, ..., \sigma_{0,n}]$ for which $D = 0$ but keep $w\rho = M_i/A(z_i)$ at each step of this method.
5. Determine z_I that satisfies the mass conservation equation: $A(z_I) = M_i/[\rho(\boldsymbol{\sigma}_0) \cdot w(\boldsymbol{\sigma}_0)]$. Point $I(z_I, \boldsymbol{\sigma}_0)$ lies on the approximation of the $D(\boldsymbol{\sigma}_0) = 0$ curve.
6. If all N_i at point I have different signs than in point H, then repeat the previous steps with smaller Δz until the required accuracy is reached (if the accuracy is reached, I is the sought approximation of the singular saddle point S). Otherwise, go to the first step but replace G with H and H with I.

The gradient descent method (also called the steepest descent method) is a first-order iterative optimisation algorithm for finding the minimum of a function [32]. However, here the algorithm was used to find $\boldsymbol{\sigma}_0$ at which $D = 0$. This is based on the fact that between the starting point where $D > 0$ and the point where D has a negative minimum value there is a point at which $D = 0$.

The proposed method is generalised in the sense that it may be applied for any model described by Eq. (14) regardless of the equations number. The singular point found by means of the above algorithm corresponds to certain inlet conditions. Those conditions may be thought as the better approximation of the original inlet conditions (Fig. 1, point B) since points G and H are located close to point S. In other words, the higher the number of PIF iterations, the better the accuracy of the solution.

4.2. Determination of a vector tangent to the transonic trajectory at the singular point

Figure 3 shows the points L, N, P that are inflection points of the subsonic trajectories. Each of the vectors: V_L, V_N, V_P is tangent to a trajectory at a corresponding inflection point. The points M, O, R represent local pressure minima. It is worth noticing that the closer to point S the subsonic trajectory lies, the closer the inflection point of this trajectory is to the pressure minimum point of this trajectory. Finally, at the transonic trajectory those points merge together into point S. Consequently, the direction of V_1 can be approximated by the direction of V_P. Thus, to perform the considered procedure, only the last-found (by the PIF algorithm) PF trajectory is required. The higher the number of
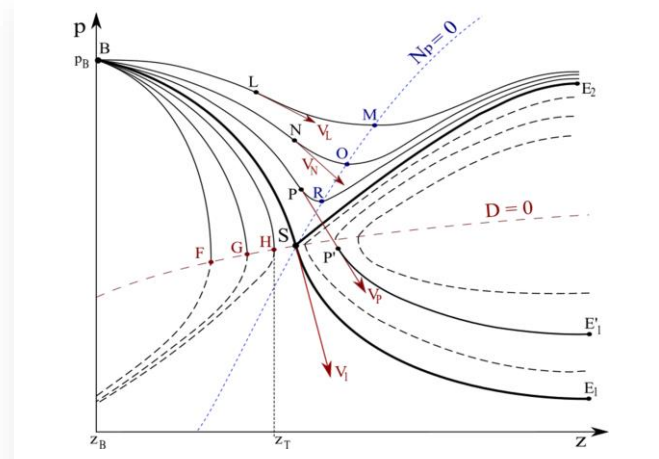
Fig. 3. Projection of the solutions to the initial-value problem on plane $p-z$ and vectors tangent to PF trajectories at inflection points.

PIF iterations, the smaller the distance between points R and S and the better accuracy of the V_1 direction approximation.

The direction of V_P can be directly used to carry out the integration "from" the found saddle singular point giving an approximation (B-P-P'-E$_1$') of the subsonic and supersonic parts of the sought transonic trajectory. Nevertheless, the higher accuracy can be reached by using V_P as a first guess for well-known iterative methods of eigenvector determination, e.g. the inverse power method [32].

The topological considerations revealed that it is impossible to start integration strictly from the singular point. Thus, it is now necessary to clarify the previously used mental shorthand: integration "from" the singular point.

Making a step (either upstream or downstream) along V_1 (or its approximation) determines a point that is eligible for starting numerical integration. The up-stream integration when it reaches z_B, determines the inlet conditions corresponding to the considered singular saddle point. Similarly, down-stream integration determines the outlet conditions. Therefore, the described procedure is a solution to an initial-value problem of the system of equations (16) with initial values: $z = z_S$ and $\sigma = \sigma_S$.

5. Proposition of after-shock trajectory determination approach

Oblique shocks, expansion waves, and complex shock interactions require at least 2D modelling to be fully represented. Mostly because they involve strong changes in both the magnitude of flow variables and the flow direction. However, since normal shock waves are perpendicular to the flow direction and cause abrupt changes in flow properties (such as pressure, temperature, density and velocity) without a flow direction change, they can be captured in 1D modelling. A normal shock wave forms when the supersonic flow decelerates to subsonic speed. In a convergent-divergent nozzle, this type of shock typically appears near the throat in the divergent section.

Figure 4 depicts a transonic trajectory (S-1-E$_1$) consisting of the subsonic part (on the left side from point S) and the supersonic part (on the right side from point S). A normal shock can theoretically occur at any point along the supersonic portion of

the trajectory (for example at an arbitrary point 1) and the already mentioned jump from the supersonic to subsonic speed must satisfy the conservation of mass, momentum and energy (or in other words the Rankine-Hugoniot relations). For the initial point 1, infinitely many possible subsonic states satisfy the required conditions.
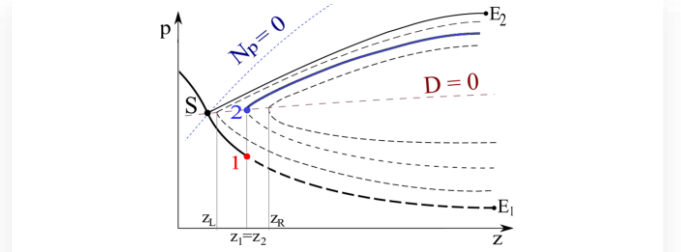

Fig. 4. Normal shock wave in 1D modelling.

However, an assumption that the jump is associated with the lowest possible entropy generation determines state 2 (that lies on the curve $D = 0$, Fig. 4) as the final (after-shock) state. Downstream integration of the system of Eqs. (16) from this state yields a subsonic after-shock trajectory depicted as the blue line in Fig. 4. However, to integrate toward the outlet section the sign of the integration step size dl must be chosen such that $Ddl > 0$. It is worth emphasizing that the brown line segment on the left side of S is distinct from the segment on the right side, even though the condition $D = 0$ is satisfied on both sides. Each point on the left part corresponds to a different mass flow rate, while the points on the right side are associated with a constant mass flow rate, specifically that of the transonic trajectory (S-1-E$_1$).

Figure 5 presents the flowchart for the point 2 determination algorithm. The blocks in the orange frame are the implementa-
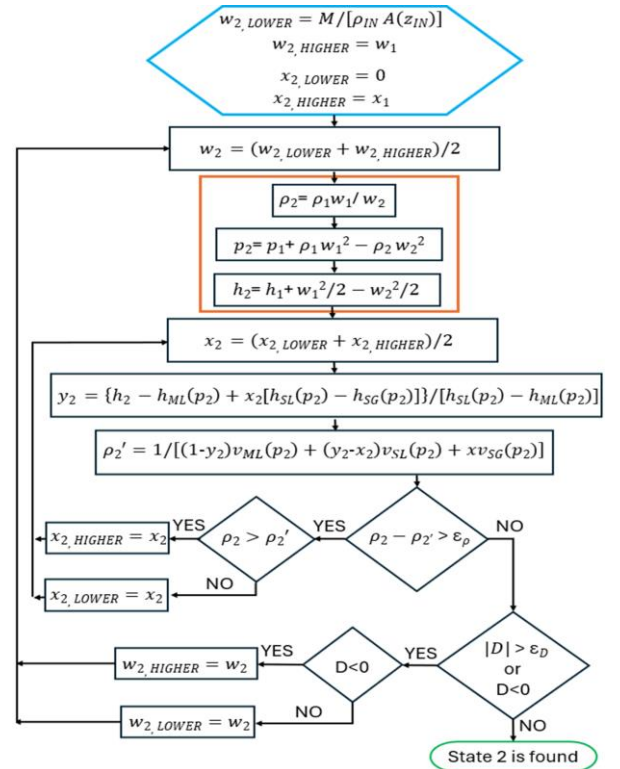

Fig. 5. Flow chart of after-shock fluid state determination approach.

tion of the Rankine-Hugoniot relations. The values of ε_ρ and ε_D determine the accuracy of the solution.

The blocks describing how to calculate y_2 and ρ_2' are correct only for the DEM but with appropriate modifications, the algorithm can be used with other models.

Figure 4 illustrates that, for a constant mass flow rate (represented by the specific brown curve), changes in the flow variables due to the jump depend on the spatial coordinate as well as the shape and orientation of the curve.

6. Implementation of the solution procedures

The methods proposed in this article, along with the author's improvements to the PIF algorithm, the model of metastable liquid properties and the Lockhart-Martinelli model were integrated into the described procedure for solving the initial-value problem and implemented in C++. The water properties were determined using library functions from the CoolProp program [33].

7. Results and discussion

The primary objective of this section is to verify the correctness of the proposed fast TTD method. Therefore, differences between the solutions determined using the proposed method and those obtained with the WAHA code are presented. Experimental data on the simulated flows are provided mostly as evidence that the simulated flows are indeed transonic. Consequently, the degree of convergence between the simulation results (obtained with the fast TTD method) and the experimental

data is insignificant (experimental validation of the DEM is not the purpose of this article). The comparison between experimental data depicting shock waves and the results obtained from the proposed shock wave modelling approach serves solely as a proof of concept, employed here due to the lack of other verification methods.

7.1. Verification of the fast transonic trajectory determination approach

Simulation result quality depends on the model chosen and the methods applied to obtain these results, and it should always be assessed through experimental validation. However, to verify the solution method (or its part), it is essential to compare its results with those obtained from another, ideally unquestionable, solution method using the same model, submodels and flow cases. Therefore, to verify the correctness of the proposed fast TTD method, simulation results of the WAHA code using the DEM model were chosen. Those results refer to selected flow cases of the Moby Dick experiment. Only cases exhibiting unquestionable shock waves have been considered, as these undeniably represent instances of transonic flow. From these cases, only those with a high probability of being normal shock waves were selected. As previously explained, the closer a shock wave forms to the nozzle throat, the more it resembles a 1D capturable shock wave (a normal shock wave). However, if the shock occurs too close to the throat, the supersonic trajectory segment is too short for adequate method verification. The cases that best meet the described requirements were used to verify the method and are presented in Figs. 6−8.
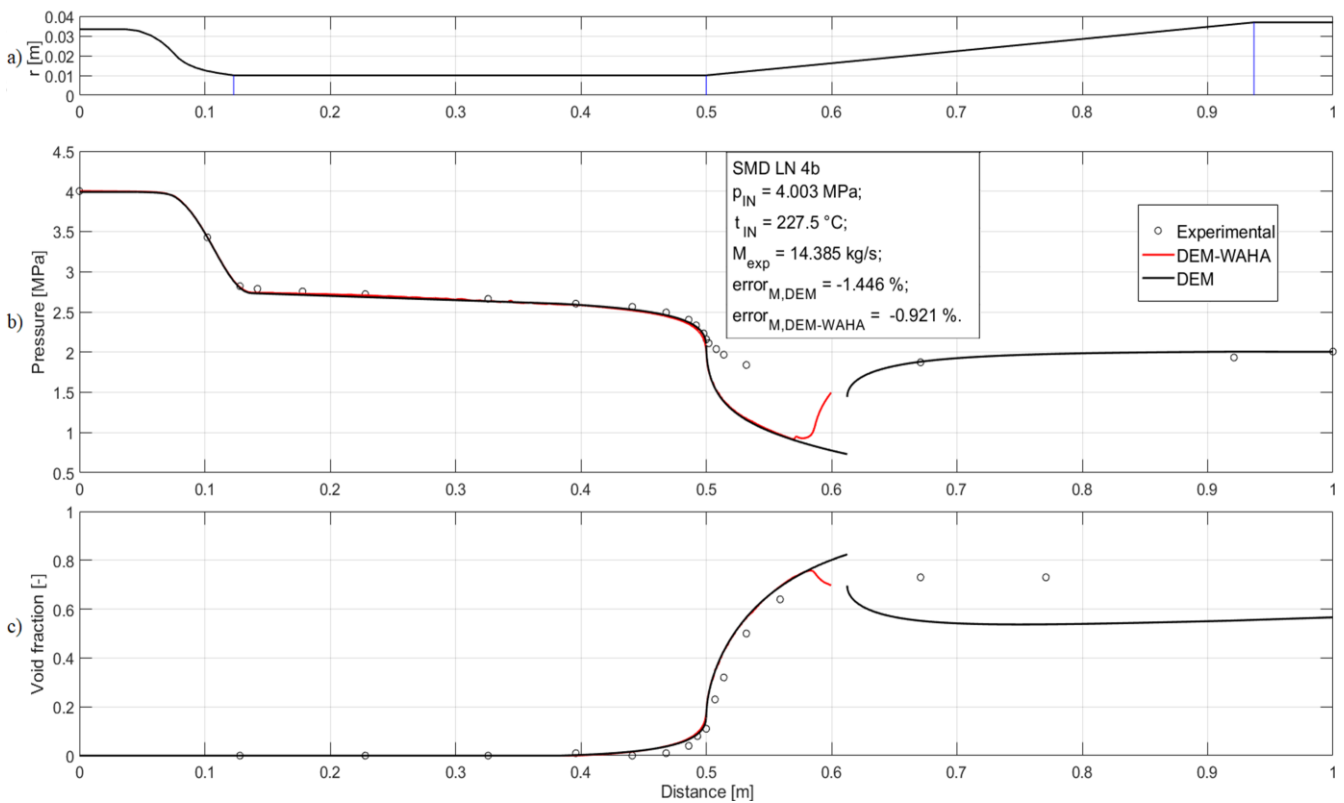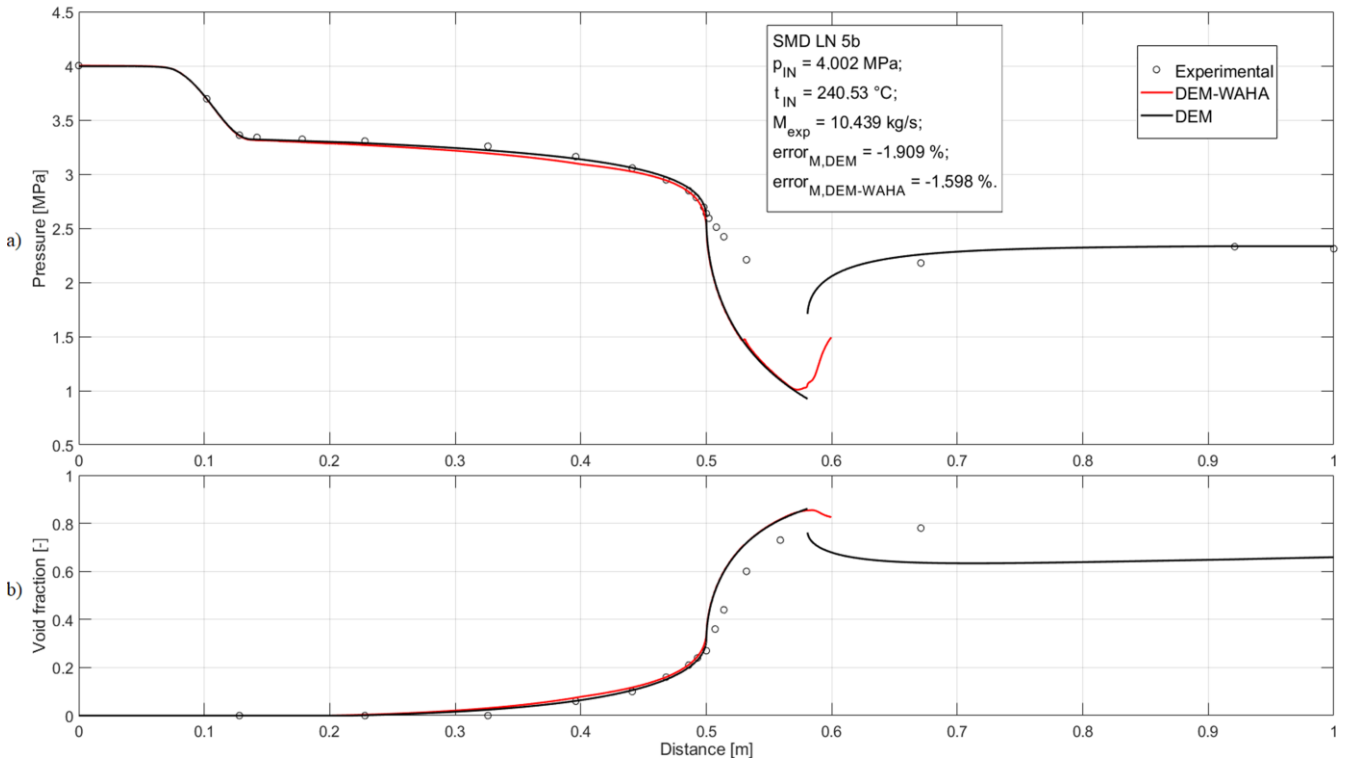

Fig. 6. Verification of the proposed TTD method by comparison with simulation results obtained from the WAHA code. Moby Dick experiment, flow case 4b: a) the experimental nozzle geometry (r – channel radius); b) the absolute static pressure distribution; c) the void fraction distribution.

Fig. 7. Verification of the proposed TTD method by comparison with simulation results obtained from the WAHA code. Moby Dick experiment, flow case 5b: a) the absolute static pressure distribution; b) the void fraction distribution.
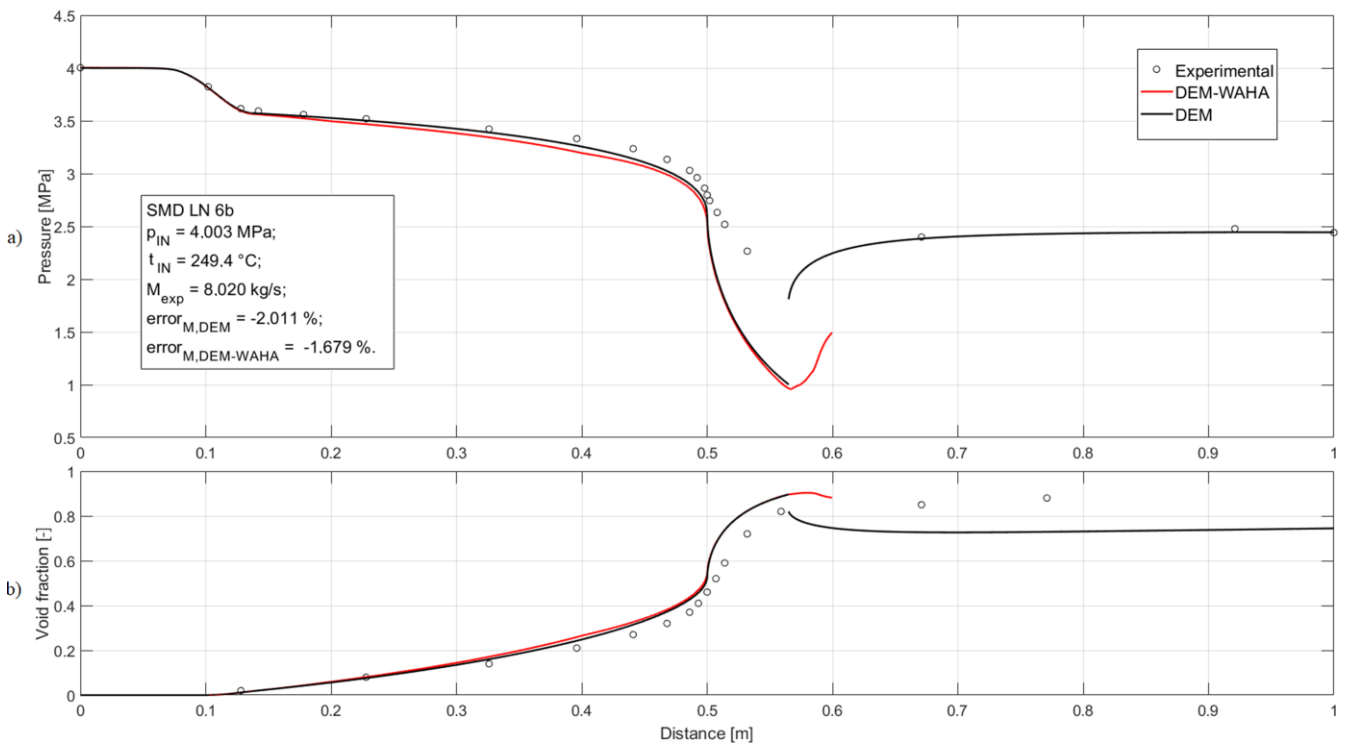

Fig. 8. Verification of the proposed TTD method by comparison with simulation results obtained from the WAHA code. Moby Dick experiment, flow case 6b: a) the absolute static pressure distribution; b) the void fraction distribution.

The WAHA code is designed to model the behaviour of shock waves and other complex flow phenomena in high-speed flows. It uses a time-dependent 1D six equation two-fluid model. The authors of the article [8] implemented the DEM using the functionality of the WAHA code and subsequently simulated the flow cases of the Moby Dick experiment. They ob-

tained results through the asymptotic convergence of the unsteady solutions to the steady-state solution. Due to the high time consumption of this method, they restricted their calculations to the nozzle cut at a distance $z = 0.6$ m from the inlet cross-section (the experimental nozzle geometry is illustrated in Fig. 6a) assuming that the absolute static pressure at this new outlet cross-section is a fraction of the pressure at the nozzle inlet:

$$p(z = 0.6 \text{ m}) = 0.37 \, p_{IN}. \tag{18}$$

Those calculations resulted in data describing water transonic flows with a shock wave (Figs. 6−8, the red lines).

For each of the three selected flow cases, the absolute static pressure distribution (shown in Figs. 6b, 7a and 8a) and the void fraction distribution (shown in Figs. 6c, 7b and 8b) along the nozzle are presented.

In all cases, the inlet pressure is nearly identical ($p_{IN} \approx$ 4 MPa), while the inlet temperatures differ. In case 4b, the liquid entering the nozzle is the most subcooled, whereas in case 6b, it is the least subcooled. This is reflected in the void fraction distributions (for both simulations and experimental data): in case 6b, the void fraction rises above zero at the smallest distance from the throat ($z_{exp} \approx 0.12$ m), while in case 4b this occurs at the largest distance ($z_{exp} \approx 0.45$ m). The initial perfect convergence of the calculated void fraction distributions (the black and red lines) confirms that the same condition for the onset of nucleation was applied in both simulations, Eq. (13).

In all cases, the differences between the two simulations are meaningful for the verification only up to $z \approx 0.52$ m. From this cross-section onward, the shock waves predicted by DEM-WAHA have a rapidly increasing impact on the preceding parts of the red trajectories. In the proposed steady flow approach marked with DEM (the black line), the shock wave does not influence the trajectory in front of it (this is a direct consequence of the features of the proposed method and can be seen in all figures as a discontinuity of the black line). In the case of the unsteady asymptotic approach (DEM-WAHA), this influence is present due to the nature of the applied solution method: the asymptotic convergence never fully captures the discontinuity (in other words, accurately reflecting this discontinuity would require an infinitely long computation time). Therefore, the discrepancy between the solutions being compared, introduced by the DEM-WAHA shock waves, should not be included in the verification process. This can be easily accomplished by analysing only the differences between DEM and DEM-WAHA distributions before $z = 0.52$ m. Such comparison is shown in Fig. 9. The relative discrepancy between pressure predictions for a cross-section located at a distance z from the nozzle inlet was calculated as follows:

$$\Delta_p(z) = \frac{p_{DEM-WAHA} - p_{DEM}}{p_{DEM-WAHA}} \, 100. \tag{19}$$

Figure 9 indicates that the maximal absolute discrepancy for all flow cases appears near the nozzle throat ($z_T = 0.5$ m). However, the absolute relative discrepancy in the worst-case scenario (flow case 4b) is slightly less than 9%. The analogue verification was conducted based on the comparison of void fraction distributions. However, for the article conciseness, it is not presented.
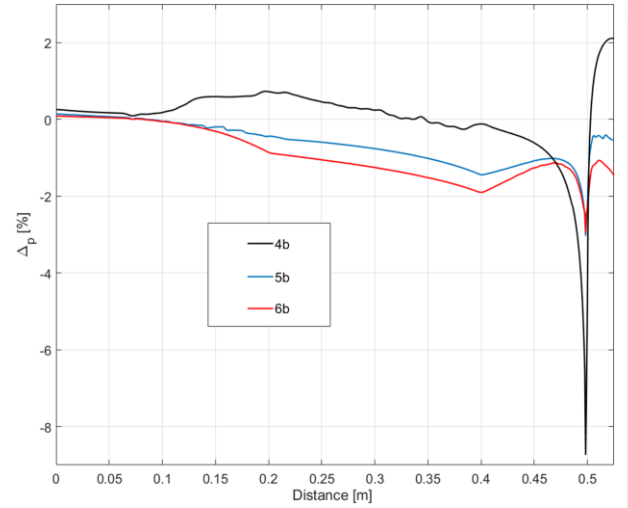

Fig. 9. Distribution of the relative discrepancy between pressure predictions, see Eq. (19).

The author decided it is sufficient to mention that the relative discrepancy in void fraction distributions is calculated in the following way:

$$\Delta_\alpha(z) = \frac{\alpha_{DEM-WAHA} - \alpha_{DEM}}{\alpha_{DEM-WAHA}} \, 100, \tag{20}$$

and achieves the maximal absolute value of approximately 6% also in case 4b.

The nature of the flows considered is such that pressure decreases monotonically until a shock wave occurs. Consequently, the denominator in Eq. (19) also decreases. This means that even if the pressure difference in the numerator (and thus the error) remained constant, the relative error would still increase. Therefore, it should be acknowledged that the relative error calculated using Eq. (19) is unfavourable for the positive verification of the proposed method, although it remains below 10%. The more favourable relative error can be obtained by putting in the denominator of Eq. (19) a mean pressure of the process ($p_{mean} \approx$ 2.37 MPa), then the absolute maximal relative discrepancy is around 7%. Even more favourable is putting in the denominator the inlet pressure, then the absolute maximal relative discrepancy is around 4.2%.

In the author's opinion, these facts lead to the conclusion that the correctness of the fast TTD method is positively verified.

It is worth noting that Fig. 9, before $z = 0.45$ m, shows oscillations − or rather noise, particularly in cases 4b and 5b − and refractions, which are most noticeable in cases 6b and 5b. The noise on the right side of Fig. 9 may stem from the shock wave predicted by the DEM-WAHA model. However, the mentioned noise observed on the left side appears exclusively in the sections associated with single-phase flows (before the nucleation onset). The author suspects that to accelerate the DEM-WAHA calculations, a single precision was used in those sections, which likely contributed to the observed noise. The mentioned refractions are due to differences in the spatial discretization of the nozzle geometry. For all presented flow cases, DEM-WAHA uses the same spatial discretization (in the range shown in Fig. 9, this consists of 693 intervals, each 0.75 mm long). In contrast, DEM, using the proposed methods, operates with an adaptive

integration step, resulting in a different spatial discretization for each flow case (that is not uniform also along the nozzle). Within the mentioned range, case 4b required the fewest intervals (3 028), while case 6b required the most intervals (5 659). The author believes that if DEM-WAHA calculations were performed with identical discretization, for each case, as that applied in DEM, the discrepancy between the simulations would be even smaller than those presented above.

7.2. Verification of after-shock trajectory determination approach

In Figs. (6)−(8), experimental data (represented by circles) show absolute static pressure distributions. In all flow cases, a monotonic pressure drop is observed up to $z = 0.532$ m. However, for all cases considered, the next data point at $z = 0.671$ m shows a pressure higher than that at $z = 0.532$ m. The substantial distance between these points, along with the convex shape formed by the four points, preceding the point at $z = 0.532$ m, indicates the presence of a shock wave between $z = 0.532$ m and $z = 0.671$ m. The flows are therefore transonic: the fluid velocity increases monotonically from the inlet to the cross-section slightly downstream of the throat, where it passes through the value of the local speed of sound and then in the divergent nozzle part (somewhere between $z = 0.532$ m and $z = 0.671$ m) the velocity decreases to a value lower than the local speed of sound.

The above-mentioned figures also present the distributions of void fraction, experimental critical mass fluxes and the error associated with each simulation in predicting these fluxes. This error was calculated as follows:

$$error = \frac{Mexp - Mcalc}{Mexp} 100. \tag{21}$$

It is evident that each of the simulations, thus DEM itself, predicts the pressure distributions and void fractions accurately up to the nozzle throat ($z = 0.5$ m). However, the pressure drops beyond the throat are highly overestimated, leading to an overestimation of the void fractions in the associated region.

The predicted shock waves in Figs. (6)−(8) are represented by the discontinuities in the black lines. It can be seen that the subsonic trajectories behind these discontinuities align well with the last three experimental pressure points in each of the flow cases. However, this alignment does not validate the proposed method: the relatively flat trajectories predicted by DEM in this region, make it easy to adjust the jump (discontinuity) location to achieve a trajectory that matches the mentioned points but the experimental void fraction distribution is not well approximated by this trajectory. This demonstrates that the implemented DEM is not capable of accurately describing the shock wave, which is not surprising given that Eq. (7) was developed based on data that only capture the distributions up to the throat − specifically related to flashing − and therefore does not account well for condensation that is caused by the shock wave and for the influence of the diffuser geometry on the following subsonic flow.

If these trajectories accurately described both the void fraction and pressure distributions, it would imply that DEM together with the proposed method are effective for predicting normal shock waves. Unfortunately, this is not the case; thus,

the presented data can only serve as proof of concept. They demonstrate that the method has been implemented and utilized with DEM. Moreover, the results obtained do not reveal any errors or inconsistencies in the method.

8. Conclusions

The proposed fast method for determining transonic trajectories is competitive with traditional, time-consuming approaches (such as the Newton Critical Point method or the asymptotic convergence of time-dependent solutions). The novelty of the proposed method lies in leveraging the well-known fast PIF algorithm to confine the phase space region, enabling the application of the author's (new) techniques for identifying the saddle singular point and determining the trajectory passing through it. The author also enhanced the PIF algorithm to achieve greater speed and ensure compatibility with the proposed approaches. This paper not only provides a mathematical description of the method but also offers a computational verification: a confrontation of results obtained by application of the mentioned method with results obtained from the well-known WAHA, utilizing DEM. The maximum absolute pressure discrepancy between the compared simulations (calculated conservatively) was less than 9%, which the author considers sufficient to prove the correctness of the method. This method can be applied to models as complex as DEM (such as HRM) as well as to simpler models (such as HEM and Isentropic Homogeneous Equilibrium model).

The presented analysis regarding the proposed normal shock wave modelling serves as proof of concept: the proposed method has been successfully implemented and it operates with DEM (however it can be used also with HRM, HEM and Isentropic Homogeneous Equilibrium model). Furthermore, the results obtained do not indicate any inconsistencies in the method. In the case of this method, the novelty is its implementation-oriented description that allows for easy implementation for all the above-mentioned models. Moreover, for DEM, such a method was never applied before this work. Thus, the presented results are unique.

For transonic flow with a constant mass flow rate, variations in flow variables across the shock depend on both the spatial location of the shock and the shape and orientation of $D = 0$ curve. The latter is influenced by the type of two-phase flow model applied.

After comparing the simulation results with experimental data, it has become clear that together with the implemented DEM, the proposed method is unable to accurately describe the shock waves: it can provide a precise representation of the pressure distribution behind the shock wave, but the corresponding void fraction distribution is significantly underestimated compared to the experimental data. The author thinks that this discrepancy partially arises from the application of Eq. (7), which was developed based on data that only consider distributions of flow variables up to the throat and does not adequately account for the condensation induced by the shock wave. However, also the proposed algorithm of the after-shock trajectory determination can be responsible as it assumes that the jump (shock) is associated with the lowest possible entropy generation. Thus,

the resulting following shock void fraction is lower than this caused by higher entropy generation. In the future, the contributions of each of these mechanisms should be thoroughly investigated and modelled accordingly. Finally, as the least probable reason, it should be pointed out that, contrary to the assumption adopted, the analysed waves may not be normal shock waves but oblique shock waves. In such a case, neither the presented modelling nor the measurement techniques used in the experiment are sufficient to describe and capture this phenomenon.

Finally, it is important to summarize the key advantages and limitations of the proposed methods. The disadvantages are relatively few, with the most significant being the need to develop a custom implementation of the calculation procedures described. While existing numerical libraries (available for many programming languages) can assist in this process, it remains a labour-intensive task that requires both programming expertise and the ability to apply numerical methods to simulate flow phenomena effectively. Integrating the proposed methods into commercial solvers such as Fluent of the ANSYS environment seems to be possible by using the User-Defined Function functionality. Probably the biggest advantage of such an implementation would be the possibility of using a user-friendly (graphical) interface when defining the boundary conditions of the simulation and performing calculations. However, the author anticipates that the biggest advantage of the presented procedures, namely the short computation time, may be compromised in such an implementation. The second major limitation is that the proposed procedures cannot be extended to determine time-dependent solutions. Consequently, these methods are not suitable for modelling unsteady flow. However, it is important to note that any unsteady flow model must first be validated against its steady-state version, for which the presented methods are indispensable.

The primary advantage of the described methods lies in their exceptional speed, making them suitable for incorporation into more complex, multi-stage, and multi-iterative analyses. Another significant benefit is that the solutions produced are considerably smoother than those obtained using the WAHA code. This smoothness simplifies interpretation of the results, as potential irregularities or non-monotonic behaviour in the trajectory are more likely to reflect actual phenomena rather than artefacts of the solution method. Furthermore, if doubts about the results arise, the high computational efficiency of these methods allows for easy repetition with a substantially increased number of steps, which would be far more challenging with conventional approaches.

Another major advantage is that, outside the vicinity of the singular saddle point, the methods enable dynamic adjustment of the integration step size. This feature enables acceleration of the calculations for specific flow channel geometries (pipes, slowly changing cross-section area channels) while making it possible to enhance the accuracy in areas where geometry remains unchanged, but the onset of nucleation requires a reduction in the integration step.

References

[1] Bilicki, Z., & Kestin, J. (1990). Physical aspects of the relaxation model in two-phase flow. *Proceedings of the Royal Society of London A: Mathematical, Physical and Engineering Sciences*, 428(1875), 379–397. doi: 10.1098/rspa.1990.0040

[2] Bilicki, Z., Dafermos, C., Kestin, J., Majda, G., & Zeng, D.L. (1987). Trajectories and singular points in steady-state models of two-phase flows. *International Journal of Multiphase Flow*, 13(4), 511–533. doi: 10.1016/0301-9322(87)90019-X

[3] De Sterck, H. (2007). Critical Point Analysis of Transonic Flow Profiles with Heat Conduction. *SIAM Journal on Applied Dynamical Systems*, 6(3), 645–662. doi: 10.1137/060677458

[4] Yee, H.C. (1994). Basins of attraction and the time-dependent approach to obtaining steady-state numerical solutions. In *Numerical Methods for Fluid Dynamics* (pp. 135−162). Oxford Academic. doi: 10.1093/oso/9780198536963.003.0009

[5] Angielczyk, W., Śmierciew, K., & Butrymowicz, D. (2019). Application of a fast transonic trajectory determination approach in 1-D modelling of steady-state two-phase carbon dioxide flow. *E3S Web of Conferences*, 128, 06005. doi: 10.1051/e3sconf/201912806005

[6] Seynhaeve, J.M., & Giot, M. (2004). The WAHA code: a numerical tool for water hammer in two-phase flow - some simulations of experiments. *117. session of the scientific and technical committee of the French hydro-technical society „Advances in the modelling methodologies of two-phase flows"*, 24-26 November, Lyon, France.

[7] Banaszkiewicz, M., & Kardaś, D. (1997). Numerical Calculations of the Moby Dick Experiment by Means of Unsteady Relaxation Models. *Journal of Theoretical and Applied Mechanics*, 35(2), 211−232.

[8] Bartosiewicz, Y., & Seynhaeve, J.M. (2013). Delayed Equilibrium Model (DEM) of Flashing Choked Flows Relevant to LOCA. *Multiphase Science and Technology*, 25(2–4), 117–131. doi: 10.1615/MultScienTechn.v25.i2-4.50

[9] Bartosiewicz, Y., Giot, M., & Seynhaeve, J.M. (2010). Revisiting Modeling Techniques and Validation Experiments for Two-Phase Choked Flows Relevant to LOCA. (2010). *The 8th International Topical Meeting on Nuclear Thermal-Hydraulics, Operation and Safety (NUTHOS-8) N8P0317*, 10–14 October, Shanghai, China.

[10] Emanuel, G. (1964). A general method for numerical integration through a saddle-point singularity with application to one-dimensional nonequilibrium nozzle flow. *Technical documentary report no. AEDC-TDR-64-29*. Stanford University, California, USA.

[11] De Sterck, H., Rostrup, S., & Tian, F. (2009). A fast and accurate algorithm for computing radial transonic flows. *Journal of Computational and Applied Mathematics*, 223(2), 916–928. doi: 10.1016/j.cam.2008.03.019

[12] Cheng, K., Meng, T., Zhao, F., & Tan, S. (2019). Development and validation of a thermal hydraulic transient analysis code for offshore floating nuclear reactor based on RELAP5/SCDAPSIM/MOD3.4. *Annals of Nuclear Energy*, 127, 215–226. doi: 10.1016/j.anucene.2018.12.004

[13] Ohnuki, A., Akimoto, H., & Murao, Y. (1993). Assessment of TRAC-PF1/MOD1 code for thermal-hydraulic behavior in pressure vessel during reflood in SCTF test with a radial power distribution. *Technical documentary report no JAERI-M--93-139*, Japan Atomic Energy Research Institute, Tokyo, Japan.

[14] Dor, I., Geffraye, G., Lavialle, G., & Mieusset, T. (2004). Recent Improvements of Physical Models in the CATHARE Code and Their Validation. 12th International Conference on Nuclear Engineering, Proceeding Paper (pp. 681–691), 25−29 April, Arlington, Virginia, USA. doi: 10.1115/ICONE12-49408

[15] Sánchez, V.H., Thieme, M., & Tietsch, W. (2012). Validation and Application of the Thermal Hydraulic System Code TRACE for Analysis of BWR Transients. *Science and Technology of Nuclear Installations*, 2012(1), 247482. doi: 10.1155/2012/247482

[16] Gale, J., Tiselj, I., & Horvat, A. (2008). Two-fluid model of the Waha code for simulations of water hammer transients. *Multiphase Science and Technology*, 20(3–4), 291–322. doi: 10.1615/MultScienTechn.v20.i3-4.40

[17] Va, B., Lee, W.-T., & Roe, P. (1991). Characteristic time-stepping or local preconditioning of the Euler equations. *10th Computational Fluid Dynamics Conference*. 24−26 June, Honolulu, USA. doi: 10.2514/6.1991-1552

[18] Angielczyk, W., Seynhaeve, J.M., Gagan, J., Bartosiewicz, Y., & Butrymowicz, D. (2019). Prediction of critical mass rate of flashing carbon dioxide flow in convergent-divergent nozzle. *Chemical Engineering and Processing - Process Intensification*, 143, 107599. doi: 10.1016/j.cep.2019.107599

[19] Angielczyk, W., Bartosiewicz, Y., & Butrymowicz, D. (2020). Development of Delayed Equilibrium Model for CO2 convergent-divergent nozzle transonic flashing flow. *International Journal of Multiphase Flow*, 131, 103351. doi: 10.1016/j.ijmultiphaseflow.2020.103351

[20] Angielczyk, W. (2024). A Review of the Relaxation Models for Phase Transition Flows Centered on the Topological Aspects of the Nonequilibrium Mass Transfer Modelling. *Acta Mechanica et Automatica*, 18(3), 526–535. doi: 10.2478/ama-2024-0056

[21] Nakagawa, M., Berana, M.S., & Kishine, A. (2009). Supersonic two-phase flow of CO2 through converging–diverging nozzles for the ejector refrigeration cycle. *International Journal of Refrigeration*, 32(6), 1195–1202. doi: 10.1016/j.ijrefrig.2009.01.015

[22] Gale, J., & Tiselj, I. (2004). Simulation of the Critical Flashing Flow with the Transient 1D Two-Fluid Model. *ASME 2004 Heat Transfer/Fluids Engineering Summer Conference*. 11−15 July, Charlotte, North Carolina, USA. doi: 10.1115/ht-fed2004-56315

[23] Ebrahimzadeh Azghadi, F. E., Mahpeykar, M.R., Pasandideh Fard, M., & Lakzian, E. (2022). Numerical simulation of nucleating flow and shock capturing in steam turbines by a simple low-dissipation upwind scheme using an Eulerian-Lagrangian model. *Computers & Fluids*, 249, 105699. doi: 10.1016/j.compfluid.2022.105699

[24] Gaballa, H., Jafari, S., Di-Lella, A., Habchi, C., & de Hemptinne, J.C. (2022). Thermodynamics analysis of CO2 condensation in supersonic flows for the potential of clean offshore natural gas processing. *Applied Energy*, 320, 118523. doi: 10.1016/j.apenergy.2022.118523

[25] Chen, Z., & Liu, G. (2024). Analysis of the Internal Flow Features of a CO2 Transonic Nozzle and Optimization of the Nozzle Shape Profile. *Applied Thermal Engineering*, 243, 121945. doi:10.1016/j.applthermaleng.2023.121945

[26] Seynhaeve, J.-M., De Crécy, A., & Bartosiewicz, Y. (2015). Uncertainty analysis of delayed equilibrium model (DEM) using the CIRCE methodology. *NURETH-16, Chicago, IL, August 30-September 4* (pp. 1143−1156).

[27] Attou, A., Bolle, L., & Seynhaeve, J.M. (2000). Experimental study of the critical flashing flow through a relief line: evidence of the double-choked flow phenomenon. *International Journal of Multiphase Flow*, 26(6), 921–947. doi: 10.1016/S0301-9322(99)00077-4

[28] Lorenzo, M.D., Lafon, P., Seynhaeve, J.-M., & Bartosiewicz, Y. (2017). Benchmark of Delayed Equilibrium Model (DEM) and classic two-phase critical flow models against experimental data. *International Journal of Multiphase Flow*, 92, 112–130. doi: 10.1016/j.ijmultiphaseflow.2017.03.004

[29] Skripov, V. P. (1992). Metastable states. *Journal of Non-Equilibrium Thermodynamics*, 17(3), 193–236. doi: 10.1515/jnet.1992.17.3.193

[30] Angielczyk, W. (2021). *Modelling of CO2 transonic flashing flow through a convergent-divergent nozzle using the Delayed Equilibrium Model*. PhD Thesis. Bialystok University of Technology, Faculty of Mechanical Engineering, Białystok, Poland.

[31] Bouré, J.A., Fritte, A.A., Giot, M.M., & Réocreux, M.L. (1976). Highlights of two-phase critical flow: On the links between maximum flow rates, sonic velocities, propagation and transfer phenomena in single and two-phase flows. *International Journal of Multiphase Flow*, 3(1), 1–22. doi: 10.1016/0301-9322(76)90030-6

[32] Press, W.H., Teukolsky, S.A., Vetterling, W.T., & Flannery, B.P. (2002). *Numerical Recipes in C++: The Art of Scientific Computing* (Third Edition, Vol. 1002). Cambridge University Press.

[33] Bell, I.H., Wronski, J., Quoilin, S., & Lemort, V. (2014). Pure and Pseudo-pure Fluid Thermophysical Property Evaluation and the Open-Source Thermophysical Property Library CoolProp. *Industrial and Engineering Chemistry Research*, 53(6), 2498–2508. doi: 10.1021/ie4033999

ARCHIVES
OF THERMODYNAMICS

Theoretical investigation for optimal thermal and thermodynamic performance of flat-plate solar collector with nanofluids

Vikash Kumar Gorai[a], Mukesh Kumar[a], Rahul Singh[b], Mukesh Kumar Sahu[c]*

[a]Cambridge Institute of Technology, Tatisilwai, Ranchi, Jharkhand, 835103, India
[b]Amity University, Ranchi, Jharkhand, 834001, India
[c]Kalinga University, Kotni, Naya Raipur, Chhattisgarh, 492101, India
*Corresponding author email: mukeshkumar.sahu@kalingauniversity.ac.in

Abstract

In this work, an analytical study is carried out on the performance of copper-based nanoparticles and water in flat-plate solar collectors. The effect of copper-based nanoparticles on various thermophysical properties of collectors has been studied and compared with water under the same conditions. The effects of temperature rise parameter from 0.0018 to 0.025, volume percentage of nanoparticles from 0 to 1 and mass flow rate in the range of 0.012 to 0.170 kg/s have been considered. The mass flow rate range covers both laminar and turbulent flow conditions. A detailed parametric study was carried out by developing appropriate MATLAB codes for various performance and energy equations to investigate the effects of volume percentage of nanoparticles and mass flow rate on the basic thermophysical properties and performance parameters, including Nusselt number, heat transfer coefficient, collector plate factor, heat removal factor, Reynolds number, collector heat gain, fluid outlet temperature and thermal efficiency. A new number has been introduced to find out the optimal value of mass flow rate for optimizing collector performance. From the analysis it was found that water collector achieved the maximum thermal efficiency of 53.7% for the highest value of mass flow rate of 0.1675 kg/s. For the nanofluid collector, the maximum efficiency is 70.5% for a nanofluid volume fraction of 0.48 and for the highest considered value of mass flow rate of 0.1675 kg/s. The nanofluid collector is predicted to provide up to 16.8% higher energy efficiency than the water collector.

Keywords: Nanofluid; Flat-plate solar collector; Density; Efficiency

1. Introduction

The use of different types of non-conventional renewable energy sources is necessary to fulfill the continuously increasing energy demands. In order to use and convert solar energy into useful thermal energy for the various mankind applications, it is essential that solar thermal energy conversion systems deliver maximum efficiencies [1]. To improve the performance of thermal systems nanofluids are also widely used for the heat transfer, cooling and others applications [2]. The use of nanofluids and nanotechnology in thermal energy conversion systems improves its performance without any harmful environmental impact.

Nanofluid is a colloidal mixture of nano-sized particles in a host (base) fluid to affect the thermophysical properties and improve the heat transfer characteristics of base fluids, which are useful for different practical applications [3]. Nanofluids are now used frequently as coolants, lubricants, hydraulic fluids and metal cutting fluids. There are many research works that concentrate on nanofluids containing different nanoparticles with various volume concentrations and sizes [4]. Various base

Nomenclature

A_c – collector surface area, m^2
C_b – bond conductance, $W/(m^2\,K)$
C_P – specific heat capacity, $J/(kg\,K)$
D – diameter of tube, m
D_i – inner diameter of tube, m
f – friction factor
F – fin efficiency
F' – collector efficiency factor
F_P – collector efficiency factor
F_R – heat removal factor
h – heat transfer coefficient, $W/(m^2\,K)$
I – intensity of solar radiation, W/m^2
k – thermal conductivity, $W/(m\,K)$
L – length of collector, m
Nu – Nusselt number
m – mass flow rate, kg/s
Pr – Prandtl number
Qu – useful heat gain, W
Re – Reynolds number
t – thickness, m
T – temperature, K
T_{fm} – mean fluid temperature, K
T_{pm} – mean plate temperature, K

TEIF– thermal efficiency improvement factor
ΔT – temperature drop, $= T_{fo} - T_{fi}$, ºC
$\Delta T/I$ – temperature rise parameter, ºC m^2/W
U_L – overall heat loss coefficient, $W/(m^2\,K)$
V – velocity of fluid in the collector, m/s
W – riser tube spacing, m

Greek symbols

η_{th} – thermal efficiency
μ – dynamic viscosity, N s/m^2
ρ – density, kg/m^3
ϕ – volume fraction
$(\tau\alpha)$ – effective transmittance-absorptance product

Subscripts and Superscripts

a – ambient
avg – average
bf – base fluid
f – fluid
in – inlet
ir – inner
out – outlet
nf – nanofluid
np – nanoparticle
p – plate

fluids such as ethylene glycol, form amide, water, etc., have been used by the researchers. The enhancement in thermal properties is achieved by mixing nano-sized particles, dispersed uniformly in the base fluids [5]. Nanoparticles have a larger relative surface area since particle size is very small, thus providing higher suspension stability that improves the thermal conductivity of the mixture [6,7].

Nanofluid is a colloidal suspension of nanoparticles of size 1 to 100 nm (10^{-9} m) in the base fluid, and this is the term first given by Choi in 1995 [8]. Depending on the application, nanofluids have been made of various materials such as metals, metal oxides, ceramics and carbon nanotubes (CNT). Alim et al. [9] carried out a theoretical study, investigating the effects of 4 different nanoparticles (NPs), namely alumina oxide (Al_2O_3), titanium oxide (TiO_2), silicon dioxide (SiO_2), and copper oxide (CuO), on thermal energy efficiency and entropy generation (EG), based on the second law of thermodynamics for the flat-plate collectors. They explored the effects of different concentrations and volume flow rates on the efficiencies of the flat-plate collector and found that CuO nanoparticles deliver the highest enhancement over the other types of nanoparticles.

Moghadam et al. [10] carried out experimental research using the CuO nanoparticles and water as base fluid in the flat-plate collector. They found an enhancement in the collector efficiency with increasing the mass flow rate for both types of flat-plate collectors, i.e. for nanofluid based and water based flat plate collectors.. Shojaeizadeh et al. [11] carried out a theoretical study for the exergy performance considering Al_2O_3–H_2O nanofluid as the heat transfer fluid (HTF) in a flat-plate collector. They investigated various parameters, including volume concentration, solar radiation, plate absorber area, mass flow rate, ambient temperature, and the fluid inlet temperature, on the flat-plate collector exergy efficiency.

Mahian et al. [12] carried out a theoretical study considering Al_2O_3 nanofluid in a flat-plate solar collector. They have investigated the effects of solar radiation and ambient temperature on the entropy generation in the collector. They took the nanoparticles with different sizes as 25, 50, 75 and 100 nm, volume percentages of up to 4 vol% and mass flow rates within the range between 0.1 and 0.8 kg/s. They reported that, as the nanofluid concentration enhances, the entropy generation rate decreases.

Said et al. [13] performed theoretical analysis for a flat-plate collector using single wall carbon nanotubes (SWCNTs) based nanofluid. They evaluated and compared the 2nd law exergetic efficiency and pumping power performance of the SWCNT nanofluid based solar collector with the Al_2O_3, SiO_2 and TiO_2 nanofluid based solar collectors. Sint et al. [14] carried out theoretical analysis using the program developed in MATLAB software in order to estimate the thermal performance of the flat-plate solar collector by using CuO and H_2O based nanofluid. They reported that the collector efficiency is a function of volume percentage and nanoparticle size. The collector efficiency was found to be maximum when the values of the total heat loss coefficient are at a minimum. Furthermore, the collector efficiency was found to be maximum when the collector heat removal factor have its maximum value.

Tong et al. [15] carried out experimental research using H_2O, Al_2O_3 with base fluid H_2O, and CuO with base fluid H_2O. They have evaluated the absorber performance for a fixed flow rate of 0.047 kg/s. They have reported that Al_2O_3 in a H_2O base fluid at a volume percentage of 0.01%, has the highest energy efficiency of 77.5% while CuO with H_2O base fluid has maximum efficiency of 73.9%. They also found that entropy generation was

the highest for H_2O based collector and the lowest for Al_2O_3 nanofluid with 1.0 %vol. fraction.

Esen et al. [16] reported the modelling of new solar air heater (SAH) efficiency by using the least-squares support vector machine (LS-SVM) method. They carried out their research for the SAH with double-pass channel. They have compared the predicted and experimental results and after that proposed that LS-SVM model can be used for estimating the efficiency of SAHs with reasonable accuracy. In another work, Esen et al. [17] carried out their study on SAH system by using artificial neural network (ANN) and wavelet neural network (WNN) models. The authors compared the predicted and experimental results and proposed that WNN model can be used for estimating some parameters of SAHs with sufficient accuracy.

Ozgen et al. [18] performed an experimental investigation using aluminium cans as an absorbing plate in the double-pass channel of a flat-plate SAH. They considered different arrangements of the aluminium cans in the absorber plate. For the first type (Type I) they were staggered as zigzag and for the second one (Type II) they were arranged in order. Type III was a flat absorber plate (without cans). They used two values of air mass flow rates, 0.03 kg/s and 0.05 kg/s. They obtained the highest thermal efficiency for the Type I configuration at a mass flow rate of 0.05 kg/s.

In the study of Esen et al. [19], experiments were performed to find out how the use of different refrigerants affects thermal performance of a two-phase thermosyphon solar collector. Three identical small-scale solar water heating systems, using refrigerants R-134a, R407C, and R410A, were constructed and tested side-by-side under various environmental and load conditions. Oflaz et al. [20] carried out experimental study to explore the thermohydraulic performance of a heat exchanger tube with the combined use of SiO2-water nanofluids with newly designed conical wire inserts. The inserts were placed in a tube with five distances ranging from 0 to 33.6 mm and SiO_2-water nanofluids were used at four volume concentrations (0.5–1.25%). They obtained the best performance evaluation criteria of 1.75 at Reynolds number of 3338 and volume concentration of 1.25% for conical wire inserts with pitch ratio of 0.

Based on the literature review it is found that most of the studies have been carried out using alumina oxide (Al_2O_3) nanoparticles. To the best knowledge of the authors, the effects of copper (Cu) nanofluid as water-based fluid on the flat plate solar collector characteristics and the comparison with a water-based collector for both, i.e. laminar and turbulent flow conditions have not been studied in detail by any investigator up to now. The effect of temperature rise parameter and nanofluid volume fraction in the range of 0–1 have also not been reported by the researchers. Thermophysical properties, and various energy and performance parameters for the collectors have been evaluated by developing suitable MATLAB code.

2. Solar collector system description and methodology

In the flat collectors, nanofluid and water enters through circular shape riser tubes (Fig. 1). For the present analysis a single trans-

parent glass cover has been considered. To minimize the losses proper insulation is provided in the bottom and on the sides of the collectors.
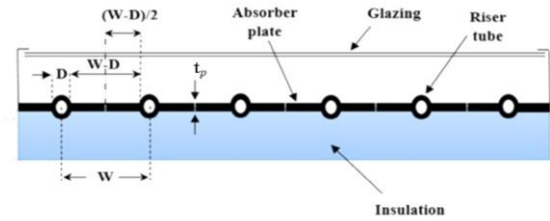

Fig. 1. A schematic of the structure and basic components of a flat-plate solar collector.

The input data for the performance evaluation of the collector, including the physical dimensions of the flat-plate collector, its operating parameters like mass flow rate and inlet temperature, as well as environmental conditions like the solar irradiance, wind velocity, and ambient temperature, were considered as given in Table 1. The arrangement of the flat-plate collector and riser tubes that were considered in the present analysis is shown in detail in Fig. 1.

Table 1. Specifications of the collector and parameters for the present analysis.

Parameter		Value	Unit
Collector dimension	length	2.0	
	width	0.95	m
	height	0.095	
Absorption area, A_c		1.90	m²
Header pipe diameter, D_H		0.022	m
Distance between two parallel tubes, W		0.145	m
Riser pipe diameter, D_o		0.01	m
Riser pipe thickness, t		0.9×10^{-3}	m
Collector tubes diameter, D		0.009	m
Working fluid		Cu nanofluid and water (H_2O) as the base fluid	
No. of glazing, Ng		1	
Thermal emission of absorption sheet, εp		0.07	
Solar absorption of absorption sheet		0.95	
Glass cover emissivity, εg		0.88	
Collector plate thickness, t		0.005	m
Collector plate thermal conductivity, k_p		383	W/(m K)
Collector tilt		35	deg
Insulation thermal conductivity, k_i		0.05	W/(m K)
Back insulation thickness, t_b		0.05	m
Solar radiation, I		900	W/m²
Wind velocity, V_w		3.2	m/s
Ambient temperature, T_a		300	K
Inlet temperature, T_i		301	K
Mass flow rate, m		0.012–0.170	kg/s

2.1. Properties of nanofluids

2.1.1. The density of the nanofluid, is evaluated based on the principle of the mixture rule as follows [20−22]:

$$\rho_{nf} = \phi\rho_{np} + (1-\phi)\rho_{bf}, \tag{1}$$

where ϕ represents volume fraction of nanoparticles, and subscripts np and bf stand for nanoparticles and base fluid, respectively.

2.1.2. The specific heat of a nanofluid is predicted by using the thermal equilibrium model:

$$C_{P,nf} = \frac{\phi(\rho C)_{np}+(1-\phi)(\rho C)_{bf}}{\rho_{nf}}. \tag{2}$$

2.1.3. The thermal conductivity of nanofluid can be evaluated as the equation given by Maxwell, which shows a good agreement with the experimental data over the other proposed models [9,10]:

$$\frac{k_{nf}}{k_{bf}} = \frac{k_{np}+2k_{bf}-2\phi(k_{bf}-k_p)}{k_{np}+2k_{bf}+\phi(k_{bf}-k_p)}. \tag{3}$$

The conductivity of the base fluid is evaluated at the average temperature (T_{avg}) from the following equation [14]:

$$k_{bf} = 0.6065\left[1.488445 + 4.12292\left(\frac{T_{avg}}{298.15}\right) - 1.63866\left(\frac{T_{avg}}{298.15}\right)\right]. \tag{4}$$

2.1.4. Dynamic viscosity of a nanofluid can be calculated by the equation that follows from the Brinkman's model

$$\frac{\mu_{nf}}{\mu_{bf}} = \frac{1}{(1-\phi)^{2.5}}, \tag{5}$$

where the viscosity of the base fluid is given as

$$\mu_{bf} = 2.414 \times 10^{-5} \times 10^{\frac{247.8}{T_{avg}-140}}. \tag{6}$$

2.1.5. The energy efficiency of the solar collector is defined by [23]

$$\eta_{th} = \frac{Qu}{A_c I}, \tag{7}$$

where A_c is a collector surface area, I is the intensity of solar radiation, and Qu represents the useful heat gain from available solar energy and is expressed by [23]

$$Qu = mC_P(T_{out} - T_{in}). \tag{8}$$

2.1.6. Useful heat gain can also be calculated as

$$Qu = A_c F_R[I(\tau\alpha) - U_L(T_{fm} - T_a), \tag{9}$$

where F_R denotes the heat removal factor, $(\tau\alpha)$ represents the effective transmittance-absorptance product, U_L is the overall heat loss coefficient, T_{fm} is the mean temperature of the fluid and T_a is the ambient temperature. It can also be calculated in terms of U_L and mean temperature of an absorber plate (T_{pm}):

$$Qu = A_c[I(\tau\alpha) - U_L(T_{pm} - T_a)]. \tag{10}$$

2.1.7. The collector heat removal factor is calculated as

$$F_R = \frac{mC_P}{A_c U_L}\left[1 - \exp\left(-\frac{U_L F' A_c}{mC_P}\right)\right]. \tag{11}$$

Here, F' is the collector efficiency factor which can be calculated as

$$F' = \frac{\frac{1}{U_L}}{W\left[\frac{1}{U_L(D+(W-D)F)}+\frac{1}{C_b}+\frac{1}{\pi D h_f}\right]}, \tag{12}$$

where: W − tube spacing, F − fin efficiency D − diameter of the tube, C_b − bond conductance. The fin efficiency can be calculated as [14]

$$F = \frac{\tanh\left(m\frac{W-D}{2}\right)}{m\frac{W-D}{2}}. \tag{13}$$

2.1.8. New mean temperature of the absorber plate is calculated as

$$T_{pm} = T_{in} + \frac{Qu}{A_c F_R U_L}(1 - F_R). \tag{14}$$

2.1.9. The collector's heat transfer coefficient can be calculated as

$$h_{nf} = \frac{Nu k_{nf}}{D_{ir}}, \tag{15}$$

where Nu is the Nusselt number and D_{ir} is the tube's inner diameter.

2.1.10. The Reynolds number can be calculated as

$$Re_{nf} = \frac{\rho_{nf} V D_{ir}}{\mu_{nf}}. \tag{16}$$

2.1.11. Prandtl number can be calculated as

$$Pr_{nf} = \frac{\mu_{nf} C_{P,nf}}{k_{nf}}. \tag{17}$$

2.1.12. The average temperature of the flow can be calculated as

$$T_{avg} = T_{fm} = \frac{T_{out}+T_{in}}{2}. \tag{18}$$

2.1.13. The Nusselt number for a flat-plate collector having nanoparticles is evaluated using the correlation [24−27]:

$$Nu_{np} = \frac{\frac{f}{8}(Re-1000)Pr}{1+12.7\left(\frac{f}{8}\right)^{\frac{1}{2}}\left(Pr^{\frac{2}{3}}-1\right)}. \tag{19}$$

2.1.14. The Nusselt number for a water-based flat-plate collector is obtained from

$$Nu_{bf} = 0.023 Re^{0.8} Pr^{0.4}. \tag{20}$$

2.1.15. The friction factor is evaluated using the formula

$$f = [0.79\ln(Re) - 1.64]^{-2}. \tag{21}$$

Table 2. Thermophysical properties of various nanoparticles and water [21−26].

Nanoparticle Type	Formula	Density, (kg/m³)	Specific heat, (J/kgK)	Thermal conductivity (W/m K)
Copper oxide	CuO	6000	551	34
Copper	Cu	8978	388	381
Alumina oxide	Al_2O_3	3960	774	40
Water	H_2O	997	4180	0.607

Fig. 3. Effect of temperature rise parameter on the density for copper-based nanofluids at different volume fractions and water.
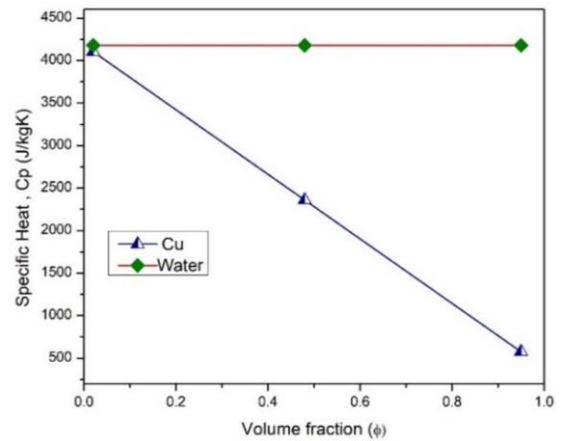
3. Results and discussion

3.1. Evaluation of thermophysical properties

The thermophysical properties of various nanoparticles and water are provided in Table 2. Figures 2 to 7 show the effect of different parameters on thermophysical properties of copper-based nanofluid flat-plate collector and their comparison with the properties of water-based collector.

Figure 2 shows the variation of nanofluid density (ρ_{nf}) with change in the nanoparticles volume fraction (ϕ) from 0.02 to 0.95 (3 values for the present analysis), which was evaluated using Eq. (1). It can be seen that the density of nanofluid is increasing with an increase in ϕ.

Figure 3 represents the effect of temperature rise parameter ($\Delta T/I$) on the nanofluid density, where $\Delta T = T_{fo} − T_{fi}$. For the present analysis, parameter ($\Delta T/I$) was taken in the range of 0.0018 to 0.026, whereas the value of solar radiation (I) is fixed at 900 W/m². Other system and operating parameters are given in detail in Table 1. It can be seen that the density of nanofluid with $\phi = 0.95$ is the highest as compared to other ϕ values. But it can also be seen that water has a higher density than the nanofluid with $\phi = 0.02$.

Figures 4 and 5 show the effect of volume fraction on the specific heat of nanofluid- and water-based collectors. It can be

Fig. 4. Variation of specific heat with volume fraction for copper nanofluid and water-based collectors.

Fig. 2. Variation of density with volume fraction for copper-based nanofluids and water.
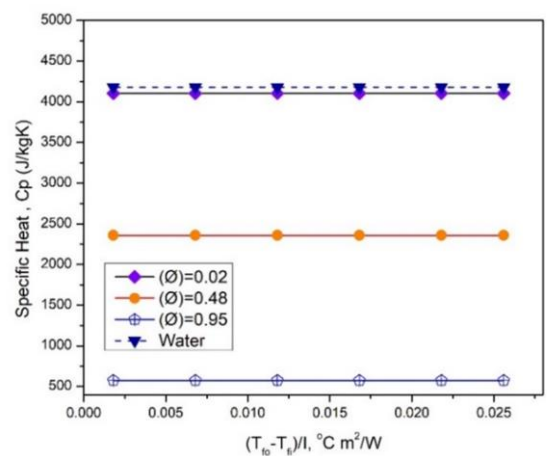

Fig. 5. Effect of temperature rise parameter on specific heat for copper nanofluid based collectors with different particle volume fractions and water based collector.

seen from Fig. 4 that the specific heat of nanofluid decreases with the increasing volume fraction of nanoparticles. From Fig. 5 it can be seen that specific heat shows inversely proportional values as ϕ increases. It can also be concluded from this figure that water have the highest specific heat compared to the considered nanofluids.

Figures 6 and 7 display thermal conductivity of a nanofluid as a function of volume fraction, and the comparison with the water thermal conductivity. It can be seen from Fig. 6 that the increase in thermal conductivity of the nanofluid is steeper when nanoparticle volume fractions exceeds 0.48. The thermal conductivity shows an enhancement which is directionally proportional to the increasing volume fraction of nanoparticles, owing to their better heat-conducting properties as compared to the base fluid. As the values of ϕ increase, more nanoparticles are added to the fluid, which enhances the thermal conductivity of nanofluid. Figure 7 demonstrates the variations of thermal conductivity with temperature rise parameter for different values of volume fraction. The thermal conductivity shows a similar trend as in Fig. 6.

3.2. Evaluation of Reynolds number

Figure 8 presents the effect of the volume fraction on the Reynolds number (Re) of the nanofluid- and water-based collectors. The Reynolds number was evaluated using Eq. (16). It can be seen that while calculating Re, the density, velocity, and viscosity play the important role. It can be seen that the Reynolds number is decreased by increasing the volume fraction for the nanofluid-based collector while for the water collector it is constant. This is because when the volume fraction is increased, the nanofluid becomes more viscous, which makes the fluid more dense and more resistant to flow. This phenomenon reduces the fluid velocity, and as the Reynolds number depends on the fluid flow velocity, hence it results in lower values of Re. Moreover, as it can be seen from the figure, the highest value of mass flow rate corresponds with the highest value of the Reynolds number.

Figure 9 is presented to show the effect of the temperature rise parameter on the Reynolds number for different values of
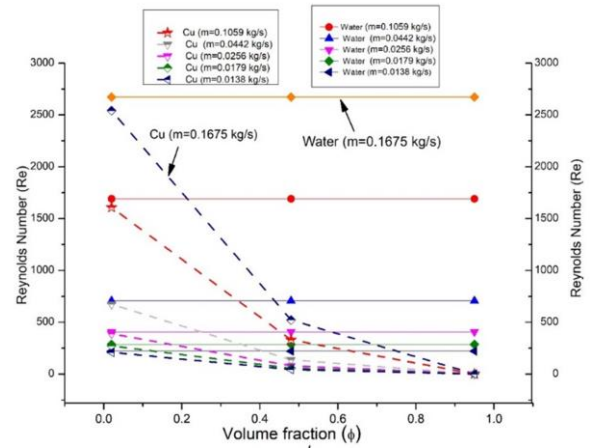

Fig. 8. Variation of Reynolds number with volume fraction
for copper nanofluid and water
for laminar and turbulent flow region.

Fig. 6. Thermal conductivity of water and copper nanofluids with
different volume fractions.
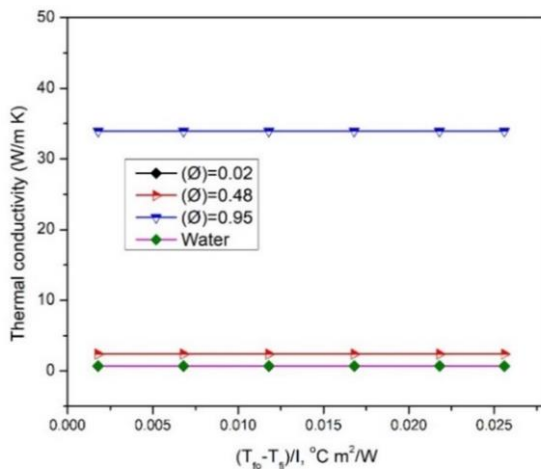
Fig. 7. Effect of temperature rise parameter for copper nanofluid
collector with different particle volume fractions
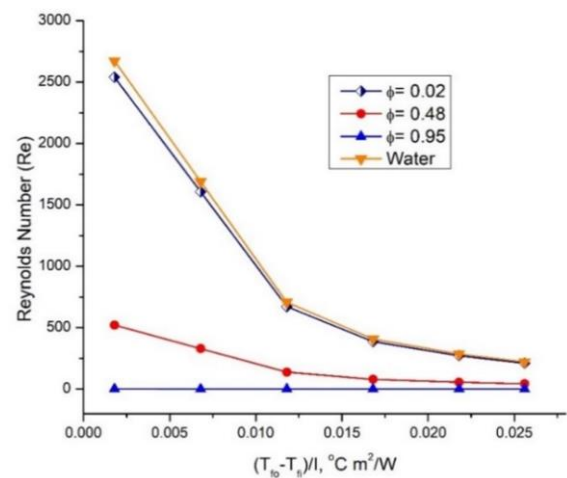and water collector.

Fig. 9. Effect of temperature rise parameter on the Reynolds
number for nanofluid-based and water solar collectors.

volume fraction. It can be seen from the figure that Re decreases with an increase in $\Delta T/I$. Among all curves, water collector has higher values of Re over the nanofluid-based collector for all values of $\Delta T/I$. Furthermore, the nanofluid-based collector with the lowest value of ϕ has higher values of Re over the collector using nanofluid with higher values of ϕ.

3.3. Evaluation of Nusselt number and heat transfer coefficient

Figure 10 shows the Nusselt number (Nu) variations with the change in volume fraction and for different values of mass flow rate (m), which has been evaluated using Eqs. (19) and (20) for nanofluid collector (Fig. 10a) and water-based collector (Fig. 10b), respectively. It can be seen that Nu of nanofluid collector decreases with an increase in ϕ. Adding more nanoparticles increases the nanofluid volume fraction, which increases the nanofluid viscosity and makes nanofluid thicker. Higher viscous fluids have less flowing ability and for the higher viscous fluid the rate of heat transfer is low, therefore the Nusselt number (Nu) decreases with an increase in the volume percentages of nanoparticles. Furthermore, it can also be concluded that the highest value of $\dot{m}$ shows the highest value of Nu for both types of collectors.
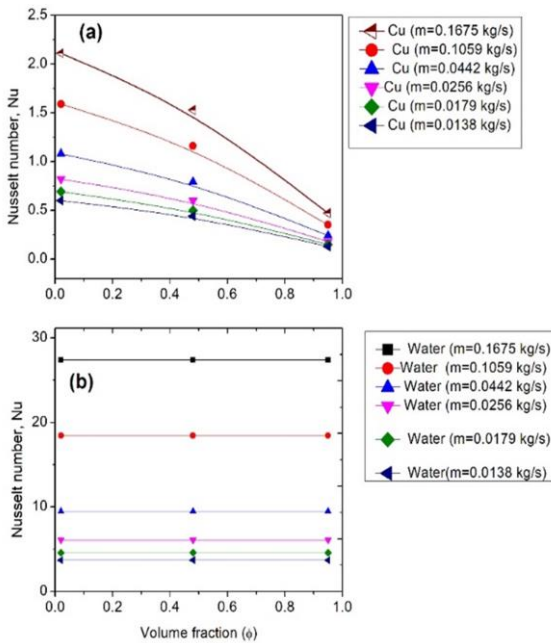

Fig. 10. Variation of Nusselt number with volume fraction for copper nanofluid (a) and water (b).

Figure 11 shows the variations of the Nusselt number with the temperature rise parameter for different volume fractions for both collectors. It can be seen that the Nu decreases with an increase in volume fraction (ϕ) from 0.02 to 0.95 for nanofluid collector. Furthermore, Nu values remain constant for all values of ϕ corresponding to increase in the values of ($\Delta T/I$). For water collector Nu decreases with an increase in the value of $\Delta T/I$ but the Nu values are higher as compared to nanofluid collector.
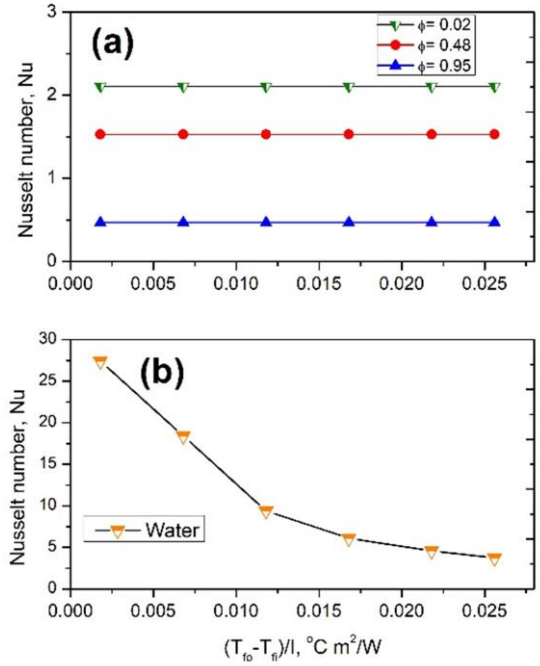

Fig. 11. Effect of temperature rise parameter on the Nusselt number for copper nanofluid at different volume fractions (a) and water (b).

3.4. Evaluation of heat transfer coefficient

Figure 12 shows the comparison of heat transfer coefficient (h) for nanofluid and water collectors for different values of volume fraction. It can be seen that for water collector (Fig. 12b), values
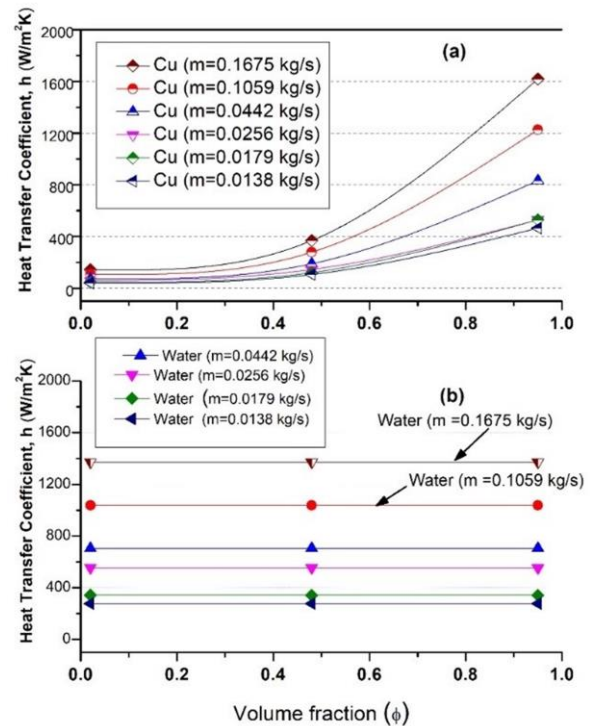

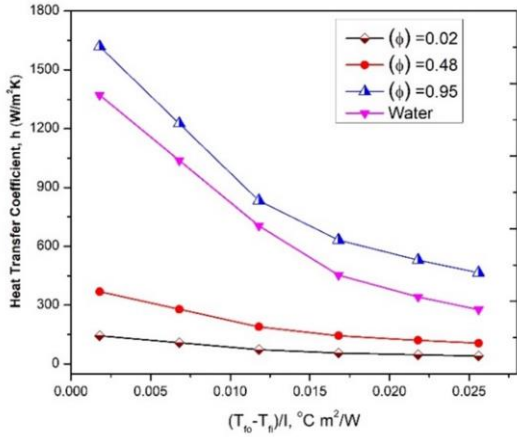Fig. 12. Variation of heat transfer coefficient with volume fraction for copper nanofluid (a) and water (b).

Fig. 13. Effect of temperature rise parameter on heat transfer coefficient for copper nanofluid collector with different particle volume fractions and water collector.

of h remain constant for all values of ϕ, but it is found that they increase with an increase in the values of m. While on the other side, it can be seen that for nanofluid collector (Fig. 12a) h is increasing with an increase in the value of ϕ and m.

Figure 13 shows the comparison of heat transfer coefficients of the nanofluid and water collectors for different values of temperature rise parameter and mass flow rate. It can be seen that for both collectors show decreasing values of h with an increase in the value of $\Delta T/I$. It can also be concluded from this figure that for nanofluid collector, the highest value of ϕ shows higher values of h over the other values of ϕ.

3.5. Evaluation of plate efficiency factor and heat removal factor

Figure 14 depicts a comparison of the collector plate efficiency factor (F_P) of the nanofluid-based and water-based collectors for different values of volume fraction and mass flow rate. As it can be seen, for both collectors F_P shows increasing values with an increase in m.
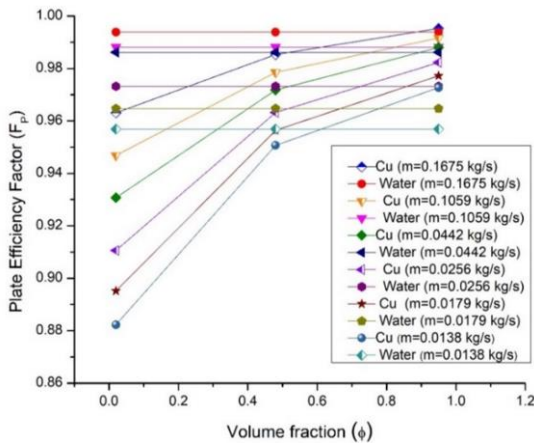

Fig. 14. Variation of plate efficiency factor with volume fraction for copper nanofluid and water collectors.

Figure 15 shows the effect of temperature rise parameter on the collector plate efficiency factor for nanofluid- and water-based collectors for different values of volume fraction. It can be seen that for both type of collectors F_P decreases with an increase in the value of $\Delta T/I$.

Figure 16 shows the collector heat removal factor (F_R) comparisons of nanofluid and water collectors for different values of volume fraction and mass flow rate. It can be seen from the figure that for nanofluid collector the value of F_R increases up to the values of $\phi = 0.45$ and declines with further increase of ϕ.
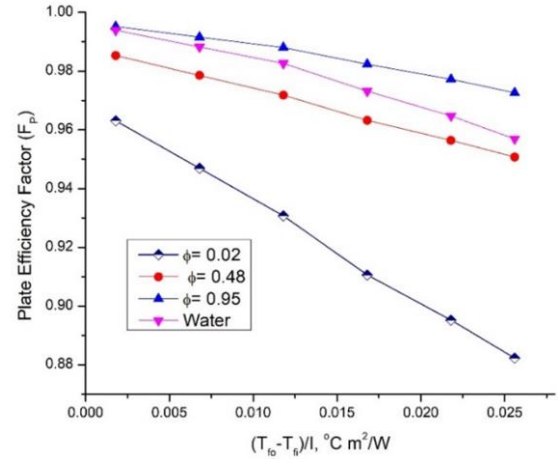

Fig. 15. Effect of temperature rise parameter on plate efficiency factor for copper nanofluid collector with different particle volume fractions and water collector.
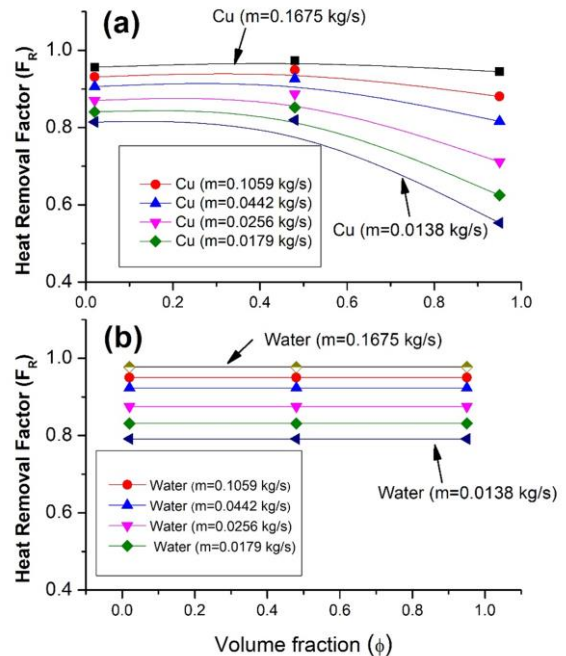

Fig. 16. Variation of heat removal factor with volume fraction for (a) copper nanofluid collector and (b) water collector.

Figure 17 shows a comparison of the heat removal factor of the nanofluid- and water-based collectors with changes in the
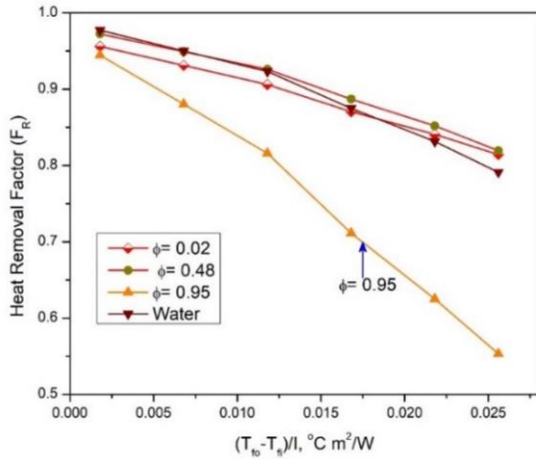
Fig. 17. Effect of temperature rise parameter on the plate efficiency factor for copper nanofluid collector with different particle volume fractions and water collector.

temperature rise parameter and volume fraction. For both collectors, it shows decreasing values of F_R with an increase in the value of $\Delta T/I$.

3.6. Evaluation of useful heat gain and energy efficiency

Figures 18−22 show variations of useful heat gain (Qu) and energy efficiency (η_{th}) of the nanofluid- and water-based collectors. It can be seen from these figures that nanofluid collector has higher values of Qu and η_{th} compared to water. This is because due to nanoparticles, nanofluid-based collector have higher thermal conductivity than water-based collector; these nanoparticles absorb more heat with the same collector surface area. In result, nanofluid collector has higher rate of heat exchange between the flowing fluid and collector surfaces (tubes).

Figure 18 shows a comparison of a collector useful heat gain between the nanofluid and water collectors for different values of volume fraction and mass flow rate. The results indicate that
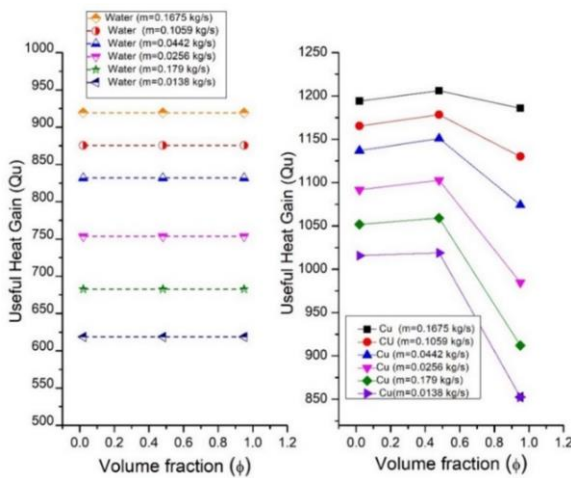
for water collector, Qu value increases with an increase in the values of m and it remain constant when ϕ increases, but for the nanofluid collector, it increases up to $\phi = 0.45$. The Qu values for the nanofluid-based collector are higher compared to the water-based collector for all values of m and ϕ.

Figure 19 depicts a comparison of the useful heat gain variations with the temperature rise parameter between the water-based collector and nanofluid-based collectors with different nanoparticle volume fractions. For both collectors, Qu decreases with an increase in the values of $\Delta T/I$. It can also be seen from this figure that values of Qu for nanofluid collector are higher compared to the water based collector for all values of ϕ which used for the present nanofluid collector.

In Fig. 20 a comparison of a collector energy efficiency (η_{th}) between the nanofluid and water collectors as a function of volume fraction and mass flow rate. From the analysis it was found that water collector has attained maximum value of $\eta_{th} = 53.7\%$ for the highest value of m. Furthermore, the nanofluid collector
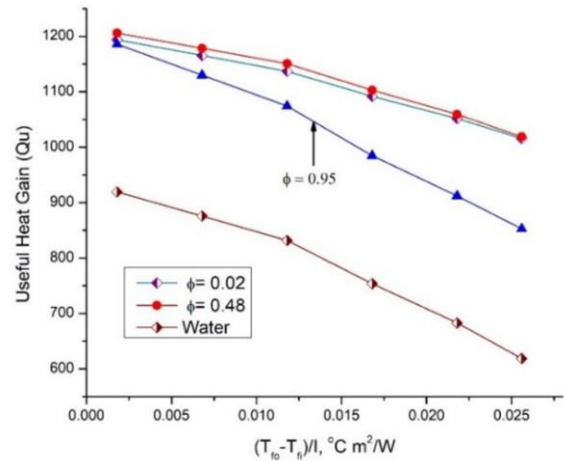

Fig. 19. Effect of temperature rise parameter on the useful heat gain for copper nanofluid collector with different particle volume fractions and water collector.
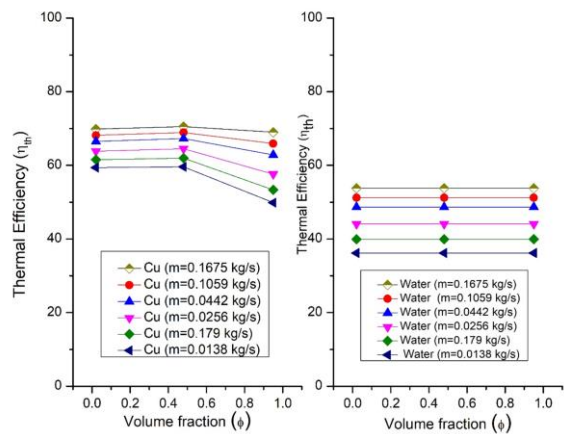

Fig. 18. Variation of useful heat gain with volume fraction for copper nanofluid and water-based collectors.

Fig. 20. Variation of energy efficiency with volume fraction for copper nanofluid and water-based collectors.

has maximum η_{th} of 70.5% for $\phi = 0.48$ and the highest considered value of m. Thus the nanofluid collector was found to have 16.8% higher energy efficiency than the water collector.

Figure 21 presents the variation of collector energy efficiency (η_{th}) with the temperature rise parameter for the nanofluid-based collectors with different volume fractions of nanoparticles and the water based collector. It can be seen that for both types of collectors the value of η_{th} decrease with increasing values of $\Delta T/I$. It can also be found from the figure that water has values of η_{th} lower than those predicted for the nanofluid collector for all ϕ values considered.
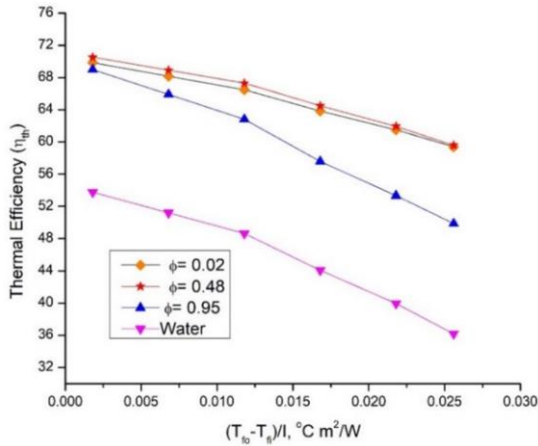

Fig. 21. Effect of temperature rise parameter on the collector energy efficiency for copper nanofluids with different particle volume fractions and water.

3.7. Evaluation of fluid outlet temperature

Figure 22 shows a comparison of the outlet fluid temperature (T_{fo}) between the nanofluid- and water-based collectors, changing with the volume fraction and for different values of mass flow rate. It can be seen that for both collector types T_{fo} decreases with an increase in m. From Fig. 22a it can be seen that for the water collector, T_{fo} is constant for all values of ϕ, i.e. no effect of ϕ is visible due to no presence of nanoparticles. Furthermore, from Fig. 22b it can be seen that T_{fo} for the nanofluid collector is increasing with enhancing the values of ϕ from 0.02 to 0.95. This is due to the fact that nanoparticles increase the surface area so that more solar energy is absorbed by the collector plate. Nanoparticles in the fluid also improve the convective heat transfer, which accelerates the heat absorption rate. So, finally the nanofluid based solar collector can extract more heat, which delivers the high fluid outlet temperature over the without nanoparticles based collector.

Figure 23 presents a comparison of the changes in the outlet fluid temperature with the temperature rise parameter between the nanofluid-based collectors at different volume fractions of nanoparticles and the water-based collector. It can be found that for both collector types, values of T_{fo} increase as the value of $\Delta T/I$ increase. It can also be seen from the figure that water collector exhibits lower T_{fo} values compared to the nanofluid collector for all considered ϕ values.
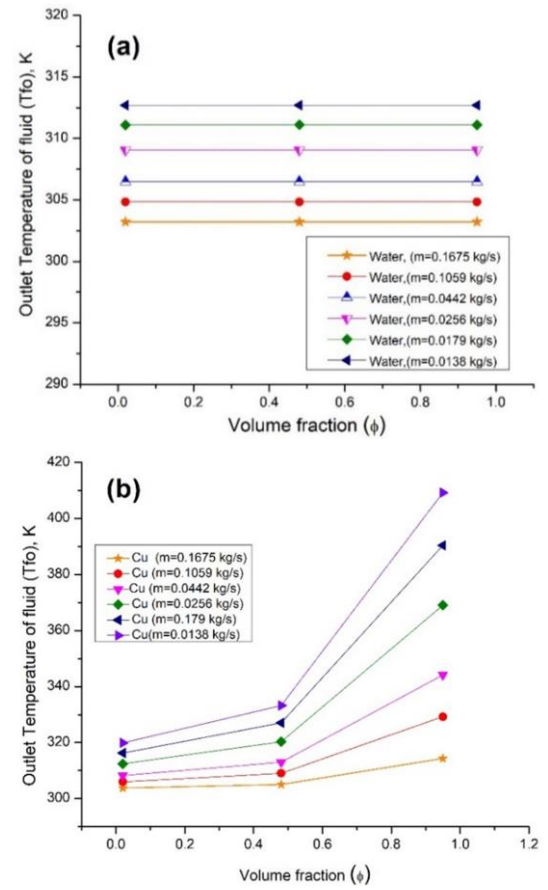

Fig. 22. Variation of the fluid outlet temperature with volume fraction for water (a) and copper nanofluid (b).
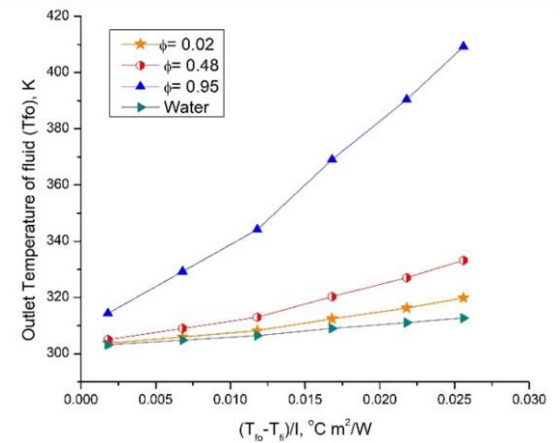

Fig. 23. Effect of the temperature rise parameter on fluid outlet temperature for water and for copper nanofluids with different particle volume fractions.

4. Optimal thermal and thermodynamic performance of collector

4.1. Evaluation of thermal efficiency improvement factor

In order to evaluate the enhancement of thermal performance of the thermal system after application of any technique and for comparison to the reference (base) system Sahu et al. [27] pro-

posed the parameter, called as thermal efficiency improvement factor (TEIF), which can be calculated as

$$\text{TEIF} = \frac{(\eta_{th})_{nf} - (\eta_{th})_{bf}}{(\eta_{th})_{bf}}. \tag{22}$$

Figure 24 shows the change of thermal efficiency improvement factor of a nanofluid collector with the volume fraction and for various values of mass flow rate. It can be seen from the figure that $\phi = 0.48$ delivers the highest value of TEIF = 64.6% for the lowest value of m, while for the highest value of m the value of TEIF for $\phi = 0.48$ is 31.1%.

Figure 25 demonstrates the variation of thermal efficiency improvement factor with the temperature rise parameter and volume fraction. It can be seen that $\phi = 0.48$ shows the highest values of TEIF, while $\phi = 0.95$ shows the lowest values of all ϕ considered for all values of $\Delta T/I$. Furthermore, TEIF values increase when the value of $\Delta T/I$ increases for all values of ϕ.

5.1. Evaluation of Sahu number

Figure 26 shows the effect of mass flow rate on the collector outlet fluid temperature (T_{fo}) for all values of volume fraction which were considered in the present analysis. It is clear from
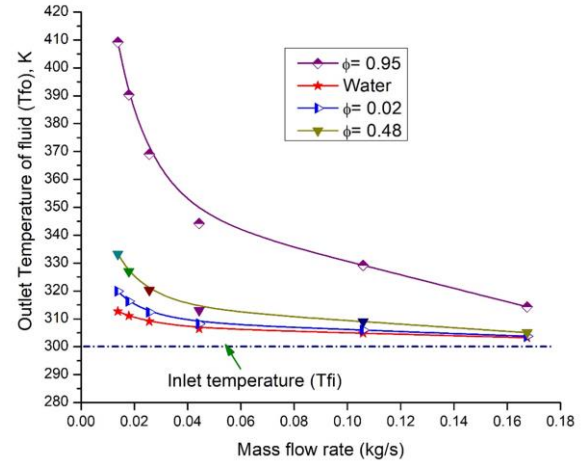

Fig. 26. Variation of fluid outlet temperature with the mass flow rate for nanofluid collector with different particle volume fractions and water collector.
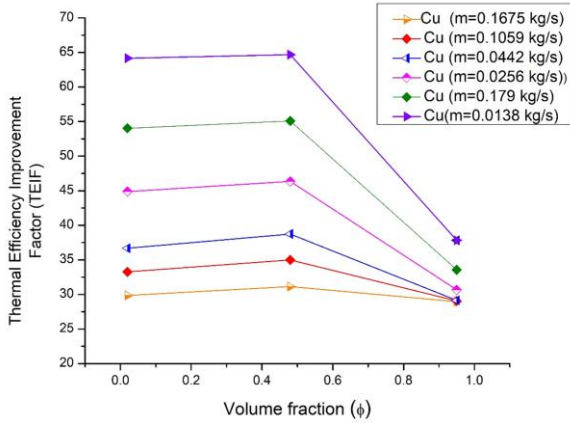

Fig. 24. Variation of thermal efficiency improvement factor of a nanofluid collector with the volume fraction and flow rate.

Fig. 25. Effect of temperature rise parameter on the thermal efficiency improvement factor for the present nanofluid collector.

this figure that for both collector types, outlet temperature decreases with an increase in the mass flow rate. For mass flow rate exceeding 0.06 kg/s, T_{fo} decreases at a higher rate. At mass flow rates larger than $m = 0.12$ kg/s, for water collector and for the nanofluid collector of $\phi = 0.02$ and 0.48, the values of T_{fo} are almost close to the collectors inlet temperature T_{fi} (shown by horizontal dotted line), i.e. both collector types show negligible temperature rise. Furthermore, it can also be concluded that as the mass flow rate increases, the outlet fluid temperature of the nanofluid collector is higher than that for the water collector. From the present analysis, it was found that the trends of changes in collector outlet fluid temperature and energy efficiency with mass flow rate are opposite.

It can be seen from Fig. 26 that collector outlet fluid temperature decreases with the increasing mass flow rate and at higher values of mass flow rate, the values of the collector outlet fluid temperature (T_{fo}) are very close to the inlet fluid temperature (T_{fi}). As per the authors' knowledge, any dimensionless number has been suggested to date by any investigator to evaluate the percentage of collector outlet fluid temperature with its operating mass flow rate. So, this manuscript fourth author suggested the following formula to evaluate this:

$$\text{Sahu Number} = 100 - \left(\frac{T_{fo}}{T_{fo} - T_{fi}}\right). \tag{23}$$

Figure 27 shows the variation of Sahu number with the mass flow rate for both collector types using Eq. (23). It can be seen from the figure that Sahu number is decreasing with m for both types of collectors. Furthermore, it can be concluded that for water and for nanofluid for all values of ϕ, after certain values of m Sahu number goes below zero (shown by vertical dotted lines for water and nanofluid solar collectors) to the negative values; this means after this value of m collectors are not able to deliver the temperature rise ($\Delta T = T_{fo} - T_{fi}$) significantly. For example, from Fig. 27 we can obtain the critical value of $m = 0.07$ kg/s for water by simply putting the vertical line towards the horizontal coordinate (flowrate–axis). Similarly, for nanofluid collector of

Gorai V.K., Kumar M., Singh R., Sahu M.K.
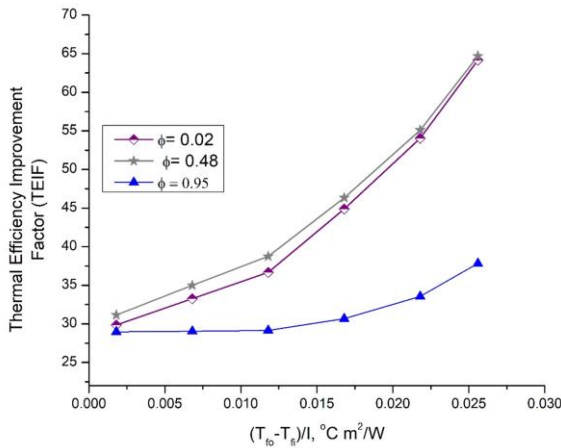
$\phi = 0.02$ the critical value of *m* is 0.095 kg/s. Thus, it can be seen that the Sahu number is an effective number to obtain the optimal value of *m* for both types of collectors.
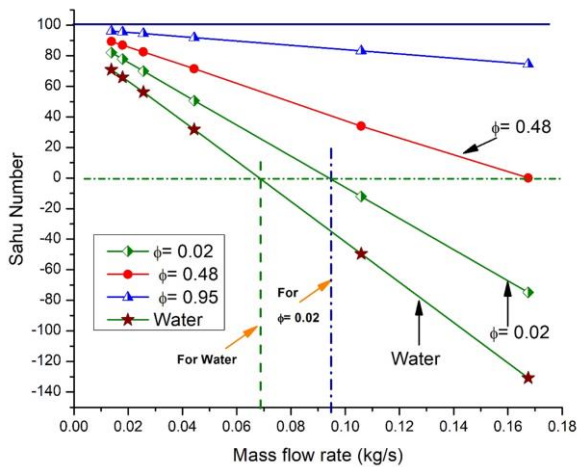

Fig. 27. Variation of Sahu number with the mass flow rate for nanofluid and water collectors.

6. Conclusions

In the present work the performances of the copper water-based flat plate solar collectors were examined theoretically using MATLAB. The effects of the temperature rise parameter, $\Delta T/I = 0.0018–0.025$, volume fraction $\phi = 0–1$ and mass flow rate, $m = 0.012–0.170$ kg/s, were considered in the investigation. Then a detailed parametric study was carried out to investigate the effects of volume fraction and mass flow rate, thermophysical properties, Nusselt number, heat transfer coefficient, collector plate factor, heat removal factor, Reynolds number, collector heat gain, fluid outlet temperature, and thermal efficiency. The Sahu number was introduced to find the optimum values of mass flow rate for both collector types. The main findings of the present work can be summarised as follows:

1. With increasing nanoparticles' volume fraction, the density and thermal conductivity of nanofluids based flat-plate collector improves, while the specific heat decreases.
2. With increasing volume fraction, the Reynolds number and Nusselt number of a nanofluid collector decreases.
3. With increasing volume fraction, the heat transfer coefficient, useful heat gain and collector fluid outlet temperature increase, but their values are higher compared to water (H$_2$O)-based collector for all values of volume fraction.
4. From the analysis it was found that the water collector has attained a maximum value of $\eta_{th} = 53.7\%$ for the highest value of mass flow rate. Furthermore, for the nanofluid collector, the maximum thermal efficiency is 70.5% for $\phi = 0.48$ and for the highest value of mass flow rate, thus a maximum of 16.8% higher efficiency compared to a water collector was obtained.
5. The highest value of the thermal efficiency improvement factor equal to 64.6% was obtained for $\phi = 0.48$ and for the

lowest value of the mass flow rate, while for the highest value of mass flow rate, the value of thermal efficiency improvement factor for $\phi = 0.48$ is 31.1%.
6. The Sahu number is an effective number to obtain the optimal value of mass flow rate for both types of collectors.

References

[1] Duffie, J.A., & Beckman, W.A. (2016). *Solar engineering of thermal processes solar engineering*, Wiley, New York. doi: 10.1002/9781118671603

[2] Kasaeian, A., Eshghi, A.T., & Sameti, M. (2015). A review on the applications of nanofluids in solar energy systems. *Renewable and Sustainable Energy Reviews*, 43, 584–598. doi: 10.1016/j.rser.2014.11.020

[3] Mahian, O., Kianifar, A., Kalogirou, S.A., Pop, I., & Wongwises, S. (2013). A review of the applications of nanofluids in solar energy. *International Journal of Heat and Mass Transfer*, 57(2), 582–594. doi: 10.1016/j.ijheatmasstransfer.2012.10.037

[4] Okonkwo, E.C., Osho, I.W., Almanassra, I.W., Abdullatif, Y.M., & Al-Ansari T. (2020). An updated review of nanofluids in various heat transfer devices. *Journal of Thermal Analysis and Calorimetry*, 145, 2817–2872. doi: 10.1007/s10973-020-09760-2

[5] Xian, H.W., Sidik, N.A.C., & Najafi, G. (2019). Recent state of nanofluid in automobile cooling systems. *Journal of Thermal Analysis and Calorimetry,* 135, 981–1008. doi: 10.1007/s10973-018-7477-3

[6] Sarsam, W.S., Kazi, S.N., & Badarudin, A. (2015). A review of studies on using nanofluids in flat-plate solar collectors. *Solar Energy*, 122, 1245–1265. doi: 10.1016/j.solener.2015.10.032

[7] Sajid, M.U., & Ali, H.M. (2019). Recent advances in application of nanofluids in heat transfer devices: A critical review. *Renewable and Sustainable Energy Reviews*, 103, 556–592. doi: 10.1016/j.rser.2018.12.057

[8] Choi, S.U.S, &. Eastman, J.A. (1995). Enhancing thermal conductivity of fluids with nanoparticles. *International Mechanical Engineering Congress and Exhibition*, 12-17 Nov., San Francisco, USA.

[9] Alim, M.A., Abdin, Z., Saidur, R., Hepbasli, A., Khairul, M.A., & Rahim, N.A. (2013). Analyses of entropy generation and pressure drop for a conventional flat plate solar collector using different types of metal oxide nanofluids. *Energy and Buildings*, 66, 289–96. doi: 10.1016/j.enbuild.2013.07.027

[10] Moghadam, A.J., Farzane-Gord, M., Sajadi, M., & Hoseyn-Zadeh, M. (2014). Effects of CuO/water nanofluid on the efficiency of a flat-plate solar collector. *Experimental Thermal and Fluid Science*, 58, 9–14. doi: 10.1016/j.expthermflusci.2014.06. 014

[11] Shojaeizadeh, E., Veysi, F., & Kamandi, A., (2015). Exergy efficiency investigation and optimization of an Al$_2$O$_3$-water nanofluid based flat-plate solar collector. *Energy and Buildings,* 101, 12–23. doi: 10.1016/j.enbuild.2015.04.04

[12] Mahian, O., Kianifar, A.,. Sahin, A.Z., & Wongwises, S. (2014). Entropy generation during Al2O3/water nanofluid flow in a solar collector: Effects of tube roughness, nanoparticle size, and different thermophysical models. *International Journal of Heat and Mass Transfer*, 78, 64–75. doi: 10.1016/j.ijheatmasstransfer. 2014.06.051

[13] Said, Z., Saidur, R., Rahim, N.A., & Alim, M.A. (2014). Analyses of exergy efficiency and pumping power for a conventional flat plate solar collector using SWCNTs based nanofluid. *Energy and Buildings*, 78, 1–9. doi: 10.1016/j.enbuild.2014.03.061

[14] Sint, N.K.C., Choudhury, I.A., Masjuki, H.H., & Aoyama, H. (2017). Theoretical analysis to determine the efficiency of a CuO-water nanofluid based-flat plate solar collector for domestic solar

water heating system in Myanmar. *Solar Energy*, 155, 608–619. doi: 10.1016/j.solener.2017.06.055

[15] Tong, Y., Lee, H., Kang, W., & Cho, H., (2019). Energy and exergy comparison of a flat plate solar collector using water, Al$_2$O$_3$ nanofluid, and CuO nanofluid. *Applied Thermal* Engineering, 159, 113959. doi: 10.1016/j.applthermaleng.2019.113959

[16] Esen, H., Ozgen, F., Esen, M., & Sengur, A. (2009). Modelling of a new solar air heater through least-squares support vector machines. *Expert Systems with Applications*, 36(7), 10673–10682. doi: 10.1016/j.eswa.2009.02.045

[17] Esen, H., Ozgen, F., Esen, M., & Sengur, A. (2009). Artificial neural network and wavelet neural network approaches for modelling of a solar air heater. *Expert Systems with Applications*, 36(8), 11240–11248. doi: 10.1016/j.eswa.2009.02.073

[18] Ozgen, F., Esen, M., & Esen, H. (2009). Experimental investigation of thermal performance of a double-flow solar air heater having aluminium cans. *Renewable Energy*, 34(11), 2391–2398. doi 10.1016/j.renene.2009.03.029

[19] Esen, M., & Esen, H. (2005). Experimental investigation of a two-phase closed thermosyphon solar water heater. *Solar Energy*, 79(5), 459–468. doi: 10.1016/j.solener.2005.01.001

[20] Oflaz, F., Keklikcioglu, O., & Ozceyhan, V. (2022). Investigating thermal performance of combined use of SiO2-water nanofluid and newly designed conical wire inserts. *Case Studies in Thermal Engineering*, 38, 102378. doi: 10.1016/j.csite.2022.102378

[21] Wole-osho, I., Okonkwo, E.C., Abbasoglu, S., & Kavaz, D. (2020). Nanofluids in solar thermal collectors: Review and limitations. *International Journal of Thermophysics*, 41, 157. doi: 10.1007/s10765-020-02737-1

[22] Meibodi, S.S., Kianifar, A., Mahian, O., & Wongwises, S. (2016). Second law analysis of a nanofluid-based solar collector using experimental data. *Journal of Thermal Analysis and Calorimetry*, 126, 617–625. doi: 10.1007/s10973-016-5522-7

[23] He, Q., Zeng, S., & Wang, S. (2015). Experimental investigation on the efficiency of flat-plate solar collectors with nanofluids. *Applied Thermal Engineering*, 88, 165–171. doi: 10.1016/j.applthermaleng.2014.09.053

[24] Mahian, O., Kianifar, A., Sahin, A.Z., & Wongwises, S. (2015). Heat transfer, pressure drop, and entropy generation in a solar collector using SiO2/water nanofluids: Effects of nanoparticle size and pH. *Journal of Heat and Mass Transfer*, 137(6), 61011. doi: 10.1115/1.4029870

[25] Sarsam, W.S., Kazi, S.N., & Badarudin, A. (2015). A review of studies on using nanofluids in flat-plate solar collectors. *Solar Energy*, 122, 1245–1265. doi: 10.1016/j.solener.2015.10.032

[26] Khanafer, K., & Vafai, K. (2018). A review on the applications of nanofluids in solar energy field. *Renewable Energy*, 123, 398–406. doi: 10.1016/j.renene.2018.01.097

[27] Sahu, M.K., & Prasad, R.K. (2017). Thermohydraulic performance analysis of an arc shape wire roughened solar air heater. *Renewable Energy*, 108, 598–614. doi: 10.1016/j.renene.2017.02.075

Yield augmentation by integrating jute wick in a single slope solar still: an experimental study

Akashdeep Negi[a], Lalit Ranakoti[a], Prabhakar Bhandari[b], Saurabh Aggarwal[c],
Rajesh P. Verma[d], Ankur Singh Bist[e], Arun Uniyal[f], Shivasheesh Kaushik[g*],
Nikhil Kanojia[h], Ayushman Srivastav[h]

[a]Department of Engineering, Graphic Era Deemed to be University, Dehradun 248 002, Uttarakhand, India
[b]Department of Mechanical Engineering, School of Engineering and Technology, K.R. Mangalam University, Gurugram, Haryana 122 103, India
[c]Department of Mechanical Engineering, Uttaranchal University, Dehradun 248 007, Uttarakhand, India
[d]Department of Aerospace Engineering, Graphic Era Deemed to be University, Dehradun 248 002, Uttarakhand, India
[e]Department of Computer Science and Engineering, Graphic Era Hill University, Bhimtal Campus, Bhimtal 263 136, Uttarakhand, India
[f]Department of Mechanical Engineering, COER University, Roorkee 247 667, Uttarakhand, India
[g]Department of Mechanical Engineering, Shivalik College of Engineering, Dehradun 248 007, India
[h]Department of Mechanical Engineering, UPES., Dehradun 248 007, India
*Corresponding author email: shivasheeshkecua@gmail.com

Abstract

The availability of freshwater is a significant challenge in today's world, especially in arid and coastal regions. As a solution, purifying existing open water reservoirs or saline water could help bridge the gap between demand and supply. Solar distillation presents a promising method, requiring low initial investment and leaving no harmful environmental impact. However, limited yield due to the traditional design of a solar system is still a problem. Therefore, in the present study, the traditional design of the solar still, i.e. single slope solar still or conventional solar still (CSS) is modified with jute wick (MSS) at an inclination angle of 30º. The length-to-width ratio was kept at 3:1 to avoid shadows at the corners. The studies were conducted to assess how jute fibre as a wick, wind speed and solar intensity affected the CSS's distillate production. The total yield was found to be 2.69 and 3.208 kg/m² per day for CSS and MSS, respectively. Additionally, daily thermal efficiency was analysed to check the feasibility and practicability of the systems. It was evident that incorporating jute wick improves the thermal efficiency of CSS by 26.6%. These findings recommend MSS as a promising and economically viable solution for enhancing solar still performance.

Keywords: Energy; Solar distillation; Solar still; Tilted wick; Jute wick; Distillate yield

1. Introduction

Needless to say, there is no life without fresh water. It is not only the water we drink, water is part of everything we do. Yet, it is increasingly becoming scary. Already, around 2/3rd of the total population faces water scarcity at least once a month. Islands and coastal areas, in particular areas, are at the forefront of climatic change due to global warming [1]. Therefore, in those places, droughts happen more frequently, and freshwater sources are drying up, resulting in critical day-zero situations (people have to stand in cue for the daily quota of water) in ma-

Nomenclature

A_{ge} – area of glass exposed, m^2
$IS_{(t)}$ – solar intensity, W/m^2
L_{vap} – latent heat of vaporisation, J/kg
$\dot{m}_p$ – hourly distillate yield, kg/h
T_w – temperature of water, K

Greek symbols

$\eta_{d(t)}$ – daily thermal efficiency of the system

Subscripts and Superscripts

ge – glass exposed
vap – vaporisation
w – water

Abbreviations and Acronyms

CSS – conventional solar still
MSS – modified solar still
SEM – scanning electron microscopy

jor cities of both developed and developing nations. So, the population depends on fresh waterfalls from nearby water sources, i.e. canals and groundwater. However, extensive use of these resources results in ecological unbalance. Generally, near coastal areas, the availability of fresh water is limited; moreover, their populations depend on nearby sources, i.e. transportation of fresh water, and ocean water if found purified [2]. The transported water is not economical and feasible in the long term. So, they need a place solution to combat the current scenario. According to the World Health Organization (WHO), the palatability of drinking water has been standardized in the form of total dissolved solids (TDS) [3]. Ocean water contains high TDS of more than 35 ppb (parts per billion). In this context, the TDS value of less than 300 ppm is highly considered for drinking water, while those between 300−600 ppm can be used for drinking water. However, a TDS value above 600 ppm is not considered for drinking purposes [4].

Various techniques such as nanofiltration [5], electrocoagulation [6], electro-oxidation [7], and reverse osmosis [8] are available to treat ocean water. However, due to sophisticated mechanisms and certain drawbacks, such as more energy consumption, these methods are limited to being used in nearby coastal areas [9]. Hence, an alternative low-cost technique named solar distillation can be used to treat saline water in nearby oceans. Solar distillation is a technique used to treat saline water or impure water with the help of solar radiation. It works on the principle of evaporation and condensation. During the process, the saline water is poured into the watershed, and sunlight that passes through the transparent covers and reaches the watershed water surface heats the water. The absorbed heat causes the water molecules to gain energy and transition from liquid to vapour through evaporation. During the process, the impurities, such as salts, bacteria, and other contaminants, are left behind in the wick. The vapour accumulates on the inner surface of the transparent cover due to temperature differences. This condensed water is collected in a separate container at the lowest point of the still. The evaporation and condensation process continues in a continuous cycle under available sunlight [10]. Wicks are materials with a high water-absorbing tendency due to capillary action such as sponges, cotton, jute fibre, khes cloth, polyester cloth, terry cloth, and so on [11]. The introduction of wick results in a higher evaporation rate, which increases the overall distillate of the solar still compared to the conventional one. Moreover, inclined wicks have better distillate output compared to horizontal wicks [12]. Literature [13] suggests the

inclination of the wick should be equal to the latitude of the location to collect maximum solar radiation throughout the day. In order to store maximum solar radiation throughout the day, some special collectors with a roughened surface (such as W-contoured, taper-contoured and reverse taper-contoured turbulators) [14] can be used and for maintaining the energy in transferring medium, micro-channel [15], mini-channel [16], and heat pipe [17] or exchanger can be employed [17]. For instance, Munisamy et al. [18] experimented by inclining the tilted wick solar still at 30ºC. Terry cloth, jute cloth, polyester, and fur fabric cloth were used as the wick material. The maximum distillate was obtained for the fur fabric followed by jute, terry cloth, and polyester fabric. The author found that fur fabric cloth has high water absorbency while low capillary rise compared to jute cloth. Furthermore, Hansen et al. [19] tested the porosity, absorbency, capillary rise, and heat transfer coefficient of various wick materials for the distillate enhancement of the inclined solar still. The results revealed that the porosity of the wick material is an important area of assessment. The high porosity of the wick material has more voids that enable water vapour to move easily toward the condensing surface. In addition, [20] has tested the various parameters affecting the distillate yield of wick-type solar still, i.e. climatic, operational, and design parameters. Janarthanan et al. [21,22] have theoretically and experimentally tested the effect of floating tilted wick solar stills. Mahdi et al. [23] used charcoal pieces to reduce the thermal inertia of watershed-type solar still. The reduction in thermal inertia provided by the wet wick extends the contact time of watershed water with the wick to enhance the evaporation rate [24]. Furthermore, Fayaz et al. [25] experimentally tested the effect of inclination and flow rate over the wick. The author found an angle of 30º as the best for the latitude of the location and the optimum flow rate value was 0.20 g/(m^{2}s). The flow rate of the watershed water was based on experimental testing and the wick should remain completely wet during the experimentation. Modi et al. [26] reported a significant improvement in the distillate yield of 23.71% by modifying conventional solar still (CSS) with jute wick.

A concise summary of results regarding the wick-based distillation is shown in Table 1. The literature review on the distillate yield of stills suggests that the inclination of the wick and materials used for the wick are the factors that influence the distillate yield. However, limited study has been conducted on the effect of the tilted wick inner part of the watershed. This creates

Table 1. Summary of distillate yield from solar stills with wick.

Solar still type	Wick material	Inclination or height	Observation	Reference
Individual watershed	khes cloth	30º	Maximum distillate yield: • CSS – 2.894 kg/m²/day • MSS with tilted wick and flat plate collector – 3.997 kg/m²/day	[13]
Double slope multi wick	black cotton cloth, jute cloth	10,13, 16, 19, 22, 25, 28,31, 34, 37 cm	Maximum productivity for 2 cm water depth: • reference still – 3020 l/day • black cotton cloth – 9012 l/day • jute wick – 7040 l/day	[27]
Inclined individual slope	jute wick	20º, 30º	Distillate enhancement compared to CSS: • jute wick with solar still – 62% • parabolic concentrator solar tracker + wick type solar still's efficiency – 276%	[28]
Individual slope	khes cloth	0, 15, 30, and 45º	Maximum distillate yield: • 0º – 3.1 kg/m²/day • 15º – 3.51 kg/m²/day • 30º – 3.60 kg/m²/day • 45º – 3.41 kg/m²/day	[28]
Individual slope	V-shaped floating jute cloth wick	24º	Winter: • daily productivity – 3.23 kg/m² Summer: • daily productivity – 6.2 kg/m²	[29]
Individual slope	jute cloth	13º	• Maximum daily yield in April – 4.57 kg/m² • Overall efficiency in the month of April – 46%	[30]
Inclined individual slope	jute cloth, terry cloth, polyester cloth, and fur fabric	30º	Productivity: • fur fabric cloth as wick – 3.63 l/day. • jute as wick – 3.39 l/day. • polyester cloth as wick - 2.56 l/day. • terry cloth as a wick – 2.85 l/day	[18]

a research gap in understanding the impact of the wick's tilt angle on the distillation process. Exploring the influence of the wick's inclination within the watershed is a crucial factor for several reasons. The tilt angle can affect the flow dynamic of heat transfer within the still. The combined effect of the low-cost jute wick material and its inclination has not been extensively studied. So, to fill this gap a low-cost jute fibre was used as a wick material of the watershed inner part to enhance the distillate yield of the solar still. The findings were not limited to the fact that a higher number of fins have always shown better performance than arrangements with lower number of fins.

A review of existing literature highlights that both the inclination of the wick and the material used significantly influence the distillate yield in solar stills. However, there is a noticeable lack of comprehensive research focusing on the use of jute material as a wick under a location latitude inclination. This gap limits our understanding of how the wick's tilt angle impacts the efficiency of the distillation process. The inclination angle plays a critical role in influencing heat transfer dynamics within the still. Despite the potential of low-cost jute material, its combined effect with varying inclinations on the performance of solar stills remains underexplored. To address this gap, this study utilizes an affordable jute fibre as the wick material and investigates its inclination within the basin to enhance distillate yield, offering a novel approach to improving solar still performance. Additionally, thermal and economic analyses were performed for better understanding.

2. Materials and methods

2.1. Fabrication of setup

The jute cloth was purchased domestically from a local shop. Raw image of the jute fiber and its microscopic images at 132× and 230× magnification are shown in Fig. 1. Upon closer examination through scanning electron microscopy (SEM) analysis, the jute fiber revealed a unique surface morphology characterized by its inherent roughness and fibrous structure. These features play a critical role in enhancing capillary action and improving water retention, both of which are crucial for the efficient functioning of the solar still. The porosity of the jute fibers, although visually identifiable from the SEM images, directly contributes to their water absorption capability. This property facilitates prolonged water retention within the wick, ensuring steady evaporation rates over time. In this study, a tilted wick inner part of the watershed solar still was constructed using stainless steel grade 304. The aspect area of the still, made of 24-gauge sheet, was 1.8 m × 0.59 m × 0.8 m. The upper part of the still was covered with 5 mm toughened glass sheet with a transmissivity of 90%. The glass was adjusted at an angle of 45º so that maximum radiation could be accumulated during the day. The low-cost jute fiber is used as a wick for the experimental study. A galvanized iron (GI) sheet that was 30° slanted under the location's latitude supported the inclined wick, Fig. 2(B). Prior to experimentation under the environmental conditions, the setup was tested with external radiation panels, Fig. 2(A).
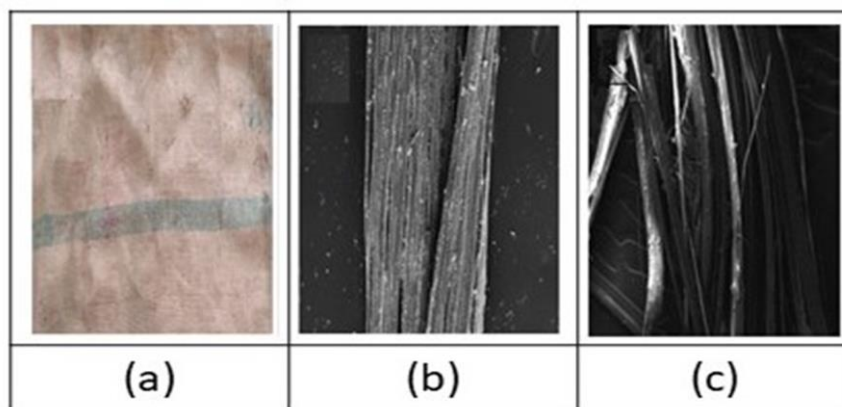
Fig. 1. Image of (a) jute fibre, and its SEM images: (b) at 132× magnification, (c) at 230× magnification.
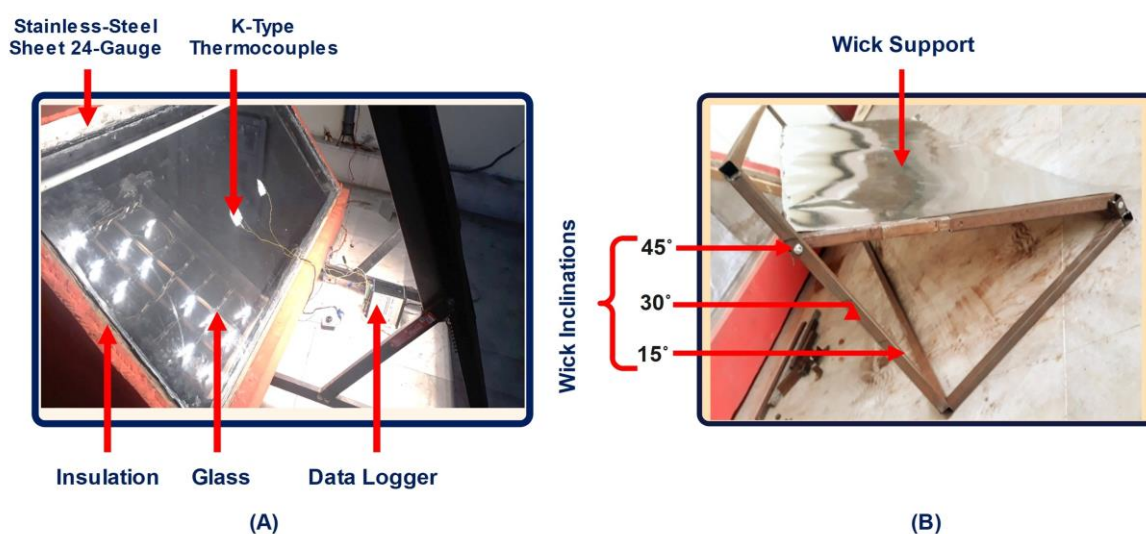

Fig. 2. Images of (A) experimental setup with external radiation panel and (B) wick adjusting stand.

2.2. Experiment procedure

The experiments were performed under the environmental conditions of Chandigarh University of Mohali, Punjab for the latitude of 30.7712° N, 76.5783° E. The experiments were carried out for 3 days in March 2020 and the best day results were disclosed in this study. The details on experimental setup are shown in Fig. 3. The solar still was oriented towards the South to obtain the maximum solar radiation throughout the day. Five K-type thermocouples were used to measure the temperature of different components of the still. The thermocouples were attached to a data logger which recorded the temperature data of the components during experiment time. Each day, the experiment was performed for the available period of solar intensity, i.e. for approximately10 hours, from 9:00 am to 7:00 pm, maintaining the level of the basin water at 3 cm. The distillate output from the setup was measured each hour using a weighing pan. The solar intensity was measured using a solarimeter, while an anemometer was used to measure the wind velocity during the day. The experiments were performed for two cases, viz.: (1) conventional solar still (CSS) and (2) modified solar still (MSS). The case of the modified solar still was the conventional solar still

modified with a tilted jute wick. The experimentation on CSS was performed on 13 March 2020 while for MSS the experimentation was performed on 15 March 2020. Table 2 shows the range and accuracy of the instruments used during experimentation.

Table 2. Details of used instruments during experimentation.

Instruments	Range	Accuracy
Solarimeter	0–1500 W/m²	±1 W/m²
K-type thermocouples	±200°C	±0.1 m/s
Anemometer	0–30 m/s	±0.1°C
Weighing pan	0–5 kg	±0.001 g
Data logger	–	–

2.3. Thermal performance

Thermal efficiency is the ratio of output to input energy of the system. The output energy is defined as the energy required to evaporate the basin water and input energy is expressed in solar intensity. Moreover, thermal efficiency serves as a modest
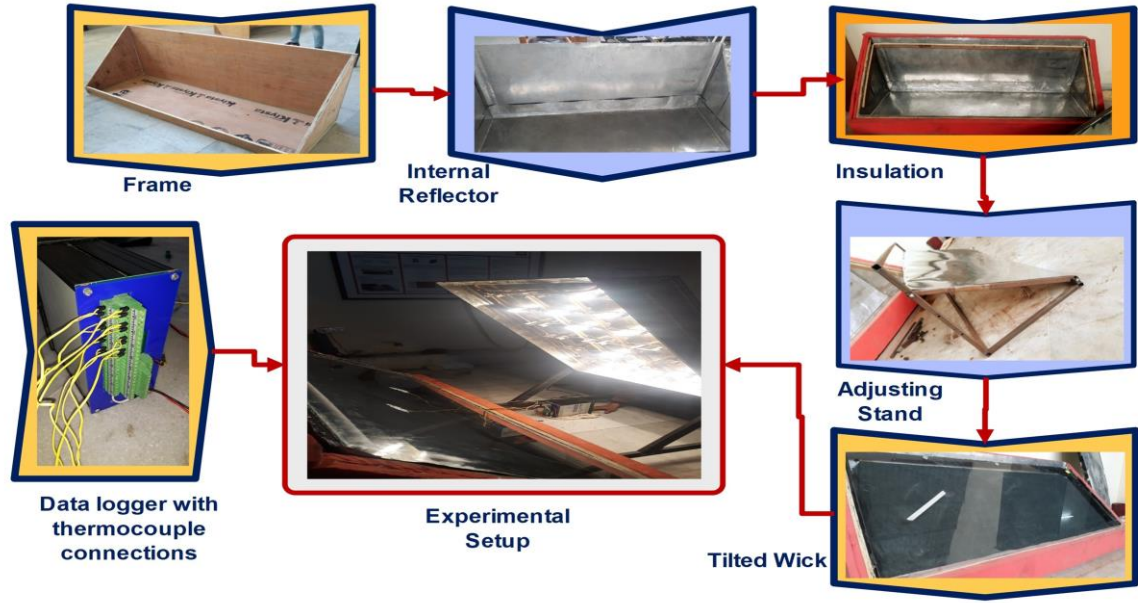
172

Fig. 3. Components of experimental setup.

measure to assess a distiller's capacity to harness the solar radiation available within its area. As such, it stands as a benchmark for comparing the thermal effectiveness between MSS and CSS.

The system's daily thermal efficiency varies with time and depends on the hourly distillate yield ($\dot{m}_p$), solar intensity ($IS_{(t)}$), latent heat of vaporization (L_{vap}), and the area of glass exposed (A_{ge}) to incident solar radiation. It can be calculated using the equation

$$\eta_{d(t)} = \frac{\sum \dot{m}_p L_{vap}}{3600 \sum IS_{(t)} A_{ge}}. \tag{1}$$

Additionally, the L_{vap} can be determined from the equation [31–32]

$$L_{vap} = 3.1615 \times 10^6 \left(1 - 7.616 \times 10^{-4} T_w\right), \tag{2}$$

where T_w stands for the temperature of water.

3. Results and discussion

The effect of jute fibre as a wick on the distillate yield of the individual watershed slope solar still was investigated under actual climatic conditions. In the present study, the distillate yield of the modified solar still is evaluated. Moreover, the results of distillate yield obtained from MSS were compared with those obtained from CSS.

3.1. Variation of solar intensity and wind velocity

The solar intensity and wind velocity during the experimental days are shown in Fig. 4, respectively. The average radiations falling on the surface are approximately similar in the trend for the experimental days. Besides this, the wind velocity fluctuates throughout the experiment duration time for both days. The maximum solar intensity of approximately 1000 W/m² and 980 W/m² was estimated at 12:00 pm − 1:00 pm for CSS and
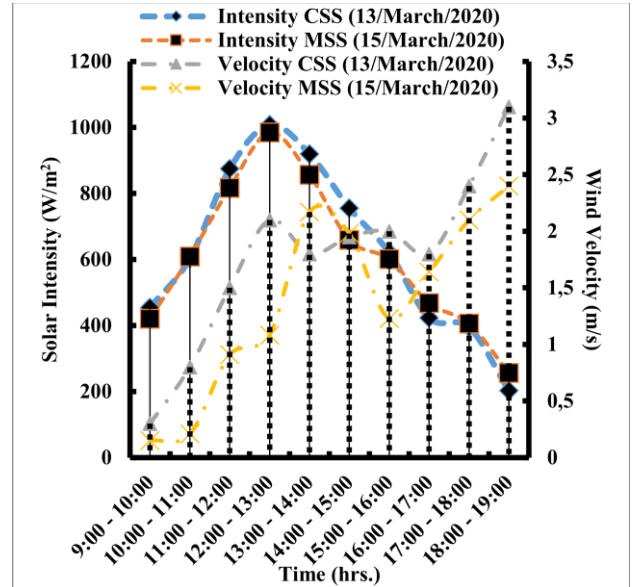

Fig. 4. Variation of solar intensity and wind velocity.

MSS, respectively. After 1:00 pm the solar intensity decreases to 220 W/m² at 6:00 pm – 7:00 pm. Similarly, the wind velocity fluctuates throughout the day. It was low during the day, and increased during the off-shine hours, the wind velocity increased and was found to be maximum during the late hours of testing.

3.2. Variation of the component's temperature and productivity of the conventional solar still

The temperatures of CSS and MSS components are shown in Fig. 5. In the case of CSS, the glass and watershed water is directly exposed to solar radiation, while in the case of MSS the
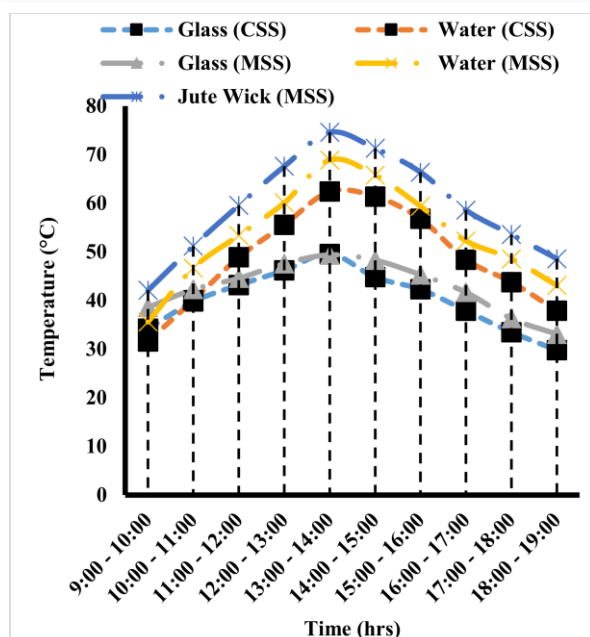
173

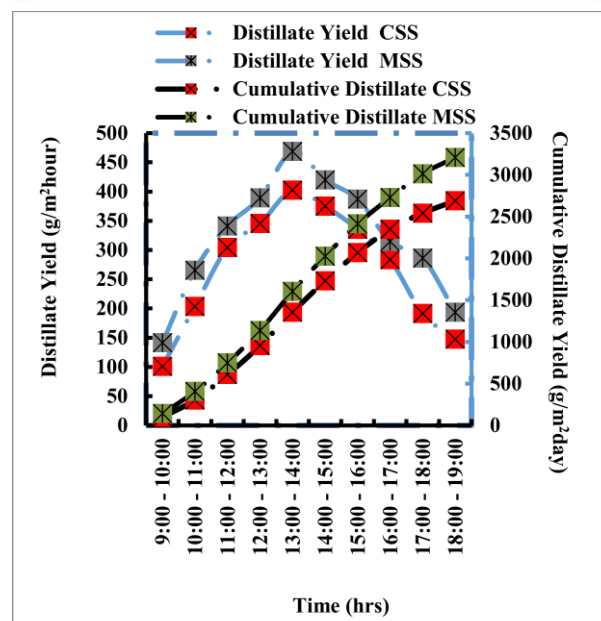Fig. 5. Temperature variations of CSS and MSS components.

Fig. 6. Hourly and cumulative distillate yield of CSS and MSS.

glass and inclined jute wick are directly subjected to solar radiation. The watershed water of the MSS is not subjected to direct solar radiation due to the placement of the wick above the watershed. In the case of CSS, the glass and watershed temperature increases with increased solar radiation until 1:00 pm, after that the energy stored in the form of latent heat of the watershed water further elevates the temperature of water for the next hour. However, due to the direct incident radiation on the glass and the increased evaporation rate of the watershed water, the glass temperature surged but remained lower than the watershed temperature. This may be due to the wind velocity and heat loss to the surroundings.

3.3. Distillate yield of the CSS and MSS

The temperatures of CSS and MSS components are the distillate yield and accumulated yield of the CSS and MSS, shown in Fig. 6. The distillate yield strictly depends on the difference between watershed water and glass temperature in the case of CSS. However, in the MSS, the tilted wick temperature plays a vital role. It is directly proportional to the daily distillate yield obtained with MSS, which is 19.2% higher compared to CSS. The jute fibre as a wick has high capillary rise, which increases the surface area thermal inertia resulting in an increase in the evaporation rate. In the case of CSS, the maximum distillate yield of 402.3 g/m^2 was obtained between 1:00 and 2:00 p.m. during the maximum temperature difference between water and glass. Similarly, the maximum distillate output of MSS was achieved between 1:00 and 2:00 p.m. and was 468 g/m^2. Furthermore, the temperature of the wick played an important role in increasing the evaporation rate. Also, the cumulative yield of 2.69 kg/m^2/day and 3.208 kg/m^2/day was achieved for CSS and MSS, respectively.

3.4. Thermal performance of the CSS and MSS

Thermal performance is a vital parameter in evaluating the performance of the solar still. Therefore, it is utmost important to compare the daily thermal efficiency of the CSS and MSS. Figure 7 portrays the comparison in the daily thermal efficiency of the respected models. It can be clearly seen that, while introducing wick to CSS, it has higher surface area, and consequently a higher distillate yield that has severely influenced the daily efficiency of the system. Figure 7 shows comparative energy efficiency for both respective models. Higher daily efficiency of 41.29% was reported for MSS, while for CSS it was 32.61%.
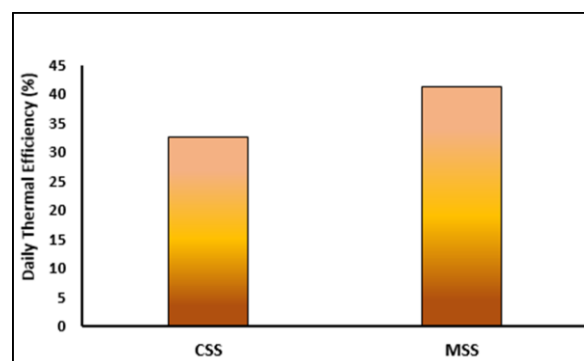

Fig. 7. Daily thermal efficiency of CSS and MSS.

4. Conclusions

The experimental investigation was performed by modifying the conventional solar still (CSS) with and without jute fibre wick at the latitude of the location. The experiments were performed on the actual environmental conditions. The following conclusions were made on the basis of experiments.

- The evaporation rate of the solar still is proportional to the solar intensity during the day.
- Jute fibre as a wick has significant benefits such as good capillary rise, low cost, and ease of availability.
- Yearly maintenance of watershed surface and glass can be helpful to increase the overall distillate yield of the still.
- The daily distillate yield obtained from MSS was 19.2% higher when compared to CSS.
- Properties such as capillary action, porosity, and wettability of the wicks should be an important assessment area and should be considered for future work.
- Investigating the effects of chemical or thermal treatments on jute fibre properties (e.g., hydrophilicity, durability) could further enhance its performance.
- Treating jute fibre with hydrophilic coatings or anti-bacterial agents can improve its longevity and performance in solar stills operating in diverse environmental conditions.
- A comprehensive environmental and economic life-cycle assessment of jute fibre-based systems is recommended to validate their sustainability and long-term viability.

Acknowledgements

References

[1] Boretti, A., & Lorenzo, R. (2019). Reassessing the projections of the World Water Development Report. *npj Clean Water, 2*, 15. doi: 10.1038/s41545-019-0039-9

[2] Hoque, M.A., Scheelbeek, P.F.D., Vineis, P., Khan, A.E., Ahmed, K.M., & Butler, A.P. (2016). Drinking water vulnerability to climate change and alternatives for adaptation in coastal South and South East Asia. *Climatic Change, 136*, 247−263. doi: 10.1007/s10584-016-1617-1

[3] Dulaimi, A., Adham, G., & Younes, M.A. (2017). Assessment of potable water quality in Baghdad City, Iraq. *Air Soil and Water Research, 10*, 1−5. doi: 10.1177/1178622117733441

[4] Chabuk, A., Hammood, Z.A., Ansari, N.A., Abed, S.A., & Laue, J. (2021). Classification maps for TDS concentrations in the GIS along Euphrates River, Iraq. *Water, Air, and Soil Pollution, 232*, 317. doi: 10.1007/s11270-021-05236-7

[5] Diawara, C.K. (2008). Nanofiltration process efficiency in water desalination. *Separation and Purification Reviews, 37*(3), 302−324. doi: 10.1080/15422110802228770

[6] Al-Raad, A.A., Hanafiah, M.M., Naje, A.S., Ajeel, M.A., Basheer, A.O., Aljayashi, T.A., & Toriman, M.E. (2019). Treatment of saline water using electrocoagulation with combined electrical connection of electrodes. *Processes, 7*(5), 242. doi: 10.3390/pr7050242

[7] Heikki, S., Bhatnagar, A., & Sillanpää, M. (2015). Recent developments of electro-oxidation in water treatment − A review. *Journal of Electroanalytical Chemistry, 754*, 46−56. doi: 10.1016/j.jelechem.2015.06.016

[8] Thomas, M.M., Ghaffour, N., Dehwah, A.H.A., Rachman, R.,

Maliva, R.G., & Amy, G. (2013). Subsurface intakes for seawater reverse osmosis facilities: Capacity limitation, water quality improvement, and economics. *Desalination, 322*, 37−51. doi: 10.1016/j.desal.2013.04.021

[9] Lauren, G.F., Lawler, D.F., Freeman, B.D., Marrot, B., & Moulin, P. (2009). Reverse osmosis desalination: Water sources, technology, and today's challenges. *Water Research, 43*(9), 2317−2348. doi: 10.1016/j.watres.2009.03.010

[10] Akashdeep, N., Dhindsa, G.S., & Satbir, S.S. (2020). Performance enhancement of solar still using heat storage medium and nanoparticles. *International Journal of Advance Science and Technology, 29*(10s), 5508−5513.

[11] Hongjie, W., Wang, H., Jin, X., Zhou, H., Wang, H., Wang, W., Ruan, F., Feng, Q., & Lin, T. (2023). Tuning in-plane wicking properties of hydrophilic fibrous membranes using hydrophobic fibrous cover layers. *Advanced Materials Interfaces, 10*(1), 2200741. doi: 10.1002/admi.202200741

[12] Al-Karaghouli, A.A., & Minasian, A.N. (1995). A floating-wick type solar still. *Renewable Energy, 6*(1), 77−79. doi: 10.1016/0960-1481(94)00047-A

[13] Akashdeep, N., Dhindsa, G.S., & Satbir, S.S. (2022). Experimental investigation on individual watershed tilted wick solar still integrated with flat plate collector. *Materials Today: Proceedings, 48*(5), 1439−1446. doi: 10.1016/j.matpr.2021.09.210

[14] Ghildyal, A., Bisht, V.S., Bhandari, P., Thapliyal, S., Kaushik, S., Ranakoti, L., Bangari, R.S., Srivastav, A., Kanojia, N., & Paul, A.R. (2024). A comparative numerical evaluation of solar air heater performance having W-contoured, taper-contoured and reverse taper-contoured turbulators. *Archives of Thermodynamics, 45*(4), 189–196. doi: 10.24425/ather.2024.152008

[15] Bhandari, P., Sharma, V., Ranakoti, L., Bisht, V.,S., Lila, M., K., Kaushik, S., Kanojia, N., Srivastava, A., Kumar, B., Kumar, S.R., Kumar, M., & Paul, A.R. (2024). Numerical investigation of increasing-decreasing stepped micro pin fin heat sink having various arrangements. *Archives of Thermodynamics, 45*(4), 37–44. doi: 10.24425/ather.2024.151995

[16] Kaushik, S., Mehta, J.S., Singh, S., Mahar, V.S., Srivastav, A., Kanoji, N., Kumar, R., Vashisth, S., Karki, S.S., Kumar, A., Bhandari, P., & Singh, D.S. (2024). Comparative study of thermal criteria and fluid-flow criteria in micro and mini channel design constrains with or without insert made of aluminum material. *International Journal of Integrated Engineering, 16*(6), 31−45. doi: 10.30880/ijie.2024.16.06.004

[17] Kaushik, S., Mahar, V.S., Singh, S., Kshetri, R., Kumar, B., Mehta, J.S., Paul, A.R., Kumar, S., Vashisth, S., Pundir, R.S., & Kumar, A. (2024). Comparative experimental analysis of fluid flow in a concentric tube exchanger having semi hollow cylindrical macro inserts with nanofluid and base fluid. *Archives of Thermodynamics, 45*(2), 205–212. doi: 10.24425/ather.2024.150866

[18] Munisamy, T.K., Mohan, A., & Veeramanikandan, M. (2019). Experimental investigation of tilted wick solar still using fabrics. *Australian Journal of Mechanical Engineering, 17*(3), 185–190. doi: 10.1080/14484846.2017.1334306

[19] Hansen, R., Samuel, C., Narayanan, S., & Murugavel, K.K. (2015). Performance analysis on inclined solar still with different new wick materials and wire mesh. *Desalination, 358*, 1−8. doi: 10.1016/j.desal.2014.12.006

[20] Yeh, H.M., & Chen, L.C. (1986). The effects of climatic, design, and operational parameters on the performance of wick-type solar distillers. *Energy Conversion and Management, 26*(2), 175−180. doi: 10.1016/0196-8904(86)90052-X

[21] Janarthanan, B., Chandrasekaran, J., & Kumar, S. (2005).

Evaporative heat loss and heat transfer for open-and closed-cycle systems of a floating tilted wick solar still. *Desalination*, 180(1-3), 291−305. doi: 10.1016/j.desal.2005.01.010

[22] Janarthanan, B., Chandrasekaran, J., & Kumar, S. (2006). Performance of floating cum tilted-wick type solar still with the effect of water flowing over the glass cover. *Desalination*, 190(1-3), 51−62. doi: 10.1016/j.desal.2005.08.005

[23] Mahdi, J.T., Smith, B.E., & Sharif, A.O. (2011). An experimental wick-type solar still system: Design and construction. *Desalination*, 267(2-3), 233−238. doi: 10.1016/j.desal.2010.09.032

[24] Sharshir, S.W., Joseph, A., Kandeal, A.W., & Hussien, A.A. (2022). Performance improvement of tubular solar still using nano-coated hanging wick thin film, ultrasonic atomizers, and cover cooling. *Sustainable Energy Technologies and Assessments*, 52(B), 102127. doi: 10.1016/j.seta.2022.102127

[25] Fayaz, Z., Dhindsa, G.S., & Sokhal, G.S. (2022). Experimental study of solar still having variable slope tilted wick in the watershed to enhance its daily yield. *Materials Today: Proceedings*, 48(5), 1421−1426. doi: 10.1016/j.matpr.2021.09.195

[26] Modi, K.V., & Modi, J.G. (2020). Influence of wick pile of jute cloth on distillate yield of double-basin single-slope solar still: theoretical and experimental study. *Solar Energy*, 205, 512−530. doi: 10.1016/j.solener.2020.05.086

[27] Pal, P., Yadav, P., Dev, R., & Singh, D. (2017). Performance analysis of modified watershed type double slope multi-wick solar still. *Desalination*, 422, 68−82. doi: 10.1016/j.desal.2017.08.009

[28] Jobrane, M., Kopmeier, A., Kahn, A., Cauchie, H.M., Kharroubi, A., & Penny, C. (2022). Theoretical and experimental investigation on a novel design of wick type solar still for sustainable freshwater production. *Applied Thermal Engineering*, 200, 117648. doi: 10.1016/j.applthermaleng.2021.117648

[29] Agrawal, A., & Rana, R.S. (2019). Theoretical and experimental performance evaluation of individual-slope individual-watershed solar still with multiple V-shaped floating wicks. *Heliyon*, 5(4), e01525. doi: 10.1016/j.heliyon.2019.e01525

[30] Shubhajyothi, H., Ganesh, R., Manikandan, V., & Bhavani, T. (2021). Performance evaluation of a tilted wick type solar still by using the concept of solar fraction. *Materials Today: Proceedings*, 37(2), 1112−1132. doi: 10.1016/j.matpr.2020.06.345

[31] El-Sebaii, A.A., Ramadan, M.R.I., Aboul-Enein, S., & Salem, N. (2008). Thermal performance of a single-basin solar still integrated with a shallow solar pond. *Energy Conversion and Management*, 49(10), 2839–2848. doi: 10.1016/j.enconman.2008.03.002

[32] Sahota, L., & Tiwari, G.N. (2016). Effect of Al2O3 nanoparticles on the performance of passive double slope solar still. *Solar Energy*, 130, 260–272. doi: 10.1016/j.solener.2016.02.018

ARCHIVES
OF THERMODYNAMICS

Numerical investigation of heat transfer enhancement in a double pipe heat exchanger using tangential perforated ring turbulators

Ganga Chauhan[a], Vijay Singh Bisht[a], Prabhakar Bhandari[b*], Sandeep Singh[c],
Rahul Shukla[d], Lalit Ranakoti[e], Ankur Singh Bist[f]

[a]Department of Thermal Engineering, Veer Madho Singh Bhandari Uttarakhand Technical University, Dehradun 248 007, Uttarakhand, India
[b]Mechanical Engineering Department, School of Engineering and Technology, K.R. Mangalam University, Gurugram, 122 103, India
[c]O.P. Jindal Global University, Sonipat 131 001, Haryana, India
[d]Mechanical Engineering Department, IET Bundelkhand University, Jhansi 284 001, Uttar Pradesh, India
[e]Department of Mechanical Engineering, Graphic Era Deemed to be University, Dehradun 248 002, Uttarakhand, India
[f]Graphic Era Hill University, Bhimtal campus, Bhimtal 26 3136, Uttarakhand, India
*Corresponding author email: prabhakar.bhandari40@gmail.com)

Abstract

This research investigates the heat transfer and fluid flow characteristics of a double pipe heat exchanger enhanced with perforated turbulators. The study focuses on the effects of varying Reynolds numbers and geometric configurations, particularly the number of perforations in the inserts, on thermal performance. Using the finite volume method and Ansys Fluent simulations, the heat exchanger was analysed under different conditions, comparing the results with a smooth tube configuration. The findings reveal that the pitch ratio of 2.5 has shown the highest heat transfer capacity followed by pitch ratios of 4.5 and 6.5. Further, irrespective of relative pitch ratio, the ring with no perforations has shown the highest value of average Nusselt number and in the case of perforation, the open area ratio of 0.068 has yielded the best thermal performance.

Keywords: Computational fluid dynamics; Double pipe heat exchanger; Perforated ring turbulators; Tangent placed turbulator; Thermohydraulic performance

1. Introduction

Heat exchange between flowing fluids is one of the most important physical processes of concern, and a variety of heat exchangers are used in different types of installations, like process industries, power plants, HVACs (heating, ventilation, and air conditioning systems), etc. The purpose of constructing a heat exchanger is to get an efficient method of heat transfer from one fluid to another, by direct contact or by indirect contact. The heat transfer occurs by three principles: conduction, convection and radiation. In a heat exchanger, the heat transfer through radiation is not taken into account as it is negligible in comparison to conduction and convection [1].

There are generally two methods observed in literature to augment heat transfer, i.e. active and passive techniques [2]. Active techniques require an external source of energy to improve heat transfer efficiency. Examples of such methods include the

Chauhan G., Bisht V.S., Bhandari P., Singh S., Shukla R., Ranakoti L., Bist A.S.

Nomenclature

C_p – specific heat, J/(kg K)
d, D – diameter, mm
D_h – hydraulic diameter, mm
Fr – friction factor
h – ring thickness, mm
H – heat transfer coefficient, W/(m^2 K)
I – uniform heat flux, W/m^2
K – thermal conductivity, W/(m K)
L – length, mm
Nu – Nusselt number, $= H D_h/K$
P – roughness pitch between the rings, mm
p – pressure, Pa
Pr – Prandtl number, $= v/\alpha$
PR – pitch ratio, $= p/D_h$
Re – Reynolds number, $= \rho v D_h/\mu$
T – temperature, K
u, v, w – velocity components, m/s

x, y, z – Cartesian coordinates, m

Greek symbols
α – thermal diffusivity, m^2/s
λ – open area ratios
μ – dynamic viscosity, Pa·s
v – kinematic viscosity, m^2/s
ρ – density, kg/m^3

Subscripts and Superscripts
i – inner
h – hydraulic
o – outer

Abbreviations and Acronyms
CFD – computational fluid dynamics
PTT – twisted tape with perforations
PCR – perforated ring

use of cams and reciprocating plungers to create induced pulsations, employing a magnetic field to disturb light particles in a fluid stream, and implementing mechanical aids. Other techniques involve surface vibration, fluid vibration, electrostatic fields, as well as methods like suction, injection, and jet impingement, all of which depend on an external power source to achieve enhanced heat transfer [3].

Passive techniques involve altering the flow channel's surface or design through various modifications, or insertion of different-sized particles (particularly nano or micro) in fluid [4]. These can include adding components like inserts or swirl flow devices, modifying the surface with treatments or roughness, extending surfaces, using displaced enhancement devices, employing coiled tubes, etc. [5]. Over time, various advanced designs have been introduced to balance acceptable pressure levels while improving heat transfer efficiency. Enhancements in heat exchanger performance have been achieved by optimizing surface area, incorporating turbulence-inducing elements, minimizing the fluid's overall thermal resistance, and lowering pumping power requirements for a given heat load [6,7]. The flow pattern within a heat exchanger's passage is inherently intricate, with the natural formation of vortices. This complexity increases significantly when the geometric configuration is altered, as such modifications amplify interruptions in the flow. By introducing elements like vortex generators or louvers, it is possible to harness this phenomenon to create intentional, large-scale vortices along the flow direction. Commonly used vortex generators include devices like twisted tapes, ring-shaped inserts, baffles, turbulators, winglets, and pins, which are widely implemented to improve the efficiency of heat exchangers. Detailed investigations into heat transfer enhancements have been conducted by researchers, such as Khoshvaght-Aliabadi et al. [8], Sinha et al. [9], and Hu et al. [10].

Researchers have explored various inserts to enhance heat transfer in heat exchangers. Thianpong et al. [11] introduced a novel approach by incorporating twisted tapes with perforations (PTT) into heat exchanger tubes. These tapes are designed with holes along their entire length, which significantly boosts the heat transfer rate. Their findings revealed an impressive improvement of 36−85% compared to plain tubes without PTT. Additionally, they discovered that reducing the pitch ratio and twist ratio of the tapes further enhances heat transfer efficiency. Eiamsa-ard [12] expanded on this concept by employing multiple twisted tapes within the same tube, ranging from two to four tapes. This configuration resulted in thermal performance factors superior to those achieved with a single twisted tape, with an observed efficiency increase of 0.94−1.4%. Murugesan et al. [13] explored the use of twisted tape inserts with trapezoidal cuts and found that these modified inserts significantly improved thermal performance. In another study, Murugesan et al. [14] investigated twisted tapes with U-shaped cuts, discovering that this design achieved a thermal enhancement factor of 1.22 with a twist ratio of 2.0. Promvonge [15] conducted an experimental study combining wire coils and twisted tapes inside a heat exchanger tube. The wire coil was wound around the twisted tape along its entire length, creating a swirl flow within the tube. This combination nearly doubled the efficiency compared to using twisted tape alone. Eiamsa-ard et al. [16] extended this concept by experimenting with variable-pitch coils, finding that adjusting the coil pitch resulted in the highest efficiency.

Arulprakasam Jothi et al. [17] focused on using conical strip inserts as turbulators inside a circular tube. They experimented with conical strips having varying twist ratios in both staggered and non-staggered arrangements. Their research showed that the staggered arrangement of conical strips with a twist ratio of 3 achieved the highest Nusselt number. Promvonge and Eiamsa-ard [18] conducted a study where they utilized a combination of conical-ring and twisted-tape inserts within a circular tube. Their findings revealed that this hybrid configuration significantly improved the heat transfer rate, achieving an enhancement of over 10% compared to using conical-ring inserts alone. This demonstrates the synergistic effect of combining different types of inserts in optimizing thermal performance in heat exchangers.

This research paper focuses on double pipe heat exchangers, and the following are the highlights of relevant work previ-

ously conducted in this field. Saud Ghani et al. [19] experimentally demonstrated that double pipe heat exchangers improve air conditioning performance by reducing compressor work and increasing efficiency. Rennie and Raghavan [20] numerically analysed double pipe helical heat exchangers, providing key design insights for enhancing temperature control and uniformity in liquid food processing. Structural modifications in double pipe heat exchangers primarily involve the incorporation of elements such as fin inserts [21,22], wire inserts [23,24], and tape inserts [25], as well as alterations to pipe designs [26,27]. Additionally, techniques like employing porous media [28] and integrating generators and turbulators [29] are also utilized. Sheikholeslami and Ganji [30] used circular perforated rings turbulators on air side in their double pipe heat exchanger. They placed turbulators in radial direction of the tube and found that thermal performance enhances with an increase in open area ratio. Salem et al. [31] performed comparative experimental study on flower and conventional segmental baffles in double pipe heat exchanger and observed that flower design achieve better characteristics than traditional baffles. Banihashemi et al. [32] investigated the impact of using moving turbulators in heat exchangers, comparing them to stationary turbulators. They found that rotating turbulators, particularly those with smaller angle ratios, greatly improved thermal efficiency and performed better than the stationary versions. Nakhchi et al. [33] studied double-pipe heat exchangers that utilized perforated, inclined elliptic turbulators. Their findings revealed a 217.4% rise in the Nusselt number and a 39.4% improvement in heat transfer. They achieved a thermal efficiency of 1.85 without notable increases in friction loss. Kumar [34] conducted a study on the impact of hemispherical turbulators in a double pipe heat exchanger. The study showed that while the turbulators enhanced heat transfer, they also led to an increase in the friction factor. The highest performance indicator recorded was 1.41.

In present research work, heat transfer and fluid flow properties in a double pipe heat exchanger that uses perforated turbulators inserts were explored. The turbulators were placed tangentially to the inner tube. The novelty of this research lies in the use of tangential perforated ring turbulators to enhance heat transfer in a double pipe heat exchanger, offering a unique design innovation compared to the perforated turbulators studied by Sheikholeslami and Ganji [30]. The tangential orientation of the turbulators induces swirling flows and enhanced turbulence near the heat transfer surfaces, leading to improved fluid mixing and thermal performance. Unlike [30], which focused on axial perforations, this study investigates the effects of open area ratio on both heat transfer and pressure drop. Additionally, demonstrating superior heat transfer rates and overall performance, it provides new insights into optimizing heat exchanger design. The heat exchanger performance were evaluated for varying operating condition, i.e. Reynolds number, and varying geometric condition, i.e. number of perforations in the inserts.

2. Materials and methods

The double-tube heat exchanger featuring perforated rings was numerically simulated using finite volume method. Using commercial code Ansys [35], the heat exchanger was analysed for different operating and geometric parameters. Further, comparison was also made with smooth tubes in heat exchanger. The working fluid for this analysis is air, which flows through a constant heat flux tube equipped with perforated rings.

The present model consists of two concentric tubes: a larger outer tube with an inner diameter (D_i) of 50 mm and an outer diameter (D_o) of 60 mm, and a smaller inner tube with an inner diameter of (d_i) 28 mm and an outer diameter (d_o) of 30 mm. The smaller tube is equipped with perforated rings, which serve to ensure a steady flow of hot air in the outer tube. The perforated rings are made of copper and vary in open area ratios and depths, affecting the fluid flow behaviour. Figure 1a depicts schematic diagram of double-tube heat exchanger with perforated rings. Two views were zoomed out from Fig. 1a. Firstly, the inlet cross section, which shows the location of perforated ring, i.e. tangentially to the inner tube.

The rings were placed at two different locations, i.e. at the top and at the bottom. In the second view, the inner tube is displayed. It shows how perforations were made on the rings, i.e. along the circumference of the circle. Further, for better understanding, 3D geometrical model of present work is shown in Fig. 1b.
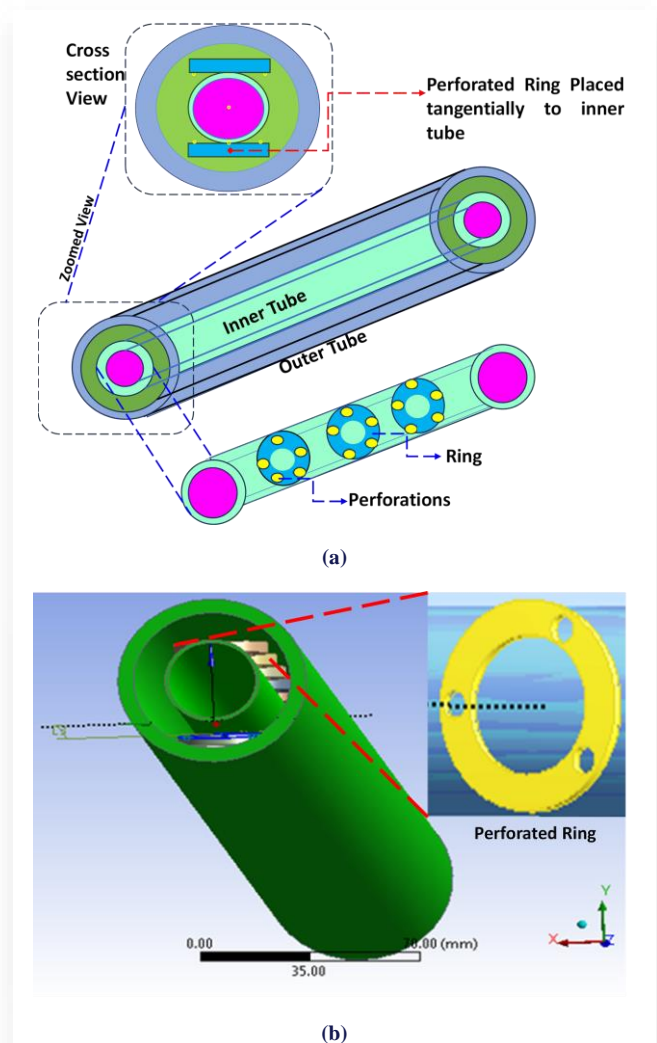

(a)

(b)

Fig. 1. (a) Schematic diagram with zoomed view; (b) 3D geometric model of double pipe heat exchanger with tangential perforated ring turbulators.

179

The study examines different mass flow rates and open area ratios (λ = 0, 0.088, 0.068 and 0.056). A constant heat flux of 1000 W/m² is applied along the entire length of the 1200 mm double-tube system, with turbulent flow conditions analysed in the range of Reynolds numbers from 6000 to 14 000 and pitch ratios (PR) of 2.5, 4.5 and 6.5. Pitch ratio is the ratio of roughness pitch to the hydraulic diameter. The k–ε turbulence renormalisation group (RNG) model with enhanced wall treatment for swirl-dominated flow and thermal effects was used for the simulation in Ansys Fluent.

The cold air flowing in the annular gap was heated by the constant heat flux provided on the inner tube wall. The perforated rings (PCR) enhance the total convective area for better heat transfer. Different PCRs characterised by their number of holes and roughness patterns, are installed on the hot water tube to analyse thermo-hydraulic performance. The entrance and exit lengths within this system are not fixed; instead, they vary based on the pitch, which can range from 75 to 195 mm. As the pitch changes within this range, both the entrance and exit lengths adjust accordingly, reflecting the dependency of these dimensions on the chosen pitch value. It was ensured that the flow reaches a fully-developed state. The complete details of the numerical models are provided in Table 1.

Table 1. Details of geometric parameters of the double-tube with perforated rings shaped roughness.

Parameters	Range of value
Total length of tubes, L	1200 mm
Air tube inner diameter	50 mm
Air tube outer diameter	60 mm
Pitch between the rings	75 mm, 135 mm, 195 mm
Pitch ratio (roughness pitch to hydraulic diameter ratio), PR = p/D_h	2.5, 4.5, 6.5
Hydraulic diameter, D_h	30 mm
Perforated ring thickness	4 mm, 5 mm, 6 mm
Uniform heat flux, I	1000 W/m²
Reynolds number, Re	6000, 8000, 10000, 12000, 14000
Number of holes used in perforated ring, N	3, 5
Diameter of holes	4 mm
Open area ratio, λ	0.0833, 0.068, 0.056
Open area ratio for perforated ring without hole, λ	0
Prandtl number, Pr	0.707

3. Numerical modelling

3.1. Governing equations

The governing equations for the flow system have been formulated for three different flow scenarios: steady laminar, unsteady laminar, and turbulent. This section concentrates on the conservation equations applicable to laminar and turbulent flow conditions. The model is very helpful in present geometry as it accurately predicts the swirling flow conditions. The RNG k–ε turbulence model is having a quite similar structure to standard k–ε

but differs in how it manages turbulent viscosity, diffusion, and heat transfer enhancement. The standard k–ε model is effective for many turbulence scenarios but less suitable for large adverse pressure gradients.

The mathematical expression of the principle of conservation of mass applied to an elemental control volume within a fluid under motion, known as continuity equation, is given by

$$\frac{\partial u}{\partial x} + \frac{\partial v}{\partial y} + \frac{\partial w}{\partial z} = 0. \tag{1}$$

The variables u, v and w are velocity components in x-, y- and z-direction, respectively.

The governing equations for momentum conservation in the fluid domain along the three coordinate axes are formulated as follows:

x-momentum equation

$$\left(u\frac{\partial u}{\partial x} + v\frac{\partial u}{\partial y} + w\frac{\partial u}{\partial z} \right) = -\frac{1}{\rho}\frac{\partial p}{\partial x} + v\left(\frac{\partial^2 u}{\partial x^2} + \frac{\partial^2 u}{\partial y^2} + \frac{\partial^2 u}{\partial z^2} \right), \tag{2}$$

y-momentum equation

$$\left(u\frac{\partial v}{\partial x} + v\frac{\partial v}{\partial y} + w\frac{\partial v}{\partial z} \right) = -\frac{1}{\rho}\frac{\partial p}{\partial y} + v\left(\frac{\partial^2 v}{\partial x^2} + \frac{\partial^2 v}{\partial y^2} + \frac{\partial^2 v}{\partial z^2} \right), \tag{3}$$

z-momentum equation

$$\left(u\frac{\partial w}{\partial x} + v\frac{\partial w}{\partial y} + w\frac{\partial w}{\partial z} \right) = -\frac{1}{\rho}\frac{\partial p}{\partial z} + v\left(\frac{\partial^2 w}{\partial x^2} + \frac{\partial^2 w}{\partial y^2} + \frac{\partial^2 w}{\partial z^2} \right), \tag{4}$$

where p is the pressure, ρ is the density and v is the kinematic viscosity.

Assuming that the flow is steady and incompressible with constant thermal conductivity and without heat generation and viscous heating, the energy equation is as follows:

$$u\frac{\partial T}{\partial x} + v\frac{\partial T}{\partial y} + w\frac{\partial T}{\partial y} = \alpha\left(\frac{\partial^2 T}{\partial x^2} + \frac{\partial^2 T}{\partial y^2} + \frac{\partial^2 T}{\partial y^2} \right), \tag{5}$$

where α is the thermal diffusivity and T is the temperature.

To simplify the numerical simulation, the following assumptions were made in present work:
- the flow is steady throughout the simulation,
- there is no pressure variation in the y-direction,
- shear forces in the y-direction are assumed to be zero,
- effect of gravity on body forces is neglected,
- the flow is incompressible,
- the flow entering the test section is fully developed,
- axial heat conduction in the fluid is considered insignificant,
- air properties are held constant at standard atmospheric conditions.

3.2. Material properties

In the present study, the inner and outer tube contain water and air, respectively. Copper was chosen as the material for the tube wall and perforated rings due to its superior thermo-physical characteristics, high thermal conductivity, machinability, and low cost. The thermo-physical properties of the working fluid and tube material considered in the simulation are tabulated in Table 2.

Table 2. Thermophysical properties of working fluid and materials considered.

Properties	Copper	Air	Water
Density, ρ (kg/m³)	8978	1.225	998.2
Specific heat, C_p, (J/(kg K))	381	1006.4	4182
Thermal conductivity, K (W/(m K))	387.6	0.028	0.6
Viscosity, μ (Pa s)	–	1.7894×10^{-5}	0.001003

Meshing in inner tube having tangential perforated circular ring turbulators

Fig. 2. Meshed image of the inner tube with tangentially placed perforated rings.

3.3. Boundary conditions

For the numerical analysis of the double-tube heat exchanger with perforated rings, the boundary conditions are set for the inlet (velocity), outlet (pressure), and wall surfaces of the model. A no-slip boundary condition is applied to all solid surfaces, and a turbulence intensity of 5% is used for these walls. The inlet flow conditions are defined by a Reynolds number range of 6000 to 14 000. The outer wall of heat exchanger holds adiabatic condition. The simulation is performed using velocity-pressure coupling, Green-Gauss node-based methods, and a second-order upwind scheme for calculating momentum, turbulent kinetic energy, and dissipation rate.

3.4. Mesh generation and grid independence test

In computational modelling, the mesh represents a discrete approximation of the geometric model of the double tube. Achieving the ideal balance of automation, validity, accuracy, and efficiency in meshing often requires compromises. The primary goals of meshing include ensuring valid simulations, enhancing accuracy, and optimizing computational efficiency through high-quality graded meshes and flexible control of mesh density. In this study, 3D uniform meshing was employed, specifically using a regular tetrahedron format. This approach involves boundary-based node smoothing and domain boundary recovery. The mesh was generated for the double tube with perforated rings with specific conditions: a span angle centre of fine resolution, smooth transitions, and an element size of 1 mm, as illustrated in Fig. 2. The perforated rings were resolved by mesh and no separate approach was opted for them. This method combines the best aspects of various meshing tools into a single environment to produce high-quality meshes. The maximum skewness observed is 0.8, with an average skewness of 0.25. The highest skewness values are found in the perforated ring. The domain's orthogonal quality is 0.95, indicating satisfactory mesh quality. Additionally, the cell wall distance y (distance of the cell centre of the first layer of elements from the wall) is set to achieve $y^+ > 1$, considering the high Reynolds number in the model. Once computations are completed, if the results remain consistent across different mesh elements, it indicates that the mesh is independent, meaning that further changes to the mesh will not affect the results. This concept is crucial for ensuring the reliability of comparative results.

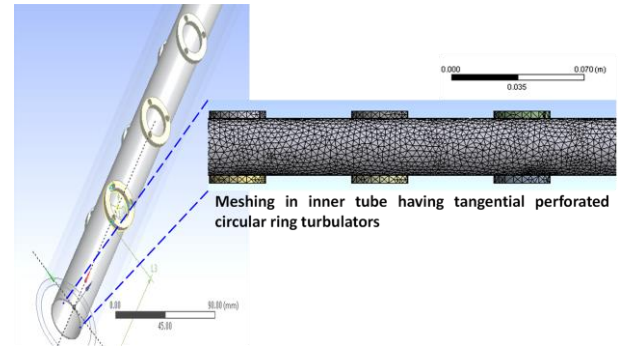A grid independence test was performed using a solution-adaptive refinement method to ensure that the mesh is optimized for the simulation. This method adjusts the mesh to be as effective as possible for solving the flow problem while avoiding unnecessary computational costs. According to Table 3, after reaching 939 124 elements, the heat transfer results stabilized and were accurate for the geometric model. At this mesh size, the Nusselt number remained constant regardless of further grid adjustments.

Table 3. Variation of Nusselt number with grid size.

Number of nodes	Number of elements	Nusselt number
79390	197 959	23.091230
131 146	404 845	33.771310
197 566	797 580	36.156780
220 502	939 124	36.182411

3.5. Validation of present work

To validate the current numerical method and model, the results were compared with those from a study by Sheikholeslami and Ganji [30]. Their research investigated heat transfer in a double pipe with perforated roughness, 1200 mm in length, with inner and outer diameters of 50 mm and 60 mm, respectively. The study evaluated Nusselt numbers and friction factors across different Reynolds numbers (6000, 8000, 10 000, 12 000, 14 000). The comparison of these results, illustrated in Fig. 3, indicated a deviation of ±9% to 12% from experimental data, which is deemed acceptable for CFD simulations using Fluent 14.0.

Further, comparisons were also made between CFD results for the smooth tube and Dittus-Boelter correlation, and a deviation of 3% was observed.

4. Results and discussion

The research focused on analysing the heat transfer performance and pressure drop characteristics of a double tube heat exchanger featuring perforated rings, comparing these results with those of a smooth tube under identical conditions. A three-dimensional model was developed using Ansys Workbench 14.0 for the numerical simulation.

The study investigated how different configurations of perforations (none, three or five) affected the heat transfer and fric-
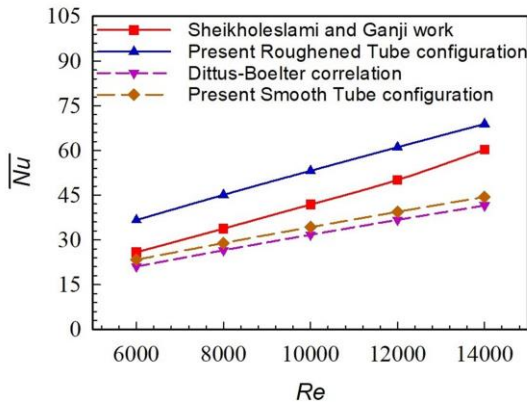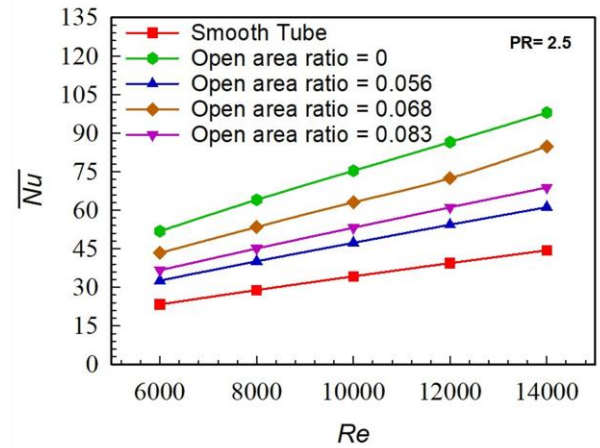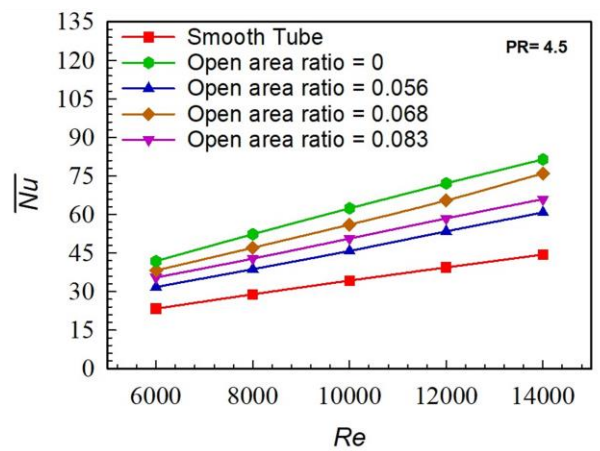
Fig. 3. Validation plot for roughened
and smooth tube configuration.

(a)

(b)

(c)

Fig. 4. Variation of average Nusselt number with Reynolds number
for different configurations of heat exchanger.

tion characteristics of the heat exchanger. The hydraulic diameter for the annular gap was 30 mm, and the simulations covered Reynolds numbers from 6000 to 14 000. The analysis results, presented through the figures, illustrate the variations in Nusselt number (Nu) and friction factor due to the presence of the PCRs.

In order to examine the heat transfer rate of any fluid flow, the importance of Nusselt number cannot be undermined. In such situation, the study of the effect on Nu due to various modification performed on the existing arrangement becomes imperative. Here, different dimension geometries were examined to analyse the variation in Nu with respect to Re. The change in Nu with the change in Re for different geometries at PR = 2.5, 4.5 and 6.5 is shown in Fig. 4a−c, respectively. It can be seen from Fig. 4 that Nu increases with the increase in Re for all geometries. For PR = 2.5, the highest increase in Nu is observed for the case of open area ratio $\lambda = 0$ followed by with an open area ratio of 0.068, 0.083 and 0.056, respectively. Apparently, the lowest rate of increase in Nu was obtained for smooth tube. The trend of Nu changes with respect to Re at PR = 4.5 and PR = 6.5 was observed to be similar to that observed for the case PR =2.5, as shown in Fig. 4b and c, respectively. Unlike the trends of Nu with respect to Re, the difference in the Nu value noted for 2.5 PR is different from that obtained for the cases PR = 4.5 and 6.5. Largest difference in Nu values was observed between the open area ratio of 0.056 and the smooth tube at PR = 2.5, which is comparable to the difference noted between Nu values for the open area ratio 0.056 and the smooth tube at PR = 4.5. The effect of open area ratio on the variation in Nu is noteworthy at PR = 2.5 and 4.5 but upon examining the case for PR = 6.5, it was found that the value of Nu for the open area ratios of 0.056 and 0.083 are very close to each other at every value of Re. Nu values suggested that the heat transfer is dominated by convection at all three values of PR for all geometries except the smooth surface where the convection effect was not found to be of much significance. The heat transfer between the fluid flow is also a function of friction factor. Since friction ratio indicates the friction loss occurring in the system during the flow, it causes reduction in the overall heat transfer from or to the system.
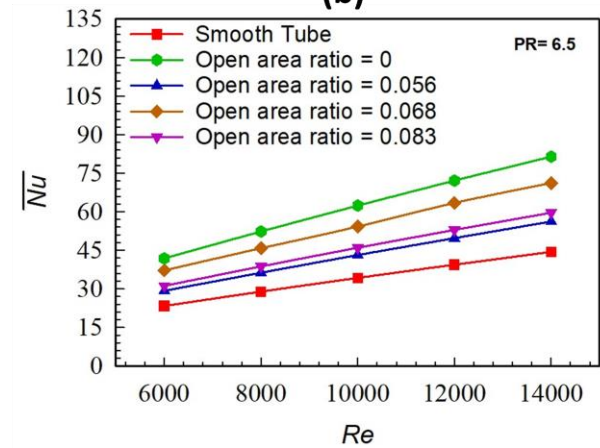
The change in the value of friction factor relative to Re for the considered geometry configurations is plotted in Fig. 5. As can be seen, Fig. 5a−c have been plotted to analyse the effect of change in Re on friction factor for different configurations at PR = 2.5, 4.5 and 6.5, respectively. At PR = 2.5, the change in the friction ratio for smooth pipe with respect to Re is obtained

as the lowest among all configurations with a negligible change. This behaviour of friction ratio for smooth pipe is similar to the behaviour obtained at PR = 4.5 and 6.5 with respect to Re values. Among different configurations, open area ratio $\lambda = 0.056$ exhibits low friction factor, followed by open area ratios $\lambda = 0.083$ and 0.068. It was found that configuration with an open area ratio of $\lambda = 0$ showed the highest friction factor at all values of Re. Interestingly, the difference in the friction ratio values at PR = 4.5 and 6.5 is less as compared to the difference in the friction ratio values obtained for PR = 2.5 at all values of Re. Hence, the improvement in the heat transfer can be achieved in the case of smooth pipe after examining the friction factor. But looking at Nu, the overall heat transfer for smooth pipe is somehow reduced when compared to other configurations.

5. Conclusions

In this study, the heat transfer and fluid flow characteristics of a double pipe heat exchanger equipped with perforated turbulators were comprehensively analysed. The findings demonstrate that the incorporation of these turbulators significantly enhances the heat transfer performance across various operating conditions and geometric configurations. The Nusselt number increased with Reynolds number for all examined geometries, with the most pronounced improvements observed for configurations with specific open area ratios. Additionally, the friction factor analysis revealed that while the use of turbulators increases frictional losses, it concurrently enhances overall heat transfer, making it a promising modification for improving the thermal efficiency of heat exchangers. This research provides valuable insights into optimizing heat exchanger designs for better thermal performance under diverse conditions.

References

[1] Singh, B.P., Bisht, V.S., Bhandari, P., & Rawat, K. (2021). Thermo-fluidic modelling of a heat exchanger tube with conical shaped insert having protrusion and dimple roughness. *Aptisi Transactions on Technopreneurship*, 3(2), 13–29. doi: 10.34306/att.v3i2.200

[2] Kharkwal, H. & Singh, S. (2022). Effect of serrated circular rings on heat transfer augmentation of circular tube heat exchanger. *Archives of Thermodynamics*, 43(2), 129–155. doi: 10.24425/ather.2022.141982

[3] Bhandari, P., Singh, J., Kumar, K., & Ranakoti, L. (2022). A review on active techniques in microchannel heat sink for miniaturization problem in electronic industry. *Acta Innovations*, 45, 45–54. doi: 10.32933/ActaInnovations.45.4

[4] Parveez, M., & Hanief, M. (2022). Enhancement of heat transfer in helical coil heat exchangers using nano-fluids. *Chemical and Process Engineering*, 43(2), 279–283. doi: 10.24425/cpe.2022.140832

[5] Aziz, A., & Rehman, S. (2020). Analysis of non-equidistant baffle spacing in a small shell and tube heat exchanger. *Archives of Thermodynamics,* 41(2), 201–221. doi: 10.24425/ather.2020.133629

[6] Xu, P., Zhou, T., Xing, J., & Fu, Z. (2022). Numerical investigation of heat transfer enhancement in helically coiled specifically shaped tube heat exchangers. *Nuclear Engineering and Design*, 396, 111896. doi: 10.1016/j.nucengdes.2022.111896

[7] Moradikazerouni, A. (2022). Heat transfer characteristics of thermal energy storage system using single and multi-phase cooled heat sinks: A review. *Journal of Energy Storage*, 49, 104097. doi: 10.1016/j.est.2022. 104097

[8] Khoshvaght-Aliabadi, M., Zangouei, S., & Hormozi, F. (2015). Performance of a plate-fin heat exchanger with vortex-generator channels: 3D-CFD simulation and experimental validation. *International Journal of Thermal Science,* 88, 180–192. doi: 10.1016/j.ijthermalsci.2014.10.001
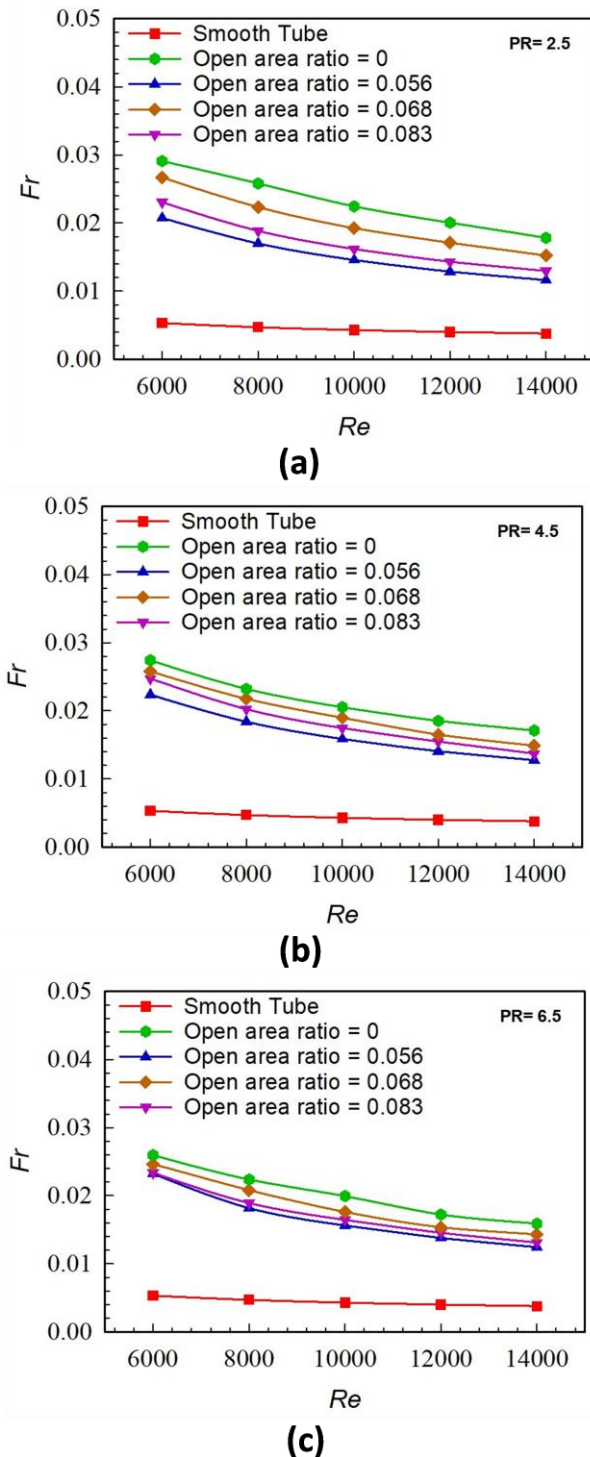
Fig. 5. Friction factor variation with Reynolds number for different configurations of heat exchanger.

[9] Sinha, A., Ashoke Raman, K., Chattopadhyay, H., & Biswas, G. (2013). Effects of different orientations of winglet arrays on the performance of plate-fin heat exchangers. *International Journal of Heat and Mass Transfer*, 57(1), 202–214. doi: 10.1016/j.ijheatmasstransfer.2012.10.034

[10] Hu, D.L., Zhang, Q., Song, K.W., Gao, C., Zhang, K., Su, M., & Wang, L.B. (2023). Performance optimization of a wavy finned-tube heat exchanger with staggered curved vortex generators. *International Journal of Thermal Science*, 183, 107830. doi: 10.1016/j.ijthermalsci.2022.107830

[11] Thianpong, C., Eiamsa-ard, P., & Eiamsa-ard, S. (2012). Heat transfer and thermal performance characteristics of heat exchanger tube fitted with perforated twisted-tapes. *Heat and Mass Transfer*, 48(6), 881-892. doi: 10.1007/s00231-011-0943-0

[12] Eiamsa-ard, S. (2010). Study on thermal and fluid flow characteristics in turbulent channel flows with multiple twisted tape vortex generators. *International Communications in Heat and Mass Transfer*, 31(6), 644–651. doi: 10.1016/j.icheatmasstransfer.2010.02.004

[13] Murugesan, P., Mayilsamy, K., Suresh, S., & Srinivasan, P.S.S. (2009). Heat transfer and pressure drop characteristics of turbulent flow in a tube fitted with trapezoidal-cut twisted tape insert. *International Journal of Academic Research*, 1(1), 123–128.

[14] Murugesan, P.K., Mayilsamy, K., & Suresh, S. (2011). Heat transfer and friction factor in a tube equipped with U-cut twisted tape insert. *Jordan Journal of Mechanical and Industrial Engineering*, 5(6), 559–565.

[15] Promvonge, P. (2008). Thermal augmentation in circular tube with twisted tape and wire coil turbulators. *Energy Conversion and Management*, 49(11), 2949–2955. doi:10.1016/j.enconman.2008.06.022

[16] Eiamsa-ard, S., Nivesrangsan, P., Chokphoemphun, S., & Promvonge, P. (2010) Influence of combined non-uniform wire coil and twisted tape inserts on thermal performance characteristics. *International Communications in Heat and Mass Transfer,* 37(7), 850–856. doi: 10.1016/j.icheatmasstransfer.2010.05.012

[17] Arulprakasajothi, M., Elangovan, K., Hema Chandra Reddy, K., & Suresh, S. (2016). Experimental investigation on heat transfer effect on conical strip inserts in a circular tube under laminar flow. *Frontiers in Energy*, 10(2), 136–142. doi: 10.1007/s11708-015-0389-z

[18] Promvonge, P., & Eiamsa-ard, S. (2007). Heat transfer behaviors in a tube with combined conical-ring and twisted-tape insert. *International Communications in Heat and Mass Transfer*, 34(7), 849–859. doi: 10.1016/j.icheatmasstransfer.2007.03.019

[19] Ghani, S., Gamaledin, S.M.A., Rashwan, M.M., & Atieh, M.A. (2018). Experimental investigation of double-pipe heat exchangers in air conditioning applications. *Energy and Buildings,* 158, 801–811. doi: 10.1016/j.enbuild.2017.10.051

[20] Rennie, T.J., & Raghavan, V.G.S. (2010). Numerical analysis of the lethality and processing uniformity in a double-pipe helical heat exchanger. *Chemical Engineering and Process: Process Intensification*, 49(7), 672–679. doi: 10.1016/j.cep. 2010.05.007

[21] Sahiti, N., Krasniqi, F., Fejzullahu, X., Bunjaku, J., & Muriqi, A. (2008). Entropy generation minimization of a double-pipe pin fin heat exchanger. *Applied Thermal Engineering,* 28(17–18), 2337–2344. doi: 10.1016/j.applthermaleng.2008.01.026

[22] Iqbal, Z., Syed, K.S., & Ishaq, M. (2011). Optimal convective heat transfer in double pipe with parabolic fins. *International Journal of Heat and Mass Transfer*, 54(25–26), 5415–5426. doi: 10.1016/j.ijheatmasstransfer.2011.08.001

[23] Sharifi, K., Sabeti, M., Rafiei, M., Mohammadi, A.H., & Shirazi, L. (2018). Computational fluid dynamics (CFD) technique to study the effects of helical wire inserts on heat transfer and pressure drop in a double pipe heat exchanger. *Applied Thermal Engineering*, 128, 898–910. doi: 10.1016/j.applthermaleng.2017.08.146

[24] Andrzejczyk, R., Muszynski, T., & Kozak, P. (2019). Experimental investigation of heat transfer enhancement in straight and U-bend double-pipe heat exchanger with wire insert. *Chemical Engineering and Process – Process Intensification,* 136, 177–190. doi: 10.1016/j.cep.2019.01.003

[25] Moya-Rico, J.D., Molina, A.E., Belmonte, J.F., Tendero, J.I.C., & Almendros-Ibanez, J.A. (2020). Experimental characterization of a double tube heat exchanger with inserted twisted tape elements. *Applied Thermal Engineering*, 174, 115234. doi: 10.1016/j.applthermaleng.2020.115234

[26] Syed, K.S., Ishaq, M., Iqbal, Z., & Hassan, A. (2015). Numerical study of an innovative design of a finned double-pipe heat exchanger with variable fin-tip thickness. *Energy Conversation and Management*, 98, 69–80. doi: 10.1016/j.enconman.2015.03.038

[27] Vaezi, S., Karbalaee, M.S., & Hanafizadeh, P. (2017). Effect of aspect ratio on heat transfer enhancement in alternating oval double pipe heat exchangers. *Applied Thermal Engineering,* 125, 1164–1172. doi: 10.1016/j.applthermaleng. 2017.07.070

[28] Alomar, O.R., Hamdoon, O.M., & Salim, B.M. (2020). Analysis of two-phase flow in a double pipe heat exchanger filled with porous media. *International Journal of Heat and Mass Transfer*, 156, 119799. doi: 10.1016/j.ijheatmasstransfer. 2020.119799

[29] Sheikholeslami, M., Gorji-Bandpy, M., & Ganji, D.D. (2016). Effect of discontinuous helical turbulators on heat transfer characteristics of double pipe water to air heat exchanger. *Energy Conversion and Management*, 118, 75–87. doi: 10.1016/j.enconman.2016.03.080

[30] Sheikholeslami, M., & Ganji, D.D. (2016). Heat transfer improvement in a double pipe heat exchanger by means of perforated turbulators. *Energy Conversion and Management*, 127, 112–123. doi: 10.1016/j.enconman.2016.08.090

[31] Salem, M.R., Ellaban, M.M., Ali, R.K., & Elmohlawy, A.E. (2024). Experimental investigation of the performance attributes of a double pipe heat exchanger equipped with baffles of conventional or flower layouts. *Applied Thermal Engineering*, 253, 123771. doi: 10.1016/j.applthermaleng.2024. 123771

[32] Banihashemi, S., Assari, M., Javadi, S., & Vahidifar, S. (2024). Study the effect of innovative active and passive methods on thermal characteristics and turbulent flow behaviour in a heat exchanger pipe. *Journal of Thermal Analysis and Calorimetry*, 149, 777–797. doi: 10.1007/s10973-023-12728-7

[33] Nakhchi, M.E., Hatami, M., & Rahmati, M. (2021). Experimental investigation of performance improvement of double-pipe heat exchangers with novel perforated elliptic turbulators. *International Journal of Thermal Sciences*, 168, 107057. doi: 10.1016/j.ijthermalsci.2021.107057

[34] Kumar, S., Dinesha, P., Narayanan, A., & Nanda, R. (2020). Effect of hemispherical turbulators in a double-pipe heat exchanger for heat transfer augmentation, *Journal of Turbulence*. 21(3), 166−185. doi: 10.1080/14685248.2020.1742344

[35] Ansys Fluent, Release 15.0: *User's Guide*. ANSYS Inc. 2013.

ARCHIVES OF THERMODYNAMICS

The influence of seasonality of microgrids connected to the power system on selected power quality parameters

Marta Bątkiewicz-Pantuła

Wrocław University of Science and Technology, Faculty of Electrical Engineering, Institute of Electrical Power Engineering.
Wybrzeże Wyspiańskiego Str. 27, 50-370 Wroclaw, Poland
Author email: marta.batkiewicz-pantula@pwr.edu.pl

Abstract

The article presents an assessment of the parameters of power quality obtained from renewable sources. The assessment was based on the Decree of the Minister of Climate and Environment of March 22, 2023 on detailed conditions for the operation of the electricity system (Dz. U. 2023 r., 819) and the EN 50160: 2010 standard – Parameters of supply voltage in public power grids. The analysis was carried out on the example of actual measurements of power quality parameters. The measurements were made with a Fluke 1760 power quality analyser. The analyser was installed at the point of connection to the renewable energy grid. The article analyses and compares renewable energy sources. The assessment of power quality parameters was carried out on the basis of the discussed analyses. The article presents the influence of seasonality on the parameters of power quality.

Keywords: Seasonality; Power quality; Microgrid; Power system

1. Introduction

Electricity has gained the status of the most popular and most frequently used form of energy [1, 2]. The process of generating, transmitting and using electricity is fully mastered. Energy has become an object of purchase and sale. The main factor determining the price the consumer must pay is, of course, the amount of energy he uses. However, the feature that determines its usefulness for electrical loads is its quality [3].

The best power quality is one in which the voltage curve is uninterrupted and perfectly sinusoidal, and its frequency is rated. The value of the rated voltage is equal to the root mean square (RMS) voltage [4]. The ideal state is impossible to achieve, so for each customer, sufficient electricity quality parameters are determined that do not adversely affect the opera-tion of the facility. All deviations from the ideal are subject to examination and evaluation [5–7]. The basic place of measurement, observation and testing is most often the point of connection to the power grid. The next measurement place is the point on the loads terminals [8].

Power quality is one of the most serious dilemmas in the modern world [9]. It is expected that in the near future, the vast majority of electricity users will have to face, to a greater or lesser extent, complications caused by the issue of energy quality.

2. Power quality parameters

The dynamic development of devices containing high-power semiconductor elements has begun a new and most dynamically

Nomenclature

a – initial value at $t = 0$
b – function trend
n – speed, rpm
P_{st} – short-term light flicker
P_{lt} – long-term light flicker
p – number of analysed data
r – height, m
S_{Oi} – cleaned seasonality indicators
S_t^i – difference between empirical and model values
T – time, month

t – time, month
$\hat{y}$ – regression function
$\hat{y}^*$ – regression function taking into account seasonality
$\hat{y}_T^P$ – forecasting

Abbreviations and Acronyms
HV – high voltage
LV – low voltage
MV – medium voltage
RES – renewable energy sources
RMS – root mean square

developing chapter in the field of power quality. The focus began to be on removing potential sources of power quality degradation by introducing new technical solutions [10–13].

Power quality is an interdisciplinary field that is difficult to interpret clearly. It means something different to the supplier and the consumer of energy, and manufacturers of electrical equipment understand the concept of power quality even differently. The most appropriate definition of power quality is as follows [3]:

"Power quality is a set of parameters describing the properties of the process of supplying energy to the user under normal operating conditions, determining the continuity of the power supply (long and short interruptions in the power supply) and characterizing the supply voltage (value, asymmetry, frequency, shape of the time course)". The normal operating conditions described in the definition mean:

- a state in which power produced is equal to demand,
- connection works in networks proceed without disruptions,
- short circuits are removed by automatic protection equipment,
- factors such as did not occur:
  - temporary electricity supply contracts,
  - a non-compliance with standards or technical requirements by users of electrical installations and devices (connections and operation),
  - extraordinary events:
    - events caused by nature (difficult atmospheric conditions, natural disasters), power shortage resulting from external events,
    - undesirable actions of third parties,
    - actions of public authorities,
    - strikes,
    - forces majeure.

The term power quality is often replaced by electromagnetic compatibility, which is not entirely correct. This is most likely due to the mutual overlap of fields, for example in the context of the emissivity of conducted disturbances and their impact on voltage parameters [14].

The PN-EN 50160 [15–17] standard applies mainly to energy suppliers and specifies the parameters of the supply voltage in terms of value, frequency, correct shape and phase voltage asymmetry. The standard also specifies the permissible levels of deviations of power quality parameters from the rated voltage.

The standard regarding electromagnetic compatibility of electrical devices PN-EN IEC 61000-4-11:2020-11 [18] describes the levels of interference emission for loads. Electromagnetic compatibility applies not only to disturbances and the impact of electrical equipment on the power quality, but also to the condition of the power system.

2.1. Power quality assessment

The measurement of quality parameters should be continuous for a period of at least one week that is representative for a given network [19]. Each measured parameter is averaged over 10 minutes. The concept of a representative week refers to the normal state of network operation (normal network operation and no emergency events). If emergency events occur, they should be omitted in the assessment of power quality parameters.

There are three methods of assessment:
- specifying the number or percentage of values that exceed the permissible values,
- comparison of maximum measured values with permissible values,
- comparison of statistical parameters of measured quantities with limits.

Permissible limits define parent and child documents. The superior document in the process of assessing the power quality is the Decree of the Minister of Climate and Environment of March 22, 2023 on detailed conditions for the operation of the electricity system (Dz. U. 2023 r., 819) [20]. A subordinate document is the PN-EN 50160 standard: Parameters of supply voltage in public distribution networks, which has been updated six times so far, i.e. in 2008, 2010, 2015, 2018, 2020 and 2023 [17].

The basic disorders encountered in installations are:
- voltage fluctuations,
- voltage dips,
- voltage increases,
- power outages.

Voltage fluctuations occurring for various reasons in low voltage (LV), medium voltage (MV) and high voltage (HV) networks are transferred to the low-voltage network, causing the phenomenon of flickering light (flicker). It is the impression of instability of visual perception caused by a light stimulus whose luminance or spectral distribution changes over time. Measuring the flicker phenomenon is an indirect way of assessing voltage fluctuations [21–23].

The measure of the nuisance of light flicker is the short-term light flicker severity factor (P_{st}) and long-term light flicker severity factor (P_{lt}). The nuisance of light flickering caused by voltage fluctuations depends on both the amplitude of the fluctuations and the frequency of their occurrence.

Table 1 specifies the permissible limits of the power quality parameter [17].

Table 1. Permissible limits for light flicker.

Param-eter	Factor	Time	Permissible limits	
			Regulation [20]	Standard PN-EN50160 [17]
Flicker	P_{st}	10 min	–	Up to 35 kV: 1.2 for 95% measurement data set Over 35 kV: 1.0 for 95% measurement data set
	P_{lt}	2h	$P_{lt} \leq 1$ for 95% measurement time	Up to 35 kV: 1.0 for 100% measurement data set Over 35 kV: 0.8 for 100% measurement data set

Analysing Table 1, it can be seen that the limit value of the power quality parameter has been increased in standard PN-EN 50160 [17] compared to previous regulations and the period fulfilling the set limit values has been increased from 95% to 100% of the observation time. Additionally, limit values have been defined for the P_{st} coefficient.

3. Evaluation of power quality parameters for renewable energy sources

Connecting renewable energy sources (RES) to the power system results in decentralized generation, which involves [24]:
- bidirectional energy flow,
- access to a large number of power electronic devices (inverters, controllers),
- stochastic nature of renewable energy generation.

The quality of energy in a microgrid is influenced by three sides at the same time:
- load side,
- distributed generation side,
- energy network site.

This approach significantly complicates the analysis and control of the power system [25]. Therefore, attention to the issue of power quality in microgrids is becoming increasingly common [26–34].

Analysis of selected power quality parameter was carried out for two different renewable energy sources: a wind farm and a hydroelectric power plant.

The analysis of only one selected parameter, which is flicker, i.e. an indirect way of assessing voltage fluctuations, was carried out due to the expected basic disturbances encountered in the network cooperating with RES. Only the values of indicators related to voltage fluctuations are analysed, while other qualitative parameters such as the value of the voltage asymmetry coefficient, voltage distortion and power are not its purpose and will not be included in this analysis. Due to the specific nature of the studied objects, it was assumed that variable weather conditions

and changes in load or energy production may lead to voltage fluctuations in the grid cooperating with RES, and the analysed P_{st} and P_{lt} are key parameters in the analysis of voltage fluctuations.

Figure 1 shows the general conceptual diagram of the measurement system for all analysed renewable sources.
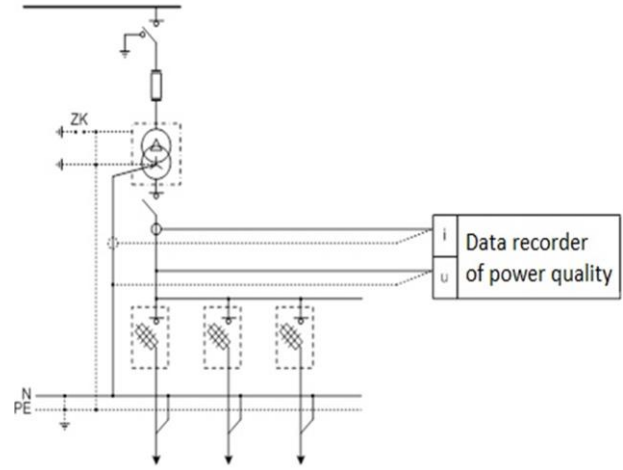

Fig. 1. General conceptual diagram of the measurement system.

The analysed wind farms consist of two wind turbine towers with a height of 24.5 m. Three-propeller wind turbines of the type: VESTAS HSW 250 T (250 kW) and VESTAS V-20-100 (100 kW) with dimensions $r = 8.75$ m, total height 33.50 m and a 0.4 kV cable line from two wind turbine towers and a 0.4 kV cable-distribution cabinet.

The VESTAS V 20-100 wind farm is equipped with an asynchronous generator with a power of 110 kW, generator voltage 400 V, frequency 50 Hz. Synchronous rotation speed $n = 45.05$ rpm. Speed in generator operation: $n = 45.86$ rpm.

The HSW 250T power plant is equipped with two asynchronous generators with a capacity of 80 kW and 250 kW. The generator voltage is 400 V, frequency 50 Hz. The generator is equipped with a set of protections that control the parameters of the power grid and prevent the generator from island operation. The generator protections will cause it to be switched off in the event of an increase or decrease in voltage and an increase in the generator frequency above 50.5 Hz and a decrease in frequency below 49.8 Hz.

The analysed small hydroelectric power plants are equipped with two asynchronous generators with a capacity of 200 kW each. The first power plant is equipped with Francis and Kaplan turbines, in a vertical arrangement with a transmission belt, while the second is equipped with Kaplan turbines, in a vertical arrangement with a transmission belt. Connection to the network via a MV/LV transformer 21000/400 400 kVA. The system is equipped with fully automated capacitor banks. Control of switching the turbines on and off is fully automated, e.g. in the event of voltage failures on the network side. Operation is sometimes switched to manual control, e.g. during maintenance activities.

The full observation time of the recorded parameters was one week, which is consistent with the assumption [17] regarding the assessment of the quality parameters of electric power concerning a representative measurement period.

The measurements of the quality of electric power for two wind power plants and two hydroelectric power plants presented in the work were carried out at the same measurement time for a given group of RES sources. The mentioned power plants of a given type were installed in similar locations. The measurement points designated in this way were intended to check the impact of the power system on the mentioned power plants and to exclude any possible interference from the network on the discussed selected parameters of the quality of electric power.

Figures 2 and 3 show sample graphs for a representative measurement period for two different wind farms. In Figs. 2 and 3, P_{lt} is marked in red, while the P_{st} coefficient is marked in blue. The description of the X-axis data in Figs. 2 and 3 is the measurement time in the format day, hour.
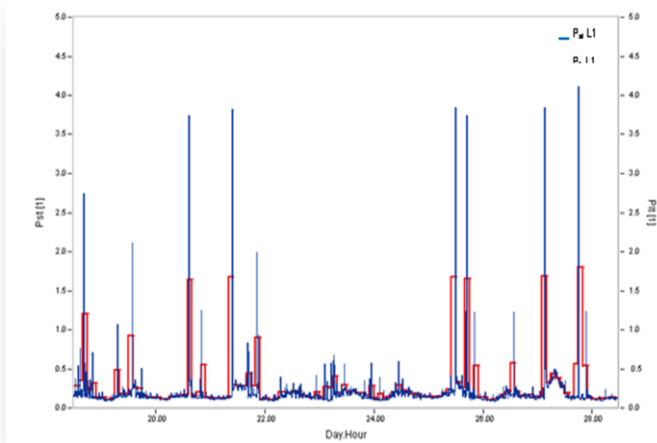
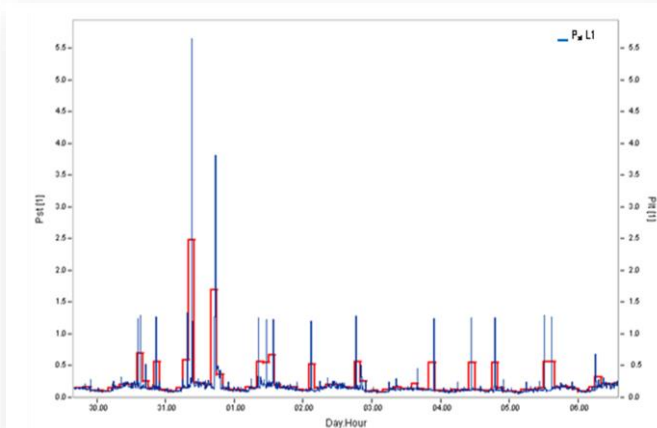Fig. 2. An example graph for a representative measurement period for the first wind farm.

Fig. 3. Sample graph for a representative measurement period for the second wind farm.

Analysing Figs. 2 and 3, it can be seen that increasing most of the limit values of power quality parameters significantly affects the conditions for meeting the normative restrictions, resulting in their failure to meet them.

Figures 4 and 5 show sample graphs for a representative measurement period for two different hydropower plants. In Figs. 4 and 5, P_{lt} is marked in red, while the P_{st} coefficient is marked in blue. The description of the X-axis data in Figs. 4 and 5 is the measurement time in the format day, hour.

Analysing Fig. 4, it can be seen that despite exceeding the P_{st} coefficient in some measurement data values, the coefficient meets the standard requirements for 95% of the measurement data set. Analysing Fig. 5, it can be seen that increasing most of the limit values of power quality parameters significantly affects the conditions for meeting the normative restrictions, resulting in their failure to meet them.
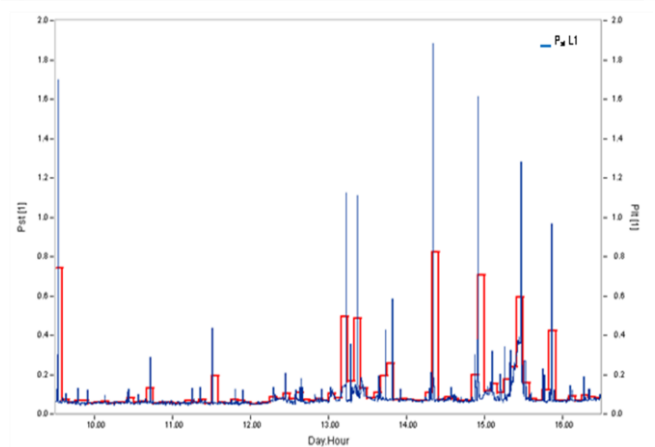

Fig. 4. Sample graph for a representative measurement period for the first hydroelectric power plant.
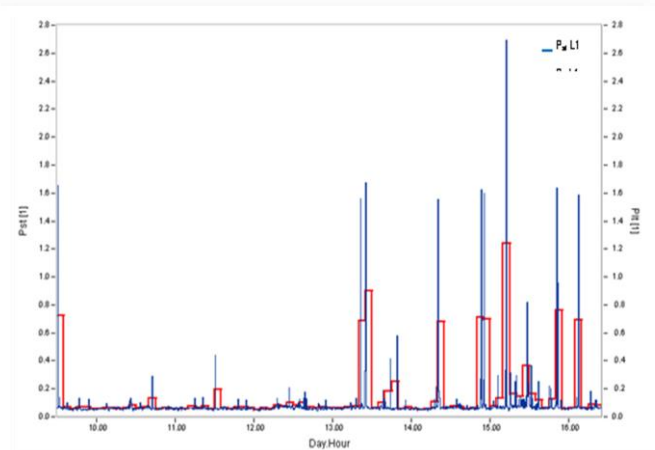

Fig. 5. Sample graph for a representative measurement period for the second hydroelectric power plant.

4. Seasonality of renewable energy sources

One type of statistical series is a time series, which can be defined as a sequence of observations of a phenomenon in subsequent units of time, e.g. years, quarters, months [35,36]. The phenomenon under consideration may be subject to certain regularities, the detection and description of which is the aim of time series analysis [37].

The basic functions of the time series include:
- the regression function described by the formula:

$$\hat{y} = a + bt, \tag{1}$$

- the difference between empirical and model values described by the formula:

$$S_t^i = y_t - \hat{y}_t, \tag{2}$$

- seasonality index described by:

$$S_i = \frac{\sum_{i=1}^{m} S_t^i}{p}, \tag{3}$$

- determination of modified theoretical values taking into account seasonality described by:

$$\hat{y}^* = \hat{y} + S_{Oi}, \tag{4}$$

- forecasting described by:

$$\hat{y}_T^P = b \times T + a + S_{Oi}. \tag{5}$$

Based on the observations of the flicker P_{st} variability, the type of seasonality can be identified. In the example discussed, it is additive in nature.

Figures 6 and 7 show example charts of the seasonality function for two different wind farms. Analysing the charts (Figs. 6
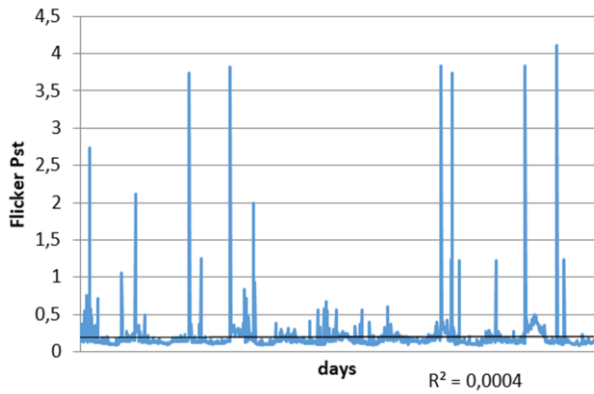
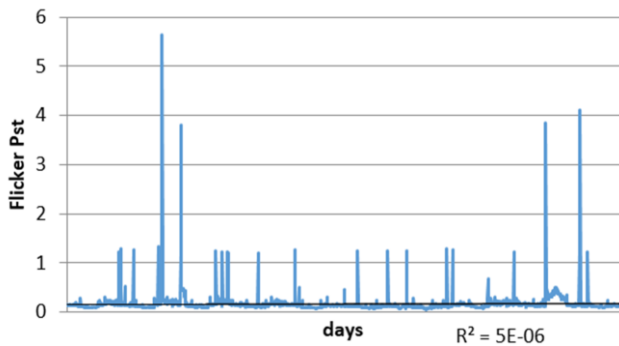Fig. 6. An example chart of the seasonality function for the first wind farm.

Fig. 7. An example of a chart of the seasonality function for the second wind farm.

and 7) it can be observed that the seasonality function has a positive trend. The measure of model fit is low. This is most likely

due to the nature of changes in the flicker coefficient for a wind farm.

Figures 8 and 9 show example charts of the seasonality function for two different hydropower plants. Analysing the charts
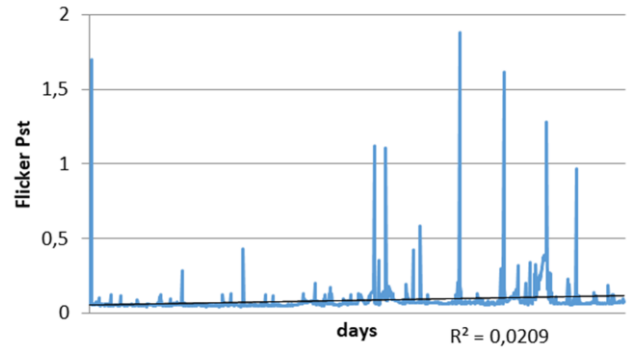

Fig. 8. An example of a seasonality function chart for the first hydroelectric power plant.
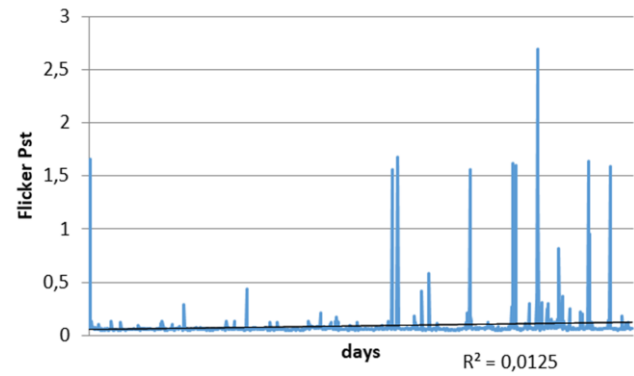

Fig. 9. An example chart of the seasonality function for the second hydroelectric power plant.

(Figs. 8, 9) it can be observed that the seasonality function has a positive trend. The model fit measure is higher. This is most likely due to lower variability of changes in the flicker coefficient for a hydropower plant.

By determining the basic functions of time series in accordance with the relationship (1) and (5), the regression function and forecasting take the form:

- for wind power plants:
  - first power plant:

$$\hat{y} = 0.19 + 0.00021t, \tag{6}$$

$$\hat{y}_T^P = 0.00021 \times 24 + 0.19 + 0.005 = 0.20004, \tag{7}$$

  - second power plant:

$$\hat{y} = 0.17 + 0.00019t, \tag{8}$$

$$\hat{y}_T^P = 0.00019 \times 24 + 0.17 + 0.007 = 0.1815, \tag{9}$$

- for hydroelectric power plants:
  - first power plant:

$$\hat{y} = 0.09 + 0.00015t, \tag{10}$$

Bątkiewicz-Pantuła M.

$$\hat{y}_T^P = 0.00015 \times 24 + 0.09 + 0.072 = 0.1656, \quad (11)$$

    o   second power plant:

$$\hat{y} = 0.09 + 0.00015t, \quad (12)$$

$$\hat{y}_T^P = 0.00015 \times 24 + 0.09 + 0.0071 = 0.1646. \quad (13)$$

From the analyses performed, it can be concluded that the seasonality for hydropower plants is constant and remains at the same level. The forecast growth of flicker for a period of 24 months is 0.16.

Data for wind farms are more volatile. This is directly related to the nature of the installation's operation. The forecast growth of flicker for a period of 24 months is between 0.18–0.20.

5. Conclusions

The seasonality of microgrids connected to the power system affects the power quality parameters only for specific renewable sources.

From the analyses carried out, it can be concluded that for wind farms, the tightening of normative requirements has an impact on the flicker, resulting in a failure to meet the requirements. Connecting the installation does not affect the values of other parameters. Based on such a modified seasonality model for a wind farm, future values can be predicted with greater precision, but the forecast accuracy is not high.

However, for a hydroelectric power plant, there are no power quality parameters that are influenced by the installation despite the stricter requirements. Flicker has no influence on the seasonality of network operation. Based on such a modified seasonality model for a hydropower plant, future values can be forecast with much greater precision and accuracy.

Research and assessment of the power quality are an important and necessary element in the reliability and safety of the power system operation [38]. In installations using renewable energy sources, various loads with non-linear current-voltage characteristics are often used. Loads such as power electronic devices, due to their widespread use and non-linear characteristics, are the most common cause of poor power quality [39]. The share of non-linear loads in the overall balance of power installed at a single consumer increased to the level that new phenomena appeared in the supply voltage. It can therefore be concluded that the structure of microgrids may be a source of additional problems with power quality. The designated measurement points were intended to exclude any possible interference from the network on the selected parameters of the power quality discussed. The measurements of selected parameters of the power quality conducted and presented in the article are the first approach to the analysis of the mutual influence of various RES located in similar locations. The analysis of selected parameters of the power quality conducted was intended to verify the need for mutual, synchronous measurements in the future in order to determine the characteristic features of the given RES. The conducted studies were also intended to check whether similar RES, located close to each other, negatively affect each other, which was not observed in the studied measurement period.

References

[1] Cierpiał-Wolan, M. (2023). *Statistics Poland. Energy consumption in households in 2021*. Warszawa, Rzeszów. Issued by the Spokesperson for the President of Statistics Poland.

[2] Marszałek, M. (2015). Freedom of business activity of the producer – seller of electric energy. *Legal Monographs*.

[3] Hanzelka, Z. (2002). *Power Quality, part 1*, online: http://twelvee.com.pl/pdf/Hanzelka/cz_1_pelna.pdf (in Polish). [accessed 06 Nov. 2023].

[4] Hanzelka, Z. (2013) *Quality of the Electricity Supply-Disturbances of the Voltage RMS Value*. AGH University of Krakow, Kraków (in Polish).

[5] Golla, M., Sankar, S., & Chandrasekaran, K. (2021). Renewable Integrated UAPF Fed Microgrid System for Power Quality Enhancement and Effective Power Flow Management. *International Journal of Electrical Power & Energy System*, 133, 107301. doi: 10.1016/j.ijepes.2021.107301

[6] Ding, Y. (2020). Analysis of Operation and Maintenance of Power Distribution Network Management Technology under the Background of Big Data Era. In *Big Data Analytics for Cyber-Physical System in Smart City. BDCPS 2019. Advances in Intelligent Systems and Computing*, vol 1117 (pp. 610-615). Springer: Singapore. doi: 10.1007/978-981-15-2568-1

[7] Jasiński, M., Sikorski, T., & Borkowski, K. (2019). Clustering as a Tool to Support the Assessment of Power Quality in Electrical Power Networks with Distributed Generation in the Mining Industry. *Electric Power Systems Research*, 166, 52–60. doi: 10.1016/j.epsr.2018.09.020

[8] Piątek, K., Firlit, A., Chmielowiec, K., Dutka, M.; Barczentewicz, S., & Hanzelka, Z. (2020). Optimal Selection of Metering Points for Power Quality Measurements in Distribution System. *12th International Conference and Exhibition on Electrical Power Quality and Utilisation (EPQU)*, 14-15 September, Kraków, Poland.

[9] Lange, A., Pasko, M., & Grabowski, D. (2021). Selected aspects of wind and photovoltaic power plant operation and their cooperation, *Bulletin of the Polish Academy of Sciences Technical Sciences*, 69(6). doi: 10.24425/bpasts.2021.139793

[10] Heping, P., Wenxiong, M,. Yong, W., Le, L., & Zhong, X. (2022). Identification method for power quality disturbances in distribution network based on transfer learning. *Archives of Electrical Engineering*, 71(3), 731−754. doi: 10.24425/aee.2022.141682

[11] Khoa, N.M., Dai, L.V., Tung, D.D, & Toan, N.A. (2021). An advanced IoT system for monitoring and analysing chosen power quality parameters in micro-grid solution. *Archives of Electrical Engineering*, 70(1), 173−188. doi: 10.24425/aee.2021.136060

[12] Nair, D.R., Nair, M.G., & Thakur, T.A (2022). Smart Microgrid System with Artificial Intelligence for Power-Sharing and Power Quality Improvement. *Energies*, 15(15), 5409. doi. 10.3390/en15155409

[13] Guo, X.-H., Chang, C.-W., & Chang-Chien, L.-R. (2022). Digital Implementation of Harmonic and Unbalanced Load Compensation for Voltage Source Inverter to Operate in Grid Forming Microgrid. *Electronics*, 11, 886. doi: 10.3390/electronics11060886

[14] Hanzelka, Z., & Kowalski, Z. (1999). Electromagnetic Compatibility (EMC) and Electrical Power Quality in Standards, *Jakość i Użytkowanie Energii Elektrycznej*, 5(1), 93−107 (in Polish).

[15] EN 50160:2010. *Voltage characteristics of electricity supplied by public electricity networks.*

[16] EN 50160:2019. *Voltage characteristics of electricity supplied by public electricity networks.*

[17] EN 50160:2023 *Voltage characteristics of electricity supplied by public electricity networks.*

[18] EN IEC 61000-4-11:2020-11 *Electromagnetic compatibility (EMC) − Part 4−11: Testing and measurement techniques − Voltage dips, short interruptions and voltage variations immunity tests for equipment with input current up to 16 A per phase.*

[19] Klajn, A., & Bątkiwicz-Pantuła, M., (2013). *Application Note - Standard EN 50 160: Voltage characteristics of electricity supplied by public electricity network.* European Copper Institute, Cu0147(02), 1− 30.

[20] *Decree of the Minister of Climate and Environment of March 22, 2023 on detailed conditions for the operation of the electricity system.* Dz. U. 2023 r., 819 (in Polish).

[21] EN 61000-4-15: 2011 *Electromagnetic Compatibility (EMC) − Test and Measurement Methods − Flicker Meter − Functional and design specifications.*

[22] EN 61000-4-30:2015 *Electromagnetic compatibility (EMC) − Part 4-30: Testing and measurement techniques − Power quality measurement methods.*

[23] "Power Quality" Working Group WG2. (2000). *Guide to Quality of Electric Supply for Industrial Installations. Part 5, Flicker and Voltage Fluctuations.*

[24] Dragicevic, T., Vazquez, S., & Wheeler, P. (2019). Advanced Control Methods for Power Converters in Distributed Generation Systems and Microgrids. *IEEE Transaction on Industrial Electronics*, 66(11), 8866–8869. doi: 10.1109/TIE.2019.2914846

[25] Liao, J., Zhou, N., Wang, Q., Li, C., & Yang, J. (2018). Definition and Correlation Analysis of Power Quality Index of DC Distribution Network. *Proc. Chinese Society for Electrical Engineering*, 38(23), 6847–6860. doi: 10.13334/j.0258-8013.pcsee.181276

[26] Ostrowska, A., Michalec, Ł. Skarupski, M., Jasiński, M., Sikorski, T., Kostyła, P., Lis, R., Mudrak, G., & Rodziewicz, T. (2022). Power Quality Assessment in a Real Microgrid-Statistical Assessment of Different Long-Term Working Conditions. *Energies*, 15, 8089. doi: 10.3390/en15218089

[27] Parol, M., Kapler, P., Marzecki, J., Parol, R., Połecki, M., & Rokicki, Ł. (2020). Effective approach to distributed optimal operation control in rural low voltage microgrids. *Bulletin of the Polish Academy of Sciences Technical Sciences*, 68(4), 661−678. doi: 10.24425/bpasts.2020.134178

[28] Shi, H., Zhuo, F., Yi, H., & Geng, Z. (2016). Control Strategy for Microgrid under Three-Phase Unbalance Condition. *Journal of Modern Power Systems and Clean Energy*, 4, 94–102. doi: 10.1007/s40565-015-0182-3

[29] Li, Y., & Nejabatkhah, F. (2014). Overview of Control, Integration and Energy Management of Microgrids. *Journal of Modern Power Systems and Clean Energy*, 2, 212–222. doi: 10.1007/s40565-014-0063-1

[30] Wang, N., Zheng, S., & Gao, W. (2022). Microgrid Harmonic Mitigation Strategy Based on the Optimal Allocation of Active Power and Harmonic Mitigation Capacities of Multi-Functional Grid-Connected Inverters. *Energies*, 15(17), 6109. doi: 10.3390/en15176109

[31] Arbab-Zavar, B., Palacios-Garcia, E.J., Vasquez, J.C., & Guerrero, J.M. (2019). Smart Inverters for Microgrid Applications: A Review. *Energies*, 12(5), 840. doi: 10.3390/en12050840

[32] Liu, B., Zhao, X., Liu, Y., Zhu, Y., & Chen, J. (2020). Control Strategy of Clustered Micro-Grids for Grid Voltage Unbalance Compensation without Communications. *IET Generation. Transmission & Distribution*, 14(20), 4410–4415. doi: 10.1049/iet-gtd.2020.0421

[33] Zhang, M., Li, Y., Liu, F., Li, W., Peng, Y., Wu, W., & Cao, Y. (2019). Cooperative Operation of DG Inverters and a RIHAF for Power Quality Improvement in an Integrated Transformer-Structured Grid-Connected Microgrid. *IEEE Transaction on Industry Applications*, 55, 1157–1170. doi: 10.1109/TIA.2018.2882504

[34] Golkhandan, N.H., Ali Chamanian, M., & Tahami, F. (2018). A New Control Method for Elimination of Current THD under Extremely Polluted Grid Conditions Applied on a Three Phase PWM Rectifier. *INTELEC. International Telecommunications Energy Conference*, 7–11 October, Torino, Italy. doi:10.1109/INTLEC.2018.8612432

[35] Kot, S., Jakubowski, J., & Sokołowski, A. (2011). *Statistics*, (2nd ed.). Difin S.A. Warszawa (in Polish).

[36] Sokołowski, A. (2010). *Time series analysis and forecasting, Statistics in research and teaching statistics.* StatSoft Polska. Kraków (in Polish).

[37] Ręklewski, M. (2020). *Descriptive statistics. Theory and examples.* State Vocational University in Włocławek (in Polish).

[38] IEA Publications. (2023). *Management Seasonal and Interannual Variability of Renewables.* https://www.iea.org/reports/managing-seasonal-and-interannual-variability-of-renewables [accessed 06 Nov. 2023].

[39] Chojnacki, A.Ł., & Kończak, Z. (2023). Seasonality and causes of damage to power distribution networks. *Elektro.info*, 7–8, 67–71 (in Polish).

ARCHIVES
OF THERMODYNAMICS

Exergetic performance analysis of a direct ammonia-fed solid oxide fuel cell

Anli Shang[a], Hanlin Song[b], Zheshu Ma[b*]

[a]School of Mechanical Engineering, Xijing University, Xi'an, 710123, China.
[b]College of Automobile and Traffic Engineering, Nanjing Forestry University, Nanjing 210037, China.
[*] Corresponding author; E-mail: mazheshu@njfu.edu.cn

Abstract

To explore the performance limit of direct ammonia-fed solid oxide fuel cells based on oxygen-ion conductivity, a finite time thermodynamic model is developed. The finite time thermodynamic indexes including exergy efficiency, exergetic performance coefficient and entropy production rate are derived to evaluate the performance of direct ammonia-fed solid oxide fuel cells from multiple perspectives. Moreover, the effects of operating temperature, operating pressure, fuel utilization, electrolyte thickness and electrode porosity on exergy efficiency and exergetic performance coefficient of the studied direct ammonia-fed solid oxide fuel cells are numerically analyzed. The derived finite time thermodynamic model can be further employed to obtain optimal operating parameters and structural parameters under different application scenarios to guide engineering design and operation control.

Keywords: DA-SOFC; Finite time thermodynamics; Exergetic performance coefficient; Exergy efficiency

1. Introduction

The overuse of fossil energy has brought serious energy crisis and environmental pollution to the world. Fuel cells are very attractive options because of their high efficiency, clean operation and fuel flexibility [1]. Since ammonia is safer, less expensive, easier to store and transport, and non-flammable at normal conditions, it has become a viable fuel for fuel cells [2]. Moreover, the technological foundation for the production of ammonia has been already established. Consequently, there is a growing interest in the use of ammonia in fuel cells, especially solid oxide fuel cells (SOFCs) [3–5].

Traditional methods of studying fuel cells are usually based on idealized assumptions. Finite time thermodynamics (FTT) takes into account the irreversibility and actual operating conditions of the actual power and energy systems, and provides more realistic models for performance optimization [6]. One of the main purposes of FTT is to provide valuable means to optimize thermal and/or fluidic systems by seeking systems performance boundaries considering under finite time and finite size constraints [7].

The primary areas of study in finite-time thermodynamics include finite-time availability, optimum routes of thermodynamic processes, and novel assessment indices [8,9]. These include conventional thermodynamic devices such as power plants [10], heat pumps [11], fuel cells [12,13], and so on. Ge et al. [14] used finite time thermodynamic theory to optimize

Nomenclature

A_{cell} – active cell area, m^2

ex – exergy, J/mol

E_r – cell reversible voltage, V

E^0 – voltage at standard pressure, V

EPC – exergetic performance coefficient

Ex – exergy, W

F – Faraday's constant, C/mol

h – molar enthalpy, J/mol

j – current density, A/m^2

$\dot{m}$ – mass flow rate, kg/h

$n_{H_2,equ}$ – equivalent molar flow rate of H$_2$, mol/s

$n_{H_2,consumed}$ – actual consumed molar flow rate of H$_2$, mol/s

n_{fuel} – amount of fuel required, mol

p – pressure, atm

p_i – partial pressure of i-th component, atm

$p_i{}^{TB}$ – partial pressure of i-th component at three-phase boundary, atm

P – power density, A/m^2

$\overline{R}$ – gas constant, J/(mol·K)

R_Ω – electrolyte resistivity, Ω m

s – molar entropy, J/(mol K)

t_{ele} – electrolyte thickness, mm

T – operating temperature, K

T_e – ambient temperature, K

T_L – temperature of the low-temperature heat source, K

U_f – fuel utilization, %

$V_{act,an}$ – anodic activation overpotential, V

$V_{act,ca}$ – cathodic activation overpotential, V

$V_{con,an}$ – anodic concentration overpotential, V

$V_{con,ca}$ – cathodic concentration overpotential, V

V_{ohm} – Ohmic overpotential, V

W – output power, W

x_i – mole fraction

Greek symbols

ϕ – exergy efficiency

Subscripts and superscripts

0 – standard conditions

act – activation

an – anode

ca – cathode

con – concentration

fc – fuel cell

H$_2$ – hydrogen

H$_2$O – water

O$_2$ – oxygen

ohm – Ohmic

Abbreviations and Acronyms

DA-SOFC – direct ammonia-fed solid oxide fuel cells

EDI – exergy destruction index

ESI – exergy sustainability index

FTT – finite time thermodynamic (model)

GA – genetic algorithm

HT-PEMFC – high temperature proton exchange membrane fuel cell

MSR – methanol steam reforming

ORC – organic Rankine cycle

PEMFC – proton exchange membrane fuel cell

the performance by setting work, power and efficiency as optimization targets and configuration of an internal combustion engine. Chen et al. [15] applied the finite time thermodynamic theory to build a novel solar driven system and analysed the effects of solar irradiance on the thermodynamic performance of the system. Li et al. [13] developed a finite-time irreversible thermodynamic model of proton exchange membrane fuel cell (PEMFC) and produced the ecological performance coefficient and the finite-time ecological objective function. Guo et al. [16] derived finite-time thermodynamic indexes such as exergy efficiency, exergy destruction index (EDI) and exergy sustainability index (ESI) to better evaluate the performance of the fuel cell. Li et al. [17] applied finite time thermodynamic theory to analyse and optimize the power system of a vehicle mounted high temperature proton exchange membrane fuel cell (HT-PEMFC) integrating methanol steam reforming (MSR) and organic Rankine cycle (ORC). The results showed that higher operating temperature and anode pressures are beneficial to improve overall performance and that systems operating at optimum parameters have better thermodynamic, economic and environmental performance.

To improve the performance of fuel cells in economic and ecological terms, many optimization studies have been done for different operating parameters [18]. Hajabdollahi and Fu [19] set up a SOFC cogeneration system optimized with the objective function of maximum exergy efficiency and minimum total cost

rate, and the optimal exergy economic configuration of the system was obtained. Mert et al. [20] carried out multi-objective optimization work on a vehicle-mounted proton exchange membrane fuel cell system using a genetic algorithm (GA) and optimized the system with the goals of maximizing power output, energy efficiency and minimizing power generation costs. You et al. [21] used the NSGA-II method to perform two sets of multi-objective optimizations on the SOFC system with five key objectives: energy efficiency (maximization), system energy efficiency (maximization), system net output power (maximization), freshwater production (maximization), and system total cost (minimization), achieving optimal system performance in three typical scenarios. Forough and Roshandel [22] used genetic algorithms to perform multi-objective optimization of SOFC stacks with minimum energy cost, maximum output power, minimum energy cost and maximum power efficiency as objective functions. Mojaver et al. [23] used a genetic algorithm for the multi-objective optimization of the SOFC power generation system. The current density and the inlet temperature of the stack were used as input variables when the sum of energy efficiency and product unit cost were taken as the objective function, comparing the performance of SOFC-O based and SOFC-H based power generation systems under optimal operating conditions.

In this paper, we first analyse the irreversibility of DA-SOFC from the point of view of finite time thermodynamics, and establish a mathematical model of exergetic efficiency ϕ and

EPC considering irreversible polarizations. Secondly, the performance of DA-SOFC is analysed, and the effects of operating temperature, operating pressure, fuel utilisation, electrolyte thickness and electrode porosity on the exergetic efficiency and *EPC* of DA-SOFC are studied. The results obtained can provide theoretical guidance for the optimization design and practical application of DA-SOFCs.

2. Exergetic performance analysis model of DA-SOFC

Conventional SOFCs typically use oxygen ions as the conducting electrolyte (SOFC-O), such as the commonly used yttria stabilised zirconia (YSZ). In addition, SOFC can also use protons as conductive electrolytes (SOFC-H). In solid oxide fuel cells based on oxygen ion conductivity, there are still problems to be solved such as low cell efficiency due to higher anode concentration overpotential [24]. This paper will focus on the redox reaction in solid oxide fuel cells based on oxygen ion conduction, and study the problems such as reducing the concentration overpotential at the anode, so as to improve the oxygen ion conduction and cell efficiency.

O^{2-} ions must flow through the electrolyte in solid oxide fuel cells based on oxygen ion conducting electrolytes. Air or pure oxygen gas should be supplied to the fuel cell's cathode side. Oxygen is converted to oxygen ions at the cathode-electrolyte junction. At the interface between the anode and electrolyte, these ions go through the electrolyte and react electrochemically with hydrogen gas to form water vapour. Ammonia fuel thermally breaks down to make hydrogen. At the anode side of the fuel cell, the ammonia fuel is fed in and thermally decomposes with the help of a catalyst to produce H_2 and N_2.

Decomposition-produced hydrogen diffuses to the anode-electrolyte interface, where it electrochemically interacts with oxygen ions to make water vapour. The fuel cell releases hydrogen, nitrogen and unreacted ammonia fuel, and produces water vapour. The hydrogen concentration is diluted as a result of creation of nitrogen during the thermal breakdown of ammonia, which lowers the fuel cell's reversible potential. At low temperatures and without a catalyst, the decomposition rate is slower, but at high temperatures and with a catalyst, the decomposition rate is faster.

Based on series process assumptions [15,25,26]:
- ammonia fully participates in gasification reactions,
- by volume, air is composed of 79% non-O_2 fraction and 21% O_2,
- every gas is deemed ideal and gas leakage is negligible,
- all reaction processes are steady-state within the stack,
- the temperature distribution of the stack is uniform,
- using environmental conditions (temperature and pressure of 25°C and 1 atm ≈ 1,013 bar, respectively) as reference conditions, exergy analysis is conducted under design conditions,

the mathematical expressions for the output power, output efficiency, ecological objective function and ecological coefficient of performance of the direct ammonia-fed solid oxide fuel cell were derived in [27].

The single DA-SOFC voltage can be obtained [27]:

$$V = E_r - V_{act,an} - V_{act,ca} - V_{ohm} - V_{con,an} - V_{con,ca}. \quad (1)$$

The output power density of DA-SOFC is [27]:

$$P = \frac{P_{cell}}{A_{cell}} = jV_{cell} = j(E_r - V_{act,an} - V_{act,ca} +$$

$$+ V_{con,an} - V_{con,ca}) = j(E^0 + \frac{\overline{R}T}{2F} ln(\frac{p_{H_2}(p_{O_2})^{\frac{1}{2}}}{p_{H_2O}}) +$$

$$- \frac{\overline{R}T}{F} sinh^{-1}(\frac{j}{zJ_{ca}}) - \frac{\overline{R}T}{F} sinh^{-1}(\frac{j}{zJ_{an}}) - jt_{ele}R_\Omega +$$

$$- \frac{\overline{R}T}{2F} ln\left(\frac{p_{H_2}^{TB} p_{H_2O}}{p_{H_2} p_{H_2O}^{TB}}\right) - \frac{\overline{R}T}{4F} ln\left(\frac{p_{O_2}}{p_{O_2}^{TB}}\right)). \quad (2)$$

For a more detailed derivation and working scheme chart the reader can be referred to reference [27].

Energy loss and deterioration in output performance can result from heat loss and friction between the gas and the channel during DA-SOFC operation. The second law of thermodynamics requires that exergy analysis be carried out in order to thoroughly assess the thermodynamic performance of DA-SOFC. The potential and kinetic energies of the steady state system are negligible. The logistical exergy mainly includes physical exergy and chemical exergy [28], which are calculated by the formula:

$$Ex = \dot{m} \cdot ex = \dot{m}(ex^{ch} + ex^{ph}), \quad (3)$$

$$ex^{ch} = \sum x_i ex_{0,i}^{ch} + RT_0 \sum x_i lnx_i, \quad (4)$$

$$ex^{ph} = (h - h_0) - T_0(s - s_0), \quad (5)$$

where x_i and $ex_{0,i}^{ch}$ are the mole fraction of the substance and the standardized chemical exergy, respectively; T_0 is the ambient temperature; h_0 and s_0 are the specific enthalpy and entropy of the reference state, respectively; $h–h_0$ represents the change in molar enthalpy and $s–s_0$ the change in molar entropy.

In the direct ammonia fuel cell system, the total energy input is:

$$Ex_{in}^{fc} = Ex_{NH_3,in} + Ex_{O_2,in}. \quad (6)$$

The efficient use of energy is reflected in the exergy efficiency of DA-SOFC, which is expressed as follows:

$$\phi = \frac{P}{Ex_{in}^{fc}} = \frac{j(E_r - V_{act,an} - V_{act,ca} - V_{ohm} - V_{con,an} - V_{con,ca})A}{Ex_{H_2,in} + Ex_{O_2,in}}. \quad (7)$$

The exergy balance equation of the steady-state system is expressed as:

$$Ex_D = \sum Q(1 - \frac{T_0}{T}) - W + \sum Ex_{in}^{fc} - \sum Ex_{out}^{fc}, \quad (8)$$

where Ex_D is the exergy loss rate.

The DA-SOFC thermodynamic performance is analysed using the exergetic performance coefficient (*EPC*). It is defined as the output power to exergy destruction rate ratio, combining thermodynamic and exergy performance. *EPC* may be described as follows:

$$EPC = \frac{P}{Ex_D} = \frac{j(E_r - V_{act,\text{an}} - V_{act,ca} - V_{ohm} - V_{con,an} - V_{con,ca})A}{\sum Q(1 - \frac{T_0}{T}) - P + \sum Ex_{in}^{fc} - \sum Ex_{out}^{fc}}. \quad (9)$$

3. Results and discussion

To numerically analyse and compare studied DA-SOFC performance based derived models, the same data sets of a DA-SOFC single cell as in [27] are employed.

3.1. Effects of operating temperature on DA-SOFC performance

The operating temperature of DA-SOFC is crucial for its performance. In a suitable high-temperature environment, the electrochemical reaction rate is accelerated and the electrode activity is improved, which helps to reduce the polarization loss inside the fuel cell stack and thereby increase the efficiency and power density of the fuel cell. Increasing the temperature is beneficial for the rapid conduction of electrons and oxygen ions and enhances the electrical conductivity of DA-SOFC. However, at excessively high operating temperatures, fuel cell components may be affected by corrosion and its life can be reduced. As well, inconsistent thermal expansion coefficients of components may lead to cracks and failures inside the components. In addition, high-temperature operation usually requires expensive special materials such as high-temperature alloys and ceramics, increasing manufacturing costs and also requiring the introduction of more complex thermal management systems. Therefore, accurately selecting and controlling the operating temperature is vital for ensuring the efficient and stable operation of DA-SOFC.

Figures 1 and 2 present the exergy efficiency ϕ and EPC varying with current density at different operating temperatures, respectively. One can see that the operating temperature of DA-SOFC has a significant impact on exergy evaluation indicators. The exergy efficiency ϕ and exergy performance coefficient EPC of DA-SOFC both increase with the increase of operating temperature. In the high current density range, as the operating temperature increases, the electrochemical reaction rate significantly increases, thereby improving the fuel utilization efficiency, reducing fuel waste, and effectively reducing the exergy loss of the system. At the same time, increasing the temperature also leads to an increase in ionic conductivity, significantly reducing the ionic conduction resistance and slowing down the waste heat generation caused by ionic transmission resistance. Therefore, during the operation of DA-SOFC, the unrecoverable exergy loss is significantly reduced. As shown in Fig. 2, in the low current density range, the improvement degree of EPC by increasing temperature is much smaller than that in the high current density range. This is mainly because under low current density conditions, the electrochemical reaction rate is relatively slow, so the influence of operating temperature on the activity of electrons and ions is relatively limited. However, when the current of DA-SOFC is 15 000 A/m^2 and the operating temperature is increased from 1043 K to 1103 K, EPC increases by 61%. Therefore, increasing the operating temperature can significantly improve the exergy performance of DA-SOFC.
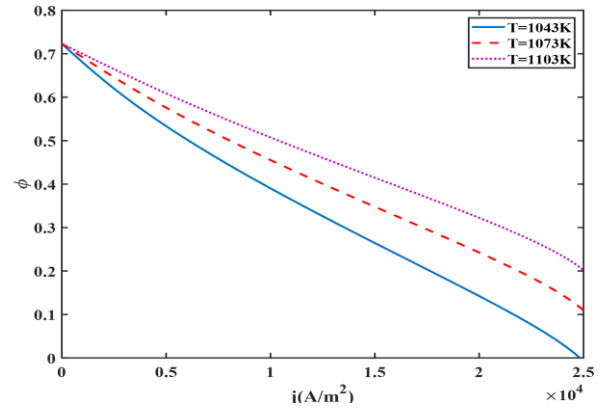

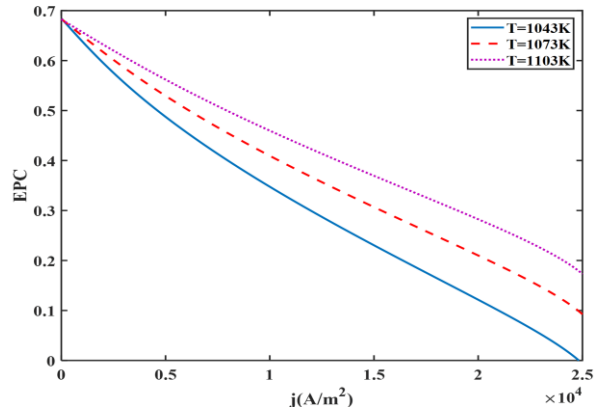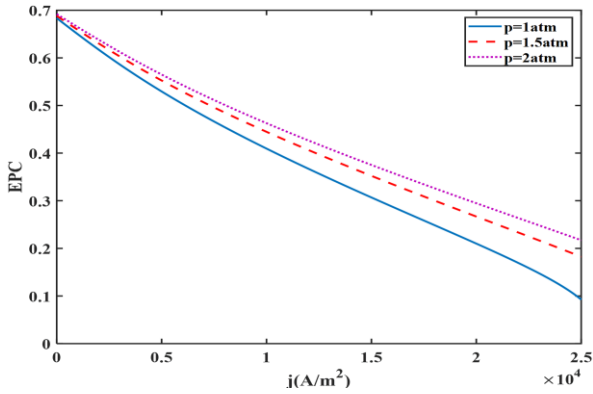Fig. 1. ϕ varying with current density at different T.

Fig. 2. EPC varying with current density at different T.

3.2. Effects of operating pressure on DA-SOFC performance

As is known to all, increasing the operating pressure can significantly improve the thermodynamic performance of DA-SOFC. First of all, increasing the operating pressure helps to increase the gas diffusion rate and makes it easier for reactants to be transported inside the fuel cell flow field, so that fuel and oxygen can be used more effectively, thereby improving the overall efficiency. Secondly, a higher operating pressure is conducive to reducing the flow resistance and improving the response speed of the fuel cell. However, increasing the operating pressure will consume more power from auxiliary equipment such as compressors, requiring higher costs, and the manufacturing and maintenance costs of the system may also increase. Therefore, when considering increasing the operating pressure, multiple factors such as performance improvement, system cost, and material strength must be comprehensively considered to find the best operating parameters to meet the needs of specific application scenarios. In general, optimizing the operating pressure is one of the important strategies to improve the performance of fuel cell systems, but various factors need a careful trade-off.

Figures 3 and 4 reflect the changes of exergy efficiency ϕ and exergy performance coefficient EPC with the current density under different operating pressures p. As can be seen from

196

the figures, the exergy efficiency ϕ and exergy performance coefficient *EPC* of DA-SOFC both increase with the increase of operating temperature. When the current density is 15 000 A/m^2 and the operating pressure changes from 1 atm to 2 atm, the exergy efficiency ϕ and exergy performance coefficient *EPC* increase by 11.1% and 22.5%, respectively. Therefore, when the current density and operating temperature are constant, increasing the operating pressure can significantly improve the exergy performance indicators of DA-SOFC.
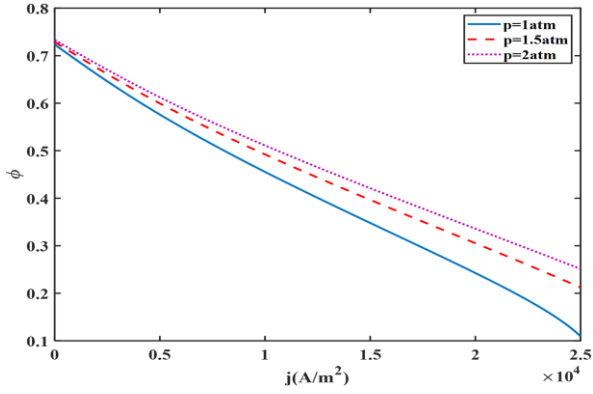
Fig. 3. ϕ varying with current density at different *p*.

Fig. 4. *EPC* varying with current density at different *p*.

3.3. Effects of fuel utilization on DA-SOFC performance

Fuel utilization rate U_f has an important impact on the performance of fuel cells. A higher fuel utilization rate U_f means more efficient conversion of fuel into electrical energy, thereby improving the overall efficiency of the fuel cell. By maximizing the available portion of fuel chemical energy, the economy and sustainability of the fuel cell system can be significantly improved. This has positive significance for realizing clean energy conversion and mitigating climate change in the field of sustainable energy. However, multiple aspects such as fuel supply, reaction kinetics, and system design need to be comprehensively considered to achieve optimal fuel utilization rate U_f. Therefore, in the development and optimization of fuel cell technology and applications, maximizing the fuel utilization rate is one of the key considerations for achieving efficient, economical and sustainable energy conversion.

Figures 5 and 6 present the influence of fuel utilization rate U_f on the exergy performance indicators of DA-SOFC under different operating pressures when the inlet flow rate and the operating temperature are constant. The exergy efficiency ϕ and exergy performance coefficient *EPC* of DA-SOFC both increase with the increase of fuel utilization rate U_f. Increasing the fuel utilization rate U_f can reduce the consumption of underutilized fuel in the system through non-electrochemical pathways, thereby reducing unnecessary heat generation. A higher fuel utilization rate U_f also means a more effective power generation process, reducing the energy loss caused by electrochemical reactions inside the system and helping to slow down the temperature rise of the system and further reducing the release of waste heat. When the operating temperature is 1073 K, the current density is 15 000 A/m^2 and the fuel utilization rate is 0.9, the exergetic performance coefficient is increased by 22.2%. Therefore, improving fuel utilization can reduce cell heat loss and improve the exergetic performance coefficient. In summary, under certain conditions, increasing fuel utilization can improve the finite time thermodynamic performance of DA-SOFC.
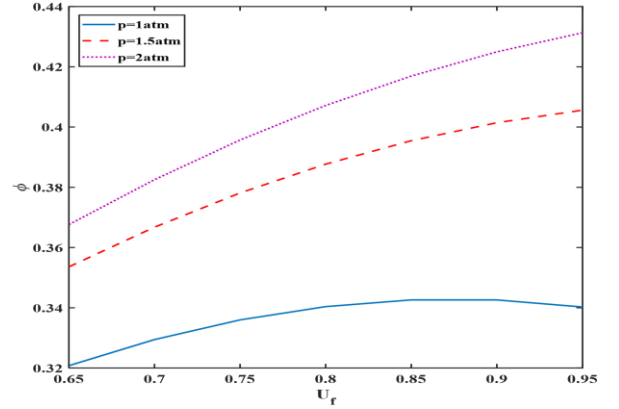

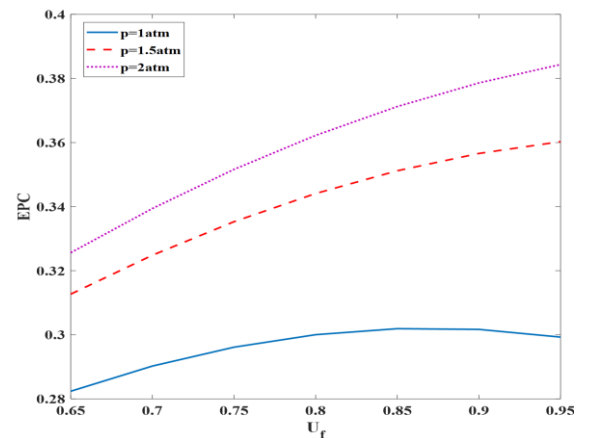Fig. 5. ϕ varying with fuel utilization at different *p*.

Fig. 6. *EPC* varying with fuel utilization at different *p*.

3.4. Effects of electrolyte thickness on DA-SOFC performance

Electrolyte thickness is a key design parameter for fuel cells and has an important impact on system performance. When the elec-

trolyte thickness is too large, the internal resistance of the fuel cell also increases due to the increase in the resistance of the ion transport path. This will increase the resistance of current transmission in the electrolyte and reduce the overall conductivity of the fuel cell, thus affecting the output power. A thicker electrolyte may also lead to an increase in the voltage drop between electrodes, thus affecting the fuel cell system efficiency. Secondly, a thicker electrolyte increases the gas diffusion path and hinders the effective transportation of fuel and oxygen. This affects the utilization efficiency of reactants and reduces the rate of electrochemical reactions. Therefore, the response speed of the fuel cell is slower, affecting its dynamic performance, which may be limited, especially in applications that require a quick response. Therefore, when designing a fuel cell, it is necessary to carefully balance the influence of electrolyte thickness on resistance and reaction rate.

Figures 7 and 8 demonstrate the influence of electrolyte thickness t_{ele} on the exergy performance indicators of DA-SOFC when the operating temperature is constant.
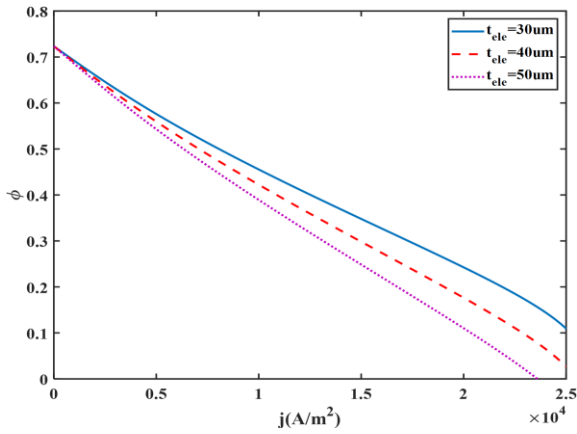

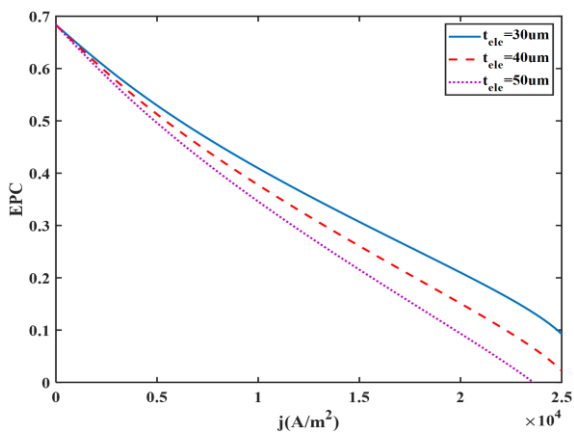Fig. 7. ϕ varying with current density at different t_{ele}.

Fig. 8. EPC varying with current density at different t_{ele}.

The exergy efficiency φ and exergy performance coefficient EPC of DA-SOFC both decrease with the increase of electrolyte thickness. Increasing the electrolyte thickness of DA-SOFC has a significant impact on waste heat generation. There are multiple reasons for the increase in waste heat generation in DA-SOFC

due to an increase in electrolyte thickness. First, increasing the electrolyte thickness will significantly increase the internal resistance of the fuel cell, leading to greater Ohmic losses. Secondly, due to the increase in electrolyte thickness, the diffusion path of fuel and oxygen in the fuel cell becomes longer, increasing the resistance to mass transfer. This leads to more diffusion limitations, reducing the utilization efficiency of fuel, thereby increasing the proportion of chemical energy that is not converted into electrical energy and is converted into thermal energy. Therefore, although an increase in electrolyte thickness is beneficial to some aspects of performance, it simultaneously brings greater resistance and diffusion limitations, resulting in additional waste heat generation. All these reasons will lead to an increase in exergy loss, resulting in a decrease in exergy efficiency ϕ and exergy performance coefficient EPC.

3.5. Effects of porosity on DA-SOFC performance

The porosity of fuel cell electrodes greatly affects DA-SOFC performance. Moderate porosity can improve gas diffusion and electron conduction, and promote the effective transmission of reactants in the electrode. Higher porosity helps to increase gas passage in the electrode, provides more active surfaces and promotes catalytic reactions. However, too high porosity may also lead to a loose electrode structure and reduce the effective electrode surface area, thereby affecting the reaction rate. Too high or too low porosity may lead to the concentration of mechanical stress and affect the stability of the electrode structure, thus affecting DA-SOFC life. An increase in porosity may lead to an extension of the gas flow path and an increase in gas diffusion resistance. Therefore, when optimizing the porosity value of fuel cell electrodes, factors such as gas diffusion, electron conduction and reaction rate need to be comprehensively considered to achieve the appropriate performance.

Figures 9 and 10 present the influence of electrode porosity ε on the exergy performance indicators of DA-SOFC when the operating temperature is constant. The exergy efficiency ϕ and exergy performance coefficient EPC of DA-SOFC both decrease with the increase of electrode porosity ε. A moderate pore structure can improve the uniform distribution of fuel in the electrode, improve the utilization efficiency of fuel, help to maximize the conversion of chemical energy into electrical energy, and reduce the proportion of unused energy converted into thermal energy, thereby improving the thermal efficiency of the fuel cell. When increasing the porosity, EPC increases. When the current density is 15 000 A/m^2 and the porosity increases from 0.6 to 0.8, EPC increases by 6.8%. From this analysis, it can be seen that the exergy performance and ecological performance of the fuel cell can be improved by adjusting the microstructure of the electrode, thereby improving the finite time thermodynamic performance of DA-SOFC.

4. Conclusions

A novel finite time thermodynamic model formulating the exergy efficiency and EPC is derived for a DA-SOFC. The effects of parameters including the operating temperature, operating pressure, fuel utilization, electrolyte thickness and electrode porosity on the finite time thermodynamic performance of the
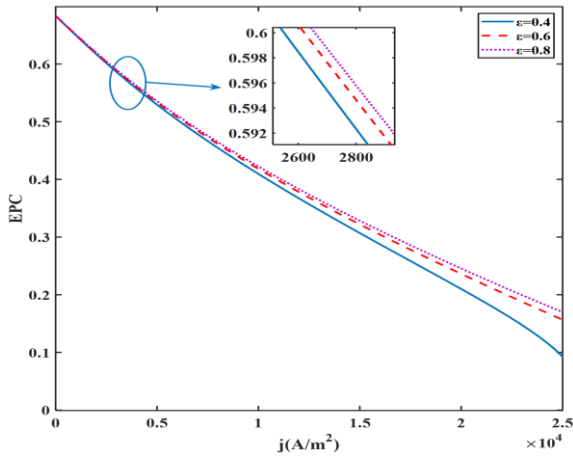
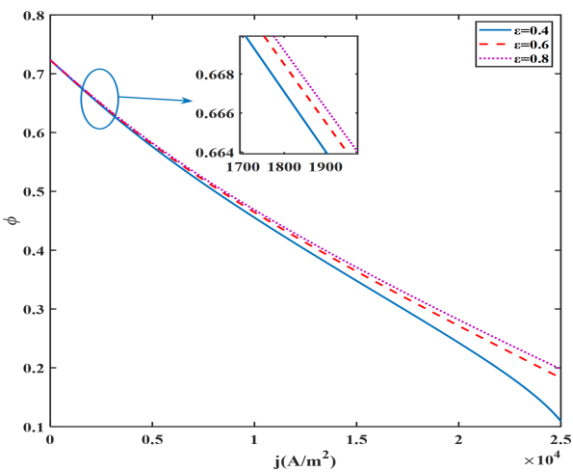Fig. 9. ϕ varying with current density at different porosity ε.

Fig. 10. *EPC* varying with current density at different porosity ε.

studied irreversible DA-SOFC are investigated. The main results of this work could be concluded as follows:

1) Increasing the operating temperature T, inlet pressure p, and fuel utilization rate U_f is beneficial for reducing waste heat generation of DA-SOFC, decreasing exergy loss and entropy production rate, and thereby improving performance indicators such as exergy efficiency and exergy performance coefficient of DA-SOFC. The increase in inlet pressure will consume additional external power, leading to a more complex system, increased cost and weight.

2) Reducing the electrolyte thickness (t_{ele}) can improve the thermodynamic performance of DA-SOFC. However, in practical work, a thinner electrolyte will make it difficult to effectively isolate the heat between the electrodes, which may lead to uneven temperature distribution and even thermal runaway, affecting the stack stability and lifespan. In the real design of DA-SOFC, a reasonable electrolyte thickness and electrode porosity need to be selected for DA-SOFC according to specific application scenarios.

3) The derived finite time thermodynamic model can be further employed to obtain optimal operating parameters and structural parameters under different application scenarios. These

optimization results can be used to guide engineering design and operation control.

Acknowledgements

References

[1] Sanaye, S., & Katebi, A. (2014). 4E analysis and multi objective optimization of a micro gas turbine and solid oxide fuel cell hybrid combined heat and power system. *Journal of Power Sources*, 247, 294–306. doi: 10.1016/j.jpowsour.2013.08.065

[2] Ma, Q., Peng, R., Tian, L., & Meng, G. (2006). Direct utilization of ammonia in intermediate-temperature solid oxide fuel cells. *Electrochemistry Communications*, 8(11), 1791–1795. doi: 10.1016/j.elecom.2006.08.012

[3] Ni, M., Leung, D.Y., & Leung, M.K. (2008). Mathematical modeling of ammonia-fed solid oxide fuel cells with different electrolytes. *International Journal of Hydrogen Energy*, 33(20), 5765–5772. doi: 10.1016/j.ijhydene.2008.07.021

[4] Fuerte, A., Valenzuela, R.X., Escudero, M.J., & Daza, L. (2009). Ammonia as efficient fuel for SOFC. *Journal of Power Sources*, 192(1), 170–174. doi: 10.1016/j.jpowsour.2008.11.037

[5] Baniasadi, E., & Dincer, I. (2011). Energy and exergy analyses of a combined ammonia-fed solid oxide fuel cell system for vehicular applications. *International Journal of Hydrogen Energy*, 36(17), 11128–11136. doi: 10.1016/j.ijhydene.2011.04.234

[6] Ahmadi, M.H., Ahmadi, M.-A., & Pourfayaz, F. (2017). Thermal models for analysis of performance of Stirling engine: A review. *Renewable and Sustainable Energy Reviews*, 68, 168−184. doi: 10.1016/j.rser.2016.09.033

[7] Andresen, B., & Salamon, P. (2022). Future Perspectives of Finite-Time Thermodynamics. *Entropy*, 24(5), 690. doi: 10.3390/e24050690

[8] Ghasemkhani, A., Farahat, S., & Naserian, M.M. (2018). Multi-objective optimization and decision making of endoreversible combined cycles with consideration of different heat exchangers by finite time thermodynamics. *Energy Conversion and Management*, 171, 1052–1062. doi: 10.1016/j.enconman.2018.06.046

[9] Dai, D., Liu, Z., Yuan, F., Long, R., & Liu, W. (2019). Finite time thermodynamic analysis of a solar duplex Stirling refrigerator. *Applied Thermal Engineering*, 156, 597–605. doi: 10.1016/j.applthermaleng.2019.04.098

[10] Li, Y., He, Y., & Wang, W. (2011). Optimization of solar-powered Stirling heat engine with finite-time thermodynamics. *Renewable Energy*, 36(1), 421–427. doi: 10.1016/j.renene.2010.06.037

[11] Tierney, M. (2020). Minimum exergy destruction from endoreversible and finite-time thermodynamics machines and their concomitant indirect energy. *Energy*, 197, 117184. doi: 10.1016/j.energy.2020.117184

[12] Li, C., Liu, Y., Xu, B., & Ma, Z. (2019). Finite Time Thermodynamic Optimization of an Irreversible Proton Exchange Membrane Fuel Cell for Vehicle Use. *Processes*, 7(7), 419. doi: 10.3390/pr7070419

[13] Li, D., Li, S., Ma, Z., Xu, B., Lu, Z., Li, Y, & Zheng, M. (2021). Ecological Performance Optimization of a High Temperature Proton Exchange Membrane Fuel Cell. *Mathematics*, 9(12), 1332. doi: 10.3390/math9121332

199

[14] Ge, Y., Chen, L., & Sun, F. (2016). Progress in Finite Time Thermodynamic Studies for Internal Combustion Engine Cycles. *Entropy*, 18(4), Article 139. doi: 10.3390/e18040139

[15] Chen, Y., Zhao, D., Xu, J., Wang, J., & Lund, P.D. (2021). Performance analysis and exergo-economic optimization of a solar-driven adjustable tri-generation system. *Energy Conversion and Management*, 233, 113873. doi: 10.1016/j.enconman.2021.113873

[16] Guo, X., Xu, B., Ma, Z., Li, Y., & Li, D. (2022). Performance Analysis Based on Sustainability Exergy Indicators of High-Temperature Proton Exchange Membrane Fuel Cell. *International Journal of Molecular Sciences*, 23(17), 10111. doi: 10.3390/ijms231710111

[17] Li, Y., Li, D., Ma, Z., Zheng, M., Lu, Z., Song, H., & Shao, W. (2022). Performance analysis and optimization of a novel vehicular power system based on HT-PEMFC integrated methanol steam reforming and ORC. *Energy*, 257, 124729 doi: 10.1016/j.energy.2022.124729

[18] Ramadhani, F., Hussain, M.A., Mokhlis, H., & Hajimolana, S. (2017). Optimization strategies for Solid Oxide Fuel Cell (SOFC) application: A literature survey. *Renewable and Sustainable Energy Reviews*, 76, 460–484. doi: 10.1016/j.rser.2017.03.052

[19] Hajabdollahi, Z., & Fu, P.-F. (2017). Multi-objective based configuration optimization of SOFC-GT cogeneration plant. *Applied Thermal Engineering*, 112, 549–559. doi: 10.1016/j.applthermaleng.2016.10.103

[20] Mert, S. O., Ozcelik, Z., Ozcelik, Y., & Dincer, I. (2011). Multi-objective optimization of a vehicular PEM fuel cell system. *Applied Thermal Engineering*, 31(13), 2171–2176. doi: 10.1016/j.applthermaleng.2011.04.031

[21] You, H., Han, J., Liu, Y., Chen, C., & Ge, Y. (2020). 4E analysis and multi-objective optimization of a micro poly-generation system based on SOFC/MGT/MED and organic steam ejector refrigerator. *Energy*, 206, 118122. doi: 10.1016/j.energy.2020.118122

[22] Forough, A.B., & Roshandel, R. (2013). Multi objective optimization of solid oxide fuel cell stacks considering parameter effects: Fuel utilization and hydrogen cost. *Journal of Renewable and Sustainable Energy*, 5(5), 053124. doi: 10.1063/1.4822253

[23] Mojaver, P., Chitsaz, A., Sadeghi, M., & Khalilarya, S. (2020). Comprehensive comparison of SOFCs with proton-conducting electrolyte and oxygen ion-conducting electrolyte: Thermoeconomic analysis and multi-objective optimization. *Energy Conversion and Management*, 205, 112455. doi: 10.1016/j.enconman.2019.112455

[24] Ishak, F., Dincer, I., & Zamfirescu, C. (2012). Energy and exergy analyses of direct ammonia solid oxide fuel cell integrated with gas turbine power cycle. *Journal of Power Sources*, 212, 73–85. doi: 10.1016/j.jpowsour.2012.03.083

[25] Beyrami, J., Chitsaz, A., Parham, K., & Arild, O. (2019). Optimum performance of a single effect desalination unit integrated with a SOFC system by multi-objective thermo-economic optimization based on genetic algorithm. *Energy*, 186, 115811. doi: 10.1016/j.energy.2019.07.141

[26] Wang, J., Cui, Z., Yao, W., & Huo, S. (2023). Regulation strategies and thermodynamic analysis of combined cooling, heating, and power system integrated with biomass gasification and solid oxide fuel cell. *Energy*, 266, 126430. doi: 10.1016/j.energy.2022.126430

[27] Song, H., Lu, Z., Ma, Z., Guo, X., & Guo, Q. (2024). Thermodynamic analysis of the performance of an irreversible ammonia-fed solid oxide fuel cell. *Archives of Thermodynamics*, 45(2), 279−290. doi: 10.24425/ather.2024.150872

[28] Maffei, N., Pelletier, L., Charland, J.P., & McFarlan, A. (2006). An ammonia fuel cell using a mixed ionic and electronic conducting electrolyte. *Journal of Power Sources*, 162(1), 165–167. doi: 10.1016/j.jpowsour.2006.06.056

ARCHIVES OF THERMODYNAMICS

Numerical study of radiative MHD hybrid nanofluid flow through porous concentric cylinders

Rudrappa Mahesha[a,b], Narasappa Nalinakshi[a], Thavada Sravan Kumar[a*]

[a]Department of Mathematics, Atria Institute of Technology, Bengaluru 560024, KA, India.
[b]Visvesvaraya Technological University, Belagavi 590018, KA, India.
*Corresponding author email: sravan.k@atria.edu

Abstract

The main objective of this study is to investigate the effects of Cu, Al$_2$O$_3$, and H$_2$O-based nanofluids on heat transfer through annulus-shaped, two concentric cylindrical regions. The quadratic convection in the flow of hybrid nanofluids in an inclined porous annulus medium is considered. The conservation laws are obeyed in a non-linear model of the flow geometry. Applying a suitable non-dimensional transformation, we solved the resultant equation using the Runge-Kutta 4th order method with a shooting technique to obtain the solution for the velocity and temperature. The flow structure and heat transfer are influenced by quadratic resistance and mixed convection mechanisms in nonlinear Boussinesq approximation, as investigated in biomedical devices, nuclear reactors as well as heat exchangers. The analysis demonstrates that radiation significantly affects heat transfer by enhancing the Lorentz force, which in turn dissipates the flow rate. This behaviour aligns well with the flow patterns reported in previous studies for various physical parameters.

Keywords: Magnetohydrodynamics; Irregular heat source; Hybrid nanofluids; Heat transfer; Concentric cylinder

1. Introduction

Many researchers have recently diverted their interest to nano-technology innovation as it offers a variety of opportunities for designing and manufacturing goods with advancements in heat transfer. Hybrid nanofluids flowing across an annular cylindrical region are used in nuclear power plants, hot rollers, heat exchangers and heat storage systems to transfer heat. The nanofluid has colloidal suspensions of nanoparticles in a base fluid. Choi and Eastman [1] reported on investigating nanofluids and heat characteristics.

The term 'hybrid' describes the combination of various unique nanoparticles that create a homogeneous phase. The metal and metal oxide nanoparticles such as Al, Cu, Fe, MgO, Al$_2$O$_3$, TiO$_2$ and SiO$_2$ are disseminated in oil, water, kerosene and ethylene glycol (base fluids). The wide range of applications of hybrid nanofluids has a revolutionary approach to heat transfer accepted among researchers. A conventional fluid that contains both metallic and non-metallic nanoparticles has enhanced thermophysical properties, which demonstrated that the hybrid nanofluids (Al$_2$O$_3$-Cu-H$_2$O) had a higher diffusivity than the mononanofluids described by Suresh et al. [2]. Devi and Devi [3] and Kanchana et al. [4] investigated stiff isothermal boundary conditions in heat transfer and show an improvement in the fraction factor for the suspension of two nanoparticles in water. Waini et al. [5] found that Cu-Al$_2$O$_3$ has a higher heat transfer

Mahesha R., Nalinakshi N., Sravan Kumar T.

Nomenclature

a – radius of the inner cylinder, m

b – radius of the outer cylinder, m

B_0 – magnetic field, T

Bi_1 – Biot number cylinder 1, $Bi_1 = \frac{h_1 a}{\kappa_f}$

Bi_2 – Biot number cylinder 2, $Bi_2 = \frac{h_2 a}{\kappa_f}$

Cp – specific heat at constant pressure, kJ/(kg K)

Da – Darcy number

Ec – Eckert number, $Ec = \frac{U_w^2}{(c_p)_f (T_w - T_\infty)}$

g –gravitational acceleration, m/s^2

h_1, h_2– convective heat transport coefficients, W/(m^2·K)

M – magnetic parameter, $M = \sqrt{\frac{\sigma \beta_0^2 a^2}{\mu_f}}$

Mc – mixed convection parameter, $Mc = \frac{g(\rho \beta_0)_f (T_w - T_0) a^2}{u_0 \mu_f}$

m – shape factor of different nanoparticles

N – radiation parameter, $N = \frac{4\sigma T_\infty^3}{\chi \kappa_f}$

Nu – Nusselt number

n – exponential index

Pr –Prandtl number, $Pr = \frac{(\mu c_p)_f}{\kappa_f}$

p – pressure, kPa

Q_0 – THS coefficient

Q_e – ESHS coefficient

Qc – quadratic convection parameter, $Qc = \frac{(\rho \beta_1)_f (T_w - T_0)}{(\rho \beta_0)_f}$

Q_E – exponential space-related heat source parameter, $Q_E = \frac{Q_e a^2}{\nu_f (\rho c_p)_f}$

Q_T – temperature related heat source parameter, $Q_T = \frac{Q_0 a^2}{\nu_f (\rho c_p)_f}$

R – dimensionless radial axis

r – radial axis

T – temperature, K

U – nondimensional velocity, m/s

u – dimensional velocity, m/s

z – common axis

Greek symbols

α – angle of inclination, rad

β – thermal expansion coefficient, K^{-1}

θ – nondimensional temperature, K

κ – thermal conductivity, W/(m·K)

λ – aspect ratio,

μ – dynamic viscosity, Pa·s

ν – kinematic viscosity, m^2/s

σ – Stefan Boltzmann constant, W/(m^2 K^4)

ρ – density, kg/m^3

τ – skin friction coefficient

ϕ – volume fraction

Subscripts and Superscripts

hnf – hybrid nanofluids

nf – nanofluids

f – fluids

Abbreviations and Acronyms

LBA – linear Boussinesq approximation

NBA – non-linear Boussinesq approximation

THS – temperature dependent heat source parameter

ESHS– exponential space-related heat source parameter

MHD– magnetohydrodynamics

rate than Cu with H$_2$O as a base fluid.

The annular cylindrical region geometry for heat transfer is very essential in industrial applications such as turbomachines, engineering, heating, chemical industries, solar collectors and heat exchangers. Shahzadi and Nadeem [6] investigated the heat transfer in an inclined annular duct filled with nanofluids and observed that silver nanoparticles can enhance more pressure gradients than pure blood. Mixed convective flow in a vertical, concentric cylinder exposed to the heat source, thermal radiation in the presence of porous matrix was observed by Oni [7]. Mebarek-Oudina et al. [8] investigated the heat source aspect ratio increment in the fluid temperature over an annular-spaced vertical cylinder. Mebarek-Oudina et al. [9] has investigated natural oscillatory convective flow in a circular inclined annulus area filled with molten metal, obtaining the best stabilization for the system tilted at a 30º angle.

The linear Boussinesq approximation (LBA) truncates the density variation expansion of the Taylor series with temperature after the second term, assuming a linear density variation with temperature, and this LBA holds good only when the temperature difference is slightly varied. The mathematical model created using LBA becomes erroneous in other circumstances. The nonlinear Boussinesq approximation (NBA) with temperature as a result $\Delta \rho = -\rho \beta (T - T_w)^2$ was identified by Goren [10] in 1996. In the investigation of free convection in the presence of buoyancy force between two plates, by considering the non-

linear quadratic fluctuations in density with temperature, an increase in heat transfer is noticed by Vajravelu and Sastri [11]. The term $\Delta \rho / \rho$ is a nonlinear Boussinesq approximation using the Taylor series expansion. The mixed convective flow over vertical wavy-shaped surface in the presence of porous medium with nanofluid, using nonlinear Boussinesq approximation was inspected by Kameshwaran et al. [12].

The magnetohydrodynamics (MHD) is interaction of electrically conducting fluids in the influence of magnetic field, plays a major role in industrial applications of heat transfer analysis such as aircraft, designs of the fins, cooling of reactors, in geophysics and astrophysicists. Numerous studies have been conducted on MHD flow over the years. Sravan Kumar [13] investigated hybrid nanofluids as copper-ferrous oxide nanoparticles with ethylene glycol as base fluid and noticed that the heat flow rate of copper-ferrous oxide is reduced compared to copper with ethylene glycol as base fluid. Aladdin et al. [14] analysed the rate of heat transfer which is diminished in copper-aluminium oxide as compared to copper with water base fluids in MHD free convection flow over a plate. The experimental observation of forced convection over concentric tubes of heat exchangers of Cu-Al$_2$O$_3$ nanoparticles as high thermal conductivity is analysed by Phanindra et al. [15]. Sheikholeslami et al. [16] examined the transient natural convection flow along a moving vertical plate in nanofluids with isothermal and isoflux boundary conditions. Sheikholeslami and Ganji [17] studied the heat and mass trans-

fer in the influence of thermal radiation between two parallel plates of unsteady flow and discovered that an increment in radiation effect increases the boundary layer thickness of concentration. Suresh et al. [18] studied that heat transfer of copper-aluminium oxide/H_2O hybrid nanofluid with variation of pressure over a uniformly heated circular tube is increased when compared with pure water.

The study of viscous dissipation effects in the usteady nanofluid flow over an exponentially moving vertical plate with Lorentz force, analysed by Sravan Kumar et al. [19], resulted in the enhancement of fluid velocity in the boundary layer. The comparative study of the dissipative and radiative flow of hybrid nanofluid between two coaxial cylinders studied by Hayat et al. [20] focuses on the viscous dissipation effects of hybrid nanofluids which are dominant when compared with nanofluids.

The novelty of the present work is nonlinear Boussinesq approximation which is $\Delta\rho/\rho = -[(T-T_0)\beta_0 + (T-T_0)^2\beta_1]$, an analysis including the MHD, radiation effects, and viscous dissipation effects of the hybrid nanofluid in a heated inclined porous concentric cylindrical region. The complicated non-dimensional set of nonlinear coupled equations is solved by a numerical method, using the 4th order RK method with a shooting technique to obtain solutions for the velocity and temperature. The outcomes are presented graphically and analysed in detail. The physical model focuses on industrial applications such as electronic cooling systems, environmental monitoring systems and medicine.

2. Mathematical formulation

The mixed convection of Cu-Al_2O_3-H_2O hybrid nanofluid of NBA approximation in an inclined two concentric cylinders is schematically depicted in Fig. 1.
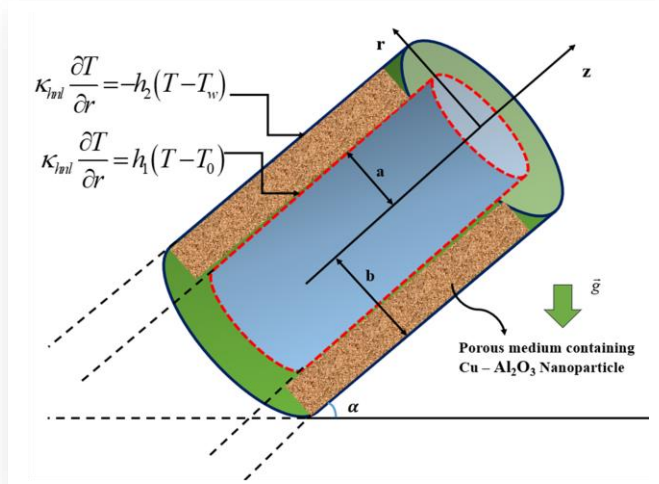

Fig. 1. Schematic representation of flow geometry.

The convective boundary conditions at the inner and outer cylinder respectively are $\kappa_{hnf}\frac{\partial T}{\partial r} = h_1(T-T_0)$ and $\kappa_{hnf}\frac{\partial T}{\partial r} = -h_2(T-T_w)$. The cylindrical coordinate system with the r-axis in the radial direction and the z-axis as the common axis is con-

sidered. The inner cylinder radius is $a \leq r \leq b$. The annulus with an unlimited length, and the fluid flow that is independent of z, is represented in the model given below (see Shahzadi and Nadeem [6], Oni [7]):

- Conservation of mass

$$\frac{1}{r}\left(\frac{\partial}{\partial r}(ru)\right) = 0, \tag{1}$$

- Conservation of momentum

$$\frac{\mu_{hnf}}{\rho_{hnf}}\frac{1}{2}\frac{\partial}{\partial r}\left(r\frac{\partial u}{\partial r}\right) - \frac{u\mu_{hnf}}{K\rho_{hnf}} - \frac{1}{\rho_{hnf}}\frac{\partial p}{\partial z} - \frac{1}{\rho_{hnf}}\sigma B_0^2 +$$

$$+\frac{g}{\rho_{hnf}}\left[(\rho\beta_0)_{hnf}(T-T_0) + (\rho\beta_1)_{hnf}(T-T_0)^2\right]\cos\alpha = 0, \tag{2}$$

- Conservation of energy

$$\frac{\kappa_{hnf}}{(\rho c_p)_{hnf}}\left[\frac{1}{r}\frac{\partial}{\partial r}\left(r\frac{\partial T}{\partial r}\right)\right] + \frac{1}{(\rho c_p)_{hnf}}\frac{\partial q_r}{\partial r} +$$

$$+\frac{Q_0}{(\rho c_p)_{hnf}}(T-T_0) + \frac{(T_w-T_0)}{(\rho c_p)_{hnf}}Q_e\,exp\left(\frac{-nr}{a}\right) + \tag{3}$$

$$+\left(\frac{\partial u}{\partial r}\right)^2\frac{\mu_{hnf}}{(\rho c_p)_{hnf}} = 0,$$

with the boundary conditions of dimensional form as given by Srinivasacharya et al. [21]:

at $r = a$: $\qquad u' = 0, \qquad \kappa_{hnf}\frac{\partial T}{\partial r} = h_1(T-T_0),$

$$\tag{4}$$

at $r = b$: $\qquad u' = 0, \qquad \kappa_{hnf}\frac{\partial T}{\partial r} = -h_2(T-T_w).$

The volume fraction, thermal expansion coefficients, density, specific heat, dynamic viscosity, and thermal conductivity of hybrid nanofluid are given by (see [3,4,22−24]):

$$\phi = \phi_{Cu} + \phi_{Al_2O_3}, \tag{5}$$

$$(\rho\beta_0)_{hnf} = ((1-\phi) + \phi_{Cu}\frac{(\rho\beta_0)_{Cu}}{(\rho\beta_0)_f} +$$

$$\phi_{Al_2O_3}\frac{(\rho\beta_0)_{Al_2O_3}}{(\rho\beta_0)_f})(\rho\beta_0)_f, \tag{6}$$

$$(\rho\beta_1)_{hnf} = ((1-\phi) + \phi_{Cu}\frac{(\rho\beta_1)_{Cu}}{(\rho\beta_1)_f} +$$

$$\phi_{Al_2O_3}\frac{(\rho\beta_1)_{Al_2O_3}}{(\rho\beta_1)_f})(\rho\beta_1)_f, \tag{7}$$

$$\rho_{hnf} = \left((1-\phi) + \phi_{Cu}\frac{\rho_{Cu}}{\rho_f} + \phi_{Al_2O_3}\frac{\rho_{Al_2O_3}}{\rho_f}\right)\rho_f, \tag{8}$$

$$(\rho C_p)_{hnf} = ((1-\phi) + \phi_{Cu}\frac{(\rho c_p)_{Cu}}{(\rho c_p)_f} +$$

$$+\phi_{Al_2O_3}\frac{(\rho c_p)_{Al_2O_3}}{(\rho c_p)_f})(\rho C_p)_f, \tag{9}$$

$$\mu_{hnf} = \frac{1}{(1-\phi)^{2.5}}\mu_{nf}, \tag{10}$$

$$\frac{\kappa_{hnf}}{\kappa_f} = \tag{11}$$

$$= \frac{\left(\frac{(\phi\kappa)_{Cu}+(\phi\kappa)_{Al_2O_3}}{\phi}\right)+(m-1)\kappa_f+(m-1)\left((\phi\kappa)_{Cu}+(\phi\kappa)_{Al_2O_3}\right)-(m-1)\kappa_f\phi}{\left(\frac{(\phi\kappa)_{Cu}+(\phi\kappa)_{Al_2O_3}}{\phi}\right)+(m-1)\kappa_f+\left((\phi\kappa)_{Cu}+(\phi\kappa)_{Al_2O_3}\right)-\kappa_f\phi}.$$

The non-dimensional quantities are given by (see [7]):

$$\left.\begin{array}{ll} U = \frac{u}{u_0}, & P = \frac{pa}{u_0\nu_l} \\[2mm] \theta = \frac{T-T_0}{T_w-T_0}, & R = \frac{r}{a}, \quad Z = \frac{z}{a} \end{array}\right\}. \tag{12}$$

The values of thermophysical properties of hybrid nanofluids are tabulated in Table 1.

Table 1. H_2O, Cu and Al_2O_3 hybrid nanofluids thermophysical properties at 300 K.

Properties	Cu	Al₂O₃	H₂O	Different shape of nanoparticle	m
ρ, kg·m⁻³	8933	3970	997.1		3
κ, W·m⁻¹·K⁻¹	401	40	0.613		5.7
$\beta \cdot 10^{-5}$, K⁻¹	1.67	0.85	21		4.8
μ, kg·m⁻¹·s⁻¹	-	-	0.00089		3.7

Further, the dimensionless quantities describing thermophysical properties are denoted by:

$$A_1 = \frac{1}{(1-\phi)^{2.5}},$$

$$A_2 = (1-\phi) + \phi_{Cu}\frac{(\rho\beta_0)_{Cu}}{(\rho\beta_0)_f} + \phi_{Al_2O_3}\frac{(\rho\beta_0)_{Al_2O_3}}{(\rho\beta_0)_f},$$

$$A_3 = (1-\phi) + \phi_{Cu}\frac{\rho_{Cu}}{\rho_f} + \phi_{Al_2O_3}\frac{\rho_{Al_2O_3}}{\rho_f},$$

$$A_4 = \frac{\left(\frac{(\phi\kappa)_{Cu}+(\phi\kappa)_{Al_2O_3}}{\phi}\right)+(m-1)\kappa_f+(m-1)\left((\phi\kappa)_{Cu}+(\phi\kappa)_{Al_2O_3}\right)-(m-1)\kappa_f\phi}{\left(\frac{(\phi\kappa)_{Cu}+(\phi\kappa)_{Al_2O_3}}{\phi}\right)+(m-1)\kappa_f+\left((\phi\kappa)_{Cu}+(\phi\kappa)_{Al_2O_3}\right)-\kappa_f\phi}.$$

Using non-dimensional quantities given by Eqs. (12) and thermophysical properties represented by Eqs. (5)−(11), Eqs. (1)−(4) are transformed to the following forms:

$$A_1\left(\frac{d^2U}{dR^2}+\frac{1}{R}\frac{dU}{dR}\right)+Mc(A_2\theta+A_3Qc\theta^2)\cos(\alpha)+$$
$$-\frac{A_1}{Da}U-p-M^2U = 0, \tag{13}$$

$$\frac{A_4}{Pr}\left(\frac{d^2\theta}{dR^2}+\frac{1}{R}\frac{d\theta}{dR}\right)+Q_T\theta+Q_E\exp(-nR)+$$
$$-\frac{N}{Pr}\frac{d^2\theta}{dR^2}+A_1Ec\left(\frac{dU}{dR}\right)^2 = 0, \tag{14}$$

at $R = 1$: $\quad U = 0, \quad \frac{d\theta}{dR} = \frac{Bi_1}{A_4}\theta,$

at $R = \lambda$: $\quad U = 0, \quad \frac{d\theta}{dR} = \frac{Bi_2}{A_4}(1-\theta).$ $\tag{15}$

The physical quantities like non-dimensional Nusselt numbers (Nu_1 and Nu_λ) and skin friction coefficients (τ_1 and τ_λ) are defined as [25]:

at $R = 1$: $\quad Nu_1 = \frac{\kappa_{hnl}}{\kappa_l}\left(\frac{d\theta}{dR}\right)_{R=1}, \quad \tau_1 = \frac{\mu_{hnl}}{\mu_l}\left(\frac{dU}{dR}\right)_{R=1}.$

at $R = \lambda$: $Nu_\lambda = \left(\frac{\kappa_{hnl}}{\kappa_l}+N\right)\left(\frac{d\theta}{dR}\right)_{R=\lambda}, \quad \tau_\lambda = \left(\frac{\mu_{hnl}}{\mu_l}+N\right)\left(\frac{dU}{dR}\right)_{R=\lambda}$ $\tag{16}$

3. Numerical method

The non-dimensional Eqs. (13)–(14) with the dimensionless boundary condition Eq. (15) are numerically solved using the 4th order RK shooting technique method [24]. By using $[U, U', \theta, \theta'] = [y_1, y_2, y_3, y_4]$, the system of equations can be written in the first-order differential equations as follows:

$$y_1'=y_2$$
$$y_2'=\frac{-1}{A_1}\left(Mc(A_2y_3+A_3Qcy_3^2)\cos\alpha-\frac{A_1y_1}{Da}-p-M^2y_1\right)-\frac{y_2}{R}, \tag{17}$$
$$y_3'=y_4$$
$$y_4'=\frac{-Pr}{A_4}\left(Q_Ty_3+Q_E\exp(-nR)-\frac{Ny_3}{Pr}+A_1Ecy_1^2\right)-\frac{y_4}{R}$$

with boundary conditions:

at $R = 1$: $\quad y_1 = 0, \quad y_4 = \frac{Bi_1}{A_4}y_3,$

at $R = \lambda$: $\quad y_1 = 0, \quad y_4 = \frac{Bi_2}{A_4}(1-y_3).$ $\tag{18}$

and corresponding initial conditions:

$$y_1(1) = 0, \quad y_2(1) = t_1,$$
$$y_3(1) = t_2, \quad y_4(1) = \frac{Bi_1}{A_4}t_2, \tag{19}$$

where t_1 and t_2 are the initial values. The initial conditions are approximated to satisfy the boundary conditions. Table 2 gives the information of Q_T for Nusselt number at $r=1$.

4. Results and discussion

The analysis of heat transfer between two concentric cylinders in an annulus is presented through graphs and tables. Figures 2−15 show various effects such as those of MHD (M), radiation (N), viscous dissipation (Ec), volume fraction (ϕ), etc. on velocity $U(R)$ and temperature $\theta(R)$. The data on graphs and in tables are obtained for the fixed effective parameters, such as $Mc = 2$, $Qc = 0.5$, $\alpha = \pi/4$, Da $= 0.1$, $Q_T = 0.01$, $Q_E = 0.1$, Pr $= 6.0674$, $Bi_1 = Bi_2 = 0.3$, $M = 0.5$, Ec $= 0.1$, $N = 1$ and $\phi = 0.01$ [25].

In the performance of magnetic field, Fig. 2 displays the velocity profiles for different magnetic parameter (M^2) values. As M^2 increases, the fluid velocity decreases. This is due to the Lorentz force, a resistive force generated by the interaction of the transverse magnetic field with in the convective fluid. This force opposes the flow, reducing the fluid velocity and leading to a thin momentum boundary layer. MHD is used in medicinal field to study plasma of human body in biological and environmental monitoring systems. The effect of viscous dissipation in

temperature graph observed in Fig. 3 shows that the thickness of thermal boundary increases with increasing Ec, which is due to the conversion of mechanical energy into thermal energy. This results in additional heating of the fluid, leading to a rise in temperature within the boundary layer and an enhancement of heat transfer.

In Figs. 4−5, we observe that the radiation effect (N) decreases the velocity for different values of N due to the temperature difference and boundary layer thickness. In the temperature plot, as temperature increases for different values of N due to its increased thermal conductivity, addition of nanoparticles may lead to influencing radiative heat transfer between the cylinders. Hybrid nanofluids can be used as a coolant in electronic devices such as computers, televisions and smartphones, so as to prevent overheating and improve dissipation of heat.
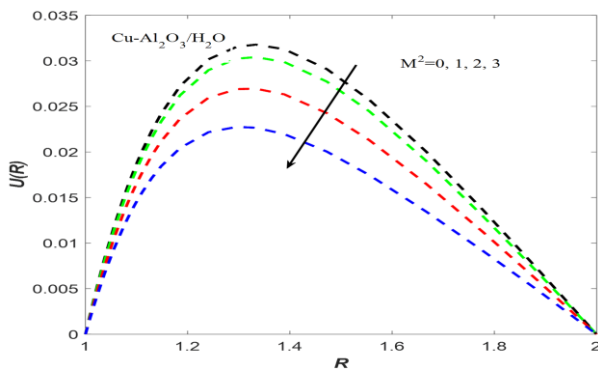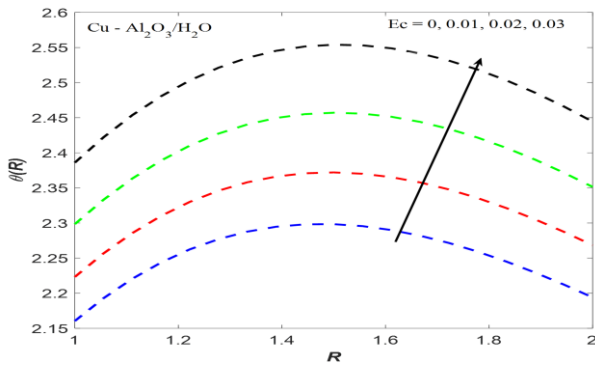

Fig. 2. Velocity for different values of M^2.

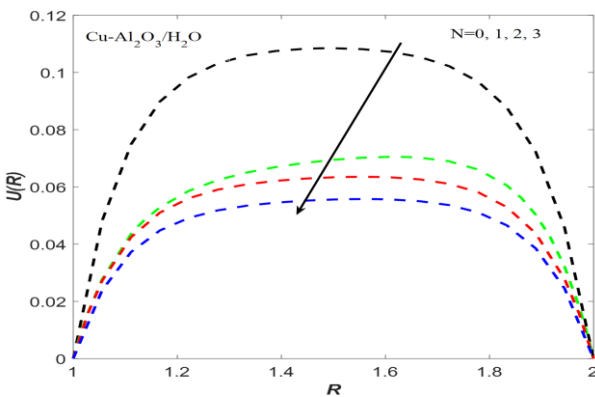Fig. 3. Temperature for different values of Ec.
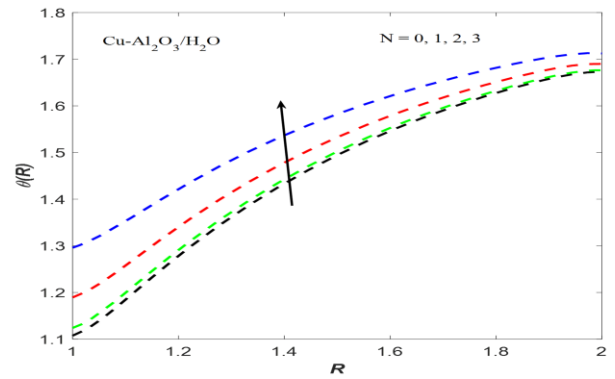

Fig. 4. Velocity for different values of N.

Fig. 5. Temperature for different values of N.

The concentration of nanoparticles refers to volume fraction (ϕ) and from Figs. 6 and 7 we noticed that the volume fraction in velocity profile decreases, as nanoparticle concentration increases. Due to the suspension of nanoparticles in the base fluids, density is increased, leading to a decrement in velocity profiles of the fluid in a porous cylinder. Whereas, in the temperature profile, the energy increases as the volume fraction increases. This is due to the good thermal conductivity of the nanofluid and larger surface area of nanoparticles, which enable more efficient heat transfer.

In Figs. 8 and 9, we observe the combined effect of exponentially related heat source parameter (ESHS) (Q_E) on $U(R)$ and $\theta(R)$, showing an increment in Q_E leading to more effective heat transfer in increased velocity. The temperature profile for varied Q_E is increased, because the ESHS mechanism gives an additional heat source to the system. It can be seen that the velocity increases for platelet-shaped nanoparticles when compared to cylinder, brick, and spherical-shaped nanoparticles, as shown in Fig. 10. The temperature profiles fluctuate, as seen in Fig. 11, with the platelet-shaped nanoparticles having a high temperature at the inner cylinder and a lower profile at the outer cylinder when compared to the cylinder, brick, and spherical-shaped nanoparticles.

In Fig. 12, we observe that as quadratic convection Qc increases, the momentum profile also increases because of its strong buoyancy force. Further, a higher momentum is observed in the quadratic convection than in LBA. The behaviour of the velocity graphs for the various values is plotted in Fig. 13, and it is observed that permeability for the lower value of Da gives an increment in the momentum of the porous region compared to the clear region Da = 0. From Fig. 14 we can visualize the effect of mixed convection (Mc) on the velocity, which increases with Mc due to the domination of buoyancy force to the inertial force. This results in an effective improvement of heat transfer. As the angle of inclination α increases , the velocity decreases due to the least domination of acceleration by gravity, as shown in Fig. 15.

By comparing results of Thriveni and Mahantesh [25] (see Table 2) we noticed that the present study outcomes are in good agreement as regards Q_T values of the Nusselt number at the lower wall. Table 3 illustrates the significance of skin friction for different effects such as M^2, Mc, Qc, and Da, showing an increasing trend of the velocity at the surface. Though the angle
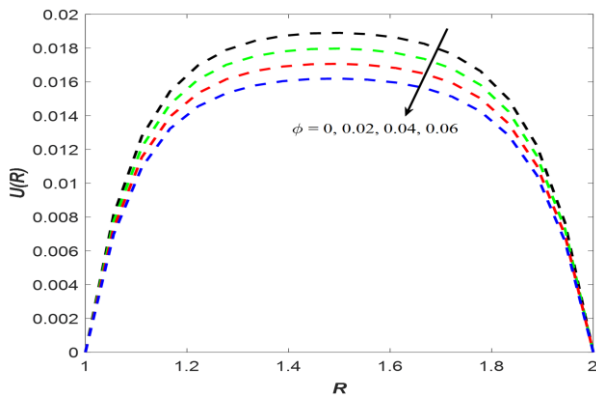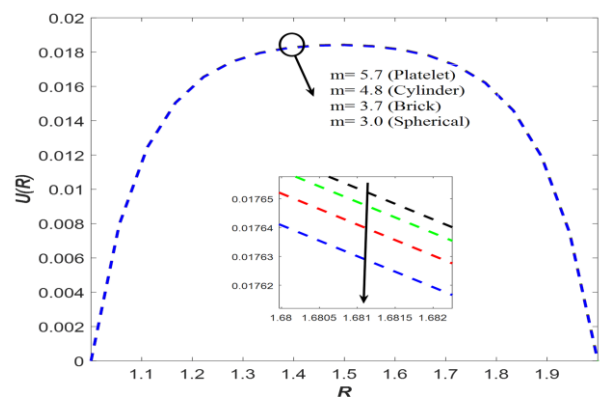
Fig. 6. Velocity for different values of ø.

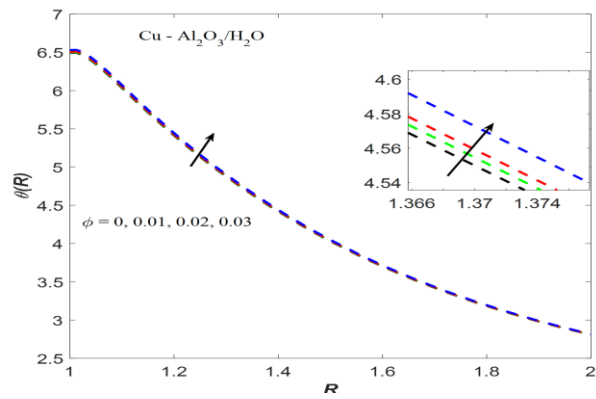Fig. 10. Velocity for different values of m.

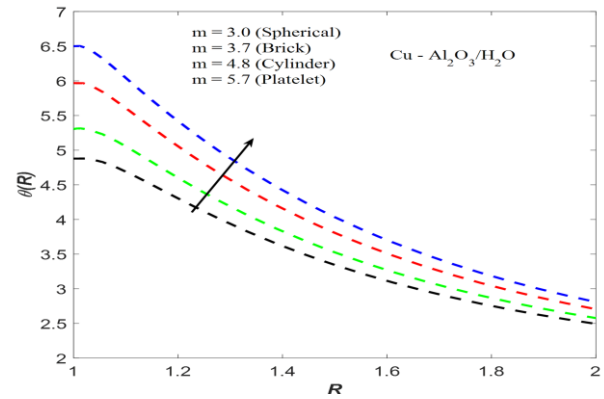Fig. 7. Temperature for different values of ø.

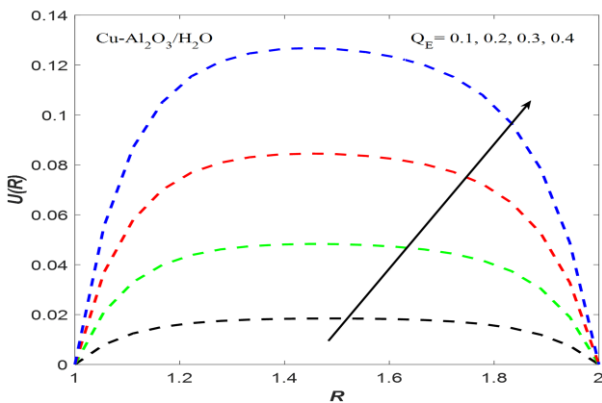Fig. 11. Temperature for different values of m.

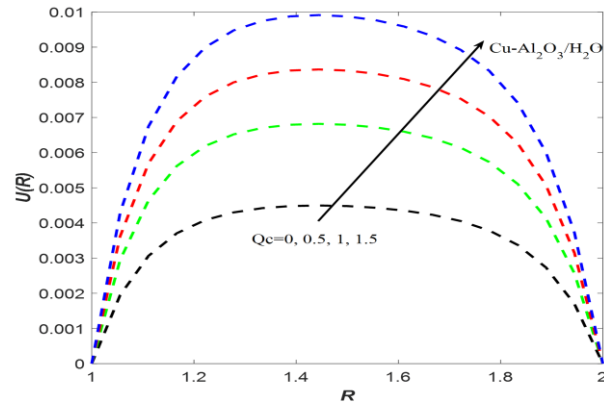Fig. 8. Velocity for different values of Q_E.

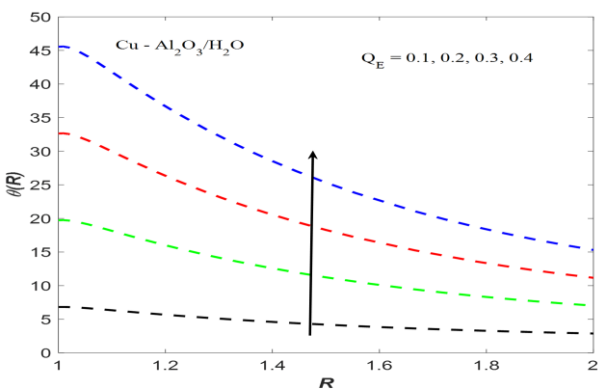
Fig. 12. Velocity for different values of Q_c.
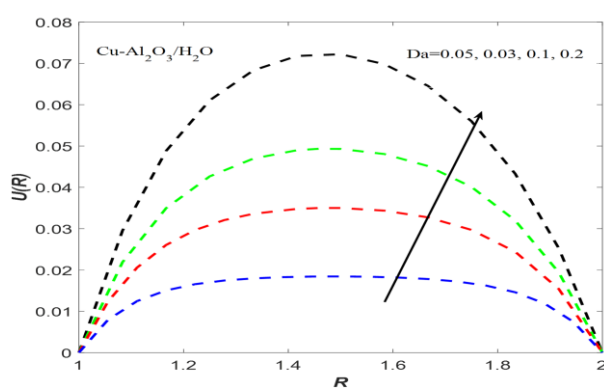

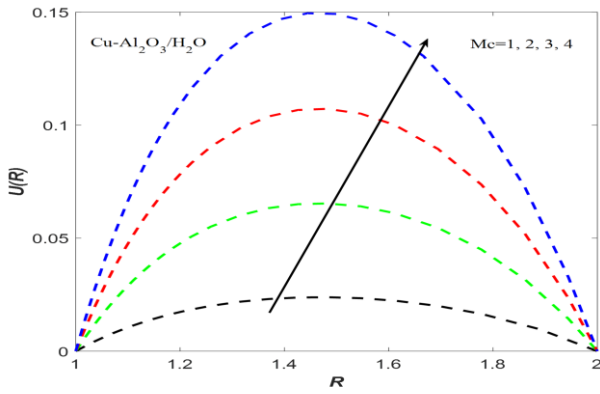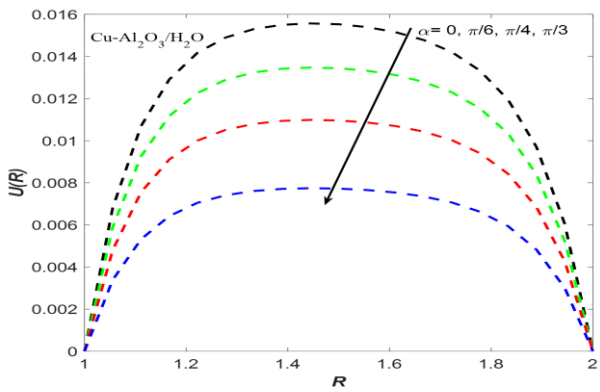Fig. 9. Temperature for different values of Q_E.

Fig. 13. Velocity for different values of Da.

206

Fig. 14. Velocity for different values of *Mc*.

Fig. 15. Velocity for different values of *α*.

Table 2. The Nusselt number for different values of Q_T at *r* =1.

Q_T	Thriveni and Mahanthesh [25]	Present work
0.5	1.571404	1.571405
1.0	1.716981	1.716982
1.5	1.882604	1.882605
2.0	2.072277	2.072278
2.5	2.291116	2.291117
3.0	2.545765	2.545766

Table 3. Numerical values of τ_1 and τ_λ for various values of M^2, *Mc*, *Qc*, Da and α when Pr = 6.0674, Q_T = 0.01, Q_E = 0.1, Bi_1 = Bi_2 = 0.03 and ϕ = 2%.

M^2	Mc	Qc	Da	α	τ_1	τ_λ
1	2	0.5	0.1	$\pi/4$	0.451468	0.484422
2					0.562719	0.594243
3					0.662388	0.683438
	2				0.481467	0.434245
	2.5				0.601915	0.542874
	3				0.722363	0.651503
		0.1			0.374082	0.333169
		0.2			0.400928	0.358438
		0.3			0.427774	0.383707
			0.05		0.351276	0.332389
			0.07		0.412666	0.381011
			0.09		0.460956	0.418489
				$\pi/6$	0.589747	0.531900
				$\pi/4$	0.481467	0.434245
				$\pi/3$	0.340353	0.306978

gets smaller, there is an increase in velocity at the lower wall of the cylinder.

5. Conclusions

The hybrid nanofluid flow in a convectively heated system of two concentric cylinders containing porous medium with the effects of MHD, thermal radiation, viscous dissipation, as well as exponential space-related heat source parameter and temperature-dependent heat source parameter was considered. The nonlinear and coupled equations were numerically solved using the shooting 4th order RK method. The analysis of MHD, thermal radiation, viscous dissipation, volume fraction, and Darcy number are discussed graphically. The findings of this study are as follows:

1. The strong magnetic effect (M^2) enhances effective heat transfer by the influence of Lorentz forces, which results in reduction of the boundary layer thickness.
2. The effect of viscous dissipation (Ec) on the temperature profiles is strong due to conversion of mechanical energy into thermal energy, and leads to an overall increase in heat transfer.
3. The thermal radiation effect (*N*) increases the heat flow rate, and enhances the potential of overall thermal performance.
4. The rate of heat transfer of hybrid nanofluids is higher when compared to pure nanofluids.

References

[1] Choi, S.U.S., & Eastman, J. (1995). Enhancing thermal conductivity of fluids with nanoparticles. *Developments and Applications of Non-Newtonian Flows*, 66, 99–105.

[2] Suresh, S., Venkitaraj, K.P., Selvakumar, P., & Chandrasekar, M. (2012). Effect of Al₂O₃–Cu/water hybrid nanofluid in heat transfer. *Experimental Thermal and Fluid Science*, 38, 54–60. doi: 10.1016/j.expthermflusci.2011.11.007

[3] Devi, S.S.U., & Devi, S.P.A. (2016). Numerical investigation of three-dimensional hybrid Cu–Al₂O₃/water nanofluid flow over a stretching sheet with effecting Lorentz force subject to Newtonian heating. *Canadian Journal of Physics*, 94(5), 490–496. doi: 10.1139/cjp-2015-0799

[4] Kanchana, C., Siddheshwar, P.G.S., & Zhao, Y. (2019). A study of Rayleigh–Bénard convection in hybrid nanoliquids with physically realistic boundaries. *The European Physical Journal Special Topics*, 228(12), 2511–2530. doi: 10.1140/epjst/e2019-900074-1

[5] Waini, I., Ishak, A., Groşan, T., & Pop, I. (2020). Mixed convection of a hybrid nanofluid flow along a vertical surface embedded in a porous medium. *International Communications in Heat and Mass Transfer*, 114, 104565. doi: 10.1016/j.icheatmasstransfer.2020.104565

[6] Shahzadi, I., & Nadeem, S. (2017). Inclined magnetic field analysis for metallic nanoparticles submerged in blood with convective boundary condition. *Journal of Molecular Liquids*, 230, 61–73. doi: 10.1016/j.molliq.2017.01.008

[7] Oni, M.O. (2017). Combined effect of heat source, porosity and thermal radiation on mixed convection flow in a vertical annulus: An exact solution. *Engineering Science and Technology, an International Journal*, 20(2), 518–527. doi: 10.1016/j.jestch.2016.12.009

[8] Mebarek-Oudina, F., Aissa, A., Mahanthesh, B., & Öztop, H.F. (2020). Heat transport of magnetized Newtonian nanoliquids in an annular space between porous vertical cylinders with discrete heat source. *International Communications in Heat and Mass Transfer*, 117, 104737. doi: 10.1016/j.icheatmasstransfer.2020. 104737

[9] Mebarek-Oudina, F., Bessaih, R., Mahanthesh, B., Chamkha, A.J., & Raza, J. (2020). Magneto-thermal-convection stability in an inclined cylindrical annulus filled with a molten metal. *International Journal of Numerical Methods for Heat & Fluid Flow*, 31(4), 1172–1189. doi: 10.1108/hff-05-2020-0321

[10] Goren, S.L. (1996). On free convection in water at 4°C. *Chemical Engineering Science*, 21(6–7), 515–518. doi: 10.1016/0009-2509 (66)85065-0

[11] Vajravelu, K., & Sastri, K.S. (1977). Fully developed laminar free convection flow between two parallel vertical walls. *International Journal of Heat and Mass Transfer*, 20(6), 655–660. doi: 10.1016/0017-9310(77)90052-7

[12] Kameswaran, P.K., Vasu, B., Murthy, P.V.S.N., & Gorla, R.S.R. (2016). Mixed convection from a wavy surface embedded in a thermally stratified nanofluid saturated porous medium with non-linear Boussinesq approximation. *International Communications in Heat and Mass Transfer*, 77, 78–86. doi: 10.1016/ j.icheatmasstransfer.2016.07.006

[13] Kumar, T.S. (2021). Hybrid nanofluid slip flow and heat transfer over a stretching surface. *Partial Differential Equations in Applied Mathematics*, 4, 100070. doi: 10.1016/j.padiff.2021.100070

[14] Aladdin, N.A.L., Bachok, N., & Pop, I. (2020). Cu-Al₂O₃/water hybrid nanofluid flow over a permeable moving surface in presence of hydromagnetic and suction effects. *Alexandria Engineering Journal*, 59(2), 657–666. doi: 10.1016/j.aej.2020.01.028

[15] Phanindra, Y., Kumar, S.D., & Pugazhendhi, S. (2018). Experimental Investigation on Al2O3 & Cu/Oil Hybrid Nanofluid using Concentric Tube Heat Exchanger. *Materials Today: Proceedings*, 5(5), 12142–12150. doi: 10.1016/j.matpr.2018.02.192

[16] Sheikholeslami, M., Bandpy, M.G., Ellahi, R., & Zeeshan, A. (2014). Simulation of MHD CuO–water nanofluid flow and convective heat transfer considering Lorentz forces. *Journal of Magnetism and Magnetic Materials*, 369, 69–80. doi: 10.1016/ j.jmmm.2014.06.017

[17] Sheikholeslami, M., & Ganji, D.D. (2014). Unsteady nanofluid flow and heat transfer in presence of magnetic field considering thermal radiation. *Journal of the Brazilian Society of Mechanical Sciences and Engineering*, 37(3), 895–902. doi: 10.1007/s40430-014-0228-x

[18] Suresh, S., Venkitaraj, K.P., Hameed, M.S., & Sarangan, J. (2014). Turbulent Heat Transfer and Pressure Drop Characteristics of Dilute Water Based Al2O3–Cu Hybrid Nanofluids. *Journal of Nanoscience and Nanotechnology*, 14(3), 2563–2572. doi: 10.1166/jnn.2014.8467

[19] Sravan Kumar, T., Dinesh, P.A., & Makinde, O.D. (2020). Impact of Lorentz Force and Viscous Dissipation on Unsteady Nanofluid Convection Flow over an Exponentially Moving Vertical Plate. *Mathematical Models and Computer Simulations*, 12(4), 631–646. doi:10.1134/s2070048220040110

[20] Hayat, T., Yazman, M., Muhammad, K., & Momani, S. (2023). Radiative and dissipative flow of hybrid nanofluid between two coaxial cylinders: A comparative numerical study. *Alexandria Engineering Journal*, 71, 79–88. doi: 10.1016/j.aej.2023.03.030

[21] Srinivasacharya D., & Hima Bindu, K. (2018). Entropy generation due to micropolar fluid flow between concentric cylinders with slip and convective boundary conditions. *Ain Shams Engineering Journal*, 9(2), 245–255. doi: 10.1016/j.asej.2015.10.016

[22] Thriveni K., & Mahanthesh, B. (2020). Nonlinear Boussinesq buoyancy driven flow and radiative heat transport of magnetohybrid nanoliquid in an annulus: A statistical framework. *Heat Transfer*, 49(8), 4759–4782. doi: 10.1002/htj.21851

[23] Lakshmi, K.M., Siddheshwar, P.G., & Laroze, D. (2020). Natural convection of water-copper nanoliquids confined in low-porosity cylindrical annuli. *Chinese Journal of Physics*, 68, 121–136. doi: 10.1016/j.cjph.2020.09.008

[24] Kierzenka, J., & Shampine, L.F. (2001). A BVP solver based on residual control and the Maltab PSE. *ACM Transactions on Mathematical Software*, 27(3), 299–316. doi: 10.1145/502800. 502801

[25] Thriveni, K., & Mahanthesh, B. (2021). Sensitivity computation of nonlinear convective heat transfer in hybrid nanomaterial between two concentric cylinders with irregular heat sources. *International Communications in Heat and Mass Transfer*, 129, 105677. doi: 10.1016/j.icheatmasstransfer.2021.105677